



**Universitat**  
de les Illes Balears

**DOCTORAL THESIS**

**2019**

**DEVELOPMENT OF SQUARAMIDE-BASED  
SELF-IMMOLATIVE SPACERS  
FOR DRUG DELIVERY**

**Marta Ximenis Campins**





**Universitat**  
de les Illes Balears

**DOCTORAL THESIS**

**2019**

**Doctoral Programme of Chemical Science and  
Technology**

**DEVELOPMENT OF SQUARAMIDE-BASED  
SELF-IMMOLATIVE SPACERS  
FOR DRUG DELIVERY**

**Marta Ximenis Campins**

**Thesis supervisor: Dr. Antonio Costa Torres**

**Thesis supervisor: Dr. M. Carmen Rotger Pons**

**Tutor: Dr. M. Carmen Rotger Pons**

**Doctor by the Universitat de les Illes Balears**





**Universitat de les  
Illes Balears**

Dr. Antonio Costa Torres and Dr. M. Carmen Rotger Pons, of the University of the Balearic Islands

WE DECLARE:

That the thesis entitled *Development of Squaramide-Based Self-Immolative Spacers for Drug Delivery*, presented by Marta Ximenis Campins to obtain a doctoral degree, has been completed under my supervision and meets the requirements to opt for an International Doctorate.

For all intents and purposes, we hereby sign this document.

Signature

Dr. Antonio Costa Torres

Dr. M. Carmen Rotger Pons

Palma de Mallorca, 02/07/2019



The results derived from this thesis have resulted in the publication of the following scientific article:

M. Ximenis, J. Pitarch-Jarque, S. Blasco, C. Rotger, E. García-España, A. Costa. Water-Soluble Squaramide Dihydrates: N-Methylation Modulates the Occurrence of One- and Two-Dimensional Water Clusters through Hydrogen Bonding and Dipolar Interactions. *Cryst. Growth Des.* **2018**, *18*, 4420–4427.

Other publications derived from collaborations during this thesis:

M. Ximenis, E. Bustelo, A. G. Algarra, M. Vega, C. Rotger, M. G. Basallote, A. Costa. Kinetic Analysis and Mechanism of the Hydrolytic Degradation of Squaramides and Squaramic Acids. *J. Org. Chem.* **2017**, *82*, 2160–2170.

C. López, M. Ximenis, F. Orvay, C. Rotger, A. Costa. Supramolecular Hydrogels Based on Minimalist Amphiphilic Squaramide–Squaramates for Controlled Release of Zwitterionic Biomolecules. *Chem. Eur. J.* **2017**, *23*, 7590-7594



## *Acknowledgements*

En primer lloc voldria dirigir-me als meus directors Toni i Carme, gràcies per donar-me l'oportunitat de desenvolupar aquesta tesi amb voltros. Gràcies per les discussions científiques que han fet despertar-me encara més la curiositat pel coneixement i la recerca.

A l'equip del científicotècnic de la UIB, en especial a en Biel, Rosa, Joan i Jose, gràcies per la vostra ajuda, dedicació i paciència.

Gràcies a tots els que conformau el Grup de Química Supramolecular, passats i presents: Ruth, Àngel, Elena, Paulino, Alberto, Susana, Manel, Edu, Tomeuet, Sergi, Santy, Pere, Jeroni, Neus, David i Toni B. Ha estat un plaer créixer com a científica i persona al vostre costat, aprenent de cadascun de vosaltres. Gràcies per fer-me sentir com a casa, deixant-me expressar la meva burreria pels laboratoris i, moltes vegades, afegint-vos-hi. Als calculístics, Toni F. i Antonio, gràcies per donar-me suport teòric i artístic, sempre amb molt bon humor. Xisca, Carlos, heu estat pilars fonamentals d'aquesta tesi. Ha estat un viatge ple de dificultats, obstacles i reptes però al vostre costat, les rialles, dinarillos i manualitats varies, han fet que tot fos més fàcil i divertit. Mil gràcies. Lluís, saps bé que a una de tantes realitats alteratives del multivers hem triomfat amb Acamelados però en aquesta, ens toca triomfar com a científics. Gràcies per treure a la llum a na Loky. Tomeu, gràcies pel teu vot de confiança, gràcies per obrir-me portes a oportunitats que mai hagués pensat, per fer-me més atractiu el *dark side*.

Gràcies a la Conselleria d'Educació, Cultura i Universitats del Govern Balear i al Fons Social Europeu per concedir-me la beca de doctorat i l'ajuda per desenvolupar l'estada, que ha fet possible tot l'aprenentatge i desenvolupament d'aquesta tesi.

I want to thank Professor Frank Würthner for giving me the opportunity to join his group at Würzburg University. Thanks also to the entire Würthner group, especially, Kazu, Anja and Chia-An for all the support at both professional and personal level. Ann Christin, thank you for your help and kindness, thanks for making me feel like at home during my stay in Würzburg. Vielen dank.

Als Wilds, gràcies per la vostra implicació i atenció, per fer-me sempre un lloc i donar-me tants moments de desconexió, ja siguin gastronòmics, lúdics, d'escapisme o de rallyes clandestins.

Als meus pares, germans i germana, gràcies pel vostre suport incondicional, per animar-me a començar aquest viatge, acompanyant-me sempre. Gràcies pel gran esforç que heu

fet ajudant-me a arribar fins aquí i, sobretot, gràcies per donar suport a les meves decisions de “*la pens i la faig*”, cada vegada amb més cara de “*ja no mos vé de nou*”.

Predina, aquesta tesi també és teva. Una vegada me vas dir que voldries haver estat més llesta i haver estudiat però també me vas dir que t’encantava mirar el cel, la mar i l’horitzó, demanant-te que hi hauria més enllà i per què passaven les coses. M’has transmès aquest esperit curiós i, que avui estigui escrivint aquestes línies, té molta part de tu. Moltíssimes gràcies.

Finalment, gràcies Gabriel, has estat el meu company de batalla des del principi, compartint èxits i fracassos, perquè saps ben bé com ha costat arribar fins aquí. Gràcies per tot el teu suport i paciència, per animar-me sempre a anar una passa més enllà i per fer-me costat, fins i tot al moments més difícils.



**Universitat**  
de les Illes Balears



*Me interesan todas las ramas del conocimiento*

GABRIEL ROMAY



## *List of Abbreviations*

BIPY	2,2'-Bipyridine
Bhc	4-bromo-7-hydroxycoumarin
CB1954	5-Aziridinyl-2,4-dinitrobenzamide
5-FC	5-fluorocytosine
A	Absorbance
CH <sub>3</sub> CN	Acetonitrile
$K_a$	Acid dissociation constant
ATP	Adenosine triphosphate
Ala	Alanine
$k_{OH}$	Alkaline hydrolysis rate constant
ANM	Aniline Nitrogen Mustard
ADEPT	Antibody Directed Enzyme Prodrug Therapy
AQPs	Aquaporins
Aq	Aqueous
AWC	Artificial Water Channels
ADHD	Attention Deficit Hyperactivity Disorder
BDEPT	Bacterial Directed Enzyme Prodrug Therapy
BBB	Blood Brain Barrier
BODIPY	Boron-dipyrromethene
CCl <sub>4</sub>	Carbon tetrachloride
CM	Carrier-mediated
CNS	Central Nervous System
Cs <sub>2</sub> CO <sub>3</sub>	Caesium Carbonate
$\delta$	Chemical shift
cf.	Compare
CPCM	Conductor-like Polarizable Continuum Model
COSY	Correlation spectroscopy
$J$	Coupling constant
CBs	Cucurbiturils
$k_c$	Cyclization rate constant
CBPQT	Cyclobis-(paraquat- <i>p</i> -phenylene)
CDs	Cyclodextrins
CPA	Cyclophosphamide
CFTR	Cystic Fibrosis Transmembrane Conductance Regulator
CYP	Cytochrome
CyD	Cytosine Deaminase
DFT	Density Functional Theory
DNA	Deoxyribonucleic Acid
CH <sub>2</sub> Cl <sub>2</sub>	Dichloromethane
Et <sub>2</sub> O	Diethyl ether
DSC	Differential Scanning Calorimetry

DMSO	Dimethylsulfoxide
DEPT	Directed Enzyme Prodrug Therapy
Boc <sub>2</sub> O	Di-tert-butyl dicarbonate
DTT	Dithiothreitol
dsDNA	Double Strand DNA
DDD	Drew-Dickerson Dodecamer
ED	Electro-Dialysis
eV	Electronvolt
ESI-MS	Electrospray Ionisation Mass Spectrometry
Eq.	Equation
Equiv	Equivalent
EtOH	Ethanol
Fmoc	Fluorenylmethyloxycarbonyl
FFNs	Fluorescent False Neurotransmitters
FDA	Food and Drug Administration
FO	Forward Osmosis
FTIR-ATR	Fourier Transform Infrared-Attenuated Total Reflection
GCV	Ganciclovir
GDEPT	Gene Directed Enzyme Prodrug Therapy
GSH	Gluthathione
g	Gram
gA	Gramicidin A
GAH	Guanine aminohydrolase
HSV-TK	Herpes Simplex Virus Thymidine Kinase
HMBC	Heteronuclear Multiple-Bond Correlation Spectroscopy
HSQC	Heteronuclear Single-Quantum Correlation Spectroscopy
HPLC	High Pressure Liquid Chromatography
HRMS	High Resolution Mass Spectrometry
His	Histidine
hAQP4	Human aquaporin 4
hiPSCs	Human-induced pluripotent stem cells
IFA	Ifosfamide
IR	Immediate Release
IMiDs	Immunomodulatory derivatives
IR	Infrared
INP	Inorganic nanoparticles
INT	Intermediate
IUPAC	International Union of Pure and Applied Chemistry
ICL	Interstrand Cross-Linking
K	Kelvin degree
KIE	Kinetic isotope effect
LBN	Latanoprostene bunod
LD	Lenalidomide

LGA	L-glutamic acid
LiCl	Lithium Chloride
LUMO	Lowest Unoccupied Molecular Orbital
Lys	Lysine
LAS	Lysine acetylsalicylate
m/z	Mass-to-charge ratio
MHz	Megahertz
MD	Membrane Distillation
mRNA	Messenger RNA
MeOH	Methanol
Met	Methionine
MW	Microwave
mL	Millilitres
$\epsilon$	Molar absorptivity
M	Molarity
MED	Multi Effect Desalination
MSF	Multi Stage Flash
ANM-OH	<i>N,N</i> -bis(2-hydroxyethyl)-1,4-phenylenediamine
DiPEA	<i>N,N</i> -Diisopropylethylamine
DMF	<i>N,N</i> -Dimethylformamide
NIH	National Institute of Health
NGP	Neighbouring Group Participation
NADH	Nicotinamide adenine dinucleotide
NADPH	Nicotinamide adenine dinucleotide phosphate
NMs	Nitrogen Mustards
NTR	Nitroreductase
NO	Nitrous oxide
NDMA	<i>N</i> -methyl-D-aspartic acid
NMR	Nuclear Magnetic Resonance
NOESY	Nuclear Overhauser Effect Spectroscopy
SN	Nucleophilic substitution
$k_{\text{obs}}$	Observed rate constant
PTX	Paclitaxel
Phe	Phenylalanine
PBS	Phosphate-buffered saline
PPGs	Photoremovable Protecting Groups
pNBzC	<i>p</i> -nitrobenzylcarbamates
PGA	Poly(glycolic acid)
PLA	Poly(lactic acid)
PLGA	Poly(lactide-co-glycolide)
PAGE	Polyacrylamide Gel Electrophoresis
PAMAM	Polyamidoamine
PEG	Polyethylene glycol

PEI	Polyethyleneimine
PEG	Polyethyleneglycol
PDEPT	Polymer Directed Enzyme Prodrug Therapy
PBLA	Poly- $\beta$ -benzyl L-aspartate
K <sub>2</sub> CO <sub>3</sub>	Potassium carbonate
PXRD	Powder X-ray diffraction
PG	Protective Group
RDS	Rate-determining step
RO	Reverse Osmosis
RNA	Ribonucleic Acid
SIL	Self-Immolative Linker
Ser	Serine
ssDNA	Single Strand DNA
SSIS	Squaramide-based Self-Immolative System
NaCl	Sodium chloride
NaHCO <sub>3</sub>	Sodium hydrogencarbonate
NaOH	Sodium hydroxide
Na <sub>2</sub> SO <sub>4</sub>	Sodium sulphate
ss-CPMAS NMR	Solid-state Cross-Polarization Magic Angle Spinning NMR
SQ	Squaramide
SR	Sustained Release
TMZ	Temozolomide
Boc	Tert-butyloxycarbonyl
TBAF	Tetra- <i>n</i> -butylammonium fluoride
TGA	Thermogravimetric Analysis
TOCSY	Total correlation spectroscopy
TS	Transition State
Et <sub>3</sub> N	Triethylamine
TFA	Trifluoroacetic acid
TML	Trimethyl lock
TCEP	Tris(2-carboxyethyl)phosphine
Tris	Tris(hydroxymethyl)aminomethane
UT-B	Urea transporter B
VMAT	Vesicular Monoamine Transporter
VDEPT	Virus Directed Enzyme Prodrug Therapy
K <sub>w</sub>	Water autoprotolysis equilibrium constant
$\lambda$	Wavelength
WHO	World Health Organization
Zn(OTf) <sub>2</sub>	Zinc trifluoromethanesulfonate

## Abstract

This PhD thesis entitled “*Squaramide-Based Self-Immolative Spacers for Drug Delivery*” describes the development of squaramide spacers able to undergo triggered-disassembly for the release of bioactive compounds.

As a starting point, we synthesised a small collection of squaramate esters to study their hydrolytic stability in biologically simulated conditions. These compounds bear different side chains with chemical functionalities that may assist the hydrolysis or cyclization reaction. The kinetic study has permitted to find that the propanediamino and the ethyl sulphur side chains successfully undergo the cyclization reaction releasing ethanol as the leaving group.

Based on the results found for squaramate ester derivatives, we designed and synthesized squaramide-based self-immolative models bearing amines as the leaving group. We explored both anilines and aliphatic amines to this purpose. The kinetic study revealed that the rate of disassembly was strongly dependent on the pH and the nucleofugacity of the leaving group. Henceforth the release of anilines was faster than *n*-butylamine. Additionally, *N*-methylated models showed faster cyclization rates and better aqueous solubility. Overall, the most suitable squaramide-based self-immolative linker should present the following key features: 1) Propanediamino chain as the nucleophile 2) Aniline as the chemical nature of the leaving group or cargo 3) *N*-methylation of the squaryl ring.

As proof of concept, we applied the optimised design in the synthesis of a prodrug. We selected the *p*-nitrobenzyl carbamate residue as the trigger group and phenylenediamine mustard as the active drug. The disassembly process was enzymatically triggered by a nitroreductase using NADH as the reductive agent. We tested the biological activity of the prodrug against glioblastoma cancer cells. The clonogenic assay performed with LN229 cells showed that the treatment with the parent mustard drug had no effect on the cell growth but, when treated with the mustard prodrug, we could observe the significant decrease in the survival factor (down to 24 %). This result was outstanding since the treatment with temozolomide, a common antitumor agent used in the treatment of brain cancer, showed a survival factor of 58 %.

In addition to the main line of this thesis, the study of the cyclosquaramide self-immolation products led to crystalline aggregates in water. The different degree of *N*-methylation produced three types of water clusters: water tapes, 2D hexagonal water layers and, 1D water chains.

## Resumen

Esta tesis, titulada “*Espaciadores Autoinmolativos de base Escuaramida para la Administración de Fármacos*” describe el desarrollo de espaciadores derivados de escuaramida capaces de desensamblarse para liberar compuestos bioactivos.

En primer lugar, se han sintetizado una colección de escuaramato ésteres y se ha estudiado su estabilidad hidrolítica en condiciones fisiológicas. Estos compuestos presentan diferentes grupos funcionales en la cadena lateral que pueden asistir la reacción de hidrólisis o la ciclación. El estudio cinético ha permitido determinar que los compuestos con cadenas de propandiamina y etilsulfuro son capaces de llevar a cabo la reacción de ciclación, liberando etanol como grupo saliente.

En base a estos resultados, se han diseñado y sintetizado modelos autoinmolativos de base escuaramida para el estudio de liberación de aminas como grupo saliente. Se han considerado tanto anilinas como aminas alifáticas. Los estudios cinéticos han demostrado la dependencia de la autoinmolación con el pH y la nucleofugacidad del grupo saliente, encontrando velocidades de liberación mayores en anilinas respecto a las aminas alifáticas. Así mismo, se ha observado que los modelos *N*-metilados presentan cinéticas de liberación más rápidas y son más solubles en medio acuoso. De estos estudios se determinan los atributos clave para el diseño de sistemas autoinmolativos: 1) el uso de la cadena de propandiamina como nucleófilo 2) el uso de anilinas como grupo saliente del compuesto de interés 3) *N*-metilación del nitrógeno escuaramídico.

Como prueba de concepto, el módulo autoinmolativo optimizado se ha introducido en la síntesis de un profármaco. Éste consta del *p*-nitrobencil carbamato como grupo protector (gatillo) y un derivado de mostaza de nitrógeno como fármaco. El proceso de autoinmolación se ha activado por efecto de la enzima nitroreductasa usando NADH como agente reductor. La actividad biológica del profármaco y la mostaza se ha probado frente a células cancerosas de glioblastoma mediante un ensayo clonogénico con células LN229. Mientras que la mostaza no presenta efecto sobre la proliferación celular, el profármaco reduce el factor de supervivencia del cultivo al 24 %. Este resultado es muy significativo ya que, el ensayo con temozolomida, un antitumoral comúnmente usado en el tratamiento de tumores cerebrales, presenta un factor de supervivencia del 58 %.

Además de la línea principal de esta tesis, el estudio de los productos de autoinmolación (cicloescuaramidas) ha llevado a la formación de cristales en agua. Se ha visto cómo el grado de metilación influye en la formación de tres tipos de redes de agua en la estructura: cintas, capas bidimensionales hexagonales y cadenas monodimensionales.

## Resum

Aquesta tesi, titulada “*Espaiadors Autoimmolatius de base Esquaramida per a l'Administració de Fàrmacs*” descriu el desenvolupament d'espaiadors derivats d'esquaramida capaços de desencadellar-se per alliberar composts bioactius.

En primer lloc, s'ha sintetitzat una col·lecció d'esquaramat èsters y s'ha estudiat la seva estabilitat hidrolítica en condicions fisiològiques. Aquests composts presenten diferents grups funcionals a la cadena lateral que poden assistir la reacció d'hidròlisi o la ciclació. L'estudi cinètic ha permès determinar que els composts amb cadenes de propandiamina i etilsulfur son capaços de dur a terme la reacció de ciclació alliberant etanol como grup sortint.

En base a aquests resultats, s'han dissenyat i sintetitzat models autoimmolatius de base esquaramida per a l'estudi d'alliberament d'amines como a grup sortint. S'han considerat tant anilines como amines alifàtiques. Els estudis cinètics han demostrat la dependència de l'autoimmolació amb el pH i la nucleofugacitat del grup sortint, trobant velocitats d'alliberament majors per anilines respecte les amines alifàtiques. Així mateix, s'ha observat que els models *N*-metilats presenten cinètiques d'alliberament més ràpides i son més solubles en medi aquós. D'aquests estudis es conclouen els atributs clau per al disseny de sistemes autoimmolatius: 1) l'ús de la cadena de propandiamina com a nucleòfil 2) l'ús d'anilines como grup sortint del compost d'interès 3) *N*-metilació del nitrogen esquaramídic.

Com a prova de concepte, el mòdul autoimmolatiu optimitzat s'ha introduït a la síntesis d'un profàrmac. La seva estructura consta del *p*-nitrobenzil carbamat com a grup protector (gallet) i un derivat de mostassa de nitrogen com a fàrmac. El procés d'autoimmolació s'ha activat mitjançant l'acció de l'enzim nitroreductasa fent servir NADH com agent reductor. L'activitat biològica del profàrmac i de la mostassa s'ha provat front cèl·lules canceroses de glioblastoma mitjançant un assaig clonogènic amb cèl·lules LN229. Mentre que la mostassa no presenta efecte sobre la proliferació cel·lular, el profàrmac redueix el factor de supervivència del cultiu al 24 %. Aquest resultat és molt significatiu ja que, l'assaig amb temozolomida, un antitumoral molt usat en el tractament de tumors cerebrals, presenta un factor de supervivència del 58 %.

A més de la línia principal d'aquesta tesi, l'estudi dels productes d'autoimmolació (cicloesquaramides) ha dut a la formació de cristalls en aigua. S'ha vist com el grau de metilació influeix en la formació de tres tipus de xarxes d'aigua a l'estructura: cintes, capes bidimensionals hexagonals y cadenes monodimensionals.



## *Table of Contents*

<b>1. Introduction</b>	25
1.1. Targeted Drug Delivery	27
1.1.1. Self-Immolative Linkers	29
1.1.2. Triggers	33
1.1.3. Carriers	36
1.1.4. Targeted Drug Delivery to Tumours	45
1.2. Squaramides: From Supramolecular Chemistry to Chemical Biology	47
1.2.1. Squaramide Compounds in Chemical Biology and Medicinal Chemistry	50
1.2.2. Squaramides as Self-Immolative Spacers for Drug Delivery	55
<b>2. Objectives</b>	59
<b>3. Towards Self-Immolative Systems: Squaramate Esters</b>	63
3.1. Motivation and Objectives	65
3.1.1. Objectives	66
3.2. Introduction	67
3.2.1. Reactivity of Squaramate Esters. Hydrolysis	68
3.2.2. Hydrolysis Kinetics. Rate Law	71
3.2.3. Anchimeric Assistance	72
3.3. Results and Discussion	78
3.3.1. Synthesis of the Squaramate Esters	78
3.3.2. Kinetics of the Squaramate Esters Hydrolysis	78
3.3.3. Intramolecular Cyclization of Esters <b>13b</b> and <b>14b</b>	88
3.4. Conclusions	106
3.5. Experimental Section	107
3.5.1. Kinetic Experiments	107
3.5.2. Theoretical Calculations	107
3.5.3. Synthesis	108
3.5.4. NMR Spectra of Selected Compounds	115

<b>4. Water-Soluble Cyclosquaramides: Supramolecular Aggregation in Solid State</b>	119
4.1. Motivation	121
4.2. Introduction	122
4.2.1. Natural Water Channels	122
4.2.2. Artificial Water Channels	124
4.3.3. Industrial Applications	127
4.3. Objectives	129
4.4. Water Soluble Squaramide Dihydrates: N-Methylation Modulates the Occurrence of 1D and 2D Water Clusters Trough Hydrogen Bonding and Dipolar Interactions ( <i>Crystal Growth and Design</i> , <b>2018</b> , <i>18</i> , 4420-4427)	131
4.4.1. Abstract	133
4.4.2. Experimental Section	136
4.4.3. Results and Discussion	138
4.4.4. Conclusions	147
4.4.5. Acknowledgments	148
4.4.6. Supporting Information	149
<b>5. Squaramide-Based Self-Immulative Spacers: Improving the Leaving Group</b>	167
5.1. Self-Immulative Systems: Design Principles	169
5.2. Objectives	173
5.3. Results and Discussion	174
5.3.1. Self-Immulative Models Releasing Anilines	174
5.3.2. Self-Immulative Models Releasing Aliphatic Amines	190
5.3.3. Transamidation-type Reaction on Compound <b>33c</b>	206
5.4. Conclusions	216
5.5. Experimental Section	217
5.5.1. Kinetic Experiments	217
5.5.2. Theoretical Calculations	217
5.5.3. Synthesis	218
5.5.4. NMR Spectra of Selected Compounds	231
5.5.5. Spectroscopic Data of Compounds <b>36a-d</b>	246

<b>6. Squaramide-Based Self-Immolative Spacers in Action</b>	249
6.1. Prodrug Design	251
6.1.1. Drug/Cargo Selection	252
6.1.2. Trigger Selection	254
6.2. Objectives	258
6.3. Results and Discussion	259
6.3.1. Synthesis of the Self-Immolative Nitrogen Mustard Prodrug	259
6.3.2. DNA Cross-Linking	264
6.3.3. Cell Viability Analysis	268
6.3.4. Further Perspectives	271
6.4. Conclusions	279
6.5. Experimental Section	280
6.5.1. Synthesis	281
6.5.2. NMR Spectra of Selected Compounds	286
6.5.3. Clonogenic Assay	289
<b>7. Conclusions</b>	291



**1**

---

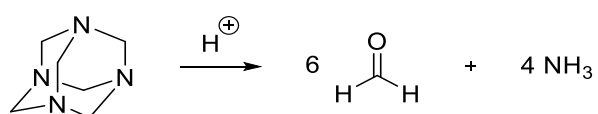
# **Introduction**



## 1.1. TARGETED DRUG DELIVERY

Common challenges for drugs when trying to reach their therapeutic target are the need of specificity, low cytotoxicity, ability to penetrate the cell membrane or avoid undesired side enzymatic reactions. Despite overcoming these demands, a drug may fail its purpose because of its intrinsic properties such as low solubility in water, inadequate stability profile and low pharmacokinetics.<sup>1</sup> To solve such problems, drug delivery systems aim to deliver a drug to its corresponding target site efficiently, within a precise period of time and dosage.

Hence, the strategy of *prodrugs* is born to define an inactive compound which under metabolization within the body is converted to its corresponding therapeutically active molecule while improving their delivery properties.<sup>2</sup> The term was firstly presented in 1958 by Adrien Albert,<sup>3</sup> discussing the effects of selective toxicity, metabolic reactions and membrane permeability of the drug, all of them, demanding challenges to overcome reaching the target site. Nonetheless, it was in 1899 when Schering introduced the first prodrug: methenamine, an inactive prodrug, which under acidic conditions, releases formaldehyde showing antibacterial activity (Scheme 1.1), without defining the term.<sup>4</sup>



**Scheme 1.1.** Acidic breakdown of methenamine to release antibiotic formaldehyde and ammonia.

Later on, in 1935, Bayer reported by serendipity the antibiotic prontosil, which was found to be the inactive form of the *para*-aminophenylsulfonamide, generated under enzymatic reduction (Scheme 1.2).<sup>5</sup>

<sup>1</sup> a) M. Hammarlund-Udenaes, E. de Lange, and R. Thorne. (2014) *Drug Delivery to the Brain*, 1st ed., AAPS Press, Springer, DOI: 10.1007/978-1-4614-9105-7. b) R. Walther, J. Rautio, A. N. Zelikin, *Adv. Drug Deliv. Rev.* **2017**, *118*, 65–77.

<sup>2</sup> J. Rautio, N. A. Meanwell, L. Di, M. J. Hageman, *Nat. Rev. Drug Discov.* **2018**, *17*, 559–587.

<sup>3</sup> A. Albert, *Nature* **1958**, *182*, 421–423.

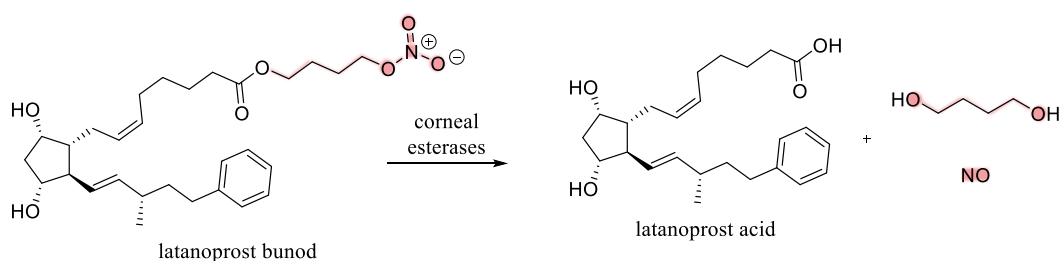
<sup>4</sup> S. Elayyan, D. Karaman, G. Mecca, L. Scrano, S. A. Bufo, R. Karaman, *World J. Pharm. Pharm. Sci.* **2015**, *4*, 1504–1529.

<sup>5</sup> R. Bentley, *J. Ind. Microbiol. Biotechnol.* **2009**, *36*, 775–786.



Typically, these built-in structural liabilities, are designed to improve intrinsic properties of the parent drug such as aqueous solubility, an increase of lipophilicity to allow passive permeability through membranes, gain in affinity to membrane transport proteins, improvement of metabolic stability, extend the duration of action, or increase the specificity to reduce side effects.

For instance, in November 2017, the prodrug latanoprostene bunod (LBN) was approved for the treatment of high intramolecular pressure in patients with open-angle glaucoma or ocular hypertension. Upon topical administration at the ocular surface, LBN is hydrolysed by corneal esterases into the active latanoprost acid (Scheme 1.3).<sup>8</sup>



**Scheme 1.3.** Biochemical transformation of LBN into its active form by enzymatic catalysis.

Additionally, the introduction of a nitro group in the prodrug complex increases water solubility but, in parallel, generates NO which plays an important role in the regulation of elevated intraocular pressure.<sup>9</sup>

### 1.1.1. Self-Immolative Linkers

Despite enzymatic selectivity and specificity, the efficient conversion of a prodrug is critically demanding on the accessibility to the substrate and thus, the steric hindrance limits drastically the prodrug cleavage. To effectively circumvent these problems, a labile spacer or *self-immolative linker* (SIL) is often conjugated between the active drug and the protecting group that must reach the enzyme reactive moiety. After the proper stimuli, the protective moiety (trigger) is removed, and the resulting linker-drug conjugate undergoes spontaneously the drug release (Figure 1.2).

<sup>8</sup> G. A. Garcia, P. Ngai, S. Mosaed, K. Y. Lin, *Clin. Ophthalmol.* **2016**, *10*, 2035–2050.

<sup>9</sup> A. H. P. Krauss, F. Impagnatiello, C. B. Toris, D. C. Gale, G. Prasanna, V. Borghi, V. Chirolì, W. K. M. Chong, S. T. Carreiro, E. Ongini, *Exp. Eye Res.* **2011**, *93*, 250–255.

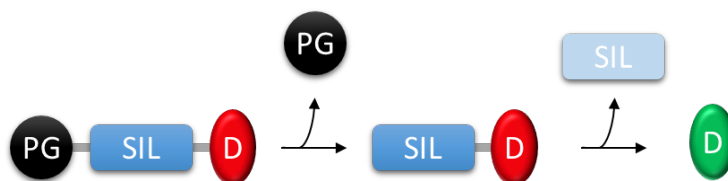


**Figure 1.2.** Schematic representation of a self-immolative spacer. First cleavage of the protecting group (PG) leads to spontaneous breakdown of the self-immolative linker (SIL) releasing the active drug (D).

For instance, in Paclitaxel (PTX) phosphate, the cleavage of the phosphonate group produces the active PTX. However, it is sterically hindered and hence difficult to be enzymatically removed from the molecule cleavage moiety (Figure 1.3a). Conversely, its analogue PTX-TML-phosphate, includes a self-immolative spacer based on a “trimethyl lock” (TML) linker<sup>10</sup> which undergoes spontaneous cyclization when the phosphate group is removed, thus releasing the active drug (Figure 1.3b).<sup>11</sup>

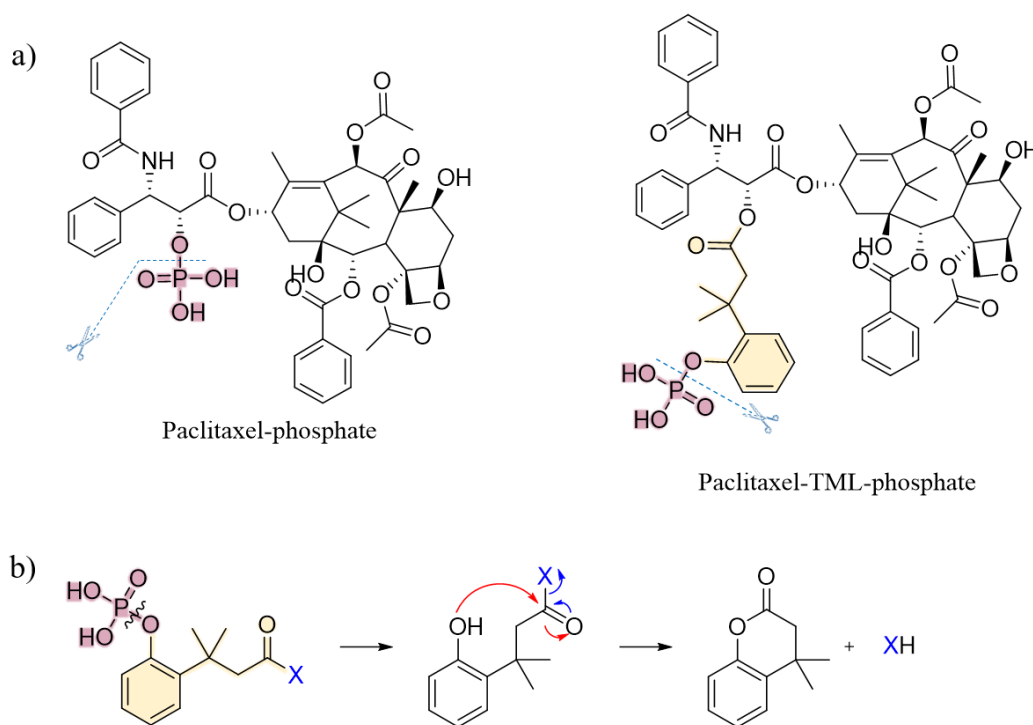


**Figure 1.3.** a) Early design of PTX prodrug. Comparison of the steric hindrance when including or not the SIL b) Cyclization mechanism of TML.

Two main categories can be distinguished for SIL depending on their mechanism of breakdown. On one hand, self-immolation by a cascade reaction of eliminations and, on the other hand, disassembly governed by cyclization processes giving final ring-closed

<sup>10</sup> O. A. Okoh, P. Klahn, *ChemBioChem* **2018**, *19*, 1668–1694.

<sup>11</sup> M. Skwarczynski, Y. Hayashi, Y. Kiso, *J. Med. Chem.* **2006**, *49*, 7253–7269.

structures.<sup>12</sup> Figure 1.4 summarizes some examples of general spacers depending on their breakdown mechanism.

Although the rate of disassembly varies depending on the mechanism, both mechanisms involve the release of a leaving group, and normally its nucleofugacity governs the last step of self-immolation. The rate of this step usually increases when the  $pK_a$  of the conjugate acid of the leaving group decreases.<sup>13</sup>

Commonly, self-immolative spacers activated by an electronic cascade (Figure 1.4) contain a donor group conjugated to an aromatic structure, being a hydroxy,<sup>14</sup> an amino<sup>15</sup> or a thiol.<sup>16</sup> As long as they are protected, their nucleophilicity is not enough to trigger the reaction cascade and the consequent release of the drug. Generally, during the disassembly, quinone or azaquinone methide derivatives are formed, hence, the resonance energy of the aromatic ring as well as the substituents involved in the aromatic moiety play a key role in the breakdown kinetics. It is also noticeable that external parameters such as pH, temperature or solvent may also be involved. Thus, the kinetics of self-immolation can be modified by stabilizing or destabilizing the cationic intermediates through modifications in the aromatic core, via substituents.

---

<sup>12</sup> A. Alouane, R. Labruère, T. Le Saux, F. Schmidt, L. Jullien, *Angew. Chem. Int. Ed.* **2015**, *54*, 7492–7509.

<sup>13</sup> M. B. Smith, J. March, (2007) March's advanced organic chemistry. *Reactions, mechanisms, and structure*, 6th ed., Wiley, New York.

<sup>14</sup> a) L. R. Staben, S. G. Koenig, S. M. Lehar, R. Vandlen, D. Zhang, J. Chuh, S. F. Yu, C. Ng, J. Guo, Y. Liu, A. Fourie-O'Donohue, M. Go, X. Linghu, N. L. Segreaves, T. Wang, J. Chen, B. Wei, G. D. Phillips, K. Xu, K. R. Kozak, S. Mariathasan, J. A. Flygare, T. H. Pillow, *Nat. Chem.* **2016**, *8*, 1112–1119. b) H. Y. Lee, X. Jiang, D. Lee, *Org. Lett.* **2009**, *11*, 2065–2068. c) A. Alouane, R. Labruère, T. Le Saux, I. Aujard, S. Dubruille, F. Schmidt, L. Jullien, *Chem. Eur. J.* **2013**, *19*, 11717–11724. d) A. Alouane, R. Labruère, K. J. Silvestre, T. Le Saux, F. Schmidt, L. Jullien, *Chem. Asian J.* **2014**, *9*, 1334–1340.

<sup>15</sup> a) F. M. H. De Groot, C. Albrecht, R. Koekkoek, P. H. Beusker, H. W. Scheeren, *Angew. Chem. Int. Ed.* **2003**, *42*, 4490–4494. b) R. Erez, D. Shabat, *Org. Biomol. Chem.* **2008**, *6*, 2669–2672. c) M. Shamis, D. Shabat, *Chem. Eur. J.* **2007**, *13*, 4523–4528.

<sup>16</sup> P. D. Senter, W. E. Pearce, R. S. Greenfield, *J. Org. Chem.* **1990**, *55*, 2975–2978.

## ELIMINATION

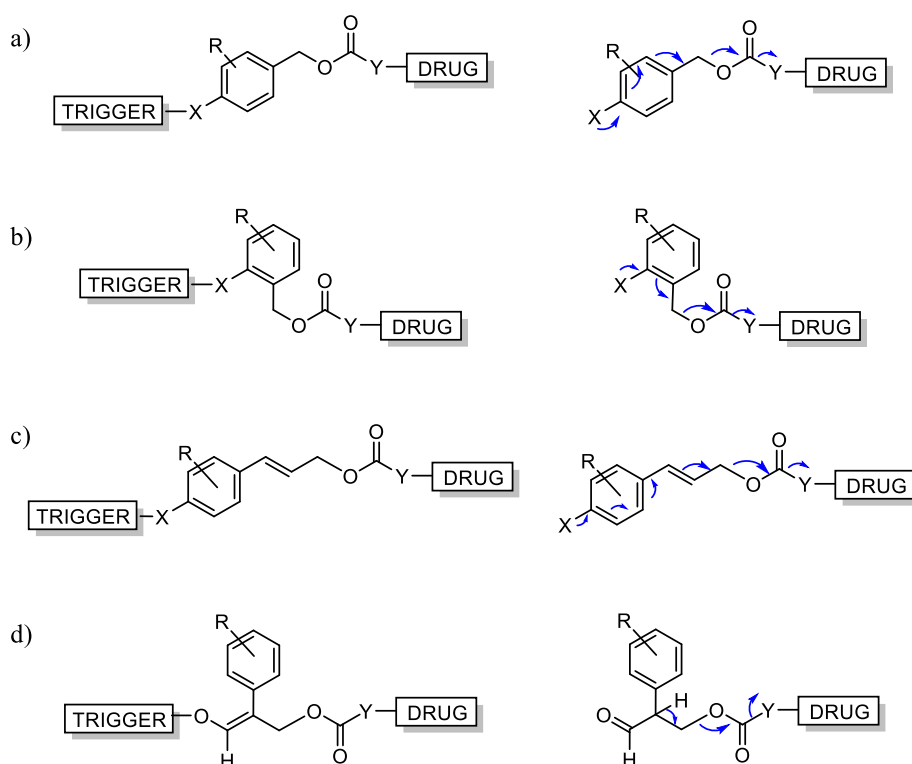


**Figure 1.4.** Self-immolative spacers based on an electronic cascade after trigger activation: Z = O, NH or S. X = O, NH or S. a) 1,6-benzyl elimination.<sup>14,15a</sup> b) 1,4-benzyl elimination.<sup>14,15a</sup> c) 1,8-elimination.<sup>14c,15b</sup> d)  $\beta$ -elimination.<sup>17</sup>

Self-immolative spacers that disassemble by cyclization usually bear nucleophile protected functionalities (Figure 1.5). The cleavage of the protecting group leads to an intramolecular reaction towards an electrophilic carbonyl or aliphatic carbon.<sup>18</sup> In general terms, the cyclization kinetics are slower than elimination by electronic cascade.<sup>19</sup> Similarly as discussed before, the modulation of kinetics can be achieved by the introduction of bulky groups in the alkyl chain, which may favour the cyclization process (Thorpe-Ingold effect<sup>20</sup> and/or reactive rotamer effect).<sup>21</sup> Moreover, nucleophilicity and electrophilicity of the sites involved in the cyclization process are key to define the rate-determining step, as well as the nature of the leaving group. In parallel, after triggering the activation of a self-immolative linker, a pH-sensitive group may be released and therefore, the pH of the media would critically influence the cyclization process. For instance, DeWit and Gillies developed a SIL based on 4-

<sup>17</sup> F. Rivault, I. Tranoy-Opalinski, J. P. Gesson, *Bioorganic Med. Chem.* **2004**, *12*, 675–682.

<sup>18</sup> A. Zheng, D. Shan, X. Shi, B. Wang, *J. Org. Chem.* **1999**, *64*, 7459–7466.

<sup>19</sup> C. De Gracia Lux, C. L. McFearin, S. Joshi-Barr, J. Sankaranarayanan, N. Fomina, A. Almutairi, *ACS Macro Lett.* **2012**, *1*, 922–926.

<sup>20</sup> R. M. Beesley, C. K. Ingold, J. F. Thorpe, *J. Chem. Soc. Trans.* **1915**, *107*, 1080–1106.

<sup>21</sup> A. L. Parrill, D. P. Dolata, *Tetrahedron Lett.* **1994**, *35*, 7319–7322.

aminobutyric acid derivatives and evaluated the rotamer and Thrope-Ingold effect as well as the reaction kinetics at different pH values. The reaction rate drastically fell when lowering the pH at 4.<sup>22</sup>

## CYCLYZATION

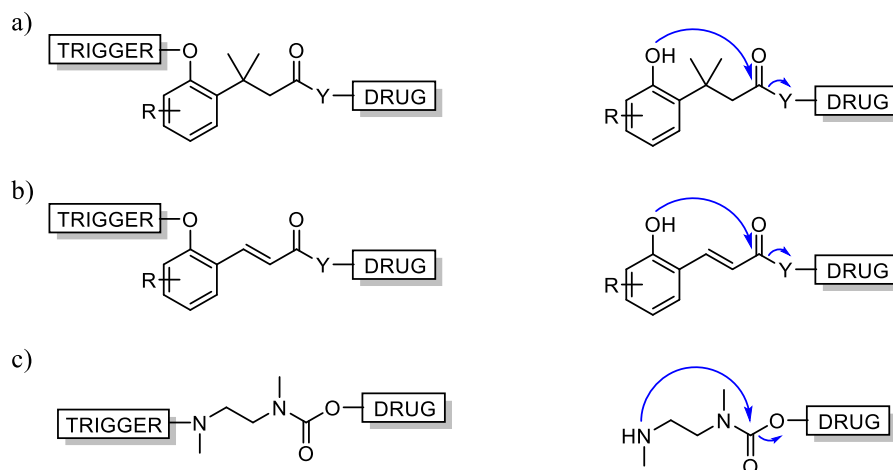


Figure 1.5. Self-immolative spacers based on 1,5- or 1,6-cyclization cascade.<sup>10,22</sup>

### 1.1.2. Triggers

Ideally, protecting groups should preserve the chemical stability of the system until reaching the target site where, under a specific stimulus or trigger, it will activate the self-immolative reaction cascade. The proper activation of self-immolation is crucial to target the right site within the right timing.

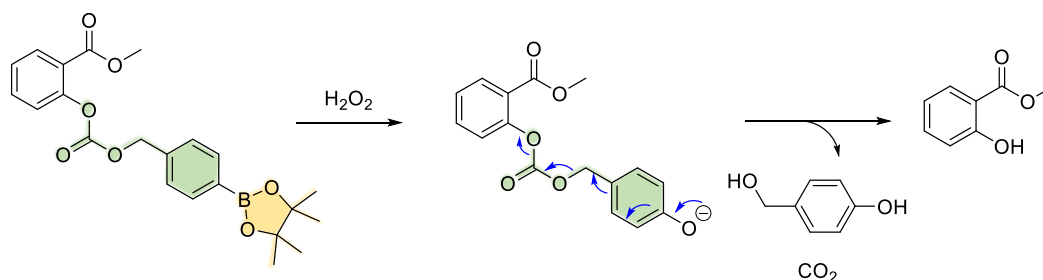
Triggers can be classified depending on their nature, being a chemical reagent, an enzyme or a light photon.

**Chemical reagents.** A common strategy to trigger the disassembly process involves the introduction of protective groups sensitive to redox processes, nucleophilic attack or proton exchange. For instance, disulfide bridges are frequently used as they disassemble under activation with free thiols, such as dithiothreitol (DTT) or glutathione (GSH).<sup>23</sup> On the other hand, phenylboronates have been used under activation by hydrogen peroxide (Scheme 1.4).<sup>24</sup>

<sup>22</sup> a) M. A. DeWit, E. R. Gillies, *Org. Biomol. Chem.* **2011**, *9*, 1846–1854. b) R. V. Kolakowski, K. T. Haelsig, K. K. Emmerton, C. I. Leiske, J. B. Miyamoto, J. H. Cochran, R. P. Lyon, P. D. Senter, S. C. Jeffrey, *Angew. Chem. Int. Ed.* **2016**, *55*, 7948–7951.

<sup>23</sup> Y. J. Pan, Y. Y. Chen, D. R. Wang, C. Wei, J. Guo, D. R. Lu, C. C. Chu, C. C. Wang, *Biomaterials* **2012**, *33*, 6570–6579.

<sup>24</sup> a) J. L. M. Jourden, S. M. Cohen, *Angew. Chem. Int. Ed.* **2010**, *49*, 6795–6797. b) J. L. M. Jourden, K. B. Daniel, S. M. Cohen, *Chem. Commun.* **2011**, *47*, 7968–7970.



**Scheme 1.4.** ROS-activated boronic ester with a carbonate linked SIL where the methyl salicylate is used as a leaving group.

Regarding the nucleophilic activation, water can smoothly activate reactions with esters;<sup>25</sup> meanwhile, the fluoride anion may react with silylated ethers.<sup>26</sup> Triggers based on proton exchange usually involve carbamates, typically Boc<sup>22,27</sup> and Fmoc,<sup>27</sup> followed by spontaneous decarboxylation.

**Enzymatic activation.** Although some enzymes may be expressed in multiple locations, the use of enzymatic activation for triggering self-immolation processes is an interesting approach to enhance specificity or directed drug delivery. For instance, cytochrome P450 (CYP) or CYP3A4 are mainly expressed in the liver;<sup>28</sup>  $\beta$ -glucuronidase,<sup>29</sup> glutathione S-transferase,<sup>30</sup> thymidine phosphorylase,<sup>31</sup> tyrosinase,<sup>32</sup> NADPH-cytochrome P450 reductase,<sup>33</sup> DT-diaphorase (also known as NQO1)<sup>34</sup> or tumour-associated proteases<sup>35</sup> are found in cancer cells; and bacterial reductases in the colon.<sup>36</sup>

<sup>25</sup> M. A. DeWit, E. R. Gillies, *J. Am. Chem. Soc.* **2009**, *131*, 18327–18334.

<sup>26</sup> a) W. Seo, S. T. Phillips, *J. Am. Chem. Soc.* **2010**, *132*, 9234–9235. b) R. Perry-Feigenbaum, E. Sella, D. Shabat, *Chem. Eur. J.* **2011**, *17*, 12123–12128.

<sup>27</sup> A. P. Esser-Kahn, N. R. Sottos, S. R. White, J. S. Moore, *J. Am. Chem. Soc.* **2010**, *132*, 10266–10268.

<sup>28</sup> Erion, M. D. in *Targeted Delivery of Small and Macromolecular Drugs* (eds Narang, A. S. & Mahato, R. I.) 277–310 (CRC Press, **2010**).

<sup>29</sup> M. Rooseboom, J. N. M. Commandeur, N. P. E. Vermeulen, *Pharmacol. Rev.* **2004**, *56*, 53–102.

<sup>30</sup> P. Labbé, H. Alout, L. Djogbénou, N. Pasteur and M. Weill. *Genetics and Evolution of Infectious Disease*, **2011**, *Chapter 14*, 363–409. DOI: 10.1016/B978-0-12-384890-1.00014-5.

<sup>31</sup> a) Y. Y. Elamin, S. Rafee, N. Osman, K. J. O'Byrne, K. Gately, *Cancer Microenviron.* **2016**, *9*, 33–43. b) C. Deves, D. C. Rostirolla, L. K. B. Martinelli, C. V. Bizarro, D. S. Santos, L. A. Basso, *Mol. Biosyst.* **2014**, *10*, 592–604.

<sup>32</sup> X. Lai, H. J. Wichers, M. Soler-Lopez, B. W. Dijkstra, *Chem. Eur. J.* **2018**, *24*, 47–55.

<sup>33</sup> D. S. Riddick, X. Ding, C. R. Wolf, T. D. Porter, A. V. Pandey, Q. Y. Zhang, J. Gu, R. D. Finn, S. Ronseaux, L. A. McLaughlin, C. J. Henderson, L. Zou, C. E. Flück, *Drug Metab. Dispos.* **2013**, *41*, 12–23.

<sup>34</sup> E.-T. Oh, H. J. Park, *BMB Rep.* **2013**, *48*, 609–617.

<sup>35</sup> J. Vandooren, G. Opdenakker, P. M. Loadman, D. R. Edwards, *Adv. Drug Deliv. Rev.* **2016**, *97*, 144–155.

<sup>36</sup> S. S. Dhaneshwar, G. Vadnerkar, *Curr. Top. Med. Chem.* **2011**, *11*, 2318–2345.

**Light-driven activation.** The last strategy to trigger the breakdown consists in the activation by light. In this regard, the most used and developed protecting group is the *ortho*-nitrobenzyl group, activated by UV photons which present a fast cleavage rate (less than 1 ms for good leaving groups).<sup>14c,d,37</sup> In addition to the *ortho*-nitrobenzyl, a large variety of photoremovable groups are currently being used for drug delivery as well as other applications (Figure 1.6).<sup>38</sup>

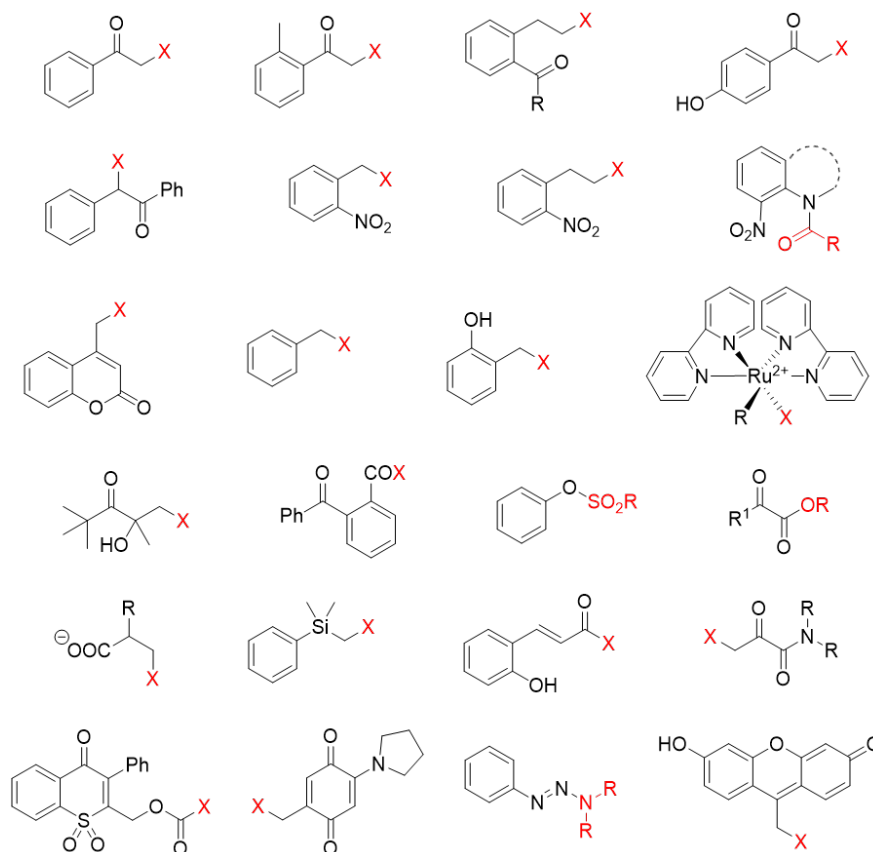


**Figure 1.6.** Examples of Photoremovable Protecting Groups (PPGs).

For drug delivery applications, a key factor needs to be taken into account: PPGs should present strong intrinsic absorption at wavelengths above 300 nm, where irradiation is less likely to be absorbed by the biological surrounding.

For instance, Figure 1.7 shows a dendritic scaffold designed by Almutairi and collaborators which undergoes disassembly under response to near-infrared light. In this example a photoremovable protecting group, 4-bromo-7-hydroxycoumarin (Bhc) is

<sup>37</sup> N. Fomina, C. Mcfearin, M. Sermsakdi, O. Edigin, A. Almutairi, *J. Am. Chem. Soc.* **2010**, *132*, 9540–9542.

<sup>38</sup> P. Klan, T. Solomek, C. G. Bochet, R. Givens, M. Rubina, V. Popik, A. Kostikov, J. Wirz, *Chem. Rev.* **2013**, *113*, 119–191.

combined with a cyclization-mediated SIL ( $N,N'$ -ethylenediamine lactonization) and an electronic cascade-mediated SIL (quinone methide) to release L-glutamic acid (LGA).<sup>39</sup>

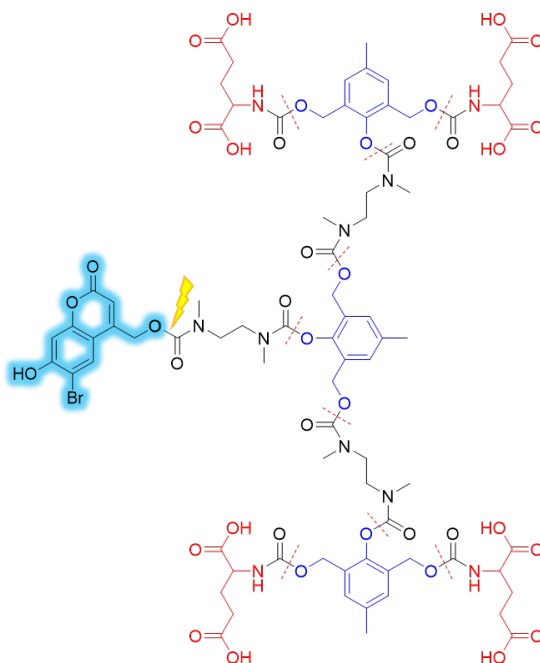


**Figure 1.7.** G2-dendritic self-immolative system. Fluorescent PPG (Bhc, fluorescent blue), SIL lactonization unit (black), SIL quinone methide (blue) and LGA (red).

### 1.1.3. Carriers

Permeability across biological membranes remains one of the most hectic challenges in drug delivery. Sugano and collaborators discussed the coexistence of both passive diffusion and carrier-mediated (CM) transport during drug delivery exhaustively.<sup>40</sup> Thus, many strategies have been developed to increase drug penetration across biological barriers to find an equilibrium between permeability and specificity.<sup>2,41</sup>

Passive diffusion relies exclusively on the ability of a compound to cross the cell membrane driven by the entropic process.<sup>42</sup> Hence, strategies in increasing lipophilicity of drugs and prodrugs are commonly employed to achieve good oral and topic

<sup>39</sup> N. Fomina, C. L. McFearn, A. Almutairi, *Chem. Commun.* **2012**, 48, 9138–9140.

<sup>40</sup> L. Di, P. Artursson, A. Avdeef, G. F. Ecker, B. Faller, H. Fischer, J. B. Houston, M. Kansy, E. H. Kerns, S. D. Krämer, H. Lennernäs and K. Sugano, *Drug Discov. Today* **2012**, 17, 905–912.

<sup>41</sup> a) A. Wicki, D. Witzigmann, V. Balasubramanian, J. Huwyler, *J. Control. Release* **2015**, 200, 138–157. b) S. M. Grassl, *16-Mechanisms of Carrier-Mediated Transport: Facilitated Diffusion, Cotransport and Countertransport*, **2001**, 249-259 in *Cell Physiology Source Book*, 3<sup>rd</sup> edition, Science Direct. DOI: 10.1016/B978-012656976-6/50108-6

<sup>42</sup> W. L. Backes, *Passive Diffusion of Drugs Across Membranes*, **2007**, 1-5. Elsevier. DOI: 10.1016/B978-008055232-3.60067-4

administration properties.<sup>43</sup> On the contrary, CM transport is based on the transport against a natural gradient.<sup>40</sup> Hence, it is particularly important for polar and charged drugs, which ability to permeate membranes by diffusion is extremely low.

Traditionally, the term “carrier” refers exclusively to transmembrane proteins that assist the molecular flow through membranes. However, research on molecular transport assisted by small molecules or macromolecules implies the need to review the definition. Hence, in drug delivery and, particularly in this thesis, the term “carrier” will refer to any species capable of transport a substance (i.e. drug) within the body.

For drug delivery purposes, when targeting a specific organ or tissue, CM transport helps to low the toxicity increasing the selectivity. It also alters the intrinsic biodistribution of the drug by allowing it to accumulate at a preferred site. Up to date, a huge variety of carriers are being investigated for drug delivery, including vectors and drug conjugates, lipid and polymer-based nanocarriers and inorganic nanoparticles.

*Lipid-based nanocarriers.* Liposomes, which are spherical closed phospholipid bilayers, were the first nanocarriers developed in nanomedicine. After their discovery by Watkins and collaborators in 1965,<sup>44</sup> their use and development have gained impact in the field. Over the last 20 years, the use of lipidic carriers has evolved significantly, from Doxil<sup>®</sup> the first nanocarrier approved by the FDA back in 1995 for doxorubicin delivery, to Onyvite<sup>®</sup> approved in 2015 for amphotericin B delivery.<sup>45</sup>

Despite liposomes provide good chemical stability of the drug and prevent it from undesirable attacks during its distribution, control over the distribution and removal *in vivo* keeps on a challenge.<sup>46</sup> To face this obstacle, in recent years, researchers have focused on modifying the liposomal surface with antibodies or proteins which confer specificity for a particular site. For instance, the first clinical trial with targeted liposomes consisted in immunoliposome-encapsulated doxorubicin, tagged with polyethylene-glycol (PEG) and the F(ab')<sub>2</sub> fragment of human monoclonal antibody GAH to treat metastatic stomach cancer (Figure 1.8a).<sup>47</sup>

*Polymeric nanocarriers.* Natural polymers, including proteins, peptides, glycans, starches, and cellulose can be used as drug carriers because of their unique properties:

---

<sup>43</sup> a) Y. Fukano, K. Kawazu, *Drug Metab. Dispos.* **2009**, *37*, 1622–1634. b) S. M. Hoy, *Drugs* **2015**, *75*, 1807–1813.

<sup>44</sup> A. D. Bangham, M. M. Standish, J. C. Watkins, *J. Mol. Biol.* **1965**, *13*, 238–252.

<sup>45</sup> U. Bulbake, S. Doppalapudi, N. Kommineni, W. Khan, *Pharmaceutics* **2017**, *9*, 1–33.

<sup>46</sup> Z. Li, S. Tan, S. Li, Q. Shen, K. Wang, *Oncol. Rep.* **2017**, *38*, 611–624.

<sup>47</sup> Y. Matsumura, M. Gotoh, K. Muro, Y. Yamada, K. Shirao, Y. Shimada, M. Okuwa, S. Matsumoto, Y. Miyata, H. Ohkura, K. Chin S. Baba T. Yamao A. Kannami Y. Takamatsu K. Ito K. Takahashi, *Ann. Oncol.* **2004**, *15*, 517–525.

they are biodegradable, metabolizable and easily modifiable in their surface.<sup>48</sup> However, only Abraxane<sup>®</sup>, an albumin-based nanoparticle to deliver PTX, is currently used in clinical studies for the treatment of breast, lung and pancreatic cancers (Figure 1.8b).<sup>41</sup> Regarding other natural polymers, none has yet been approved but promising results are being found for chitosan-based nanoparticles.<sup>49</sup>

In contrast, synthetic polymers are becoming promising candidates for nanomedicine development because of their chemical versatility. Synthetic polymers in micellar or nanoparticle forms such as polyethylene glycol – poly(glycolic acid), PEG-PGA; poly(lactide-co-glycolide) PLGA-PEG or modified polymers such as polyamidoamine-cholesterol (PAMAM-cholesterol) are succeeding in early clinical trials in the treatment of cancer.<sup>50</sup> For instance, Genexol-PM<sup>®</sup> is a marketed formulation of PTX based on PEG-PLA micelles (Figure 1.8c).<sup>51</sup>

*Inorganic nanoparticles (INP).* INP have an extended use in a variety of fields, including tumour imaging, enhancement of radiotherapy or drug delivery.<sup>52</sup> Some INP, for instance, quantum dots<sup>53</sup> and gold nanoparticles<sup>54</sup> exhibit unique optical, electrical and magnetic properties which makes them useful for medicinal applications normally focused on imaging.

Despite their widely extended use in other fields, any INP has reached marketing approval, finding obstacles in their high toxicity or lack of stability. However, Letho and collaborators, have recently developed a nanocomposite by coating porous silicon nanoparticles with two polymeric scaffolds: poly(beta-amino ester) (PAE) and Pluronic F-127. Then, PTX and DOX were separately loaded inside (Figure 1.8d).<sup>55</sup>

---

<sup>48</sup> W. Lohcharoenkal, L. Wang, Y. C. Chen, Y. Rojanasakul, *Biomed Res. Int.* **2014**, *2014*, 1–12.

<sup>49</sup> S. Naskar, K. Koutsu, S. Sharma, *J. Drug Target.* **2018**, *0*, 1–15.

<sup>50</sup> R. H. Prabhu, V. B. Patravale, M. D. Joshi, *Int. J. Nanomedicine* **2015**, *10*, 1001–1018.

<sup>51</sup> K.S. Lee, H.C. Chung, S.A. Im, Y.H. Park, C.S. Kim, S.-B. Kim, S. Y. Rha, M. Y. Lee, *J. Ro Breast Cancer Res. Treat.* **2008**, *108*, 241–250.

<sup>52</sup> H. C. Huang, S. Barua, G. Sharma, S. K. Dey, K. Rege, *J. Control. Release* **2011**, *155*, 344–357.

<sup>53</sup> P. Zrazhevskiy, M. Sena, X. Gao, *Chem. Soc. Rev.* **2010**, *39*, 4326–4354.

<sup>54</sup> F. Y. Kong, J. W. Zhang, R. F. Li, Z. X. Wang, W. J. Wang, W. Wang, *Molecules* **2017**, *22*, 1–13

<sup>55</sup> W. Xu, R. Thapa, D. Liu, T. Nissinen, S. Granroth, A. Närvänen, M. Suvanto, H. A. Santos, V. P. Lehto, *Mol. Pharm.* **2015**, *12*, 4038–4047.

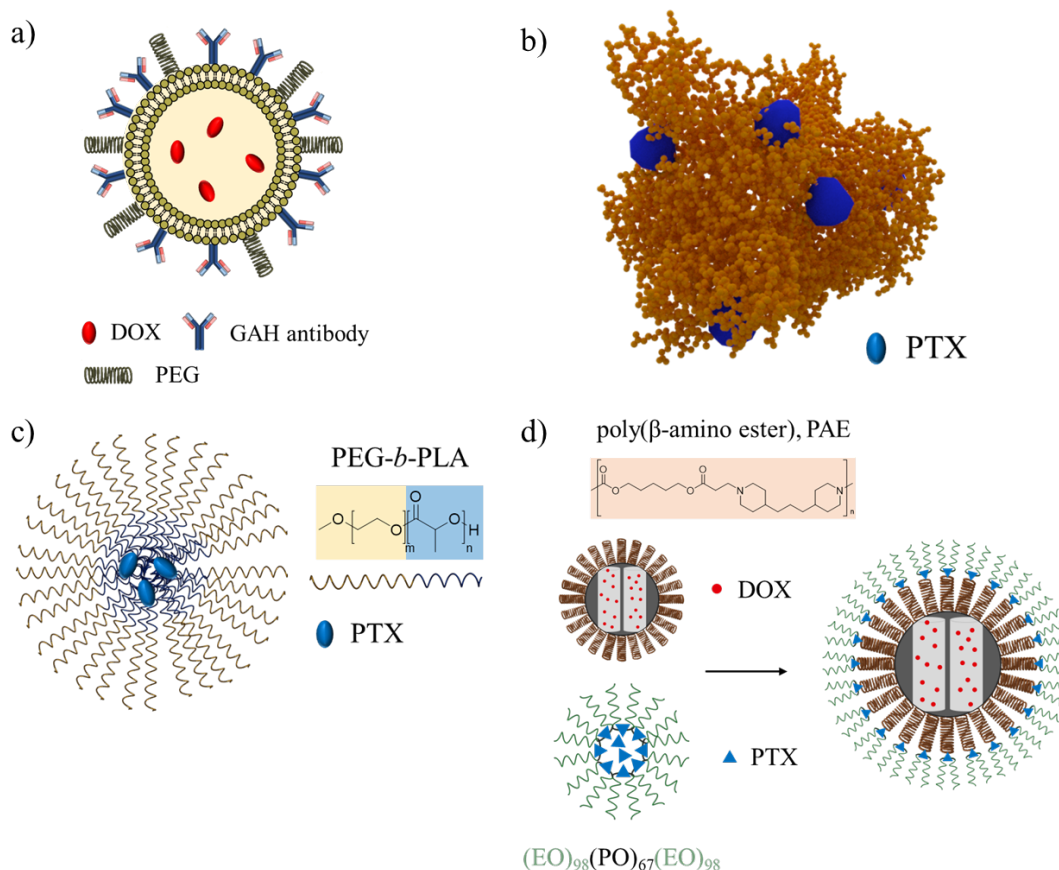


**Figure 1.7.** Schematic representations of a) PEG immunoliposome for DOX delivery. b) Abraxane<sup>®</sup>, albumin-PTX conjugate. c) Genexol<sup>®</sup>, PEG-*b*-PLA based micelle for PTX transport. d) Silicon-polymer coated nanoparticle for simultaneous delivery of DOX and PTX.

*Vectors and drug conjugates.* In general terms, most strategies used to design prodrug compounds rely on enzymatic reactions to trigger the formation of the active drug. However, high demands exist on finding enzymes capable of trigger the desired reaction and being specific to the prodrug substrate. Thus, Directed Enzyme Prodrug Therapies (DEPTs) use exogenous enzymes to activate the prodrugs and are particularly interesting in cancer chemotherapies.<sup>56</sup> Depending on the strategy used to reach the target site and introduce the exogenous genetic information or the enzyme itself by the help of vectors, DEPTs can be further classified in: antibody-directed enzyme prodrug therapy (ADEPT),<sup>57</sup> polymer-directed enzyme prodrug therapy (PDEPT),<sup>58</sup> gene-directed enzyme prodrug therapy (GDEPT),<sup>59</sup> virus-directed enzyme prodrug therapy

<sup>56</sup> V. V. Padma, *BioMedicine* **2015**, *5*, 1–6.

<sup>57</sup> S. K. Sharma, K. D. Bagshawe, *Adv. Drug Deliv. Rev.* **2017**, *118*, 2–7.

<sup>58</sup> A. Scomparin, H. F. Florindo, G. Tiram, E. L. Ferguson, R. Satchi-Fainaro, *Adv. Drug Deliv. Rev.* **2017**, *118*, 52–64.

<sup>59</sup> J. Zhang, V. Kale, M. Chen, *AAPS J.* **2015**, *17*, 102–110.

(VDEPT)<sup>60</sup> and, bacterial-directed enzyme prodrug therapy (BDEPT).<sup>61</sup> Figure 1.9 shows a schematic representation of such therapies.

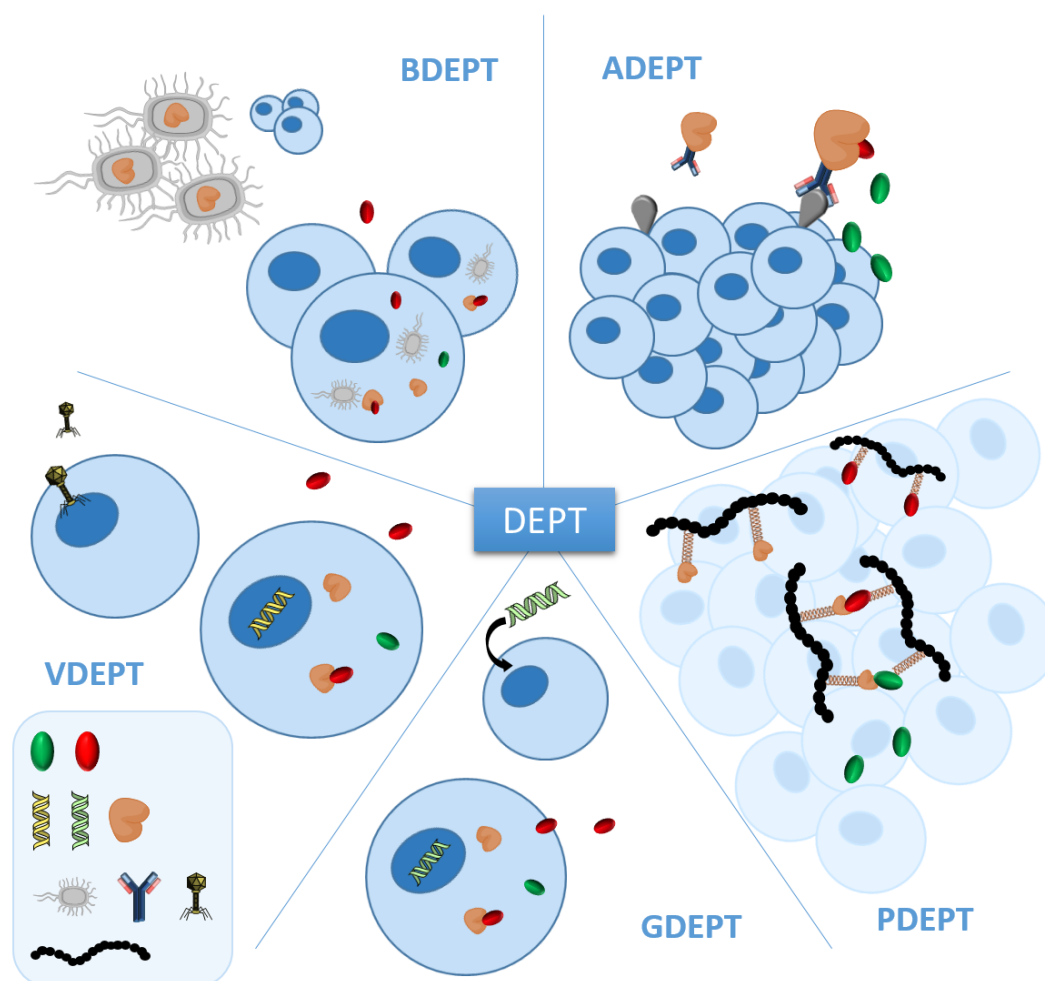


**Figure 1.9.** Directed Enzyme Prodrug Therapies. Legend, from left to right and up to bottom: Active drug, prodrug, viral genome, gene, enzyme, bacteria, antibody, virus, and polymer.

Among all therapies, ADEPT is widely used and consists of an antibody designed against a tumour antigen linked to the prodrug-activating enzyme (Figure 1.9). After exposure to tumour cells (blue), the prodrug (red) is administered and then converted into the active drug (green) by reaction with the enzyme (orange). For instance, between 1991 and 1993 Bagshawe carried out the first clinical trials with ADEPT in humans.<sup>62</sup> Then, monoclonal antibody A5B7<sup>63</sup> was conjugated to carboxypeptidase

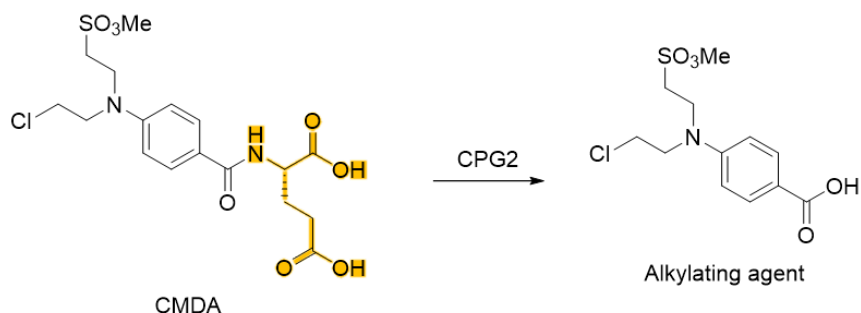
<sup>60</sup> N. Habbabeh, R. Karaman (2014) *Virus directed Enzyme Prodrug Therapy (VDEP) in Prodrugs Design-A New Era*, Nova Publisher, DOI: 10.13140/2.1.2198.5606

<sup>61</sup> P. Lehouritis, C. Springer, M. Tangney, *J. Control. Release* **2013**, *170*, 120–131.

<sup>62</sup> K. D. Bagshawe, *Adv. Pharmacol.* **1993**, 99–121.

<sup>63</sup> P. J. Harwood, D. W. Britton, P. J. Southall, G. M. Boxer, G. Rawlins, G. T. Rogers, *Br. J. Cancer* **1986**, *54*, 75–82.

G2<sup>64</sup> and N-(4-((2-chloroethyl) (2-mesyloxyethyl)- amino)benzoyl)-L-glutamic acid prodrug (CMDA, Scheme 1.5).<sup>65</sup>



**Scheme 1.5.** Nitrogen Mustard Prodrug used in Antibody Directed Enzyme Therapy.

Further clinical studies<sup>66</sup> unveiled promising results for the use of ADEPT in targeting and treating tumours. In parallel, around 1997 Marais and collaborators faced the same challenge using GDEPT.<sup>67</sup>

**Supramolecular carriers.** In addition to covalent bondage between the drug and the carrier, supramolecular chemistry offers the possibility of non-covalent transport. In the context of drug delivery, supramolecular materials have gained relevance and use during the last decades.<sup>68</sup> Hence, the supramolecular approach offers the ability of specific molecular recognition, selective transport or control release, being those significant outlines in drug delivery.

**Supramolecular affinity: drug guest-macrocylic host.** Drug-Macrocycle complexes were firstly used in drug delivery to enhance the aqueous solubility of the drugs, increase their chemical stability or prevent them from undesired metabolic reactions before reaching the target site. Normally, macrocycles used for this purpose are amphiphilic, with the ability to accommodate the drug in their hydrophobic cavity (Figure 1.10).

<sup>64</sup> S. Rowsell, R. A. Pauptit, A. D. Tucker, R. G. Melton, D. M. Blow, P. Brick, *Structure* **1997**, *5*, 337–347.

<sup>65</sup> C. J. Springer, P. Antoniw, K. D. Bagshawe, F. Searle, G. M. F. Bisset, M. Jarman, *J. Med. Chem.* **1990**, *33*, 677–681.

<sup>66</sup> a) M. P. Napier, S. K. Sharma, C. J. Springer, K. D. Bagshawe, A. J. Green, J. Martin, S. M. Stribbling, N. Cushen, D. O'Malley, R. H. J. Begent, *Clin. Cancer Res.* **2000**, *6*, 765–772. b) R. J. Francis, S. K. Sharma, C. Springer, A. J. Green, L. D. Hope-Stone, L. Sena, J. Martin, K. L. Adamson, A. Robbins, L. Gumbrell, D. O'Malley, E. Tsiompanou, H. Shahbakhti, S. Webley, D. Hochhauser, A. J. Hilson, D. Blakey, R. H. J. Begent, *Br. J. Cancer* **2002**, *87*, 600–607.

<sup>67</sup> R. Marais, R. A. Spooned, S. M. Stribbling, Y. Light, J. Martin, C. J. Springer, *Nat. Biotechnol.* **1997**, *15*, 1373–1377.

<sup>68</sup> a) M. J. Webber, R. Langer, *Chem. Soc. Rev.* **2017**, *46*, 6600–6620. b) M. J. Webber, E. A. Appel, E. W. Meijer, R. Langer, *Nat. Mater.* **2015**, *15*, 13–26.

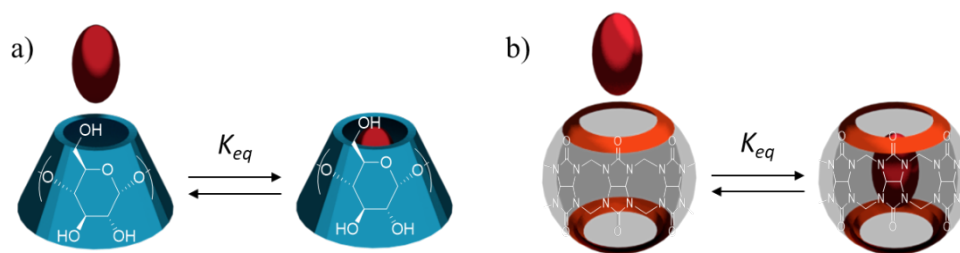


**Figure 1.10.** Schematic representation of a) cyclodextrin-drug complex and b) cucurbituril-drug complex.  $K_{eq}$  represents the binding constant with the guest (red).

First molecules used in this field were cyclodextrins (CDs),<sup>69</sup> which are glucose-based macrocycles produced as a result of enzymatic degradation of starch.<sup>70</sup> From a 3D point of view, they present a torus or truncated cone shape because of the chair conformation of the oligosaccharides. Commonly, the CDs can be formed by 6, 7, and 8 glucose units: named  $\alpha$ ,  $\beta$ , and  $\gamma$ , respectively.

Cyclodextrins were firstly introduced in the pharmaceutical market as excipients due to their properties as solubility enhancers and drug carriers,<sup>71</sup> while increasing the stability of the drug by its isolation from the medium. Nowadays cyclodextrins are the most clinically advanced supramolecular entities used for drug delivery and are used in at least 35 clinically approved pharmaceutical products (as of 2013).<sup>69</sup>

An interesting example of drug complexation with cyclodextrins is the work published by Monnaert and collaborators.<sup>72</sup> In their research, they studied the transport of DOX across the blood-brain barrier (BBB) with the use of  $\gamma$ -CD and HP- $\gamma$ -CD (hydroxypropyl) finding a significant increase in permeability.

In a similar vein, cucurbit[ $n$ ]urils (CB[ $n$ ]) are macrocycles, also used for drug delivery. CBs are formed by condensing glycoluril and formaldehyde under acidic conditions.<sup>73</sup> The common numbers of glycoluril units found for CBs are 5, 6, 7, 8, and 10. In particular, CB[7] is widely used because of its great ability to complex a variety of guests, and in some cases, showing higher binding constants than its CD analogues.<sup>74</sup> In

<sup>69</sup> a) S. V. Kurkov, T. Loftsson, *Int. J. Pharm.* **2013**, *453*, 167–180. b) R. Challa, A. Ahuja, J. Ali, R. K. Khar, *AAPS PharmSciTech* **2005**, *6*, 329–357. c) J. Zhang, P. X. Ma, *Adv. Drug Deliv. Rev.* **2013**, *65*, 1215–1233

<sup>70</sup> B. Gidwani, A. Vyas, *Biomed Res. Int.* **2015**, *2015*, 198268.

<sup>71</sup> M. E. Brewster, T. Loftsson, *Adv. Drug Deliv. Rev.* **2007**, *59*, 645–666.

<sup>72</sup> V. Monnaert, D. Betbeder, L. Fenart, H. Bricout, A. M. Lenfant, C. Landry, R. Cecchelli, E. Monflier, S. Tilloy, *J. Pharmacol. Exp. Ther.* **2004**, *311*, 1115–20.

<sup>73</sup> S. J. Barrow, S. Kasera, M. J. Rowland, J. Del Barrio, O. A. Scherman, *Chem. Rev.* **2015**, *115*, 12320–12406.

<sup>74</sup> a) W. S. Jeon, K. Moon, S. H. Park, H. Chun, Y. H. Ko, J. Y. Lee, E. S. Lee, S. Samal, N. Selvapalam, M. V. Rekharsky, V. Sindelar, D. Sobransingh, Y. Inoue, A. E. Kaifer, K. Kim, *J.*

addition to small-molecules complexation, CB[ $n$ ]s have been used in specific recognition of peptide units.<sup>75</sup> For instance, Figure 1.11 shows two examples of cucurbit[ $n$ ]uril receptors. (a) Urbach and Kim took advantage of the ability of CB[7] to specifically bind Phenylalanine residue in a peptide chain, to enhance protein analysis by mass spectrometry.<sup>75a</sup> (b) Structure of CT008, a dinuclear platinum drug (up, blue), which is highly reactive to thiol-containing plasma proteins. The corresponding binding to CB[7] and CB[8], below, left and right respectively, protects the drug from premature chemical degradation.<sup>76</sup>

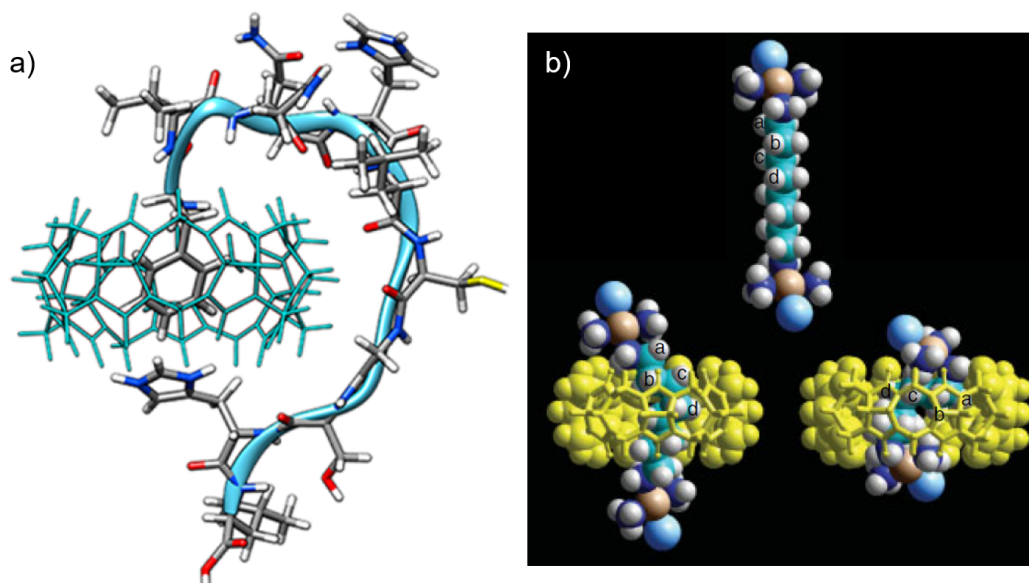


**Figure 1.11.** a) Lowest-energy theoretical structure of InsB peptide in complex with CB[7]. b) Dinuclear platinum CT008 and the corresponding complexes with CB[7] and CB[8]. Modified from reference 75a and 76 respectively.

In addition to CDs and CBs, other macrocyclic structures such as pillar[ $n$ ]arenes or calix[ $n$ ]arenes may be used in the field of drug delivery as solubility enhancers or drug encapsulators.<sup>77</sup> Unlike CBs and CDs, these macrocycles can be asymmetrically tuned in the face positions, which may be of interest for the design of drug delivery systems.<sup>78</sup>

*Am. Chem. Soc.* **2005**, *127*, 12984–12989. b) J. Mohanty, A. C. Bhasikuttan, W. M. Nail, H. Pal, *J. Phys. Chem. B* **2006**, *110*, 5132–5138.

<sup>75</sup> a) J. W. Lee, M. H. Shin, W. Mobley, A. R. Urbach, H. I. Kim, *J. Am. Chem. Soc.* **2015**, *137*, 15322–15329. b) L. C. Smith, D. G. Leach, B. E. Blaylock, O. A. Ali, A. R. Urbach, *J. Am. Chem. Soc.* **2015**, *137*, 3663–3669.

<sup>76</sup> A. I. Day, J. G. Collins (2012). *Supramolecular Chemistry: From Molecules to Nanomaterials*. John Wiley & Sons, Ltd. DOI: 10.1002/9780470661345

<sup>77</sup> Y. Zhou, H. Li, Y. W. Yang, *Chinese Chem. Lett.* **2015**, *26*, 825–828.

<sup>78</sup> a) R. Lavendomme, S. Zahim, G. De Leener, A. Inthasot, A. Mattiuzzi, M. Luhmer, O. Reinaud, I. Jabin, *Asian J. Org. Chem.* **2015**, *4*, 710–722. b) N. L. Strutt, H. Zhang, S. T. Schneebeli, J. F. Stoddart, *Acc. Chem. Res.* **2014**, *47*, 2631–2642.

*Encapsulation with supramolecular network materials.* An important aspect of drug delivery and design takes into account the need for controlled release. In this regard, supramolecular chemistry can be used to build three-dimensional porous materials or hydrophilic-hydrophobic multi-phase structures to entrap drugs which may be further released in a specific environment. To date, hydrogels are the most used supramolecular biomaterials for drug and protein release.<sup>68</sup>

Hydrogels are 3D hydrophilic cross-linked polymer networks<sup>79</sup> with the ability to encapsulate drugs by controlling the degree of supramolecular crosslinking during the hydrogel formation.<sup>80</sup> For instance, Hartgerink and collaborators developed a peptide-based nanofibrous hydrogel for release of suramin.<sup>81</sup> In this example, the highly sulfonated drug stabilizes the cationic fibre structure.

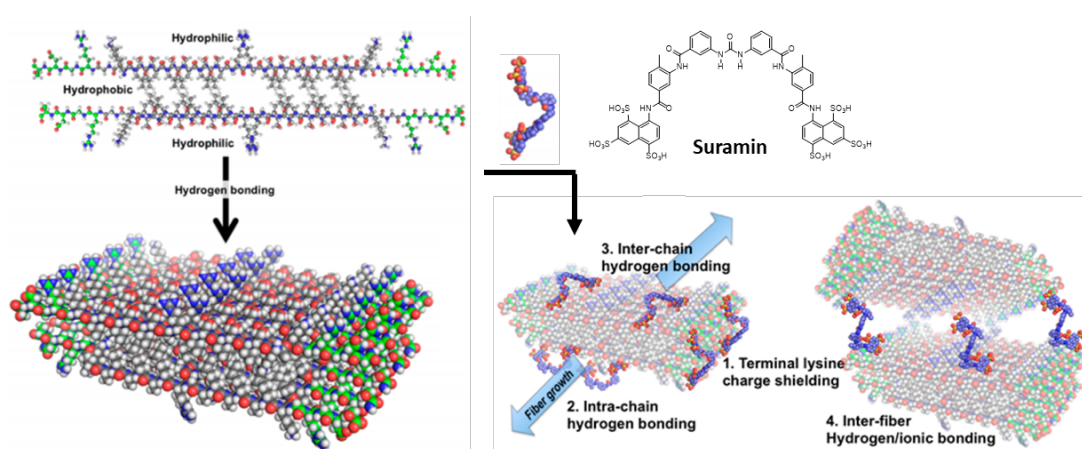


**Figure 1.12.** Hartgerink's supramolecular hydrogel for controlled release of suramin. Modified from ref. 81.

*Encapsulation with nanoscale supramolecular carriers.* In addition to entangled supramolecular materials for drug encapsulation, discrete nanocarriers can selectively transport guests in a nanoscale. For example, Ma and collaborators developed polymeric-based nanoparticles for drug and gene delivery. Supramolecular assembly was achieved through a host-guest interaction between a cationic polymer and a hydrophobic polymer. (Figure 1.13).<sup>82</sup>

<sup>79</sup> a) R. Dong, Y. Pang, Y. Su, X. Zhu, *Biomater. Sci.* **2015**, *3*, 937–954. b) D. Yuan, B. Xu, *J. Mater. Chem. B* **2016**, *4*, 5638–5649.

<sup>80</sup> a) V. Yesilyurt, M. J. Webber, E. A. Appel, C. Godwin, R. Langer, D. G. Anderson, *Adv. Mater.* **2016**, *28*, 86–91. b) S. Fleming, R. V. Ulijn, *Chem. Soc. Rev.* **2014**, *43*, 8150–8177.

<sup>81</sup> V. A. Kumar, S. Shi, B. K. Wang, I. C. Li, A. A. Jalan, B. Sarkar, N. C. Wickremasinghe, J. D. Hartgerink, *J. Am. Chem. Soc.* **2015**, *137*, 4823–4830.

<sup>82</sup> J. Zhang, H. Sun, P. X. Ma, *ACS Nano* **2010**, *4*, 1049–1059.

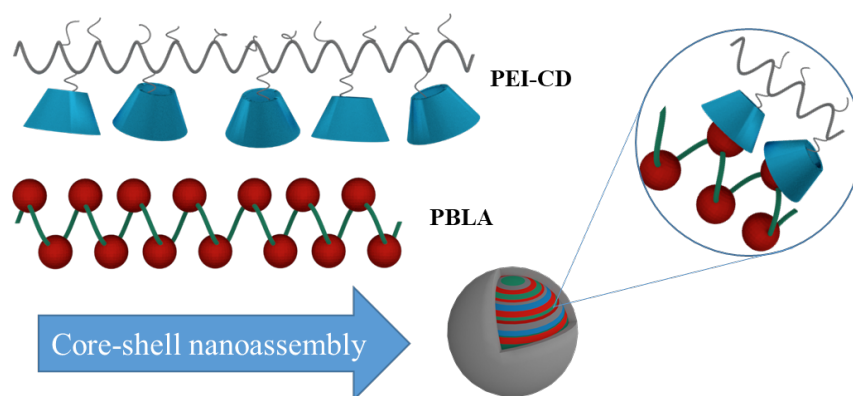


**Figure 1.13.** Branched polyethyleneimine-cyclodextrin conjugate (PEI-CD) assembled to poly- $\beta$ -benzyl L-aspartate (PBLA) forming nanoparticles. Complexation occurs between benzyl groups from PBLA (red) and cyclodextrins from PEI-CD (blue).

#### 1.1.4. Targeted Drug Delivery to Tumours

The unregulated growth of malignant cells which have the potential to spread to other body parts results in a range of diseases called cancer. When this excessive growth develops in a mass, it is considered a tumour. The World Health Organization (WHO) estimates around 18 million new cancer cases and almost 10 million cancer deaths in 2018. In 91 of 172 countries, cancer represents the first or second cause of death before age 70 (Figure 1.14), led by lung cancer (almost 20% of total cancer deaths) and followed by breast cancer (11.6% of incidence) and colorectal cancer (9.2% of mortality).<sup>83</sup>

Despite the success to some extent of several chemotherapeutics, the main drawbacks that face chemotherapy are the poor bioavailability, high-dose requirements, adverse side effects, low therapeutic indices of anticancer drugs together with the development of multiple drug resistance, and non-specific targeting. Hence, researchers are focused on developing new strategies and designs for targeted drug delivery to accomplish the demands of effective treatments for complex diseases like cancer.

<sup>83</sup> F. Bray, J. Ferlay, I. Soerjomataram, R. L. Siegel, L. A. Torre, A. Jemal, *CA Cancer J. Clin.* **2018**, *68*, 394–424

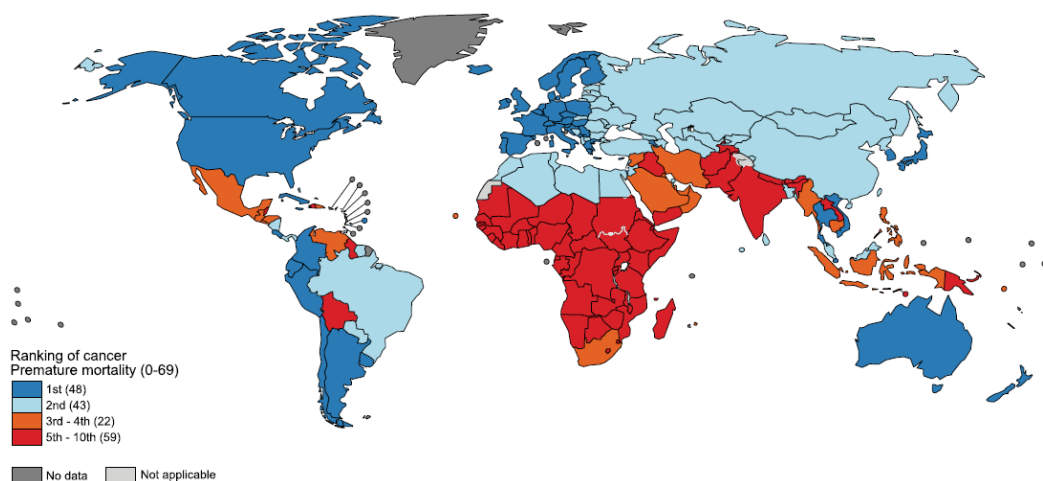


**Figure 1.14.** Ranking of cancer premature mortality (0-69 years of age). Reproduced from ref. 83.

The early stage of cancer treatment starts by prevention, the most cost-effective long-term strategy for the control of the disease. Raising awareness and reducing the exposure to cancer risk factors ensure that people are provided with the information to adopt healthy lifestyles. However, when the disease appears, early detection and diagnosis increases the chances for successful treatment and thus the survival. From the medicinal chemistry point of view, researchers play a key role in the treatment stage of cancer and it is necessary to find specific and selective chemotherapies, reducing their toxicity and side effects to develop sophisticated targeting strategies for an effective treatment.

In the Supramolecular Chemistry Group at the UIB, part of our research focuses on the use of squaramides as building blocks in medicinal chemistry and chemical biology. Their remarkable properties, especially their easy synthetic access, good solubility properties, and good biocompatibility, have led us to explore their potential in drug delivery.

## 1.2. SQUARAMIDES: FROM SUPRAMOLECULAR CHEMISTRY TO CHEMICAL BIOLOGY

Squaramides are the 3,4-diamino derivatives of squaric acid. The structure consists of a cyclobutenedione ring with two amino groups bonded directly to the ring. The lone pair on the nitrogen atom is delocalized through the cyclobutenedione system which shortens the C-N bond and consequently, confers a rotational restriction through it of approximately ( $63 \text{ kJ}\cdot\text{mol}^{-1}$ )<sup>84</sup> (Figure 1.15a). Thus, squaramides can exist in different conformations (Figure 1.15b) being the E,E the less preferred due to the steric hindrance.

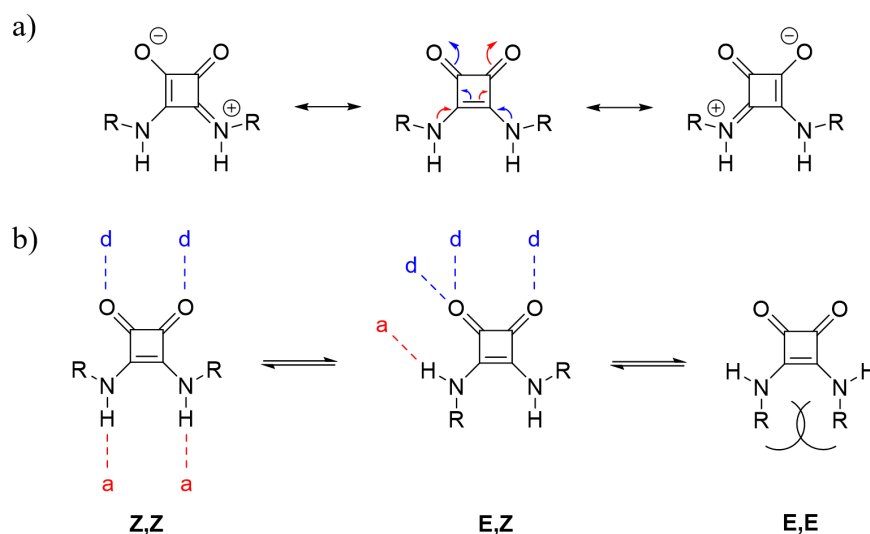


**Figure 1.15.** a) Zwitterionic resonant forms for a secondary squaramide. b) Conformational equilibrium for secondary squaramides and corresponding hydrogen bond pattern.

Secondary squaramides can form up to four hydrogen bonds, combining two donor squaramidic protons and two acceptor carbonyl groups. In addition to the conformational properties, delocalization of the charge over the cyclobutenedione ring strengthens the hydrogen bonding ability of squaramides. Depending on the conformation adopted, the resulting hydrogen bond pattern is different.

Costa, Frontera, and collaborators have reported their ability to hydrogen bond to acceptors, donors and mixed acceptor-donor groups making them unique scaffolds for complexing both cationic and anionic species.<sup>85</sup> Their remarkable hydrogen bond donor

<sup>84</sup> M. C. Rotger, M. N. Piña, A. Frontera, G. Martorell, P. Ballester, P. M. Deyà, A. Costa, *J. Org. Chem.* **2004**, *69*, 2302–2308.

<sup>85</sup> a) D. Quiñero, A. Frontera, P. Ballester, P. M. Deyà, *Tetrahedron Lett.* **2000**, *41*, 2001–2005. b) S. Tomàs, R. Prohens, M. Vega, M. C. Rotger, P. M. Deyà, P. Ballester, A. Costa, *J. Org. Chem.* **1996**, *61*, 9394–9401. c) R. Prohens, M. C. Rotger, M. N. Piña, P. M. Deyà, J. Morey, P. Ballester, A. Costa, *Tetrahedron Lett.* **2001**, *42*, 4933–4936.

and acceptor character comes from the enhancement of the aromaticity of the squaramide scaffold upon hydrogen bond formation which sets a clear difference with their chemical analogues ureas (Figure 1.16).<sup>86</sup>

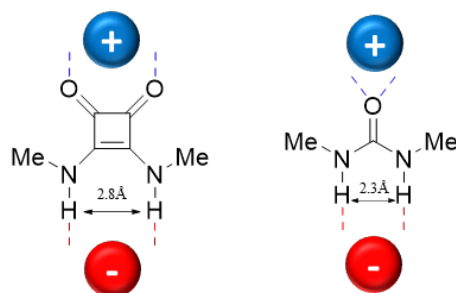


**Figure 1.16.** Comparison between squaramide and urea hydrogen bond patterns and N-H distances.

Due to its properties, squaramides are widely used in organo- and H-bond catalysis. In comparison with thioureas, extensively used in the field,<sup>87</sup> the larger distance between the NH centres of the squaramide moiety and their higher acidity, usually implies the formation of stronger hydrogen-bonds with nitro, carbonyl, or imino substrates among others (Figure 1.17a), converting squaramides in good modifiable scaffolds for catalysis. Additionally, chiral functionalization of squaramide-catalysts may lead to enantioselective reactions (Figure 1.17b).<sup>88</sup>

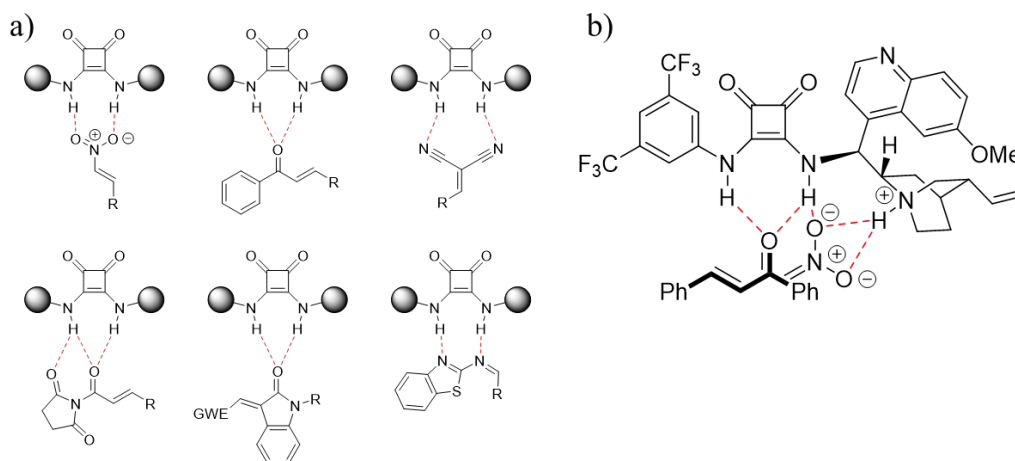


**Figure 1.17.** a) Hydrogen bond-activation of substrates by squaramides. b) Transition state of enantioselective Michael addition of nitroalkanes to chalcones by a chiral squaramide catalyst described by Du.

<sup>86</sup> R. Ian Storer, C. Aciro, L. H. Jones, *Chem. Soc. Rev.* **2011**, *40*, 2330–2346.

<sup>87</sup> a) O. V. Serdyuk, C. M. Heckel, S. B. Tsogoeva, *Org. Biomol. Chem.* **2013**, *11*, 7051–7071.

b) Žabka, M.; Šebesta, R. *Molecules* **2015**, *20*, 15500–15524.

<sup>88</sup> B. L. Zhao, J. H. Li, D. M. Du, *Chem. Rec.* **2017**, *17*, 994–1018.

The concept of self-assembly was firstly defined by Jean-Marie Lehn as *the process by which specific components spontaneously assemble in a highly selective fashion into a well-defined, discrete supramolecular architecture*.<sup>89</sup>

The self-assembly process is mainly driven by non-covalent interactions, leading to a cooperative aggregation which shows different properties than the corresponding discrete monomeric unit. Taking advantage of their ability of hydrogen bonding, squaramides are excellent scaffolds for supramolecular and self-assembly based applications<sup>90</sup> such as molecular recognition,<sup>91</sup> supramolecular catalysis,<sup>92</sup> materials science,<sup>93</sup> and sensing.<sup>94</sup>

---

<sup>89</sup> A. Pfeil, J. M. Lehn, *J. Chem. Soc. Chem. Commun.* **1992**, 838–840.

<sup>90</sup> L. A. Marchetti, L. K. Kumawat, N. Mao, J. C. Stephens, R. B. P. Elmes, *Chem* **2019**, *5*, 1–88.

<sup>91</sup> a) J. Alemán, A. Parra, H. Jiang, K. A. Jørgensen, *Chem. Eur. J.* **2011**, *17*, 6890–6899.

<sup>92</sup> a) P. Chauhan, S. Mahajan, U. Kaya, D. Hack, D. Enders, *Adv. Synth. Catal.* **2015**, *357*, 253–281. b) F. E. Held, S. B. Tsogoeva, *Catal. Sci. Technol.* **2016**, *6*, 645–667. c) X. Han, H. Zhou, C. Dong, *Chem. Rec.* **2016**, *16*, 897–906. d) Q. Sun, H. Zhu, Y. Chen, X. Yang, X. Sun, Q. Lin, *Angew. Chem. Int. Ed.* **2015**, *54*, 13253–13257. e) X. Zhang, Z. Zhang, J. Boissonault, S. M. Cohen, *Chem. Commun.* **2016**, *52*, 8585–8588.

<sup>93</sup> a) B. Soberats, L. Martínez, E. Sanna, A. Sampedro, C. Rotger, A. Costa, *Chem. Eur. J.* **2012**, *18*, 7533–7542. b) Y. Ohsedo, M. Miyamoto, A. Tanaka, H. Watanabe, *New J. Chem.* **2013**, *37*, 2874–2880. c) V. Saez Talens, P. Englebienne, T. T. Trinh, W. E. M. Noteborn, I. K. Voets, R. E. Kieltyka, *Angew. Chem. Int. Ed.* **2015**, *54*, 10502–10506. d) C. López, M. Ximenis, F. Orvay, C. Rotger, A. Costa, *Chem. Eur. J.* **2017**, *23*, 7590–7594. e) S. Park, J. Uchida, K. Urushibara, H. Kagechika, T. Kato, A. Tanatani, *Chem. Lett.* **2018**, *47*, 601–604.

<sup>94</sup> a) R. Prohens, G. Deslongchamps, P. Ballester, A. Costa, *Angew. Chem. Int. Ed.* **1999**, *38*, 2208–2211. b) A. Rostami, C. J. Wei, G. Guørin, M. S. Taylor, *Angew. Chem. Int. Ed.* **2011**, *50*, 2059–2062. c) P. Manesiotis, A. Riley, B. Bollen, *J. Mater. Chem. C* **2014**, *2*, 8990–8995.

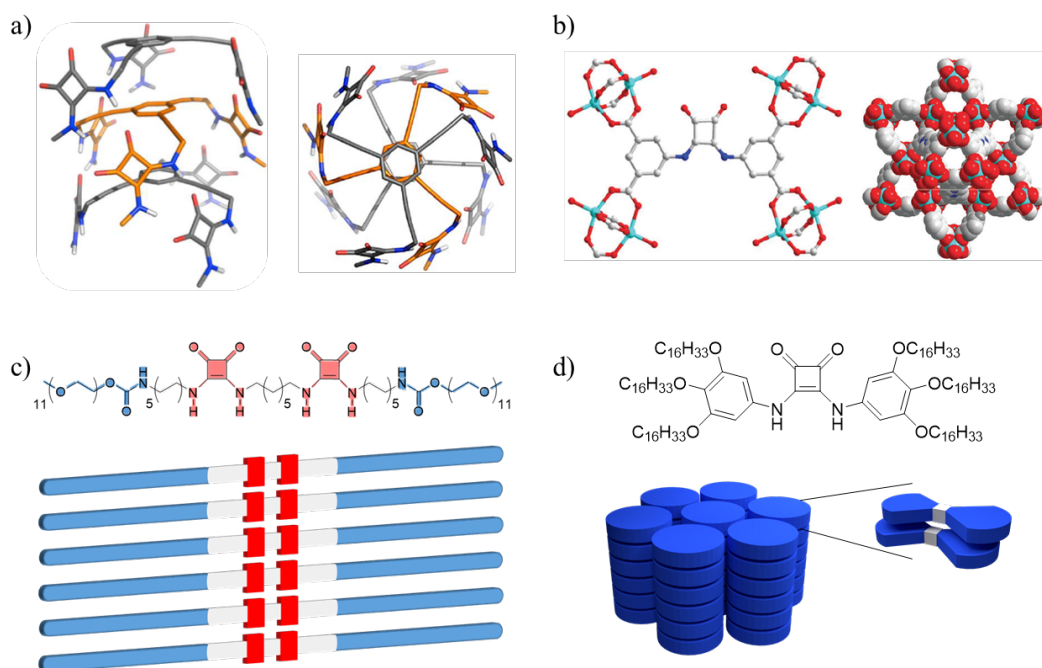


**Figure 1.18.** Hydrogen bond-based self-assembly of squaramides: a) tripodal receptor<sup>93a</sup>, b) MOF<sup>92e</sup>, c) supramolecular polymer<sup>93c</sup> and d) liquid crystal.<sup>93e</sup>

### 1.2.1. Squaramide Compounds in Chemical Biology and Medicinal Chemistry

Given the unique described properties of squaramides, their developed synthetic access<sup>95</sup> and their chemical stability in aqueous media<sup>96</sup> researchers have paid attention to their potential use in biological applications.

One of the first introductions of squaramides in the biological field was their use as isosteric replacements for a large variety of carboxylate groups and amino acids. Since the first published incorporation of a squarate in replacement of a carboxylic acid in phosphonoformic acid by Kim and Misco in 1992,<sup>97</sup> expansion to other substrates has followed.

<sup>95</sup> a) A. H. Schmidt, *Synthesis*, **1980**, 961 and references therein. b) A. Muktanti, M. Periasamy, *ARKIVOC*, **2005**, 48 and references therein. c) E. W. Neuse, B. R. Green, *J. Org. Chem.* **1974**, *39*, 3881–3886. d) L. F. Tietze, M. Arlt, M. Beller, K. H. Gluesenkamp, E. Jaehde, M. F. Rajewsky, *Chem. Ber.*, **1991**, *124*, 1215–1221. e) A. Rostami, A. Colin, X. Y. Li, M. G. Chudzinski, A. J. Lough, M. S. Taylor, *J. Org. Chem.* **2010**, *75*, 3983–3992.

<sup>96</sup> a) P. Sejwal, Y. Han, A. Shah, Y. Y. Luk, *Org. Lett.* **2007**, *9*, 4897–4900. b) M. Ximenis, E. Bustelo, A. G. Algarra, M. Vega, C. Rotger, M. G. Basallote, A. Costa, *J. Org. Chem.* **2017**, *82*, 2160–2170.

<sup>97</sup> U. Kim, P. F. Misco, *Tetrahedron Lett.* **1992**, *33*, 3961–3962.

For instance, squaramic acid was introduced as a bioisostere in the design of antagonists of angiotensin II by Wyeth researchers.<sup>98</sup> They further developed the idea and applied it to convert amino acids to their respective squaric isosters;<sup>99</sup> their application and incorporation to a *N*-methyl-D-aspartic acid (NDMA) antagonist program ended in the design of EAA-90 (Perzinfotel).<sup>100</sup> In the particular case of this drug, a prodrug strategy had to be carried out to improve its bioavailability (Figure 1.19).<sup>101</sup>

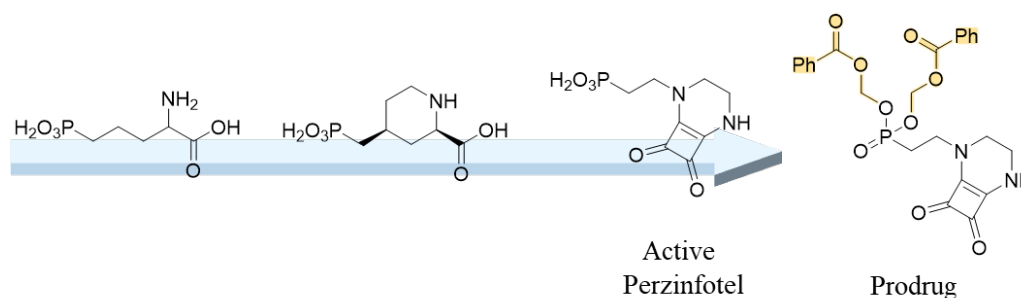


**Figure 1.19.** Structural evolution of Perzinfotel via isosterism-based rational design and final structure of prodrug.

Bioisosterism with phosphates has also been used in the modified-nucleotide design. Sekine and collaborators explored the properties of squaramide-based nucleotide analogues being of interest as potential biologically active compounds as antiviral and anticancer agents (Figure 1.20a).<sup>102</sup>

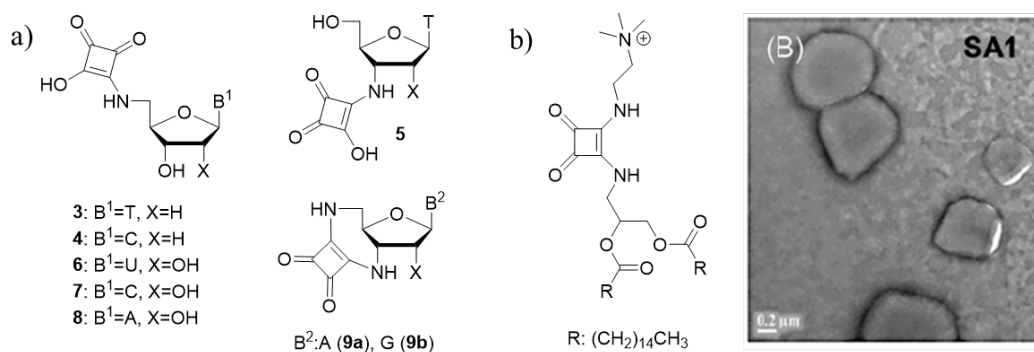


**Figure 1.20.** a) Structures of squaramide-type nucleotide analogues. b) TEM image of squaramide-based liposomes.

<sup>98</sup> R. M. Soll, W. A. Kinney, J. Primeau, L. Garrick, R. J. McCaully, T. Colatsky, G. Oshiro, C. H. Park, D. Hartupée, V. White, J. McCallum, A. Russo, J. Dinish, A. Wojdanb, *Bioorganic Med. Chem. Lett.* **1993**, *3*, 757–760.

<sup>99</sup> E. F. Campbell, A. K. Park, W. A. Kinney, R. W. Fengl, L. S. Liebeskind, *J. Org. Chem.* **1995**, *60*, 1470–1472.

<sup>100</sup> W. A. Kinney, M. Abou-Gharbia, D. T. Garrison, J. Schmid, D. M. Kowal, D. R. Bramlett, T. L. Miller, R. P. Tasse, M. M. Zaleska, J. A. Moyer, *J. Med. Chem.* **1998**, *41*, 236–246.

<sup>101</sup> R. B. Baudy, J. A. Butera, M. A. Abou-Gharbia, H. Chen, B. Harrison, U. Jain, R. Magolda, J. Y. Sze, M. R. Brandt, T. A. Cummins, D. Kowal, M. N. Pangalos, B. Zupan, M. Hoffmann, M. May, C. Mugford, J. Kennedy, W. E. Childers, *J. Med. Chem.* **2009**, *52*, 771–778.

<sup>102</sup> K. Seio, T. Miyashita, K. Sato, M. Sekine, *Eur. J. Org. Chem.* **2005**, 5163–5170.

Recently, Manna and collaborators have described a new series of squaramide-based amphiphiles leading to stable liposomes in aqueous solution (Figure 1.20b).<sup>103</sup>

Meanwhile, control over the formation or preference on the E,Z conformation can be achieved by establishing intramolecular hydrogen bonds. Recently, our group has developed several foldable squaramide-based modules as a strategy to fold peptidomimetic compounds.<sup>104</sup>

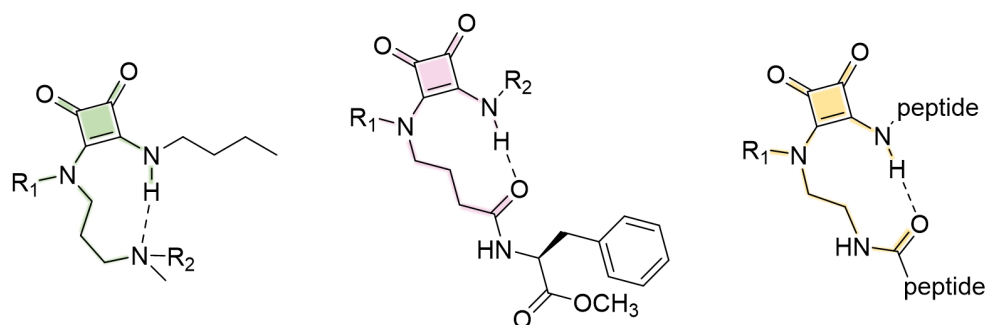
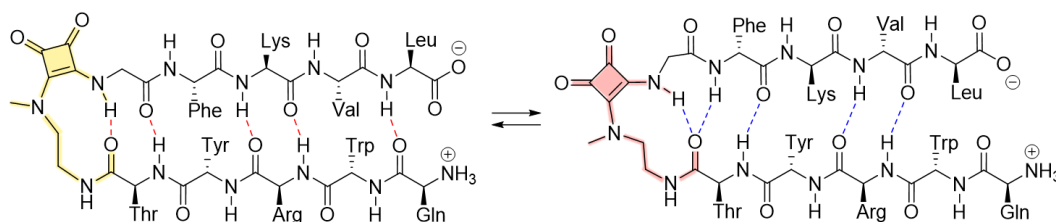


**Figure 1.21.** Structures of the E,Z squaramides. Foldable modules are highlighted in green, purple and yellow, where nine- and ten-membered rings are formed respectively.

Figure 1.21 shows three hydrogen bond-driven squaramidic turns. Stabilization is achieved by forming nine (green) and ten (pink and yellow respectively) membered rings which result in the folding of the peptidomimetic compounds.

The incorporation of the turning module into the  $\alpha$ -peptide sequence of a decapeptide by conventional solid-phase peptide synthesis, promoted its folding leading to hairpin structures in water, giving both  $\beta$ - and  $\alpha$ -turns.<sup>105</sup> (Scheme 1.6).



**Scheme 1.6.** Representation of the conformational equilibrium of the hairpin in water, giving both  $\alpha$ SQ- and  $\beta$ SQ-turns.

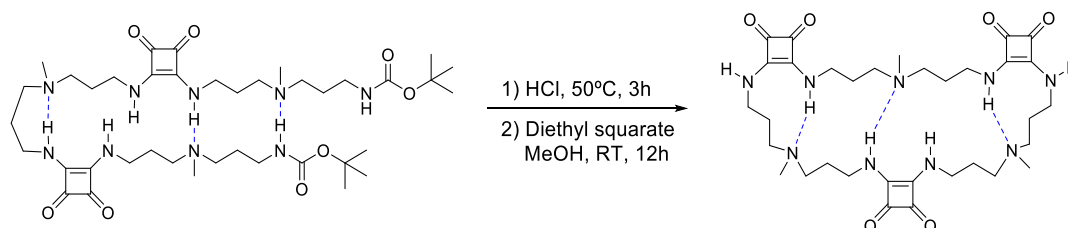
The ability to form hydrogen bonds has already been exploited in our group to study the macrocyclization on oligomeric squaramide compounds promoting the formation of

<sup>103</sup> A. Saha, S. Panda, S. Paul, D. Manna, *Chem. Commun.* **2016**, 52, 9438–9441.

<sup>104</sup> L. Martínez-Crespo, E. C. Escudero-Adán, A. Costa, C. Rotger, *Chem. Eur. J.* **2018**, 24, 1–13.

<sup>105</sup> L. Martínez, G. Martorell, Á. Sampetro, P. Ballester, A. Costa, C. Rotger, *Org. Lett.* **2015**, 17, 2980–2983.

intramolecular hydrogen bonds.<sup>106</sup> In particular, the condensation of hydrogen bond-preorganized oligomers led to efficient macrocyclization (Scheme 1.7).



**Scheme 1.7.** Preorganized macrocyclization reaction for the preparation of a macrocycle with three squaramide units.

Additionally, some of the synthesized cyclic-oligosquaramides have shown kinase inhibition and antitumor activity.<sup>107</sup>

Like squaramides, squaramide-based macrocycles present the ability to interact and complex anions such as the phosphate groups of cell membrane phospholipids. Specifically, the 2-squaramide macrocycle functionalized with a BODIPY fluorophore (Figure 1.22) demonstrated its capacity to interact with the cell membrane triggering its internalization through endocytosis mechanism. Colocalization studies showed their location at late endosomes.<sup>108</sup>

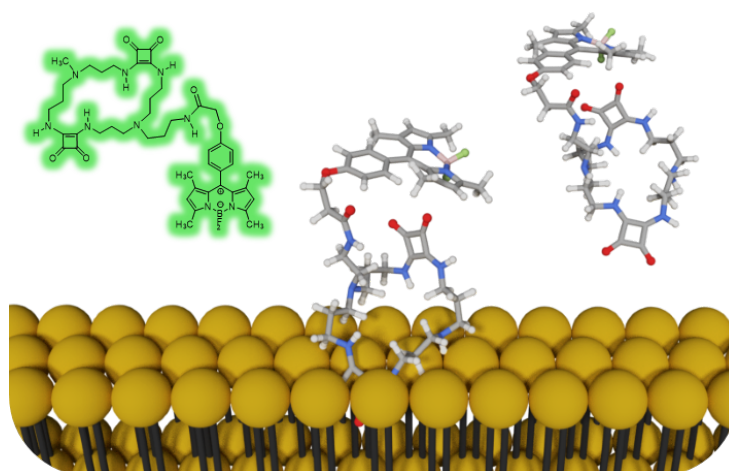


**Figure 1.22.** Structure of fluorescent macrocyclic squaramide and schematic representation of its cell internalization.

Interesting breakthroughs have resulted in recent years regarding the ability of squaramides to complex anions and cations. Pioneered by Gale and collaborators, they

<sup>106</sup> C. Rotger, M. N. Piña, M. Vega, P. Ballester, P. M. Deyà, A. Costa, *Angew. Chem. Int. Ed.* **2006**, *45*, 6844–6848.

<sup>107</sup> P. Villalonga, S. Fernández de Mattos, G. Ramis, A. Obrador-Hevia, A. Sampedro, C. Rotger, A. Costa, *ChemMedChem* **2012**, *7*, 1472–1480.

<sup>108</sup> A. Sampedro, R. Villalonga-Planells, M. Vega, G. Ramis, S. Ferna, P. Villalonga, A. Costa, C. Rotger, *Bioconj. Chem.* **2014**, *25*, 1537–1546.

explored the squaramide-based transport to carry anions and small molecules across the cell membrane by a combination of their lipophilicity and hydrogen-bond capacity (Figure 1.23).<sup>109</sup>

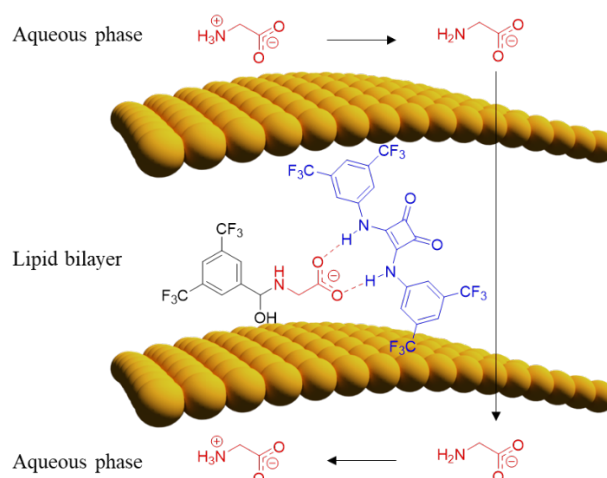


**Figure 1.23.** Squaramide-facilitated transport of glycine, involving a hemiaminal formation.

Recently, they have also demonstrated the mechanism of transport, defining the key role of squaramides acting as carriers instead of ion channels.<sup>110</sup>

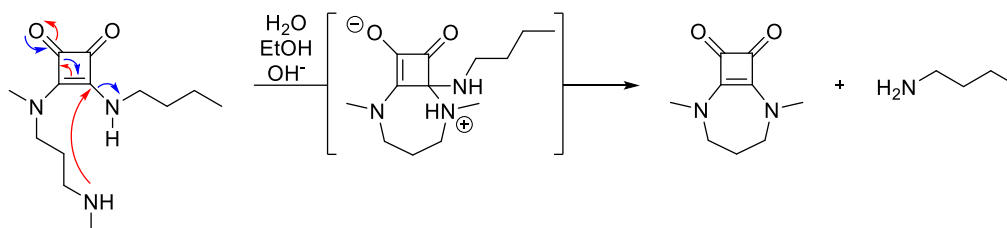
Meanwhile, hydrogen-bond driven self-assembly of squaramides has led to the formation of hydrogels. As discussed before, hydrogels stand for one of the most extended supramolecular materials for drug delivery. Precisely, our group has recently developed a biocompatible and non-cytotoxic supramolecular hydrogel based on a minimalist squaramide-squaramate hydrogelator. The resulting material is injectable and can be loaded with small zwitterionic molecules such as L-carnitine,  $\gamma$ -aminobutyric acid or a dipeptide D,L-Ala–D,L-Ala. Controlled release of such molecules is achieved and modulated by saline solutions (Figure 1.24a).<sup>93d</sup>

<sup>109</sup> X. Wu, N. Busschaert, N. J. Wells, Y. B. Jiang, P. A. Gale, *J. Am. Chem. Soc.* **2015**, *137*, 1476–1484.

<sup>110</sup> I. Marques, P. M. R. Costa, M. Q. Miranda, N. Busschaert, E. N. W. Howe, H. J. Clarke, C. J. E. Haynes, I. L. Kirby, A. M. Rodilla, R. Pérez-Tomás, P.A. Gale, V. Félix *Phys. Chem. Chem. Phys.* **2018**, *20*, 20796–20811.



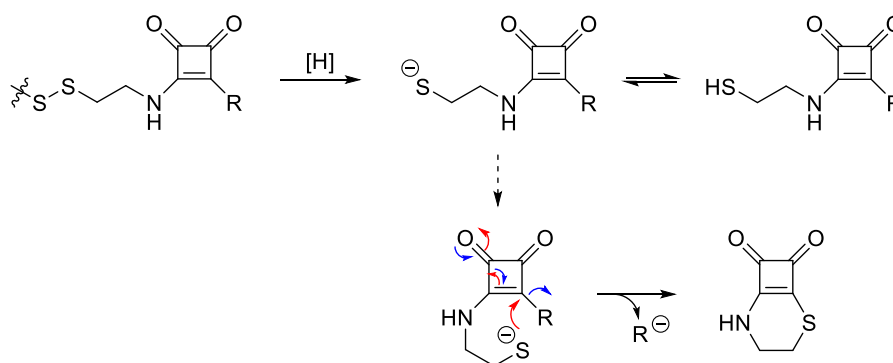
squaramides, in polar solvents or basic pH, cyclization spontaneously occurs by an intramolecular reaction (Scheme 1.8).<sup>112</sup>



**Scheme 1.8.** Intramolecular cyclization of a squaramide derivative.

We suggest that the presence of a methyl group in the squaramidic nitrogen favours the *E,Z* conformation. Consequently, spatial proximity between nucleophilic  $\gamma$ -methylamine and electrophilic carbon leads to a 1,4-addition. Then, the elimination of a primary amine (*n*-butylamine) gives the 7-membered dimethylated-squaramide ring.

From these results, Dr. Sampedro, a former member of our group, carried a further exploration of self-immolative squaramidic systems in his doctoral thesis. Briefly, he explored the possibility of introducing a thiol group as a trigger for the nucleophilic cyclization to further release the payload (Scheme 1.9).



**Scheme 1.9.** General mechanism of disulfide squaramide-based self-immolative systems.

As discussed before, disulfide groups are good triggers that activate under reductive conditions. In this example, free thiolate may undergo intramolecular cyclization to give the corresponding thiosquaramide. Thus, Dr. Sampedro developed self-immolative systems based on thiol triggers conjugated to fluorophores of different chemical nature to explore their kinetics of release. Hence, when a fluorogenic molecule is conjugated to the squaramide framework, the intrinsic fluorescence of the system decreases dramatically due to the squaramide quenching so the efficiency of the release can be monitored by the increase of fluorescence intensity in time.

<sup>112</sup> Unpublished results obtained by Dr. Luis Martínez, part of his doctoral thesis.

For instance, Figure 1.25 shows two compounds formed by a squaramide SIL conjugated to an off-on fluorescent system (**1** and **2**) and a trigger unit; both developed by Dr. Sampedro. Here, to trigger the fluorophore release reaction, tris(2-carboxiethyl) phosphine (TCEP), a reducing agent, was used. Both systems evolved to the desired free fluorophores (**3** and **4**) at physiologic pH and 37 °C.<sup>113</sup>

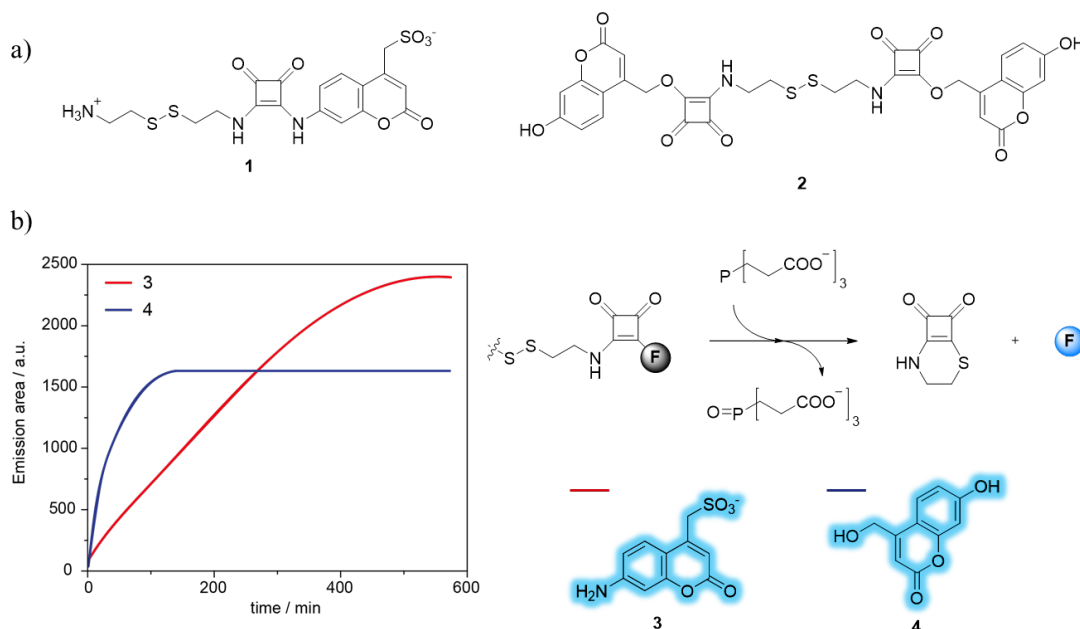


**Figure 1.25.** a) Chemical structures of fluorescent self-immolative systems. b) Evolution of fluorescence intensity spectra of aniline- (red) and alcohol- (blue) systems over time when triggering the reaction with TCEP at physiologic pH.

After 10 h, system **1** led to a 12 % release of **3**. On the other hand, the complete release of **4** was achieved in only 2h. As previously commented, the nucleofugacity of leaving group determines the release rate,<sup>13</sup> so the alkoxide is removed faster than the amine.

Taking into account all these precedents, this thesis explores the ability of squaramides to act as self-immolative linkers. From a minimalist model, to study the cyclization and release process, to a true drug-SIL-trigger conjugate.

<sup>113</sup> Unpublished results obtained by Dr. Ángel Sampedro, part of his doctoral thesis.



**2**

---

## **Objectives**



The project proposed in this thesis is based on the precedents found on the ability of some squaramides to undergo self-immolative disassembly through cyclization reactions. Hence, the main aim of this work is the development of squaramide-based self-immolative linkers applied to drug delivery.



**Scheme 2.1.** Self-immolative spacer base on a squaramidic scaffold.

In order to carry out this work, we establish the following objectives:

1. *Study of the chemical stability of squaramic esters in water.* In a first screening, we will study a small collection of squaramic ethyl ester derivatives bearing different terminal functionalities. Thus, we will define their chemical stability in aqueous solutions at different pH conditions, using 37 °C as the reference temperature to mimic biological environments.
2. *Define the chemical functionalities capable of act as nucleophiles (X) in the self-immolative squaramidic scaffold.* With the study of the aqueous stability of squaramate esters, we also pretend to define their hydrolysis pathway and the chemical functionalities capable of undergo the cyclisation reaction.
3. *Definition of the scope of chemical functionalities acting as leaving groups (Y) in the self-immolative squaramidic scaffold.* Using the optimised nucleophiles for triggering the cyclisation, we will explore the nature of leaving groups suitable to be released under physiological conditions. Hence, we will design and synthesise minimalist self-immolative systems bearing different leaving groups to study their release in different pH conditions.
4. *Study the effect of N-methylation of the squaramidic scaffold (R) in the cyclization process.* Previous work performed in our group showed that squaryl N-methylation would induce the folded conformation of some peptidomimetic squaramides. For our purpose, the folded conformation would increase the rate of cyclization, by placing more close in space the reactive centres. Therefore, based on these precedents, we will include squaryl N-methylated analogues in the design of the minimalist self-immolative systems mentioned in point 3 to evaluate their effect on the cyclization kinetics.
5. *Obtain a minimalist self-immolative system able to release a model bioactive relevant compound.* As proof of concept, and using the previously optimized design on the trigger nucleophile and the leaving group, we will synthesise a

---

representative self-immolative system bearing an antitumor drug. Thus, we will study the disassembly kinetics upon external activation in physiological conditions.

6. *Study of the biological activity of the self-immolative prodrug.* We will compare the biological activity of our prodrug with the intrinsic activity of the parent drug. Thus, we will explore both *in vitro* and cell culture studies to define the effect of the prodrug towards tumour cells.

3

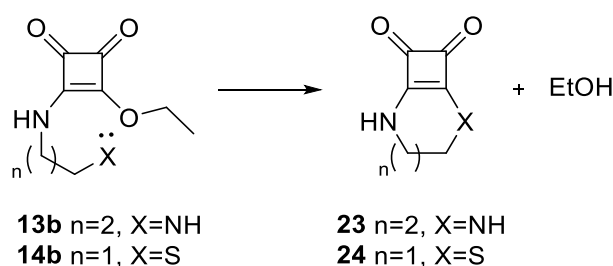
---

**Towards Self-Immolative Systems:  
Squaramate Esters**



### 3.1. MOTIVATION AND OBJECTIVES

Dr. Santiago Cañellas developed his Master Thesis under the title: *Squaramide-based Self-immolative Linkers: Kinetic Studies of Release*, where the hydrolytic stability of several squaramate esters was evaluated by UV spectroscopy at different pH values ranging from 3-9. The apparent rate constants were calculated for each process and preliminary results showed no hydrolysis under acidic conditions. Additionally, anchimeric assistance was observed when an amino-terminal group was present in the squaramate alkyl chain, increasing the hydrolysis rate in alkaline media. Noteworthy, for esters **13b** and **14b**, shown in Scheme 3.1, the intramolecular cyclization reaction competed with hydrolysis leading only to the corresponding cyclosquaramides **23** and **24** respectively.



**Scheme 3.1.** Intramolecular cyclization of squaramate esters **13b** and **14b**.

Based on the ability of squaramate esters **13b** and **14b** to easily undergo cyclization in aqueous media and taking into account the self-immolative capability of the fluorescent compounds **1** and **2**, explained in Chapter 1, it is sensible to assume that amino- and thio-squaramate derivatives are able to act as self-immolative linkers (SIL) through a cyclization mechanism.

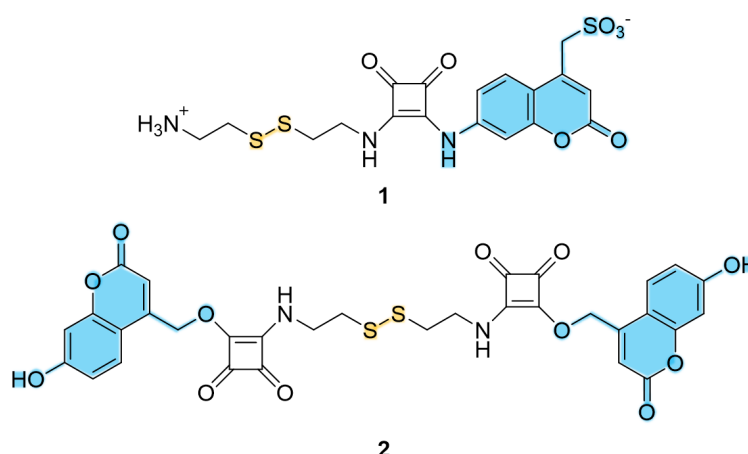


**Chart 3.1.** Chemical structures of disulfide-based self-immolative systems **1** and **2** synthesized by Dr. Sampedro. The fluorescent leaving group is highlighted in blue.

### 3.1.1. Objectives

Thus, the main goal of this chapter is to define the rate law for the aqueous degradation of squaramate ester derivatives and explore their potential as self-immolative linkers. The specific aims of this chapter are:

- The definition of the hydrolytic degradation pathway of esters **5-11**, **12b**, **13b**, and **14b**.
- The establishment of the rate law and the calculation of the rate constants for each reaction mechanism.
- The determination of the key parameters affecting the reactivity rate in order to design a minimalist squaramide-based SIL.

### 3.2. INTRODUCTION

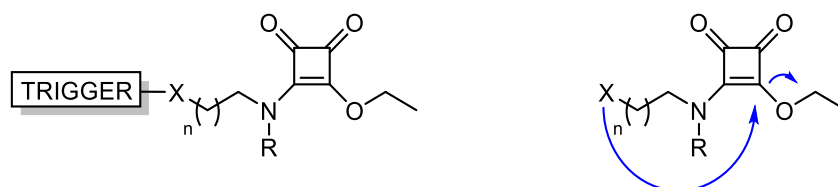
As aforementioned, self-immolative linkers that undergo disassembly by intramolecular cyclization mechanisms bear a nucleophile and an electrophile in their bone structure and the intramolecular reaction results in the release of the leaving group. Those features are illustrated in Scheme 3.2, which shows our first design on a squaramide-based self-immolative system. The terminal nucleophile is represented by  $X$  and the electrophile is the squaryl carbon, bonded to the leaving group ( $Y$ ).



**Scheme 3.2.** Self-immolative spacer based on a squaramidic scaffold and the corresponding cyclization disassembly.

For a successful self-immolation process, it is necessary to define the scope of nucleophiles able to undergo the cyclization, therefore leaving group release. Hence, it is also fundamental to assess the hydrolytic stability of the self-immolative system. The intramolecular cyclization reaction designed is aimed for the release of bioactive molecules in physiological conditions, which implies that such reactions occur in a buffered aqueous environment at around 37 °C. Those conditions can also compromise the stability of the self-immolative systems and, in addition to the cyclization process, the leaving group may also be released by hydrolysis reactions. Additionally, the presence of the nucleophilic group may affect the hydrolysis rate of the self-immolative linker through anchimeric assistance.

In order to define the most suitable functionality to act as nucleophile in the self-immolative linker, and determine the role of the Neighbouring Group Participation (NPG), some squaramate ethyl esters were chosen as minimalist self-immolative systems to study their disassembly in aqueous media:



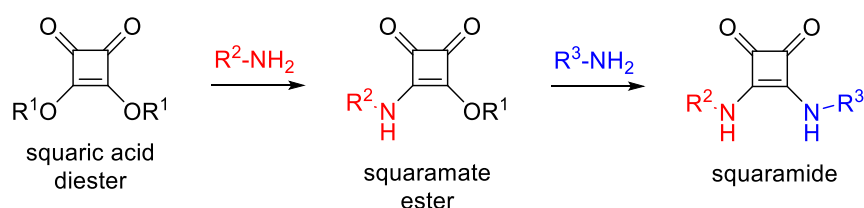
**Scheme 3.3.** Minimalist squaramate ester self-immolative system for the release of an EtOH molecule.

Along with this chapter, their chemical stability in simulated physiological conditions will be explored, by evaluating the ability of some nucleophiles to release ethanol as a representative leaving group of the esters family. In this regard, the convenience to

directly link the cargo or drug to the squaramidic unit through a squaramate ester bond will also be evaluated.

### 3.2.1. Reactivity of Squaramate Esters. Hydrolysis

Squaric acid diesters are often used as starting materials to synthesize symmetrically and unsymmetrically substituted squaramides.<sup>114</sup> Their particular reactivity permits a relatively easy control to obtain squaramate esters. After the first amide-type bond formation in polar aprotic solvents, the aromaticity of the squaryl ring increases lowering its subsequent reactivity.<sup>115</sup> Hence, the further reaction of the squaramate ester with a second amine molecule may afford the desirable unsymmetrically substituted squaramide<sup>116</sup> as shown in Scheme 3.4:



**Scheme 3.4.** General scheme for sequential amidation of squaric acid esters.

Although the squaric acid esters and the squaramate esters have a key implication in synthetic routes towards squaramides, only a few studies deal on their physicochemical properties or kinetic resistance to hydrolytic degradation. For instance, in 2008 Kováč and collaborators, studied the hydrolytic stability of several squaramate alkyl esters varying the length of the alkyl chain.<sup>117</sup> Results from these authors showed that the longer the alkyl chain, the higher the stability against hydrolysis of the ester. In parallel, they also found no influence of this chain on its further reactivity against amines to afford the corresponding squaramide. On these bases, they prepared glycoconjugates with bovine serum albumin (BSA) using the squaryl moiety as a linker (Figure 3.1).

<sup>114</sup> a) F. R. Wurm, H. A. Klok, *Chem. Soc. Rev.* **2013**, *42*, 8220–8236. b) R. Ian Storer, C. Aciro, L. H. Jones, *Chem. Soc. Rev.* **2011**, *40*, 2330.

<sup>115</sup> D. Quiñero, R. Prohens, C. Garau, A. Frontera, P. Ballester, A. Costa, P. M. Deyà, *Chem. Phys. Lett.* **2002**, *351*, 115–120.

<sup>116</sup> Normally carried out in protic polar solvents like EtOH or H<sub>2</sub>O.

<sup>117</sup> S. Hou, R. Saksena, P. Kováč, *Carbohydr. Res.* **2008**, *343*, 196–210.

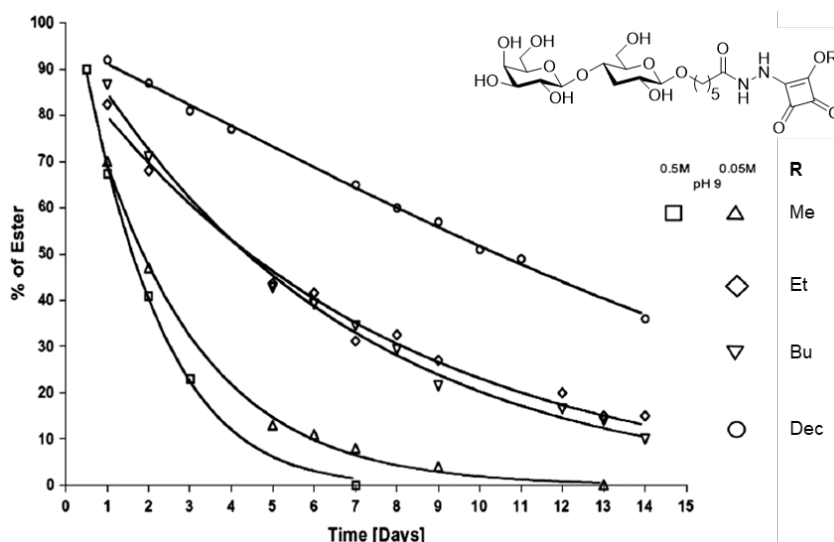
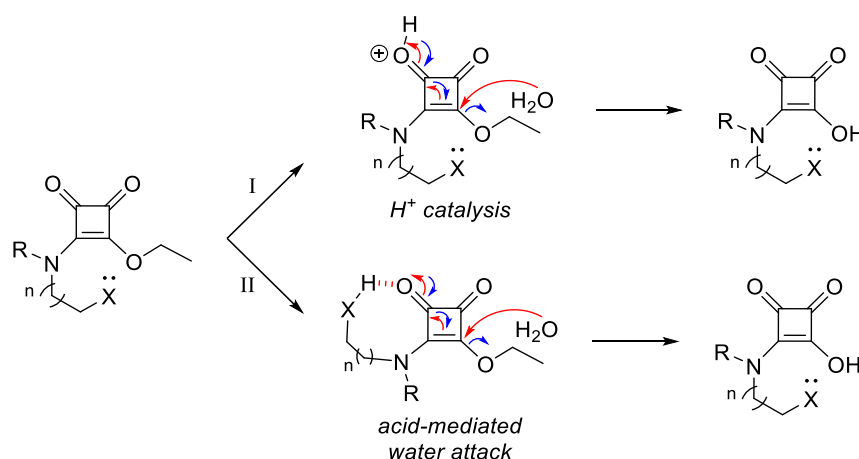


**Figure 3.1.** HPLC-monitored kinetic stability of squaramate esters bearing different alkyl chains in 0.5 and 0.05 M borate buffer pH 9 at room temperature. Modified from reference 117.

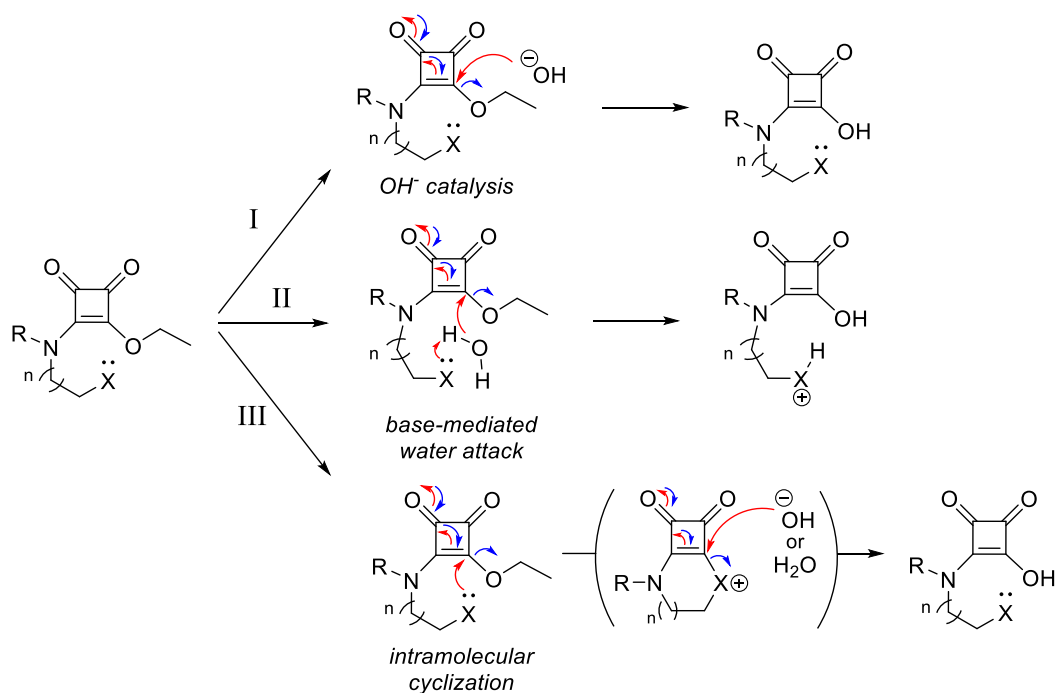
In addition to the intrinsic properties of the electrophilic centre of the squaramate ester, the presence of a proximal nucleophilic group within the molecule may also assist such hydrolysis by an intramolecular reaction, resulting in the enhancement of the reaction rate.

The hydrolysis of squaramate esters would proceed in analogy to carboxylic esters, therefore following a conventional addition-elimination mechanism. Analogously, both acid and alkaline catalysis should be considered. In the first place, acidic hydrolysis could proceed by the protonation of the carbonyl oxygen followed by water attack on the electrophilic carbon (Scheme 3.5, path I); or by intramolecular acid-mediated assistance by the neighbouring group (Scheme 3.5, path II).



**Scheme 3.5.** Proposed mechanism for the acidic hydrolysis of squaramate esters. I) acid catalysis by carbonyl protonation and II) assisted acid-mediated water attack.

On the other hand, and taking Mautner's study on choline esters as a reference,<sup>118</sup> the alkaline hydrolysis could proceed in three different pathways, proposed in Scheme 3.6. Thus, the alkaline hydrolysis could proceed by the direct hydroxide addition on the electrophilic carbon followed by the elimination of the alcohol as the leaving group (Scheme 3.6, path I). However, if the molecule contains a basic or nucleophilic group proximal to the electrophilic centre, it may assist the hydrolysis by acting as a base towards water (Scheme 3.6, path II), or by an intramolecular nucleophilic addition on the electrophilic centre, followed by a subsequent ring opening (Scheme 3.6, path III).



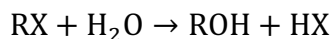
**Scheme 3.6.** Proposed mechanism for the alkali hydrolysis of squaramate esters. I) alkaline catalysis by direct hydroxide anion attack; II) assisted base-mediated water attack and, III) assisted intramolecular cyclization and subsequent intermediate-ring opening.

Throughout this chapter, we will explore the difference in the hydrolytic reactivity of several squaramide esters and how the presence of neighbouring groups on the alkyl chain can affect the reaction rate.

<sup>118</sup> P. Y. Bruice, H. G. Mautner, *J. Am. Chem. Soc.* **1973**, *95*, 1582–1586.

### 3.2.2. Hydrolysis Kinetics. Rate Law

Hydrolysis refers to “the reaction of a compound in water with a net exchange of some group with OH at the reaction centre”:<sup>119</sup>



Depending on the nature of the electrophilic substrate, the reaction mechanism may involve a protonated or unprotonated intermediate species, but eventually, the global rate law may be written as follows:

$$-\frac{d(\text{RX})}{dt} = k_h[\text{RX}] = k_{\text{OH}}[\text{OH}][\text{RX}] + k_{\text{H}}[\text{H}][\text{RX}] + k_{\text{N}}'[\text{H}_2\text{O}][\text{RX}] \quad (1)$$

where  $k_{\text{OH}}$ ,  $k_{\text{H}}$  and  $k_{\text{N}}'$  are the second order rate constants for the base- and acid-catalysed and the neutral processes, respectively. Assuming that the three hydrolysis processes are first order respect the substrate and taking into account that, in water, the product  $k_{\text{N}}'[\text{H}_2\text{O}]$  is a constant value ( $k_{\text{N}}$ ), Eq. 1 can be transformed into Eq. 2:

$$k_h = k_{\text{OH}}[\text{OH}] + k_{\text{H}}[\text{H}] + k_{\text{N}} \quad (2)$$

Considering the autoprotolysis water equilibrium (Eq. 3), Eq. 2 may be rewritten as Eq. 4:

$$[\text{OH}][\text{H}] = K_w \quad (3)$$

$$k_h = k_{\text{OH}} \frac{K_w}{[\text{H}]} + k_{\text{H}}[\text{H}] + k_{\text{N}} \quad (4)$$

Thus, Eq. 4 evidences the strong dependence of pH on the global reaction rate. Under alkali or acid conditions (high  $\text{OH}^-$  or  $\text{H}^+$ ) the first or second term respectively, dominates and the rest are negligible while at neutral pH (7), the last term gains relevance. Such behaviour is illustrated in Figure 3.2. Hlaïbi and collaborators reported the hydrolysis of lysine acetylsalicylate (**LAS**), exploring the pH dependence of the reaction kinetics.<sup>120</sup>

<sup>119</sup> W. Mabey, T. Mill, *J. Phys. Chem. Ref. Data* **1978**, 7, 383–415.

<sup>120</sup> S O. Kamal, A. Benlyamani, F. Serdaoui, M. Riri, A. Cherif, M. Hlaïbi, *Open J. Phys. Chem.* **2012**, 2, 81–87.

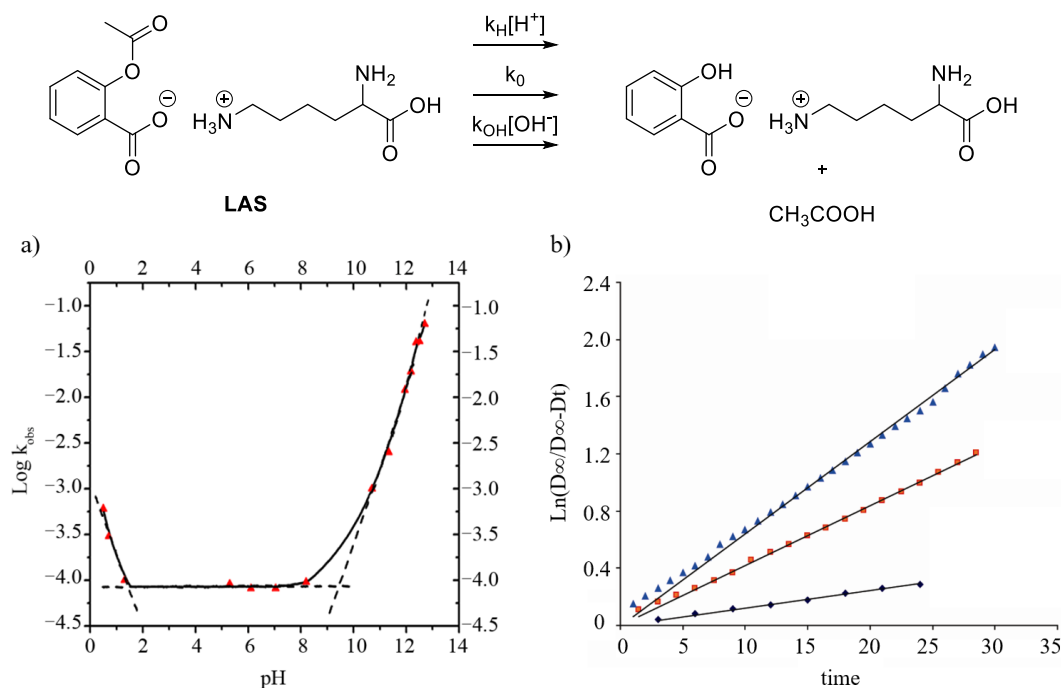


**Figure 3.2.** Example of the pH influence on the rate profile for the hydrolysis reaction of LAS at 298 K. a) pH-rate profile. b) Kinetics for the hydrolysis at pH 11.95, 12.5, and 12.7 (black, red and blue, respectively). Modified from reference 120.

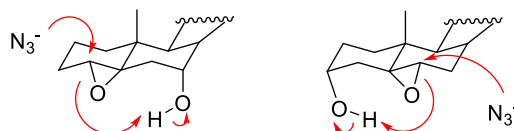
The hydrolytic kinetic profile (Figure 3.2a) is pH dependent, finding the maximum rate constants at both extremes of the pH scale ( $< 2$  and  $> 12$ ). It is worth to notice that the fastest hydrolysis occurs under strong alkali conditions. Figure 3.2b shows the enhancement of the hydrolysis rate when increasing the pH from 11.95 to 12.7 (black to blue).

### 3.2.3. Anchimeric Assistance

The anchimeric assistance or Neighbouring Group Participation (NGP) is defined by IUPAC as “*The direct interaction of the reaction centre (usually, but not necessarily, an incipient carbenium centre) with a lone pair of electrons of an atom or with the electrons of a  $\sigma$ - or  $\pi$ -bond contained within the parent molecule but not conjugated with the reaction centre*”. Such interaction decreases the activation energy of the process, increasing the reaction rate.<sup>121</sup> Despite the definition is limited to the implication of a nucleophilic neighbouring participation, the use of the term NGP has been broadly extended to any group that lows the energy of the process, increasing the reaction rate. Some examples are described below.

<sup>121</sup> IUPAC. Compendium of Chemical Terminology, 2nd ed. (the "Gold Book"). Compiled by A. D. McNaught and A. Wilkinson. Blackwell Scientific Publications, Oxford (1997).

Organic reactions involving NGP have been reported since the beginning of the 40s.<sup>122</sup> First reports are based on replacement reactions such as SN2 and SN1, where a neighbour group to the electrophilic centre assists the formation of the reaction intermediates, decreasing the energies of the transition states in the main reaction. For example, Houminer described the nucleophilic opening of steroidal epoxides by azide anions (Scheme 3.7).<sup>123</sup> In this case, the regioselectivity of the reaction is governed by the neighbour proton assistance from the axial hydroxyl group which participates in the stabilization of the transition state by the delocalization of the negative charge.



**Scheme 3.7.** Electrophilic anchimeric assistance by a hydroxy-group in the opening of steroidal epoxides by azide anions.

Currently, the presence of NGP has been reported in a different variety of reactions such as radical reactions,<sup>124</sup> acylation reactions,<sup>125</sup> acidolysis,<sup>126</sup> phosphoramidate cleavage<sup>127</sup> or polymer fragmentation,<sup>128</sup> among others. Conveniently, the anchimeric assistance is interesting to provide stereocontrol in asymmetric synthesis.<sup>129</sup> For instance, Poisson and collaborators achieved the total synthesis of (-)-Omuralide, a specific proteasome inhibitor, through the stereoselective desymmetrization of a spiro cyclic oxadisilane assisted by a neighbour hydroxyl group (Scheme 3.8).<sup>130</sup> In this particular case, after the treatment with tetra-*n*-butylammonium fluoride (TBAF) the starting alcohol is

<sup>122</sup> a) W. A. Cowdrey, Hughes E. D., C. K. Ingold, S. Masterman, A. D. Scot, *J. Chem. Soc.* **1937**, 1252–1271. b) L. C. Bateman, M. G. Church, Hughes E. D., C. K. Ingold, N. A. Taher, *J. Chem. Soc.* **1940**, 0, 979–1011. c) S. Winstein, R. E. Buckles, *J. Am. Chem. Soc.* **1942**, 12, 2780–2786. d) Y. Houminer, *J. Chem. Soc., Perkin Trans I* **1975**, 0, 277–281.

<sup>123</sup> Y. Houminer, *J. Chem. Soc., Perkin Trans I* **1975**, 0, 1663–1669.

<sup>124</sup> N. P. Dunham, W. C. Chang, A. J. Mitchell, R. J. Martinie, B. Zhang, J. A. Bergman, L. J. Rajakovich, B. Wang, A. Silakov, C. Krebs, A. K. Boal, J. M. Bollinger, *J. Am. Chem. Soc.* **2018**, 140, 7116–7126.

<sup>125</sup> R. Fjellaksel, D. Dugalic, T. B. Demissie, P. J. Riss, O. K. Hjelstuen, R. Sundset, J. H. Hansen, *J. Phys. Org. Chem.* **2018**, 31, 1–12.

<sup>126</sup> J. M. Fraile, J. I. García, Z. Hormigón, J. A. Mayoral, C. J. Saavedra, L. Salvatella, *ACS Sustain. Chem. Eng.* **2018**, 6, 1837–1847.

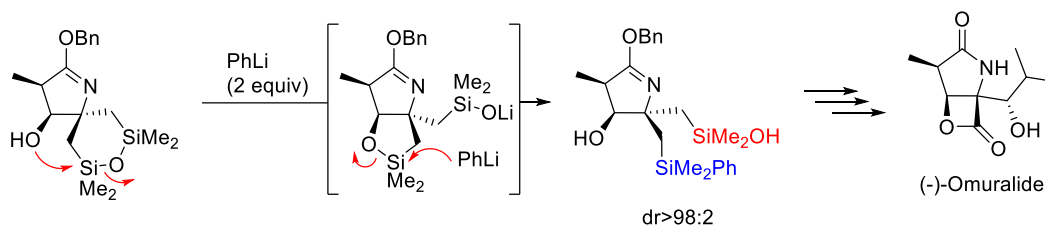
<sup>127</sup> A. Okon, M. R. Matos De Souza, R. Shah, R. Amorim, L. J. Da Costa, C. R. Wagner, *ACS Med. Chem. Lett.* **2017**, 8, 958–962.

<sup>128</sup> Z. Geng, M. G. Finn, *Chem. Mater.* **2016**, 28, 146–152

<sup>129</sup> a) A. de la Fuente, X. Verdager, A. Riera, *European J. Org. Chem.* **2017**, 2017, 7179–7185. b) S. Hajra, A. Hazra, P. Mandal, *Org. Lett.* **2018**, 20, 6471–6475. c) S. S. Pertel, S. A. Seryi, E. S. Kakayan, *Tetrahedron* **2018**, 74, 4857–4867.

<sup>130</sup> P. Rullière, A. Cannillo, J. Grisel, P. Cividino, S. Carret, J. F. Poisson, *Org. Lett.* **2018**, 20, 4558–4561.

deprotonated by one equivalent of phenyl lithium. Its further reaction with the proximal silyl atom leads to the five-membered ring oxasilane.



**Scheme 3.8.** Desymmetrization of spiro-oxadisilinine via selective ring-opening by the proximal alcohol.

Over the last years, the NGP has become of great importance in supramolecular catalysis<sup>131</sup> and its influence has also been described in non-covalent supramolecular processes. Very recently, Sir James Fraser Stoddart and collaborators published the first evidence of NGP in a rotaxane with an analogous behaviour to the role of a conventional NGP through covalent bonds.<sup>132</sup> This tri-stable [2]rotaxane shown in Figure 3.3 presents a mechanically interlocked  $\pi$ -electron rich cyclobis-(paraquat-*p*-phenylene), CBPQT, able to shuttle through three different positions: CBPQT<sup>4+</sup> (blue) interacts with triazole rings (pink), CBPQT<sup>2(+)</sup> (purple) forms radical pairs with BIPY<sup>+</sup> unit (purple) and CBPQT<sup>(0)</sup> (red) interacts with the Ar<sup>F</sup> units (green). This latter species is stabilized by charge transfer interactions with the  $\pi$ -electron-deficient Ar<sup>F</sup> units (green hexagon) demonstrating that an otherwise very weak interaction between the recognition unit and the ring upon reduction to the fully reduced state can be enhanced and supports the notion of neighbouring component effect.

<sup>131</sup> a) P. K. Biswas, S. Saha, T. Paululat, M. Schmittel, *J. Am. Chem. Soc.* **2018**, *140*, 9038–9041.

<sup>132</sup> Y. Wang, T. Cheng, J. Sun, Z. Liu, M. Frascioni, W. A. Goddard, J. F. Stoddart, *J. Am. Chem. Soc.* **2018**, *140*, 13827–13834.

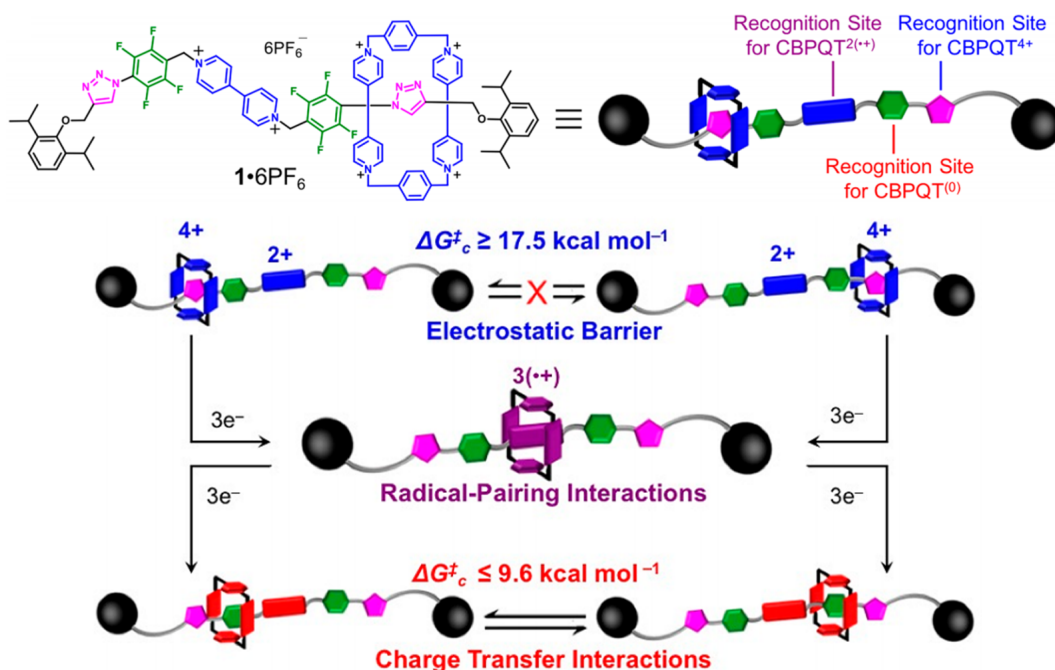


**Figure 3.3.** Structure of Stoddard's rotaxane. NGP is demonstrated by the additional charge transfer interactions found between  $\text{CBPQT}^{(0)}$  and  $\text{Ar}^{\text{F}}$ , red and green respectively. Reproduced from reference 132.

*Anchimeric assistance in hydrolytic reactions.* The influence of an NGP has been observed in a large variety of substrates and different types of reactions.<sup>133</sup> However, the most widely studied are hydrolytic reactions and particularly, those on ester substrates.<sup>134</sup> In general, the presence of a neighbour coordinating group stabilizes the transition state during the hydrolysis reaction and, consequently, the energy of the transition state decreases, thus facilitating the subsequent nucleophilic attack of a water molecule. For example, Figure 3.4, shows the anchimeric assistance due to an adjacent hydroxyl group in the hydrolysis reaction of gibberellin 7-methyl esters.<sup>134c</sup>

<sup>133</sup> a) J. L. García, A. M. Martín, J. H. Rodríguez, *Tetrahedron Lett.* **1996**, 37, 4569–4572. b) J. R. Yerabolu, C. L. Liotta, R. Krishnamurthy, **2017**, 23, 8756–8765.

<sup>134</sup> a) B. Capon, M. I. Page, *J. Chem. Soc. B Phys. Org.* **1971**, 0, 741–744. b) M. Balakrishnan, G. Venkoba Rao, N. Venkatasubramanian, *Aust. J. Chem.* **1974**, 27, 2325–2330. c) S. J. Castellaro, J. Macmillanb, C. L. Willis, A. Sciences, *J. Chem. Soc., Perkin Trans 1* **1991**, 2999–3003. d) K. Bowden, *Adv. Phys. Org. Chem.* **1993**, 28, 171–206.

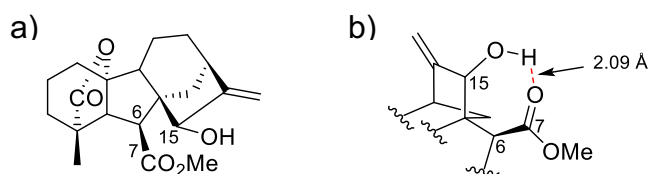


**Figure 3.4.** Representative example of anchimeric assistance of a hydroxyl group in hydrolytic reactions: a) structure of a gibberellin derivative with a 15-alcohol. b) The gibberellin structure detail showing the hydrogen bond between the 15 $\alpha$ -OH and the carbonyl group. The calculated C=O  $\cdots$ OH distance is 2.09 Å.

The existence of the hydrogen bond between the hydroxyl and the carbonyl groups was initially demonstrated by IR spectroscopy in CCl<sub>4</sub>. The methyl ester carbonyl stretch appears at 1740 cm<sup>-1</sup>, at a higher frequency than the corresponding analogue lacking the hydroxyl group at C-15 (1732 cm<sup>-1</sup>). Then, <sup>1</sup>H NMR experiments revealed a sharp doublet corresponding to the OH proton which did not appear in the corresponding unbonded analogues. Therefore, the hydroxyl proton on the C-15 stabilizes the tetrahedral intermediate formed after the addition of water in the carbonyl and consequently, the rate of alkaline hydrolysis increased by intramolecular assistance of C-15 OH.

Another representative example of the role of a particular NGP in hydrolysis reactions is the study of the intramolecular catalysis in the hydrolysis of benzylcholine and the dimethylated analogue reported by Mautner and colleagues.<sup>118</sup>

The plot of the observed rate constants against pH for benzoylcholine shows a linear tendency and the hydrolysis rate increases with the concentration of hydroxide anion (Figure 3.5, dots). The hydrolysis mechanism responds to Eq. 2', where the second and third term from Eq. 2 are negligible:

$$k_h = k_{OH}[OH] + k_H[H] + k_N \quad (2)$$

$$k_h = k_{OH}[OH] \quad (2')$$

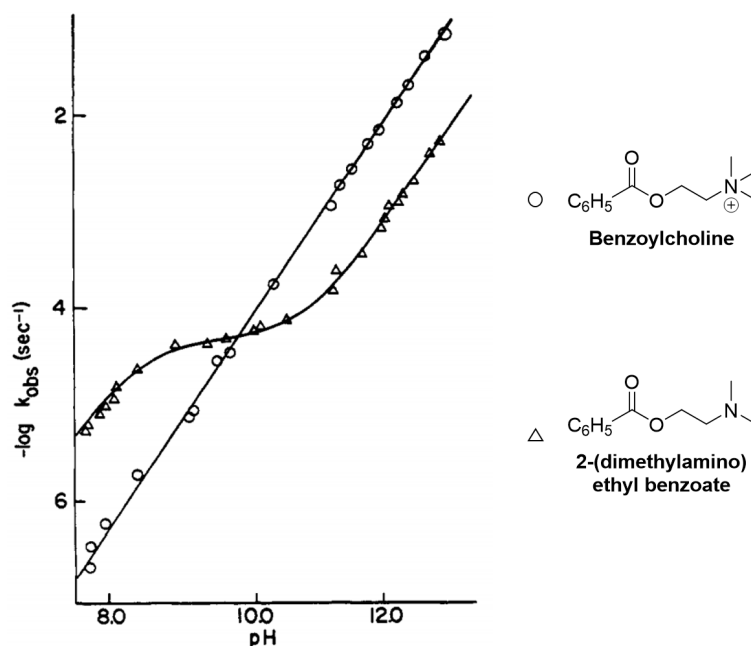
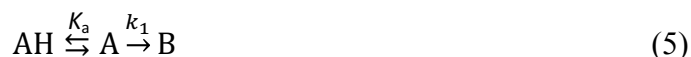


**Figure 3.5.** Observed rate constants for the hydrolysis at different pH of benzoylcholine (dots) and its dimethylated analogue (triangles). Reproduced from reference 118.

Conversely, the dimethylated analogue shows a hyperbolic profile (Figure 3.5, triangles) because of the intramolecular anchimeric assistance of the dimethylamino terminal group. In this case, in addition to the hydroxide anion hydrolysis, the substrate itself catalyses the hydrolysis reaction. Thus, the assisted process can be described as a protonic preequilibrium followed by the intramolecular assisted hydrolysis:



Where A corresponds to the substrate and B to the final hydrolysis product. The rate law of this reaction responds to Eq. 6, where the substrate-dependent term is included:

$$k_h = k_{\text{OH}}[\text{OH}] + k_1[\text{A}] = k_{\text{OH}} \frac{K_w}{[\text{H}]} + k_1 \frac{K_a}{K_a + [\text{H}]} \quad (6)$$

$K_a/(K_a + [\text{H}])$  is the concentration of ester in its free unprotonated amino base form ( $[\text{A}]$ ) and  $k_1$  is the rate constant for the assisted hydrolysis to form the hydrolytic process.

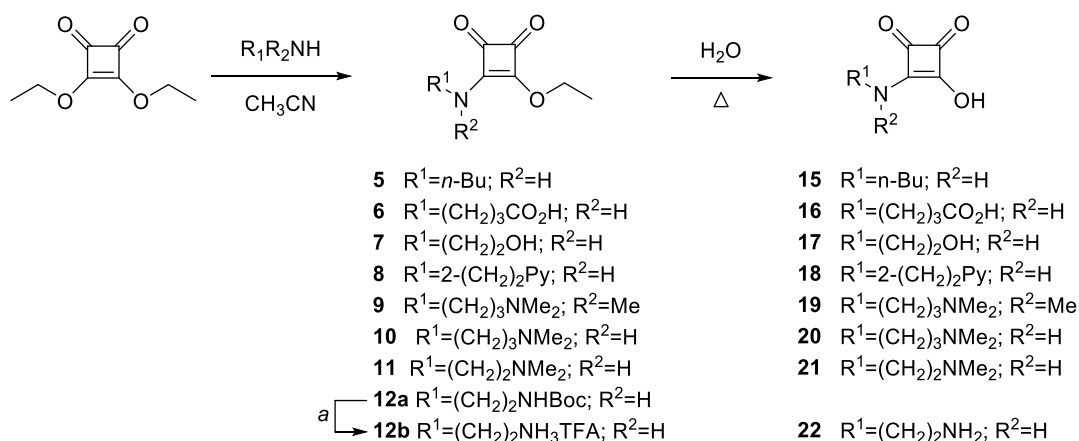
The second order rate constant for the hydrolysis of benzoylcholine found in this study is  $k_{\text{OH}} = 0.56 \text{ M}^{-1} \text{ s}^{-1}$  while for the dimethylated analogue is  $k_{\text{OH}} = 0.06 \text{ M}^{-1} \text{ s}^{-1}$  and the assisted hydrolysis rate constant is  $k_1 = 4.8 \times 10^{-5} \text{ M}^{-1} \text{ s}^{-1}$ . Although this constant is four orders of magnitude lower than  $k_{\text{OH}}$ , the hydrolysis rate at pH ranging 8-10 is significantly higher than the hydrolysis of benzoylcholine.

### 3.3. RESULTS AND DISCUSSION

Recent reports from our group states that the hydrolytic degradation of secondary squaramides requires strong alkaline pH conditions for extended periods.<sup>96b</sup> However, it is well known that squaramate esters suffer hydrolysis under mild conditions producing 3-hydroxy-4-amino derivatives of squaric acid, henceforth named as squaramate acids. Here, we present the results of the hydrolytic study performed on different squaramate esters where the anchimeric assistance (or NGP) of amidic alkyl chains has been evaluated.

#### 3.3.1. Synthesis of the Squaramate Esters

Squaramate esters **5-11** and **12b** were prepared according to a modified procedure<sup>135</sup> by condensation of diethyl squarate with one equivalent of the corresponding amine. The recorded spectroscopic data of these compounds were obtained in agreement with the previously reported. Complete hydrolysis of esters led to the corresponding squaramate acid salts (**15-22**) that were isolated, fully characterized and used as a reference for the kinetic study.



**Scheme 3.9.** Synthetic scheme of procedure for the preparation of squaramate esters **5-11** and **12b** and the corresponding squaramate acids **15-22**. (a) TFA/CH<sub>2</sub>Cl<sub>2</sub>

#### 3.3.2. Kinetics of the Squaramate Esters Hydrolysis

The structure of the squaramate esters **5-11** and **12b** differs on the nature of the *N*-alkyl chains. These compounds allowed us to explore their hydrolytic stability at pH ranging from 3 to 9. The squaramidic alkyl chains were selected as representatives of different chemical functionalities that might potentially assist the hydrolytic process being amino,

<sup>135</sup> F. Olmo, C. Rotger, I. Ramírez-Macías, L. Martínez, C. Marín, L. Carreras, K. Urbanová, M. Vega, G. Chaves-Lemaur, A. Sampedro, M. J. Rosales, M. Sánchez-Moreno, A. Costa, *J. Med. Chem.* **2014**, *57*, 987–99.

pyridine, alcohol and carboxylic acid groups. Squaramide ester **5**, bearing a butyl residue, was used as the negative control for anchimeric assistance.

In aqueous solution and with the independence of the pH, squaramate esters show intense absorption bands ( $\epsilon > 6 \times 10^4 \text{ M}^{-1} \text{ cm}^{-1}$ ) in the UV range with the maximum absorption around 272 nm, while their squaramate acid analogues present a maximum around 283 nm. Thus, the study of the hydrolytic process was performed by monitoring the time-dependent changes in the UV-vis spectra of the corresponding ester at 37 °C.<sup>136</sup> The experiments were carried out under pseudo-first order conditions (constant concentration of ester) at different pH values, and the apparent rate constants ( $k_{\text{obs}}$ ) were calculated by performing a global analysis of the absorption spectra acquired during the hydrolysis. Adjustment of data to a model was carried out with ReactLab<sup>TM</sup> Kinetics (Jplus Consulting Ltd.),<sup>137</sup> a software package used for global fitting of time-dependent kinetic measurements.

As an example, Figure 3.6a shows the full conversion of squaramate ester **5** (blue spectra) into the corresponding squaramate (red spectra) at pH 10 at 37 °C. The analysis of the UV data allowed us to calculate the apparent rate constant. The plot of the percentage of the disappearance of the starting material vs the reaction time at different pH is shown in Figure 3.6b, obtained with ReactLab<sup>TM</sup> Kinetics software.

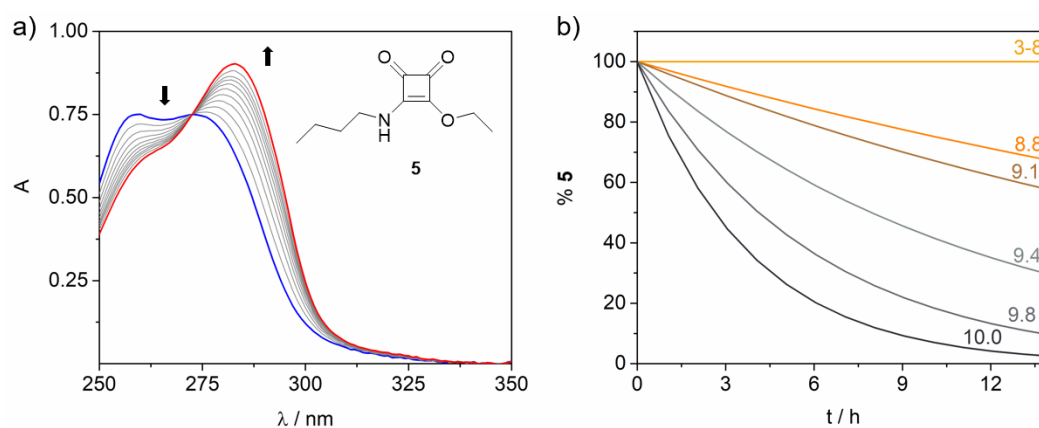


**Figure 3.6.** a) Representative example of the changes in the UV spectra observed during the hydrolysis of 30  $\mu\text{M}$  squaramate ester **5** (10 mM carbonate buffer pH 10, 37 °C). b) Calculated disappearance of 30  $\mu\text{M}$  squaramate ester **5** from the UV spectrum at 37 °C at different pH (10 mM buffer). \*From pH 3 to 8, no hydrolysis was observed after 1 week.

Table 3.1 collects the  $k_{\text{obs}}$  calculated for squaramate esters **5-11** and **12b** at pH 3-9.

<sup>136</sup> The kinetic studies were performed at 37 °C to explore the stability of the squaramide derivatives and their kinetic properties at physiological conditions.

<sup>137</sup> P. King, M. Maeder, *JPlus Consulting*, Multivariate Analytical Technologies, East Fremantle, Australia, 2009.

**Table 3.1.** Summary of pseudo-first order observed rate constants for the hydrolysis of squaramate esters **5-11** and **12b** at different pH (3-9).

Substrate / pH	$k_{\text{obs}}, 10^{-5} \text{ s}^{-1}$				
	3	5	7	8	9
<b>5</b>	-	-	-	-	$1.10 \pm 0.04$
<b>6</b>	-	-	-	-	$0.34 \pm 0.03$
<b>7</b>	-	-	-	-	$0.86 \pm 0.01$
<b>8</b>	-	-	-	-	$0.73 \pm 0.04$
<b>9</b>	-	-	$0.02 \pm 0.01$	$0.43 \pm 0.03$	$3.62 \pm 0.02$
<b>10</b>	-	-	$0.31 \pm 0.01$	$1.03 \pm 0.01$	$4.85 \pm 0.02$
<b>11</b>	-	-	$0.46 \pm 0.01$	$2.38 \pm 0.03$	$8.56 \pm 0.14$
<b>12b</b>	-	-	$1.06 \pm 0.01$	$2.91 \pm 0.01$	$16.1 \pm 0.2$

From these results, the kinetic behaviour of the studied squaramate esters can be classified in two groups: 1) esters **5-8**, which are kinetically stable under pH 9 and 2) esters **9-11** and **12b**, which suffer hydrolysis from pH 7 and, at pH 9, their hydrolysis is considerably faster than esters **5-8**.

To get a deeper inside in the knowledge of the reactivity of squaramate esters under hydrolytic conditions, first, some kinetic and mechanistic studies using compound **5** were performed, as a model of the unassisted hydrolysis reaction.

*Study of the hydrolysis of squaramate ester 5.* Contrary to that observed in neutral or acidic media, hydrolysis of the squaramate ester **5** ( $3 \times 10^{-5} \text{ M}$ ) at  $37 \text{ }^\circ\text{C}$  occurs within hours under alkaline conditions. The observed rate constants ( $k_{\text{obs}}$ ) show a linear dependence on the pH range studied (pH = 8.7-10), thus excluding the ionization of the squaramidic NH hydrogen in this pH interval, as that would lead to a nonlinear dependence of  $k_{\text{obs}}$  on the pH.

Hence, in analogy with Eq. 3 and 4 and since the experiments were carried under pseudo-first order conditions (constant concentration of ester), the rate constant could be defined as Eq. 2':

$$k_{\text{obs}} = k_{\text{OH}}[\text{OH}] = k_{\text{OH}} \frac{K_{\text{w}}}{[\text{H}]} \quad (2')$$

Data fitting to Eq. 2' leads to the second order rate constants  $k_{\text{OH}} = 0.52 \pm 0.02 \text{ M}^{-1}\text{s}^{-1}$  (Fig. 3.7b, blue). We used  $K_{\text{w}} = 2.04 \times 10^{-14}$  (reference at  $37 \text{ }^\circ\text{C}$ ).<sup>138</sup>

<sup>138</sup> A. K. Covington, M. I. A. Ferra, R. A. Robinson, *JCS Faraday Trans. I* **1977**, *73*, 1721–1730.

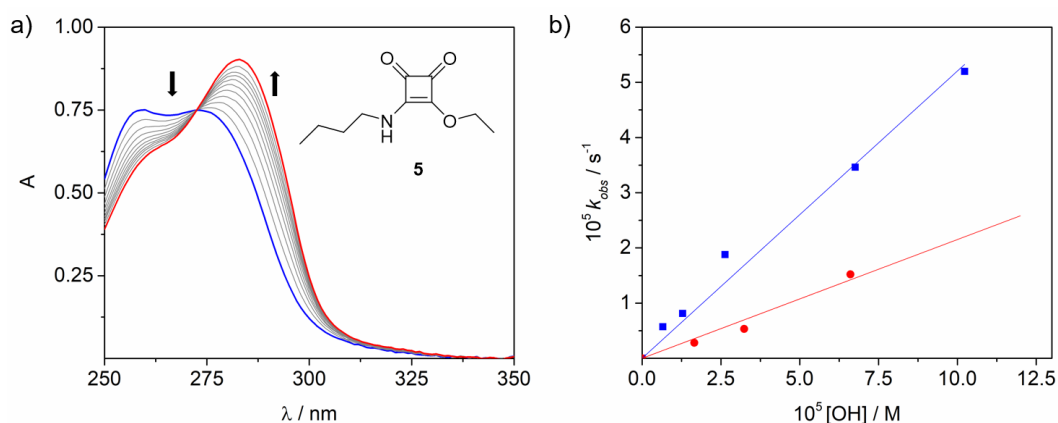
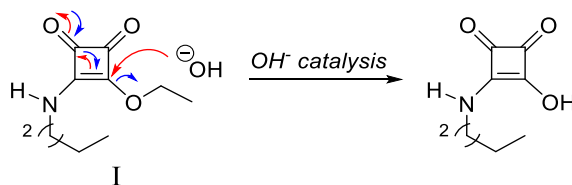


**Figure 3.7.** a) Representative example of the changes in the UV spectra observed during the hydrolysis of 30  $\mu\text{M}$  squaramate ester **5** (10 mM carbonate buffer pH 10, 37  $^{\circ}\text{C}$ ). b)  $k_{\text{obs}}$  vs  $[\text{OH}(\text{D})]$  plots for hydrolysis of ester **5** in  $\text{H}_2\text{O}$  (blue) and  $\text{D}_2\text{O}$  (red).

The same linear dependency was observed when the above experiments were performed in deuterated water ( $3 \times 10^{-5}$  M of **5**, pD = 9.1-10.2, 37  $^{\circ}\text{C}$ ) affording a value of  $k_{\text{OD}} = 0.21 \pm 0.02 \text{ M}^{-1}\text{s}^{-1}$  (Figure 3.7b, red).<sup>139</sup> From these data, the solvent Kinetic Isotope Effect (KIE) for this reaction was obtained, calculated as  $k_{\text{OH}}/k_{\text{OD}} = 2.42 \pm 0.02$ . This value is in agreement with the typically solvent KIEs values arising from the transfer of a proton from nitrogen or oxygen that are in the range values of 1.5-3.<sup>140</sup> The magnitude of the KIE obtained for the hydrolysis of squaramate ester **5** supports the implication of a water molecule in the rate-determining step (RDS). These results agree with the general base-catalysed mechanism proposed for the hydrolysis of esters, and therefore, the same mechanism can be proposed for the studied squaramate ester **5** (Scheme 3.10).



**Scheme 3.10.** Hydrolysis pathway of squaramate ester **5** through hydroxide nucleophilic catalysis (I).

In analogy to ester **5**, and assuming the same reactivity, the obtained pseudo-first order constants  $k_{\text{obs}}$  for the hydrolysis of esters **6-8** were fitted to Eq. 2'. The second order rate  $k_{\text{OH}}$  constants and the corresponding half-lives are summarized in Table 3.2.

<sup>139</sup> pD = pH + 0.4. P. K. Glasoe, F. A. Long, *J. Phys. Chem.* **1960**, *64*, 188-190.

<sup>140</sup> P.F. Fitzpatrick, *Biochim. Biophys. Acta*, **2014**, *1854*, 1746-1755.

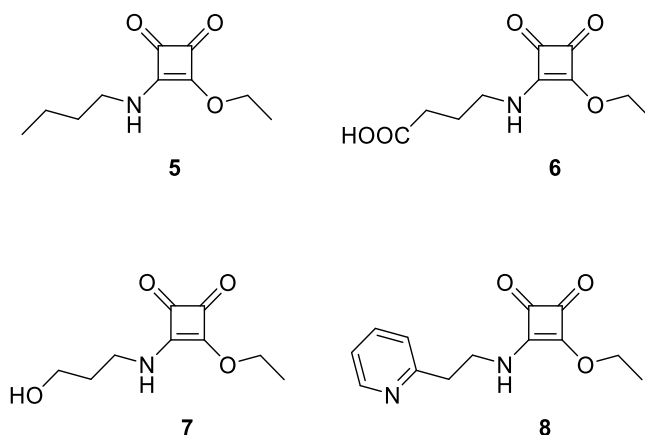


**Chart 3.2.** Chemical structure of squaramate esters **5-8**.

**Table 3.2.** Summary of second order rate constants calculated and the corresponding half-lives for the hydrolysis of squaramide esters **5-8**.

Entry	$k_{\text{OH}}, \text{M}^{-1} \text{s}^{-1}$	$t_{1/2}, \text{h}$
<b>5</b>	$0.47 \pm 0.02$	16.7
<b>6</b>	$0.34 \pm 0.03$	23.3
<b>7</b>	$0.86 \pm 0.01$	9.3
<b>8</b>	$0.73 \pm 0.04$	10.9

As can be observed from these results, the hydrolysis rate constants for compounds **5-8** have roughly the same magnitude so the studied squaramate esters bearing poor nucleophilic groups (carboxylic acid, alcohol, and pyridine; **6**, **7**, and **8** respectively) do not show an enhancement on the reaction rate in comparison with squaramate ester **5**, unable to show NGP. Thus, in these cases, the process would be only governed by the electrophilic character of the squaryl ester carbon.

*Assisted hydrolysis.* Conversely to the behaviour of esters **5-8**, the hydrolysis of squaramate esters **9-11** and **12b** at 37 °C occurs in neutral and alkaline solutions, noticeably faster than those observed for esters **5-8**.

In this case, compounds **9-11** are functionalized with a tertiary alkyl amine ( $\text{NMe}_2$ ) and **12b** with a primary amine at the end of the squaramide substituent of different length.

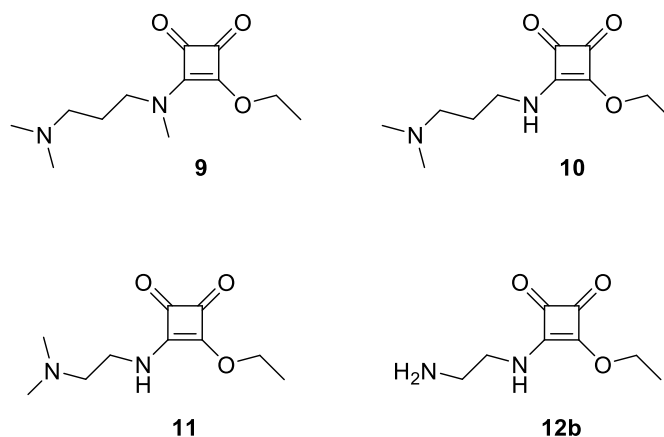


**Chart 3.3.** Chemical structure of squaramate esters **9-11** and **12b**.

The initial kinetic studies suggested that anchimeric assistance of the amino terminal groups of esters **9-11** and **12b** could enhance the rate of the hydrolytic process. Additionally, we found as per esters **5-8** that the hydrolysis of squaramate esters **9-11** and **12b** at 37 °C in moderate acidic media (pH 3-5) does not progress for longer than three weeks.

In analogy with the aforementioned study by Mautner on benzoylcholine ester and its dimethylated analogue where the hydrolysis of this latter is affected by NGP,<sup>118</sup> the kinetic of hydrolysis of squaramate esters **9-11**, and **12b** was investigated. Considering the nature of the NGP, an amine group, the *N*-protonation pre-equilibrium was taken into account. Assuming that only the free amino group would be able to catalyse the hydrolysis, the reaction rate would be sensitive to the pH. Then the rate constant may be described as shown in Eq. 6:<sup>141</sup>

$$k_{\text{obs}} = k_1[A] + k_{\text{OH}}[\text{OH}] = k_1 \frac{K_a}{K_a + [\text{H}]} + k_{\text{OH}} \frac{K_w}{[\text{H}]} \quad (6)$$

where  $K_a/(K_a + [\text{H}])$  is the concentration of squaramate ester in its free unprotonated amino base form ( $[A]$ ) and  $k_1$  is the rate constant for the assisted hydrolysis. Besides, as occurs for esters **5-8**, direct hydrolysis would also compete with the NGP process and it is included in the equation. In Eq. 6 we also assume that the ionization of the squaramidic nitrogen of **9** is negligible ( $\text{p}K_a \geq 12$ ).

As we did for compound **5**, the hydrolysis of **9** was studied in more detail at different pH, and the corresponding  $k_{\text{obs}}$  were obtained for each.

<sup>141</sup> a) H. Bundgaard, A. Buur, S. C. Chang, V. H. L. Lee, *Int. J. Pharm.* **1986**, *33*, 15–26. b) B. Steffansen, H. Bundgaard, *Int. J. Pharm.* **1989**, *56*, 159–168.

The  $K_a$  value for compound **9**, used in Eq. 6, was obtained by potentiometric titration and data fitting with Hyperquad.<sup>142</sup>

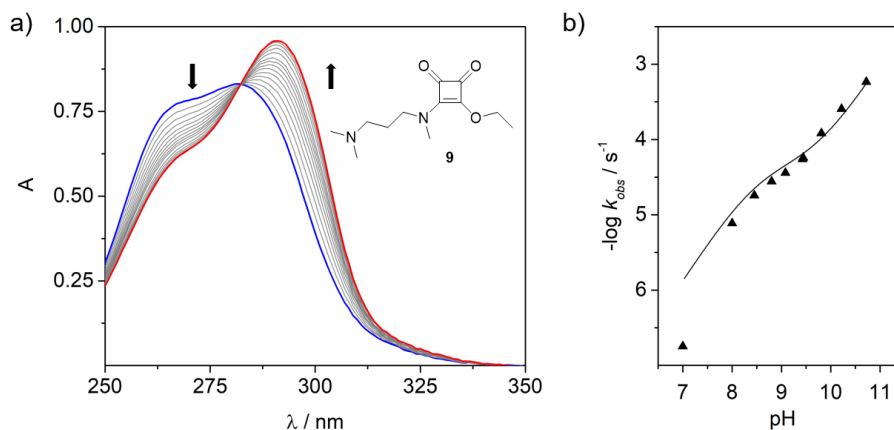


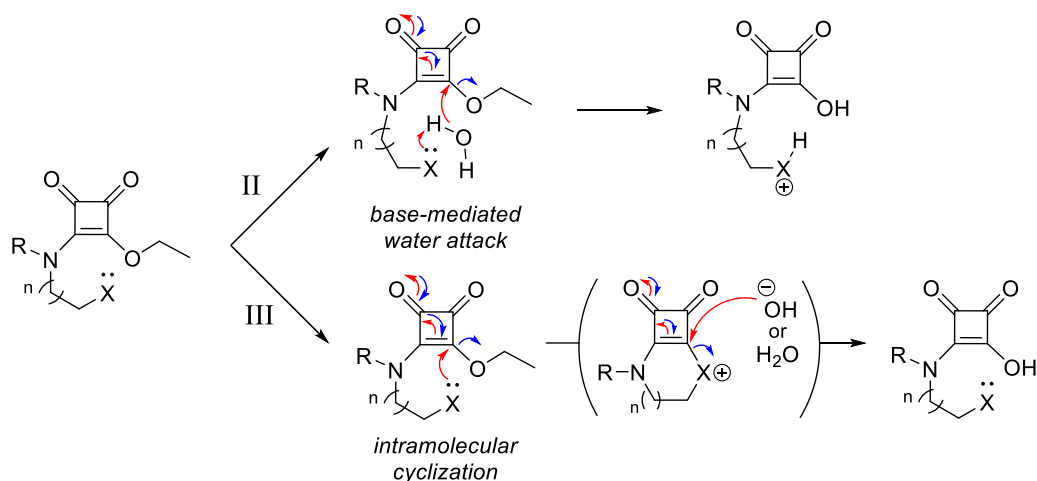
**Figure 3.8.** a) Representative example of the UV changes observed for the hydrolysis of **9** (30  $\mu\text{M}$ ) at 10 mM borate buffer pH 9 at 37  $^{\circ}\text{C}$  b) Fitting to Eq. 6 of the data obtained for hydrolysis of ester **9** at different pH.

The variation of the obtained  $k_{\text{obs}}$  against  $[\text{H}_3\text{O}^+]$  fits well to Eq. 6 in the pH range 7-10.5. The corresponding logarithmic representation is plotted for clarity (Figure 3.8b). Moreover, from this fitting both second order rate constants  $k_1$  and  $k_{\text{OH}}$  were calculated, included in Table 3.3.

Although the calculated  $k_1$  values are  $10^5$  times smaller than those obtained for  $k_{\text{OH}}$ , still are significant enough to strongly enhance the hydrolysis rate when increasing the pH. This fact is consistent with the concurrence of the two proposed mechanisms, since the concentration of the free base increases with the pH favouring the assisted hydrolysis; but also implies an increment in the hydroxide concentration which means a rate enhancement by the direct hydrolysis, observed in non-assisted hydrolysis reactions.

Accordingly, the mechanism of the hydrolysis assisted by a NGP could be considered as an intramolecular general base-mediated nucleophilic attack of a water molecule (II) or, as a consequence of a direct nucleophilic attack of the nitrogen atom on the electrophilic squaryl carbon (III), as shown in Scheme 3.11:

<sup>142</sup> Hyperquad2013 program (Protonic Software. <http://www.hyperquad.co.uk>)



**Scheme 3.11.** Proposed assisted hydrolysis pathways for squaramate esters **9-11** and **12b**: II) base-mediated water attack and III) intramolecular cyclization followed by water or hydroxide attack.

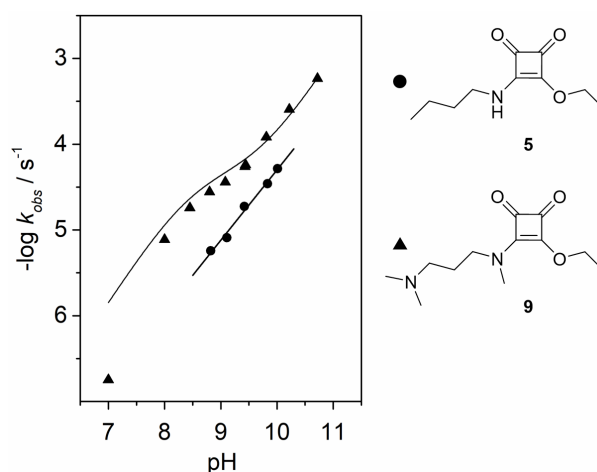
Noteworthy, squaramate esters bearing poor nucleophilic and basic substituents such as those containing O or pyridine N, are unable to assist the process. Consequently, the outcome of the reaction is analogue to that of *n*-butylamine squaramate ester **5**, a compound lacking any heteroatom suitable for anchimeric assistance

Analogously to **9**, we estimated the kinetic constant  $k_1$  for the squaramate esters **10**, **11** and **12b** by fixing the rate constant for the direct hydrolysis ( $k_{\text{OH}}$ ) and fitting the data to Eq. 6. The  $k_1$  values obtained for these compounds have roughly the same order of magnitude than the  $k_1$  obtained for compound **9**. This fact evidences the role of either the tertiary and primary alkyl amino groups as neighbour assistant groups enhancing the overall hydrolysis rate.

**Table 3.3.** Summary of second order rate constants for the hydrolysis of squaramate esters **9-12**. <sup>a</sup>pK<sub>a</sub> values used in the fitting were calculated by potentiometric titration and fitted with Hyperquad<sup>142</sup>. <sup>b</sup>To calculate  $k_1$  for compounds **10**, **11** and **12b** we assumed the same  $k_{\text{OH}}$  found for **9**.

Entry	pK <sub>a</sub> <sup>a</sup>	$k_{\text{OH}}$ , M <sup>-1</sup> s <sup>-1</sup>	$k_1$ , 10 <sup>-5</sup> M <sup>-1</sup> s <sup>-1</sup>
<b>9</b>	8.82	1.03 ± 0.04	5.2 ± 0.9
<b>10</b>	8.61	1.03 <sup>b</sup>	12 ± 2
<b>11</b>	7.95	1.03 <sup>b</sup>	3.9 ± 0.3
<b>12b</b>	8.50	1.03 <sup>b</sup>	30 ± 6

The profile obtained for the assisted hydrolysis of **9** compared with compound **5** profile reveals a global increase of the hydrolysis in neutral to alkaline solutions when an amino neighbour group is present. Hence, the hydrolytic stability of compounds exhibiting NGP is compromised even in neutral media (Figure 3.9).

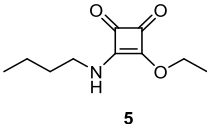
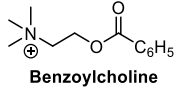
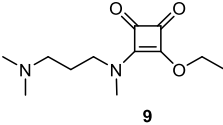
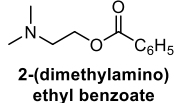


**Figure 3.9.** Comparison between hydrolysis rate pH-dependent profiles obtained for the hydrolysis of **5** (dots) and **9** (triangles) at 37 °C.

In summary, the data obtained for the hydrolysis of the squaramate esters **5-11** and **12b** showed two main kinetic profiles: (1) direct hydroxide attack on the squaramide ester moiety for all esters and an additional (2) intramolecular assisted amino attack for esters **9-11** and **12b**. In general, the magnitude of the rate constants is roughly around  $1 \text{ M}^{-1} \text{ s}^{-1}$  for (1) and  $10^{-5} \text{ M}^{-1} \text{ s}^{-1}$  for (2).

When comparing these results with those reported for the carboxylic ester analogues, squaramate esters behave similarly. For instance, in Mautner's study of the hydrolytic stability of some benzoyl esters,<sup>118</sup> benzoyl choline ester showed direct hydroxide hydrolysis, corresponding to the aforementioned kinetic profile (1). The presence of a quaternary ammonium group did not alter the ester hydrolysis rate. However, the hydrolysis of its dimethylated analogue 2-dimethylaminoethyl benzoate was faster because of the intramolecular assistance of the amino terminal group (2). The rate constants for these carboxylic esters are shown in Table 3.4, and are comparable with those found for squaramate esters **5** and **9**.

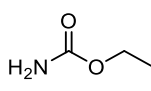
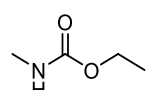
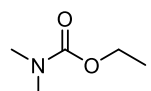
**Table 3.4.** Rate constants for the hydrolysis of squaramate esters **5** and **9** and the reported benzoylcholine esters, respectively.<sup>118</sup> <sup>a</sup>At 37 °C. <sup>b</sup>At 25 °C.

Squaramate Ester <sup>a</sup>	$k_{\text{OH}}$ , $\text{M}^{-1} \text{ s}^{-1}$	$k_1$ , $10^{-5} \text{ M}^{-1} \text{ s}^{-1}$	Carboxylic Ester <sup>b</sup>	$k_{\text{OH}}$ , $\text{M}^{-1} \text{ s}^{-1}$	$k_1$ , $10^{-5} \text{ M}^{-1} \text{ s}^{-1}$
	$0.47 \pm 0.02$	-	 Benzoylcholine	0.56	-
	$1.03 \pm 0.04$	$5.2 \pm 0.9$	 2-(dimethylamino)ethyl benzoate	0.06	4.8

It is worth to take into account that the constants reported for carboxylic esters are given at 25 °C while the constants found for squaramate esters are calculated at 37 °C. Despite this, the magnitude of direct hydrolysis and assisted hydrolysis is comparable. Thus, since the temperature enhances the reaction rate, we can point out that squaramate esters are moderately more stable than their carboxylic ester analogues.

Structurally, squaramate esters are related to carbamates and their hydrolysis rates are comparable. In the early 60s, Dittert and Higuchi performed a study on the alkaline hydrolysis of carbamate and carbonate esters finding second order rate constants around the magnitude of  $10^{-2} \text{ M}^{-1} \text{ s}^{-1}$  (Table 3.5):<sup>143</sup>

**Table 3.5.** Second order rate constants for the hydrolysis of some reported carbamate esters at 25, 30 and 55 °C.

Carbonate Ester	$k_{\text{OH}}, \text{M}^{-1} \text{s}^{-1}$ 25 °C	$k_{\text{OH}}, \text{M}^{-1} \text{s}^{-1}$ 30 °C	$k_{\text{OH}}, \text{M}^{-1} \text{s}^{-1}$ 55 °C
 urethane	$7.2 \times 10^{-2}$	0.12	1.44
 ethyl N-methyl-carbamate	$2.0 \times 10^{-2}$	$3.3 \times 10^{-2}$	0.31
 ethyl dimethyl-carbamate	$1.6 \times 10^{-2}$	-	0.18

As for squaramate esters, the carbamate hydrolysis also proceeds by an addition-elimination mechanism which results in the elimination of the alcohol residue. In comparison with the rate constants obtained for the squaramate ester analogue **5**, where only the hydroxide attack is responsible for the hydrolysis reaction, carbamates show slower rate constants and, consequently, higher hydrolytic stability. However, when compared with the hydrolysis in acidic conditions, squaramate esters are highly stable and no reaction is observed during several days while the corresponding carbamate ester analogues are hydrolysed in a relatively short time (hours).<sup>144</sup>

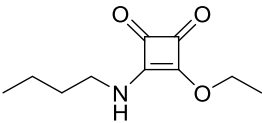
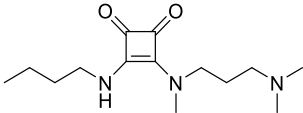
In conclusion, squaramate esters showed kinetic profiles akin to those of the hydrolysis of carboxylic or carbamate esters in alkaline media. However, in contrast to carboxylic and carbamates esters, they are highly stable in moderate acidic solutions ( $\text{pH} \geq 3$ ).

<sup>143</sup> L. W. Dittert, T. Higuchi, *J. Pharm. Sci.* **1963**, 52, 852–857.

<sup>144</sup> V. C. Armstrong, D. W. Farlow, R. B. Moodie, *J. Chem. Soc. B Phys. Org.* **1968**, 1099.

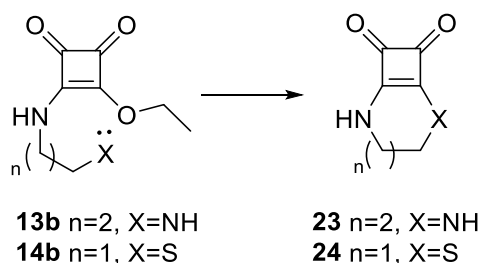
In general, the hydrolysis of squaramate esters run similar to that of carboxylic acid esters. These latter suffer hydrolysis around 1000 times faster than their counterpart amides.<sup>119</sup> Such results are in agreement for the squaramate analogues, esters and amides since, as has been recently found, the rate constant values found for the hydrolysis of squaramides are around  $10^{-4} \text{ M}^{-1}\text{s}^{-1}$ . Accordingly, the magnitude of the direct hydrolysis ( $k_{\text{OH}}$ ) for the squaramate ester **5** is also around 1000 times larger than the reported value for a related squaramide analogue (Table 3.6).<sup>96b</sup>

**Table 3.6.** Comparison of the rate constant values between the hydrolysis of *n*-butylamine squaramate ester **5** and a representative squaramide compound.

Squaryl derivative	$k_1, \text{M}^{-1} \text{s}^{-1}$
 <p style="text-align: center;"><b>5</b></p>	$4.7 \pm 0.2 \times 10^{-1}$
 <p style="text-align: center;">Related squaramide</p>	$5.4 \pm 0.5 \times 10^{-4}$

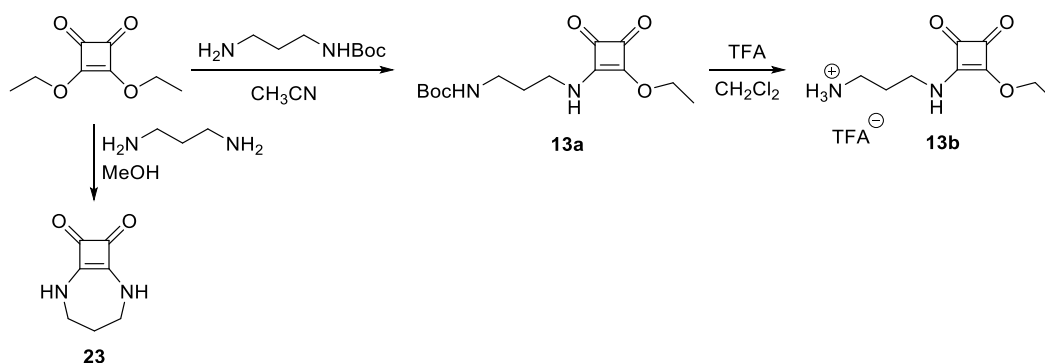
### 3.3.3. Intramolecular Cyclization of Esters **13b** and **14b**

The particular cases of the squaramate esters **13b** and **14b** were also studied. Unlike esters **5-11** and **12b**, under hydrolytic conditions, their UV spectra did not show the apparition of the typical squaramate band at 283 nm. Instead, the formation of cyclic products was observed. The presence in **13b** and **14b** of a nucleophilic primary amino and thiol terminal groups, respectively, led us to assume that in these compounds the irreversible direct intramolecular cyclization predominated over the solvent-assisted hydrolytic process (Scheme 3.12).



**Scheme 3.12.** Cyclization mechanism of esters **13b** and **14b**.

*Synthesis of ester 13b and its corresponding cyclosquaramide analogue 23.* The synthesis of ester **13b** was carried out following the same procedure than for ester **12b**, using the mono Boc-protected 1,3-propanediamine that is one methylene unit longer than ethylenediamine, used to obtain **12b** (Scheme 3.13). The corresponding trifluoroacetate ammonium salt **13b** was obtained after the treatment of **13a** with trifluoroacetic acid (TFA) in dichloromethane. On the other hand, and for comparison purposes, cyclic squaramide **23** was obtained by reaction of ethyl squarate with 1,3-propanediamine.



**Scheme 3.13.** Synthesis of squamate ester **13b** and the corresponding cyclosquaramide **23**.

The cyclic squaramide **23** was purified by crystallization obtaining **23** as a dihydrate. Details on the exploration of the formation of hydrates of **23** and derivatives together with their crystallographic properties and possible applications will be further discussed in Chapter 4.

Full characterisation of **23** was achieved by NMR and X-ray crystallography. Figures 3.10 and 3.11 show the  $^1\text{H}$  NMR and  $^{13}\text{C}$  NMR spectra of the cyclic compound **23**, respectively.

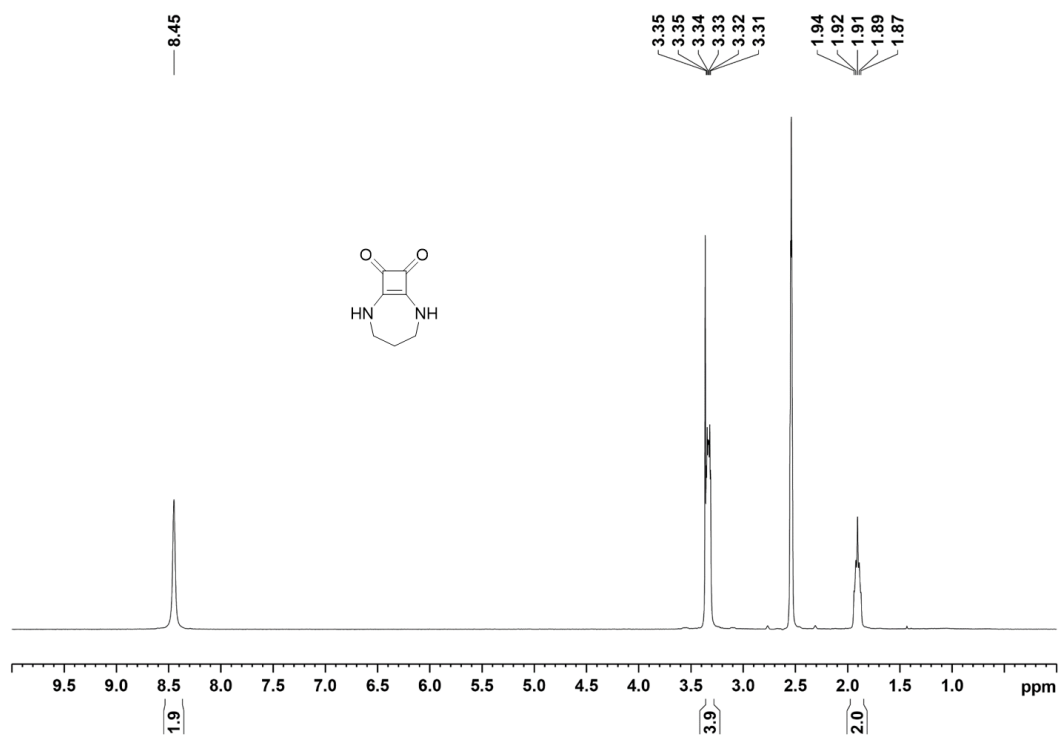


**Figure 3.10.**  $^1\text{H}$  NMR spectrum of **23** in  $\text{D}_2\text{O}$ , 300 MHz, 298 K.

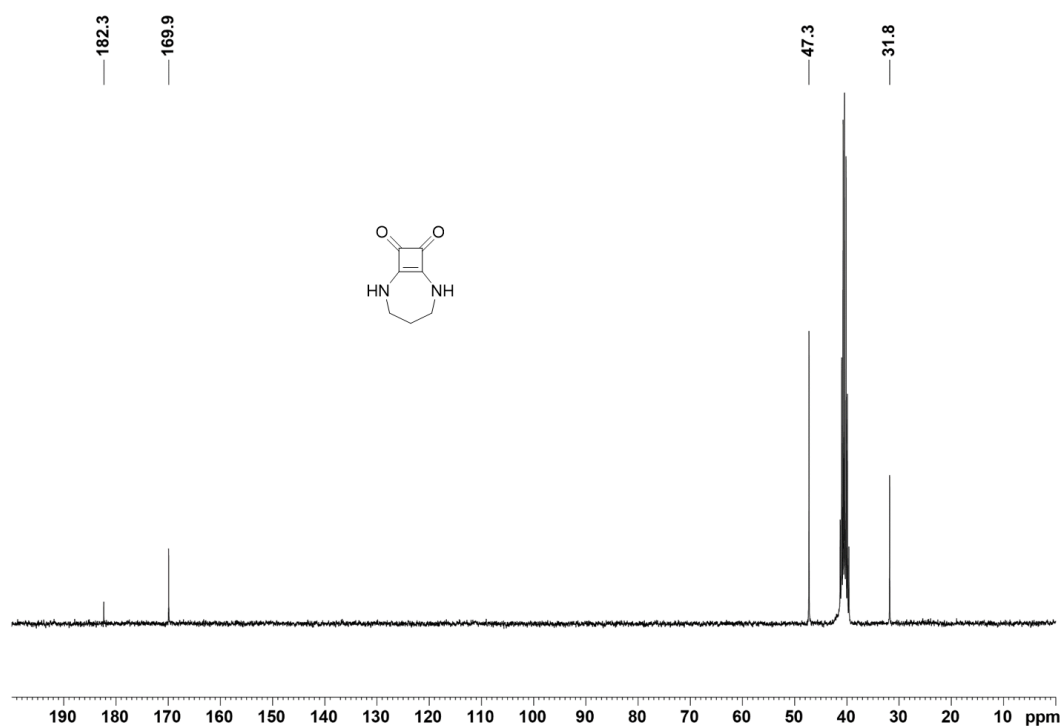


**Figure 3.11.**  $^{13}\text{C}$  NMR spectrum of **23** in  $\text{DMSO}-d_6$ , 300 MHz, 298 K.

*Cyclization of squaramate ester 13b.* Unlike ester **12b** which bears an ethylamine chain, the propylamine chain in ester **13b** is long enough to allow the intramolecular nucleophilic attack of the terminal amino group on the squaryl electrophilic centre leading to the cyclic compound **23**. As mentioned before, under hydrolytic conditions the formation of the corresponding squaramic acid as a result of the hydrolysis reaction

was not detected. The kinetic analysis showed an extremely fast cyclization to afford **23** even in moderate acidic conditions (pH 5, Table 3.7). Besides, at pH 8 and 9 the reaction was too rapid to be measured and only the final product was observed.

**Table 3.7.** Observed rate constants for the cyclization reaction of squaramate ester **13b** at different pHs. \*Not calculable.

Substrate / pH	$k_{\text{obs}}, 10^5 \text{ s}^{-1}$				
	3	5	7	8	9
<b>13b</b>	-	$0.65 \pm 0.01$	$3.68 \pm 0.05$	*	*

To confirm the formation of the cyclic squaramide **23**,  $^1\text{H-NMR}$  kinetic experiments were performed at 24 °C in 0.1 M deuterated PBS at pH 7.0 (Figure 3.12). Evidence of intramolecular cyclization was found by following the appearance of a shaped triplet at 3.7 ppm and a multiplet at 2.3 ppm (red). Analogously, the starting squaramate ester disappearance was evidenced by the decrease of the ethyl squaramate ester signals (blue).

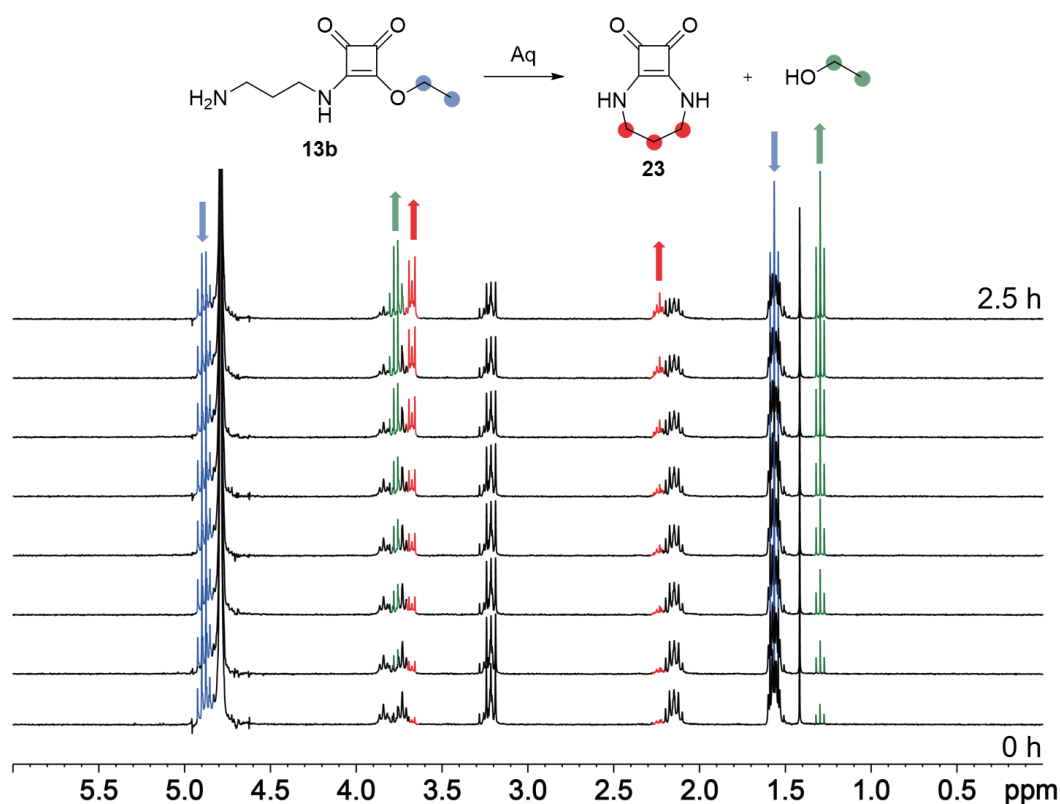


**Figure 3.12.**  $^1\text{H-NMR}$  evolution over time of 1 mM squaramate ester **13b** at 0.1 M PBS at pH 7.0 (24 °C).

The apparent kinetic constant corresponding to the formation of **23** was evaluated by following the appearance of EtOH (triplet at 1.4 ppm and quadruplet at 3.7 ppm, green). The rate constant for the formation of cyclic squaramide **23** was obtained by using the

integral of the triplet signal corresponding to EtOH, to measure the increment of this compound concentration at the solution, as expressed in Eq. 7 and Eq. 8. Thus, the observed rate constant was obtained by adjusting the integration data to a pseudo-first order reaction:

$$-\frac{d[13b]}{dt} = \frac{d[23]}{dt} = \frac{d[EtOH]}{dt} = k_{obs}[EtOH] \quad (7)$$

$$[EtOH] = [EtOH]_0 e^{-k_{obs}t} \quad (8)$$

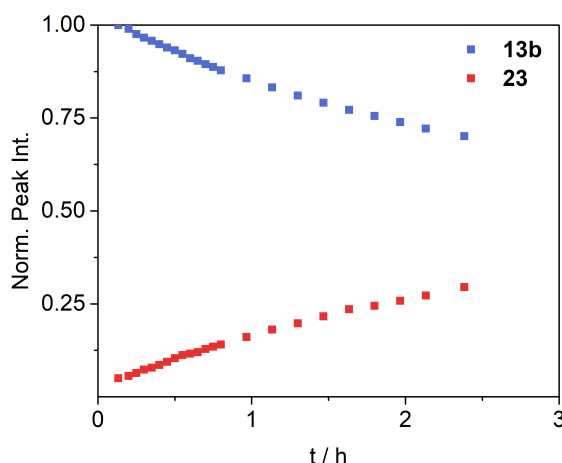
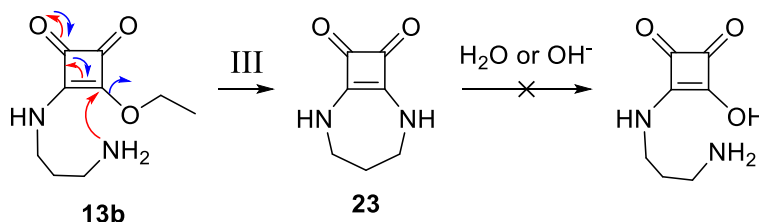


**Figure 3.13.** Representation of the calculated concentrations of **13b** and **23** against time from Eq. 8.

From these data, the calculated apparent pseudo-first order constant was  $4.5 \times 10^{-5} \text{ s}^{-1}$ . As seen on the NMR spectra where any other signals appear, only the cyclization reaction was observed in contrast with the corresponding assisted hydrolysis observed for the amino analogues **9-11** and **12b**.

Thus, the observed irreversible condensation should take place by nucleophilic attack of the terminal amino group followed by loss of ethanol. The mechanism of this cyclization agrees with the previously hypothesized intramolecular nucleophilic attack III where the cyclic key intermediate does not evolve to the corresponding squaramic acid:



**Scheme 3.14.** Aqueous cyclization mechanism for ester **13b** to afford squaramide **23**.

From the preliminary UV data obtained at 37 °C, the cyclization reaction was measurable in a range between pH 5 to 7. At this pH range, the amino group responsible

for the initial nucleophilic attack is pH sensitive. Thus, the rate law responds to a zero order reaction (intramolecular process), and the reaction kinetic constant depends on the  $pK_a$  of such amine and may be written as follows:

$$r = k_{\text{obs}} \quad (9)$$

$$k_{\text{obs}} = k_c[A] = k_c \frac{K_a}{K_a + [\text{H}]} \quad (10)$$

where  $[A]$  is the concentration of the unprotonated form of the amino group of ester **13b**, which is dependent on the pH of the solution. As can be deduced from the Eq. 10, the observed rate constant tends to reach an asymptotic value ( $k_c$ ). This is coherent with a zero order reaction when the concentration of protons is very low.<sup>145</sup> However, because of the high reactivity of ester **13b** and its rapid evolution to cyclic squaramide **23**,  $pK_a$  of the amino terminal group could not be measured by potentiometric titration. Here, we assumed a value around 8.5 based on the previous results obtained for homologous amines (see Table 3.3).

In order to better define the rate constant for the cyclization process ( $k_c$ ) a kinetic study in the acidic pH range 4.5-7 for the cyclization of **13b** (30  $\mu\text{M}$ ) at 37 °C to give **23** was performed (Figure 3.14a). The plot of the observed rate constants against pH led to an asymptotic profile, thus indicating the strong dependence on the pH (Figure 3.14b).

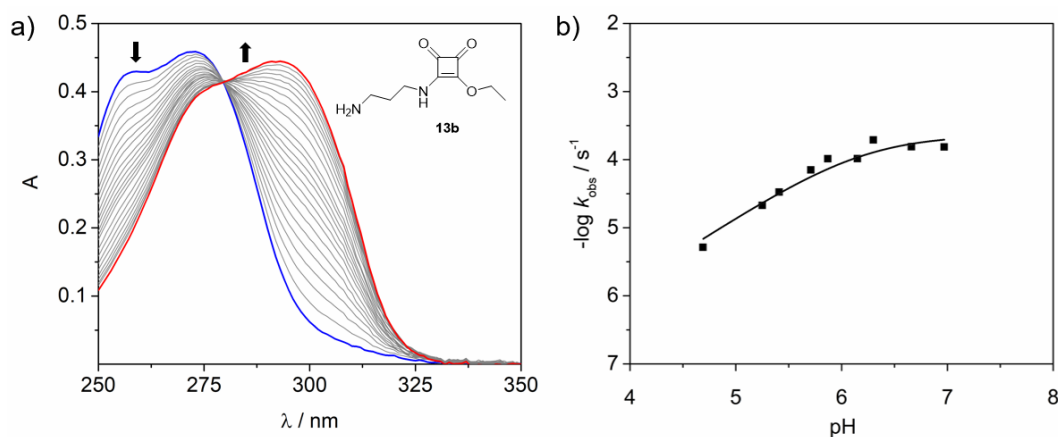


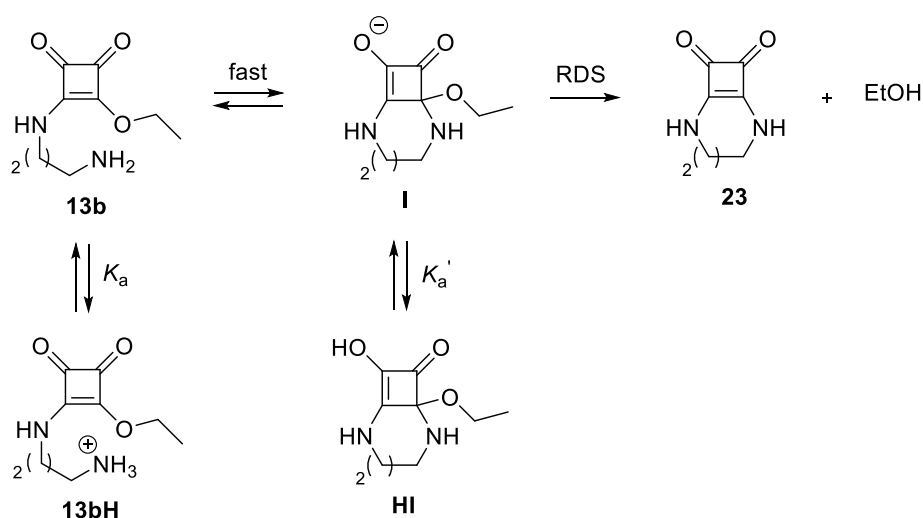
**Figure 3.14.** a) Representative example of the UV changes observed for the cyclization of **13b** (30  $\mu\text{M}$  at 10 mM cacodylate buffer pH 5.7 at 37 °C). b) Plot of the data for  $k_{\text{obs}}$  at pH range 4.5-7. The curve shows the fitting of the experimental data to Eq. 11.

Unlike the results obtained for amino esters **9-11** and **12b**, the aqueous cyclization of squaramate ester **13b** took place in moderate acidic conditions (4.5-7) where the amino terminal group ( $pK_a \approx 8.5$ ) should be fully protonated. To obtain the cyclization constant ( $k_c$ ) and following the procedure for relative esters **9-11** and **12b**, remarkably, the fit of

<sup>145</sup> D. Murzin, T. Salmi. (2005) *Catalytic Kinetics*, Elsevier Science, DOI: 10.1016/B978-0-444-51605-3.X5000-X.

the data to Eq. 10 did not converge when introducing the  $pK_a$  value of the substrate ( $pK_a = 8.5$ ,  $K_a = 3.2 \times 10^{-9}$ ) as a constant value. However, when that  $K_a$  value was also modified in the fitting, a good result was obtained (Figure 3.14b). The results obtained were  $K_a = 6.3 \times 10^{-7}$  ( $pK_a$  6.2) and  $k_c = 2.3 \times 10^{-4} \text{ s}^{-1}$  (half-life of 50 min) with a surprising low  $K_a$  value for an alkylamine.

Considering that the reaction should follow a conventional addition-elimination mechanism and taking into account the moderate acidic media, the process could be written as follows:



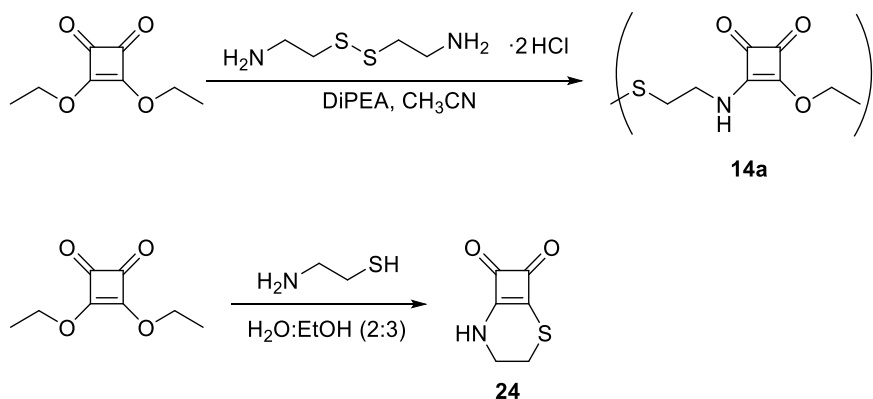
**Scheme 3.15.** Putative intramolecular addition-elimination mechanism for ester **13b** under mildly acidic conditions.

In this rationale, the fact that there is an apparent acidic constant around 6.2 ( $pK_a'$ ), significantly lower than the  $pK_a$  of the amino terminal group ( $pK_a \approx 8.5$ ) suggests that the first nucleophilic attack should not be the rate-determining step (RDS) but a fast process instead. Hence, the elimination of the leaving group could be the limiting step for this reaction and from any of the tautomeric species with an acidic constant of 6.2. In this regard the expression of the observed rate constant should be rewritten as a function of the concentration of an intermediate species, [I]:

$$k_{\text{obs}} = k_c[\text{I}] = k_c \frac{K_a'}{K_a' + [\text{H}]} \quad (11)$$

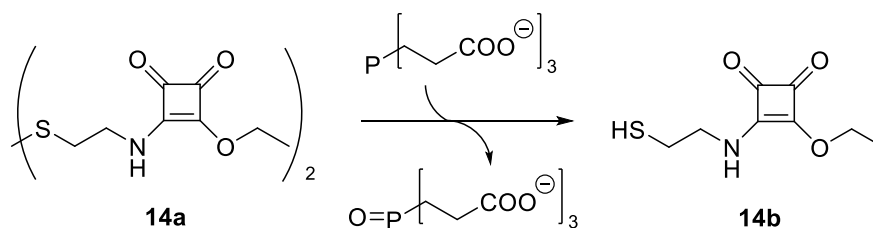
Taking into account the possible prototropic equilibria and, after a fast intramolecular nucleophilic addition reaction, the intermediate species would eliminate an ethanol molecule to form **23** to favour the gain of aromaticity. This fact could be the driving force to increase the acidity of the protonated species.

*Synthesis of diester 14a and its corresponding cyclosquaramide analogue 24.* Diester **14a** was prepared by reaction of cystamine dihydrochloride with two equivalents of diethyl squarate in CH<sub>3</sub>CN in the presence of DiPEEA as a base. On the other hand and also for comparison purposes, the corresponding cyclic squaramate thioester **24** was prepared by reaction of diethyl squarate with cysteamine in a mixture of water:ethanol (2:3).



**Scheme 3.16.** Synthesis of squaramate ester **14a** and cyclic thiosquaramide **24**.

*Cyclization of the squaramate ester 14b.* Unlike the rest of squaramate esters, compound **14b** was prepared in situ by reduction of its disulfide precursor **14a** to afford the reduced thiol form by the action of tris(2-carboxyethyl)phosphine (TCEP) reducing agent (see details in the experimental section).



**Scheme 3.17.** *In situ* reduction of the parent ester **14a** in the presence of a water-soluble phosphine to afford the reduced thiol **14b**.

A priori, the reactivity of the thiol derivative was expected to be similar to that of the amino ester **13b** but, while analysing the UV kinetic evolution of ester **14b** in alkaline hydrolytic conditions, Dr. Cañellas observed an unexpected decomposition of the cyclic thiosquaramide (Figure 3.15).

The hydrolysis reaction performed in acidic and neutral buffered solutions showed, as expected, the appearance of a maximum around 309 nm corresponding to the tethered cyclothiosquaramide **24** (Figure 3.15a, in black). However, when the reaction was performed in alkaline solutions, the maximum at 309 nm disappeared and a second maximum appeared (332 nm, Figure 3.15b, in red).

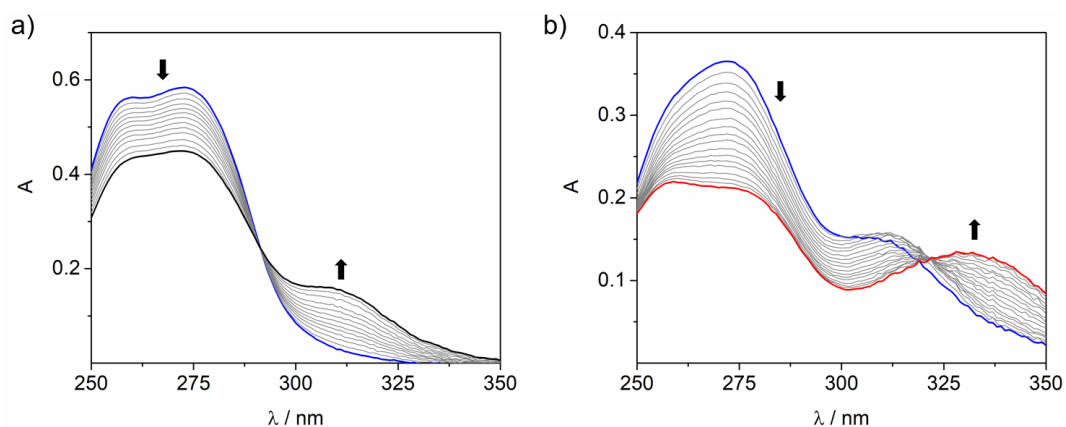
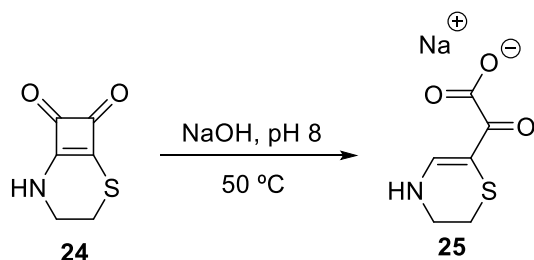


**Figure 3.15.** Representative example of the UV changes observed for the reaction of **14b** ( $30 \mu\text{M}$ ) at  $37 \text{ }^\circ\text{C}$  in a)  $10 \text{ mM}$  acetate buffered solution at pH 5 and b)  $10 \text{ mM}$  PBS buffered solution at pH 8.

To identify the aqueous degradation product, cyclic thiosquaramide **24** was suspended in  $\text{H}_2\text{O}$  and the pH was adjusted to 8 by adding  $\text{NaOH}$   $1\text{N}$  (Scheme 3.18). The suspension was heated up to  $50 \text{ }^\circ\text{C}$  to form a clear solution that was stirred for 5h keeping the pH between 7.5 and 8.5. The final removal of the solvent afforded product **25** as a pale yellow solid.



**Scheme 3.18.** Synthesis of  $\alpha$ -keto carboxylate **25** from cyclic thiosquaramide **24**.

Characterization of product **25** was achieved by mass spectrometry and 1D- and 2D-NMR experiments. The structure characterization of the isolated compound let us propose the structure of the  $\alpha$ -ketocarboxylate showed in Scheme 3.18 as a result of the cyclobutenedione ring-opening. The regioselectivity of the ring-opening reaction to afford **25** was confirmed by the coupling of  $\text{Hd}$  with the nitrogen proton ( $\text{Hc}$ ), observed as a doublet at  $7.72 \text{ ppm}$  ( $J = 6.6\text{Hz}$ ) and the corresponding correlations in COSY, TOCSY and  $^1\text{H}$ - $^{15}\text{N}$ -HSQC and HMBC.

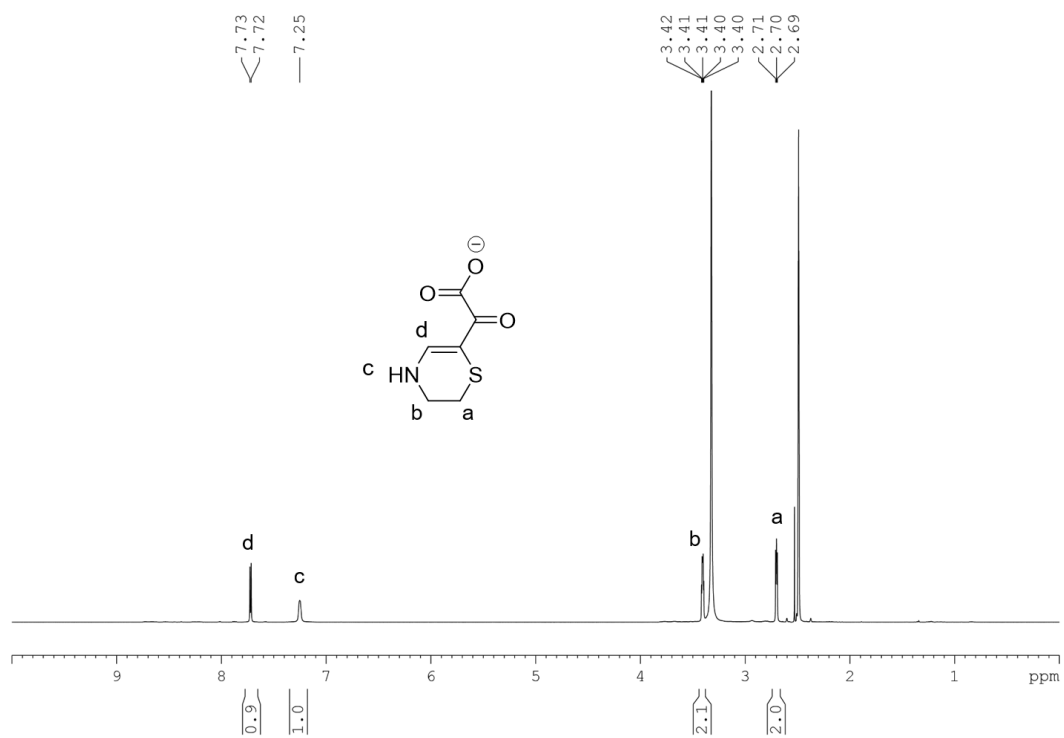


Figure 3.16.  $^1\text{H-NMR}$  of **25** (DMSO- $d_6$ , 298K) and the corresponding signal assignment.

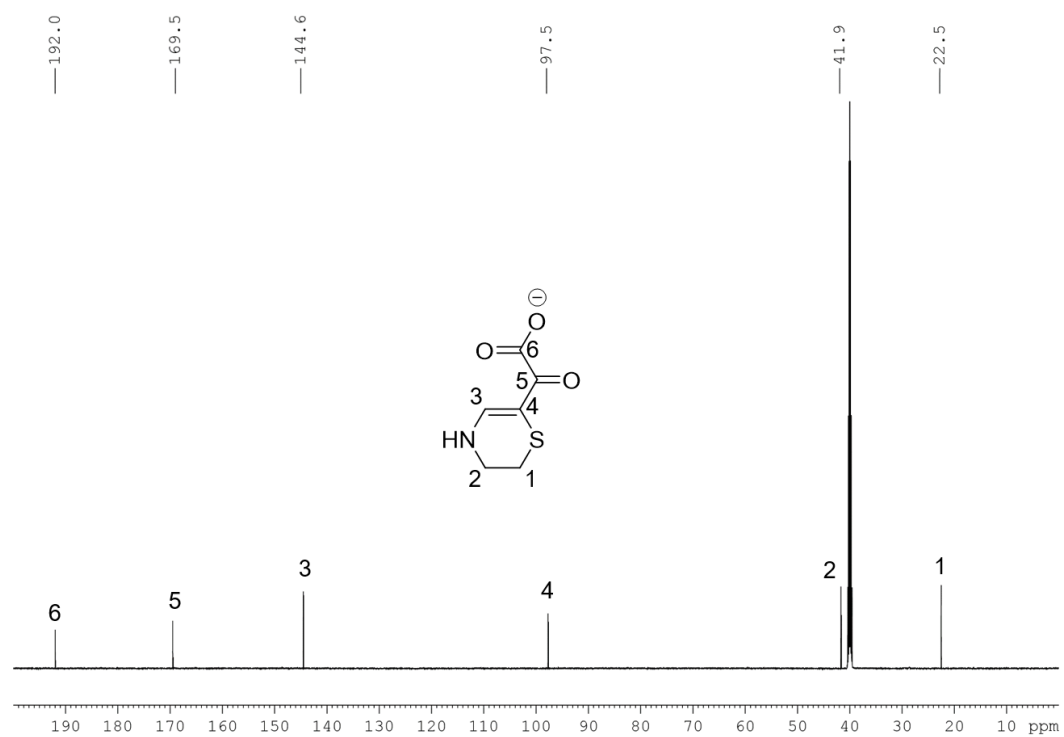
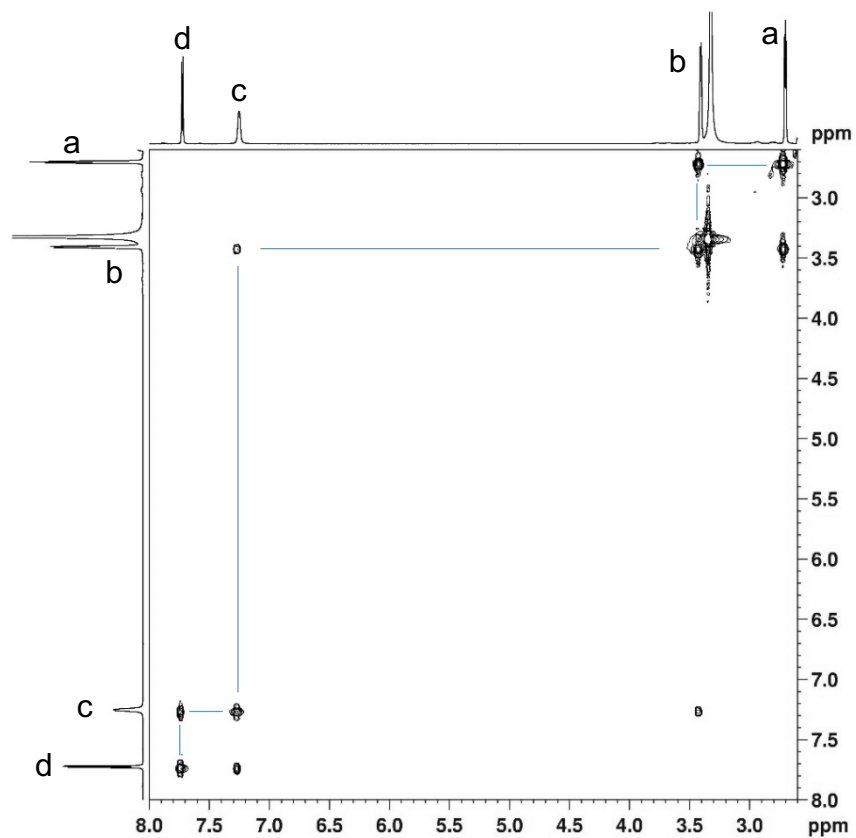
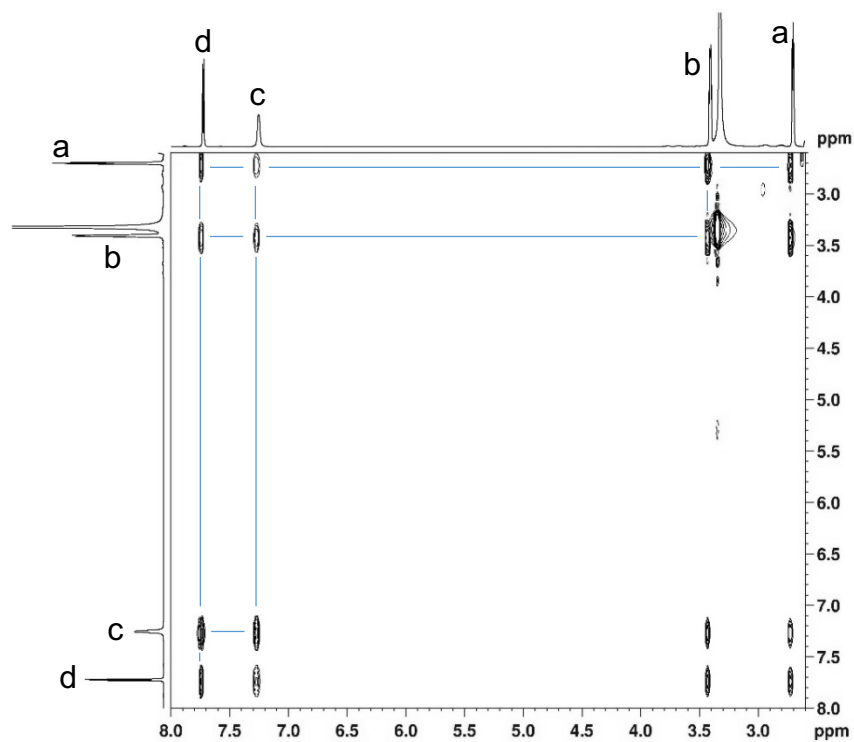


Figure 3.17.  $^{13}\text{C-NMR}$  of **25** (DMSO- $d_6$ , 298K) and the corresponding signal assignment.



**Figure 3.18.**  $^1\text{H}$ - $^1\text{H}$ -COSY experiment of **25** (DMSO- $d_6$ , 298K) and the corresponding signal correlations.



**Figure 3.19.**  $^1\text{H}$ - $^1\text{H}$ -TOCSY experiment of **25** (DMSO- $d_6$ , 298K) with correlation of coupled protons.

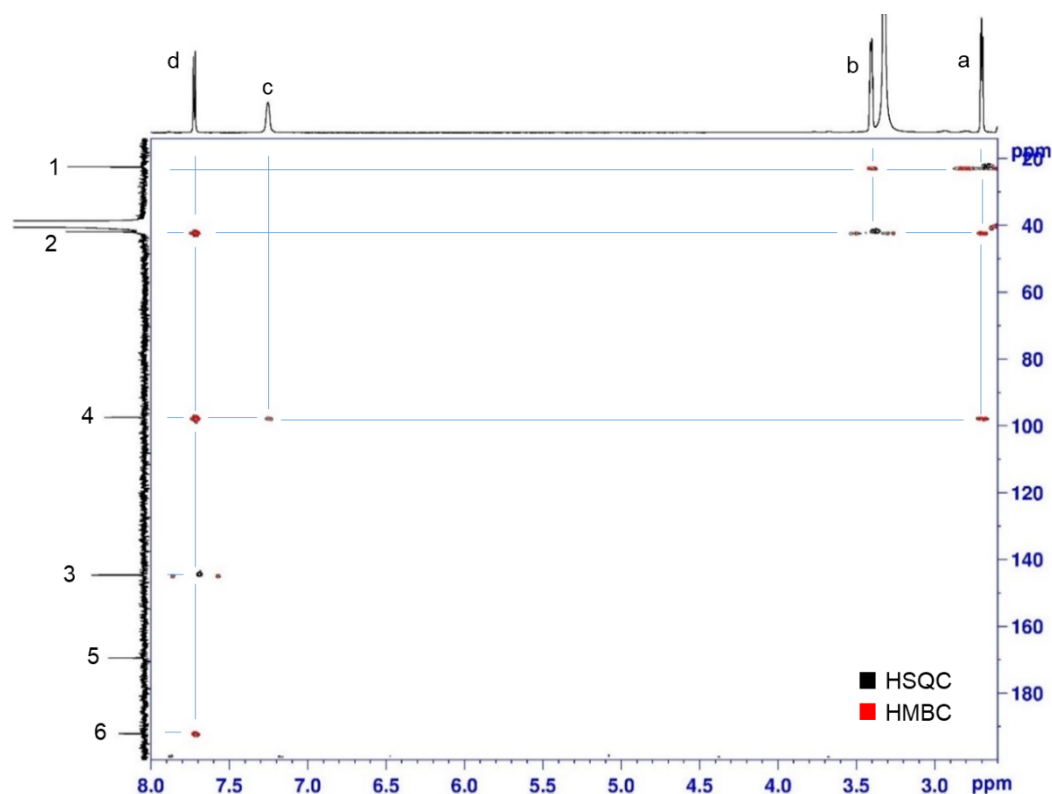


**Figure 3.20.**  $^1\text{H}$ - $^{13}\text{C}$ -HSQC and HMBC (black and red respectively) experiments of **25** (DMSO- $d_6$ , 298K) with the corresponding correlations.

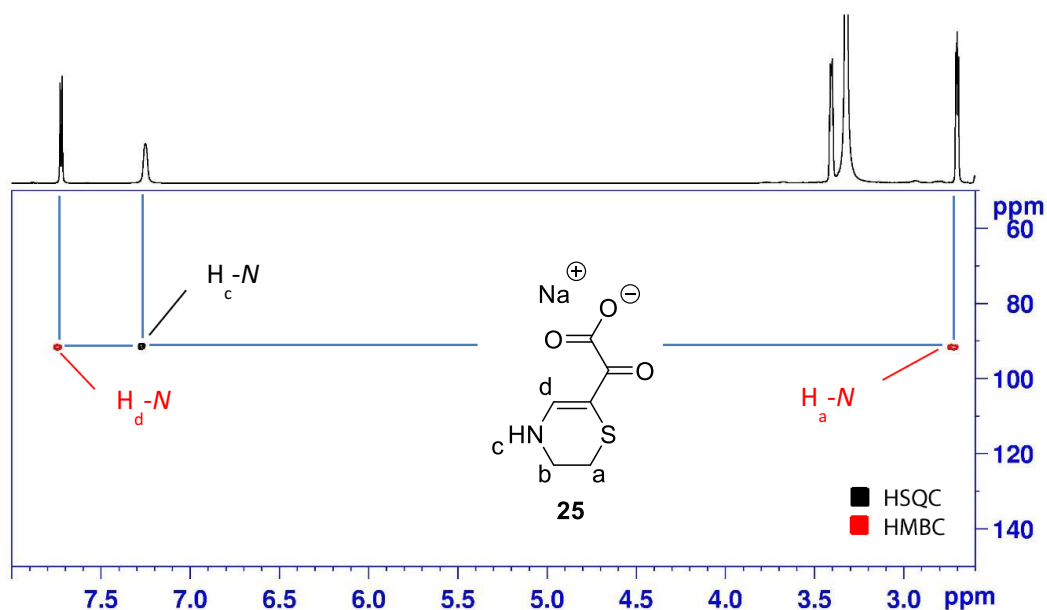
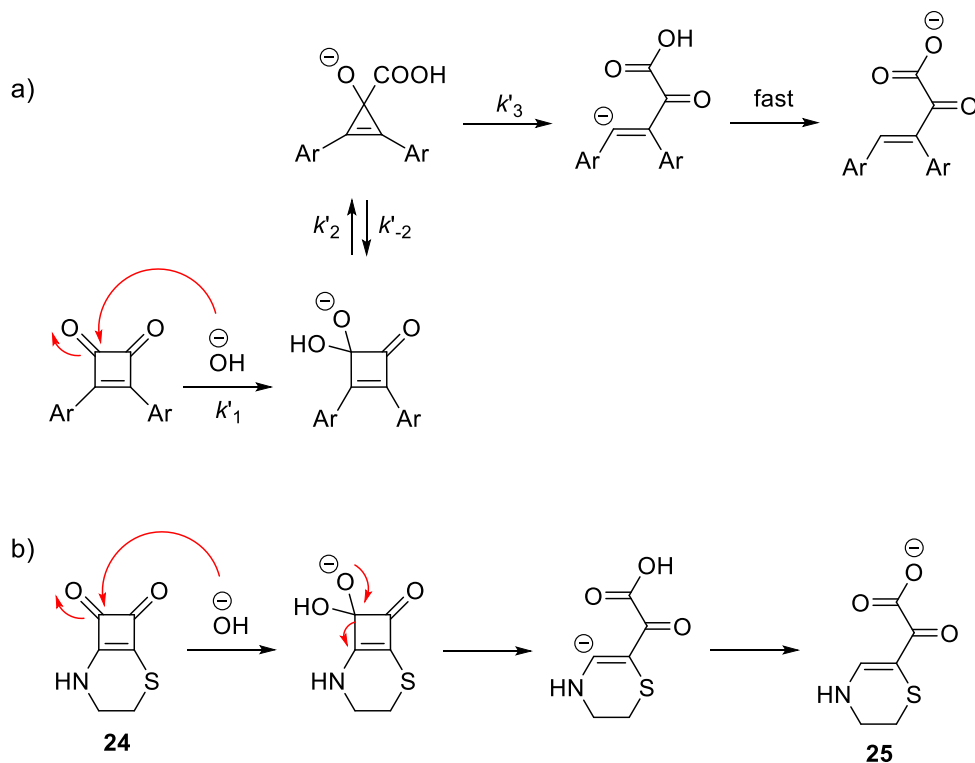


**Figure 3.21.**  $^1\text{H}$ - $^{15}\text{N}$ -HSQC and HMBC (black and red respectively) experiments of **25** (DMSO- $d_6$ , 298K) with the corresponding assignment.

The conversion of the cyclic thiosquaramide **24** into product **25** in alkaline aqueous media suggested a nucleophilic attack of the hydroxide anion to the squaramide carbonyl group followed by a ring opening. A similar reaction was described in 1997 by Horri and collaborators in particular for 3,4-diphenylcyclobut-3-ene-1,2-diones

(Scheme 3.19a). Such squaryl derivatives undergo a rapidly reversible addition of hydroxide anion to the dione, followed by a benzylic acid-type rearrangement to afford a 1-hydroxycyclopropene-1-carboxylic acid that, later, suffers ring fission to give the final product (Scheme 3.19b).<sup>146</sup>



**Scheme 3.19.** a) Proposed mechanism for the ring fission of 3,4-diphenylcyclobut-3-ene-1,2-diones from reference 146. b) Putative squaryl ring fission by 1,2-addition of hydroxide on squaramate thioester **24**.

As deduced from the structure of the 1,2-dicarbonyl compound **25**, the regioselectivity of the process is consistent with the attack of the hydroxide anion to the C4 carbonyl (Table 3.8).

To further understand the reactivity of the squaramate thioester **24**, the LUMO maps (wB97X-D/6-31G\*) of a model squaramate ester and a squaramate thioester were compared (Table 3.8). In a LUMO map, the absolute value of the LUMO is mapped onto an electron density surface. This anticipates where an electron pair (a nucleophile) might attack.

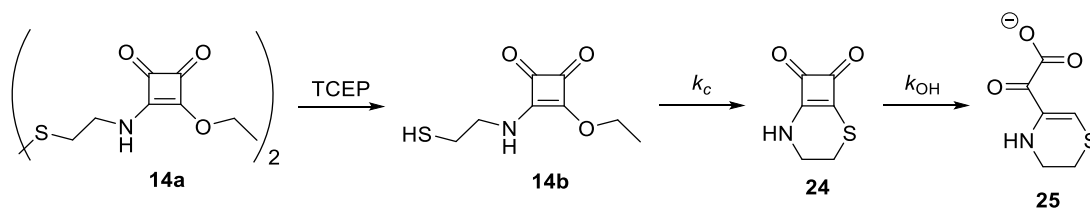
<sup>146</sup> A. Al-Najjar, K. Bowden, M. V. Horri, *J. Chem. Soc. Perkin Trans. 2* **1997**, 993–996

**Table 3.8.** LUMO maps and corresponding Natural Atomic Charges for model squaramate ethyl ester and squaramate ethylthioester.

Label	Natural Atomic Charges, eV	
C1	+ 0.115	+ 0.152
C2	+ <b>0.237</b>	- <b>0.325</b>
C3	+ 0.415	+ 0.460
C4	+ 0.460	+0. 469

Surprisingly, the Natural Atomic Charge of the substituted carbon (C2) changes dramatically from +0.237 eV (*O*-ethyl substitution) to -0.325 (*S*-ethyl substitution). Hence, the reactivity found for squaramate esters in alkali media in C2 was completely different for the thio analogues. In consequence, the electrophilicity of the carbonyl C4 is prone to be attacked by nucleophiles, in this case, hydroxide anion, which leads to the squaryl ring fission.

Once known the aqueous reaction pathway of squaramate ester **14b**, two reaction steps could be distinguished: i) intramolecular cyclization to afford squaramide thioester **24** and ii) degradation of **24** by hydroxide-induced ring-fission to give  $\alpha$ -ketoacid **25** (Scheme 3.20).

**Scheme 3.20.** In situ reduction of **14a** by TCEP and subsequent aqueous cyclization of squaramide ester **14b** to afford intermediate **24** and degradation product **25**.

Hence, the first quick reduction with TCEP of **14a** is followed by the intramolecular cyclization of **14b**. This last reaction is governed by the kinetic constant  $k_c$  that is, a priori, independent of pH (the deprotonation of thiol was not considered). However, if the reaction occurs in alkaline media, the squaramate thioester **24** reacts with hydroxide anion to afford **25** in a reaction step defined by pH-dependent  $k_{OH}$ .

To define both  $k_c$  and  $k_{\text{OH}}$ , the hydrolytic degradation of **24** was studied. Compound **24** (30  $\mu\text{M}$ ) was incubated at 37  $^\circ\text{C}$  at different pH and the corresponding observed pseudo-first order rate constants were obtained ( $k_{\text{obs}}^{\text{OH}}$ ):

**Table 3.9.** Summary of observed pseudo-first order rate constants obtained for the conversion of squaramate thioester **24** into  $\alpha$ -ketoacid **25** at different pH at 37  $^\circ\text{C}$ .

Substrate / pH	$k_{\text{obs}}^{\text{OH}}, 10^5 \text{ s}^{-1}$				
	3	5	7	8	9
<b>24</b>	-	-	$0.74 \pm 0.05$	$4.5 \pm 0.2$	$33.4 \pm 0.7$

The analysis on the UV changes for the conversion of cyclic squaramate thioester **24** into  $\alpha$ -ketoacid **25** revealed a linear dependence on the concentration of hydroxide fitting well to Eq. 2' (Figure 3.22b). Hence, the second order rate constant obtained is  $k_{\text{OH}} = 33.5 \pm 0.7 \text{ M}^{-1} \text{ s}^{-1}$ :

$$k_{\text{obs}} = k_{\text{OH}}[\text{OH}] = k_{\text{OH}} \frac{K_w}{[\text{H}]} \quad (2')$$

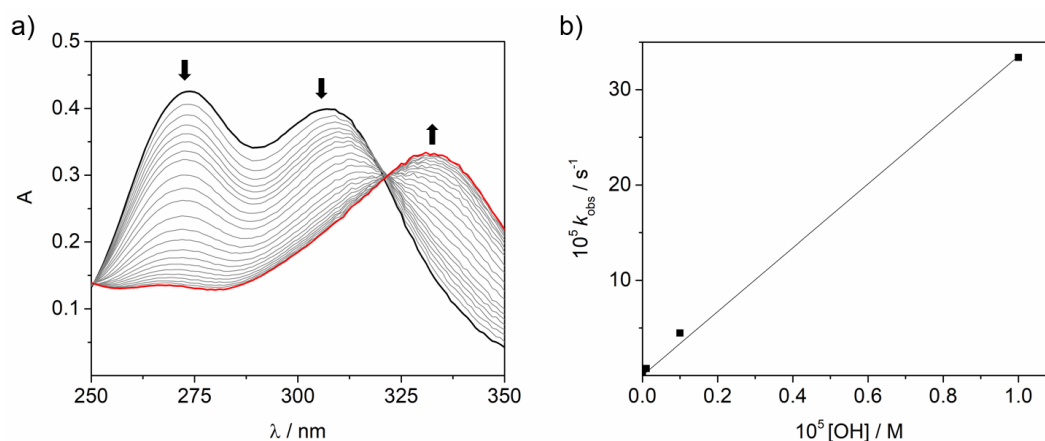


**Figure 3.22.** a) Representative example of the UV changes observed for the degradation of **24** (30  $\mu\text{M}$ ) at 10 mM PBS pH 8 at 37  $^\circ\text{C}$ . b)  $k_{\text{obs}}$  vs  $[\text{OH}]$  plot for squaryl ring fission of ester **24**.

Once the decomposition process kinetics was defined, we could calculate the apparent rate constants for the cyclization process at each pH. We defined the reaction kinetics of **14b** as a sequence of consecutive reactions. Thus, we fixed the previously obtained values for apparent degradation constant at each pH ( $k_{\text{obs}}^{\text{OH}}$ ) to obtain the value of apparent cyclization constant ( $k_{\text{obs}}^{\text{c}}$ ) after the fitting.

**Table 3.10.** Observed pseudo-first order reaction constants for the cyclization of squaramate ester **14** to afford cyclic squaramate thioester **24**.

Substrate / pH	$k_{\text{obs}}^c, 10^5 \text{ s}^{-1}$				
	3	5	7	8	9
<b>14b</b>	$0.72 \pm 0.02$	$0.78 \pm 0.01$	$2.00 \pm 0.03$	$16.1 \pm 0.3$	$1.23 \pm 0.02$

Figure 3.23a shows a representative example of the changes on the UV spectra of 30  $\mu\text{M}$  **14b** in a 10 mM PBS solution at pH 8. The starting material **14b** (blue) is converted into **24** (appearance of a maximum around 330 nm) which is further converted into **25** (maximum at 332 nm). Figure 3.23b shows the calculated speciation diagram in PBS pH 8. The fast consumption of **14b** (blue line) leads to the formation of the intermediate species **24** (black line) which eventually disappears to form **25** (red line).

Thus, after intramolecular cyclization, squaramate thioester **24** reacts with hydroxide to form **25**. The calculation of the apparent rate constants  $k_{\text{obs}}^c$  and  $k_{\text{obs}}^d$  helped us to simulate the distribution in time of all three species. For instance, at pH 8, ester **14b** rapidly evolves to form the cyclic intermediate **24** which within approximately 20 hours is fully converted into **25**.

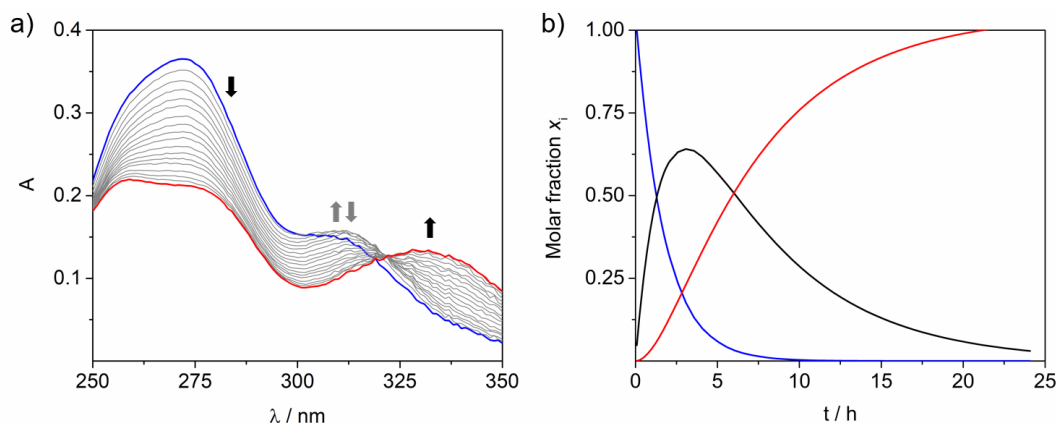
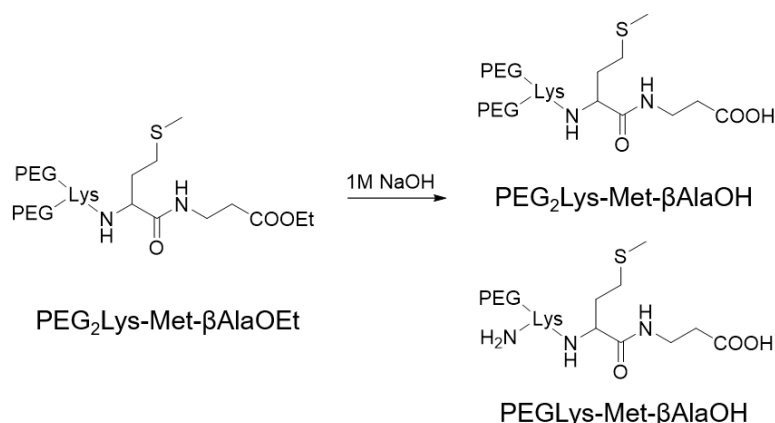


**Figure 3.23.** Example of a) spectral evolution of the hydrolysis of ester **14b** in PBS buffered solution at pH 8. b) Calculated distribution of species for the area of **14b** (blue) over the cyclic product **24** (black) and degradation product **25** (red).

Unlike esters **5-11** and **12b**, both esters **13b** and **14b** do not lead to the corresponding squaramate acids. Instead, they suffer exclusively intramolecular cyclization in aqueous solution, leading to the corresponding cyclic squaramide through the release of an ethanol molecule.

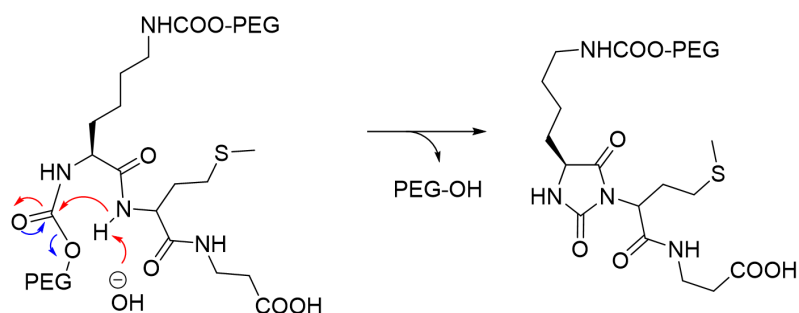
Such behaviour has also been reported for carbamate esters. While exploring the hydrolytic stability and anchimeric assistance of some polyethylene glycol (PEG)-

tagged peptide carboxylic esters, Veronese and collaborators found an unexpected carbamate hydrolysis.<sup>147</sup>



**Scheme 3.21.** Hydrolysis of  $\text{PEG}_2\text{Lys-Met-}\beta\text{AlaOEt}$  with aqueous 1M NaOH and the resulting hydrolysis products  $\text{PEG}_2\text{Lys-Met-}\beta\text{AlaOH}$  and  $\text{PEGLys-Met-}\beta\text{AlaOH}$ .

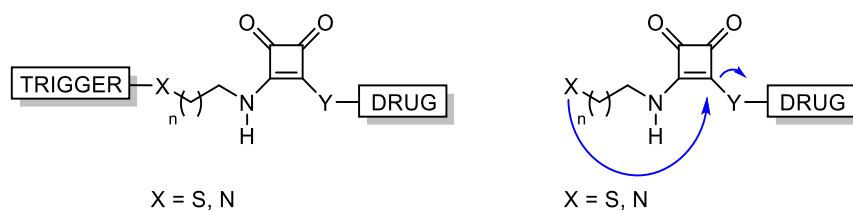
During the synthesis of the branched  $\text{PEG}_2\text{Lys-Met-}\beta\text{AlaOH}$ , the  $\alpha$ -amino residue carbamate of lysine (Lys) suffered an intramolecular nucleophilic attack of the adjacent amide catalysed by a hydroxide anion.



**Scheme 3.22.** Proposed intramolecular cyclization mechanism for the hydrolysis of  $\alpha$ -carbamate PEG ester.

In the previous chapter (Section 1.1.1) we discussed the self-immolative prodrug conjugation as a strategy for drug delivery. In addition to the  $\beta$ -elimination, cyclization mechanisms of disassembly are commonly found and normally, they are based on an intramolecular nucleophilic attack on carbamate or ester conjugates. Formally, the intramolecular cyclization reaction that esters **13b** and **14b** suffer can be considered analogous to a simple self-immolative model for the release of EtOH. Since either amino and thiol groups can undergo the cyclization process, both systems are suitable candidates to be modified under the proper rational design to develop potential prodrugs (Scheme 3.23).

<sup>147</sup> A. Guiotto, M. Canevari, M. Pozzobon, S. Moro, P. Orsolini, F. M. Veronese, *Bioorg. Med. Chem.* **2004**, *12*, 5031–5037.



**Scheme 3.23.** General schematic representation of a squaramide-based self-immolative linker (SIL).

The use of squaramides in medicinal chemistry and chemical biology is increasingly extended because they offer easy synthetic access and high biocompatibility. In this regard, it is advisable to take into account such compounds to contribute to the drug delivery field from the SIL-prodrug approximation.

Along the next chapters, we will discuss the importance of the chemical nature of the payload ( $Y$ ) and its implication on the disassembly rate, but from the results obtained in this chapter we can assume that squaramate esters are perhaps too prone to hydrolysis at physiological conditions, especially in the presence of certain nucleophiles on the SIL structure. Additionally, in Chapter 6 we will explore the tuning of the trigger moiety to activate selectively the immolation process.

### 3.4. CONCLUSIONS

In summary, the squaramate esters studied so far showed different kinetic stability profiles at 37 °C and variable pH. We found a strong relationship between the nature of the alkyl chain and their intrinsic stability in aqueous media. The esters **5-8**, which contained a terminal C, O or sp<sup>2</sup> N were stable until pH 9, where the hydrolysis becomes measurable. The hydrolytic degradation of these compounds follows a conventional second order rate law, with a linear dependency on the concentration of hydroxide species. The reaction rate constant ( $k_{\text{OH}} \approx 10^{-1} \text{ M}^{-1}\text{s}^{-1}$ ) was coherent with the rates obtained for their squaramide analogues ( $k_{\text{OH}} \approx 10^{-4} \text{ M}^{-1}\text{s}^{-1}$ ), that is, the ester hydrolysis is 1000 times faster than that of the corresponding squaramides. These results, together with the previous data found for the hydrolysis of squaramides, compare well with the difference in reactivity observed between carboxylic esters and amides.

Esters **9-11** and **12b**, containing an sp<sup>3</sup> N, showed a pH-dependent hydrolysis rate influenced by the anchimeric assistance of the terminal amino group on the alkyl chain. The anchimeric assistance coexists with the direct hydroxide hydrolysis, decreasing the hydrolytic stability of the squaramate ester residue in comparison with the analogues **5-8**.

The aqueous reactivity of squaramate esters **13b** and **14b**, with a presence of a terminal nucleophile, *NH*<sub>2</sub>, and *SH* respectively, led exclusively to the corresponding cyclic squaramide and squaramate thioester respectively when the alkyl chain is long enough. Formally, the reaction kinetics was fast enough to release an EtOH molecule. Hence, we have found two systems that are potential candidates from which develop self-immolative linkers for their application as prodrugs in drug delivery.

### 3.5. EXPERIMENTAL SECTION

Chemicals were of commercial origin (Aldrich or Scharlau) and were used as received.  $^1\text{H}$ ,  $^{13}\text{C}$  and 2D NMR spectra (at 300 and 600 MHz) and  $^{13}\text{C}$  (at 75 and 150 MHz) spectra were recorded on 300 and 600 MHz spectrometers in  $\text{CDCl}_3$  DMSO- $d_6$  solutions at room temperature. The residual proton signal was used as a reference. Chemical shifts ( $\delta$ ) are given in ppm and coupling constants ( $J$ ) in Hz. ESI-HRMS mass spectra were recorded on a magnetic sector on an Orbitrap mass spectrometer.

#### 3.5.1. Kinetic Experiments

The experiments were carried out on a VARIAN Cary 300 Bio UV-vis spectrophotometer at  $37.0 \pm 0.1$  °C in water. Squaramate esters were dissolved in  $10^{-2}$  M buffered solutions (formic acid, acetic acid, cacodylate, PBS and borate) at a final concentration of 30  $\mu\text{M}$ . The ionic strength was 0.15 M NaCl. For the study of squaramate ester **14b**, the parent disulfide **14a** is dissolved in DMSO (30 mM) and reduced *in situ* by addition of 3 equiv of TCEP. The solution is stirred for 10 min to obtain quantitatively **14b**. The resulting solution is diluted to a final concentration of 30  $\mu\text{M}$  with the corresponding buffer for the kinetic studies. The changes in the UV range were analysed with the ReactLab<sup>TM</sup> Kinetics software (Jplus Consulting Ltd.).<sup>137</sup>

#### 3.5.2. Theoretical Calculations

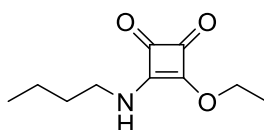
Molecular modelling and calculation of the LUMO maps were performed with Spartan '18 Wavefunction, Inc. Irvine, CA.<sup>148</sup>

---

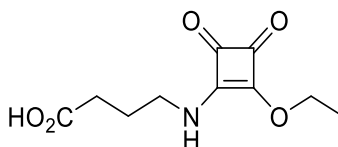
<sup>148</sup> Y. Shao, L.F. Molnar, Y. Jung, J. Kussmann, C. Ochsenfeld, S.T. Brown, A.T.B. Gilbert, L.V. Slipchenko, S.V. Levchenko, D.P. O'Neill, R.A. DiStasio Jr., R.C. Lochan, T. Wang, G.J.O. Beran, N.A. Besley, J.M. Herbert, C.Y. Lin, T. Van Voorhis, S.H. Chien, A. Sodt, R.P. Steele, V.A. Rassolov, P.E. Maslen, P.P. Korambath, R.D. Adamson, B. Austin, J. Baker, E.F.C. Byrd, H. Dachsel, R.J. Doerksen, A. Dreuw, B.D. Dunietz, A.D. Dutoi, T.R. Furlani, S.R. Gwaltney, A. Heyden, S. Hirata, C-P. Hsu, G. Kedziora, R.Z. Khallulin, P. Klunzinger, A.M. Lee, M.S. Lee, W.Z. Liang, I. Lotan, N. Nair, B. Peters, E.I. Proynov, P.A. Pieniazek, Y.M. Rhee, J. Ritchie, E. Rosta, C.D. Sherrill, A.C. Simmonett, J.E. Subotnik, H.L. Woodcock III, W. Zhang, A.T. Bell, A.K. Chakraborty, D.M. Chipman, F.J. Keil, A. Warshel, W.J. Hehre, H.F. Schaefer, J. Kong, A.I. Krylov, P.M.W. Gill and M. Head-Gordon, *Phys. Chem. Chem. Phys.*, **2006**, *8*, 3172–3191.

## 3.5.3. Synthesis

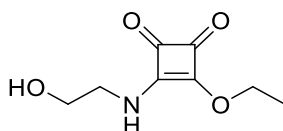
*General procedure for the synthesis of esters 5-11 and 12b:* Diethyl squarate (500 mg, 2.94 mmol) in CH<sub>3</sub>CN (3 mL) and one equivalent of the corresponding amine were mixed in a round-bottom flask and the mixture was stirred under nitrogen at room temperature for 16h. The crude mixture was concentrated to dryness under reduced pressure and purified by column chromatography (SiO<sub>2</sub>) to afford squaramate esters **5-11** and **12a** and **13a**. Boc-protected **12a** and **13a** were treated with TFA in CH<sub>2</sub>Cl<sub>2</sub> to afford the ammonium salts **12** and **13** as trifluoroacetate salts.



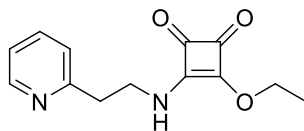
*3-(butylamino)-4-ethoxycyclobut-3-ene-1,2-dione (5).* White solid, 562 mg, 97% yield. Analytical data are in accordance with those reported in literature.<sup>96b</sup>



*4-((2-ethoxy-3,4-dioxocyclobut-1-en-1-yl)amino)butanoic acid (6).* Yellow solid, 554 mg, 83% yield. Analytical data are in accordance with those reported in literature.<sup>96b</sup>

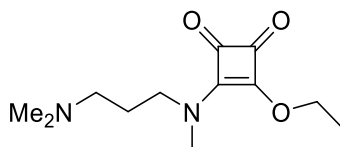


*3-ethoxy-4-((2-hydroxyethyl)amino)cyclobut-3-ene-1,2-dione (7).* White solid, 424 mg, 78% yield. Analytical data are in accordance with those reported in literature.<sup>96b</sup>

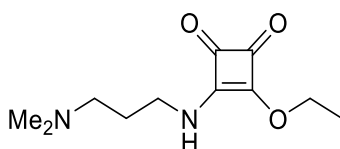


*3-ethoxy-4-((2-(pyridin-2-yl)ethyl)amino)cyclobut-3-ene-1,2-dione (8).* White solid, 51 mg, 41% yield. Analytical data are in accordance with those reported in literature.<sup>149</sup>

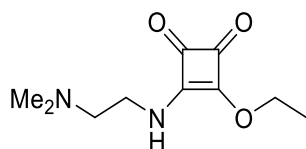
<sup>149</sup> R. Prohens, A. Portell, M. Font-Bardia, A. Bauzá, A. Frontera, *CrystEngComm* **2017**, *19*, 3071–3077.



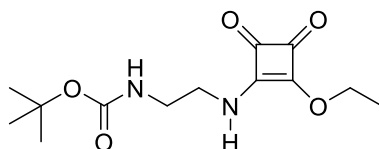
3-((3-(dimethylamino) propyl) (methyl) amino) - 4 - ethoxycyclobut-3-ene-1,2-dione (**9**). Pale yellow oil, 692 mg, 98% yield. Analytical data are in accordance with those reported in literature.<sup>96b</sup>



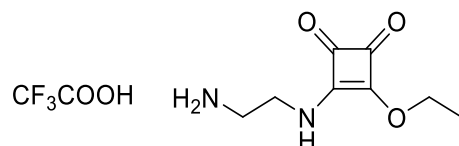
3 - ( ( 3- (dimethylamino) propyl) amino) - 4-ethoxycyclobut-3-ene-1,2-dione (**10**). Pale yellow solid, 605 mg, 91% yield. Analytical data are in accordance with those reported in literature.<sup>96b</sup>



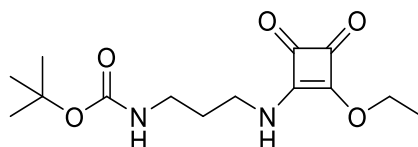
3-((2-(dimethylamino)ethyl)amino)-4-ethoxycyclobut-3-ene-1,2-dione (**11**). Pale yellow solid, 592 mg, 95% yield. Analytical data are in accordance with those reported in literature.<sup>96b</sup>



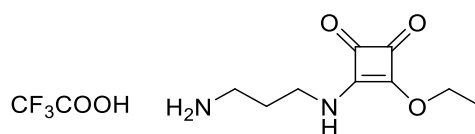
*tert-butyl* (2 -((2-ethoxy-3,4-dioxocyclobut-1-en-1-yl) amino) ethyl) carbamate (**12a**). Silica-gel column chromatography (dichloromethane/tetrahydrofuran gradient = 20:1). Pale oil, 519 mg, 61%. <sup>1</sup>H-RMN (300 MHz, CDCl<sub>3</sub>):  $\delta$  1.43 (dd,  $J = 4.8$  Hz,  $J = 6$  Hz, 2H), 1.48 (t,  $J = 7.2$  Hz, 3H), 3.36 (dd,  $J = 4.8$  Hz,  $J = 6$  Hz, 2H), 3.56 (br s, 1.3H), 3.75 (br s, 0.7H), 4.74 (q,  $J = 7.2$  Hz, 1.3H), 4.86 (br s, 0.7H), 5.93 (br s, 0.5H), 6.37 (br s, 0.5H). <sup>13</sup>C-RMN (75 MHz, CDCl<sub>3</sub>):  $\delta$  16.0, 28.4, 40.8, 45.3, 69.9, 79.9, 156.3, 172.9, 177.8, 182.8, 189.8. ESI (+)-HRMS:  $m/z$  (%) calcd for C<sub>13</sub>H<sub>21</sub>N<sub>2</sub>O<sub>5</sub><sup>+</sup> [M+H]<sup>+</sup> 285,1445; found 285,1446.



2-((2-ethoxy-3,4-dioxocyclobut-1-en-1-yl)amino)ethan-1-aminium trifluoroacetate (**12b**). Boc-protected ester **12a** (500 mg, 1.76 mmol) was dissolved in DCM (20 ml) followed by 700  $\mu$ L of TFA (8.80 mmol). The reaction was stirred at room temperature for 8h and the solvent was removed under rotary evaporation. The remaining TFA was removed by suspending the resulting oil in hexane ( $\times$  3) yielding **12b** as a white amorphous solid, 514 mg, yield 98%.  $^1\text{H-RMN}$  (300 MHz,  $\text{DMSO-}d_6$ ):  $\delta$  = 1.37 (t,  $J$  = 6.9 Hz, 3H), 3.00 (m,  $J$  = 6 Hz, 2H), 3.52 (br, 0.9H), 3.70 (br, 1.1H), 4.66 (q,  $J$  = 6.9 Hz, 2H), 7.864 (br s, 3H), 8.576 (br s, 0.5H), 8.72 (br s, 0.5H).  $^{13}\text{C-RMN}$  (75 MHz,  $\text{CDCl}_3$ ):  $\delta$  = 15.6, 41.1, 41.5, 69.0, 172.1, 176.9, 182.4, 188.2. ESI (+)-HRMS:  $m/z$  (%) calcd for  $\text{C}_8\text{H}_{13}\text{N}_2\text{O}_3^+$   $[\text{M}+\text{H}]^+$  185,0921; found 185,0921.

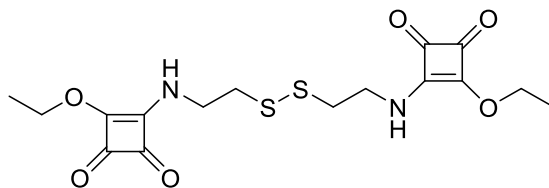


tert-butyl (3-((2-ethoxy-3,4-dioxocyclobut-1-en-1-yl)amino)propyl)carbamate (**13a**). Silica-gel column chromatography (dichloromethane/tetrahydrofuran gradient = 20:1). Pale oil, 479 mg, 91% yield.  $^1\text{H-RMN}$  (300 MHz,  $\text{CDCl}_3$ ):  $\delta$  1.44 (s, 9H), 1.46 (t,  $J$  = 6.9 Hz, 3H), 1.72 (m, 2H), 3.23 (br s, 2H), 3.47 (br s, 1.1H), 3.69 (br, 0.9H), 4.77 (q,  $J$  = 6.9 Hz, 2H), 6.68 (br, 1H), 6.93 (br s 1H).  $^{13}\text{C-RMN}$  (75 MHz,  $\text{CDCl}_3$ ):  $\delta$  16.0, 28.5, 30.5, 31.5, 32.2, 36.5, 36.9, 41.0, 41.7, 69.8, 80.0, 156.8, 157.5, 172.8, 177.2, 177.8, 183.2, 183.4, 189.1, 189.4. ESI (+)-HRMS:  $m/z$  (%) calcd for  $\text{C}_{14}\text{H}_{22}\text{N}_2\text{NaO}_5^+$   $[\text{M}+\text{Na}]^+$  321.1421; found 321.1420.



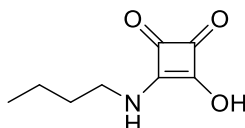
3-((2-ethoxy-3,4-dioxocyclobut-1-en-1-yl)amino)propan-1-aminium trifluoroacetate (**13b**). Boc-protected ester **13a** (120 mg, 0.40 mmol) was dissolved in DCM (10 ml) followed by 157  $\mu$ L of TFA (2.00 mmol). The reaction was stirred at room temperature for 8h and the solvent was removed under rotary evaporation. The remaining TFA was removed by suspending the resulting oil in hexane ( $\times$  3) yielding a white solid, 122 mg, 97%.  $^1\text{H-RMN}$  (300 MHz,  $\text{DMSO-}d_6$ ):  $\delta$  1.38 (t,  $J$  = 7.0 Hz, 2.7H), 1.79 (m,  $J$  = 7.5 Hz, 2H), 2.83 (m,  $J$  = 6.5 Hz, 2.2H), 3.35 (q,  $J$  = 6.9 Hz, 1.3H), 3.53 (q,  $J$  = 7.2 Hz, 1.5H), 4.66 (q,  $J$  = 7.1 Hz, 2.3H), 7.68 (br s, 2.8H), 8.62 (br s, 0.5H), 8.79 (br s, 0.5H).  $^{13}\text{C-}$

RMN (75 MHz, DMSO- $d_6$ ):  $\delta$  16.2, 29.2, 36.9, 41.1, 69.9, 174.8, 186.0. ESI (+)-HRMS:  $m/z$  (%) calcd for  $C_9H_{15}N_2O_3^+$   $[M+H]^+$  199.1077; found 199.1077.

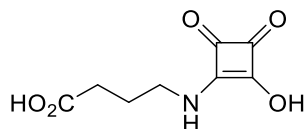


*4,4'* - ((disulfanediy)bis(ethane-2,1-diyl)) bis (azanediyl) bis(3-ethoxycyclobut-3-ene-1,2-dione) (**14a**). Cystamine dihydrochloride (330 mg, 1.47 mmol) was suspended in  $CH_3CN$  (20 mL). After the addition of DIPEA (1.5 mL, 17.64 mmol) the mixture was stirred at room temperature for 10 minutes and then, diethyl squarate (500 mg, 2.94 mmol) was added at once. The reaction was stirred at 50 °C for 6h and the solvent was removed under rotary evaporation. The resulting crude mixture was purified by silica-gel column chromatography ( $CH_2Cl_2/CH_3CN$  1:1 v/v) to afford **14a** as an amorphous white solid, 383 mg (yield 76%).  $^1H$ -RMN (300 MHz, DMSO- $d_6$ ):  $\delta$  1.37 (t,  $J = 7.2$  Hz, 6H), 2.91 (t,  $J = 6.0$  Hz, 4H), 3.59 (q,  $J = 6.0$  Hz, 2.1H), 3.77 (q,  $J = 6.0$  Hz, 1.9H), 4.65 (q,  $J = 7.2$  Hz, 4H), 8.69 (br s, 0.9H), 8.88 (br s, 1.1H).  $^{13}C$ -RMN (75 MHz, DMSO- $d_6$ ):  $\delta = 15.7, 37.8, 38.2, 42.6, 69.0, 172.4, 172.8, 176.9, 177.1, 182.2, 182.4, 189.1, 189.2$ . ESI (+)-HRMS:  $m/z$  (%) calcd for  $C_{16}H_{20}N_2NaO_6S_2^+$   $[M+Na]^+$  423.0660; found 423.0663.

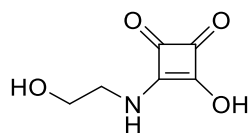
*General procedure for the synthesis of acids 15-22*: Squaramate acids **15-22** were obtained by treatment of the corresponding esters with  $H_2O$  at 60 °C for 16h. Removal of the solvent by rotary evaporation afforded the final product.



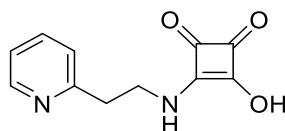
*3-(butylamino)-4-hydroxycyclobut-3-ene-1,2-dione (15)*. White solid, 38 mg, 89% yield. Analytical data are in accordance with those reported in literature.<sup>96b</sup>



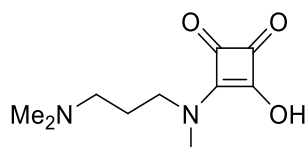
*4-((2-hydroxy-3,4-dioxocyclobut-1-en-1-yl)amino)butanoic acid (16)*. White solid, 40 mg, 88% yield. Analytical data are in accordance with those reported in literature.<sup>96b</sup>



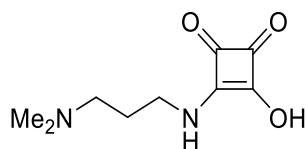
3-((2-aminoethyl)amino)-4-hydroxycyclobut-3-ene-1,2-dione (**17**). White solid, 26 mg, yield 99%.  $^1\text{H-RMN}$  (300 MHz,  $\text{D}_2\text{O}$ ):  $\delta = 3.56$  (t,  $J = 5.4$  Hz, 2H), 3.61 (t,  $J = 5.4$  Hz, 2H).  $^{13}\text{C-RMN}$  (75 MHz,  $\text{DMSO-}d_6$ ):  $\delta = 25.7, 43.0, 183.1, 184.5, 185.2$ . ESI (-)-HRMS:  $m/z$  (%) calcd for  $\text{C}_6\text{H}_6\text{NO}_4^-$  [M] $^-$  156.0302; found 156.0299.



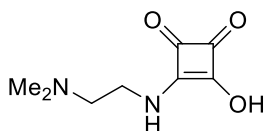
3-hydroxy-4-((2-(pyridin-2-yl)ethyl)amino)cyclobut-3-ene-1,2-dione (**18**). White solid, 16 mg, 95% yield. Analytical data are in accordance with those reported in literature.<sup>149</sup>



3-((3-(dimethylamino)propyl)(methyl)amino)-4-ethoxycyclobut-3-ene-1,2-dione (**19**). White solid, 23 mg, 97% yield. Analytical data are in accordance with those reported in literature.<sup>96b</sup>

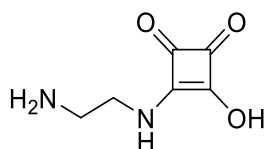


3-((3-(dimethylamino)propyl)amino)-4-ethoxycyclobut-3-ene-1,2-dione (**20**). Pale ochre amorphous solid, 18 mg, 94% yield. Analytical data are in accordance with those reported in literature.<sup>96b</sup>

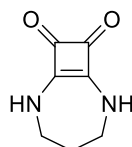


3-((2-(dimethylamino)ethyl)amino)-4-hydroxycyclobut-3-ene-1,2-dione (**21**). White solid, 22 mg, yield 85%. Analytical data are in accordance with those reported in literature.<sup>150</sup>

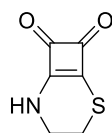
<sup>150</sup> A. Portell, M. Font-Bardia, R. Prohens, *Cryst. Growth Des.* **2013**, *13*, 4200–4203.



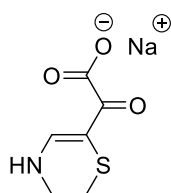
3-((2-aminoethyl)amino)-4-hydroxycyclobut-3-ene-1,2-dione (**22**). White solid, 39 mg, yield 92%.  $^1\text{H-RMN}$  (300 MHz,  $\text{D}_2\text{O}$ ):  $\delta$  2.67 (t,  $J = 6.0$  Hz, 2H), 3.43 (t,  $J = 6.0$  Hz, 2H).  $^{13}\text{C-RMN}$  (75 MHz,  $\text{DMSO-}d_6$ ):  $\delta$  25.7, 43.0, 183.1, 184.5, 185.2. ESI (-)-HRMS:  $m/z$  (%) calcd for  $\text{C}_6\text{H}_7\text{N}_2\text{O}_3^-$  [ $\text{M}$ ] $^-$  155.0462; found 155.0456.



2,6-diazabicyclo[5.2.0]non-1(7)-ene-8,9-dione (**23**). White prisms, 760 mg, yield 84%. Prepared as reported in the literature.<sup>151</sup>



2-thia-5-azabicyclo[4.2.0]oct-1(6)-ene-7,8-dione (**24**). To 453 mg (5.88 mmol) of cysteamine dissolved in 21 mL of  $\text{H}_2\text{O}$  were added 1 g (5.88 mmol) of ethyl squarate dissolved in 30 mL of EtOH. The crude reaction was stirred at room temperature for 1h and the resulting precipitate was filtered out and washed with  $\text{H}_2\text{O}$  ( $3 \times 5$  mL) and  $\text{Et}_2\text{O}$  ( $3 \times 5$  mL). Pale yellow solid, 411 mg, yield 45%.  $^1\text{H-RMN}$  (300 MHz,  $\text{DMSO-}d_6$ ,  $\text{D}_2\text{O}$ : 20%):  $\delta$  = 3.22 (m,  $J = 4.8$  Hz, 2H), 3.81 (m,  $J = 4.8$  Hz, 2H).  $^{13}\text{C-RMN}$  (75 MHz,  $\text{DMSO-}d_6$ ):  $\delta$  = 25.2, 46.2, 161.2, 178.4, 186.2, 187.0. ESI (+)-HRMS:  $m/z$  (%) calcd for  $\text{C}_6\text{H}_6\text{NO}_2\text{S}^+$  [ $\text{M}+\text{H}$ ] $^+$  156.0114; found 156.0113.



Sodium 2-(3,4-dihydro-2H-1,4-thiazin-6-yl)-2-oxoacetate (**25**). 100 mg of cyclosquaramide **24** were suspended in 75 mL of  $\text{H}_2\text{O}$ . Then, the pH was adjusted to 8 with NaOH 1M. The solution was heated up to 50  $^\circ\text{C}$  for 5h adjusting the pH between 7.5 and 8.5. After the reaction time, the solvent was removed by rotary evaporation resulting a pale yellow solid. 120 mg, yield 95%.  $^1\text{H-RMN}$  (600 MHz,  $\text{DMSO-}d_6$ ):  $\delta$

<sup>151</sup> M. Ximenis, J. Pitarch-Jarque, S. Blasco, C. Rotger, E. García-España, A. Costa, *Cryst. Growth Des.* **2018**, *18*, 4420–4427.

2.70 (t,  $J = 4.8$  Hz, 2H), 3.41 (m, 2H), 7.25 (br s, 1H), 7.72 (d,  $J = 6.6$  Hz, 2H).  $^{13}\text{C}$ -RMN (150 MHz,  $\text{DMSO-}d_6$ ):  $\delta$  22.5, 41.9, 97.5, 144.6, 169.5, 192.0. ESI (-)-HRMS:  $m/z$  (%) calcd for  $\text{C}_6\text{H}_6\text{NO}_3\text{S}^- [\text{M}]^-$  172.0074; found 172.0074.

### 3.5.4. NMR Spectra of Selected Compounds

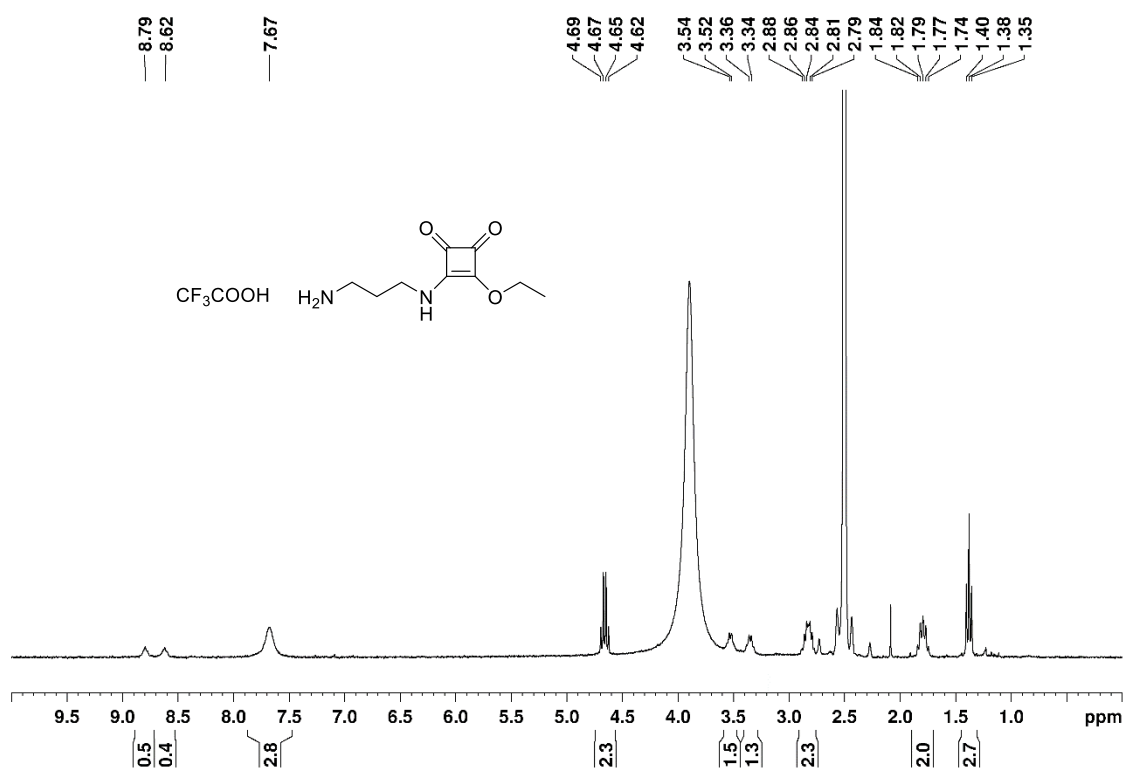


Figure 3.24.  $^1\text{H}$  NMR spectrum of **13b** in  $\text{DMSO-}d_6$ , 300 MHz, 298 K.

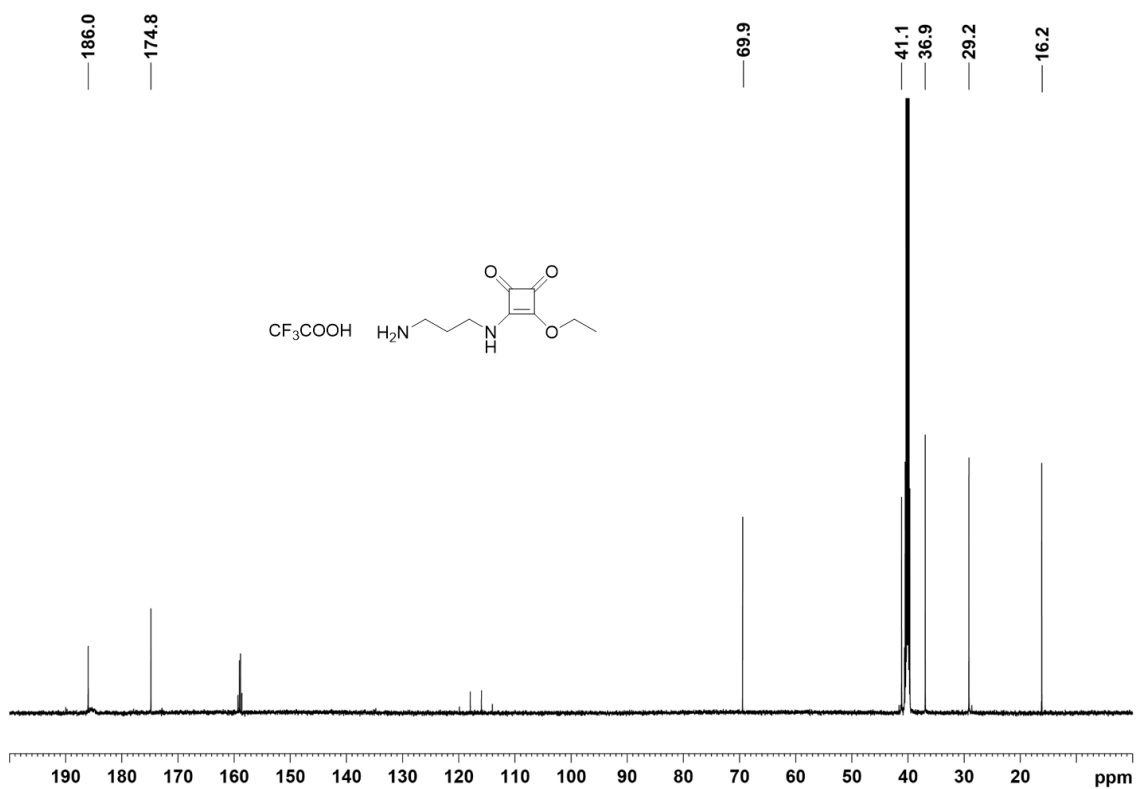


Figure 3.25. <sup>13</sup>C NMR spectrum of **13b** in DMSO-*d*<sub>6</sub>, 300 MHz, 298 K.

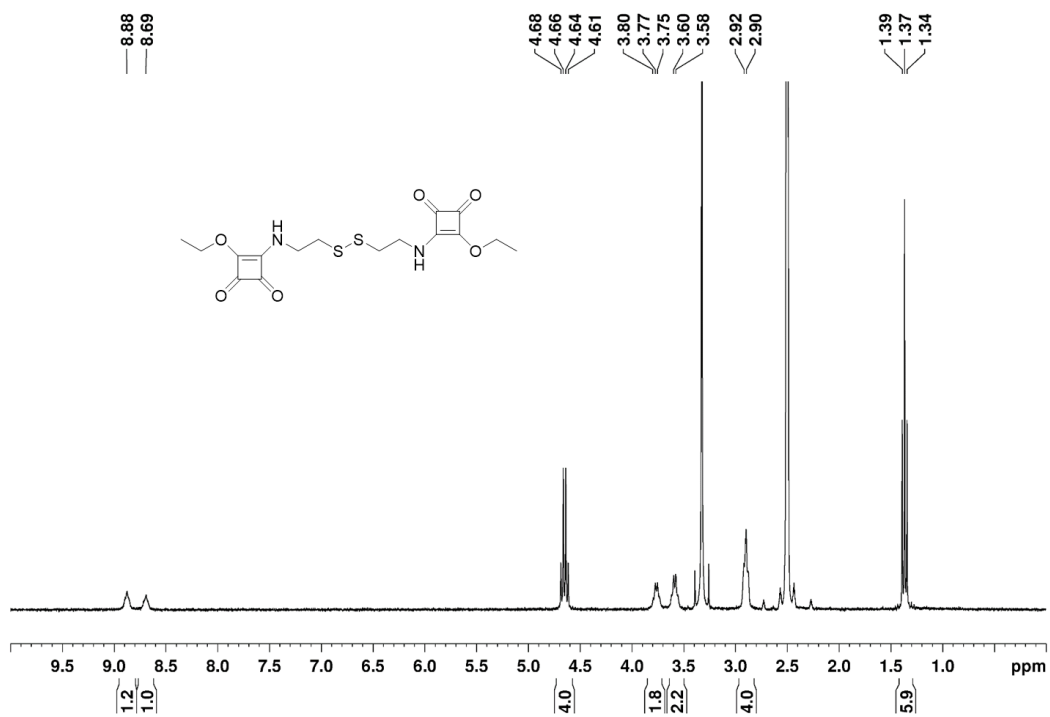


Figure 3.26. <sup>1</sup>H NMR spectrum of **14a** in DMSO-*d*<sub>6</sub>, 300 MHz, 298 K.

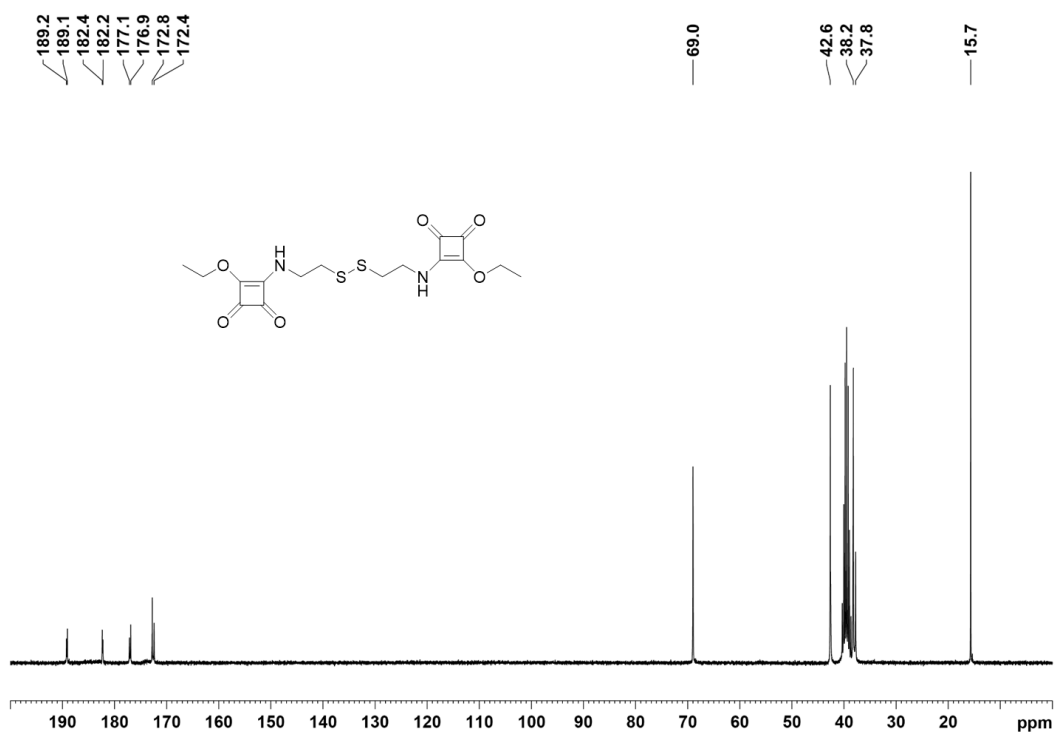


Figure 3.27.  $^{13}\text{C}$  NMR spectrum of **14a** in  $\text{DMSO-}d_6$ , 75 MHz, 298 K.

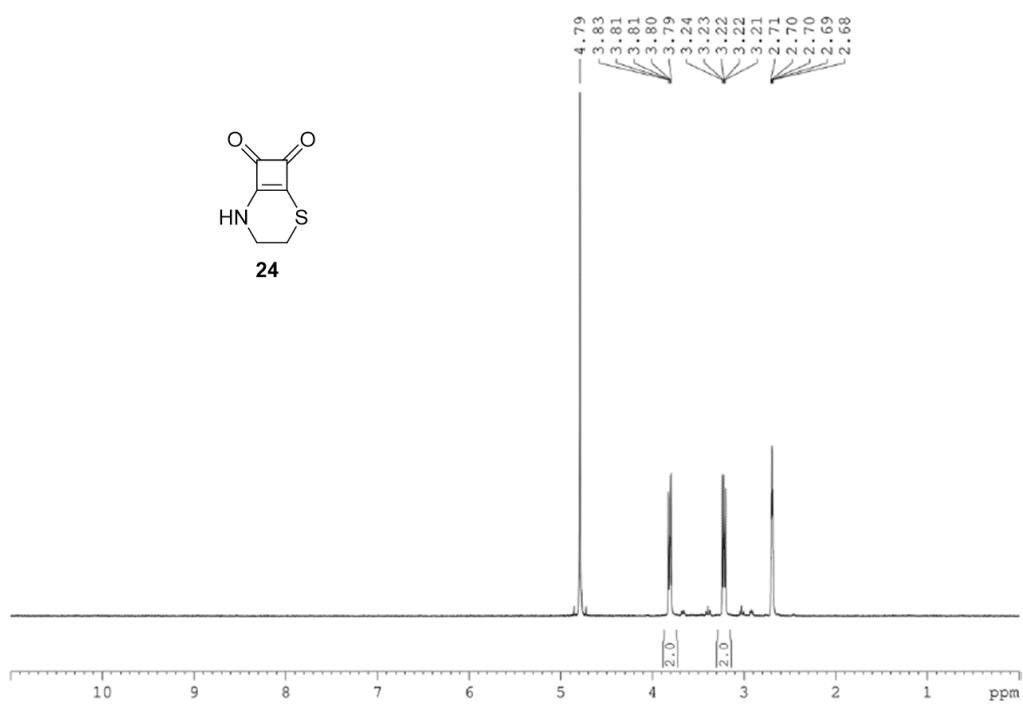
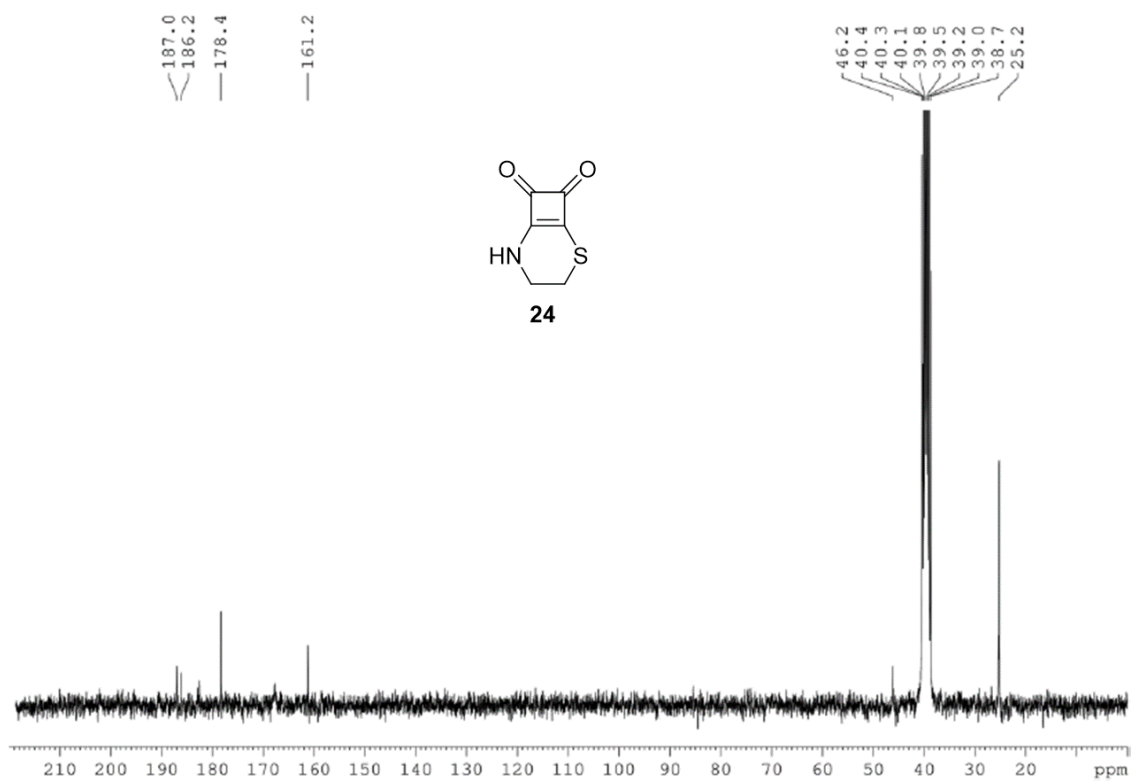


Figure 3.28.  $^1\text{H}$  NMR spectrum of **24** in  $\text{DMSO-}d_6$ ,  $\text{D}_2\text{O}$ : 20%, 300 MHz, 298 K.



**Figure 3.29.**  $^{13}\text{C}$  NMR spectrum of **24** in  $\text{DMSO-}d_6$ ,  $\text{D}_2\text{O}$ : 20%, 75 MHz, 298 K.



4

---

**Water-Soluble Cyclosquaramides:  
Supramolecular Aggregation in  
Solid State**



## 4.1. MOTIVATION

In the previous chapter, the tethered cyclosquaramide **23** was obtained as the main product of the aqueous cyclization of ester **13**. The purification of product **23** afforded transparent colourless crystalline prisms which structure was solved by X-ray crystallography. This compound crystallises exhibiting infinite H-bond ribbons between adjacent squaramide units forming a rectangular-shaped pore of coordinated water molecules. Based on this result we decided to explore the influence of N-methylation of the squaramide in the self-assembly pattern and investigate if it would also affect the occurrence of water clusters in the 3D assemblies.

## 4.2. INTRODUCTION

Hydrogen bonding is the leading driving force to predict the properties of bulk water.<sup>152</sup> The confinement of water in cavities alters that hydrogen-bond network substantially modifying the intrinsic structural, thermodynamic and dynamic properties.<sup>153</sup> For instance, near hydrophilic protein chains, the hydrogen bonding slows the dynamics of water<sup>154</sup> but, conversely, in a hydrophobic carbon nanostructure such interactions are weakened speeding up the dynamics.<sup>155</sup>

### 4.2.1. Natural Water Channels

At a biological level, confined water governs many processes on the molecular scale from electrochemical and enzymatic reactions to protein folding.<sup>156</sup> Among them, the regulation of transcellular water flow is crucial in homeostatic processes of living organisms.

A remarkable example of selective water transport occurs along with the family of aquaporins (AQPs). AQPs are transmembrane proteins capable of transport water across cell membranes with high osmotic permeability and perfect rejection of anions.<sup>157</sup> Figure 4.1 shows the resolved structure of human aquaporin 4 (hAQP4) and some highlighted features published by Stroud and colleagues.<sup>158</sup>

---

<sup>152</sup> J. Liu, X. He, J. Z. H. Zhang, L. W. Qi, *Chem. Sci.* **2018**, *9*, 2065–2073.

<sup>153</sup> S. Chakraborty, H. Kumar, C. Dasgupta, P. K. Maiti, *Acc. Chem. Res.* **2017**, *50*, 2139–2146.

<sup>154</sup> B. Bagchi, *Chem. Rev.* **2005**, *105*, 3197–3219.

<sup>155</sup> J. K. Holt, H. G. Park, Y. Wang, M. Stadermann, A. B. Artyukhin, C. P. Grigoropoulos, A. Noy, O. Bakajin, *Science* **2006**, *312*, 1034–1038.

<sup>156</sup> a) N. E. Levinger, *Science* **2002**, *298*, 1722–3. b) Y. Pocker, *Cell. Mol. Life Sci.* **2000**, *57*, 1008–1017. c) K. Rezaei, E. Jenab, F. Temelli, *Crit. Rev. Biotechnol.* **2007**, *27*, 183–195. d) S. Sen, H. P. Voorheis, *J. Theor. Biol.* **2014**, *363*, 169–187.

<sup>157</sup> a) P. Agre, G. M. Preston, B. L. Smith, J. S. Jung, S. Raina, C. Moon, W. B. Guggino, S. Nielsen, *Am. J. Physiol. Renal Physiol.* **1993**, *265*, F463–F476. b) E. Tajkhorshid, P. Nollert, M. Ø. Jensen, L. J. W. Miercke, J. O'Connell, R. M. Stroud, K. Schulten, *Science* **2002**, *296*, 525–531. c) B. L. De Groot, T. Frigato, V. Helms, H. Grubmüller, *J. Mol. Biol.* **2003**, *333*, 279–293.

<sup>158</sup> J. D. Ho, R. Yeh, A. Sandstrom, I. Chorny, W. E. C. Harries, R. A. Robbins, L. J. W. Miercke, R. M. Stroud, *PNAS* **2009**, *106*, 1–6.

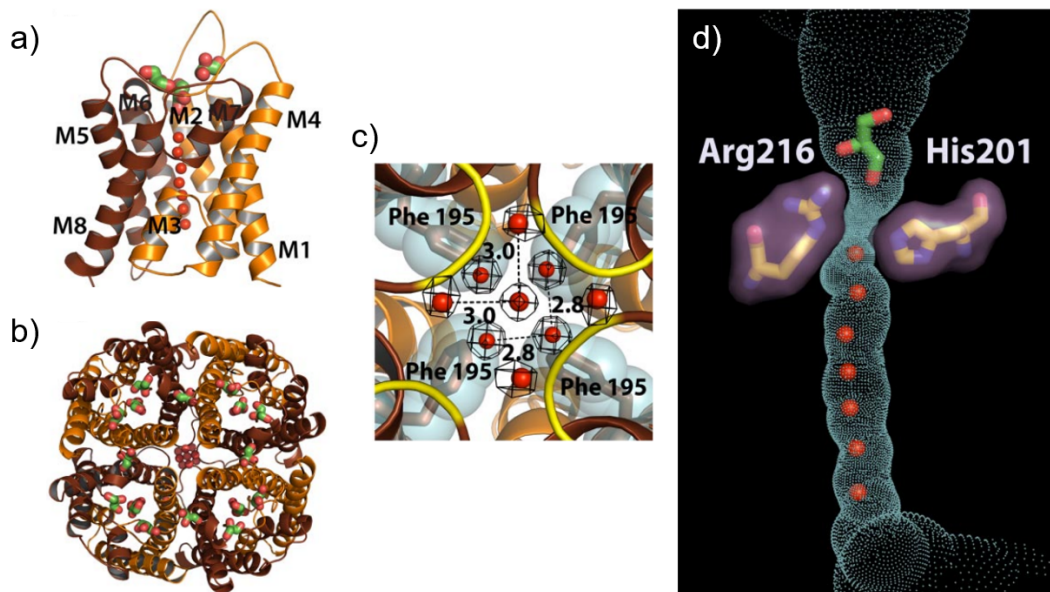


**Figure 4.1.** General features of hAQP4. a) and b) Monomer and tetramer views. Brown and orange colours represent the N- and C- terminal pseudo-2-fold related portions. Water molecules are represented as red spheres, and glycerol molecules are shown as green sticks. c) Central pore formed by the tetramer and water molecules found at the intracellular side of it. The backbone amides of Ser-188 and Gly-189 are coloured yellow in diagram representation. Phe-195 is shown as a brown stick and cyan surface. d) The conducting pore. The trace of the pore inner surface is shown in cyan. The selectivity filter residues, Arg-216 and His-201, are shown as sticks with surfaces in purple. The glycerol molecule is shown as a green stick, and the water molecules in the channel are shown as red spheres. Modified from reference 158.

The selectivity-filter for water is achieved in hAQP4 by the presence of His 201 residue which lies at the end of the protein pore, reducing the channel diameter to  $\approx 1.5 \text{ \AA}$  (external diameter  $\approx 5 \text{ \AA}$ ). Such selectivity is represented in Figure 4.1. Crystallization of hAQP4 was performed in 5% (v/v) glycerol (0.7M) and 3 glycerol molecules are found outside the channel, in the extracellular vestibule (green sticks) while water molecules (red spheres) are found within the pore channel.

In addition to AQPs, water may be indirectly transported by protein transporters of specific substrates.<sup>159</sup> The gramicidin family,<sup>160</sup> Urea transporter UT-B,<sup>161</sup> Cystic Fibrosis Transmembrane Conductance Regulator (CFTR)<sup>162</sup> or cotransporters as such as K-Cl cotransporter<sup>163</sup> or Na-K-Cl cotransporter<sup>164</sup> are some examples of porous

<sup>159</sup> B. Huang, H. Wang, B. Yang, *Adv. Exp. Med. Biol.* **2017**, 969, 251–261.

<sup>160</sup> B. L. De Groot, D. P. Tieleman, P. Pohl, H. Grubmüller, *Biophys. J.* **2002**, 82, 2934–2942.

<sup>161</sup> B. Yang, A. S. Verkman, *J. Biol. Chem.* **2002**, 273, 9369–9372.

<sup>162</sup> R. Schreiber, R. Greger, R. Nitschke, K. Kunzelmann, *Pflugers Arch. Eur. J. Physiol.* **1997**, 434, 841–847.

<sup>163</sup> T. Zeuthen, *J. Physiol.* **1994**, 478, 203–219.

<sup>164</sup> S. Hamann, J. J. Herrera-Pérez, T. Zeuthen, F. J. Alvarez-Leefmans, *J. Physiol.* **2010**, 588, 4089–4101.

channels able to transport water. Figure 4.2 shows an example of the simulation of the water pore of gramicidin A (gA) in the two possible conformations.

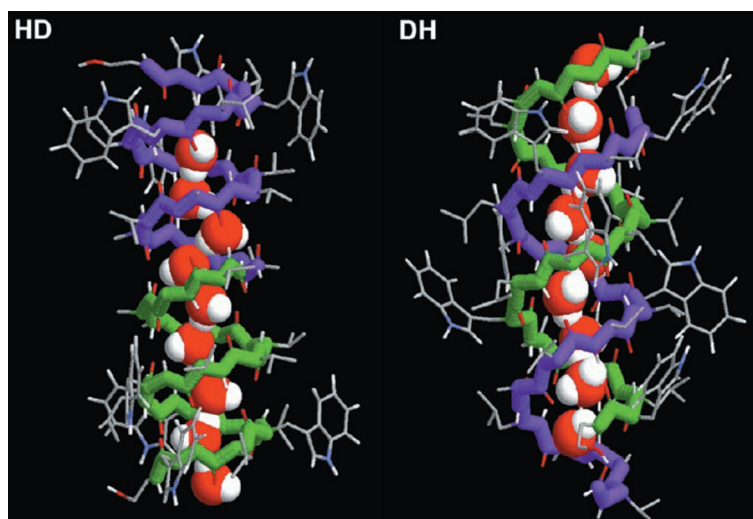


**Figure 4.2.** Water distribution in the simulated conformations of gA: helical dimer (HD, left) and double-helix conformation (DH, right). Reproduced from reference 160.

Highlighted along the channel pore, a single-file hydrogen-bonded water column is observed finding seven to nine water molecules present inside each of two conformations.

#### 4.2.2. Artificial Water Channels

Artificial water channels (AWC) constitute an alternative proposal to biological membranes which aim to mimic their water permeability and solute exclusion. AWCs are constituted by a central pore (hydrophilic or hydrophobic) which allows the passage of water and a hydrophobic shell that permits their insertion into lipidic membranes. Depending on the structure of the channels, two main approaches towards the design can be found: 1) *single-molecular channels*, constituted by one molecular entity which can span the length of the bilayer; and 2) *supramolecular channels*, which imply supramolecular assemblies of discrete molecular components to form the water channels.

Percec and colleagues pioneered the first report on diffusion of water and facilitated transport of protons with other ions exclusion. Their system was based on the self-assembly of dendritic dipeptides through  $\pi$ -stacking forming stable helical pores in the bilayers (Figure 4.3).<sup>165</sup>

<sup>165</sup> a) V. Percec, A. E. Dulcey, V. S. K. Balagurusamy, Y. Miura, M. Peterca, S. Nummelin, U. Edlund, S. D. Hudson, P. A. Heiney, H. Duan, S. N. Magonov, S. A. Vinogradov, *Nature* **2004**, *430*, 764–768. b) V. Percec, E. Dulcey, M. Peterca, M. Ilies, M. J. Sienkowska, P. A. Heiney, *J. Am. Chem. Soc.* **2005**, *51*, 17902–17909.

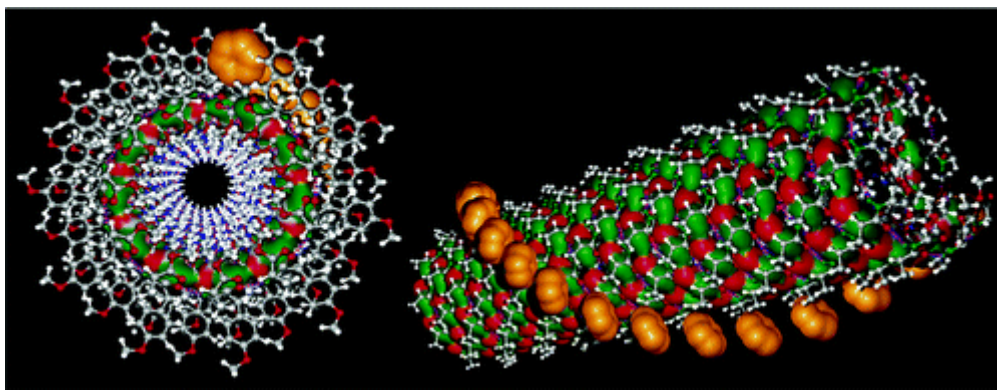


**Figure 4.3.** Percec's dendritic peptides. Hydrogen bond-driven self-assembly of monomers leads to helicoidal pores. Reproduced from reference 165.

Years later, Barboiu and co-workers reported the imidazole (I) quartets, forming water and proton dipolar channels.<sup>166</sup> Here, ureido imidazole compounds define stable supramolecular assemblies driven by H-bond interactions between the urea residues and the imidazole quartets, defining tubular architectures including water-wire arrays. The resulting architectures remind of those found on the cation-stabilized G-quartet structure.<sup>167</sup>

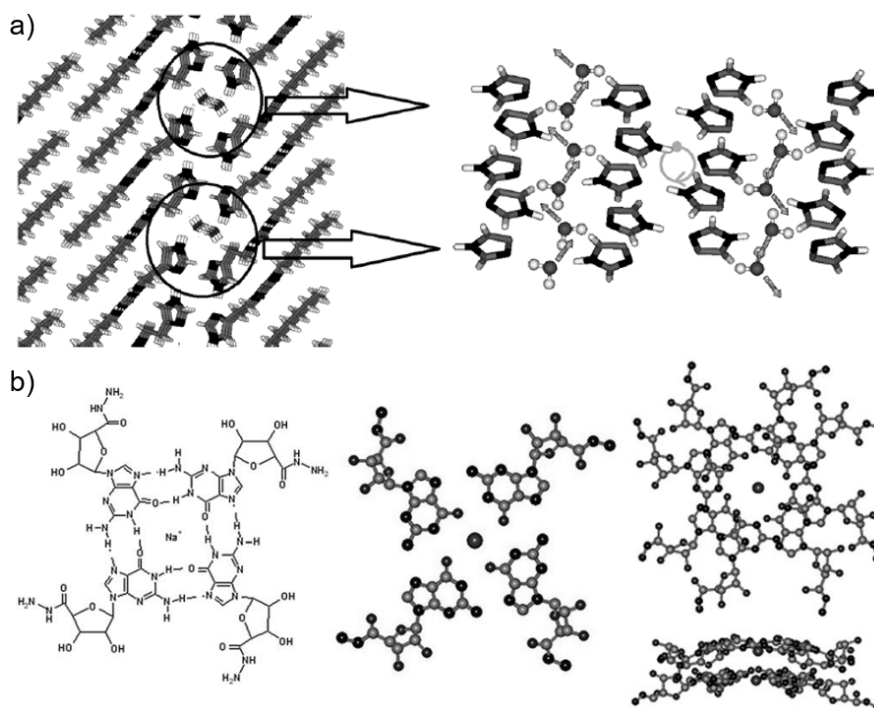


**Figure 4.4.** a) Barboiu's imidazole quartets and comparison with b) Structure of hydrogen-bonded g-quartets. Modified from references 166 and 167.

<sup>166</sup> Y. Le Duc, M. Michau, A. Gilles, V. Gence, Y. M. Legrand, A. Van der Lee, S. Tingry, M. Barboiu, *Angew. Chem. Int. Ed.* **2011**, *50*, 11366–11372.

<sup>167</sup> J. T. Davis, *Angew. Chem. Int. Ed.* **2004**, *43*, 668–698.

Unlike Percec's and Barboiu's approach which imply supramolecular assemblies of molecular components to form the water channels, in 2012 Hou's group presented single-molecular channels, constituted by molecular entities of hydrazide-functionalized pillar[5]arenes.<sup>168</sup> Intramolecular hydrogen bonding induced tubular conformations which were subsequently included in lipidic vesicles for water transport.

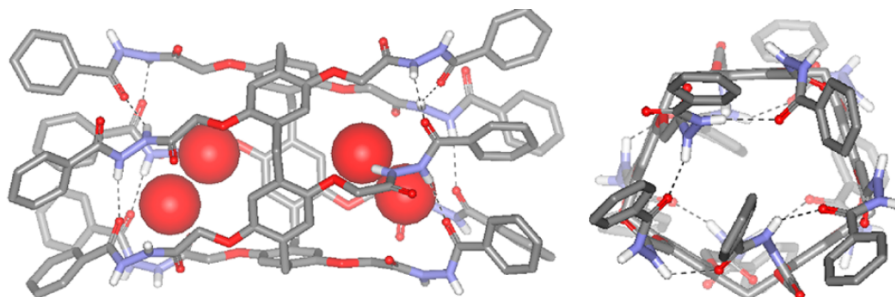


**Figure 4.5.** Crystal structure (stick model) of Hou's pillar[5]arene. Side and top view respectively. Reproduced from reference 168.

Figure 4.6 summarises the three AWC described above highlighting their ability to transport water through lipidic membranes.<sup>169</sup>

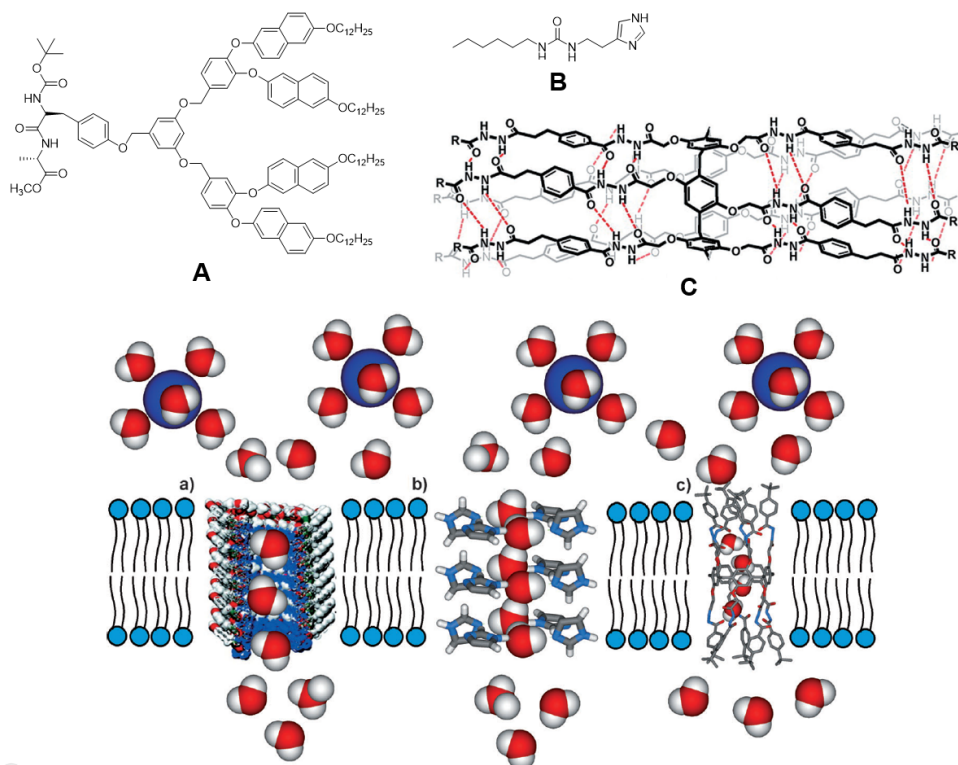


**Figure 4.6.** AWC: a) cross-section of the helical pore assembled from Percec's dendritic peptides A. b) Barboiu's I-quartet B and the oriented dipolar water wires towards the channel. c) Hou's hydrazide functionalised pillar[5]arenes C and the resulting single-molecule water channel. Modified from reference 169.

<sup>168</sup> X. Hu, Z. Chen, G. Tang, J. Hou, Z. Li, *J. Am. Chem. Soc.* **2012**, *134*, 8384–8387.

<sup>169</sup> M. Barboiu, *Angew. Chem. Int. Ed.* **2012**, *51*, 11674–11676.

### 4.2.3. Industrial Applications

Inspired by nature, materials bearing artificial water channels that can regulate the transport of water molecules through them are of great interest for industrial applications.

In the last Global Risks Report (2019) water scarcity was listed as one of the largest worldwide crisis in terms of potential impact over the next decade.<sup>170</sup> In addition to the huge increment in population and economic activities, the lack of access to water has become a serious threat and could lead to severe conflict.<sup>171</sup> During decades researchers have put their efforts to address this issue.<sup>172</sup> Oceans represent the largest source of water on the Earth and thus, desalination can be faced from two main approaches 1) thermal processes (multi-effect desalination, MED and multi-stage flash, MSF) and 2) membrane processes (pressure driven reverse osmosis, RO; voltage driven electro-dialysis, ED; membrane distillation, MD and forward osmosis, FO). Among them, RO technologies are the most extended and, for the past 30 years, have been implemented in the construction of new desalination plants (Figure 4.7a).<sup>173</sup>

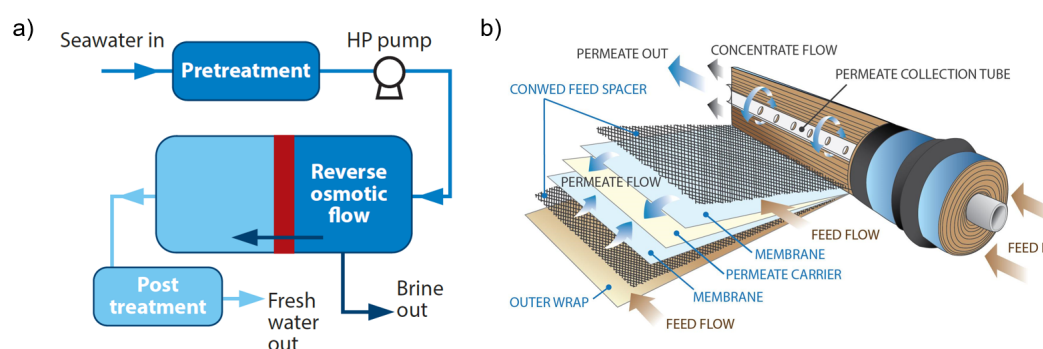


**Figure 4.7.** Schematic representation of a) RO industrial system.<sup>173</sup> b) domestic RO membrane structure.<sup>174</sup>

Despite of it had been huge industrial developments on energy efficiency to reduce the costs of RO, the most hectic technological demand keeps being membrane innovation. Along with water permeability, it is a must for RO membranes to increase their selectivity to water molecules and exclude ions (Figure 4.7b).<sup>175</sup>

<sup>170</sup> *Global Risks Report 2019*. World Economic Forum. Accessed 16 April 2019, <<http://www.weforum.org>>

<sup>171</sup> J. Eliasson, *Nature* **2015**, *517*, 6.

<sup>172</sup> M. M. Mekonnen, Y. A. Hoekstra, *Sci. Adv.* **2016**, *2*, 1–7.

<sup>173</sup> J. Imbrogno, G. Belfort, *Annu. Rev. Chem. Biomol. Eng.* **2016**, *7*, 29–64.

<sup>174</sup> Seal Water Tech. Eastern Cape, South Africa. (<https://www.sealwatertech.co.za/reverse-osmosis-systems>)

<sup>175</sup> Kumar, M., Culp, Y. & Shen Y.-X., *Water Desalination: History, Advances, and Challenges*, The Bridge, 22–29, (National Academy of Engineering, 2016).

In this vein, the efficient permeability of AQP has inspired their incorporation into RO membrane systems. However, their large scale industrial application is handicapped by the high costs of the AQP production, low stability, and fabrication limitations. To overcome this issue, AWCs have become promising architectures for designing more selective and efficient membranes for water purification applications. From an engineering point of view, the large cross-sectional area of AQPs ( $\sim 9.0 \text{ nm}^2$ ) results disproportionate in comparison with the size of its pore and results difficult to implement in an RO system. However, the AWCs channels in 2D layers would take up significantly less space than proteins reducing the active space and consequently, the costs on the design of new membranes.

### 4.3. OBJECTIVES

In analogy with Barboiu's imidazole quartet, the main aim of this chapter is to explore the effect of *N*-methylation on the self-assembly behaviour of related squaramides and study their ability to form water channels.

In particular, the aims of this chapter are defined as the following:

- To synthesise and crystallise the monomethyl and dimethyl analogues of cyclosquaramide **23** and solve their 3D crystal packing structure by X-ray crystallography.
- To investigate the effect of *N*-methylation in the self-assembly behaviour of the squaramides.
- To describe and measure the supramolecular interactions of the water confined in the crystal nanochannels.

The results obtained in this chapter have been published in *Crystal Growth and Design*, **2018**, *18*, 4420-4427.



# Water Soluble Squaramide Dihydrates: *N*-Methylation Modulates the Occurrence of 1D and 2D Water Clusters Through Hydrogen Bonding and Dipolar Interactions

*Marta Ximenis,<sup>†</sup> Javier Pitarch-Jarque,<sup>‡</sup> Salvador Blasco,<sup>‡</sup> Carmen Rotger,<sup>†</sup> Enrique García-España,<sup>‡</sup> and Antonio Costa<sup>†,\*</sup>*

<sup>†</sup> Department of Chemistry, Universitat de les Illes Balears, Ctra. Valldemossa km 7.5, 07122, Palma (Spain).

<sup>‡</sup> Instituto de Ciencia Molecular (ICMOL). Universidad de Valencia, C/ Catedrático José Beltrán 2, 46980 Valencia (Spain).

*Crystal Growth and Design*, **2018**, *18*, 4420-4427

Received: March 15, 2018

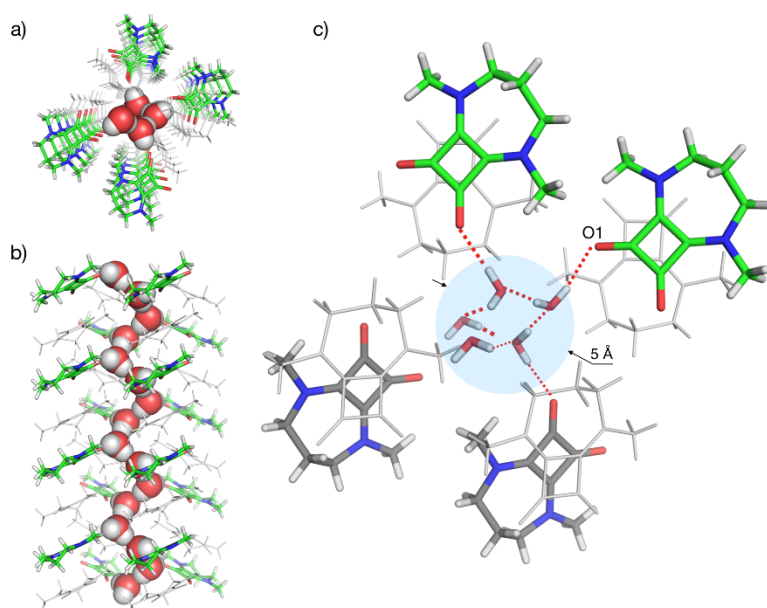
Revised: June 25, 2018

Published: July 10, 2018



#### 4.4.1. Abstract

Water confined in molecular size domains is distinct to bulk water. The altered interactions between adjacent water molecules, and between water molecules and molecular wall components of the confinement system, determine aspects of important phenomena in material science, biology, and nanotechnology. The structural determination of confined water, however, has proven to be challenging. Here, we describe the crystal structures of three related squaramides **1-3** whose molecular structures are modulated by the gradual incorporation of N-methyl groups to the squaramide moiety. The three squaramides differ in their hydrogen bonding capabilities due to the different degree of *N*-methylation of each one. Thus, while **1**·2H<sub>2</sub>O forms narrow tapes of water molecules, the monomethylated squaramide **2**·2H<sub>2</sub>O produces 2D water layers, and the dimethylated squaramide **3**·2H<sub>2</sub>O develops polymeric 1D water chains. Our observations show that *N*-methylation heavily alters the interplay between H-bonding and dipolar stacking, the two supramolecular interactions that govern the structural arrangement of squaramides **1-3** and, hence modulating the arrangement of the water molecules within the crystals.



Water confined in molecular size domains, i.e. pores, channels, and cavities, is different to bulk water.<sup>176</sup> In pure liquid water and ice, the  $sp^3$  oxygen creates a tetrahedral coordination geometry with each water molecule, H-bonded to four others. In confined spaces, water structure is disturbed due to the partial loss of hydrogen bonding within water molecules, and the interactions of water molecules with surface molecular components of the confinement system. Disturbed hydrogen bond clusters and networks of water molecules are ubiquitous in nature, where they are involved in cell organization and water transport through pores and channels that regulate water homeostasis.<sup>177</sup> The physicochemical properties of confined water are also of extremely important for emerging water purification technologies.<sup>178</sup> Therefore, there is a widespread interest in understanding the factors that control the structure and dynamic properties of confined water at a supramolecular scale.<sup>179</sup> Molecular entrapment of water in synthetic porous or channel systems offer a way to explore the properties of confined water; self-assembly of molecular crystals is, among others, a successful strategy for organizing well-defined solid structures having voids or pores with controlled dimensions.<sup>180</sup>

In this regard, squaramides offer distinctive aggregation patterns that would be highly useful for designing water confinement systems. Squaramides are partially aromatic and highly dipolar compounds featuring two adjacent carbonyl and amide-type functionalities.<sup>181</sup> Thanks to their high hydrolytic resistance across a broad range of temperatures and pH,<sup>96b</sup> squaramides find applications in supramolecular catalysis, molecular recognition and, recently, in the design of aggregated systems. For example, it has been reported that the synergy existing between aromaticity and hydrogen bonding of a bis-secondary squaramide lead to supramolecular polymers.<sup>93c</sup> Hydrogen-bonded squaramides produce organogels.<sup>182</sup> In this vein, we have recently shown the

---

<sup>176</sup> a) G. Cicero, J. C. Grossman, E. Schwegler, F. Gygi, G. Galli, *J. Am. Chem. Soc.* **2008**, *130*, 1871–1878. b) T. Nanok, N. Artith, P. Pantu, P. A. Bopp, J. Limtrakul, *J. Phys. Chem. A* **2009**, *113*, 2103–2108.

<sup>177</sup> P. Ball, *Chem. Rev.* **2008**, *108*, 74–108.

<sup>178</sup> a) L. Ding, Y. Wei, Y. Wang, H. Chen, J. Caro, H. Wang, *Angew. Chem. Int. Ed.* **2017**, *56*, 1825–1829. b) D. Jang, J. C. Idrobo, T. Laoui, R. Karnik, *ACS Nano* **2017**, *11*, 10042–10052.

<sup>179</sup> a) P. S. Cremer, A. H. Flood, B. C. Gibb, D. L. Mobley, *Nat. Chem.* **2017**, *10*, 8–16. b) S. Cervený, F. Mallamace, J. Swenson, M. Vogel, L. Xu, *Chem. Rev.* **2016**, *116*, 7608–7625. c) Fujita, *J. Am. Chem. Soc.* **2005**, *127*, 2798–2799.

<sup>180</sup> a) G. R. Desiraju, *J. Chem. Soc. Chem. Commun.* **1991**, 426–428. b) L. J. Barbour, *Nat. Chem.* **2015**, *7*, 97–99.

<sup>181</sup> a) D. Quiñero, C. Garau, A. Frontera, P. Ballester, A. Costa, P. M. Deyà, *Chem. Eur. J.* **2002**, *8*, 433–438. b) D. Quiñero, R. Prohens, C. Garau, A. Frontera, P. Ballester, A. Costa, P. M. Deyà, *Chem. Physics Lett.* **2002**, *351*, 115–120.

<sup>182</sup> a) Y. Ohseido, M. Miyamoto, A. Tanaka, H. Watanabe, *New J. Chem.* **2013**, *37*, 2874–2880. b) J. Schiller, J. V. Alegre-Requena, E. Marqués-López, R. P. Herrera, J. Casanovas, C.

formation of hydrogels based on bis-secondary squaramides combined with squaramic acid salts.<sup>93d</sup>

In all these precedents, a combination of hydrogen bonding and dipolar stacking interactions induce the aggregation of the squaryl moieties.

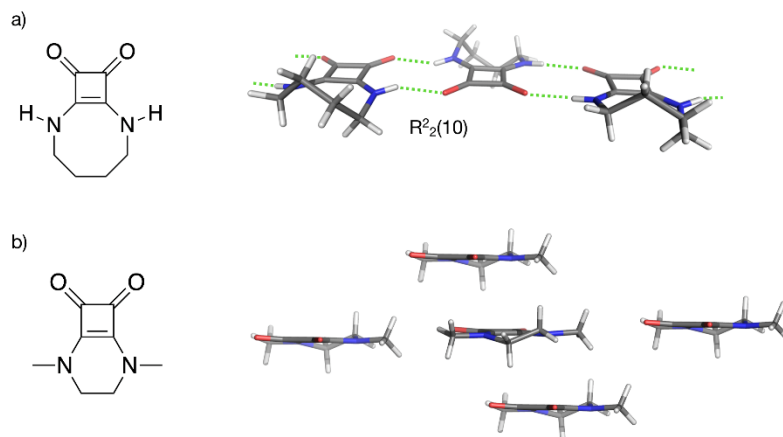


**Figure 4.8.** Molecular and X-ray structures of two tethered cyclic squaramides with E,E geometries around the C-N bonds: (a) bis-secondary, (b) bis-tertiary.

As in amides, bis-secondary squaramides show conformational isomerism due to restricted rotation around the C-N bonds.<sup>183</sup> In solid state, squaramide compounds having Z,Z and Z,E geometries are usually observed.<sup>184</sup> However, due to mutual steric hindrance between N-substituents E,E bis-secondary squaramides can only be observed in tethered cyclic squaramides. Intramolecular cyclization of dialkyl squarates with alkyl diamines is an efficient method for the synthesis of cyclic E,E squaramides. Recent work by Prohens and colleagues reported the structure of a tethered E,E bis-secondary squaramide (-NHR) that forms ribbons connected through hydrogen bonded  $R_2^2(10)$  ring motifs (Figure 4.8a). This compound, however, does not show  $\pi$ - $\pi$  contacts between adjacent ribbons.<sup>185</sup> Conversely, the N,N-methylated squaramide reported by Tidwell and coworkers (Figure 4.8b) exhibits columns of antiparallel  $\pi$ - $\pi$  stacked squaramides. Thus, the disruption of the energetically favourable  $NH\cdots O=C$  H-bond

Alemán, D. Díaz Díaz, *Soft Matter* **2016**, *12*, 4361–4374. c) B. Soberats, L. Martínez, E. Sanna, A. Sampedro, C. Rotger, A. Costa, *Chem. Eur. J.* **2012**, *18*, 7533–7542.

<sup>183</sup> a) M. C. Rotger, M. N. Piña, A. Frontera, G. Martorell, P. Ballester, P. M. Deyà, A. Costa, *J. Org. Chem.* **2004**, *69*, 2302–2308. b) K. Sato, K. Seio, M. Sekine, *J. Am. Chem. Soc.* **2002**, *124*, 12715–12724.

<sup>184</sup> R. Prohens, A. Portell, C. Puigjaner, S. Tom, K. Fujii, K. D. M. Harris, X. Alcob, *Cryst. Growth Des.* **2011**, *11*, 3725–3730. b) C. Rotger, B. Soberats, D. Quiñonero, A. Frontera, P. Ballester, J. Benet-Buchholz, P. M. Deyà, A. Costa, *Eur. J. Org. Chem.* **2008**, 1864–1868. c) L. Martínez, G. Martorell, Á. Sampedro, P. Ballester, A. Costa, C. Rotger, *Org. Lett.* **2015**, *17*, 2980–2983

<sup>185</sup> R. Prohens, A. Portell, C. Puigjaner, R. Barbas, X. Alcobé, M. Font-Bardia, S. Tomàs, *CrystEngComm* **2012**, *14*, 5745.

pattern by N-methylation allows the  $\pi$ - $\pi$  dipolar stacking pattern to manifest.<sup>186</sup> The same principle holds true not only for squaramides but for other dipolar aromatic compounds.<sup>187</sup>

Based on these precedents and our previous observations,<sup>188</sup> we planned to use cyclic squaramides as model compounds. We expected the 1,2-dicarbonyl moiety and balanced hydrophobic to hydrophilic functionalities to organize the squaramide molecules in an antiparallel manner to produce columnar assemblies in the hope of entrapping water clusters within their crystal lattices. In the present study, we synthesized three structurally related squaramides. We solved their structure by X-ray crystallography and studied the changes in the aggregation of the squaramides and water clustering promoted by N-methylation.

#### 4.4.2. Experimental Section

*Instrumental Methods.* Solution  $^1\text{H}$  and  $^{13}\text{C}$  NMR spectra were recorded on a Bruker AVANCE 300 ( $^1\text{H}$  at 300 MHz and  $^{13}\text{C}$  at 75 MHz) in  $\text{D}_2\text{O}$  and  $\text{CDCl}_3$  using the residual proton signal as reference. Chemical shifts ( $\delta$ ) are in ppm and coupling constants ( $J$ ) in Hz. For aggregation studies in  $\text{D}_2\text{O}$ , 10% dioxane was added to use its signal as internal reference. Thermogravimetric Analysis (TGA) were recorded on a SDT2960 TGA analyser (TA instruments) with an automated vertical overhead thermobalance. The experiments were performed on 5-10 mg samples, over a temperature range of 25-600 °C at a constant heating rate of 10 °C  $\text{min}^{-1}$  with a purge of dry nitrogen flowing at 30  $\text{mL min}^{-1}$ . The samples were crushed, blotted dry and placed in open Pt pans for TG experiments. Differential Scanning Calorimetry (DSC) measurements were carried out using a DSC2920 modulated DSC (TA instruments). The experiments were performed on 5-10 mg samples over a temperature range of 0 - 200 °C at a constant heating rate of 2 °C  $\text{min}^{-1}$  with a purge of dry nitrogen flowing at 30  $\text{mL min}^{-1}$ . The samples were crushed, blotted dry and placed in crimped but vented aluminium pans for DSC experiments.

ss-CP MAS  $^{13}\text{C}$  NMR experiments were performed on a Bruker Avance 600 MHz NMR spectrometer using a 4-mm double resonance broadband MAS probe (HX) at room temperature. Samples were prepared by packing the crystals in a 4 mm zirconia rotor. A spinning speed of 13 kHz was employed for all measurements. Data were collected using cross-polarization sequence at Hartmann-Hahn condition with magic angle spinning and dipolar decoupling. A contact time of 1.7 ms and repetition recycle

<sup>186</sup> N. Fu, A. D. Allen, S. Kobayashi, T. T. Tidwell, S. Vukovic, S. Arumugam, V. V. Popik, M. Mishima, *J. Org. Chem.* **2007**, 72, 1951–1956.

<sup>187</sup> E. May, R. Destro, C. Gatti, *J. Am. Chem. Soc.* **2001**, 123, 12248–12254.

<sup>188</sup> Z. Wang, V. Enkelmann, F. Negri, K. Müllen, *Angew. Chem. Int. Ed.* **2004**, 43, 1972–1975.

delay of 3 s were used. A spinal-64 decoupling sequence was used and 2500 transients were collected for signal averaging. Glycine carbonyl resonance at 176.46 was used as an external standard for chemical shift calibration. PXRD profiles were recorded using a BRUKER D8 Advance with monochromated Cu-K $\alpha$  radiation ( $\lambda = 1.54060$  Å, 40kV, 40 mA, scan speed 2.0°/min, scan range 5–45°). Data were evaluated using DIFFRAC.Eva (Bruker AXS Inc.) software. FTIR-ATR Infrared spectra were recorded on a Bruker Tensor 27 equipped with a PLATINUM Diamond ATR accessory interfaced with Opus software version 6.2 over a range of 400-4000 cm<sup>-1</sup>. An average of 16 scans was taken for each spectrum obtained.

**X-ray Crystallography.** Single-crystal X-ray diffraction data for **1**·2H<sub>2</sub>O, **2**·2H<sub>2</sub>O, **3**·2H<sub>2</sub>O. were collected on a Xcalibur diffractometer (Agilent Technologies, Sapphire 3 CCD detector) using a single wavelength X-ray source with MoK $\alpha$  radiation,  $\lambda = 0.71073$  Å and 120(1) K in all cases.

Pre-experiment, data collection, analytical absorption correction, and data reduction were performed with the Oxford program suite CrysAlisPro.<sup>189</sup> Empirical absorption correction was applied using spherical harmonics, implemented in SCALE3 ABSPACK scaling algorithm.

The crystal structures were solved with SHELXT,<sup>190</sup> using direct methods and were refined by full-matrix least-squares methods on F<sup>2</sup> with SHELXL2014. All programs used during the crystal structure determination process are included in the OLEX2 software.<sup>191</sup> All the non-hydrogen atoms were anisotropically refined. Hydrogen atoms were introduced in calculated position and their coordinates were refined according to the linked atoms. The water hydrogen atoms were located by means of the analysis of the F map. The crystallographic details of the crystal structures are summarized in Table S4.

**General Procedure for the Synthesis of Squaramides.** A solution of the diamine (6.47 mmols) in MeOH (10 mL) and diethyl squarate (1.0 g, 5.88 mmol) in MeOH (10 mL) were simultaneously added into a flask containing 80 mL of MeOH using a syringe pump (Harvard Apparatus Inc.) (0.25 mL/min). After the complete addition, a white precipitate appeared and the suspension was stirred at room temperature overnight. The solid was filtered, washed with MeOH and crystallized from water. For analysis and characterization, part of the crystallized material was dried overnight at 40°C under vacuum.

<sup>189</sup> CrysAlis PRO; Agilent Technologies Ltd: Yarnton, Oxfordshire, England, 2014.

<sup>190</sup> G. M. Sheldrick, *Acta Crystallogr., Sect. A: Found. Adv.* **2015**, *71*, 3–8.

<sup>191</sup> O. V Dolomanov, L. J. Bourhis, R. J. Gildea, J. A. K. Howard, H. Puschmann, *J. Appl. Crystallogr.* **2009**, *42*, 339-341.

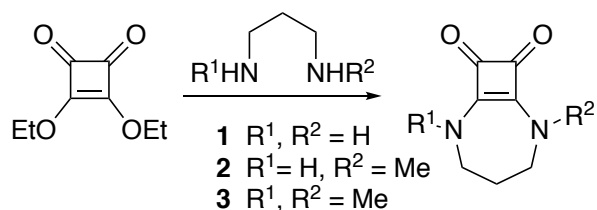
*2,6-diazabicyclo[5.2.0]non-1(7)-ene-8,9-dione (1)*. White prisms 0.76 g, yield 84%. mp 290 °C (dec.).  $^1\text{H}$  NMR ( $\text{D}_2\text{O}$ )  $\delta$  3.53 (t,  $J = 5.1$  Hz, 4H), 2.10 (m,  $J = 5.1$  Hz, 2H).  $^{13}\text{C}$  NMR ( $\text{D}_2\text{O}$ )  $\delta$  182.3, 169.9, 47.3, 31.8. ESI-HRMS(+)  $m/z$  (%): calcd for  $\text{C}_7\text{H}_9\text{N}_2\text{O}_2$   $[\text{M}+\text{H}]^+$  153.06585; found 153.0118. Anal. Calcd for  $\text{C}_7\text{H}_8\text{N}_2\text{O}_2$ : C, 55.26; H, 5.30; N, 18.41. Found: C, 55.03; H, 5.28; N, 18.18.

*2-methyl-2,6-diazabicyclo[5.2.0]non-1(7)-ene-8,9-dione (2)*. White needles. 0.75 g, yield 77%. mp 255 °C (dec.).  $^1\text{H}$  NMR ( $\text{D}_2\text{O}$ , ppm)  $\delta$  3.52 (s, 4H), 3.38 (s, 3H), 2.14 (s, 2H);  $^{13}\text{C}$  NMR ( $\text{DMSO}-d_6$ )  $\delta$  181.4, 180.9, 168.3, 167.7, 55.1, 45.7, 37.3, 29.6. ESI-HRMS(+)  $m/z$  (%): calcd for  $\text{C}_8\text{H}_{10}\text{N}_2\text{NaO}_2$  189.06345; exp. 189.06345  $[\text{M} + \text{Na}]^+$ . Anal. Calcd for  $\text{C}_8\text{H}_{10}\text{N}_2\text{O}_2$ : C, 57.82; H, 6.07; N, 16.86. Found: C, 57.64; H, 5.92; N, 16.73.

*2,6-dimethyl-2,6-diazabicyclo[5.2.0]non-1(7)-ene-8,9-dione (3)*. White needles. 0.71 g, yield 67%. mp 285 °C (melting/dec.).  $^1\text{H}$  NMR ( $\text{D}_2\text{O}$ , ppm)  $\delta$  3.59 (t,  $J = 5.1$  Hz, 4H), 3.49 (s, 6H), 2.27 (m,  $J = 5.0$  Hz, 2H);  $^{13}\text{C}$  NMR ( $\text{DMSO}-d_6$ , ppm)  $\delta$  180.8, 166.9, 54.3, 37.2, 28.3. ESI-HRMS(+)  $m/z$  (%): calcd for  $\text{C}_9\text{H}_{12}\text{N}_2\text{NaO}_2$  203.07910; exp. 203.07882  $[\text{M} + \text{Na}]^+$ . Anal. Calcd for  $\text{C}_9\text{H}_{12}\text{N}_2\text{O}_2$ : C, 59.99; H, 6.71; N, 15.55. Found: C, 59.91; H, 6.55; N, 15.42.

#### 4.4.3. Results And Discussion

Z,Z or Z,E (E,Z) bis-secondary squaramides are poorly soluble in water due to self-aggregation into head-to-tail aggregates governed by  $\text{NH}\cdots\text{O}=\text{C}$  interactions. Squaramides **1-3** (Scheme 4.1) were designed to disrupt the formation of homomeric ladder-type aggregates. In addition, we expected N-methylation to alter physical properties such as aqueous solubility and lipophilicity.<sup>192</sup>



**Scheme 4.1.** Synthesis of tethered squaramides **1-3**.

The study presented here shows how compounds **1-3** form dihydrates in solid-state and self-assemble into pillars of stacked squaramide units. We have also observed marked structural differences among them in the allocation of water molecules, thus highlighting the influence of N-methylation in self-assembly events.

<sup>192</sup> T. J. Ritchie, S. J. F. Macdonald, S. D. Pickett, *MedChem Comm* **2015**, *6*, 1787–1797.

The synthesis of **1-3** was straightforward: diethyl squarate was treated with the stoichiometric amount of corresponding 1,3-diamines (EtOH, r.t. 12 h) to provide cyclic squaramides **1-3** as white powders in near quantitative yields.  $^1\text{H}$  and  $^{13}\text{C}$  NMR, as well as ESI-HRMS spectra, were in line with the molecular structures shown in Scheme 1 (Supporting Information). Crystals suitable for X-ray analysis were obtained by dissolution in hot water followed by slow cooling to room temperature. Transparent colourless crystals of **2** and **3** up to 2 mm in diameter and two cm in length grew upon further standing and slow solvent evaporation for two to three weeks. We characterized the solid-state structures of **1-3** by elemental analysis, thermogravimetric analysis (TGA), differential scanning calorimetry (DSC), powder X-ray diffraction (PXRD), single crystal X-ray diffraction, solid-state  $^{13}\text{C}$  NMR and Fourier Transform Infrared-Attenuated Total Reflection (FTIR-ATR).

The elemental analysis of recrystallized samples of **1-3** revealed that the three squaramides were dihydrates. In turn, the TGA of **1-3** revealed respective experimental (calculated) weight losses of 20.14 (19.14), 16.90 (17.80) and 16.36 (16.36), % at relatively low temperatures ( $< 100^\circ\text{C}$ ), corresponding to irreversible release of water (Figures S10–S15). Moreover, the weight losses observed by TGA in the temperature range  $0\text{--}100^\circ\text{C}$  agrees with sharp endotherms observed in the first DSC curves. Furthermore, the crystals turned opaque during dehydration affording a visual indication that the water release processes were associated with total or partial loss of crystallinity. Finally, in situ variable-temperature PXRD was used to verify that dehydration changed the crystal structures of the three squaramides. These results indicate that the water molecules are retained loosely in the hydrated samples due to weak interactions between water molecules and critical wall components of the confinement system.

The structures of  $\mathbf{1}\cdot 2\text{H}_2\text{O}$ - $\mathbf{3}\cdot 2\text{H}_2\text{O}$  were characterized by single-crystal X-ray diffraction at 120(1) K. The structure of  $\mathbf{1}\cdot 2\text{H}_2\text{O}$  is shown in Figures 4.9 and 4.10. This compound crystallizes in the triclinic space group P-1. Each asymmetric unit of **1** contains two molecules of water and one squaramide molecule.

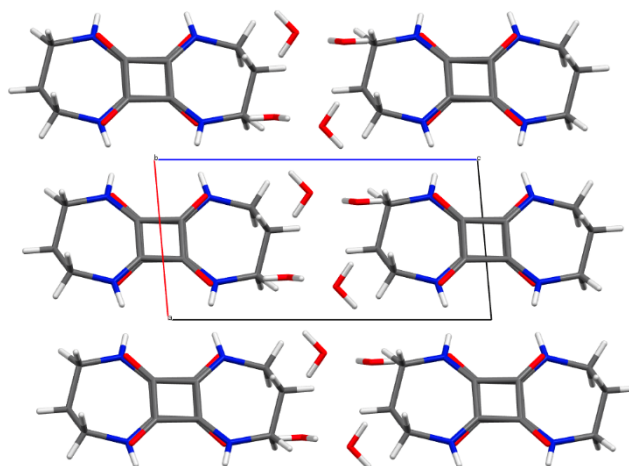


**Figure 4.9.** Crystal packing  $1 \cdot 2\text{H}_2\text{O}$  projected along the  $b$ -axis, showing the antiparallel arrangement of the squaramide molecules located in adjacent layers.

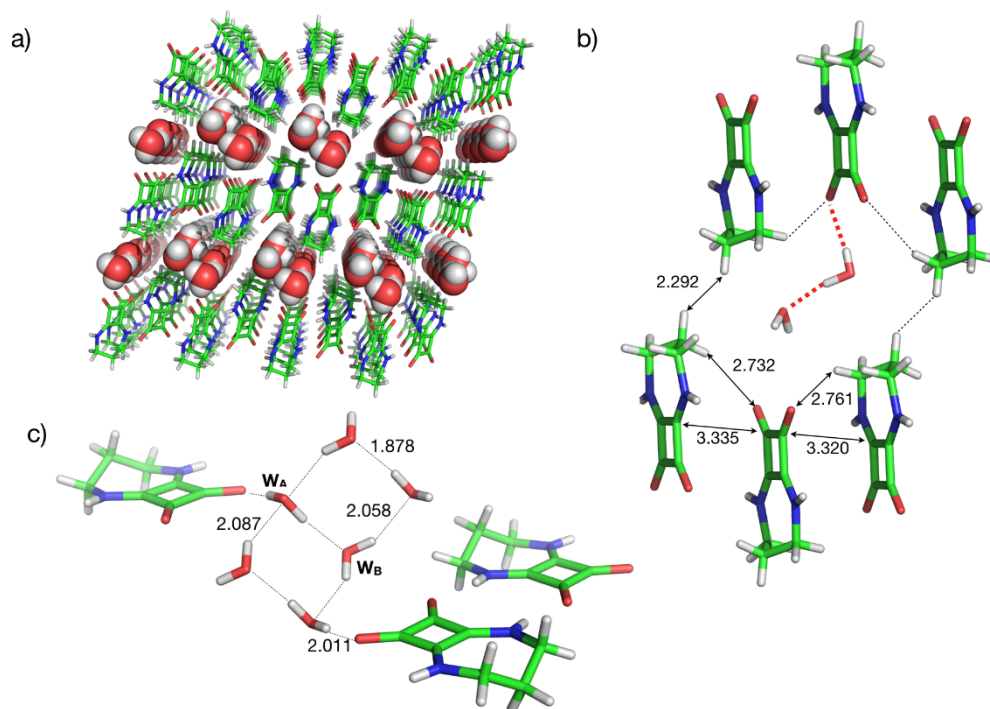


**Figure 4.10.** (a) Top view perspective of the crystal structure of squaramide  $1 \cdot 2\text{H}_2\text{O}$  showing the 1D channels of water molecules. (b) Detail of the rectangular water channel, c.a. created by six squaramide molecules. The approximate dimensions of the channel are  $7.5 \times 3.5 \text{ \AA}$ . (c) Partial view of a water channel showing the relative arrangement of the inner water molecules ( $w_A$ ,  $w_B$ ) relative to wall components. All distances are in  $\text{\AA}$ .

Somewhat as expected, the squaramide motifs in  $1 \cdot 2\text{H}_2\text{O}$  are planar and exhibit infinite H-bond  ${}^2R_2(10)$  ribbons between adjacent squaramide units. The ribbons comprise antiparallel arranged squaramides uniformly offset stacked with an intermolecular distance of  $3.773 \text{ \AA}$  between squaramide centroids. The hydrogen atoms of the two types of water molecules ( $w_A$ ,  $w_B$ ) are engaged in H-bonding. One water molecule is tetracoordinated ( $w_A$ ) and establishes strong H-bonds with water molecules ( $w_B$ ) at

distances of  $O_{wA}-O_{wB}$ , 2.790, 2.884 and 2.888 Å respectively, and one squaramide carbonyl ( $O_1-O_{wA}$ , 2.789 Å). In turn,  $w_B$  is tricoordinated with three adjacent  $w_A$  molecules (Figure 4.10b,c). Moreover, four  $C-H\cdots O$  contacts with  $d$  values of 2.62–2.97 Å and  $C-H\cdots O$  angles of 130–163° help to hold the structure in place.<sup>193</sup> The channel comprises six squaramide molecules delimitating a fully rectangular-shaped pore with approximate dimensions of c.a.  $7.5 \times 3.5$  Å.

In contrast to **1**, squaramide **2** in its anhydrous form is soluble in  $CDCl_3$ , indicating weak aggregation in this solvent. The marked increase of solubility of **2** compared to **1** is assigned to the presence of one N-methyl group in **2** that precluded the formation of extended H-bond ribbons. Nonetheless, H-bond dimerization is still likely to occur.  $^1H$  NMR dilution experiments in  $CDCl_3$  at 294 K allowed us to calculate the stability constant of the dimerization process. In particular, the NH proton of **2** exhibited a relatively large ( $> +2.1$  ppm) downfield shift upon aggregation. Dilution data of the NH proton were fitted to a dimerization model of aggregation affording a value of  $140 \pm 5 M^{-1}$  (Figures S16 and S17). Noticeably, squaramide **2** is also highly soluble ( $> 50$  mM) in  $H_2O$ . However, dilution experiments of **2** in water covering the 1-100 mM range were inconclusive. We observed small (c.a. - 0.14 ppm) and reproducible upfield shifts for the N-Me and aliphatic protons of **2**. Overall, the NMR experiments indicate the favoured dimerization of **2** and suggest further aggregation events to take place in water (figures S18 and S19).

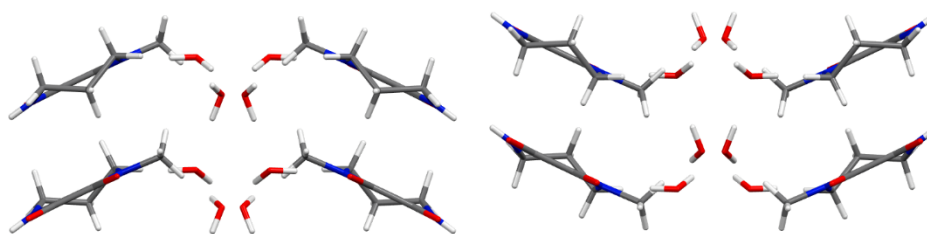


**Figure 4.11.** Crystal structure of  $2 \cdot 2H_2O$  projected along the b-axis showing the herringbone arrangement of the squaramide units. Disorder in the aliphatic  $-(CH_2)_3-$  chain of **2** was removed for clarity.

Squaramide dihydrate  $2 \cdot 2H_2O$  crystallizes in the orthorhombic space group Pbcn. Each asymmetric unit contains two molecules of water and one squaramide molecule. The methylene chain of  $2 \cdot H_2O$  shows some disorder between two close configurations with 50% occupancy in each. The crystal structure consists of cyclic  $R_2^2(10)$  dimers and displays a herringbone packing pattern with an intermolecular distance of 3.757 Å between squaramide centroids (Figure 4.11 and Supporting Information). The observed solid-state dimeric structure shows strong agreement with the  $^1H$  NMR data obtained in  $CDCl_3$  and  $H_2O$  solutions.

<sup>193</sup> S. Horowitz, R. C. Trievel, *J. Biol. Chem.* **2012**, 287, 41576–41582.

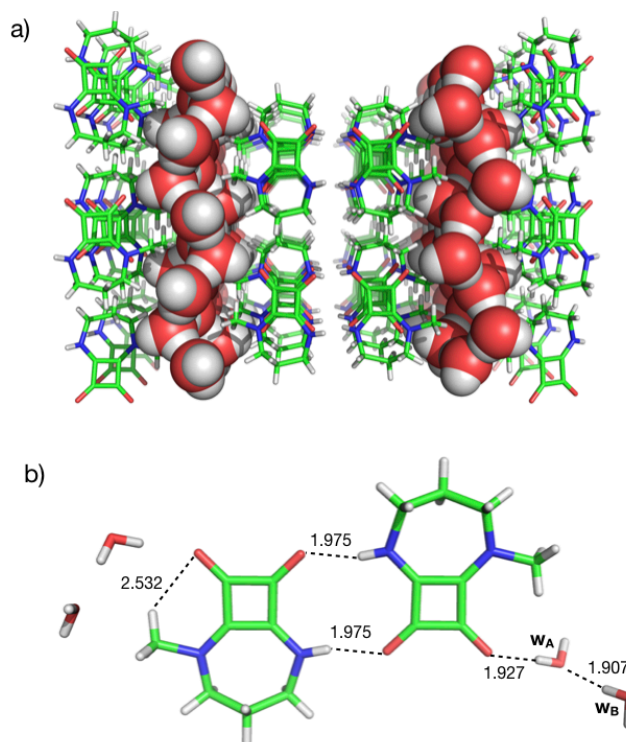


**Figure 4.12.** (a) Top view perspective of the crystal structure of squaramide  $2 \cdot 2H_2O$  showing the 2D layers of water molecules sandwiched by columnar arrays of H-bond dimeric squaramide **2** motifs. (b) Detail of a squaramide H-bond dimer motif showing the mutual intermolecular CN-H $\cdots$ O=C hydrogen-bonding existing between them (CN-H $\cdots$ O angle 178°). All distances are in Å.

Furthermore, there is one intramolecular and several intermolecular C-H $\cdots$ O=C contacts in the 2.37 – 2.70 Å range that rigidify the methylene portion of  $2 \cdot 2H_2O$  and reinforce the columnar assemblies of the tethered squaramides (Figure 4.12 and Table S5). The 2D layers of water molecules are stabilized between columnar assemblies of squaramide  $2 \cdot 2H_2O$  dimers. Water layers comprise a continuous sheet of six-membered ice-like rings of water molecules. The two types of water molecules ( $w_A$ ,  $w_B$ ) are engaged in H-bonding. One water molecule is tetracoordinated ( $w_A$ ) and establishes strong H-bonds with  $w_B$  ( $O_{w_A}-O_{w_B}$ , 2.725 Å) and one squaramide carbonyl ( $O_1-O_{w_A}$ , 2.774 Å). In turn, water molecule  $w_B$  is tricoordinated to three adjacent  $w_A$  water molecules (Figures 4.12b and 4.13). Overall,  $w_A$  and  $w_B$  form 2D monolayers of edge-sharing hexameric water clusters. Each hexameric cluster unit shows a highly distorted boat conformation (Figure 4.13) compared to the regular hexameric structure of ice.<sup>194</sup> The OH $\cdots$ O average distance within the water layer is around 2.72–2.78 Å. This value

<sup>194</sup> B. K. Saha, A. Nangia, *Chem. Commun.* **2006**, 1825–1827.

compares well with the OH $\cdots$ O distance in related 2D water layers already reported<sup>195</sup> and ice  $I_h$  (2.759 at 200 K).

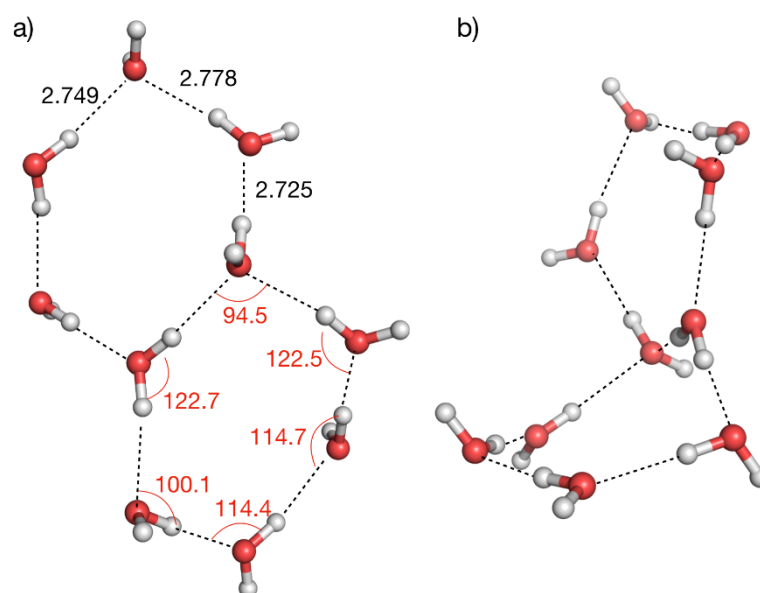


**Figure 4.13.** Top (a) and side (b) views of two hexameric clusters of water molecules showing ice-like structure in a distorted boat conformation. Distances are in Å. Angles are labelled in red.

As with N-monomethylated squaramide  $2 \cdot 2\text{H}_2\text{O}$ , the dimethylated squaramide  $3 \cdot 2\text{H}_2\text{O}$  is markedly soluble in water (*ca* 0.1 M) and crystallizes in the orthorhombic space group  $\text{Pca}2_1$ . The single-crystal structure of  $3 \cdot 2\text{H}_2\text{O}$  (Figure 4.14 and Table S6) reveals the columnar assembly of the squaramide molecules. However, there are significant differences compared to the aforementioned squaramide hydrates  $1 \cdot 2\text{H}_2\text{O}$  and  $2 \cdot 2\text{H}_2\text{O}$ . Each carbonyl-oxygen in  $3 \cdot 2\text{H}_2\text{O}$  ( $\text{O}_1$  and  $\text{O}_2$ ), hydrogen bonded to one molecule of water. The measured distances between  $\text{O}_1 \cdots \text{O}_{\text{w}1}$  and  $\text{O}_2 \cdots \text{O}_{\text{w}2}$  are 2.779 and 2.802 Å, associated to  $\text{O}_{\text{w}}\text{-H} \cdots \text{O}=\text{C}$  angles of  $173^\circ$  and  $162^\circ$  respectively. The strong dipolar interactions between squaramides induced the stacked offset arrangement of squaramide molecules along the *c*-axis with an intermolecular distance of 3.717 Å between squaramide centroids. In contrast to  $1 \cdot 2\text{H}_2\text{O}$  and  $2 \cdot 2\text{H}_2\text{O}$ , the molecules of  $3 \cdot 2\text{H}_2\text{O}$  do not show the typical antiparallel arrangement of the squaryl moiety but rather overlap each other with a rotation angle of  $135^\circ$ . Moreover, two weak  $\text{C-H} \cdots \text{O}=\text{C}$  intermolecular H-bonds between methylene protons and the squaramide carbonyls at respectively,  $\text{O}_1 \cdots \text{H}_{6\text{A}}\text{-C}_6$  2.648 and  $\text{O}_1 \cdots \text{H}_{7\text{B}}\text{-C}_7$  2.696 Å with  $\text{C-H} \cdots \text{O}$  angles of  $131.21$  and  $140.53^\circ$ , contribute synergistically to lock the columnar assembly of squaramide molecules in  $3 \cdot 2\text{H}_2\text{O}$ .

<sup>195</sup> a) R. Miyamoto, T. Hamazawa, M. Hirotsu, T. Nishioka, L. J. Wright, *Chem. Commun.* **2005**, 4047–4049. b) S. Upreti, A. Datta, A. Ramanan, *Cryst. Growth Des.* **2007**, *7*, 966–971. c) Y. Zhu, F. Wang, J. Bai, X. C. Zeng, H. Wu, *ACS Nano* **2015**, *9*, 12197–12204.

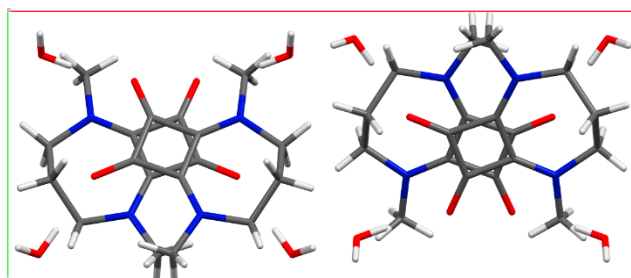


**Figure 4.14.** Crystal packing of **3**·2H<sub>2</sub>O viewed down the *c*-axis showing the overlapped layers of squaramides with a rotation angle of 135°.

The assembly of the squaramide **3**·2H<sub>2</sub>O generates channels with an interior diameter averaging 5 Å. This value is akin to those reported in the literature for other non-related synthetic self-assembled systems<sup>196</sup> and is near those for gramicidin and aquaporins, two archetypal molecular water channels, at around 4 Å.<sup>197</sup> Chain-like structures have been previously observed in *N*-alkylated six-membered cyclic chiral squaramides. However, in these instances no water molecules were present and the contacts between the different moieties were established through Ar-CH···O=C hydrogen bonds and edge-to-face  $\pi$ - $\pi$  stacking.<sup>198</sup>

In **3**·2H<sub>2</sub>O, each channel is filled with an infinite one-dimensional (1D) water chain. Each water molecule is hydrogen bonded to one carbonyl-oxygen and two neighbouring water molecules (see Figure 4.15c and Table S7). The water molecules within the channels show four relative orientations defining a left-handed helical chain (Figure 4.15) surrounded by four right-handed water chains and vice-versa with four water molecules per turn and a pitch of 7.36 Å.

<sup>196</sup> a) M. Barboiu, M. Michau, Y. Le Duc, A. Gilles, P. Parvizi, J. Post, T. Fyles, Y. M. Legrand, A. Van Der Lee, B. Coasne, P. Parvizi, J. Post, T. Fyles, *Nat. Commun.* **2014**, *5*, 1–8. b) E. Licsandru, I. Kocsis, Y. Shen, S. Murail, Y. Legrand, A. Van Der Lee, D. Tsai, M. Baaden, M. Kumar, M. Barboiu, *J. Am. Chem. Soc.* **2016**, *138*, 5403–5409. c) B. S. Kumar, P. K. Panda, *CrystEngComm* **2014**, *16*, 8669–8672. d) A. Dolgoplov, K. N. Grafkskaia, D. V Anokhin, D. E. Demco, X. Zhu, D. A. Ivanov, *Phys. Chem. Chem. Phys.* **2017**, *19*, 7714–7720.

<sup>197</sup> a) B. M. Burkhardt, N. Li, D. A. Langs, W. A. Pangborn, W. L. Duax, *Proc. Natl. Acad. Sci. U. S. A.* **1998**, *95*, 12950–12955. b) A. Finkelstein, O. S. Andersen, *J. Membr. Biol.* **1981**, *59*, 155–171.

<sup>198</sup> X. Jin, Q. Min, Y. Zheng, P. Wang, J. Zhu, H. B. Zhou, *ARKIVOC* **2010**, *11*, 322–335.

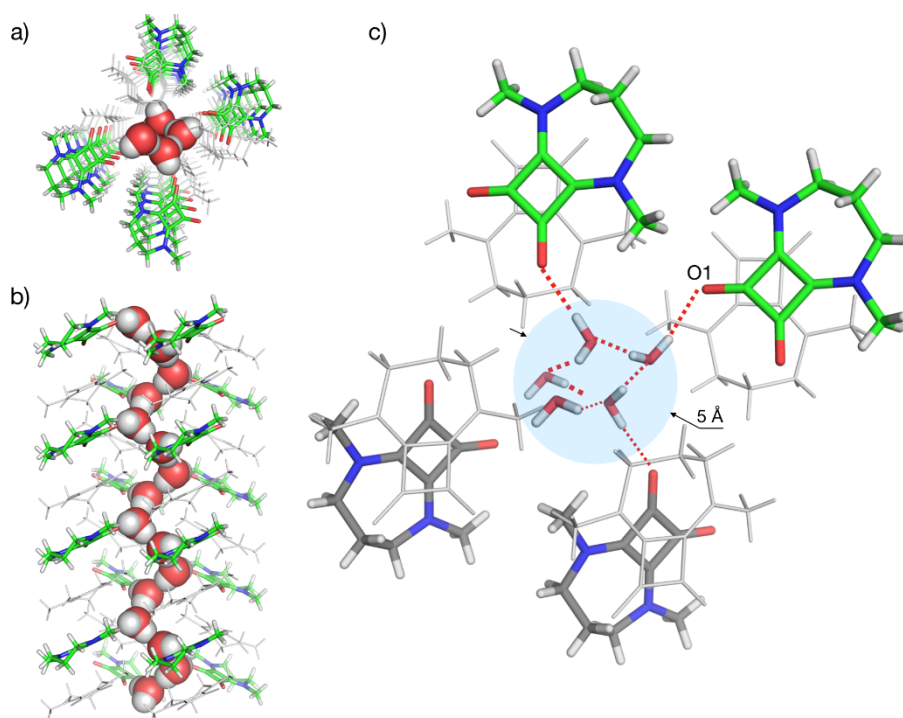


**Figure 4.15.** (a, b) Top and side view perspective of the crystal structure of squaramide **3**·2H<sub>2</sub>O showing the 1D helicoidal arrangement of water molecules. (c) Detail of a tetrameric squaramide motif showing the intermolecular O-H···O=C H bond defining a 1D pore of 5 Å on an average diameter. The helix has four water molecules per turn with a pitch of 7.36 Å.

To further characterize the solid-state structure of the squaramides we analysed the solid-state (ss) ss-<sup>13</sup>C CPMAS NMR spectra of **1**·2H<sub>2</sub>O - **3**·2H<sub>2</sub>O and their anhydrates. We deem, that the chemical shifts of the carbonyl carbons of squaramides would be sensitive to the spatial arrangement of the nuclei comprising the hydrogen bonds since the electronic environment of the carbonyl groups is affected by hydrogen bonding.<sup>199</sup> On examination, the recorded chemical shifts for the squaramide hydrates and their corresponding anhydrates appear to be well separated and close to those observed in solution thus allowing assignment. The squaramide low-field region between 160-180 ppm shows relatively sharp signals for **2**·2H<sub>2</sub>O and **3**·2H<sub>2</sub>O (Figures S20-S24). It implies that these squaramides are essentially crystalline solids. However, the enhanced mobility of the methylene carbons caused broadening and the concomitant loss of intensity in the 20-60 ppm region of the spectra. The most characteristic feature of these spectra was the presence of (at least) two carbonyls, two cyclobutene carbons and, two methyl signals, indicating inequivalence of the squaramide carbons. The separation between these pairs of signals ranged from 0.7 to 1.8 ppm. At first sight, the observed signal splitting for symmetrical squaramides **1** and **3**, both in the hydrated and anhydrate forms, is unexpected. In fact, their spectra in solution afforded only one carbonyl and

<sup>199</sup> S. Ando, I. Ando, A. Shoji, T. Ozaki, *J. Am. Chem. Soc.* **1988**, 110, 3380-3386.

cyclobutene signal, as anticipated for symmetrical squaramides (cf.  $^{13}\text{C}$  NMR in solution). Noticeably, non-equivalent squaramide carbons also occur in their corresponding anhydrates. Therefore, we cannot assign the splitting to preferential hydrogen bonding between water and a squaramide carbonyl. Inspection of the crystal structures  $1\cdot 2\text{H}_2\text{O}$  -  $3\cdot 2\text{H}_2\text{O}$  reveal that in both cases the adjacent squaramides are stacked off-centre with respective interplanar distances from the squaramide centroids in the 3.773 and 3.717 Å. As a consequence, we attributed the splitting of signals in the ss-CP MAS  $^{13}\text{C}$  NMR spectra to desymmetrization of the electronic environment of the squaramide moiety due to off-centre stacking of individual molecules.<sup>200</sup>

Because of its ability to detect hydrogen bonding to carbonyl groups, changes produced by confined water in the squaramide hydrates were also studied by (Fourier Transform Infrared-Attenuated Total Reflection) FTIR-ATR spectroscopy. Crystals of  $1\cdot 2\text{H}_2\text{O}$ - $3\cdot 2\text{H}_2\text{O}$  were studied at room temperature and compared with their corresponding microcrystalline anhydrates obtained after removing water by heating at 40°C under vacuum and  $\text{P}_2\text{O}_5$  for 16-24 h. In this regard, the FTIR-ATR spectrum of compound  $3\cdot 2\text{H}_2\text{O}$  is particularly informative since its anhydrate **3** fails to absorb in the region 4000-2000  $\text{cm}^{-1}$  region (Figure 4.16). Therefore, the absorption bands observed in this region must be exclusively attributed to water molecules.

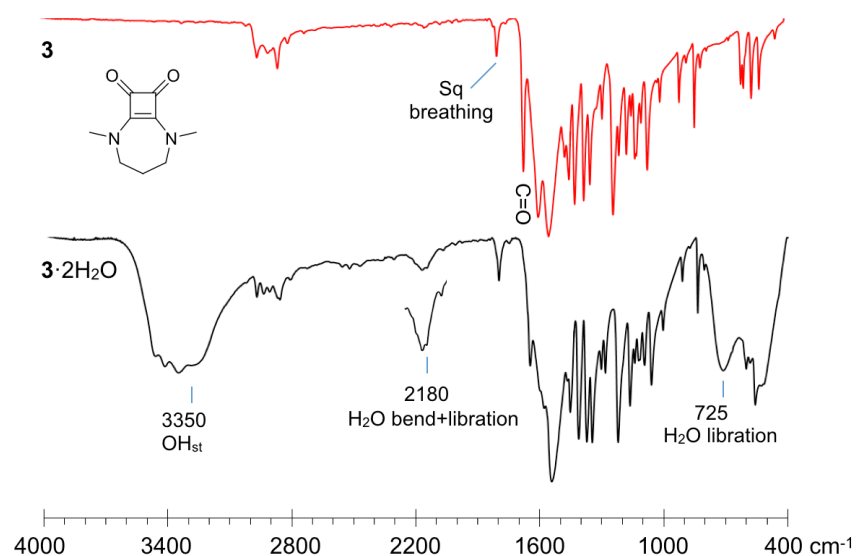


**Figure 4.16.** FTIR-ATR spectra of  $3\cdot 2\text{H}_2\text{O}$  (black) and its anhydrate (red) showing distinctive peaks due to confined water.

<sup>200</sup> a) S. P. Brown, H. W. Spiess, *Chem. Rev.* **2001**, *101*, 4125-4156. a) N. Bampos, M. R. Prinsep, H. He, A. Vidal-Ferran, A. Bashall, M. McPartlin, H. Powell, J. K. M. Sanders, *J. Soc., Perkin Trans 2*, **1998**, 715-724.

We assigned the bands at 3400-3350  $\text{cm}^{-1}$ , to O–H stretching vibrations of water molecules engaged in various local hydrogen-bonded networks.<sup>201</sup> Furthermore, the N–H stretching bands at around 3200  $\text{cm}^{-1}$  indicated strong hydrogen bonding of squaramides **1** and **2**, both in anhydrides and dihydrates (Supporting Information). Remarkably, the characteristic squaramide ring-breathing band at around 1800  $\text{cm}^{-1}$  is blue-shifted (5-10  $\text{cm}^{-1}$ ). On the other hand, the squaramide carbonyl band at around 1660  $\text{cm}^{-1}$  appears red-shifted (10-15  $\text{cm}^{-1}$ ) in the dihydrates compared to the anhydrides, indicating a weakening of the squaramide carbonyl bond due to hydrogen bonding. In addition, we identified a particular water band for **2**·2H<sub>2</sub>O and **3**·2H<sub>2</sub>O at around 2180  $\text{cm}^{-1}$ . The weak water combination (libration + bend) bands detected are useful for reporting the relative strength of the water H-bonding networks.<sup>202</sup> In our case, the combinatorial band of the dihydrates **1**·2H<sub>2</sub>O - **3**·2H<sub>2</sub>O appears blue-shifted compared to deionized water at around 2130  $\text{cm}^{-1}$  suggesting a stronger interaction between water and the squaramide carbonyls than water with the bulk phase. Similar blue shifting have recently observed with kosmotropic (structure makers) anions such as carbonate, acetate and fluoride, indicating that these anions interact with water more strongly than water with water.<sup>49</sup> Thus, the FTIR-ATR spectra of **1**·2H<sub>2</sub>O - **3**·2H<sub>2</sub>O indicate that confined water molecules heavily interact with the squaramides in agreement with the X-ray structures.

#### 4.4.4. Conclusions

In conclusion, we have shown that spontaneous self-assembly and crystallization in water is a useful approach to study the effect of *N*-methylation in the architecture of the resulting crystalline hydrates. *N*-methyl groups block the formation of N-H···O=C H-bonding that dominate the self-assembly of bis-secondary squaramides, thus favouring the manifestation of dipolar stacking and weak C-H···O=C interactions. The arrangement of the squaramide units studied so far enabled the observation of three types of water clusters, namely: water tapes from **1**·2H<sub>2</sub>O, 2D hexagonal water layers from **2**·2H<sub>2</sub>O and 1D water chains from **3**·2H<sub>2</sub>O. In all three instances, water molecules are held in place by establishing strong H-bonding with oxygen carbonyls in the squaramides, while weak CH···O=C interactions help to maintain the columnar assemblies of squaramides. These results are remarkable since, apart from the unusual solubility, the structural modification introduced by methylation induced dramatic changes in the arrangement of water molecules in confined spaces. Our study paves the

<sup>201</sup> a) Q. Sun, *Chem. Phys. Lett.* **2013**, 568–569, 90–94. b) R. Custelcean, C. Afloroaei, M. Vlassa, M. Polverejan, *Angew. Chem. Int. Ed.* **2000**, 39, 3094–3096.

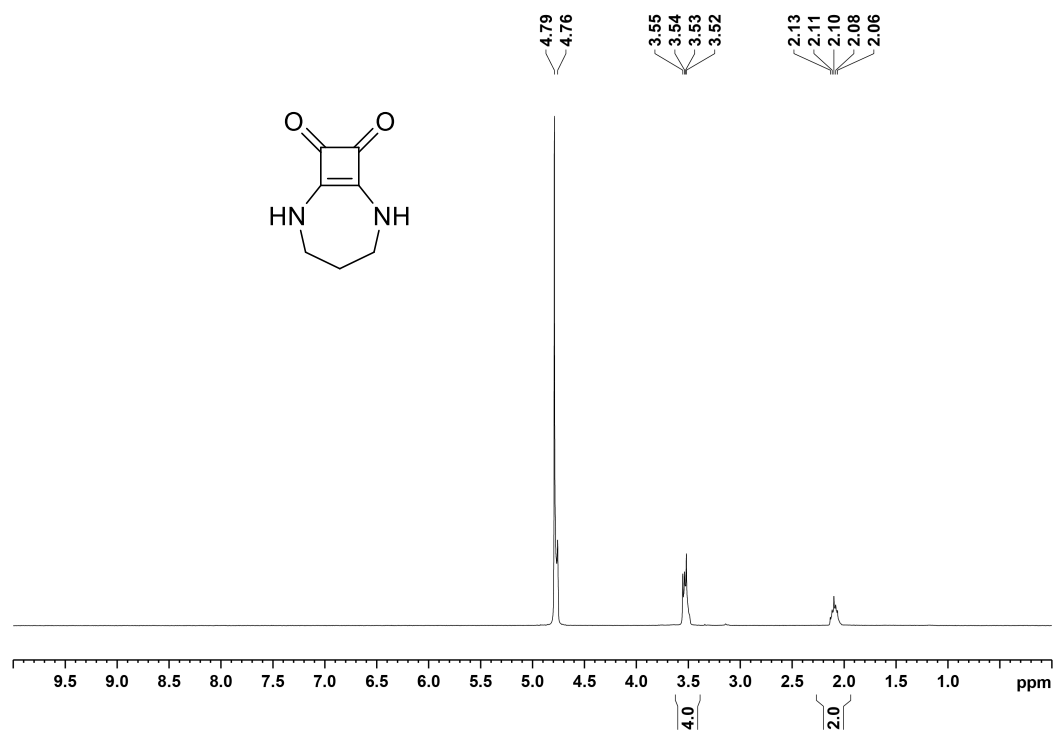
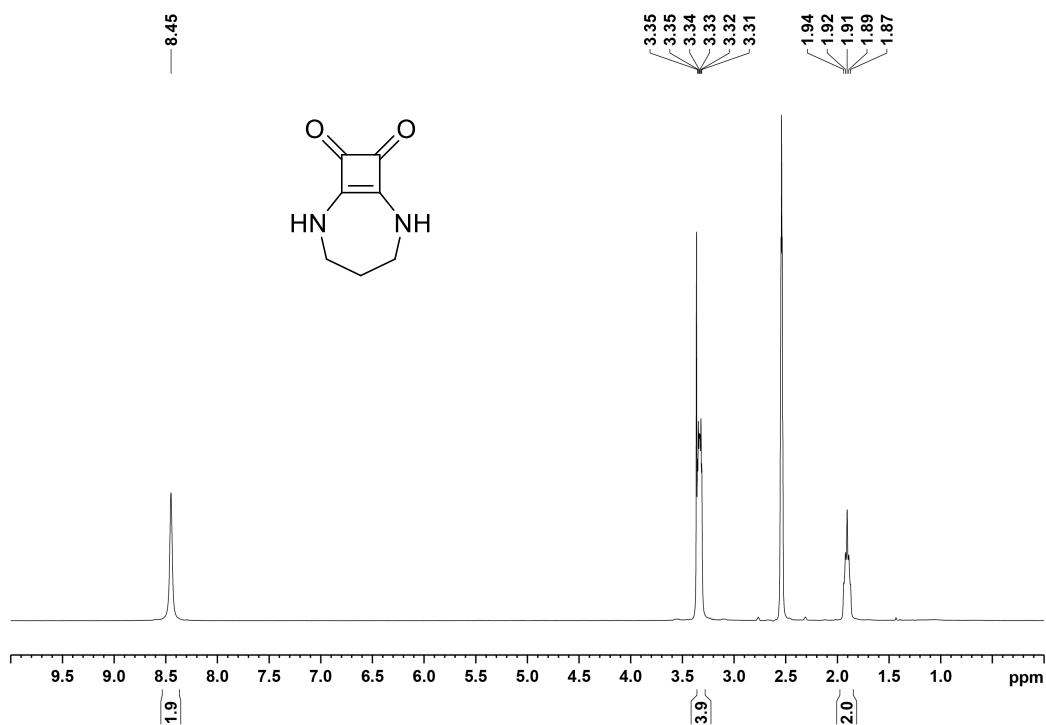
<sup>202</sup> P. K. Verma, A. Kundu, M. S. Poretz, C. Dhooonmoon, O. S. Chegwidden, C. H. Londergan, M. Cho, *J. Phys. Chem. B* **2018**, 122, 2587-2599

way for the design of water confinement and transport systems based on cyclic squaramides.

#### ***4.4.5. Acknowledgments***

Financial support from the Spanish Ministry of Economy and Competitiveness (MINECO) (CTQ2014-57393-C2-1P, CTQ2017-85821-R and CONSOLIDER-INGENIO 2010 CSD2010-00065, FEDER funds and Unidad de Excelencia María de Maeztu MDM-15-0538) are gratefully acknowledged. M. X. thanks Govern de les Illes Balears for a predoctoral fellowship, FSE funds).

## 4.4.6. Supporting Information

 $^1\text{H}$  and  $^{13}\text{C}$  NMR spectra of the new compoundsFigure S1.  $^1\text{H}$  NMR spectrum of **1** in  $\text{D}_2\text{O}$ , 300 MHz, 298 KFigure S2.  $^1\text{H}$  NMR spectrum of **1** in  $\text{DMSO}-d_6$ , 300 MHz, 298 K

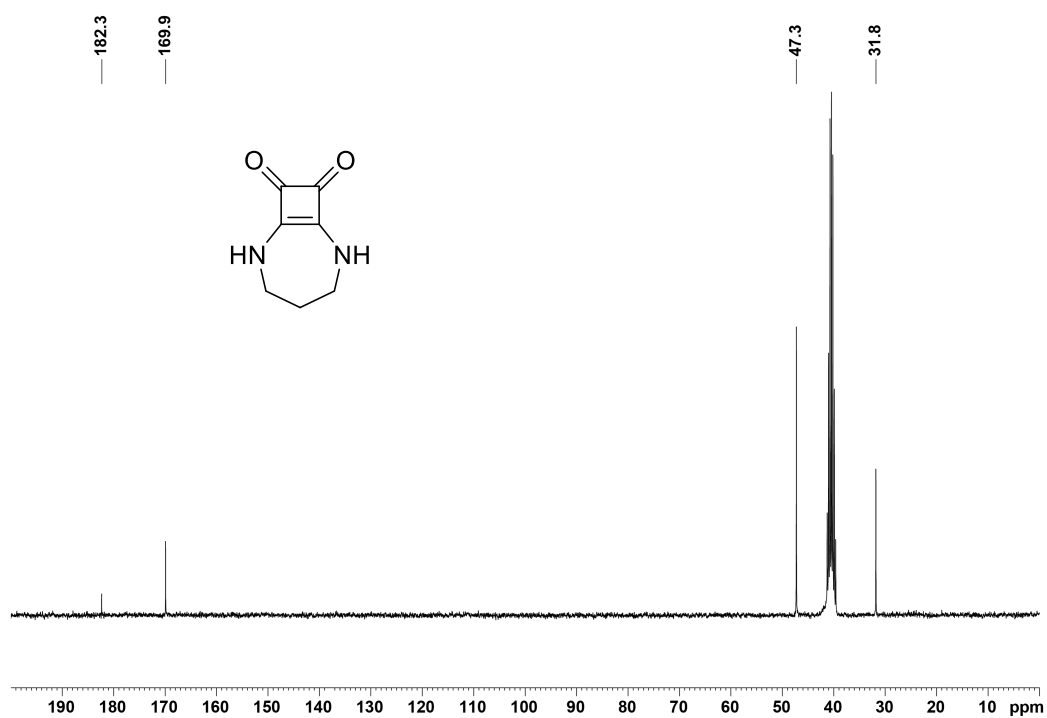


Figure S3. <sup>13</sup>C NMR spectrum of **1** in DMSO-*d*<sub>6</sub>, 300 MHz, 298 K

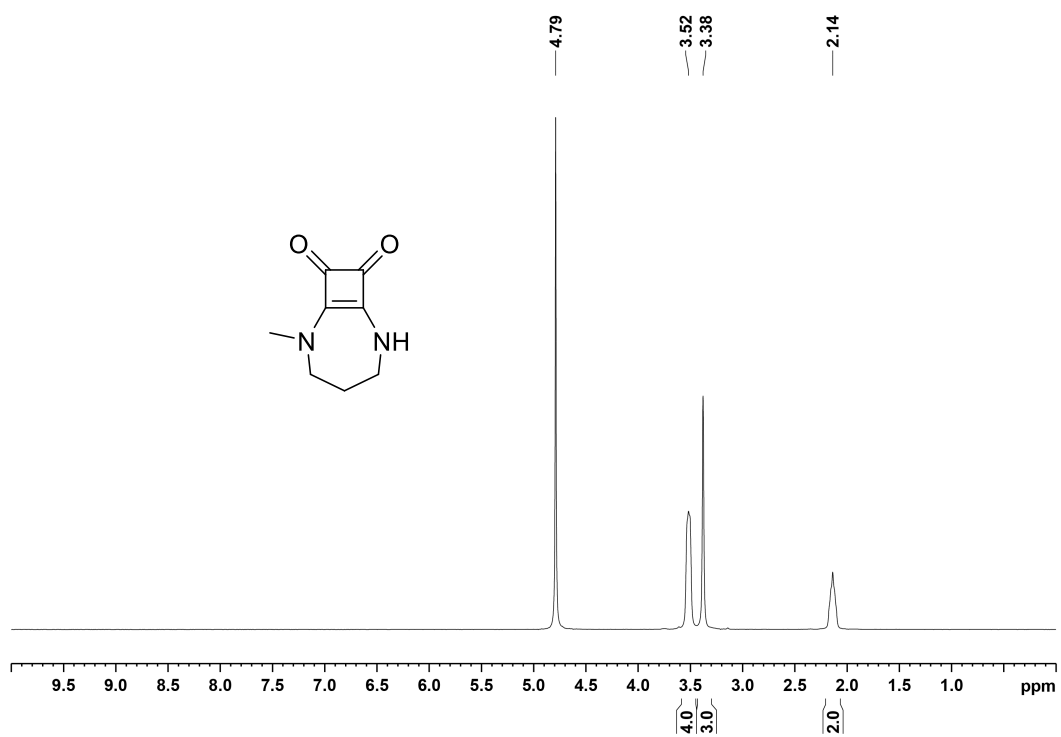


Figure S4. <sup>1</sup>H NMR spectrum of **2** in D<sub>2</sub>O, 300 MHz, 298 K

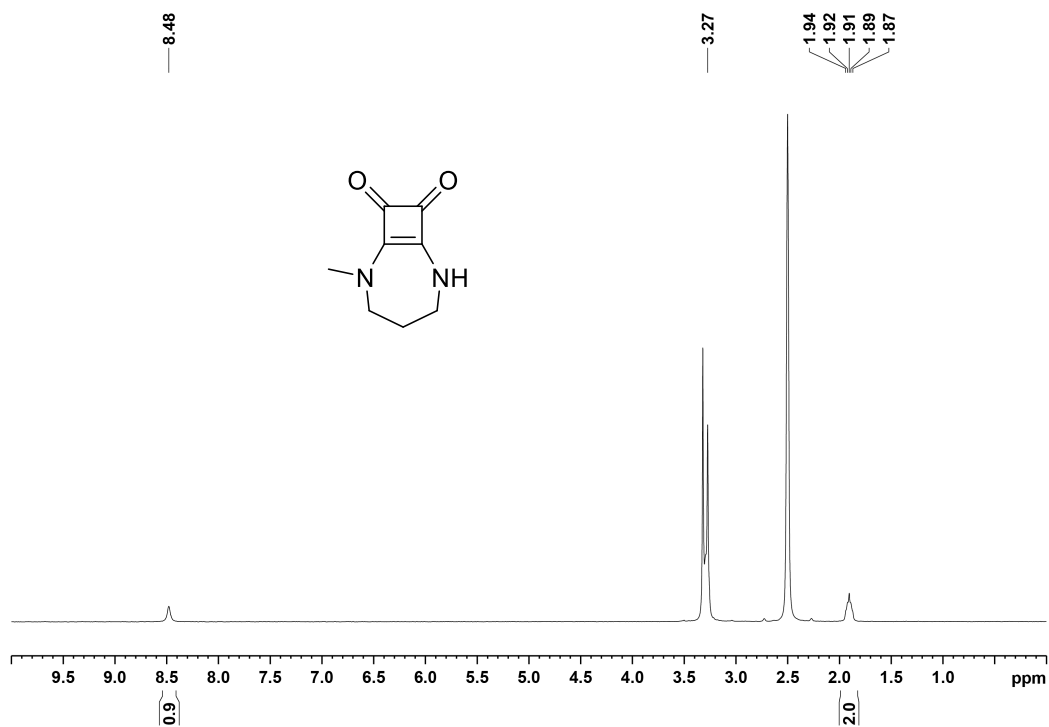


Figure S5. <sup>1</sup>H NMR spectrum of 2 in DMSO-*d*<sub>6</sub>, 300 MHz, 298 K

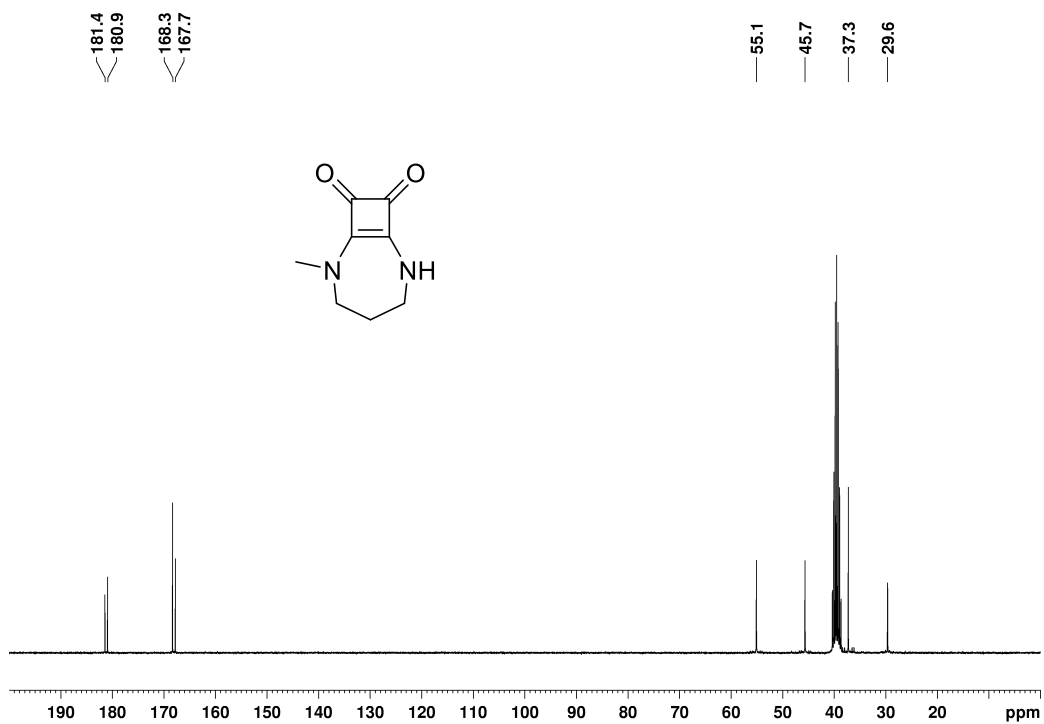


Figure S6. <sup>13</sup>C NMR spectrum of 2 in DMSO-*d*<sub>6</sub>, 300 MHz, 298 K

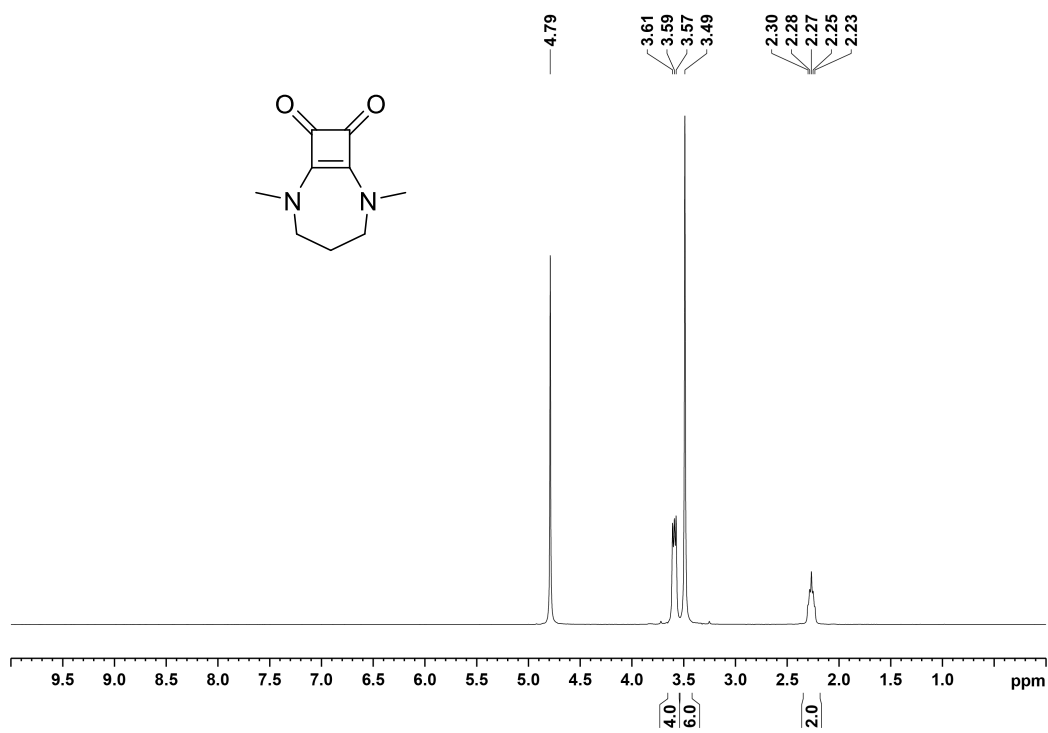


Figure S7.  $^1\text{H}$  NMR spectrum of **3** in  $\text{D}_2\text{O}$ , 300 MHz, 298 K

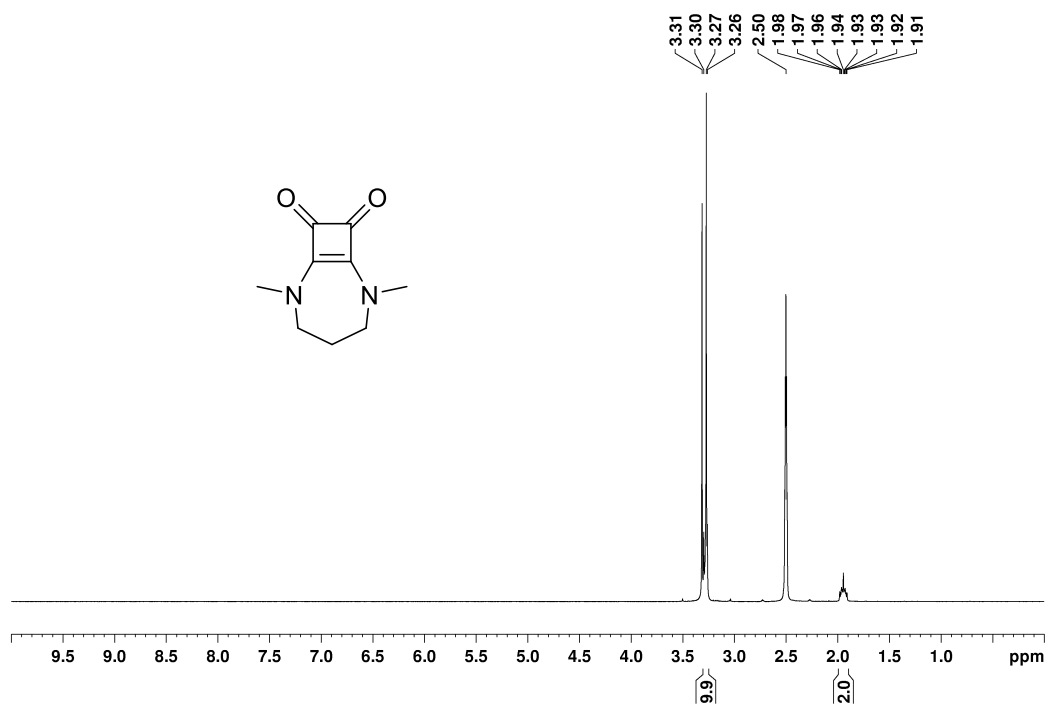
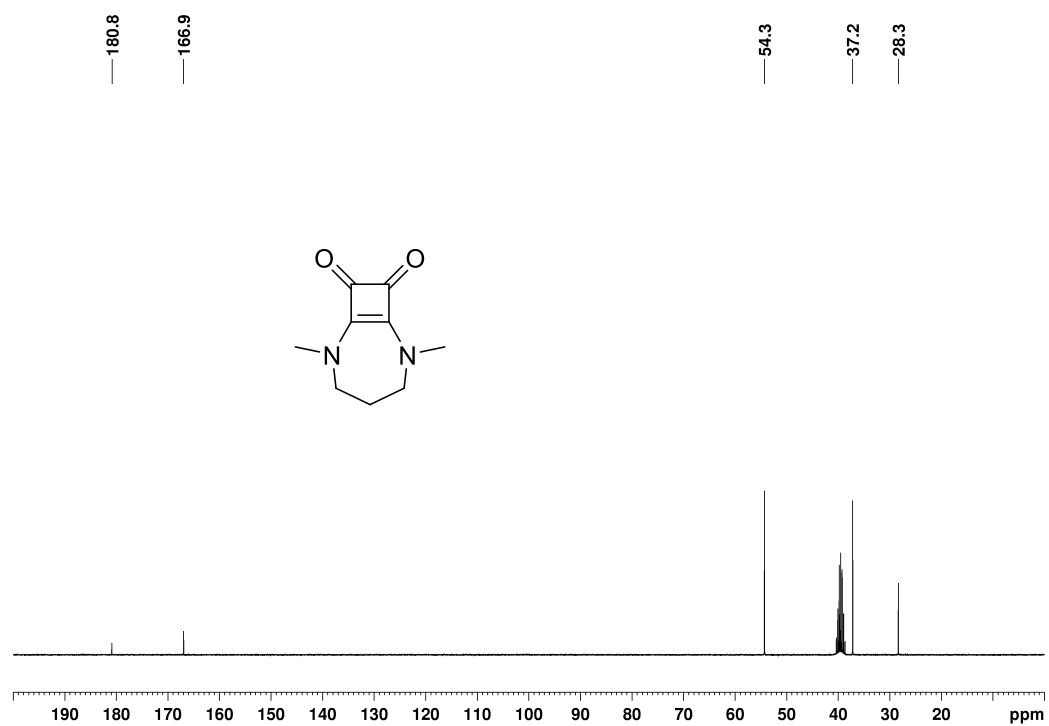


Figure S8.  $^1\text{H}$  NMR spectrum of **3** in  $\text{DMSO-}d_6$ , 300 MHz, 298 K



**Figure S9.**  $^{13}\text{C}$  NMR spectrum of **3** in  $\text{DMSO-}d_6$ , 300 MHz, 298 K

## TGA/DSC and variable temperature PXRD

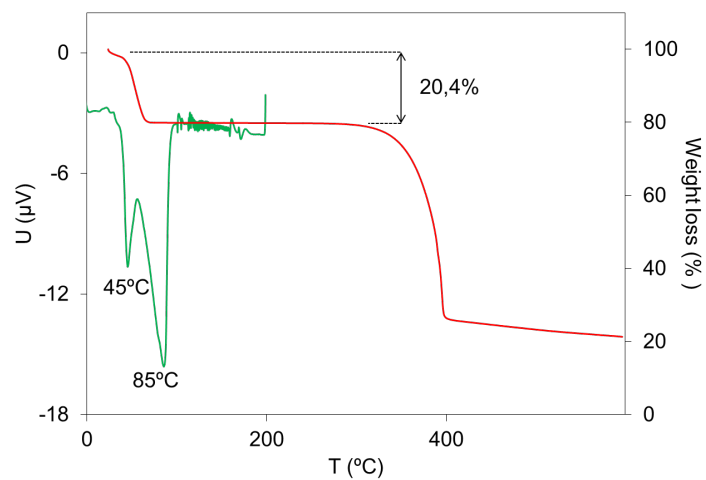


Figure S10. Thermogravimetric analysis in red and DSC trace in green of **1**.

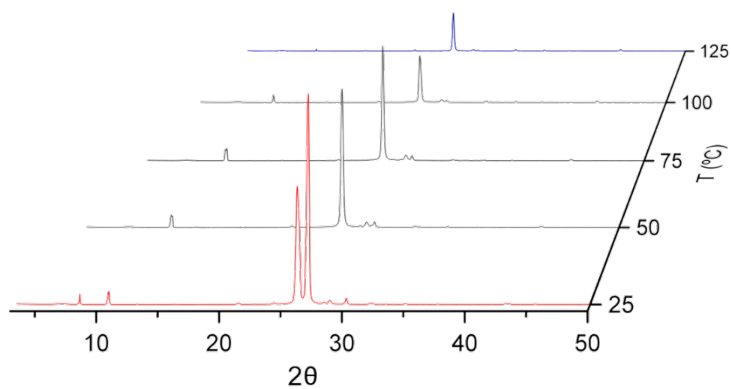


Figure S11. PXRD of **1**. 25-125°C

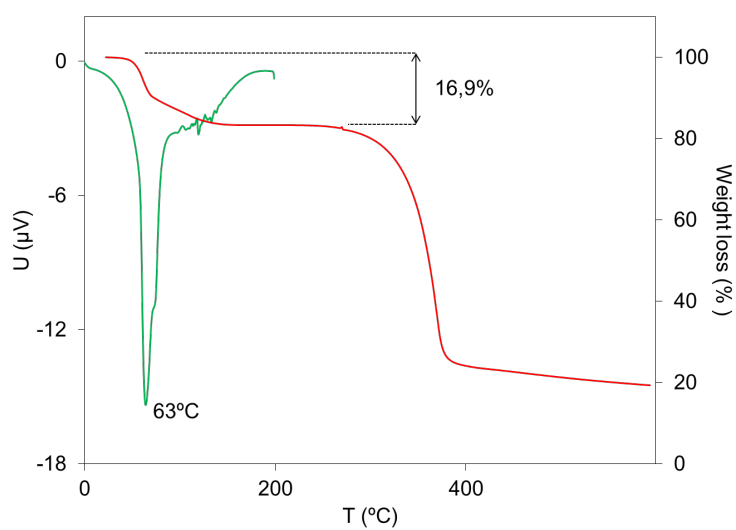


Figure S12. Thermogravimetric analysis in red and DSC trace in green of **2**.

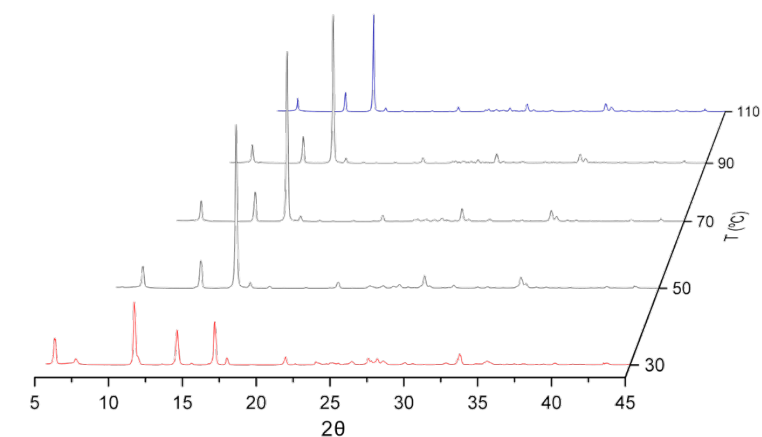


Figure S13. PXRD of 2. 30-110°C

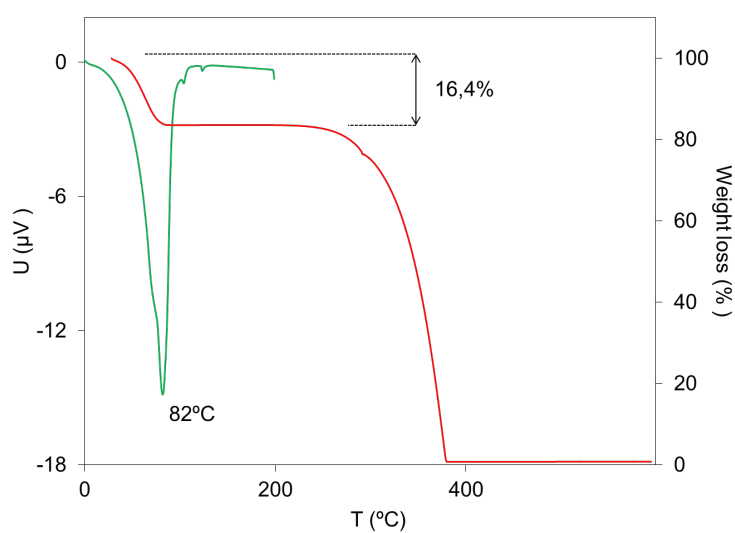


Figure S14. Thermogravimetric analysis in red and DSC trace in green of 3.

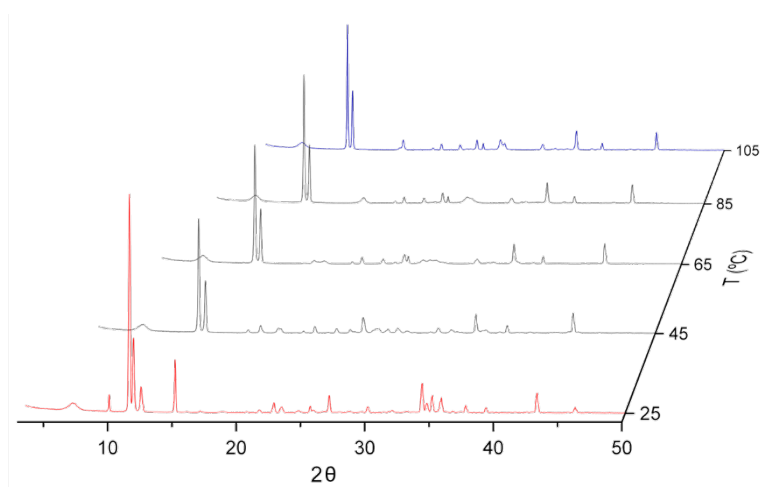
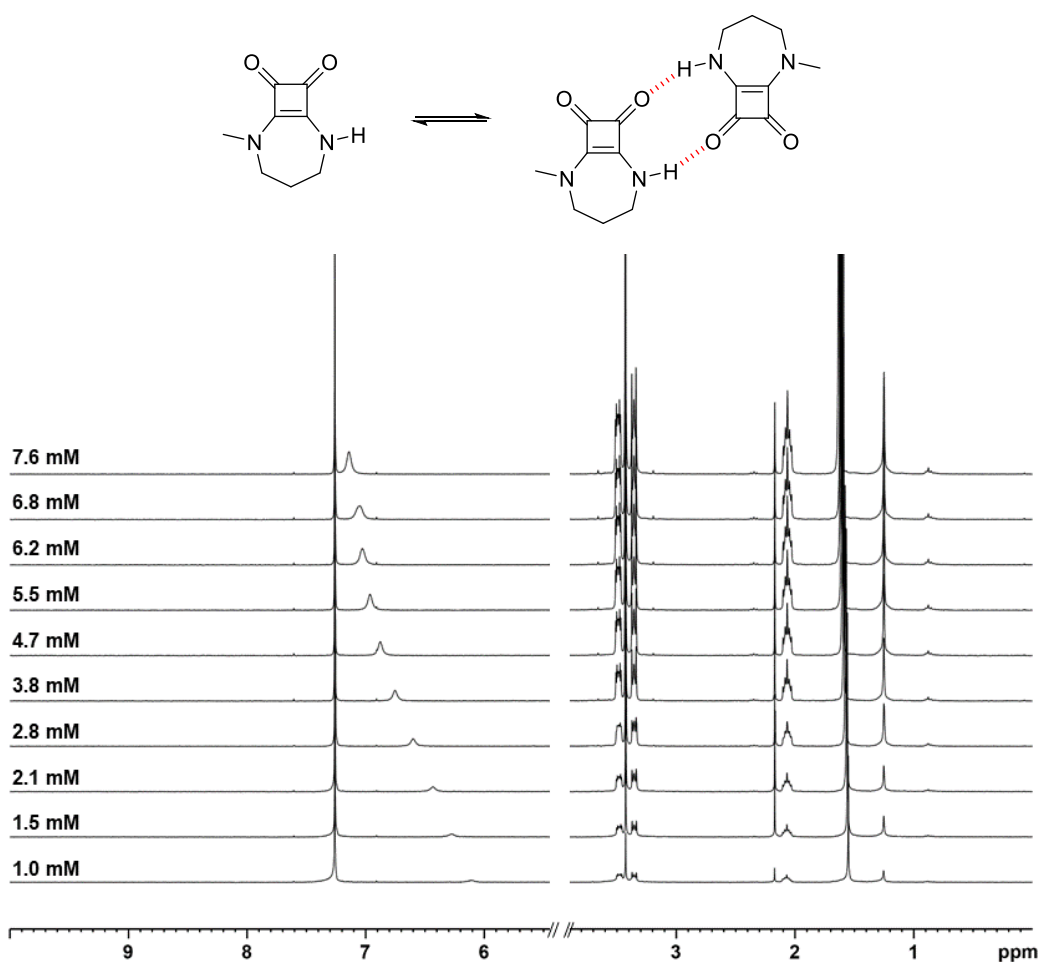
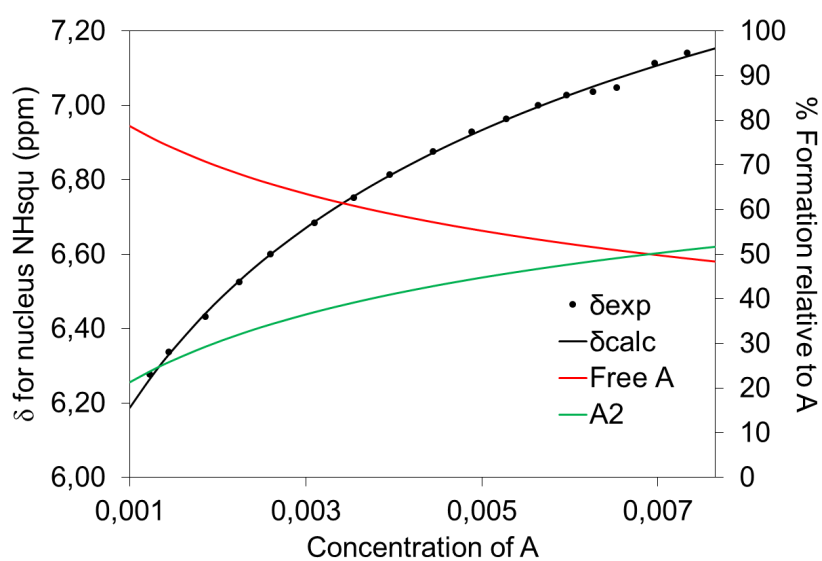


Figure S15. PXRD of 3. 25-105°C

$^1\text{H}$  NMR dimerization and aggregation experiments in  $\text{CDCl}_3$ 

**Figure S16.**  $^1\text{H}$  NMR ( $\text{CDCl}_3$ , 298K) spectra for **2** showing the upfield shift of NH protons depending on the concentration.



**Figure S17.**  $^1\text{H}$  NMR ( $\text{CDCl}_3$ , 298K) fitting of experimental data for nucleus NH of **2** to a model of dimerization ( $2\text{A}=\text{A}_2$ ) using HypNMR2008

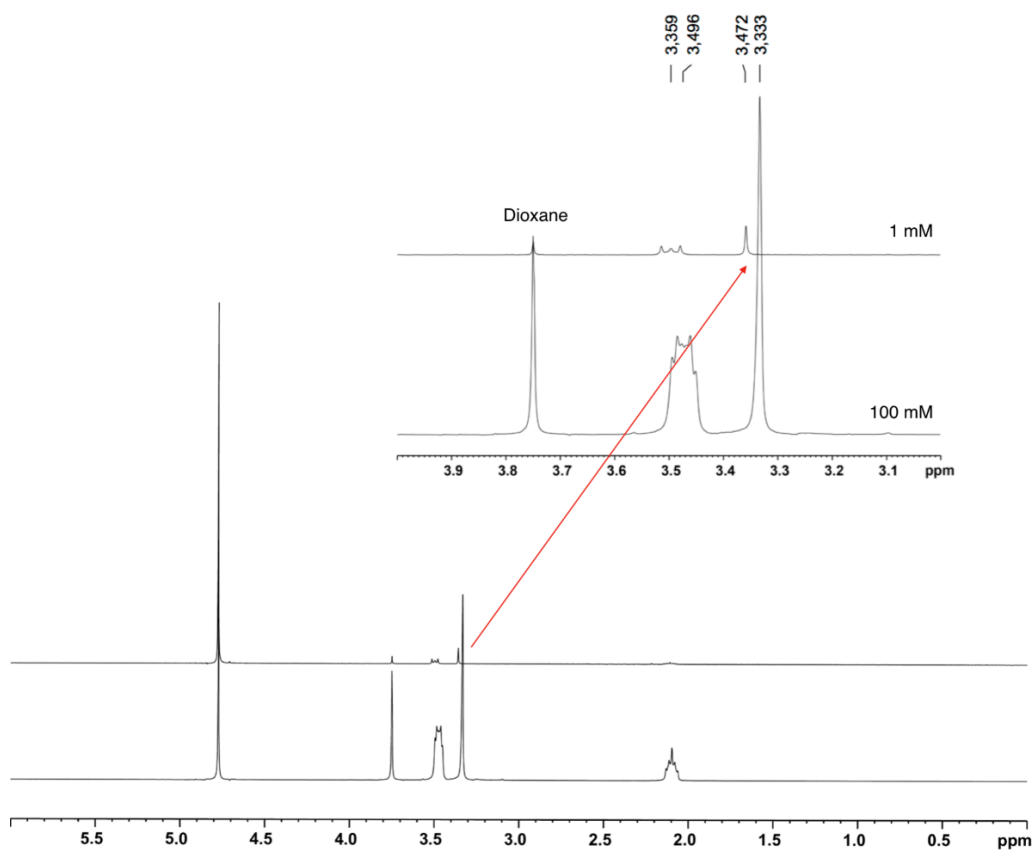


**Figure S18.**  $^1\text{H}$  NMR ( $\text{D}_2\text{O}$ , 298K) spectrums for **2** at 1 and 100 mM, respectively. Dioxane was added as internal reference.

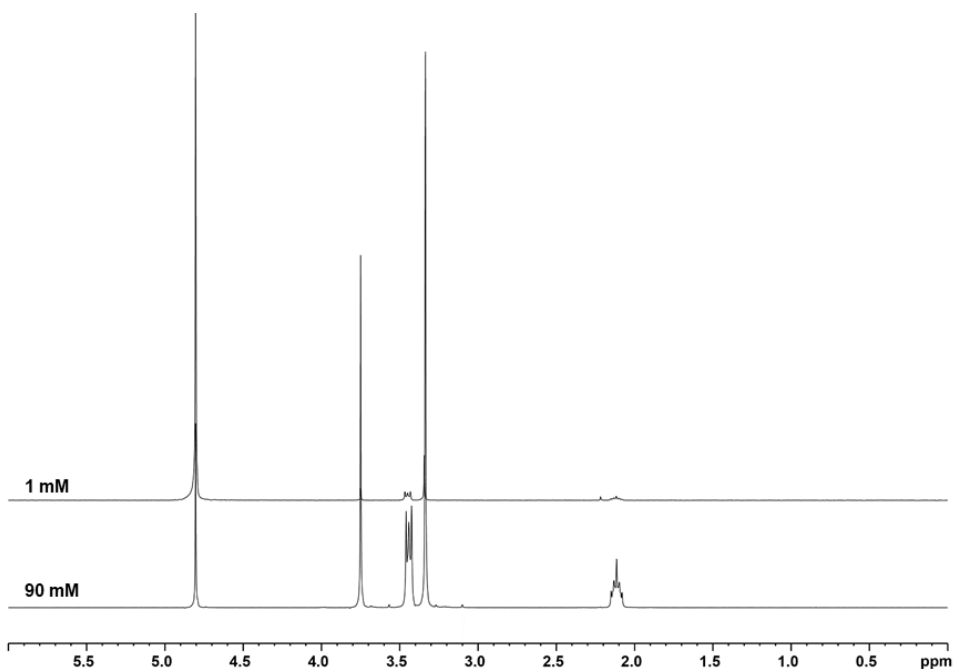


**Figure S19.**  $^1\text{H}$  NMR ( $\text{D}_2\text{O}$ , 298K) spectrums for **3** at 1 and 90 mM, respectively. Dioxane was added as internal reference.

## ORTEP views and selected X-Ray distances

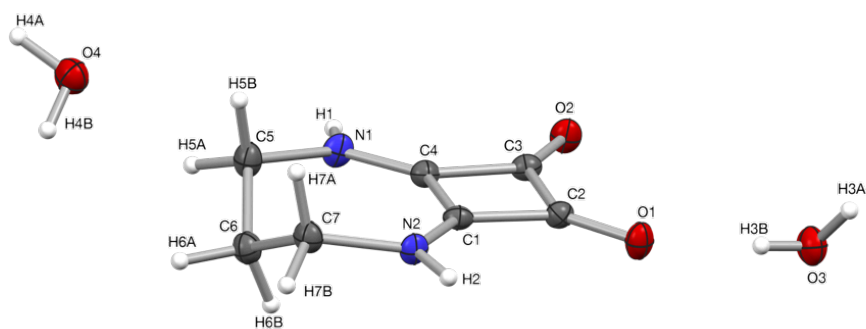


Table S1. Significant distances (Å) in 1

Interlayer squaramide contacts		Intralayer squaramide contacts (H bond)		Squaramide-water contacts		Water-water contacts	
C1–C2'	3.320	O2–N1'(NH)	2.821	O1–O3	2.789	O3–O4	2.790
C4–C3'	3.335	N2–O1'(NH)	2.821	C5H–O3	2.645	O3–O4	2.884
				C7H–O4	2.624	O3–O4	2.888

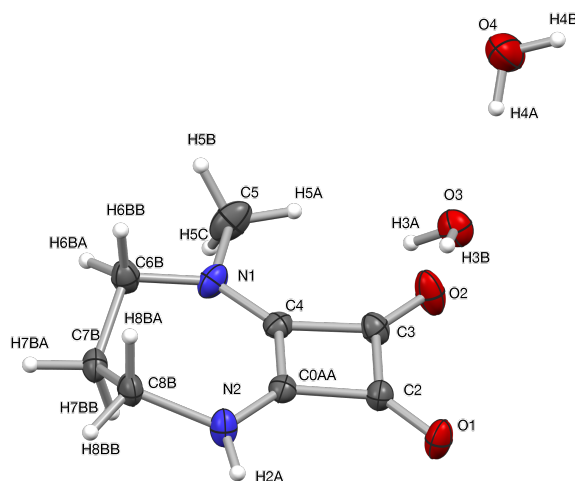
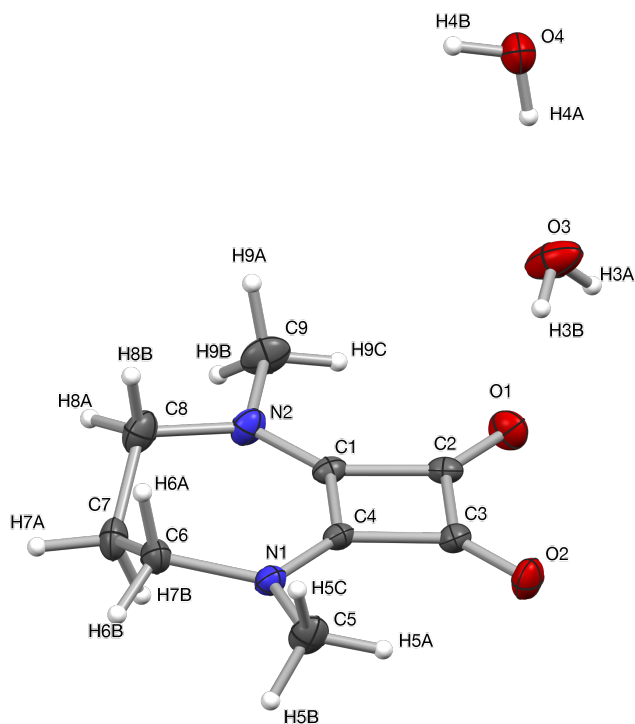


Table S2. Significant distances (Å) in 2

Interlayer squaramide contacts		Intralayer/Intramolecular squaramide contacts		Squaramide-water contacts		Water-water contacts	
C2–C4'	3.388	O1–H2'(NH)	1.975	O2–H3B	1.927	O3–H4B	1.936
C4–C2'	3.388	H2A–O1'	1.975			O3–H4A	1.907
O1–H7BB	2.375	O2–H5A	2.532			O4–H3A	1.876
O1–H7AA	2.490						
O1–H8BA	2.658						
O2–H7BA	2.490						
O2–H7BB	2.375						



**Table S3.** Significant distances (Å) in **3**

Interlayer squaramide contacts		Intralayer/Intramolecular squaramide contacts		Squaramide-water contacts		Water-water contacts	
C2–C4'	3.379	O2–H5A	2.476	O1–O3	2.779	O3–O4	2.728
C4–C2'	3.379	O1–H9C	2.551	O2–O4	2.802	O3–O4	2.716
O1–H6A	2.648	C2–C4'	3.379				
O1–H7B	2.696	C4–C2'	3.379				

## Crystallographic collection and refinement data

Table S4. Crystal data and structure refinement for 1·2H<sub>2</sub>O, 2·2H<sub>2</sub>O, 3·2H<sub>2</sub>O.

	3·2H <sub>2</sub> O	2·2H <sub>2</sub> O	1·2H <sub>2</sub> O
<b>Empirical formula</b>	C <sub>9</sub> H <sub>16</sub> N <sub>2</sub> O <sub>4</sub>	C <sub>8</sub> H <sub>14</sub> N <sub>2</sub> O <sub>4</sub>	C <sub>7</sub> H <sub>12</sub> N <sub>2</sub> O <sub>4</sub>
<b>Formula weight</b>	216.24	202.21	188.19
<b>Temperature / K</b>	120.0(1)	120.0(1)	120.0(1)
<b>Crystal system</b>	orthorhombic	orthorhombic	triclinic
<b>Space group</b>	Pca2 <sub>1</sub>	Pbcn	P-1
<b>a / Å</b>	18.2312(6)	31.9377(10)	5.3915(5)
<b>b / Å</b>	7.7893(3)	8.3100(3)	7.5525(8)
<b>c / Å</b>	7.4334(3)	7.4876(4)	10.9894(10)
<b>α / °</b>	90	90	77.404(8)
<b>β / °</b>	90	90	83.206(8)
<b>γ / °</b>	90	90	80.944(8)
<b>V / Å<sup>3</sup></b>	1055.60(7)	1987.23(14)	429.63(7)
<b>Z</b>	4	8	2
<b>ρ<sub>calc</sub> / g/cm<sup>3</sup></b>	1.361	1.352	1.455
<b>μ / mm<sup>-1</sup></b>	0.107	0.109	0.12
<b>F(000)</b>	464	864	200
<b>2θ range</b>	6.88 to 52	7.44 to 52	7.37 to 52
<b>Radiation</b>	0.71073	0.71073	0.71073
<b>Refl. collected</b>	2674	4832	2759
<b>Independent refl.</b>	1641	1951	4487
<b>R<sub>int</sub></b>	0.0214	0.0223	0.0263
<b>restraints/param</b>	1/144	0/161	0/124
<b>GOF</b>	1.048	1.027	1.051
<b>R<sub>1</sub>, wR<sub>2</sub>[I ≥ 2σ (I)]</b>	0.0373, 0.0781	0.0417, 0.1005	0.0446, 0.1039
<b>R<sub>1</sub>, wR<sub>2</sub>[all data]</b>	0.0459, 0.0863	0.0552, 0.1099	0.0623, 0.1198

Table S5. Hydrogen bond table for 1·2H<sub>2</sub>O. Distances in Å, angles in degrees.

Bond	d(D–A)	d(D–H)	d(H...A)	ang(D–A...H)
N(1)–H(1)..O(2)[–x, 1–y, –z]	2.811(2)	0.86	1.99	160
N(2)–H(2)...O(1)[2–x, –y, –z]	2.821(2)	0.86	1.98	164
O(3)–H(3A)...O(4)[1–x, –y, –z]	2.791(2)	0.924(14)	1.878(13)	168.7(8)
O(3)–H(3B)...O(1)	2.7886(18)	0.781(12)	2.011(12)	173.5(5)
O(4)–H(4A)...O(3)[–1+x, y, –1+z]	2.894(2)	0.909(11)	2.056(11)	152.8(9)
O(4)–H(4B)...O(3)[x, y, –1+z]	2.888(2)	0.889(11)	2.087(11)	149.4(9)

**Table S6.** Hydrogen bond table for 2·2H<sub>2</sub>O. Distances in Å, angles in degrees.

Bond	d(D–A)	d(D–H)	d(H...A)	ang(D–A...H)
N(2)–H(2A)...O(1)[1–x, 1–y, –z]	2.7981(17)	0.86	1.98	159
N(2)–H(2B)...O(1)[1–x, 1–y, –z]	2.7981(17)	0.86	2.00	153
O(3)–H(3A)...O(4)[ <sup>3</sup> / <sub>2</sub> –x, <sup>1</sup> / <sub>2</sub> –y, – <sup>1</sup> / <sub>2</sub> +z]	2.725(2)	0.85	1.88	177
O(3)–H(3B)...O(2)	2.7739(18)	0.85	1.93	176
O(4)–H(4A)...O(3)	2.749(2)	0.85	1.91	170
O4–H4B...O3[x, –y, <sup>1</sup> / <sub>2</sub> +z]	2.778(2)	0.85	1.94	170

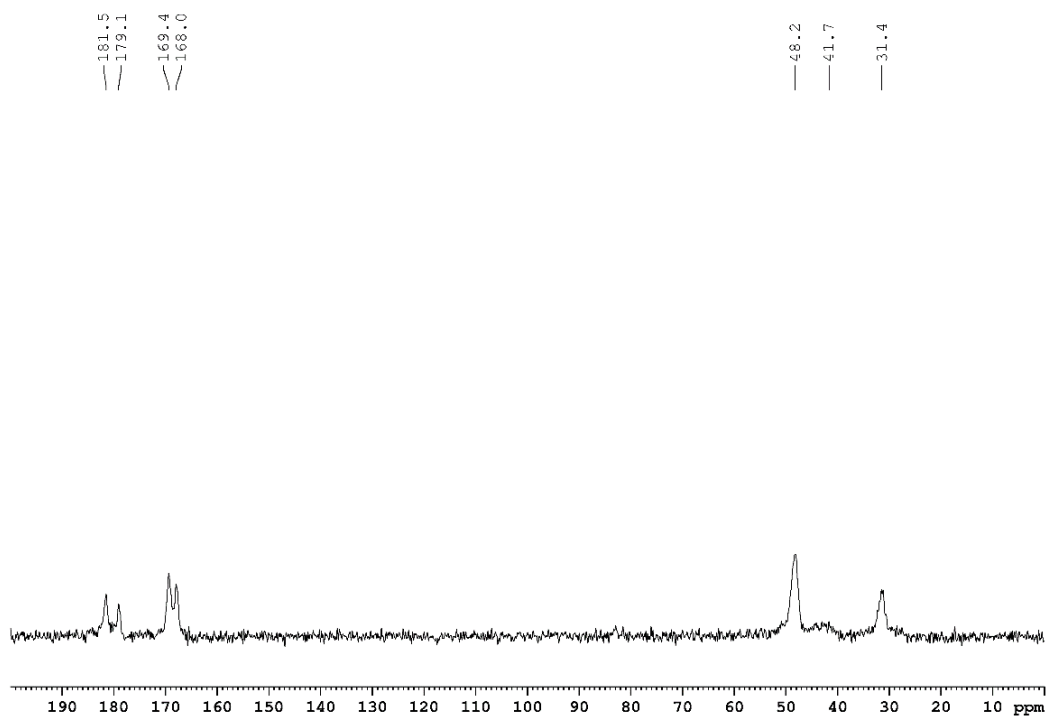
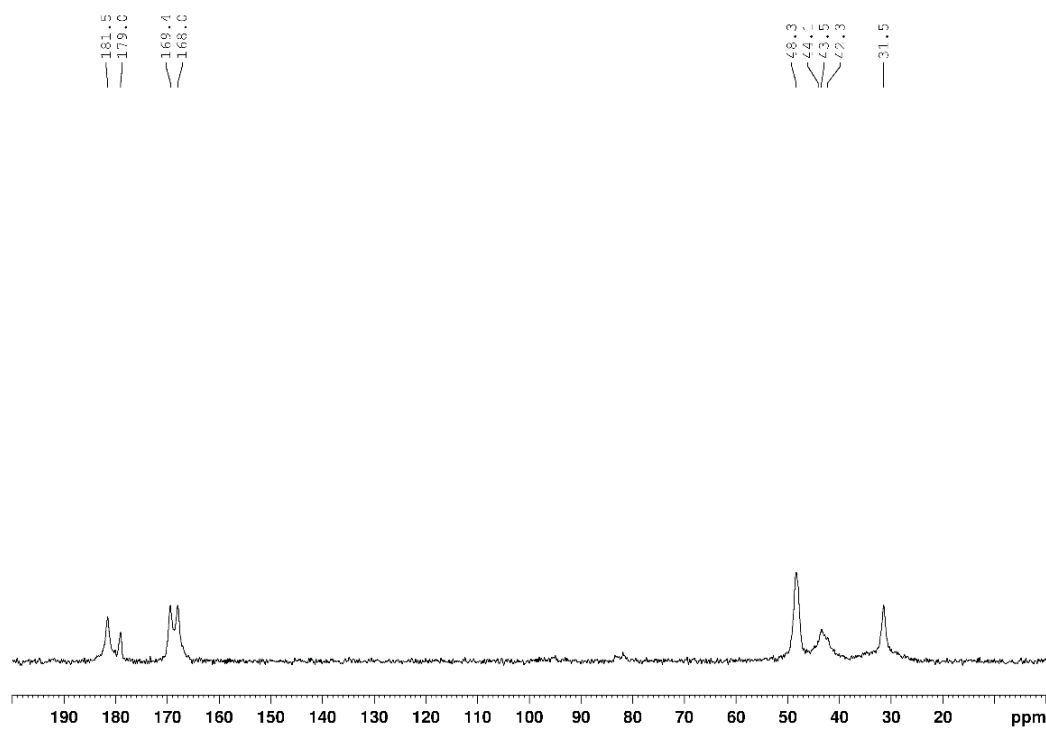
**Table S7.** Hydrogen bond table for 3·2H<sub>2</sub>O. Distances in Å, angles in degrees.

Bond	d(D–A)	d(D–H)	d(H...A)	ang(D–A...H)
O(3)–H(3A)...O(4)[1–x, –y, – <sup>1</sup> / <sub>2</sub> +z]	2.716(3)	0.85	1.87	175
O(3)–H(3B)...O(1)	2.779(2)	0.85	1.93	173
O(4)–H(4A)...O(3)	2.728(3)	0.85	1.88	174
O(4)–H(4B)...O(2)[x, –1+y, z]	2.802(2)	0.85	1.97	167

**Table S8.** Thermal parameters for the water molecules in the structures.<sup>a</sup>

		1·2H <sub>2</sub> O	2·2H <sub>2</sub> O	3·2H <sub>2</sub> O
Average U		0.0241 <sup>a</sup>	0.0211	0.0167
O3	U <sub>eq</sub>	0.0292	0.0301	0.0237
	Increment <sup>b</sup>	+21%	+43%	+42%
	No. Hydrogen bonds	4	3	4
O4	U <sub>eq</sub>	0.0486	0.0391	0.0250
	Increment	+102%	+85%	+50%
	No. Hydrogen bonds	3	3	3

<sup>a</sup>Average of U values for all atoms in the crystal. <sup>b</sup>Increment of U<sub>eq</sub> of the oxygen atom of the water above the average value.

Solid – State  $^{13}\text{C}$  CP MAS NMRFigure S20. ss- $^{13}\text{C}$  NMR spectrum of  $1 \cdot 2\text{H}_2\text{O}$ , 298KFigure S21. ss- $^{13}\text{C}$  NMR spectrum of **1**, 298K

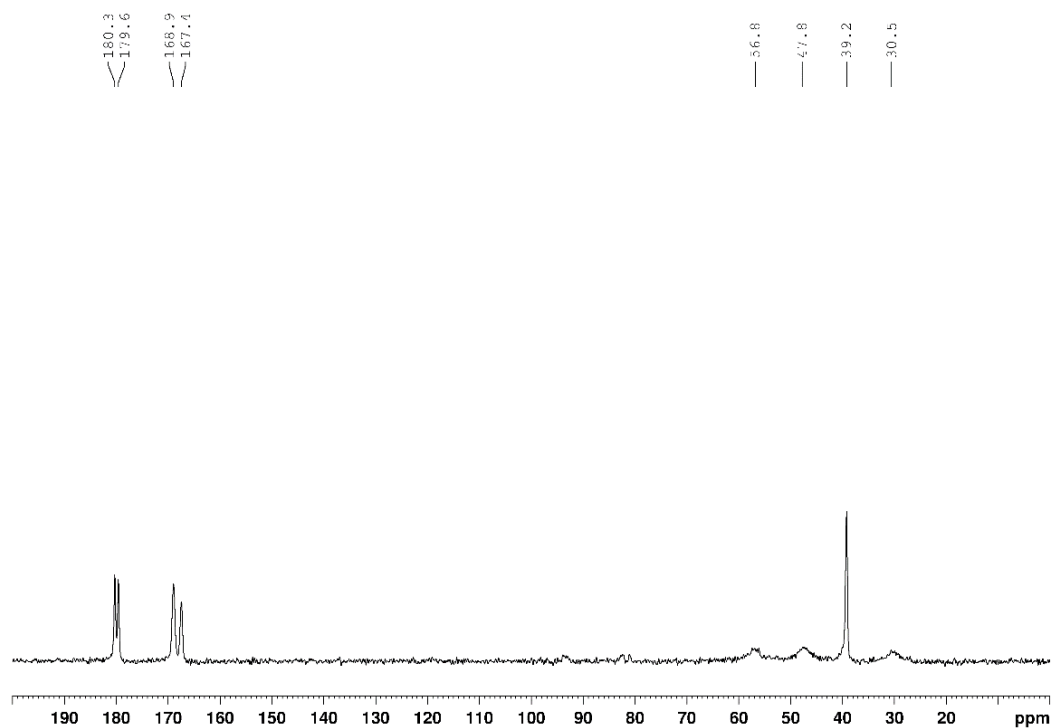


**Figure S22.** ss-<sup>13</sup>C NMR spectrum of 2·2H<sub>2</sub>O, 298K

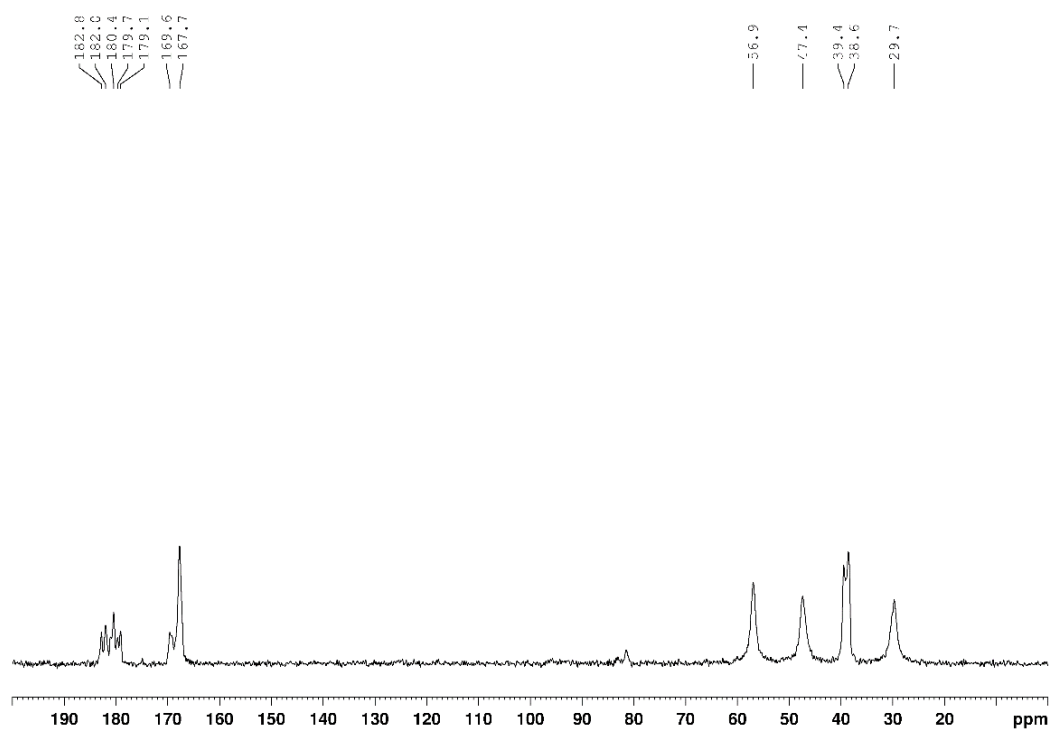


**Figure S23.** ss-<sup>13</sup>C NMR spectrum of 2, 298K

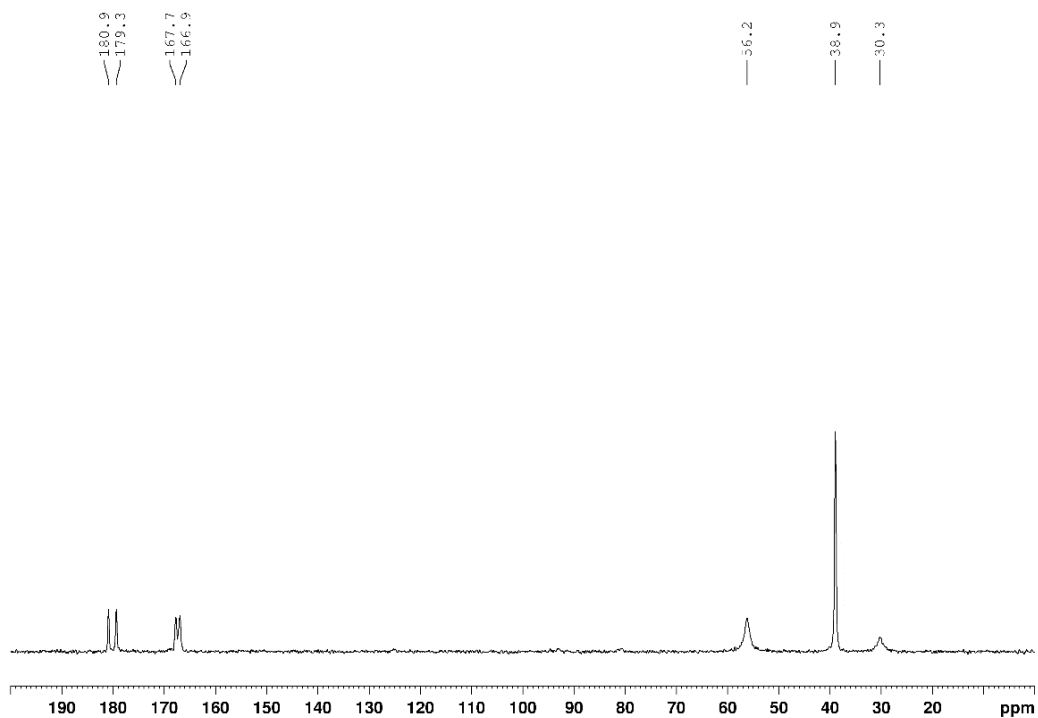


Figure S24. ss- $^{13}\text{C}$  NMR spectrum of  $3 \cdot 2\text{H}_2\text{O}$ , 298K

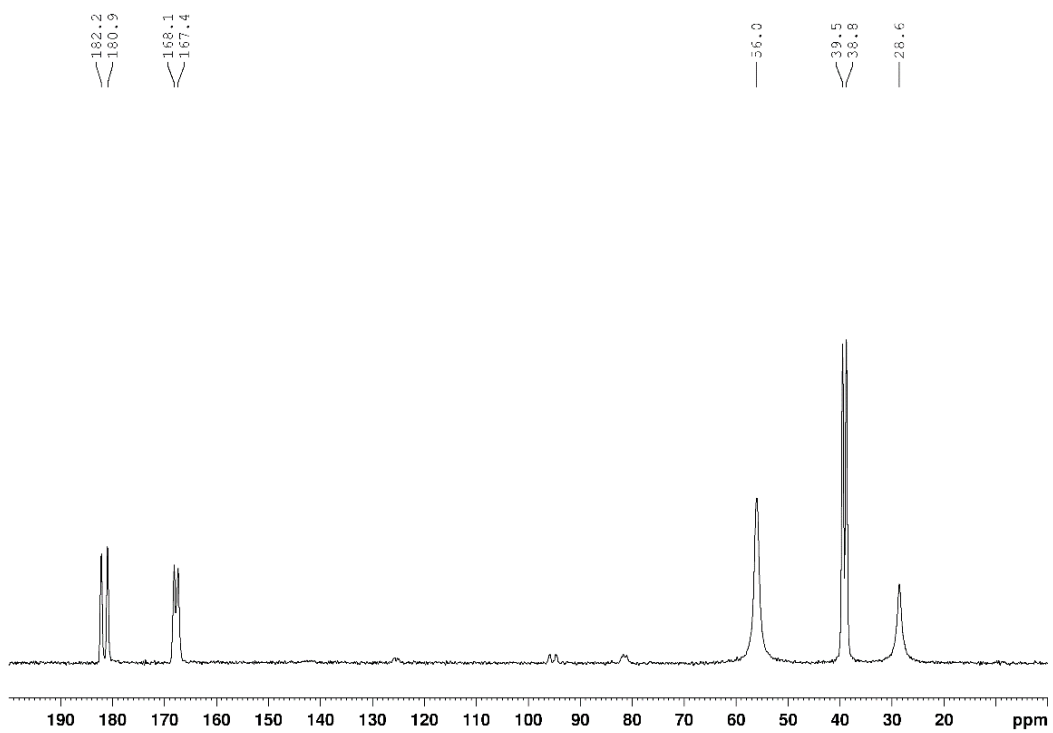
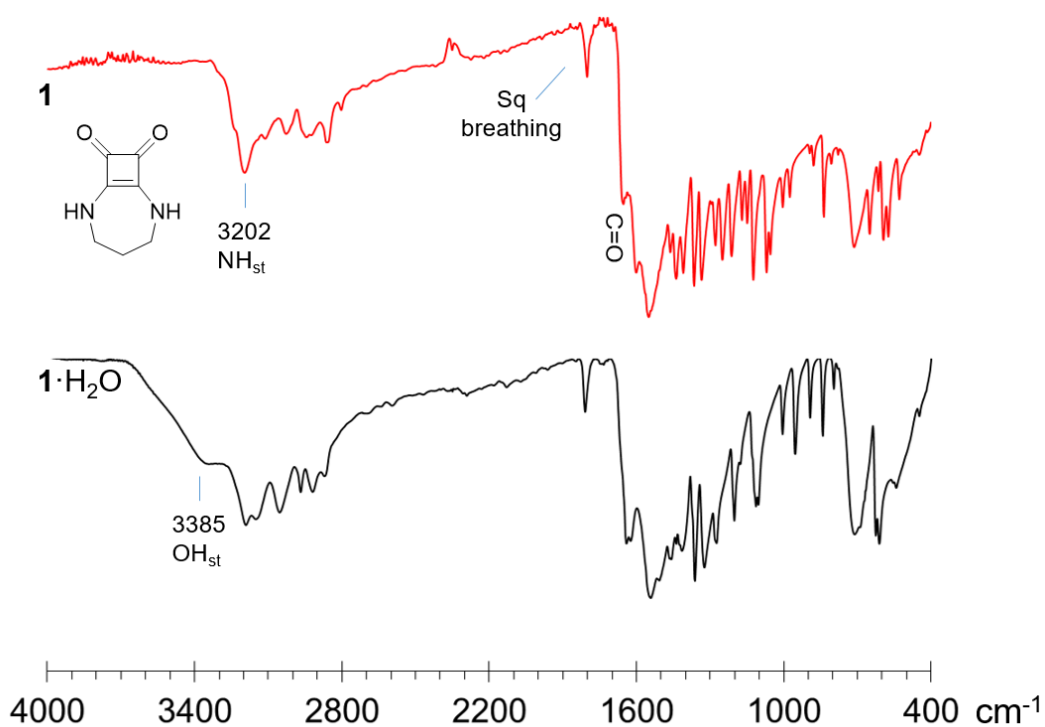
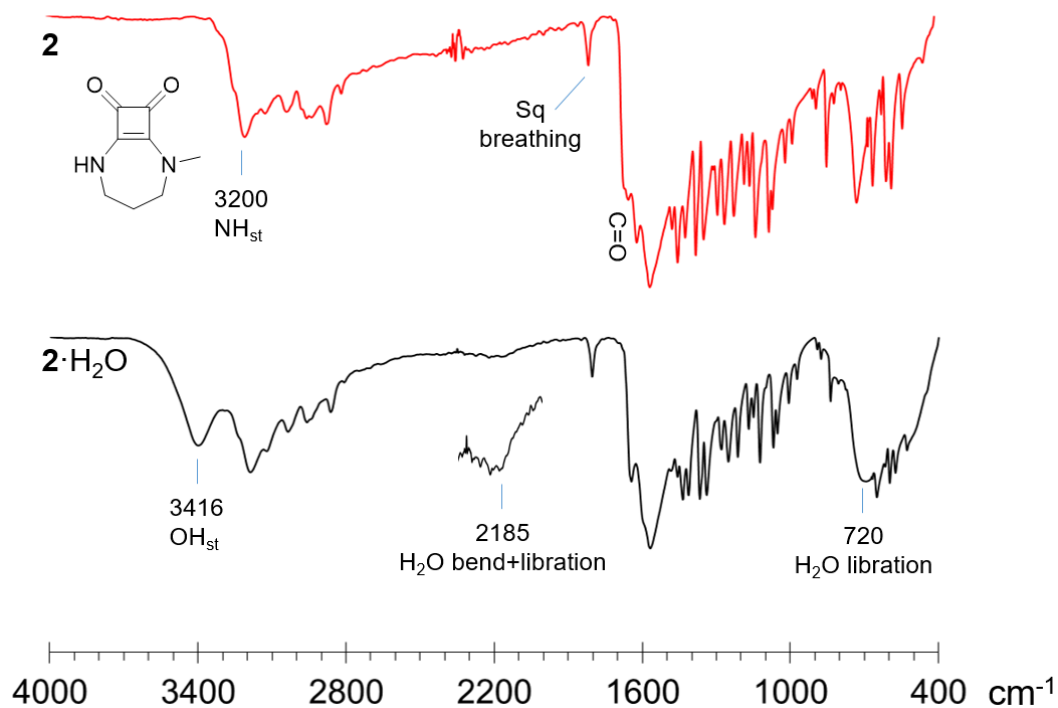


Figure S25. ss- $^{13}\text{C}$  NMR spectrum of  $3$ , 298K

## FTIR-ATR spectra



**Figure S26.** FTIR-ATR spectra of **1**·2H<sub>2</sub>O (black) and its anhydrate (red) showing distinctive peaks due to confined water



**Figure S27.** FTIR-ATR spectra of **2**·2H<sub>2</sub>O (black) and its anhydrate (red)

**Table S9.** Selected FTIR-ATR frequencies of squaramide hydrates and their anhydrides

Assignment	Wavenumber (cm <sup>-1</sup> )					
	<b>1</b>	<b>1·2H<sub>2</sub>O</b>	<b>2</b>	<b>2·2H<sub>2</sub>O</b>	<b>3</b>	<b>3·2H<sub>2</sub>O</b>
N-H (st)	3202	3196	3200	3198	-	-
Squaramide ring breathing	1798	1811	1800	1805	1792	1800
C=O (st)	1657	1643	1659	1647	1660	1649
O-H···O (st)	-	3370	-	3416	-	3350
HOH (lib. + bend.)	-	(2140) <sup>a</sup>	-	2181	-	2180
H-O-H (libration)	-	717	-	720	-	725

<sup>a</sup>tentative assignation (very weak band)

**5**

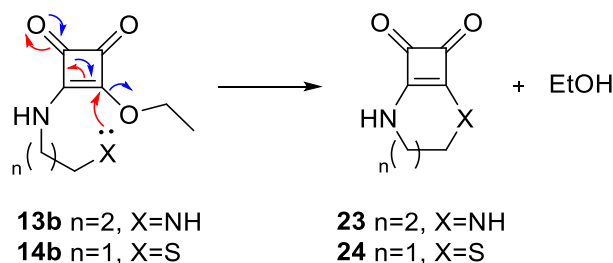
---

**Squaramide-Based Self-Immolative  
Spacers: Improving the  
Leaving Group**



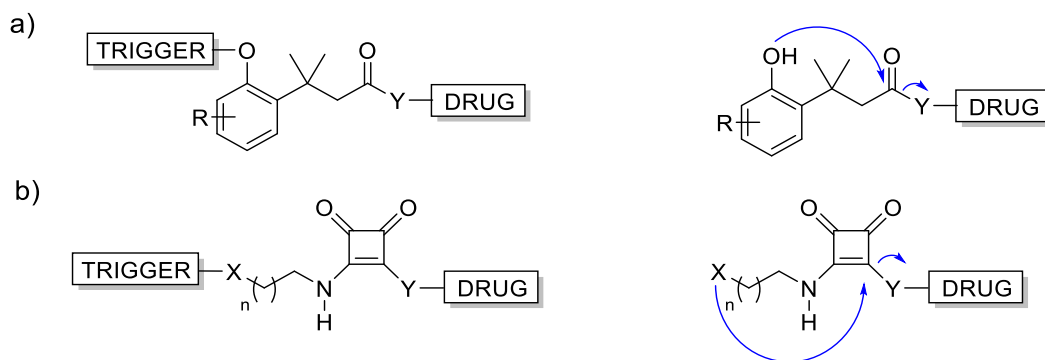
## 5.1. SELF-IMMOLATIVE SYSTEMS: DESIGN PRINCIPLES

In Chapter 3 two small squaramate ester-based systems, **13b** and **14b** were studied. These compounds spontaneously disassemble through an intramolecular cyclization mechanism which results in the release of an EtOH molecule in a relatively fast period (Scheme 5.1).



**Scheme 5.1.** Intramolecular cyclization of squaramate esters **13b** and **14b**.

In analogy to a conventional SIL which undergo cyclization, such as the trimethyl lock (TML), the immolation kinetics will depend on the nucleophilicity of the triggered group ( $X$ ) and the nucleofugacity of the leaving group ( $Y$ ). Based on our precedents, squaramide-based SIL bearing both N and S as nucleophiles, showed good self-immolative capability against the removal of EtOH (Scheme 5.2). However, chemical tunability of the leaving group ( $Y$ ) still remains unclear.



**Scheme 5.2.** General schematic representation of self-immolative linkers. a) TML and b) squaramide-based SIL.

Nucleofugacity of the leaving group is commonly related to its  $pK_a$ .<sup>13</sup> Hence, the stability of the SIL will be strongly related to the  $pK_a$  of the leaving group (Figure 5.1).

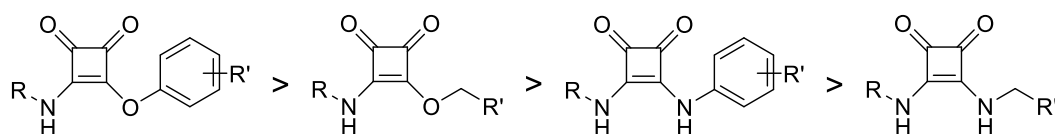


**Figure 5.1.** Assumed reactivity of squaramide derivatives depending on the  $pK_a$  of the leaving group.

According to this rationale, phenols ( $pK_a \approx 10$ ) would be removed easily, followed by aliphatic alcohols ( $pK_a \approx 16-18$ ), anilines ( $pK_a \approx 30$ ) and aliphatic amines ( $pK_a \approx 36-38$ ) respectively.<sup>203</sup> Because of the fast kinetics found for the release of EtOH, the ability of the system to release an aniline and an aliphatic amine was yet to be explored.

Another important feature of a self-immolative system based on cyclization reactions is the distance between the nucleophilic and electrophilic center. Curiously, the chain length necessary for the cyclization to take place was different for ester **13b** and **14b**. While cyclization of thiolate was achieved only with an ethyl chain, the reaction with an amine demanded a propyl chain. The corresponding ethylene analogue to **13b** (ester **12b**) did not undergo cyclization but only provides anchimeric assistance in the hydrolysis reaction. Thus, at the moment, it seemed unnecessary to explore chain length modifications to optimize the self-immolation disassembly.

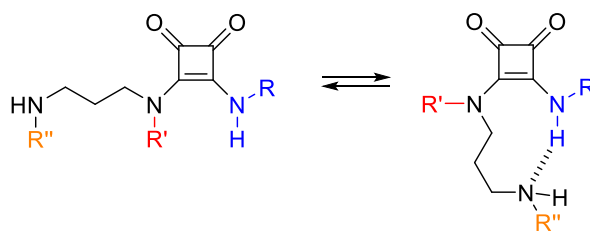
Squaramate ester **13b** was able to rapidly evolve to cyclic squaramide **23** even in moderate acidic conditions. Based on this excellent result, the next step in the design of a potential SIL-drug complex was the tunability of the cargo. Since most marketed drugs bear polar groups to effectively dissolve in blood, commonly amine or hydroxy groups, the SIL system should be conjugable to such functionalities and then, be able to release them under the proper stimulus.

In order to explore the versatility of the system to suit such requirements, a minimalist self-immolative model was designed, where the leaving group, that would be the future active payload, was modified. To this purpose, three different substituted anilines and *n*-butylamine as model functionalities were chosen, which in comparison with alcohols, are handicapped by their poor nucleofugacity (Scheme 5.3, **R**).

In addition to the payload influence, as introduced in Chapter 1, squaramides show a rotational barrier through the C-N bond which leads to the coexistence of different conformations in solution. Such phenomena are key for the cyclization reaction of the self-immolative process since, a folded conformation would place close in space both the nucleophile and electrophile centres enhancing the reaction rate. To evaluate this feature, the effect of *N*-methylation of the squaramide trigger substituent was also evaluated (Scheme 5.3, **R'**).

---

<sup>203</sup> D. E. Levy (2008) *Arrow Pushing in Organic Chemistry: An Easy Approach to Understanding Reaction Mechanisms*, 1<sup>st</sup> ed., Wiley Online Library, DOI:10.1002/9780470378885.



**Scheme 5.3.** Minimalist model of an amino-based self-immolative linker.

Finally, the presence of substituents on the nucleophilic amino group was also considered. In 1994, Mayr and Patz defined a linear free energy relationship between nucleophilicity ( $N$ ) and electrophilicity ( $E$ ) as the following equation.<sup>204</sup>

$$\log(k) = s(N + E) \quad (12)$$

In a relatively recent report, Mayr and collaborators describe the  $\alpha$ -effect in hydrazine reactivities with benzydrylium ions and quinone methides in  $\text{CH}_3\text{CN}$ .<sup>205</sup> Here they also studied the methylation effect on the nucleophilicity of amines, finding a significant increase on the  $N$  parameter, when increasing the methylation degree.

Hence, methylation on the terminal amino group on our SIL should lead to an increase of the reaction rate in comparison with the non-methylated analogue (Scheme 5.3,  $R''$ ).

Conversely, squaramate ester **14b** successfully evolved to the release of an ethanol molecule after the reduction of the disulfide bond. The Intracellular disulfide reshuffling is an extensively used strategy for intracellular drug release.<sup>206</sup> Despite the overall redox potential in the human blood is oxidative, there are some reductive cellular environments.<sup>207</sup> Thus, the presence of reductive species bearing free thiolates such as glutathione,<sup>208</sup> dithiothreitol<sup>209</sup> or cysteine<sup>208b</sup> may promote the thiol-disulfide exchange. The redox process is spontaneous and fast, and undergo efficient intracellular decomposition of the disulfide SIL. Figure 5.2 shows a general structure of a disulfide SIL (a). When the disulfide disassembles through shuffling, the resulting free thiolate attacks the electrophilic moiety which normally is a carbonyl group. Such linkage

<sup>204</sup> H. Mayr, M. Patz, *Angew. Chem. Int. Ed.* **1994**, *33*, 938–957.

<sup>205</sup> T. A. Nigst, A. Antipova, H. Mayr, *J. Org. Chem.* **2012**, *77*, 8142–8155.

<sup>206</sup> a) G. Saito, J. A. Swanson, K.-D. Lee, *Adv. Drug Deliv. Rev.* **2003**, *55*, 199–215. b) M. H. Lee, Z. Yang, C. W. Lim, Y. H. Lee, S. Dongbang, C. Kang, J. S. Kim, *Chem. Rev.* **2013**, *113*, 5071–5109.

<sup>207</sup> a) H. J. Grosz, B. B. Farmer, *Nature* **1967**, *213*, 717–718. b) H. R. López-Mirabal, J. R. Winther, *Biochim. Biophys. Acta - Mol. Cell Res.* **2008**, *1783*, 629–640.

<sup>208</sup> a) X. Wang, X. Cai, J. Hu, N. Shao, F. Wang, Q. Zhang, J. Xiao, Y. Cheng, *J. Am. Chem. Soc.* **2013**, *135*, 9805–9810. b) A. Santoro, N. Ewa Wezynfeld, M. Vašák, W. Bal, P. Faller, *Chem. Commun.* **2017**, *53*, 11634–11637.

<sup>209</sup> H. Wu, J. Li, J. Wei, Y. Dai, Z. Peng, Y. Chen, T. Liu, *Chem. Res. Chinese Univ.* **2015**, *31*, 890–894.

allows diverse chemical functionalities (Y) finding amines, alcohols, carboxylic acids, and amides.<sup>210</sup>

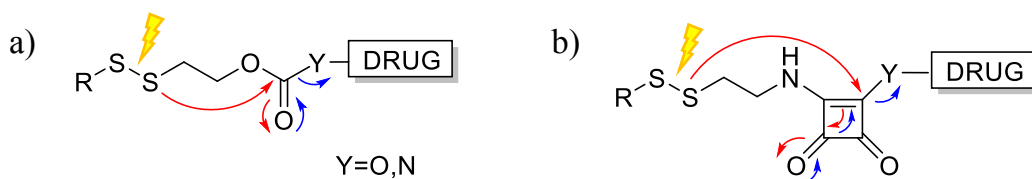


**Figure 5.2.** a) Generic mechanism of disulfide reshuffling and consequent self-immolation by cyclization releasing the parent drug. b) Extrapolation to a model squaramide-based disulfide SIL.

For compound **14b**, the disulfide shuffling reaction was triggered with tris-carboxyethyl phosphine (TCEP), a water-soluble phosphine, which reduced the disulfide affording a free thiolate. The further intramolecular cyclization was fast with a rate constant of  $2.3 \times 10^{-4} \text{ M s}^{-1}$ .

Despite the success of the minimalist model **14b**, self-immolative systems **1** and **2**, developed by Dr. Sampedro, resulted synthetically tedious and low in yield. Additionally, the most important challenge to overcome was their low water solubility, which made them hard to study in simulated physiological conditions. For this reason, the subsequent design and development of disulfide-based SIL-drug conjugates should include cunning chemical modifications to enhance the solubility of the resulting structure which requires an additional synthetic handicap. Besides, it is worth to mention that the unexpected degradation of cyclothiosquaramide **24**, the main product of such disassembly processes, hinders the spectroscopic study of the reaction kinetics.

With such precedents, we decided to discard in this thesis, the design and development of disulfide-based SIL and focus on the potential of amino derivatives.

<sup>210</sup> C. F. Riber, A. A. A. Smith, A. N. Zelikin, *Adv. Healthc. Mater.* **2015**, *4*, 1887–1890.

## 5.2. OBJECTIVES

Along with this chapter the tunability of the squaramide-amino-based SIL payload will be discussed, where the latest goal is to find the most suitable functionality that can be released under simulated biological conditions in a relatively short period. The particular aims are the following:

- To study the cyclization rate of minimalist self-immolative models for the release of differently substituted aromatic amines and study the effect of the substituents on the reaction rate.
- To use the previously developed squaramide-based self-immolative linker for the release of a bioactive aniline.
- To study the cyclization rate of minimalist self-immolative models for the release of *n*-butylamine as an example of aliphatic amines and study the effect of *N*-methylation on the reaction rate.
- To use the previously developed squaramide-based self-immolative linker for the release of a bioactive aliphatic amine.

### 5.3. RESULTS AND DISCUSSION

Based on the minimalist self-immolative model system, already studied, several squaramides bearing substituted anilines and *n*-butylamine (as a representative of an aliphatic amine) as leaving groups were designed and synthesised to study their release at different pH solutions at 37 °C. In all cases, the systems were build-up from a propylene diamine chain which, after conjugation to the squaryl moiety, would leave a free amine to act as a trigger to undergo the cargo disassembly.

#### 5.3.1. Self-immolative Models Releasing Anilines

The first group of compounds to be studied were aniline derivatives. The aromatic amine substituents were particularly suited to study the influence of the electron richness (related with  $pK_a$  and consequently, nucleofugacity) on the reaction kinetics (Chart 5.1, highlighted in blue). As aforementioned, the methylation on the squaramidic nitrogen of the trigger chain was used in the design to promote the folded conformation of the tertiary-secondary squaramide and thus enhance the intramolecular cyclization rate (Chart 5.1, **28b,d** and **e**, depicted in red). *N*-methylation was achieved using *N,N'*-Dimethyl-1,3-propanediamine as starting material due to its ease of synthetic access.

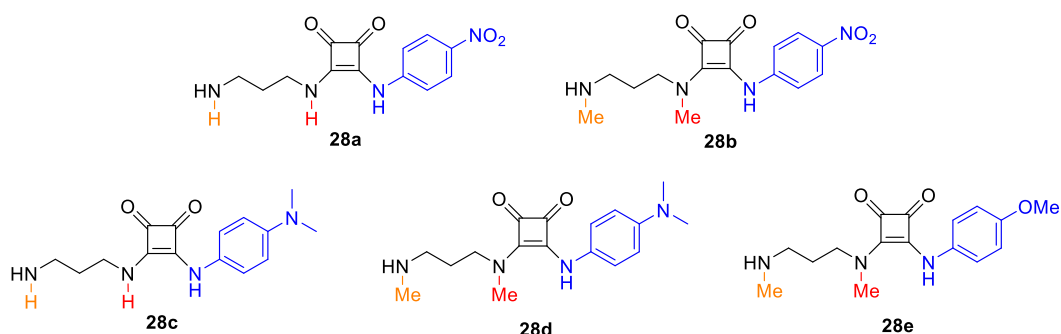


**Chart 5.1.** Chemical structures of the aniline-substituted squaramides evaluated for their self-immolative capability. Leaving group is depicted in blue.

The use of *N,N'*-Dimethyl-1,3-propanediamine in the synthesis of the model squaramides would also increment the nucleophilicity on the terminal amino group in comparison with the non-methylated analogues (Chart 5.1, depicted in orange).

In analogy to the studies performed for squaramate esters, the dimethylation reaction product was also prepared (**23b**, Chart 5.2) following the same procedure as for **23** (renamed as **23a**).

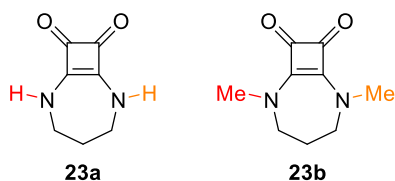
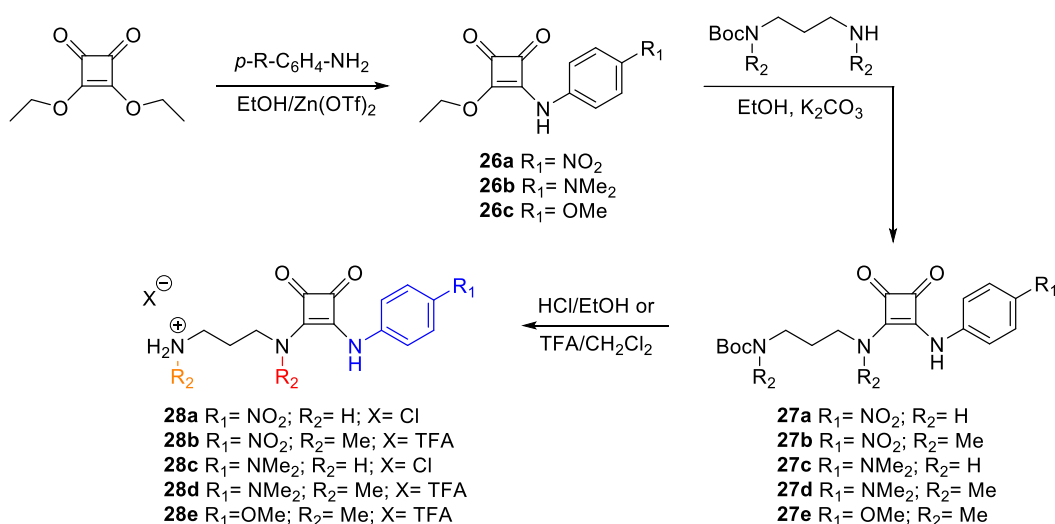


**Chart 5.2.** Chemical structures of the cyclosquaramide self-immolation products **23a** and **23b**.

*Synthesis of self-immolative models 28a-e.* The reactivity of aromatic amines as nucleophiles is lower than that of aliphatic amines. Thus, conjugation to squaramate esters is demanding. Normally it requires more drastic conditions or even catalysis to reach the final compounds. To overcome the limited reactivity the strategy developed by Taylor and collaborators was followed, using zinc trifluoromethanesulfonate as the catalyst.<sup>95e</sup> In a step-wise methodology, the aniline squaramate ester was firstly prepared and was then coupled with the corresponding Boc-protected diamine. Final acidic cleavage of the protecting group led to the corresponding self-immolative model:

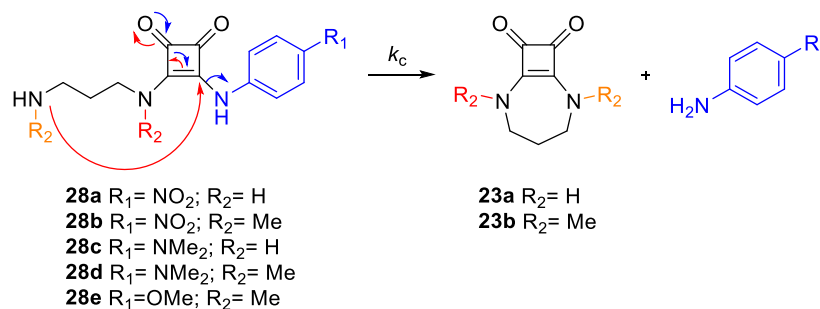


**Scheme 5.4.** Synthetic pathway to access aromatic self-immolative model **28a-e**.

The solubility of the final products was adequate to perform the subsequent experiments in aqueous solution. However, dissecondary squaramides (**a** and **c**) were less soluble than their corresponding methylated analogues (**b**, **d**, and **e**) because of their hydrogen bonding ability forming head to tail aggregates.<sup>211</sup> Thus, the final deprotection step of **27a** and **27c** had to be performed in more polar conditions (HCl/EtOH, compared to TFA/CH<sub>2</sub>Cl<sub>2</sub> for **27b**, **27d**, and **27e**).

<sup>211</sup> A. Portell, R. Barbas, D. Braga, M. Polito, C. Puigjaner, R. Prohens, *CrystEngComm* **2009**, *11*, 52–54.

*UV-Vis kinetic study of self-immolative systems 28a-e.* The high molar absorptivity of aniline-derivative squaramides allowed the study of the disassembly kinetics by UV-Vis spectroscopy.



**Scheme 5.5.** Cyclization reaction of self-immolative models **28a-e**.

In addition to the squaramide band found around 290-300 nm, the presence of a second band due to the aniline chromophore also contributed to the UV spectrum. The second band appears at a variable wavelength depending on the nature of the substituent attached to it. For instance, methoxy and dimethylamino electron donor groups showed maximums around 320 nm while electron withdrawing nitro derivative was found around 400 nm (Figures 5.3 and 5.4).

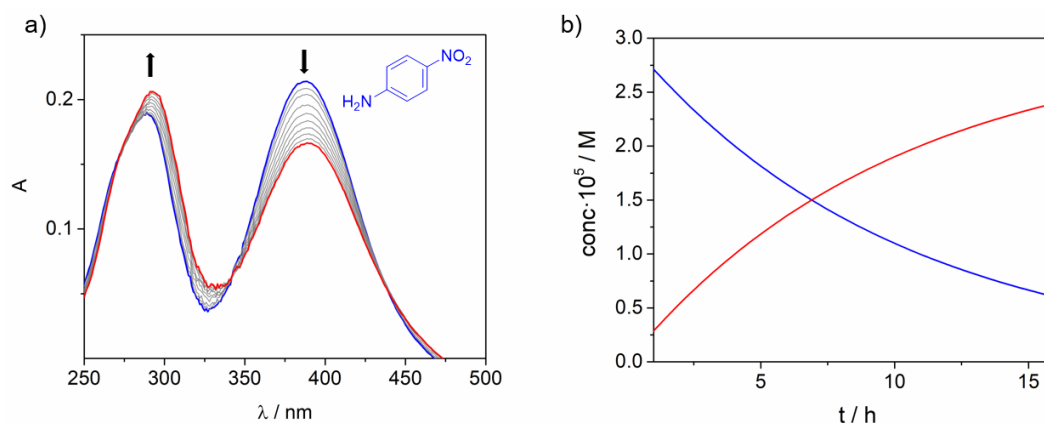


**Figure 5.3** a) Representative example of the UV changes observed for the cyclization of 30  $\mu\text{M}$  squaramide **28a** at 10 mM PBS pH 8 at 37°C. b) Corresponding speciation diagram of squaramide **28a** (blue) over the release of *para*-nitroaniline (red) at PBS pH 8 at 37°C.

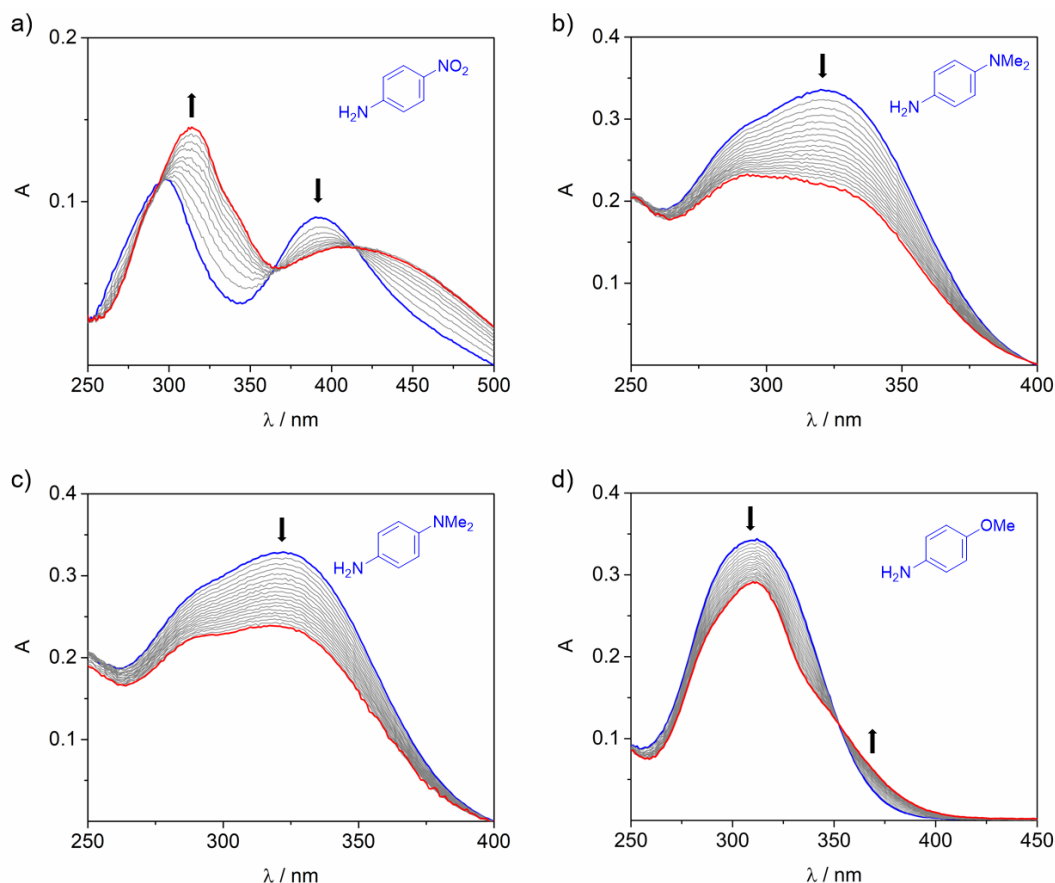
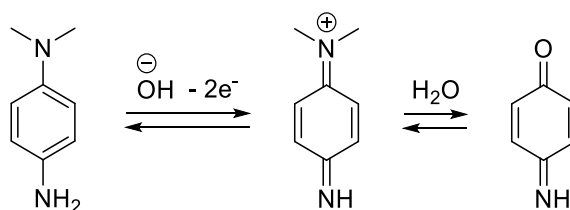


**Figure 5.4.** Representative example of the UV changes observed for the cyclization of 30  $\mu\text{M}$  a) **28b**, b) **28c**, c) **28d** and d) **28e** at 10 mM PBS pH 8 at 37  $^{\circ}\text{C}$ .

Self-immolative models **28b** and **28c** disassembled releasing *N,N*-Dimethyl-*p*-phenylenediamine which decomposed in water to afford the oxidized quinonediimine.<sup>212</sup> The change in the UV cuvette solution was observed with the naked eye, which turned purple in time due to the formation of *N,N*.dimethyl-*p*-phenylenediamine.



**Scheme 5.6.** Aqueous degradation of *N,N*-Dimethyl-*p*-phenylenediamine.

In analogy to the kinetic study performed on squaramate esters, the changes in the UV spectrum of 30  $\mu\text{M}$  solutions of model compounds were monitored in different pH buffered solutions at 37  $^{\circ}\text{C}$  (10 mM, pH 3-9, 0.15 M NaCl). The analysis of the data and

<sup>212</sup> a) L. K. J. Tong, *J. Phys. Chem.* **1954**, *58*, 1090–1097. b) L. K. J. Tong, M. C. Glesmann, R. L. Bent, *J. Am. Chem. Soc.* **1960**, *82*, 1988–1996.

evaluation of the apparent rate constants was performed with ReactLab™ Kinetics software.<sup>137</sup> Table 5.1 summarizes the obtained rate constants for **28a-e**:

**Table 5.1.** Summary of pseudo-first order rate constants for the cyclization of the self-immolative models **28a-e**.

Substrate / pH	$k_{\text{obs}}, 10^5 \text{ s}^{-1}$				
	3	5	7	8	9
<b>28a</b>	-	-	$1.02 \pm 0.01$	$11.16 \pm 0.03$	$56.3 \pm 0.5$
<b>28b</b>	-	-	$5.74 \pm 0.04$	$43.3 \pm 0.2$	$104.0 \pm 0.3$
<b>28c</b>	-	-	$2.42 \pm 0.01$	$10.04 \pm 0.02$	$9.20 \pm 0.05$
<b>28d</b>	-	-	$1.52 \pm 0.04$	$4.80 \pm 0.02$	$10.11 \pm 0.04$
<b>28e</b>	-	-	-	-	$16.1 \pm 0.1$

Analogously to squaramate esters, the reaction does not occur under acidic conditions. As expected, the analysis of the apparent constant rates reveals a pH-dependent kinetic profile. The rate of aniline release is directly related to the  $pK_a$  of the conjugate acid of the leaving group. The fastest rates are obtained for the nitro derivatives while the electron rich systems show significantly slower kinetics.

In order to properly determine the second order cyclization kinetic constant, an extended pH-variable kinetic analysis was performed. Hence, compounds **28b** and **28e** were taken as self-immolative models due to their good UV profiles and the chemical stability of the reaction products. Additionally, the effect on the difference in nucleofugacity of the leaving group due to the nitro and methoxy substituents, respectively, could be compared. Incubation of the systems in 10 mM buffered solutions at 37°C led to the pH-dependent kinetic curve. Figure 5.5 shows a comparison between both kinetic cyclization profiles. In both cases, an asymptotic profile is obtained which is coherent with the intramolecular reaction mechanism proposed in chapter 3 (Eq. 10).

$$k_{\text{obs}} = k_c[A] = k_c \frac{K_a}{K_a + [\text{H}]} \quad (10)$$

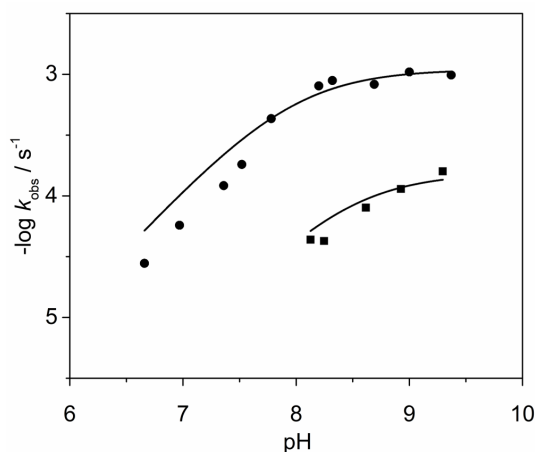


**Figure 5.5.** Fitting to Eq. 10 of the data obtained for cyclization of self-immolative system **28b** (dots) and **28e** (squares) at different pH.

By fitting of the data to Eq. 10 we could obtain the cyclization constant,  $k_c$  for all self-immolative models. Analogously, the fitting gave the corresponding values of  $pK_a$ . Results are summarized in Table 5.2.

**Table 5.2.** Summary of the second-order cyclization constants for self-immolative compounds **28a-e**.<sup>a</sup> Values obtained from fitting of Eq 10.

Entry	R <sub>2</sub>	pK <sub>a</sub> <sup>a</sup>	$k_c, 10^{-4} \text{ M}^{-1} \text{ s}^{-1}$	t <sub>1/2</sub> , min
<b>28a</b>	NO <sub>2</sub>	8.37	3.71 ± 0.1	31
<b>28b</b>	NO <sub>2</sub>	7.96	11.0 ± 0.7	11
<b>28c</b>	NMe <sub>2</sub>	7.33	1.0 ± 0.2	111
<b>28d</b>	NMe <sub>2</sub>	8.10	1.1 ± 0.1	102
<b>28e</b>	OMe	8.89	2.9 ± 0.2	39

All the first order cyclization constants obtained are about the same magnitude ( $1-10 \times 10^{-4} \text{ s}^{-1}$ ) and are comparable with those obtained for squaramate ester **13** ( $k_c = 2.3 \times 10^{-4} \text{ s}^{-1}$ ). On the other hand and considering the experimental error, the data fitting give  $pK_a$  values in agreement to the expected for alkyl amino groups. Thus, the self-immolative models **28a-e** disassemble relatively fast but show a strong dependence on the medium pH. It is noticeable that the faster kinetic constants are obtained for the cyclization of the *p*-nitroaniline derivatives that are the most electron deficient leaving groups of the set studied here (with the highest acidity,  $pK_a$  1.0).<sup>213</sup> So, the results are in agreement with the expected initial hypothesis on the effect of the nucleofugacity of the leaving group on the reaction kinetics. On the other hand, the reaction rates for the non-methylated and methylated analogue pairs **28a** and **28b** or **28c** and **28d**, respectively, are found around the same order of magnitude. Taking into account that the most determining factor appears to be the nucleofugacity of the leaving group, the

<sup>213</sup> A. Yu, Y. Liu, Z. Li, J. P. Cheng, *J. Phys. Chem. A* **2007**, *111*, 9978–9987.

methylation effect seems negligible. Thus, the release of anilines appears to be predominantly governed by the nucleofugacity of the cargo. Such dependency is reflected when representing the Hammett plot<sup>214</sup> of the analogue systems **28b**, **28d** and **28e**. In accordance, the plot of their kinetic constants as a function of substituent-para Hammett constants ( $\sigma_p$ ) suggests a linear bias:

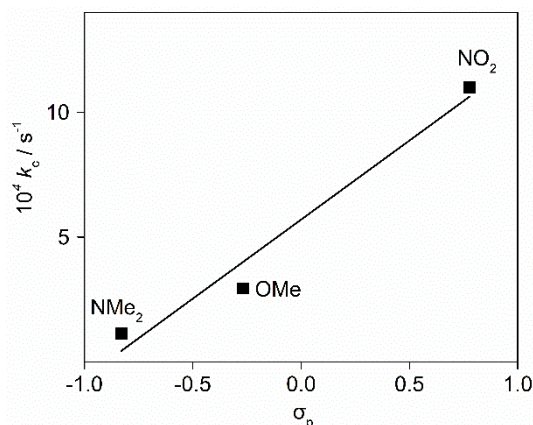
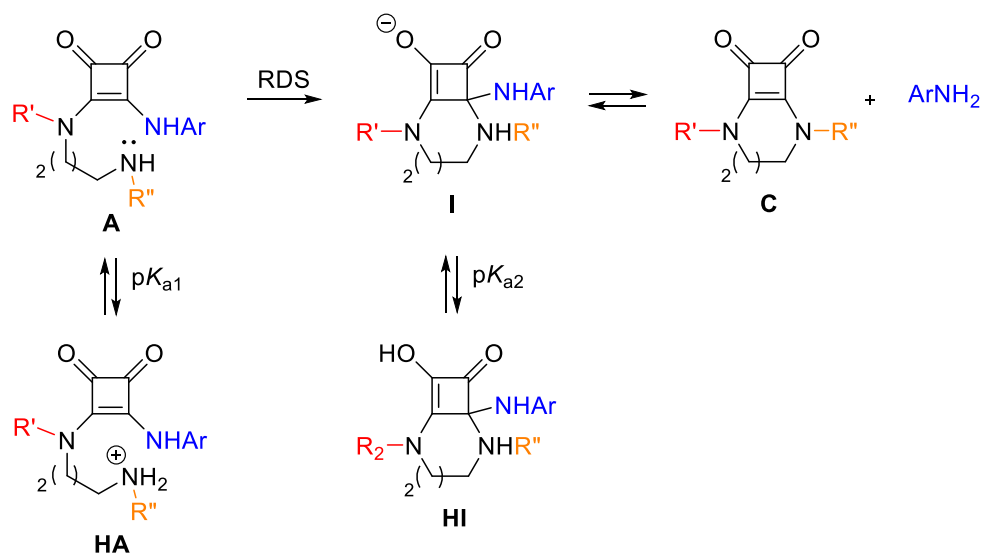


**Figure 5.6.** Hammett correlation plot for the intramolecular cyclization reaction of self-immolative systems **28b**, **28d** and **28e**.

**Reaction mechanism.** In all cases, the fitting to Eq. 10 leaves a  $pK_a$  value around 8 for the alkyl amine group, which means that the reaction would be dependent on the protonation state of the amino terminal group ( $pK_{a1}$ ) and thus, the RDS would correspond to the first nucleophilic attack on the squaramidic electrophilic carbon. These would agree with a first slow step (addition) followed by a rapid second step (elimination). Scheme 5.7 shows the proposed reaction mechanism.



**Scheme 5.7.** Proposed general reaction mechanism for the release of substituted anilines.

<sup>214</sup> a) L. P. Hammett, *J. Am. Chem. Soc.* **1937**, *59*, 96–103. b) C. Hansch, A. Leo, R. W. Taft, *Chem. Rev.* **1991**, *91*, 165–195.

In general terms, the overall rate constants were found to be similar to those found for cyclization of squaramate esters ( $\sim 10^4 \text{ s}^{-1}$ ). However, the  $\text{p}K_{\text{a}}$  calculated for the squaramate esters was significantly lower ( $\sim 6$ ) meaning that the first nucleophilic addition was faster than the elimination process. Conversely, for aniline substrates, the first step is not so advantageous, maybe due to the loss of reactivity of the electrophilic center.

To support this latter hypothesis, the LUMO maps calculated for a model squaramate ester and squaramide were compared. The LUMO maps are used to visualize the absolute magnitudes of the respective LUMO orbitals. Therefore, indicating the relative electrophilicity of the C2 carbon as a function of the attached leaving group.

**Table 5.3.** LUMO maps and corresponding Natural Atomic Charges for model squaramate ester and squaramide. Blue region is the highest reactive electrophilic site.

Label	Natural Atomic Charges, eV	
C1	+ 0.115	+ 0.116
C2	+ <b>0.237</b>	+ <b>0.105</b>
C3	+ 0.415	+ 0.454
C4	+ 0.460	+ 0.451

A close analysis in the modelled squaramides reveals a significant change in the natural atomic charge of the electrophilic carbon, depending on the chemical functionality bonded to it. Thus, the electronic deficiency of the substituted C2 carbon decreases from + 0.237 to + 0.105 eV when changing from oxygen to nitrogen. Interestingly, the natural charge is more positive for the C1 than that for the electrophilic position C2. The analysis of LUMO maps, wherein the absolute value of the LUMO coefficient is mapped onto the total calculated electron density, displays a positive electronic flux (blue) along with the N-Ph substitution to the C4 carbonyl. These results support the mechanistic hypothesis. Thus, for squaramate esters, the first nucleophilic attack is fast (favoured by the high electrophilicity of C2) and the RDS would be the elimination step. On the contrary, for squaramide derivatives, the first nucleophilic attack is handicapped, limiting the reaction kinetics. Once the intramolecular intermediate forms, the reaction rapidly evolves to the final cyclic squaramide.

*Application of the squaramide-based self-immolative system to the release of a biologically relevant aniline.* Once proved the viability of releasing anilines in a relatively short time, we decided to apply these results to the release of a bioactive aniline. To this end, we selected Lenalidomide (**LD**) as a key candidate. This compound is used in the treatment of multiple myeloma presenting both tumouricidal and immune modulatory activity.<sup>215</sup> Lenalidomide is commercialized under the name REVLIMID<sup>®216</sup> and structurally belongs to the family of thalidomide and its immunomodulatory derivatives (IMiDs<sup>®</sup>).<sup>217</sup>

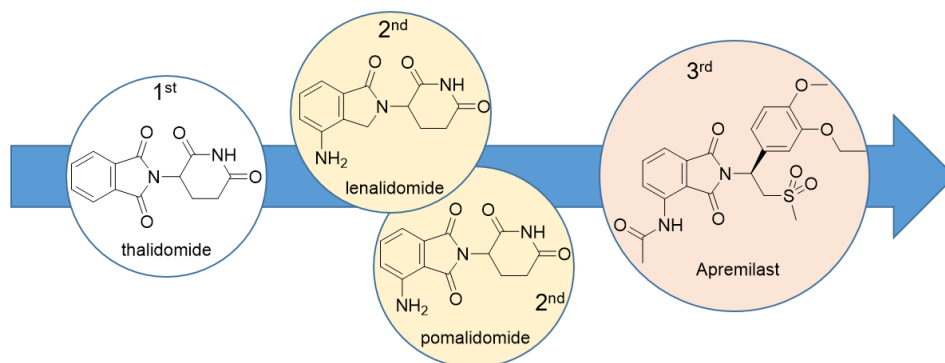
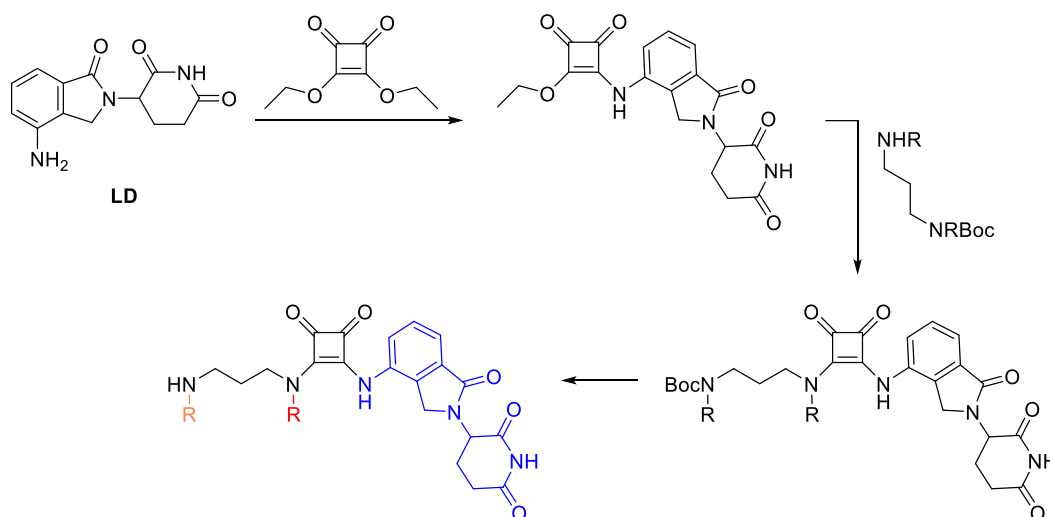


**Figure 5.7.** Evolution of IMiDs<sup>®</sup> generations showing improvement in patient tolerance and highest activity against malignant conditions.

According to the previously synthetic procedure for the synthesis of systems **28a-e**, the synthesis of the **LD**-self-immolative system was proposed as follows:



**Scheme 5.8.** Designed synthetic pathway to access **LD**-self-immolative system.

<sup>215</sup> A. Lopez-Girona, D. Heintel, L-H Zhang, D. Mendy, S. Gaidarova, H. Brady, J. B. Bartlett, P. H. Schafer, M. Schreder, A. Bolomsky, B. Hilgarth, N. Zojer, H. Gisslinger, H. Ludwig, T. Daniel, U. Jäger, R. Chopra *Br. J. Haematol.* **2011**, *154*, 325–336.

<sup>216</sup> International Narcotics Control Board **1999**, United Nations, accessed 1 October 1999, <<http://www.incb.org>>

<sup>217</sup> R. Knight, *Semin. Oncol.* **2005**, *32*, 24–30.

Despite the apparent straightforward of synthesis, the first reaction step failed to form the LD-squaramate ester. In any case, a significant amount of this compound was obtained even after a small survey of the reaction conditions. Some of the reaction conditions tried are summarized in Table 5.4:

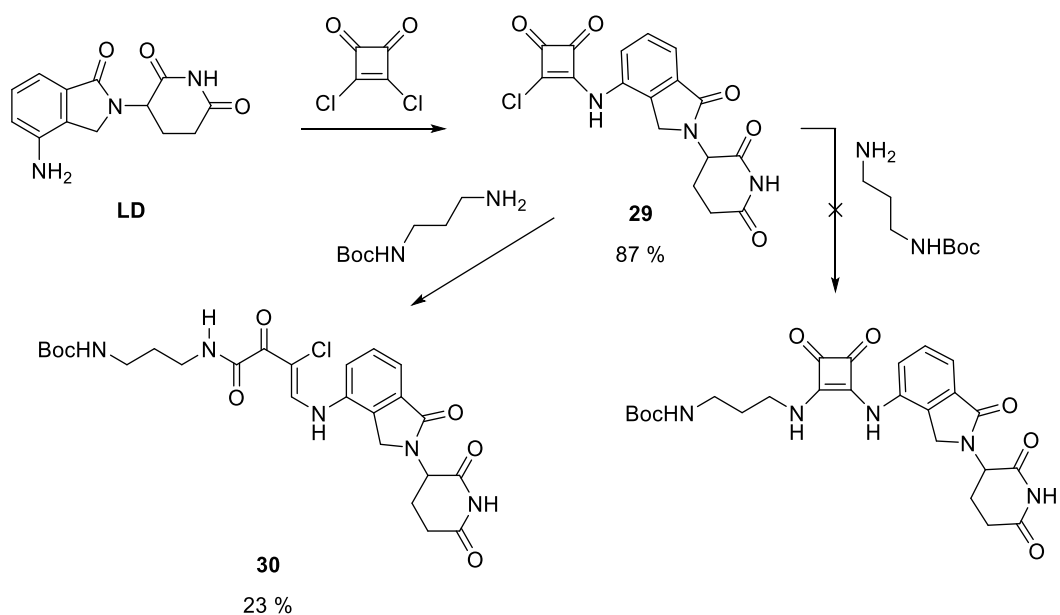
**Table 5.4.** Summary of the conditions tested for the synthesis of LD-squaramate ethyl ester.

LD (equiv)	Ethyl squarate (equiv)	Base (equiv)	Zn(OTf) <sub>2</sub> (equiv)	Temp. (°C)	time (h)	Solvent
1	1.2	-	-	25	16	EtOH
1	1.2	-	-	Rflx	16	EtOH
1	1.2	-	0.1	25	16	EtOH
1	1.2	-	0.1	130, MW	0.5	EtOH
1	1.2	2 (K <sub>2</sub> CO <sub>3</sub> )	0.1	25	16	EtOH
1	1.2	2 (K <sub>2</sub> CO <sub>3</sub> )	0.1	130, MW	1	EtOH
1	1.2	2 (K <sub>2</sub> CO <sub>3</sub> )	0.1	130, MW	1	EtOH:H <sub>2</sub> O
1	1.2	2 (Cs <sub>2</sub> CO <sub>3</sub> )	0.1	110	16	DMF

To overcome this unexpected problem, the lenalidomide conjugation was tried with squaric acid dichloride (1,2-dichlorocyclobuten-3,4-dione), a more reactive analogue of ethyl squarate. Thus, following Lunelli's reported procedure we prepared the dichloride using squaric acid and oxalyl chloride as starting materials.<sup>218</sup> LD was then coupled with the squaric acid dichloride in mild conditions affording the lenalidomide squaramate chloride **29** in good yield. Finally, chloride **29** was mixed with *N*-Boc-propane-1,3-diamine but, instead of obtaining the desired unsymmetrical squaramide, the cyclobutenedione ring underwent ring fission leading to the corresponding 1,2-dicarbonyl compound **30** (Scheme 5.9).

A complete NMR study was needed to characterise the obtained product **30**, but yet, the double bond cis-trans stereoisomerism could not be defined. Additionally, HRMS was useful to unequivocally find the exact mass in agreement with the chlorine isotope pattern (exact mass found 570.1734 [M+Na]<sup>+</sup>).

<sup>218</sup> B. Lunelli, *Tetrahedron Lett.* **2007**, 48, 3595–3597.



**Scheme 5.9.** Squaryl ring fission obtained by reaction of Boc-protected propane-diamine with squaramate chloride **29**.

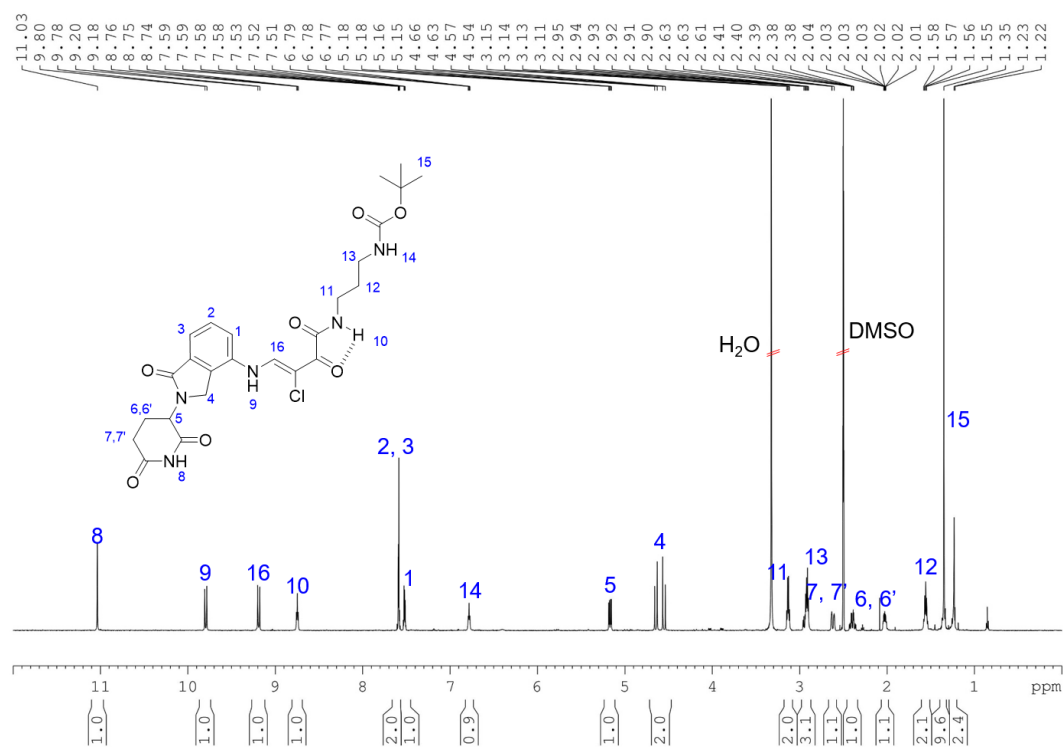


**Figure 5.8.**  $^1\text{H-NMR}$  of **30** ( $\text{DMSO-}d_6$ , 298K, 600 MHz) and the corresponding signal assignment.

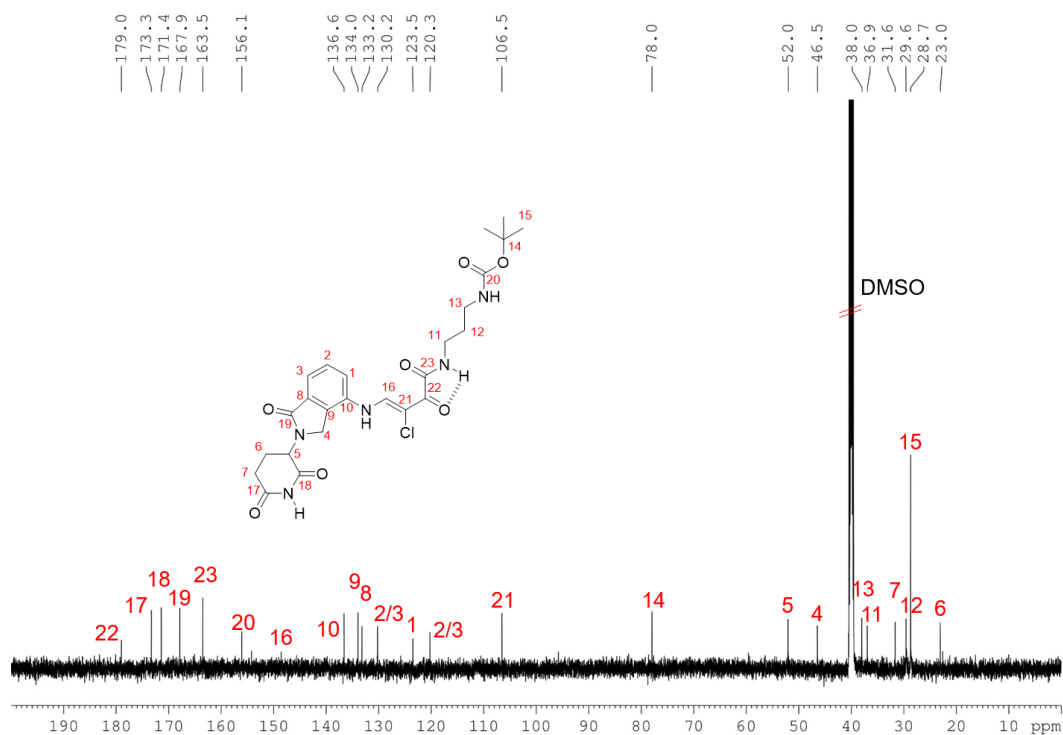


**Figure 5.9.**  $^{13}\text{C}$ -NMR of **30** (DMSO- $d_6$ , 298K, 150 MHz) and the corresponding signal assignment.

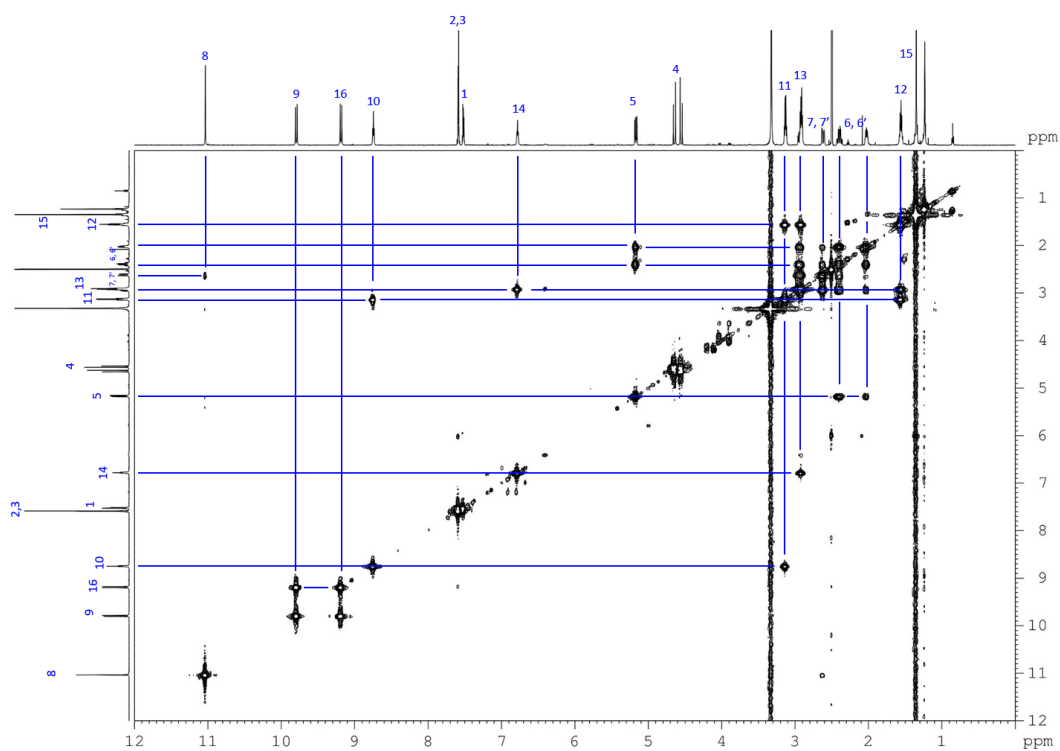


**Figure 5.10.**  $^1\text{H}$ - $^1\text{H}$ -COSY of **30** (DMSO- $d_6$ , 298K) and the corresponding signal assignment.

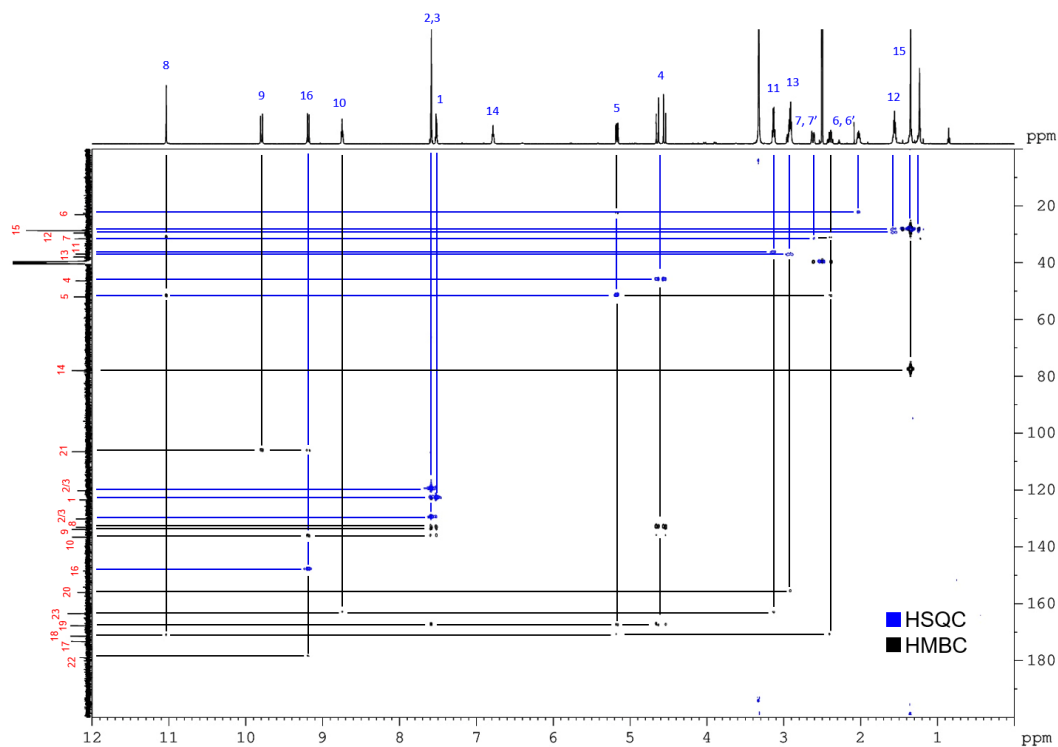


**Figure 5.11.**  $^1\text{H}$ - $^{13}\text{C}$ -HSQC and HMBC (blue and black respectively) of **30** ( $\text{DMSO-}d_6$ , 298K) and the corresponding signal assignment.

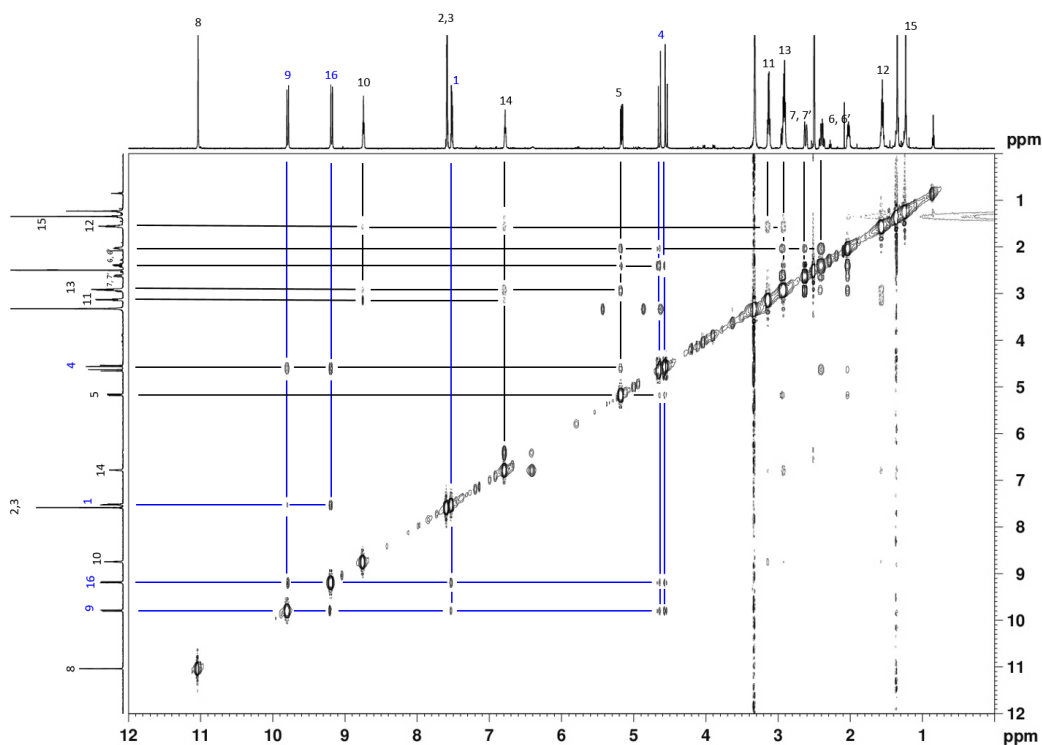


**Figure 5.12.**  $^1\text{H}$ - $^1\text{H}$ -NOESY of **30** ( $\text{DMSO-}d_6$ , 298K) and the corresponding signal assignment. Highlighted in blue, the contacts between  $\text{NH}_9$  and  $\text{H}_{16}$  with  $\text{H}_1$  and  $\text{H}_4$ .

The regioselectivity of the ring fission reaction could be identified by finding  $\text{NH}_9$  and  $\text{H}_{16}$  as doublets. Their coupling constant  $^3J_{\text{HH}}$  was 12 Hz, which indicates that they are

in *trans* conformation. The  $^1\text{H}$ - $^1\text{H}$  COSY experiment (Figure 5.10) confirmed their coupling and allowed us to assign the rest of the signals. The complementary NOESY experiment (Figure 5.12 and Chart 5.3, highlighted in blue) showed the lenalidomide protons  $\text{H}_7$  and  $\text{H}_4$  in spatial proximity with both  $\text{NH}_9$  and  $\text{H}_{16}$ .

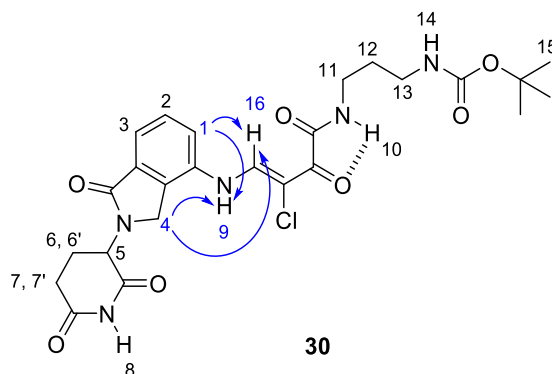
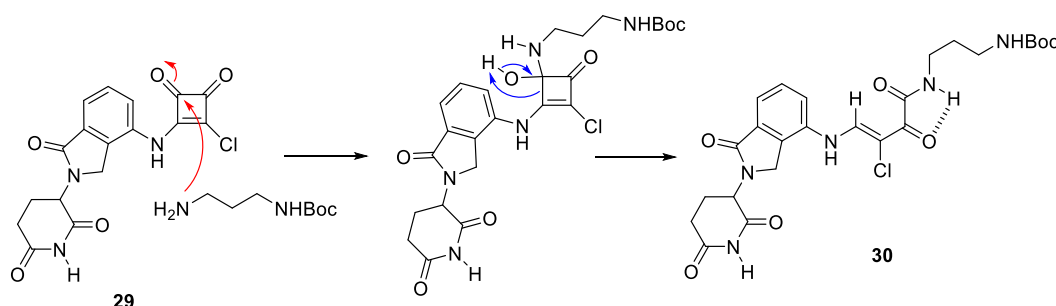


**Chart 5.3.** Relevant NOESY contacts found in compound **30** between protons  $\text{H}_7$  and  $\text{H}_4$  with  $\text{NH}_9$  and  $\text{H}_{16}$ .

Similarly to the degradation found for cyclic squaramate thioester **24** to  $\alpha$ -ketoacid **25**, it seems that squaramate chloride **29** suffered analogous ring fission when reacting with the amine:



**Scheme 5.10.** Proposed mechanism for the formation of 1,2-dicarbonyl compound **30** by 1,2 addition on the squaryl carbonyl in **29**.

As it was seen by squaramate thioesters, the presence of a sulphur atom heavily modifies the electron density of the squaryl substituted carbon (C2) forcing the reaction to take place in the opposite electrophilic carbonyl (C4). In analogy to those results, it also appears to occur when the substituent is a chlorine atom. To support this mechanistic hypothesis, the LUMO maps of a representative squaramate acid chloride, squaramate thioester and diethyl squarate were calculated. Table 5.5 shows the graphical output of the DFT calculations (wB97X-D/6-31G\*) together with the natural atomic charges of relevant atoms.

**Table 5.5.** LUMO maps and corresponding Natural Atomic Charges for model squaramate ethyl ester, ethyl thioester and acid chloride.

Label	Natural Atomic Charges, eV		
C1	+ 0.115	+ 0.152	+ 0.153
C2	+ <b>0.237</b>	- <b>0.325</b>	- <b>0.196</b>
C3	+ 0.415	+ 0.460	+ 0.463
C4	+ 0.460	+0. 469	+ 0.483

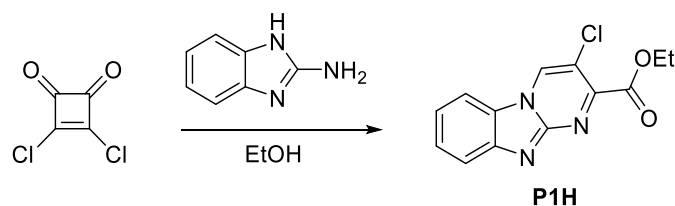
In agreement to the squaramate thioester **24** behaviour, squaramate acid chloride **29** reacts with the nucleophilic amine through the distal squaryl carbonyl (C4). The presence of a chlorine atom modifies the nature of the C2 carbon on the squaryl moiety by changing its former electrophilic nature (blue spot on the LUMO map) and revising the atomic charges (+ 0.237 eV for esters to - 0.196 eV for the acid chloride). Such structural modification caused by S and Cl atoms on C2 of the squaryl moiety, changes the common expected reactivity leading to the squaryl ring fission by the action of an external nucleophilic molecule, in this case, the *N*-Boc-propane-1,3-diamine. This result is quite impressive since, a priori, chlorine is considered a relatively good leaving group and squaramate acid dichloride has been reported successfully in the synthesis of squaric diphenyl esters,<sup>219</sup> and some poor reactive amines such as secondary hindered amines or anilines.<sup>220</sup>

Looking for similar reactions in the literature, Wang and collaborators reported the synthesis of a pyrimido[1,2-*a*]benzimidazole derivative which, by the reaction of 2-aminobenzimidazole with squaric acid dichloride in anhydrous ethanol, leads to the ethyl ester **PIH**.<sup>221</sup>

<sup>219</sup> D. Prashar, D. Cui, D. Bandyopadhyay, Y. Y. Luk, *Langmuir* **2011**, 27, 13091-13096.

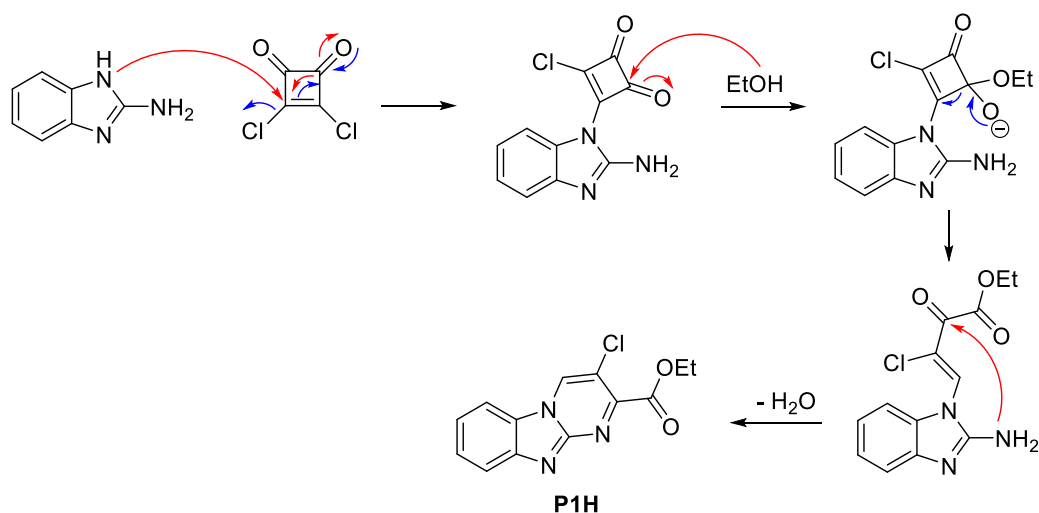
<sup>220</sup> a) G. Zinner, J. Grünefeld, *Arch. Pharm.* **1985**, 318, 992-998. b) G. Zinner, J. Grünefeld, M. Baehr, *Arch. Pharm.* **1985**, 318, 977-983. c) J. Grunefeld, G. Zinner, *Arch. Pharm.* **1985**, 318, 1062-1070. d) S. A. Ivanovsky, M. V. Dorogov, D. V. Kravchenko, A. V. Ivachtchenko, *Synth. Commun.* **2007**, 37, 2527-2542.

<sup>221</sup> G. Xia, C. Ruan, H. Wang, *Analyst* **2015**, 140, 5099-5104.



**Scheme 5.11.** Synthesis of Wang's pyrimido[1,2-*a*]benzimidazole derivative **P1H**.

Despite the reaction mechanism is not described, and the authors focus mainly in the properties of the resulting product, the reaction mechanism for the formation of **P1H** could be the same as we describe for the formation of **30**. The presence of one chlorine atom and an ethyl ester group in the resulting **P1H**, suggests a first conventional reaction of the aminobenzimidazole with the squaric acid dichloride. Thus, the resulting chloride would react with the EtOH solvent by 1,2-addition to the carbonyl followed by squaryl ring fission:



**Scheme 5.12.** Hypothesised mechanism for Wang's formation of **P1H**.

After the ring fission, the  $\alpha$ -ketoester intermediate would undergo an intramolecular reaction with the ketone to form the final cyclic **P1H**. It seems that the formation of **P1H** agrees with the reactivity of squaramate acid chlorides, where the squaryl carbonyl centre reacts with nucleophiles leading to the ring fission.

Despite our synthetic efforts, obtaining the designed lenalidomide self-immolative system proved impossible by this route and we needed a different strategy to proceed. At this moment, the main aim was to define the kinetic constants for the release of different amino-derivative cargos so we decided to keep our focus on that purpose.

### 5.3.2. Self-Immolative Models Releasing Aliphatic Amines

Once the kinetics for the release of anilines was defined, the next step was to study the capability of our self-immolative systems to release aliphatic amines. Thus, the systems **33a-c** featuring an *n*-butylamine chain as a model aliphatic cargo were designed and synthesised. As mentioned in Section 5.1, aliphatic amines have higher  $pK_a$  values in comparison with alcohols and anilines, which makes them demanding leaving groups for the self-immolation process. Thus, our attention was focused on the effect of the methylation to promote the folded conformation as well as the influence of the nucleophilicity to increase the handicapped cyclization.

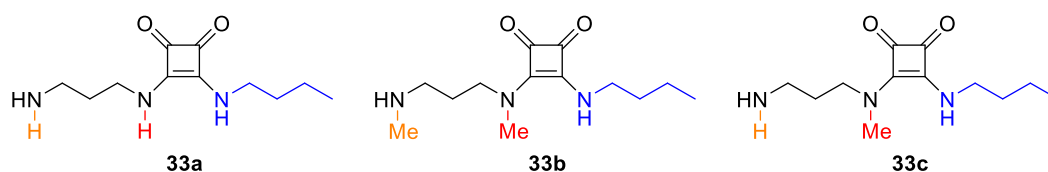
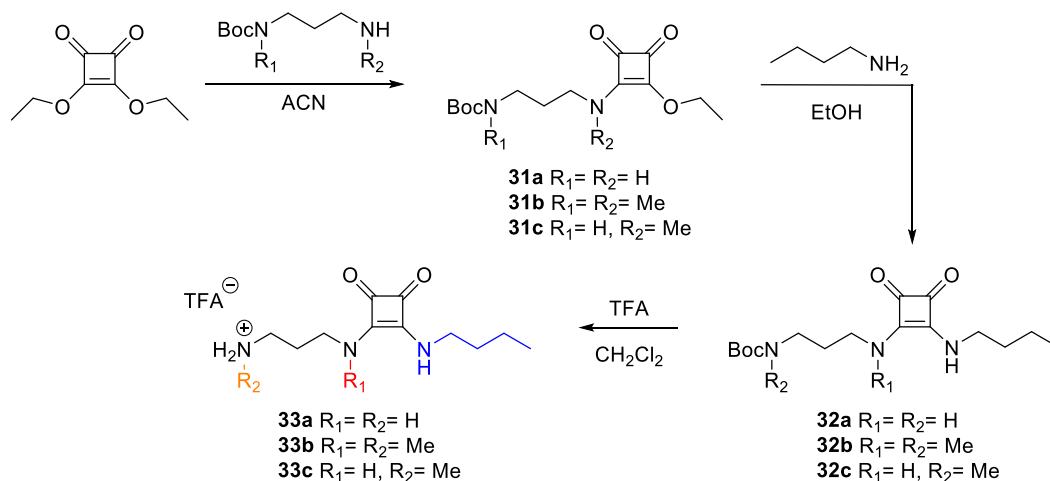


**Chart 5.4.** Chemical structures of the aliphatic squaramides evaluated by their self-immolative capability. Leaving group is depicted in blue.

**Synthesis of self-immolative systems 33a-c.** The synthesis of the amino trigger was achieved by the reaction of diethyl squarate with the corresponding Boc-protected diamine in mild conditions. Further reaction with *n*-butylamine followed by deprotection of Boc led to the aliphatic self-immolative model compounds **33a-c** (Scheme 5.13).



**Scheme 5.13.** Synthetic pathway to access aliphatic self-immolative models **31a-c**.

**Kinetic study of self-immolative models 33a-c.** Formally, the chemical transformation that occurs in the self-immolation process keeps the squaramide as the only chromophore. Hence, the change in the UV-vis spectrum was not significant enough to properly study the reaction kinetics so the reaction was followed by  $^1H$ -NMR. Thus,

model compounds **33a-c** were incubated in 0.1 M deuterated PBS solutions (pH 8, 10% DMSO, 0.15M NaCl) at 37 °C and the changes in their spectrum were studied in time.

Starting with the system **33a**, Figure 5.13 shows the corresponding assignment of the signals in the  $^1\text{H}$  spectrum. 2D correlation experiments TOCSY and COSY were performed to achieve the correct assignment (see experimental section).

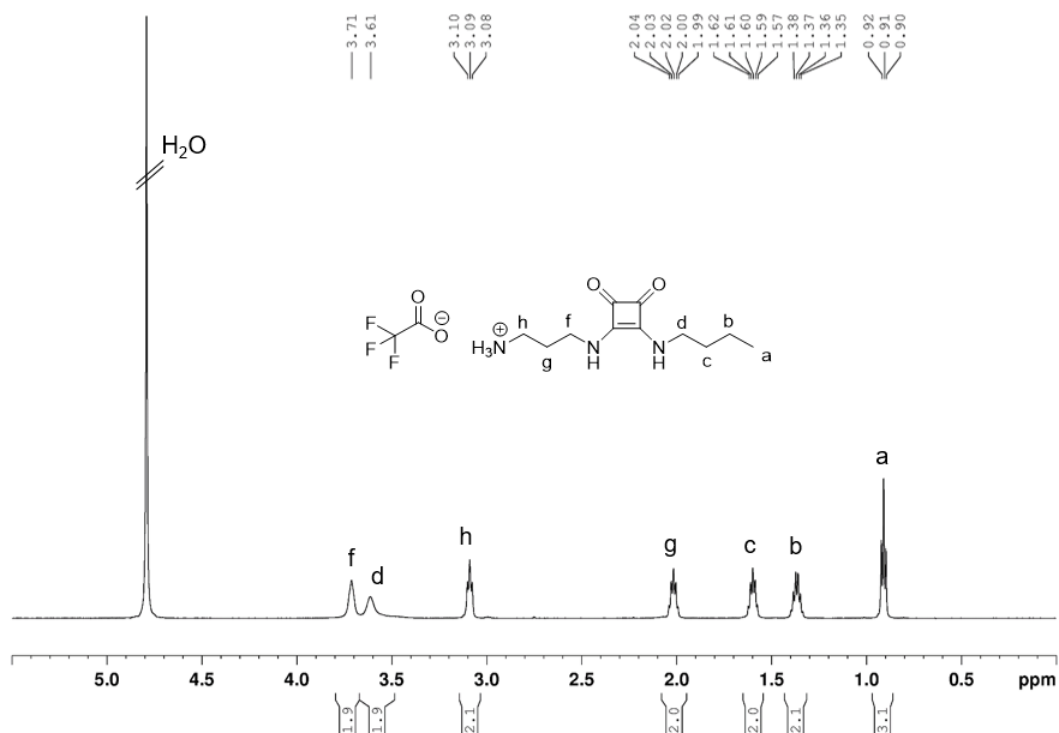


**Figure 5.13.**  $^1\text{H}$ -NMR of **33a** ( $\text{D}_2\text{O}$ , 298K) and the corresponding signal assignment.

As for the aniline analogues, deprotonation of the terminal amino group by dissolution in the buffer would trigger the 1,7-cyclization reaction to afford cyclosquaramide **23a** and *n*-butylamine. Once all the signals were identified and assigned, the reaction kinetics was followed by recording the  $^1\text{H}$ -NMR spectra every 24h.

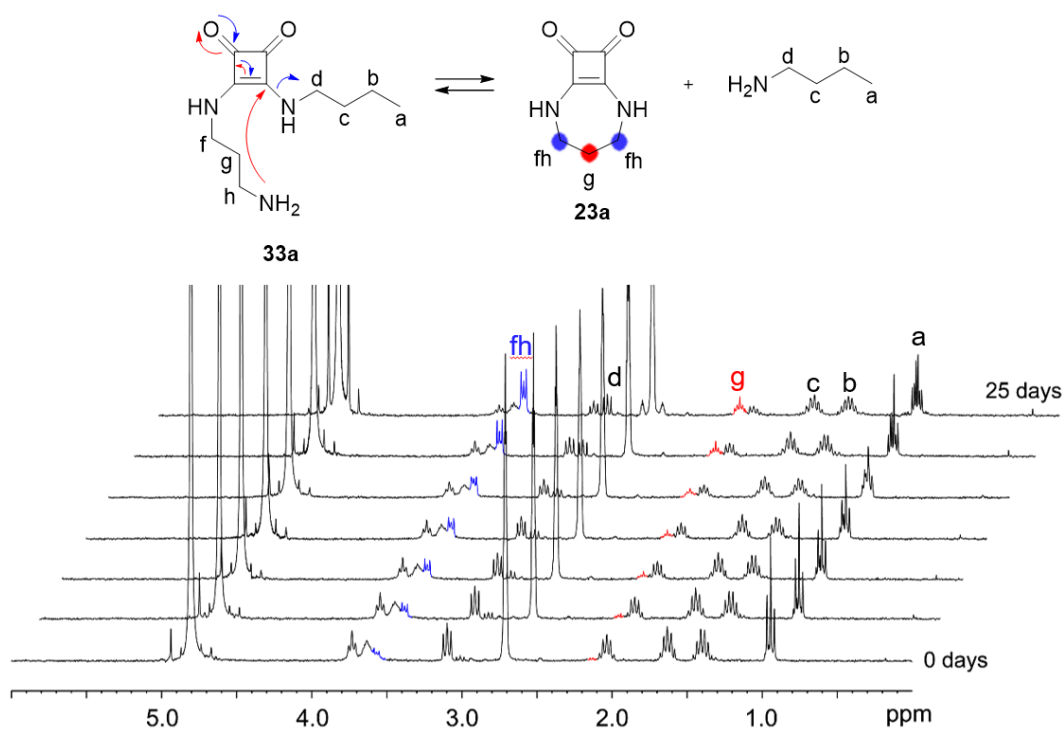


**Figure 5.14.**  $^1\text{H-NMR}$  kinetic study of intramolecular cyclization of 1mM **33a** at 0.1M PBS pH 8 (10%  $\text{DMSO-}d_6$ ), 310 K.

The most significant changes in the evolution of the cyclization process were detected in the appearance of a distorted multiplet ( $Hfh$ , blue) around 3.6 ppm along with a broad quintuplet around 2.2 ppm ( $Hg$ , red) corresponding to the cyclic **23a**. In parallel, the triplet corresponding to  $h$  protons around 3.1 ppm disappeared. The calibration with the residual signal of  $\text{DMSO-}d_6$  helped to follow the evolution of the concentration of each species with time. Figure 5.14 reflects the disappearance of self-immolative system **33a** and the concomitant appearance of the cyclic squaramide **23a** ( $Hfh$  and  $Hg$  peaks). The apparent rate constant was estimated in analogy to the cyclization of ester **13** to form **23** (Chapter 3):

$$-\frac{d[\mathbf{33a}]}{dt} = \frac{d[\mathbf{23a}]}{dt} = k_{\text{obs}}[\mathbf{23a}] \quad (12)$$

$$[\mathbf{23a}] = [\mathbf{23a}]_0 e^{-k_{\text{obs}}t} \quad (13)$$

The fitting of the data to Eq. 13 gives the pseudo-first order constant  $k_{\text{obs}} = 1.7 \times 10^{-7} \text{ s}^{-1}$ .

In the same way, assignation of signals for the  $^1\text{H}$  spectrum of **33b** was performed by COSY and TOCSY experiments (Figure 5.15 and experimental section).

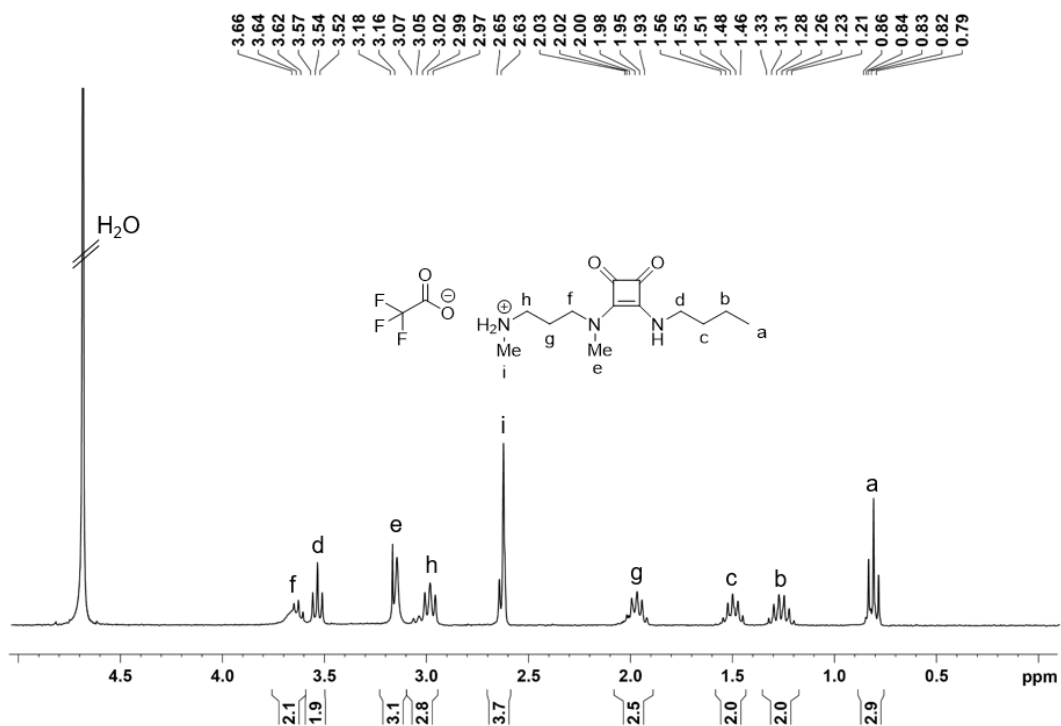


**Figure 5.15.**  $^1\text{H-NMR}$  of **33b** ( $\text{D}_2\text{O}$ , 298K) and the corresponding signal assignment.

As seen for model **33a**, the kinetic study of cyclization reaction for compound **33b** was performed in deuterated 0.1 M PBS at pH 8, 37 °C. Water suppression was performed to increase the resolution of the experiment. Figure 5.16 shows the evolution of spectra in time. Highlighted in colours are the signals corresponding to the formation of cyclic squaramide **23b**. Its formation was easily observed by the appearance of a quintuplet around 2.2 ppm (Hg, red), a singlet around 3.4 ppm (Hei, green) and a distorted multiplet around 3.5 ppm (Hfh, blue).

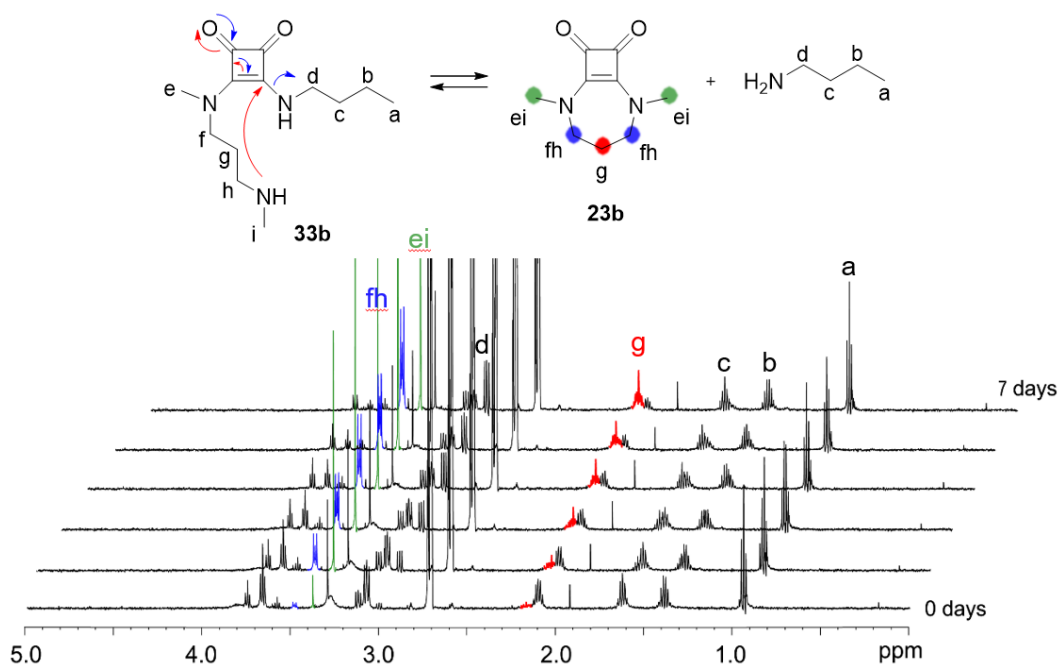


**Figure 5.16.**  $^1\text{H-NMR}$  kinetic study of intramolecular cyclization of **33b** at 0.1M PBS pH 8 (10%  $\text{DMSO-}d_6$ ), 310 K. All spectra recorded were registered using a WATERGATE pulse system for water suppression.

The representation of the changes in concentration of both species with time and fitting to Eq. 13, leads to an apparent rate constant of  $1.44 \times 10^{-5} \text{ s}^{-1}$ , a value significantly higher than the one found for cyclization of its non-methylated analogue **33a**. Such increment could be explained by the increase of nucleophilicity of the nitrogen by methylation, which directly increases the kinetic constant (Meyr equation, section 5.1.1). Additionally, the presence of a methyl group would also favour the folded conformation and thus accelerate the reaction rate. To prove this last hypothesis, a kinetic study on self-immolative system **33c** was performed.

A priori, if the methylation of the squaramide led to the folded conformation and, consequently, the reaction rate was enhanced, the observed pseudo-first order rate constant should be higher than the one obtained for model **33a** (Figure 5.17, red substituent). Conversely, that rate constant should be also lower than the one found for model **33b**, since the nucleophilicity of the terminal amino group of model **33c** is lower than the methylated amino group of analogue **33b** (Figure 5.17, orange substituent).

$$k_{\text{obs}}(\mathbf{33a}) < k_{\text{obs}}(\mathbf{33c}) < k_{\text{obs}}(\mathbf{33b})$$

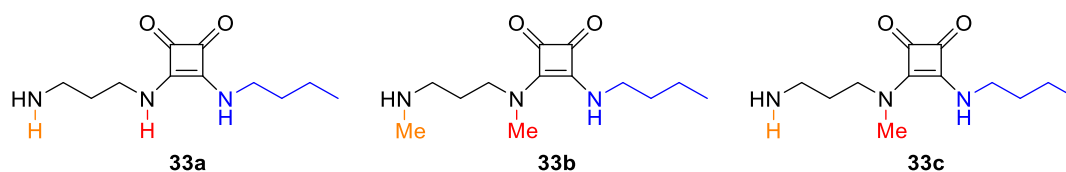


**Figure 5.17.** Hypothesised rate constant relationship depending on the *N*-methylation effect.

Thus, compound **33c** was also characterized by NMR and the assignment of the signals was performed by 2D experiments (see experimental section). The kinetic study was performed in the same conditions as for **33a** and **33b**. (Figures 5.18 and 5.19).

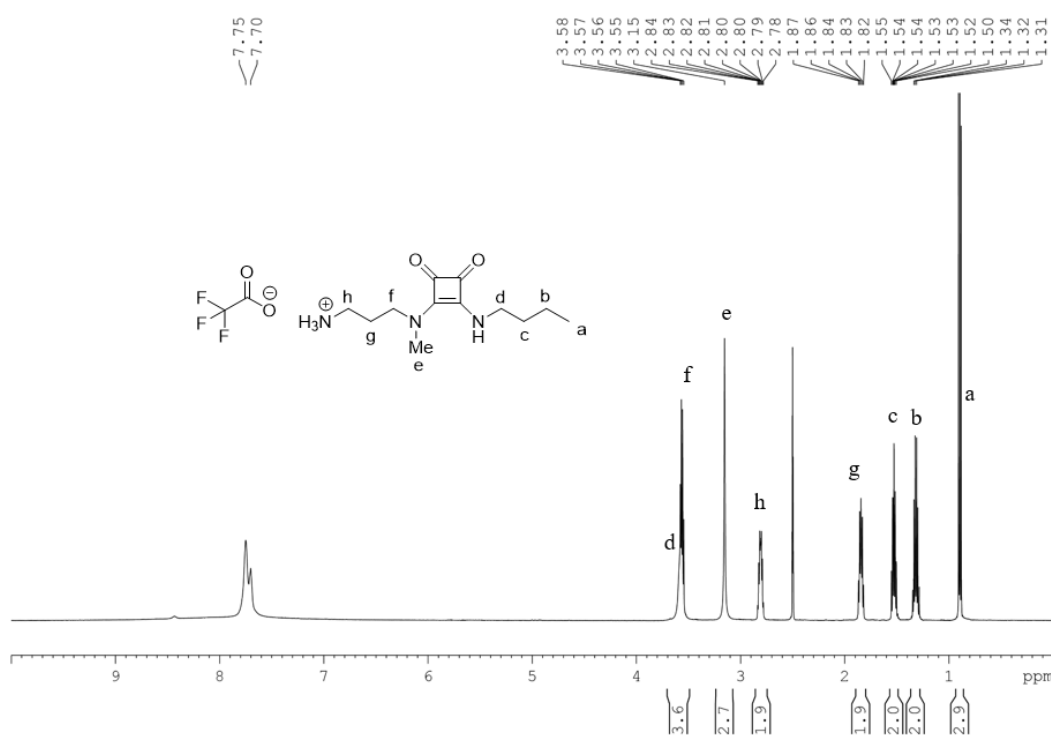


**Figure 5.18.**  $^1\text{H-NMR}$  of **33c** ( $\text{DMSO-}d_6$ , 298K) and the corresponding signal assignment.

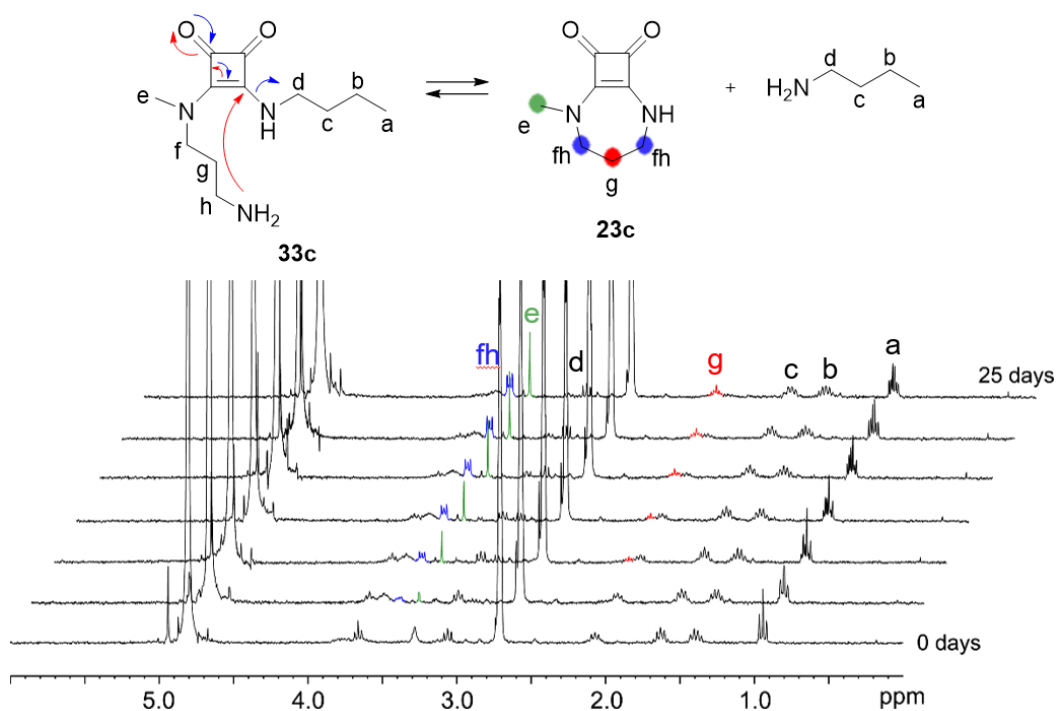


**Figure 5.19.**  $^1\text{H}$ -NMR kinetic study of intramolecular cyclization of **33c** at 0.1 M PBS pH 8 (10%  $\text{DMSO-}d_6$ ), 310 K.

In analogy to **23a** and **23b**, the cyclic mono-methylated squaramide **23c** was synthesised and fully characterised in order to unequivocally follow the cyclization process of self-immolative model **33c**. Figure 5.19 shows the  $^1\text{H}$  NMR spectra of the reaction kinetics and, highlighted in colour, the signals corresponding to the appearance of cyclosquaramide **23c**. Analogously, the relative concentrations of system **33c** and product **23c** were plotted with time. The fitting of the data to Eq. 13 gave a pseudo-first order rate constant of  $6.6 \times 10^{-7} \text{ s}^{-1}$ .

Figure 5.20 summarizes the speciation of the products obtained with time for the self-immolative models **33a-c** and the corresponding formation of cyclic products **23a-c** (a-c) along with the corresponding apparent rate constants (d).

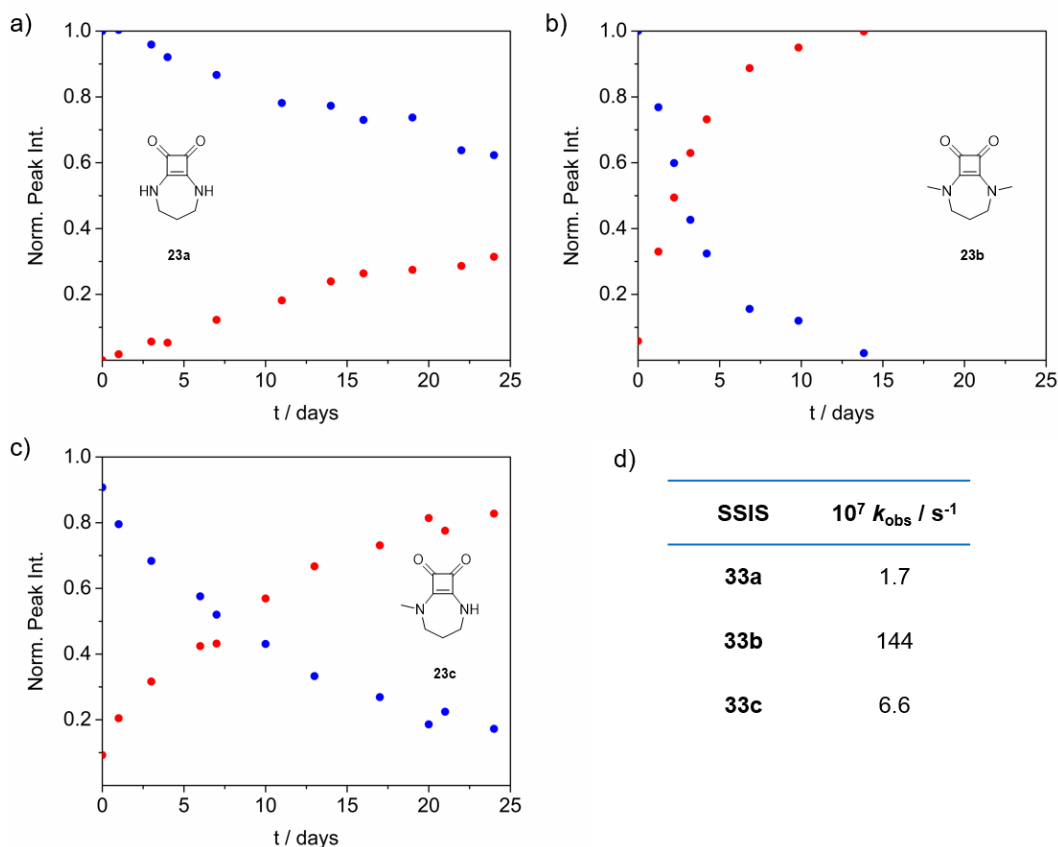


**Figure 5.20.** Evolution of the concentration of self-immolative system **33a-c** (a,b and c respectively) over the formation of cyclic squaramide **23a-c** (a,b and c respectively) at pH 8 at 37 °C and d) summary of the respective calculated observed constants.

Compounds **33a-c** were studied to test the ability of the designed squaramides to undergo intramolecular cyclization to release an *n*-butylamine molecule. Two structural modifications were taken into account: 1) the influence of *N*-methylation at the squaryl nitrogen to favour the folded conformation and 2) the *N*-methylation at the trigger amino group to increase its nucleophilicity.

The results obtained seem to agree with the initial hypothesis (Figure 5.17). When comparing the  $k_{\text{obs}}$  obtained from the NMR kinetic experiments, the rate constant is five-fold increased when the squaryl nitrogen is methylated. Thus, the folding may be favoured leading to a rate enhancement. On the other hand, the particular case of system **33b**, where both *N* are methylated, shows a dramatic increment on the reaction constant being a 100 times higher than the one found for the non-methylated **33a** or the monomethylated **33c**. Here, we should consider both the folding conformation as well as the significant increase on the nucleophilicity of the attacking group. Comparing all three values of  $k_{\text{obs}}$ , the nucleophilicity increment is the factor that outstands the highest rate increase.

Despite the compounds **33a-c** were only studied at pH 8 we cannot consider such systems the best candidates to explore the intrinsic cyclization kinetics for the release of

aliphatic amines due to the  $^1\text{H-NMR}$  signal overlapping and relatively large experimental error in the calculation of the species distribution. Hence, we decided to redesign such aliphatic model to easily monitor the reaction and then build the pH-dependent rate curves.

*Application of the squaramide-based self-immolative system to the release of a biologically relevant aliphatic amine.* Squaramide models **28a-e** and the particular cases of squaramate esters **13** and **14**, showed a measurable change in the UV-vis spectrum during their cyclization process and the study of the reaction kinetics was performed in good detail, obtaining the corresponding cyclization constants ( $k_c$ ). However, the squaramide chromophore in the self-immolative models **33a-c** did not change enough respect the corresponding cyclic products (**23a-c** and *n*-butylamine).

To successfully overcome this issue, we designed a new series of self-immolative systems bearing a fluorophore bonded to the squaramide moiety through an aliphatic amine which could be studied by fluorescence spectroscopy. Besides finding a convenient functionality to study the release of aliphatic amines, we also wanted to test our system to bind bioactive molecules, since the ultimate aim of this thesis was the development of an antitumor prodrug. Thus, after a bibliographic revision, we found in **FFN102** a suitable candidate to be used for such purpose.

Fluorescent False Neurotransmitters (FFNs) are probes that act as optical tracers that enable the visualization of neurotransmitter release at individual presynaptic terminals in the brain.<sup>222</sup> Thus, researchers can study the cell uptake and release of neurotransmitters as well as the interference of agonists and antagonists during the signalling cascade.<sup>223</sup>

In particular, **FFN102** and **FF202** are pH-responsive blue FFN probes developed by Sames and Gubernator which selectively label dopaminergic synaptic terminals.<sup>224</sup> Optical monitoring of function (or malfunction) of dopamine signalling is essential since dopamine neurotransmission has key implications in motor function, habit learning, reward, and motivation.<sup>225</sup> In consequence, alterations in dopamine neurotransmission are normally associated with disorders such as Parkinson's disease, schizophrenia or attention deficit hyperactivity disorders (ADHD).<sup>226</sup>

---

<sup>222</sup> D. Evanko *Nat. Methods* **2009**, *7*, 486-486.

<sup>223</sup> M. Lee, N. G. Gubernator, D. Sulzer, D. Sames, *J. Am. Chem. Soc.* **2010**, *132*, 8828-8830.

<sup>224</sup> P. C. Rodriguez, D. B. Pereira, A. Borgkvist, M. Y. Wong, C. Barnard, M. S. Sonders, H. Zhang, D. Sames, D. Sulzer, *Proc. Natl. Acad. Sci.* **2013**, *110*, 870-875

<sup>225</sup> R. A. Wise, *Nat. Rev. Neurosci.* **2004**, *5*, 483-494.

<sup>226</sup> J. H. Ko, A. P. Strafella, *Neuroscientist* **2012**, *18*, 149-168.

Figure 5.21 shows a schematic illustration of vesicular uptake of monoamine neurotransmitters (i.e. dopamine or epinephrine) and coumarin-based FFNs by the action of vesicular monoamine transporter (VMAT), an integral membrane protein. VMAT imports the neurotransmitter by the release of  $H^+$  and, at the same time, ATPase imports  $H^+$  at the expense of ATP hydrolysis.

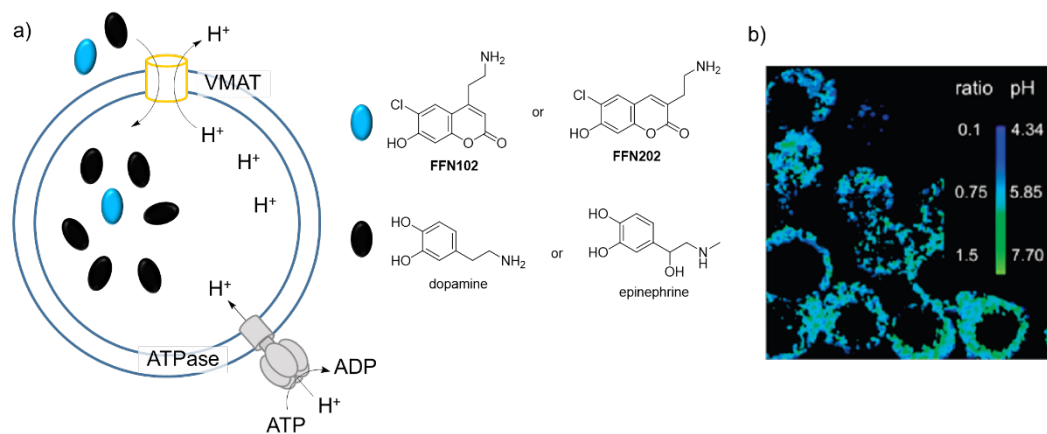
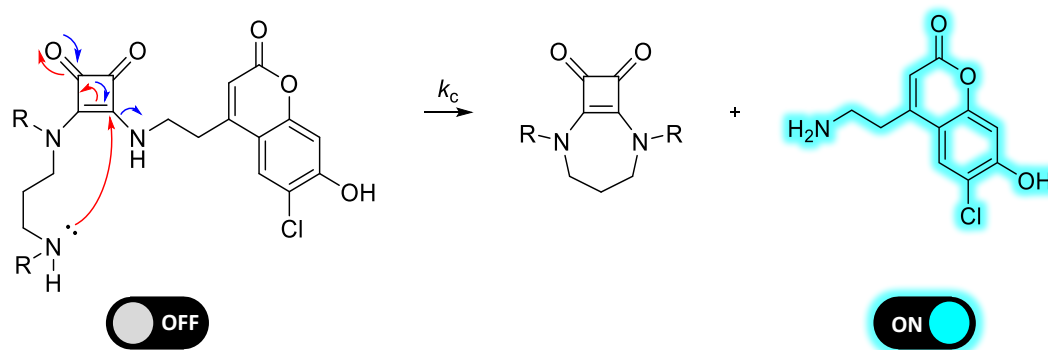


**Figure 5.21.** Schematic illustration of a) vesicular uptake of endogenous substrates (dopamine or epinephrine, black) and exogenous fluorescent substrates (FFN102 or FFN202, blue) by vesicular monoamine transporter (VMAT) and assisted by the ATPase. b) pH measurement of catecholamine secretory vesicles in PC-12 cells with FFN202 via two-photon fluorescence microscopy. Modified from reference 223.

Thus, the pH gradient between the cytoplasm and the vesicular lumen constitute the driving force for the uptake and accumulation of neurotransmitters in the vesicles. The development of pH-responsive FFNs have also allowed the *in situ* pH measurement of specific vesicles (Figure 5.21b).

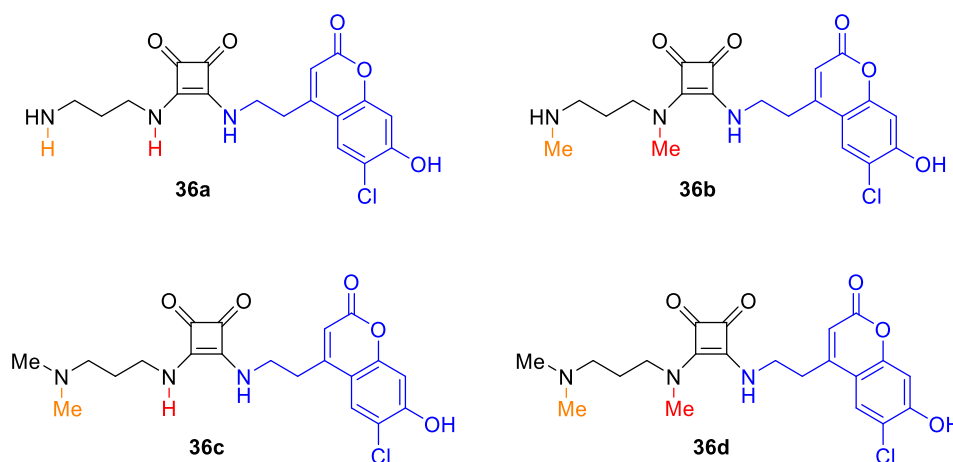
Regarding our field of interest, **FFN102** was chosen over **FFN202** as the fluorescent candidate to be released by our self-immolative system due to its easier synthetic pathway. Since the squaramides fluorescence quenching ability of both, the amino group and squaryl moiety is well known,<sup>227</sup> a priori the conjugation of a **FFN102** to our system would result in a significant decrease in the fluorescence having an “off” system. The subsequent release of the cargo by the self-immolative squaramide should turn on the fluorescence (Scheme 5.14):

<sup>227</sup> a) R. Prohens, G. Deslongchamps, P. Ballester, A. Costa, *Angew. Chem. Int. Ed.* **1999**, *38*, 2208-2211. b) R. Prohens, G. Martorell, P. Ballester, A. Costa, *Chem. Commun.* **2001**, *1*, 1456-1457.



**Scheme 5.14.** Designed blue fluorescent *off-on* self-immolative systems for the release of **FFN102**.

In analogy with the already described aliphatic models **33a-c** where the *N*-methylation was explored as a tool to enhance the cyclization reaction rate, here the same strategy was pursued. Due to their handicapped synthesis, *N*-squaryl monomethylated analogue was not prepared and only non-methylated **36a** and dimethylated **36b** models were synthesized. Additionally, to prove the release by self-immolation and not by thermal hydrolysis, the model compounds **36c** and **36d** were also prepared, where the intramolecular cyclization is not possible due to the dimethylation of the terminal amine.

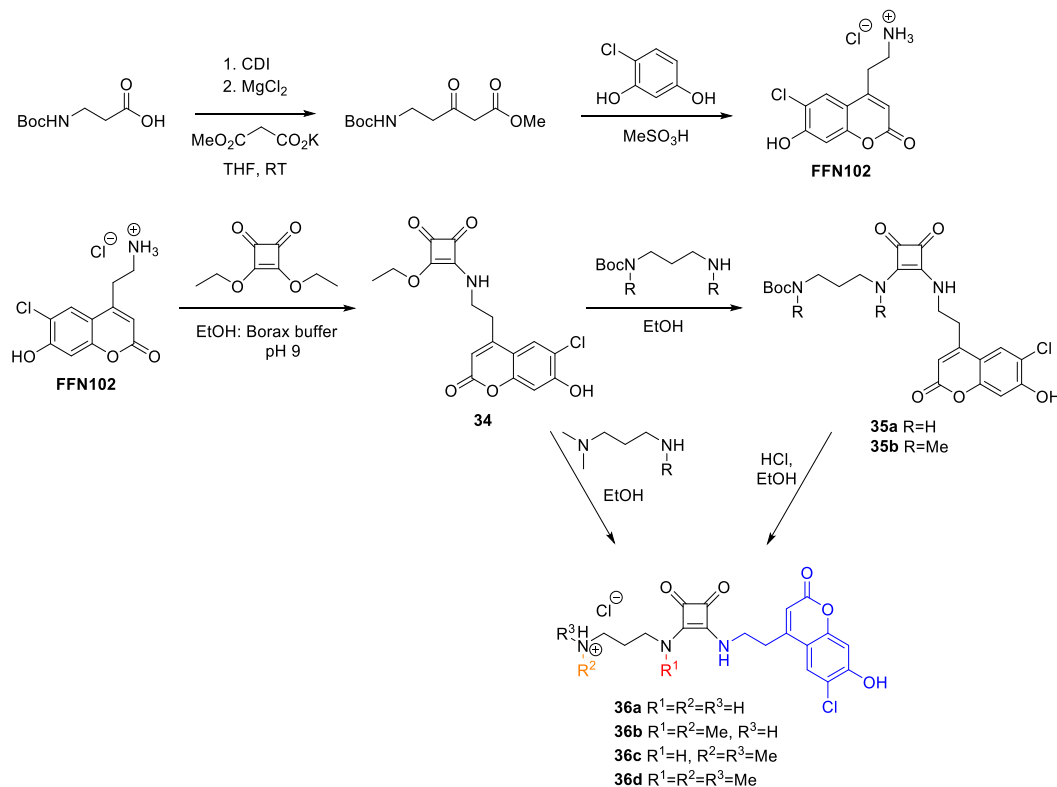


**Scheme 5.15.** Designed self-immolative models bearing **FFN102** as the amine aliphatic cargo (blue). *N*-methylation to increase nucleophilicity is highlighted in red and *N*-methylation to favor the folded conformation is shown in orange.

*Synthesis of self-immolative systems 36a-d.* **FFN102**, was prepared following the procedure reported in the literature.<sup>223,228</sup> **FFN102** was then coupled in EtOH and borax buffer at pH 9 mixture (1:1) with ethyl squarate to form the squaramate ethyl ester **33**. The reaction with the corresponding mono Boc-protected diamine in EtOH afforded

<sup>228</sup> X. Liu, A. Savy, S. Maurin, L. Grimaud, F. Darchen, D. Quinton, E. Labbé, O. Buriez, J. Delacotte, F. Lemaître, M. Guille-Collignon, *Angew. Chem. Int. Ed.* **2017**, *56*, 2366-2370.

squaramides **35a** and **35b** which were further deprotected to obtain the final self-immolative systems **36a** and **36b** as hydrochloric salts. In parallel, the reaction of ester **34** with *N*-dimethylamino propylene diamines in EtOH and further precipitation with HCl 1N led to the analogues **36c** and **36d**.



**Scheme 5.16.** Synthetic pathway to access coumarin self-immolative systems **36a-d** as hydrochloride salts.

**FFN102** and systems **36a-d** were characterised by spectroscopy in aqueous 10  $\mu\text{M}$  (0.1% DMSO) buffered solutions at pH 3, 5, 6, 7 and 8 (10 mM formic acid, acetic acid, cacodylate, and PBS respectively) at room temperature. Figure 5.22 shows a representative example of the variation of the spectroscopic properties for parent coumarin **FFN102** which is in agreement with the data reported in the literature.<sup>228</sup> The corresponding characterisation of fluorescent systems **36a-d** can be found in the experimental Section 5.4.

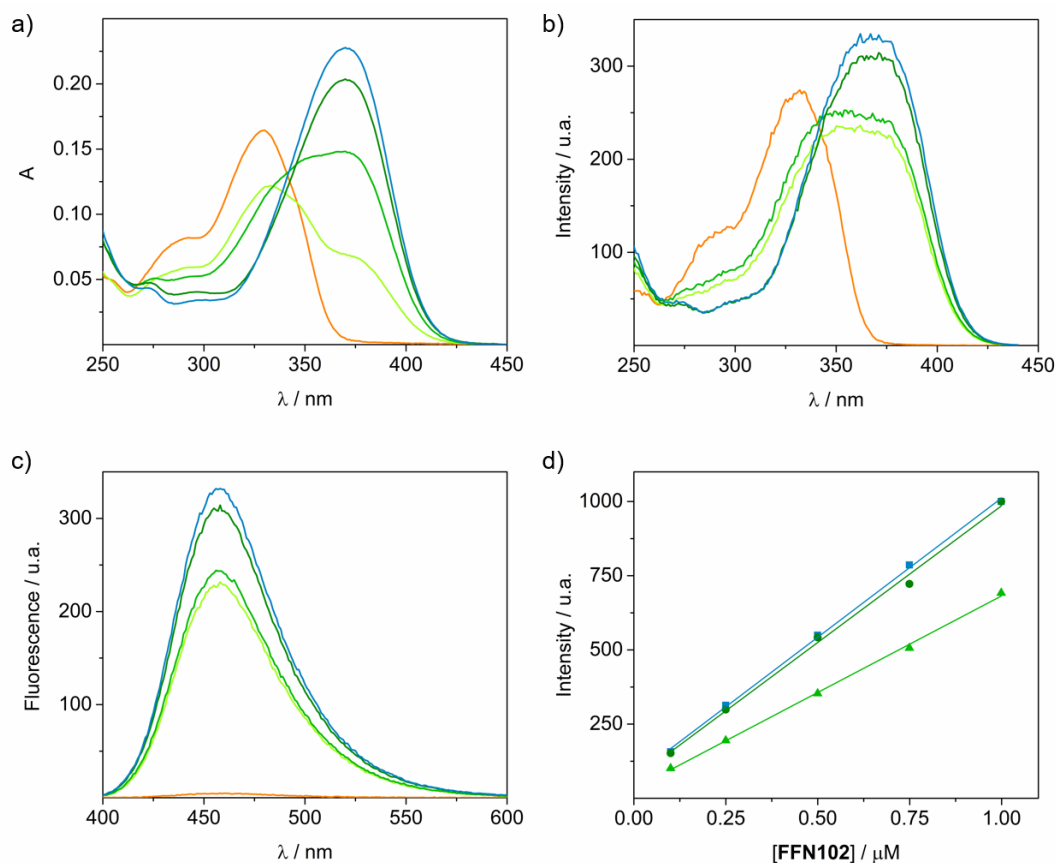


**Figure 5.22.** Absorption a), excitation b) and emission c) spectra of 10  $\mu$ M FFN102 in aqueous buffered solutions at pH 3 (orange), 5 (light green), 6 (green), 7 (dark green) and 8 (blue). All the emission spectra of FFN102 were obtained at optimal excitation wavelengths at different pH values according to their excitation spectra obtained in b). The acquisition bandwidth used was 5 nm. d) Calibration plots for FFN102 at pH 6 (green), 7 (dark green) and 8 (blue).

*Kinetic study of self-immolative systems 36a-d.* Systems **36a-d** present a quenched fluorescence in comparison with the parent FFN102 caused by the presence of the squaramide moiety. The self-immolation process results in the release of FFN102 increasing the overall fluorescence. Such increment can be easily measured by fluorescence spectroscopy and it is directly proportional to the amount of fluorophore released.

To properly determine the cyclization kinetic constant of the self-immolation process ( $k_c$ , Scheme 5.14) pH-variable experiments were performed (buffered solutions at pH 6, 7 and 8 respectively) at 37 °C. The intensity of fluorescence of the self-immolative models **36a-d** was measured and recorded every 24 h. In analogy to squaramate esters (Chapter 3) and squaramide anilines (Section 5.3.1), the analysis of the data and calculation of the apparent rate constants was performed with ReactLab<sup>TM</sup> Kinetics software.<sup>137</sup>

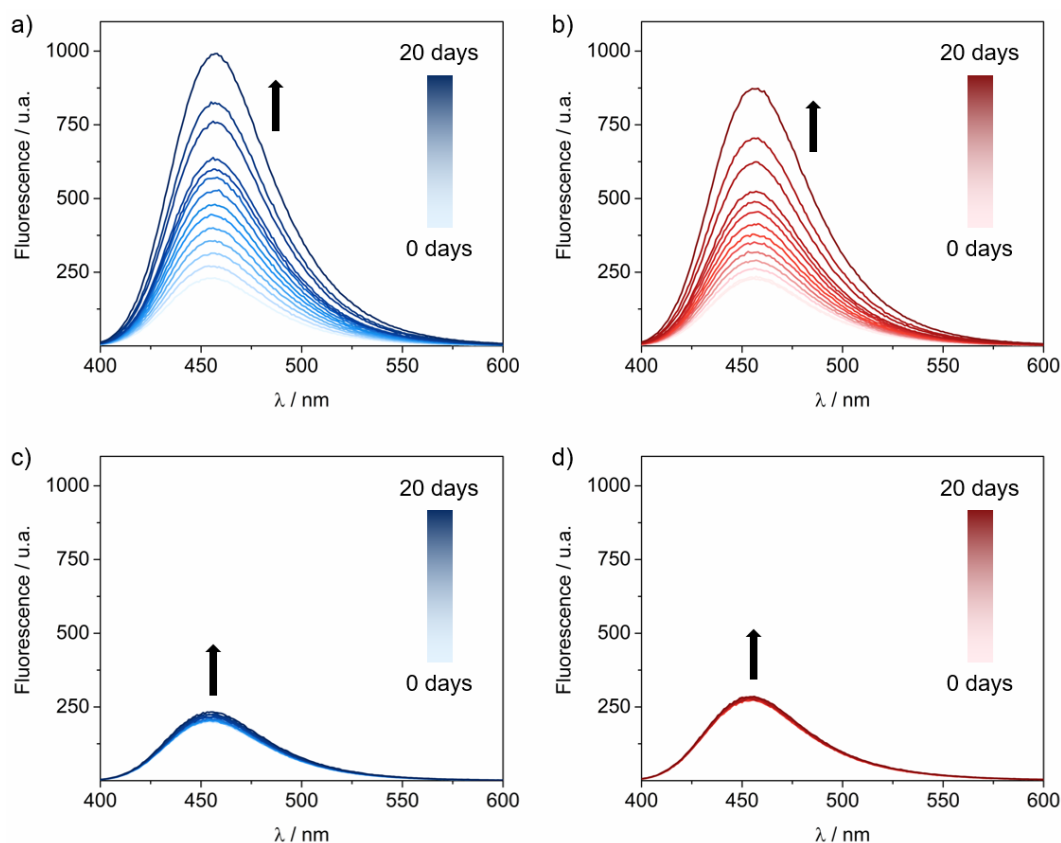


**Figure 5.23.** Representative example of the changes in the fluorescence spectra at 10 mM PBS buffered solution pH 8 at 37 °C of 10  $\mu$ M a) **36a**, b) **36b**, c) **36c** and d) **36d**. Squaramide non-methylated and methylated analogues are shown in blue and red respectively.

Figure 5.23 shows an example of the evolution of fluorescence spectra of compounds **36a-d** at PBS buffered solution at pH 8. As expected, systems **36a** and **36b** show an incremental evolution of fluorescence intensity derived from their ability to release **FFN102** by intramolecular cyclization. In contrast, dimethylation of the terminal amine as in compounds **36c** and **36d** prevents the release of the fluorophore and thus their fluorescence keeps invariable within the same period.

By fitting the changes of the fluorescence intensity over time with ReactLab Kinetics the pseudo-first order cyclization constants were obtained for each compound at the different solutions tested (pH 6, 7 and 8 respectively). Analogously to the squaramide-aniline self-immolative systems, the reaction is pH sensitive and the reaction kinetics responds to Eq. 10:

$$k_{\text{obs}} = k_{\text{c}}[A] = k_{\text{c}} \frac{K_{\text{a}}}{K_{\text{a}} + [\text{H}]} \quad (10)$$

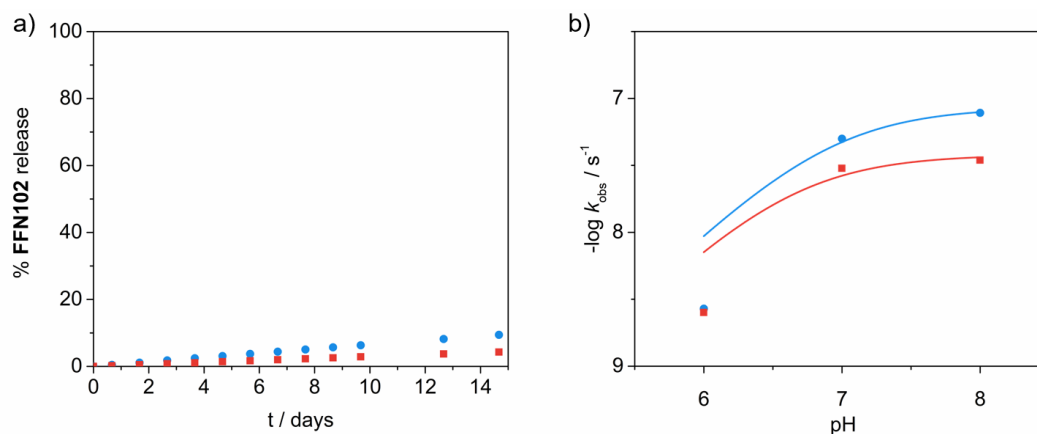


**Figure 5.24.** a) Representative plot of FFN102 release in a buffered solution at pH 8 and 37 °C by self-immolative model compounds **36a** (blue) and **36b** (red). b) Fitting to Eq. 6 for the observed cyclization constants at different pH of self-immolative compounds **36a** (blue) and **36b** (red).

The  $k_c$  obtained from the fitting are summarized in Figure 5.24b and Table 5.6.

**Table 5.6.** Cyclization constants obtained for **36a** and **36b** and their corresponding half-lives in a PBS buffered solution at pH 8 and 37 °C.

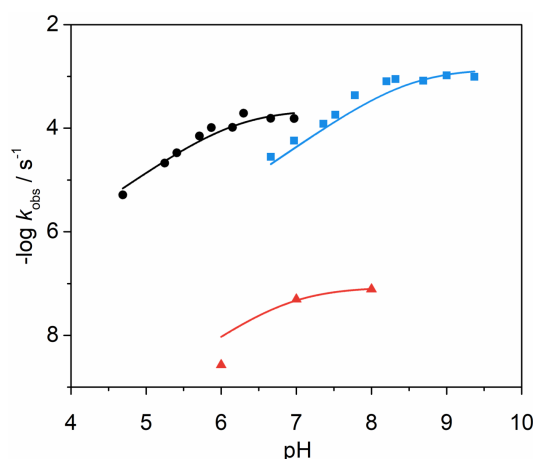
Entry	$k_c, 10^{-7} \text{ M}^{-1}\text{s}^{-1}$	$t_{1/2}$ (pH 8), days
<b>36a</b>	$3.2 \pm 0.1$	103
<b>36b</b>	$1.6 \pm 0.7$	232

The cyclization kinetic constants obtained ( $k_c \approx 10^{-7} \text{ M}^{-1}\text{s}^{-1}$ ) are significantly smaller than those found for the release of alcohols or anilines ( $k_c \approx 10^{-4} \text{ M}^{-1}\text{s}^{-1}$ ). Given that the LUMO maps of the aromatic and aliphatic amine models are similar (Table 5.7), the main difference in reactivity remains in the huge difference of nucleofugacity of the leaving group, driven by its  $pK_a$  value.

**Table 5.7.** LUMO maps and corresponding Natural Atomic Charges for model squaramides, distinguishing between aromatic and aliphatic radicals.

Label	Natural Atomic Charges, eV	
C1	+ 0.116	+ 0.105
C2	+ 0.105	+ 0.107
C3	+ 0.451	+ 0.446
C4	+ 0.454	+0. 446

The apparent rate constants obtained for the release of **FFN102** (parent self-immolative systems **36a** and **36b**) are around the same magnitude than those obtained for the non-fluorescent models **33a-c** ( $10^{-7} \text{ s}^{-1}$ , at pH 8). Overall, the release of aliphatic amines is relatively low and only around 2–3% of cargo is released after two weeks. In comparison with the results found for the release of alcohols (squaramate ester **13b**) or the release of differently substituted anilines (**28a-e**) the kinetic constant varies up to four orders of magnitude. Figure 5.25 summarizes the representative kinetic profiles of self-immolative systems studied so far. For clarity, only one model compound is shown for each cargo: alcohol (black), aniline (blue) and aliphatic amine (red).

**Figure 5.25.** Summary of pH-rate kinetic profiles of squaramate ester **13b** (black), nitroaniline derivative **28b** (blue) and coumarin system **36a** (red).

As shown in the chart, the release of aliphatic amines is significantly slower than the corresponding release of alcohols or anilines. Despite the imminent release is quite

slow, such behaviour may find its application in the sustained release of drugs. Figure 5.26 shows the plot of concentration-time behaviour of a drug depending on its kinetic release.<sup>229</sup> Unlike immediate release (IR) formulations, the controlled sustained release (SR) seeks maintaining a constant concentration of the drug with time. To satisfy this purpose, numerous variety of formulations can be found in the literature, including liposomes and drug conjugates such as hydrogels.<sup>230</sup>

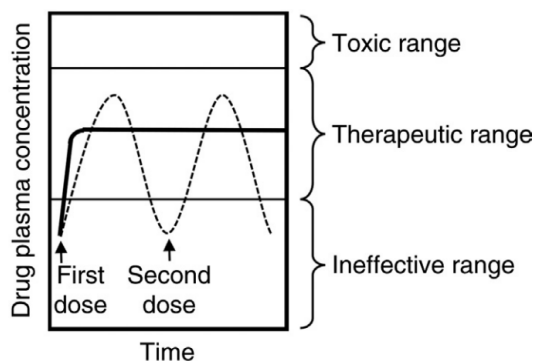


**Figure 5.26.** Two administrations of the Immediate Release (IR, dashed line) and Sustained Release (SR, solid line) formulation profiles. Reproduced from reference 229.

### 5.3.3. Transamidation-Type Reaction on Compound 33c

During long-term kinetic experiments performed on compound **33c** we detected the formation of a reaction intermediate during the first reaction hours. Initially, we attributed it to a conformational equilibrium, derived from the ability of squaramides to exist as mixtures of two conformers in solution. However, such conformational equilibrium is driven by concentration and temperature and not by the intramolecular reaction itself.

To contextualise, the conformational preferences of squaramides were firstly described by Costa *et al.* in 2004.<sup>231</sup> Taking as a simple model the squaramate ester of *n*-butylamine, they evaluated its temperature-dependent conformational behaviour by <sup>1</sup>H-NMR spectroscopy. Normally, in non-polar solvents, squaramides show both Z,E and Z,Z conformations resulting in a significant shift on the proton signals caused by the change in their chemical environment. As shown in Figure 5.27, the influence of the squaryl carbonyl on the adjacent proton results in a deshielding, shifting the proton to a

<sup>229</sup> E. Y. Chen, W. F. Liu, L. Megido, P. Díez, M. Fuentes, C. Fager, E. Olson, I. Gessner, S. Mathur, *Nanotechnologies in Preventive and Regenerative Medicine*, chapter 3 (2018), Elsevier. DOI: 10.1016/B978-0-323-48063-5.00003-4

<sup>230</sup> D. Bikiaris, E. Koutris, E. Karavas, *Recent Pat. Drug Deliv. Formul.* **2007**, *1*, 201–213.

<sup>231</sup> M. C. Rotger, M. N. Piña, A. Frontera, G. Martorell, P. Ballester, P. M. Deyà, A. Costa, *J. Org. Chem.* **2004**, *69*, 2302–2308.

lower field. Thus, in the *Z,E* conformation, the N-H proton, named as Hc, appears around 6.2 ppm while in the *Z,Z* conformation appears around 5.4 ppm, at a higher field (Hc'). Likewise, the CH<sub>2</sub> named as d suffers the same influence but, in the opposite direction, from high (*Z,E*) to a low (*Z,Z*) field, (Hd and Hd' respectively).

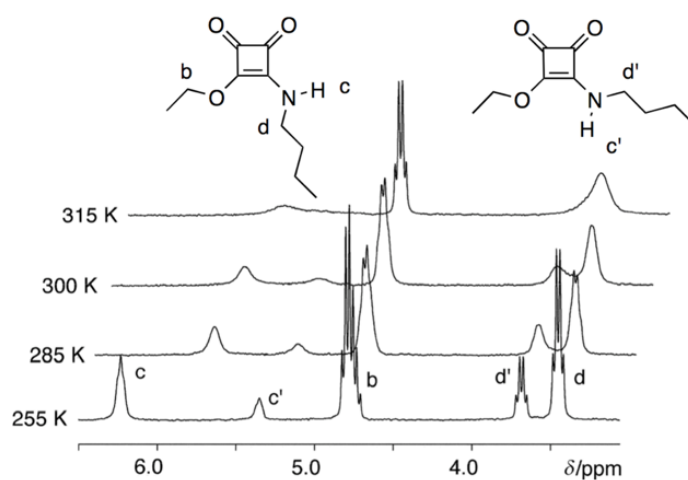


**Figure 5.27.** Temperature-dependent <sup>1</sup>H-NMR spectrum of *n*-butylamine squaramate ester in CDCl<sub>3</sub>. Reproduced from reference 231.

The proportion of each conformer in the equilibria can be calculated from their integrals, which in this example, shows the preference on the *Z,E* conformer.

Figure 5.28 shows the first five-hour period of the reaction for compound **33c**. The reaction was performed in a deuterated PBS (5% DMSO) solution at pH 8 and 37 °C and registered on a 600 MHz NMR spectrometer. During the reaction, a significant change in the chemical shift of protons H<sub>h</sub>, H<sub>f</sub> and H<sub>e</sub> (red, blue and green, respectively) was observed. The most noticeable shift was registered for methyl signal (H<sub>e</sub>, green) which shifted to a higher field from 3.30 to 2.75 ppm. Such remarkable shielding implies that the methyl group has to move away from the influence of the carbonyl group. Taking into account that the reaction evolves through intramolecular cyclization releasing *n*-butylamine, the folded conformation (*Z,E*) needs to be formed to proceed with the reaction. Thus, the methyl group should be deshielded by the influence of the carbonyl, if the *Z,E* conformation was detectable in water. Independently, a methyl shielding occurred so, before the cyclization, a previous reaction process should be considered to explain such shielding phenomenon.

Hence, we suggest that the terminal nitrogen would perform an attack to the C1 electrophilic carbon, through a 6-membered cyclic intermediate (**INT33c'**), releasing the *N*-methyl chain (Figure 5.28). Thus, if this intramolecular transamidation-type reaction took place, the resulting *N*-methyl group would become a substituent of an amino functionality (H<sub>e'</sub>), more shielded than in the former squaramide (H<sub>e</sub>). In

consequence, we should see also a significant change in the proton signals  $H_h$  and  $H_f$ . Actually, in addition to the evident methyl shift, we can distinguish the appearance of a triplet around 3.1 ppm and a triplet around 3.7 ppm, which could correspond to those protons. We renamed the transamidation product as **33c'**.

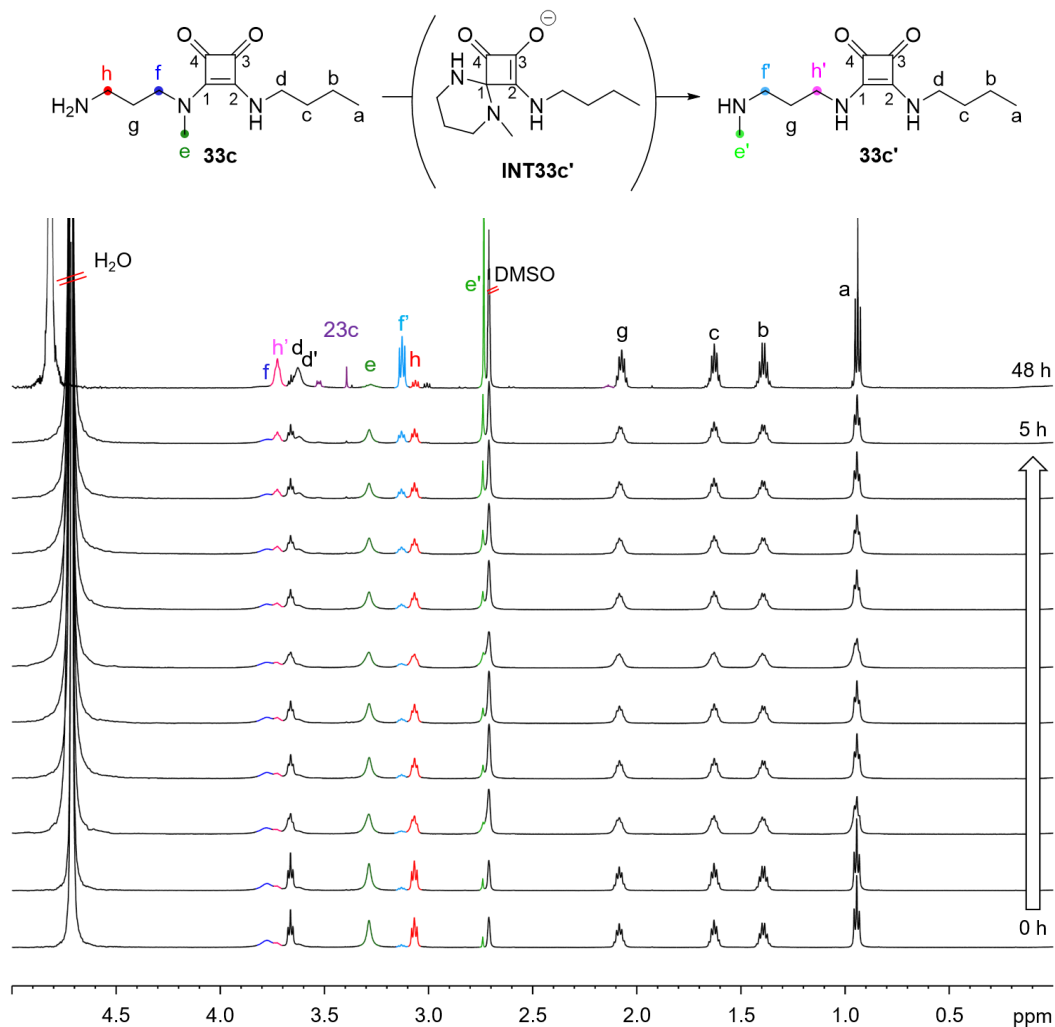


**Figure 5.28.** Changes in the  $^1\text{H-NMR}$  spectra of system **33c** during the first 5h of reaction. PBS (22 mM,  $\text{D}_2\text{O}$ , 5%  $\text{DMSO-}d_6$ ) pH 8, 310 K. Last spectrum was acquired after 48 h of incubation.

The chemical shifts described above are depicted in colours in figure 5.28. Dark green, blue and red correspond to the signals from **33c** while the transamidation signals from product **33c'** are coloured in pale green, blue and pink respectively. If the reaction is let to evolve on time, the formation of **23c** and  $n$ -butylamine is observed (purple peaks), thus suggesting that after the addition to the C1 squaryl carbon forming compound **33c'**, this latter evolves by addition to the C2 squaryl carbon affording the stable 7-membered cyclic squaramide **23c**.

In the synthesis of **33c**, the last step implied the removal of the Boc-protecting group by treatment with TFA. Thus, the final product was obtained as a pale oil, which is a TFA

ammonium salt. Surprisingly, after keeping that ammonium salt at room temperature for three months an approximately 30% conversion of **33c** into **33c'** was detected. Despite the protonation of the amino terminal group and the absence of solvent, the reaction took place. To confirm the hypothesised transamidation-type reaction, the 2D correlation experiment TOCSY allowed the identification of the signals for both **33c** and **33c'** by finding the contacts with the protons belonging to the same spin system (Figure 5.29). *Habcd* chain is shown in black, which is indistinguishable for **33c** and **33c'**. However, *Hfgh* and *Hf'gh'* proton systems are discerned (blue and red crossed peaks respectively). Besides they are both correlated with *Hg* (blue-red dashed line).

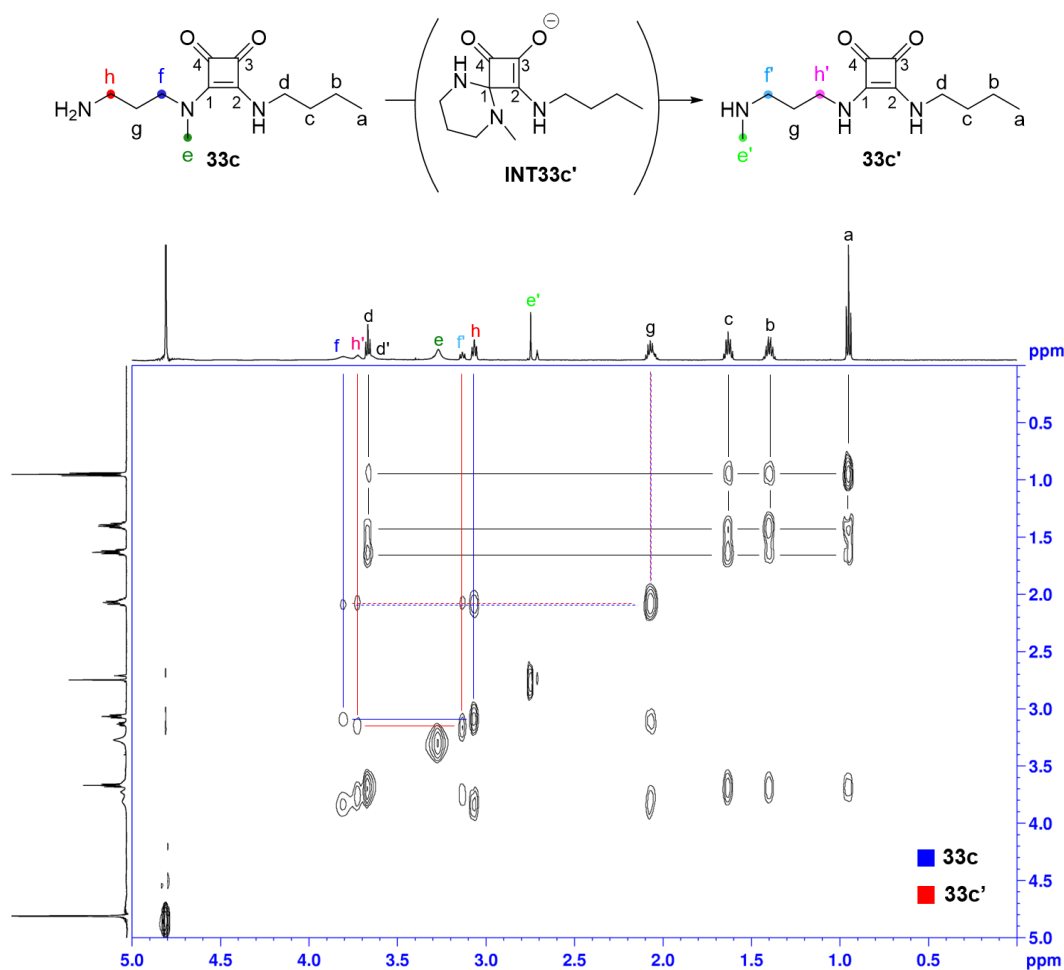


**Figure 5.29.**  $^1\text{H}$ - $^1\text{H}$  TOCSY experiment showing the correlation among coupled spin systems on 30% transformed **33c**, 22 mM,  $\text{D}_2\text{O}$ , 5%  $\text{DMSO-}d_6$  298 K, 600 MHz.

In order to shed light about the prevalence of observed C1- and/or C2-additions, theoretical calculations at M06-2X/def2-TZVP level of theory were carried out. According to experimental evidences a transamidation-type reaction occurs. We have theoretically explored both C1- and C2-additions from compound **33c**. General solvent effects have been considered by using a continuum dielectric model. Besides, we have used three explicit water molecules in the theoretical models. The utilization of at least three water molecules is necessary to locate the transition states **TS1-23c** and **TS-33c'**

along the reaction pathway (Figure 5.30). The role of the water molecules is to promote the hydrogen transfer from the nucleophilic amino group to the carbonylic O-atom of squaramide in addition to stabilize the TSs by the formation of several hydrogen-bonding interactions. The DFT results show that squaramide **23c** is the thermodynamically favoured product (compared **33c'**  $\Delta\Delta E = -2.7$  kcal/mol) while **33c'** is the kinetic one ( $\Delta\Delta E^\ddagger = 6.3$  kcal/mol), leading to the transamidation-type reaction as the preferential path. In both optimized TS structures, the *N*-atoms of the amino groups acting as nucleophiles are similarly located over C1 and C2 carbons, C $\cdots$ N distances of 1.97 and 1.96 Å, respectively. Therefore, we suggest that the origin of additional stabilization of **TS-33c'** is related to the more favoured chair conformation found in this transition state (six-membered ring). In fact, these TSs end up with the formation of intermediates **INT1-23c** and **INT-33c'** being the most stable **INT-33c'** also having a 6-membered ring in a perfect chair conformation.

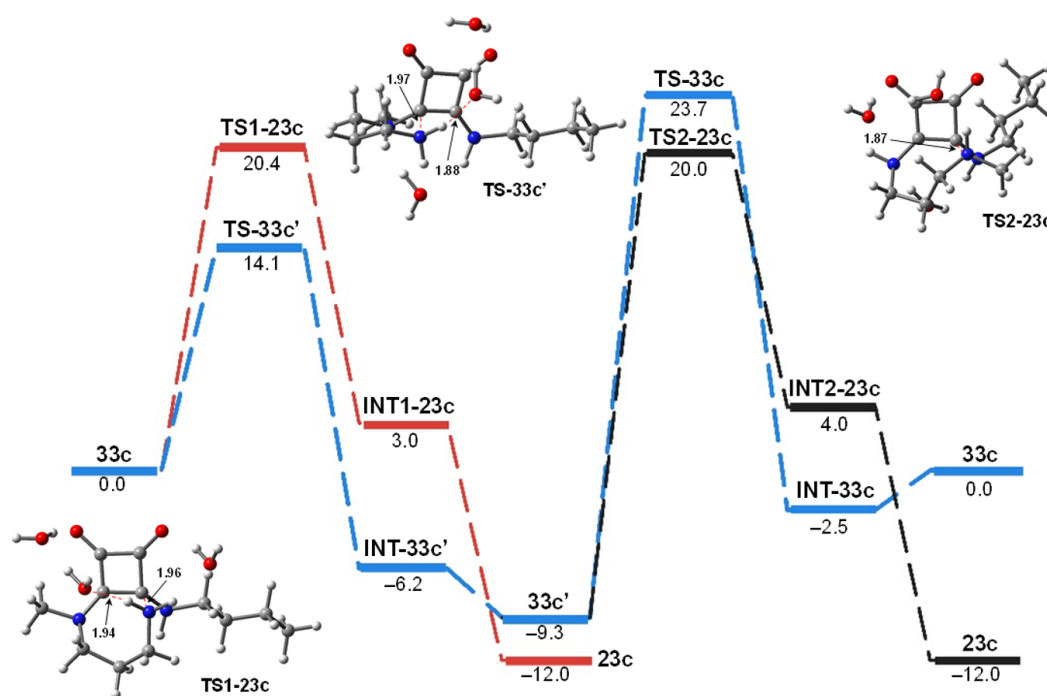


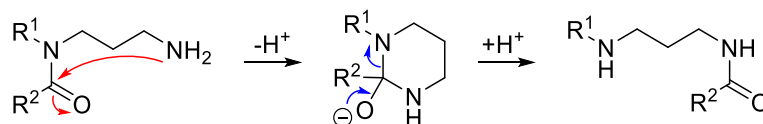
**Figure 5.30.** The calculated energy profile showing the competitive pathways of C1- (red) and C1'- (blue) additions at M06-2X/def2-TZVP level of theory. The energy profile in black corresponds to the reaction pathway once compound **33c'** is formed. The corresponding calculated structures of TS structures are also shown. All values of energies (in kcal/mol) are relative to reactants. Distances are given in Å.

To explain the formation of cyclic squaramide **23c**, we envisioned that once the transamidation reaction takes place affording compound **33c'**, it can be transformed to compound **23c** by means of the nucleophilic attack of terminal *N*-methylamino group as a jumping-off point. Firstly, it is necessary to highlight that inverse reaction **33c'**  $\rightarrow$  **33c** has a penalty of 23.3 kcal/mol whereas the corresponding energy of **TS-33c** is up to 27.3 kcal/mol, and therefore, this reaction pathway is even more difficult to pass

through it. However, the energy barrier of C2-addition (**TS2-23c**) is herein lower than the corresponding C1 attack ( $\Delta\Delta E = -3.7$  kcal/mol) being the most accessible pathway to finally reach **23c**. Moreover, **TS2-23c** is 0.4 kcal/mol lower in energy than **TS1-23c**, thus the generation of **23c** via **33c'** is slightly more favoured, although both routes probably contribute to final the formation of **23c**, which is clearly dominated by thermodynamic effects.

This point raises the question about if C1-intramolecular reactions are common in squaramides. We have serendipitously detected the transamidation product of system **33c** due to its particular asymmetric substitution.

As far as we know, such a particular reaction has never been described in squaramides and related compounds; however, it is known in amides.<sup>232</sup> Schmid and collaborators defined the isomerization of trimethylenediamine derivatives in the presence of a nucleophilic nitrogen atom (Scheme 5.17).<sup>233</sup> The reaction was favoured when one of the amino groups is primary and the other is part of a *N,N*-disubstituted carboxamide.

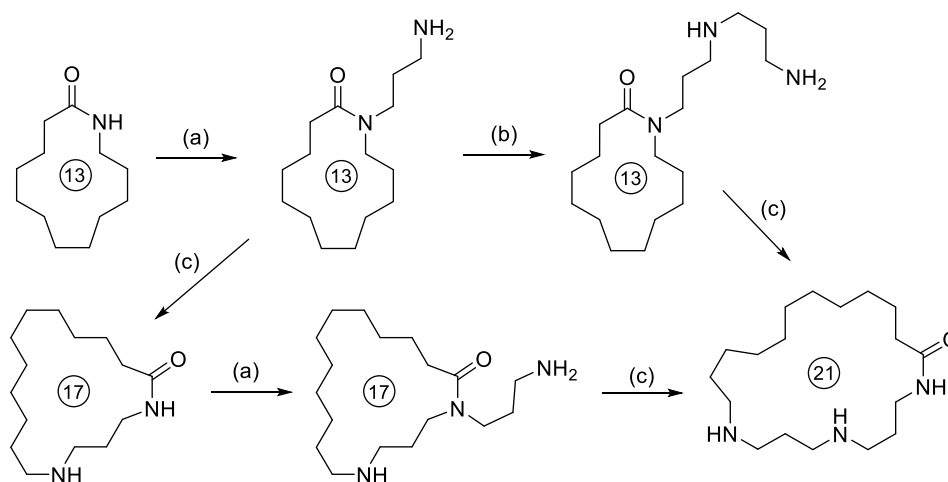


**Scheme 5.17.** Schmid's isomerization of *N,N*-disubstituted carboxamide.

The high yield of the process allowed them to use the transamidation reaction as a strategy to expand lactam rings. Starting from a 13-membered lactam ring, the introduction of a propylamine moiety by reaction with acrylonitrile followed by its reduction with hydrogen led to a 4-member ring expansion (Scheme 5.18). The reaction worked good enough to proceed using one, two or more trimethyleneamino expansion, so they described it as a “zip” reaction in analogy to the behaviour of a zip fastener.

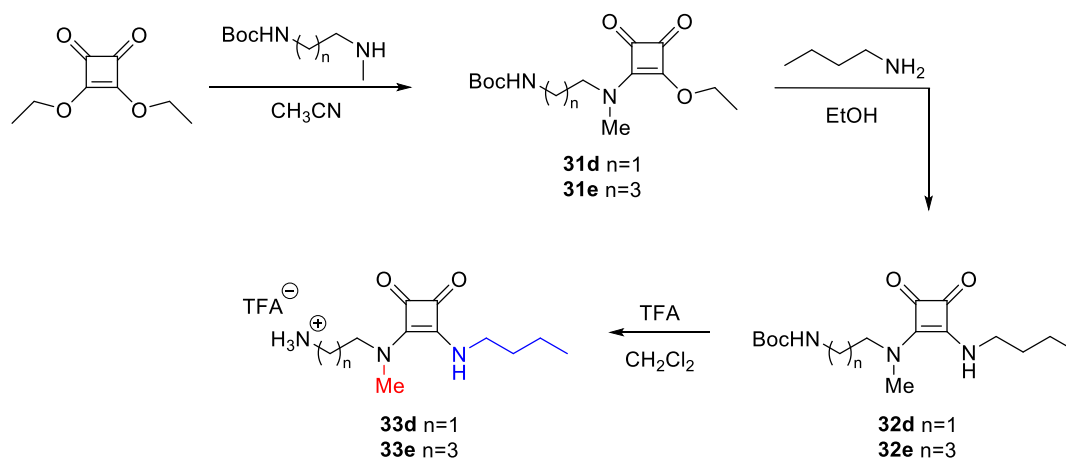
<sup>232</sup> a) T. H. Fife, B. R. DeMark, *J. Am. Chem. Soc.* **1977**, *99*, 3075-3080. b) U. Kramer, A. Guggisberg, M. Hesse, H. Schmid, *Angew. Chem. Int. Ed.* **1978**, *17*, 200–202. c) J. P. Tam, Y. A. Lu, Q. Yu, *J. Am. Chem. Soc.* **1999**, *121*, 4316–4324

<sup>233</sup> U. Kramer, A. Guggisberg, M. Hesse, H. Schmid, *Angew. Chem. Int. Ed.* **1977**, *16*, 861-862.



**Scheme 5.18.** Schmid's *zip* ring expansion for amino lactams. (a) Na salt of the amide and  $\text{CH}_2=\text{CHCN}$ ;  $\text{H}_2/\text{Pt}$ ; (b)  $\text{CH}_2=\text{CHCN}$ ;  $\text{H}_2/\text{Pt}$ ; (c)  $\text{K}[\text{NH}(\text{CH}_2)_3\text{NH}_2]$  and  $\text{H}_3\text{O}^+$ .

With such precedents, we decided to explore the influence of the diamino alkyl chain length on the effectiveness of the transamidation. Thus, the commercially available Boc-*N*-protected *N*'-methyl diamines were purchased and the ethyl and butyl analogues of **33c** were synthesised. The synthetic procedure used was analogous to that used on the synthesis of **33a-c**.



**Scheme 5.19.** Synthetic scheme to access tertiary-secondary squaramides **33d** and **33e**.

First, we assigned all the signals by performing 2D COSY and TOCSY experiments (experimental section).

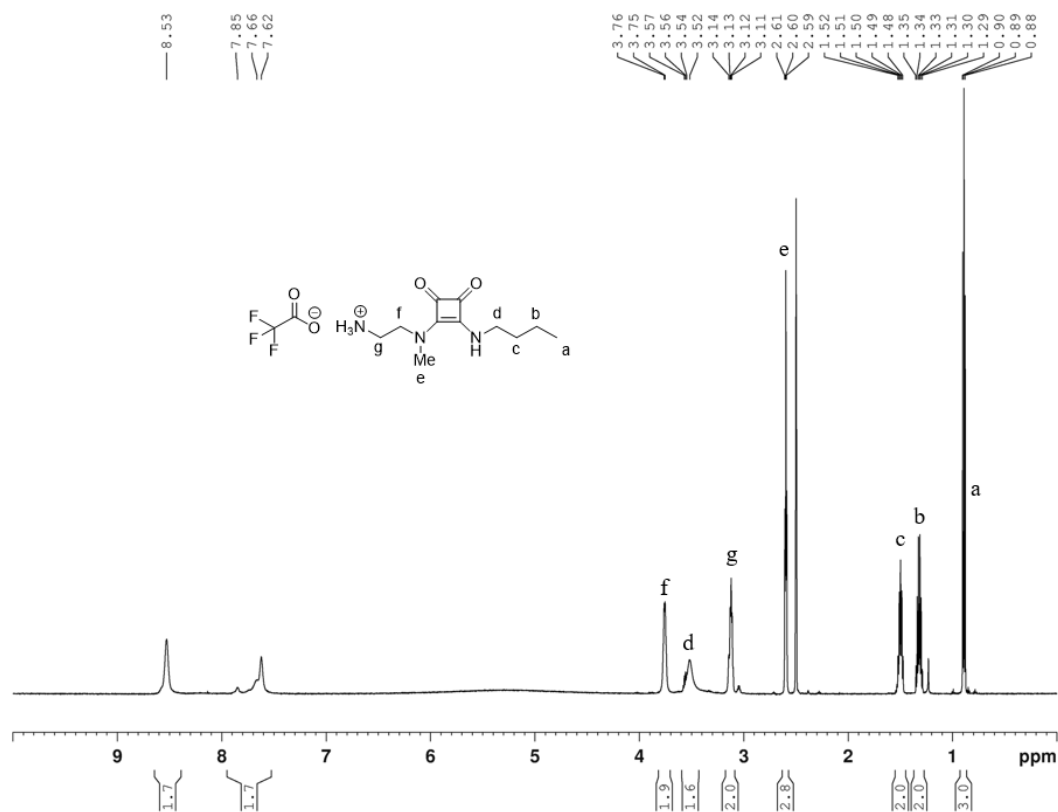


Figure 5.31.  $^1\text{H-NMR}$  of **33d** (DMSO, 298K) and the corresponding signal assignment.

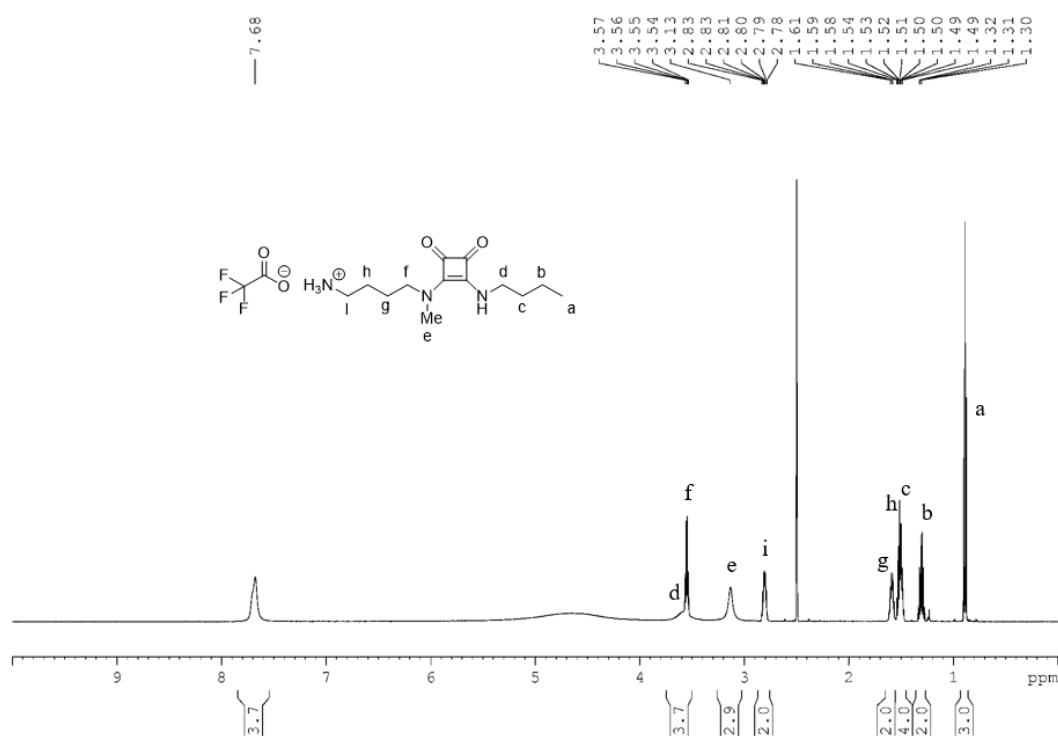
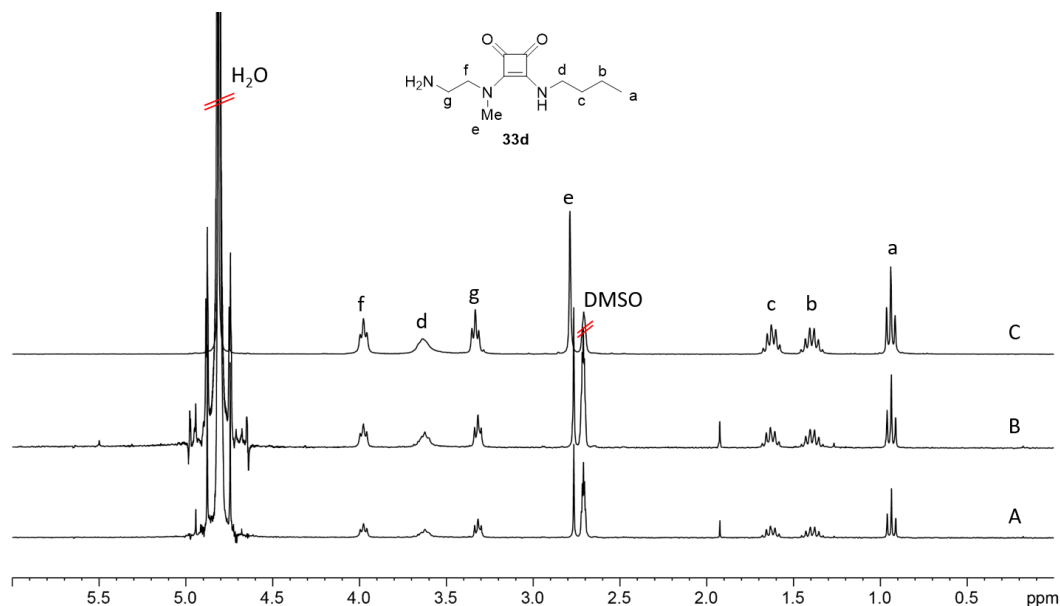


Figure 5.32.  $^1\text{H-NMR}$  of **33e** (DMSO, 298K) and the corresponding signal assignment.

Then, in analogy with the kinetic experiment performed on system **33c**, the evolution of  $^1\text{H-NMR}$  spectra of **33d** and **33e** was studied, using deuterated PBS (10% DMSO- $d_6$ ) at pH 8 at 37 °C. Incubation of both samples at 37 °C for one week (Figure 5.33A and

5.34A) led to no change in the spectra, therefore the temperature was increased to 50 °C. After three days, the  $^1\text{H}$  spectrum was collected and compared the changes with the initial spectrum (Figure 5.33B and 5.34B). To finally toughen up the conditions compounds **33d** and **33e** were heated, both in the solid state, to 100 °C for three days (figure 5.33C and 5.34C). As a result, any change was observed in the spectrum of **33d**. On the other hand, compound **33e** changed dramatically.



**Figure 5.33.**  $^1\text{H}$ -NMR of 1  $\mu\text{M}$  **33d** (0.1 M PBS, 10% DMSO- $d_6$ , pH 8) after incubation in different experimental conditions. A) seven days at 37 °C, B) three days at 50 °C and C) three days at 100°C.

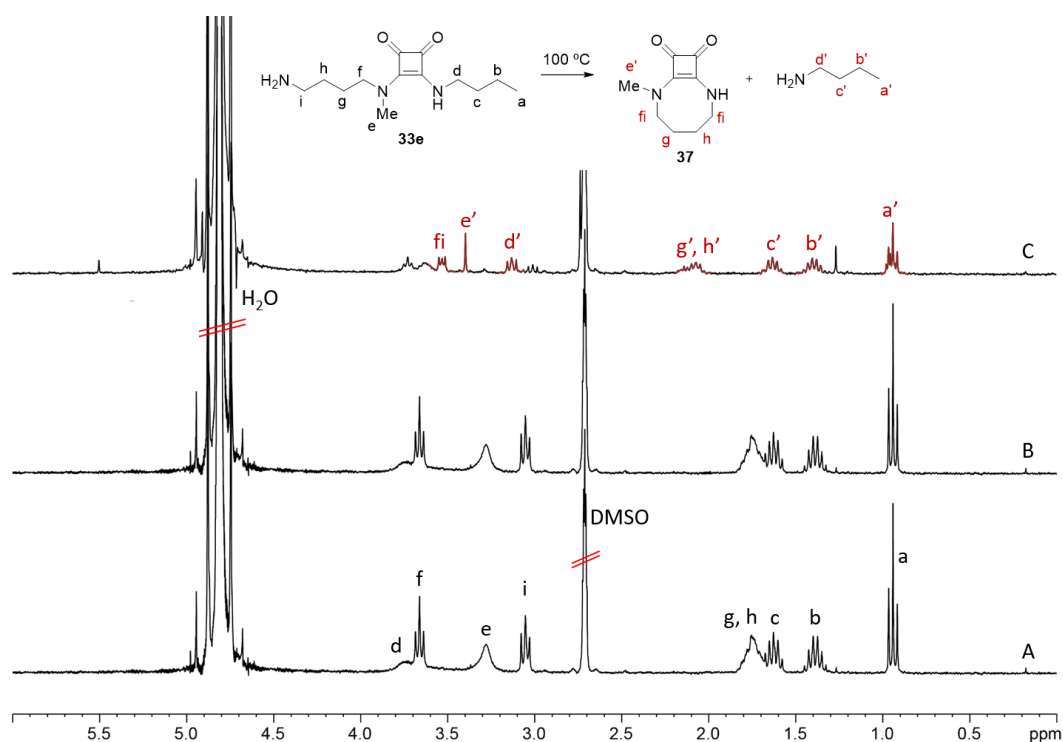


**Figure 5.34.**  $^1\text{H-NMR}$  of 1  $\mu\text{M}$  **33e** (0.1 M PBS, 10%  $\text{DMSO-}d_6$ , pH 8) after incubation in different experimental conditions. A) seven days at 37 °C, B) three days at 50 °C and C) three days at 100°C.

As evidenced by the appearance of characteristic conformational-restricted signals, we deduced that the cyclic 8-membered squaramide **37** was formed (signals highlighted in red). Confirmation of the mixture composition was achieved by analysing the NMR crude mixture by ESI-HRMS (Figure 5.35).

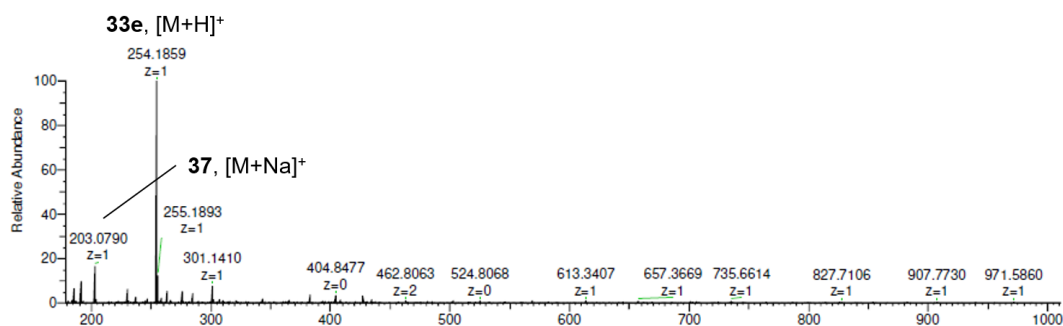


**Figure 5.35.** HRMS of **31e** heated in the solid state at 100 °C.

The confirmation of cyclization is observed by the detection of a peak at 203.0790, corresponding to the mass of cyclosquaramide **37** ( $[\text{M}+\text{Na}]^+$ ) which in comparison with the parent self-immolative system **33e**, shows a weight loss of 73 (butylamine).

It seems that the transamidation-type reaction in squaramides is taking place only with propanediamines, when the free amino is primary and the other amine is *N,N*-disubstituted in the squaramide system.

## 5.4. CONCLUSIONS

In conclusion, we designed and synthesised a new series of minimalist squaramide-based self-immolative systems. The studied self-immolative systems (**28a-e**) bearing anilines as leaving groups showed the fastest kinetics, finding the second-order reaction rates  $k_c \approx 10^{-3}$ - $10^{-4} \text{ M}^{-1}\text{s}^{-1}$ . The cyclization rate was sensitive to pH and was also enhanced by the  $pK_a$  of the conjugated acid of the leaving group (better nucleofugacity). The *N*-methylation of the squaramide significantly improved the water solubility of the system and also suggested a rate enhancement favouring the folded conformation and thus, the cyclization. Additionally, *N*-methylation of the terminal amine would increase the reaction rate due to the enhancement on the amine nucleophilicity.

The synthetic attempts to afford a lenalidomide-self-immolative system conjugate led to the squaryl ring fission of the squaramic acid chloride **29**, forming the 1,2-dicarbonyl compound **30**. In analogy to the reactivity found for squaramate thioester **24**, it seems that 3<sup>rd</sup> period atoms like sulphur and chlorine modify the intrinsic electrophilicity of C2 squaryl carbons. Hence, the corresponding squaryl derivatives suffer nucleophilic attacks on the electrophilic carbonyl C4 leading to 1,2-dicarbonyl compounds.

On the other hand, the self-immolative systems bearing *n*-butylamine as a representative of an aliphatic cargo (**33a-c**) showed pseudo-first order rate constants around  $10^{-5}$ - $10^{-7} \text{ s}^{-1}$ . The second-order rate cyclization constants for similar aliphatic systems were calculated for the corresponding fluorescent analogues (**36a** and **36b**) finding values of  $10^{-7} \text{ M}^{-1} \text{ s}^{-1}$ , 1000 times slower than those found for the analogues **28a-e**.

Self-immolative system **33c** showed the particular intramolecular transamidation-type reaction (attack on C1), previous to the cyclization process (attack on C2). DFT calculations support that **33c'** is the kinetic product while **23c** is the thermodynamic one. In this rationale, **33c** is firstly converted into **33c'** by a transamidation-type reaction, and it is therefore converted into **23c** by the 1,7-cyclization, releasing an *n*-butylamine molecule. This transamidation-type reaction was particularly detected in propanediamine *N,N*-disubstituted squaramide system **33c** but it did not occur in the related ethanediamine and butanediamine analogues **33d** and **33e** respectively.

In summary, the exploration of different minimalist self-immolative systems allowed us to define the most suitable building block for the squaramide-based self-immolative system (SSIS) bearing the following features: 1) propane diamino chain as the nucleophile 2) Aniline as the chemical nature of the leaving group or cargo 3) Improvement of the solubility of the system by *N*-methylation of the squaramide trigger chain.

## 5.5. EXPERIMENTAL SECTION

The various chemicals were of commercial origin (Aldrich or Scharlau) and were used as received.  $^1\text{H}$ ,  $^{13}\text{C}$  and 2D NMR spectra (at 300 and 600 MHz) and  $^{13}\text{C}$  (at 75 and 150 MHz) spectra were recorded on 300 and 600 MHz spectrometers in  $\text{CDCl}_3$  DMSO- $d_6$  solutions at room temperature. The residual proton signal was used as a reference. Chemical shifts ( $\delta$ ) are given in ppm and coupling constants ( $J$ ) in Hz. ESI-HRMS mass spectra were recorded on a magnetic sector on an Orbitrap mass spectrometer.

### 5.5.1. Kinetic Experiments

The UV-vis experiments were carried out on a VARIAN Cary 300 Bio UV-vis spectrophotometer and the fluorescence measurements were obtained on a Varian Cary Eclipse spectrophotometer at  $37.0 \pm 0.1$  °C in water. Squaramides were dissolved in  $10^{-2}$  M buffered solutions at a final concentration of 30  $\mu\text{M}$  and 10  $\mu\text{M}$  for UV-vis and fluorescence analysis respectively. The ionic strength was 0.15 M NaCl. The changes in the UV or fluorescence range were analysed with ReactLab<sup>TM</sup> Kinetics software (Jplus Consulting Ltd.).<sup>137</sup> For the kinetic analysis we assumed no significant contribution from the anion.

### 5.5.2. Theoretical Calculations

All DFT calculations were performed employing the Gaussian 09 package.<sup>234</sup> Geometry optimizations were carried out using the hybrid Minnesota functional of Truhlar and Zhao (M06-2X)<sup>235</sup> and the def2-TZVP basis set. In order to characterize the nature (minimum or transition state) of optimized structure, analyses of frequencies were also conducted. Minima are described by the absence of imaginary frequencies whereas one imaginary frequency was obtained for transition states. Implicit solvent effects ( $\text{H}_2\text{O}$ )

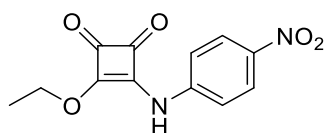
<sup>234</sup> Gaussian 09, Revision B.01, Frisch, M. J.; Trucks, G. W.; Schlegel, H. B.; Scuseria, G. E.; Robb, M. A.; Cheeseman, J. R.; Scalmani, G.; Barone, V.; Mennucci, B.; Petersson, G. A.; Nakatsuji, H.; Caricato, M.; Li, X.; Hratchian, H. P.; Izmaylov, A. F.; Bloino, J.; Zheng, G.; Sonnenberg, J. L.; Hada, M.; Ehara, M.; Toyota, K.; Fukuda, R.; Hasegawa, J.; Ishida, M.; Nakajima, T.; Honda, Y.; Kitao, O.; Nakai, H.; Vreven, T.; Montgomery, J. A., Jr.; Peralta, J. E.; Ogliaro, F.; Bearpark, M.; Heyd, J. J.; Brothers, E.; Kudin, K. N.; Staroverov, V. N.; Kobayashi, R.; Normand, J.; Raghavachari, K.; Rendell, A.; Burant, J. C.; Iyengar, S. S.; Tomasi, J.; Cossi, M.; Rega, N.; Millam, J. M.; Klene, M.; Knox, J. E.; Cross, J. B.; Bakken, V.; Adamo, C.; Jaramillo, J.; Gomperts, R.; Stratmann, R. E.; Yazyev, O.; Austin, A. J.; Cammi, R.; Pomelli, C.; Ochterski, J. W.; Martin, R. L.; Morokuma, K.; Zakrzewski, V. G.; Voth, G. A.; Salvador, P.; Dannenberg, J. J.; Dapprich, S.; Daniels, A. D.; Farkas, Ö.; Foresman, J. B.; Ortiz, J. V.; Cioslowski, J.; Fox, D. J. Gaussian, Inc., Wallingford CT, 2009.

<sup>235</sup> Zhao, Y.; Truhlar, D. G. *Theor. Chem. Acc.* **2008**, *120*, 215–241.

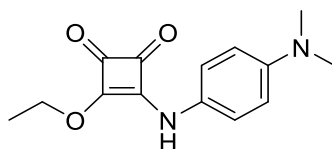
were considered applying the CPCM polarizable conductor calculation model<sup>236</sup> by means of single-point calculations. Molecular modelling and calculation of the LUMO maps were performed with *Spartan '18* Wavefunction, Inc. Irvine, CA.<sup>148</sup>

### 5.5.3. Synthesis

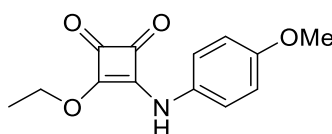
*General procedure for the synthesis of squaramate esters 26a-c.* Diethyl squarate (1.2 equiv) was dissolved in 10 mL of EtOH with 0.1 equiv of Zn(OTf)<sub>2</sub> and stirred at room temperature. To this solution 1 equiv of the corresponding amine dissolved in 4 mL of EtOH was added dropwise and the reaction mixture was stirred for 2-6 hours. After the reaction time, the resulting precipitate was filtered out, washed with EtOH (3 × 5 mL) and Et<sub>2</sub>O (3 × 5 mL) and dried under vacuum.



*3-ethoxy-4-((4-nitrophenyl)amino)cyclobut-3-ene-1,2-dione (26a).* Recrystallization from CH<sub>3</sub>CN, orange needles, 300 mg (yield 73%). <sup>1</sup>H-RMN (300 MHz, DMSO-*d*<sub>6</sub>): δ = 1.45 (t, *J* = 7.1 Hz, 3H), 4.81 (q, *J* = 7.0 Hz, 2H), 7.60 (d, *J* = 9.0 Hz, 2H), 8.25 (d, *J* = 9.0 Hz, 2H), 11.24 (br s, 1H). ESI-HRMS(+) *m/z* (%): calcd for C<sub>12</sub>H<sub>11</sub>N<sub>2</sub>O<sub>5</sub><sup>+</sup> [M+H]<sup>+</sup> 263.0662; found 263.0661 and 285.0480 [M+Na]<sup>+</sup>.



*3-((4-(dimethylamino)phenyl)amino)-4-ethoxycyclobut-3-ene-1,2-dione (26b).* Pale yellow amorphous solid 352 mg (yield 91%). <sup>1</sup>H NMR (300 MHz, CDCl<sub>3</sub>) δ 1.49 (t, *J* = 6.0Hz, 3H), 2.96 (s, 6H), 4.85 (q, *J* = 6.0Hz, 2H), 6.70 (d, *J* = 9.0Hz, 2H), 7.14 (br s, 2H). ESI-HRMS(+) *m/z* (%): calcd for C<sub>14</sub>H<sub>17</sub>N<sub>2</sub>O<sub>3</sub><sup>+</sup> [M + H]<sup>+</sup> 261.1234; found 261.1234, 283.1053 [M + Na]<sup>+</sup>, 521.2399 [2M + H]<sup>+</sup>, 543.2218 [2M + Na]<sup>+</sup>.

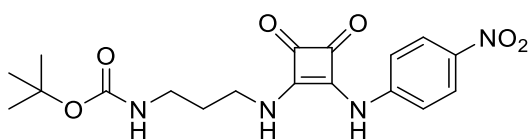


*3-ethoxy-4-((4-methoxyphenyl)amino)cyclobut-3-ene-1,2-dione (26c).* White yellow amorphous solid 384 mg (yield 58%). <sup>1</sup>H NMR (300 MHz, CDCl<sub>3</sub>) δ 1.49 (t, *J* = 6.0Hz,

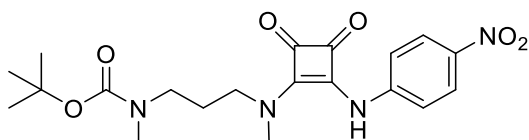
<sup>236</sup> a) Barone, V.; Cossi, M. *J. Phys. Chem. A*, **1998**, *102*, 1995–2001 b) Cossi, M.; Rega, N.; Scalmani, G.; Barone, V. *J. Comp. Chem.* **2003**, *24*, 669-681

3H), 2.96 (s, 6H), 4.85 (q,  $J = 6.0\text{Hz}$ , 2H), 6.70 (d,  $J = 9.0\text{Hz}$ , 2H), 7.14 (br s, 2H). ESI-ESI-HRMS(+)  $m/z$  (%): calcd  $\text{C}_{13}\text{H}_{14}\text{NO}_4^+$   $[\text{M} + \text{H}]^+$  248.0917; found 248.0914, 270.0734  $[\text{M} + \text{Na}]^+$ , 517.1585  $[2\text{M} + \text{Na}]^+$ .

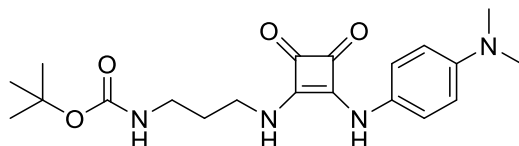
*General procedure for the synthesis self-immolative systems 28a-e.* Squaramate ester **26a-c** (1 equiv, partially dissolved), the corresponding *N*-Boc-protected diamine (1.2 equiv) and  $\text{K}_2\text{CO}_3$  (2 equiv, partially dissolved) were mixed in 15 mL of EtOH and stirred at 50 °C for 16h. After the reaction time the crude residue was evaporated to vacuum to remove the solvent and then purified either by precipitation or column chromatography. The resulting Boc-protected compounds were treated in HCl 1N or pure TFA and evaporated to vacuum to afford systems **28a-e**.



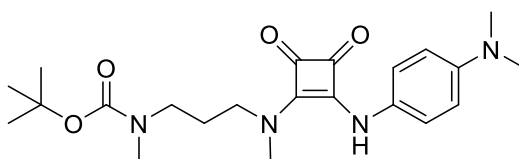
*tert-butyl (3-((2-((4-nitrophenyl)amino)-3,4-dioxocyclobut-1-en-1-yl)amino)propyl) carbamate (27a).* The crude solid was digested with  $\text{Et}_2\text{O}$  and the resulting solid was filtered and dried under vacuum. Yellow amorphous solid, 87 mg (yield 41%).  $^1\text{H}$  NMR (300 MHz,  $\text{DMSO}-d_6$ )  $\delta$  1.37 (s, 9.3H), 1.69 (m,  $J = 6.6$  Hz, 2H), 3.02 (q,  $J = 6.6$  Hz, 2H), 3.62 (q,  $J = 6.4$  Hz, 2H), 6.89 (t,  $J = 6.9$  Hz, 0.9H), 7.60 (d,  $J = 8.9$  Hz, 1.9H), 7.80 (t,  $J = 6.9$  Hz, 0.9H), 8.22 (d,  $J = 9.1$  Hz, 2H), 10.24 (br s, 0.9H). ESI-HRMS(+)  $m/z$  (%): calcd  $\text{C}_{18}\text{H}_{22}\text{N}_4\text{O}_6\text{Na}^+$   $[\text{M} + \text{Na}]^+$  413.1432; found 413.1432, 803.2297  $[2\text{M} + \text{Na}]^+$ .



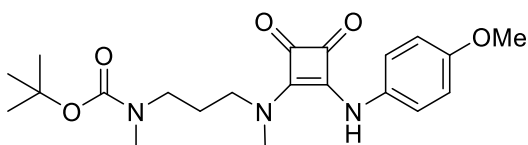
*tert-butyl methyl (3-(methyl(2-((4-nitrophenyl)amino)-3,4-dioxocyclobut-1-en-1-yl)amino)propyl) carbamate (27b).* The crude solid was digested with  $\text{Et}_2\text{O}$  and the resulting solid was filtered and dried under vacuum. Yellow amorphous solid 234 mg (yield 73%).  $^1\text{H}$  NMR (300 MHz, DMSO, ppm)  $\delta$  1.36 (s, 9.5H), 1.82 (m, 2.2H), 2.78 (s, 3.5H), 3.19 (br s, 3.5H), 3.21 (br m, 2.1H), 3.70 (br m, 2H), 7.36 (d,  $J = 8.8$  Hz, 2.1H), 8.18 (d,  $J = 9.0$  Hz, 2H), 9.89 (br s, 1H). ESI-HRMS (+)  $m/z$  (%): calcd  $\text{C}_{20}\text{H}_{26}\text{N}_4\text{O}_6\text{Na}^+$   $[\text{M} + \text{Na}]^+$  441.1745; found 441.1745.



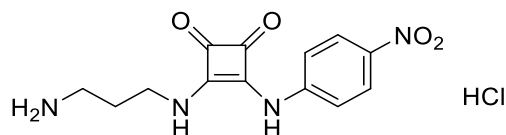
*tert-butyl (3-((2-((4-(dimethylamino)phenyl)amino)-3,4-dioxocyclobut-1-en-1-yl)amino)propyl)carbamate (27c)*. The crude residue was digested with  $\text{CH}_2\text{Cl}_2$ . The resulting pale yellow solid was filtered and dried under vacuum: 34 mg (yield 46%).  $^1\text{H}$  NMR (300 MHz, DMSO, ppm)  $\delta$  1.38 (s, 9H), 1.55 (m, 2H), 2.77 (s, 6H), 2.98 (br t, 2H), 6.56 (br s, 2H), 7.12 (br s, 2H), 12.06 (br s, 0.2H). ESI-HRMS (+)  $m/z$  (%): calcd  $\text{C}_{20}\text{H}_{29}\text{N}_4\text{O}_4^+$   $[\text{M} + \text{H}]^+$  389.2183; found 389.2183, 411.2003  $[\text{M} + \text{Na}]^+$ , 427.1743  $[\text{M} + \text{K}]^+$ .



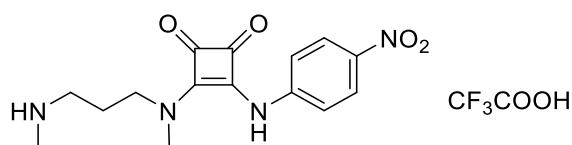
*tert-butyl (3-((2-((4-(dimethylamino)phenyl)amino)-3,4-dioxocyclobut-1-en-1-yl(methyl)amino)propyl)(methyl)carbamate (27d)*. The crude solid was digested with  $\text{Et}_2\text{O}$  and the resulting pale brown solid was filtered and dried under vacuum: 32 mg (yield 27%).  $^1\text{H}$  NMR (300 MHz, DMSO- $d_6$ )  $\delta$  1.38 (s, 9H), 1.79 (m, 2H), 2.77 (s, 3H), 2.86 (s, 6H), 3.18 (t, 2H), 3.21 (s, 3H), 3.62 (br t, 2H), 6.68 (d,  $J = 9.0\text{Hz}$ , 2H), 7.06 (d,  $J = 9.0\text{Hz}$ , 2H), 9.21 (s, 1H). ESI-HRMS (+)  $m/z$  (%): calc.  $\text{C}_{22}\text{H}_{32}\text{N}_4\text{O}_4\text{Na}^+$   $[\text{M} + \text{Na}]^+$  439.2316; found 439.2316, 455.2055  $[\text{M} + \text{K}]^+$ .



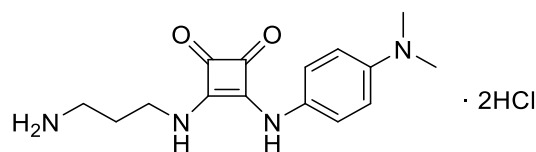
*tert-butyl (3-((2-((4-methoxyphenyl)amino)-3,4-dioxocyclobut-1-en-1-yl) (methyl)amino)propyl)(methyl)carbamate (27e)*. The crude solid was purified by column chromatography ( $\text{SiO}_2$ ,  $\text{CH}_2\text{Cl}_2$ :MeOH, 95:5). White amorphous solid, 75 mg (yield 54%).  $^1\text{H}$  NMR (300 MHz, DMSO- $d_6$ )  $\delta$  1.37 (s, 9.4H), 1.80 (m, 2.1H), 2.77 (s, 3H), 3.19 (m, 5H), 3.63 (br m, 1.9H), 3.73 (s, 3.1H), 6.89 (d,  $J = 8.9\text{ Hz}$ , 2H), 7.16 (d,  $J = 8.9\text{ Hz}$ , 2.1H), 9.28 (s, 1H). ESI-HRMS (+)  $m/z$  (%): calcd  $\text{C}_{21}\text{H}_{29}\text{N}_3\text{O}_5\text{Na}^+$   $[\text{M} + \text{Na}]^+$  426.1999; found 426.2001.



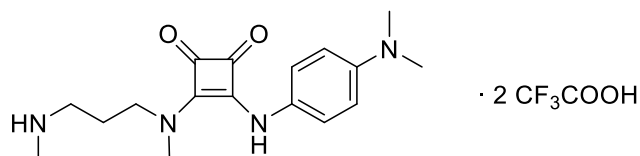
3-((2-((4-nitrophenyl)amino)-3,4-dioxocyclobut-1-en-1-yl) amino) propan-1-aminium chloride (**28a**). Yellow amorphous solid, 45 mg (yield 62%).  $^1\text{H}$  NMR (300 MHz, PBS, 10% DMSO- $d_6$ )  $\delta$  2.09 (m,  $J = 6.9$  Hz, 2.2H), 3.14 (t,  $J = 7.5$  Hz, 2.1H), 3.81 (t,  $J = 6.6$  Hz, 2.1H), 7.58 (d,  $J = 8.7$ , 2H), 8.28 (d,  $J = 9.1$  Hz, 2H).  $^{13}\text{C}$  NMR (150 MHz, DMSO- $d_6$ )  $\delta$  28.6, 36.4, 41.0, 117.3, 125.6, 141.3, 145.7, 162.8, 170.3, 179.8, 185.0. ESI-HRMS (+) m/z (%): calcd  $\text{C}_{13}\text{H}_{14}\text{N}_4\text{O}_4$   $[\text{M} + \text{H}]^+$  291.1088; found 289.1658, 313.0906  $[\text{M} + \text{Na}]^+$ .



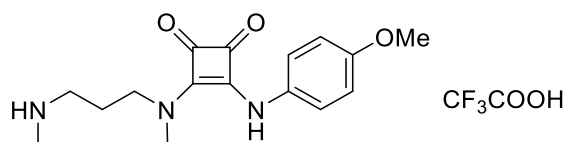
*N*-methyl-3-(methyl(2-((4-nitrophenyl)amino)-3,4-dioxocyclobut-1-en-1-yl)amino)propan-1-aminium trifluoroacetate (**28b**). Dark brown oil, 46 mg (yield 82%).  $^1\text{H}$  NMR (300 MHz, DMSO- $d_6$ )  $\delta$  1.92 (m, 2.1H), 2.57 (s, 3.3H), 2.92 (br m, 2.4H), 3.28 (s, 3.2H), 3.28 (br s, 2.9H), 7.39 (d,  $J = 9.1$  Hz, 2.1H), 8.20 (d,  $J = 9.1$  Hz, 2.0H), 8.38 (br s, 1.9H), 9.93 (br s, 1H).  $^{13}\text{C}$  NMR (150 MHz, DMSO- $d_6$ )  $\delta$  23.9, 32.4, 45.4, 48.7, 55.5, 118.9, 124.9, 141.4, 145.5, 162.1, 171.0, 180.9, 186.9. ESI-HRMS (+) m/z (%): calc.  $\text{C}_{15}\text{H}_{19}\text{N}_4\text{O}_4^+$   $[\text{M} + \text{H}]^+$  319.1401; found 319.1399.



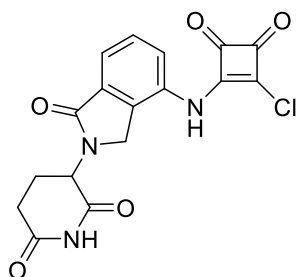
4-((2-((3-ammoniopropyl)amino)-3,4-dioxocyclobut-1-en-1-yl)amino)-*N,N*-dimethylbenzenaminium chloride (**28c**). Pale grey solid, 28 mg (yield 88%).  $^1\text{H}$  NMR (300 MHz, DMSO- $d_6$ )  $\delta$  1.87 (m, 2H), 2.90 (m, 2H), 3.04 (s, 6H), 3.64 (s), 7.59 (s, 3.3H), 8.01 (s, 2.6H), 9.13 (s, 0.8H), 11.31 (s, 0.8H).  $^{13}\text{C}$  NMR (75 MHz, DMSO- $d_6$ , ppm)  $\delta$  28.7, 30.7, 36.4, 44.8, 118.6, 120.2, 159.4, 161.0, 163.8, 169.5, 180.0, 183.7. ESI-HRMS (+) m/z (%): calcd  $\text{C}_{15}\text{H}_{21}\text{N}_4\text{O}_2^+$  289.1659; found 289.1658  $[\text{M} + \text{H}]^+$ , 327.1217  $[\text{M} + \text{K}]^+$  (504)



*N,N*-dimethyl-4-((2-(methyl(3-(methylammonio)propyl)amino)-3,4-dioxocyclobut-1-en-1-yl)amino)benzenaminium trifluoroacetate (**28d**). Pale brownish oil, 40 mg (yield 96%).  $^1\text{H}$  NMR (300 MHz, DMSO- $d_6$ )  $\delta$  1.90 (m, 2H), 2.73 (s, 1.5H), 2.89 (s, 1.6H), 2.91 (br t, 2H), 2.98 (s, 6H), 3.71 (br t, 2H), 7.02 (br s, 2H), 7.18 (d,  $J = 9.0\text{Hz}$ , 2H), 8.37 (br s, 2H), 9.40 (s, 1H).  $^{13}\text{C}$  NMR (75 MHz, DMSO- $d_6$ )  $\delta$  24.1, 27.5, 32.5, 41.0, 43.4, 45.5, 113.3, 123.4, 147.5, 152.8, 164.7, 169.4, 180.6, 185.0. ESI-HRMS (+)  $m/z$  (%): calcd  $\text{C}_{17}\text{H}_{25}\text{N}_4\text{O}_2^+$  317.1972; found 317.1972  $[\text{M} + \text{H}]^+$ .

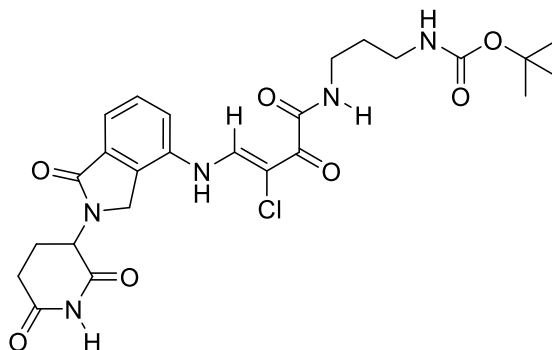


3-(2-((4-methoxyphenyl)amino)-3,4-dioxocyclobut-1-en-1-yl)(methyl)amino-*N*-methylpropan-1-aminium trifluoroacetate (**28e**). Pale yellow oil, 40 mg (yield 79%).  $^1\text{H}$  NMR (300 MHz, DMSO- $d_6$ )  $\delta$  1.91 (m, 2.1H), 2.58 (s, 3.4H), 2.93 (br m, 2.1H), 3.23 (s, 2.9H), 3.74 (s + m, 4.8H), 6.90 (d,  $J = 9.0\text{ Hz}$ , 2.1H), 7.17 (d,  $J = 8.9\text{ Hz}$  2.0H), 8.35 (br s, 2.0H), 9.34 (br s, 0.9H).  $^{13}\text{C}$  NMR (75 MHz, DMSO- $d_6$ , ppm)  $\delta$  24.0, 32.4, 45.4, 55.2, 113.7, 114.5, 122.5, 131.6, 155.8, 168.9, 180.5, 184.5. ESI-HRMS (+)  $m/z$  (%): calcd  $\text{C}_{16}\text{H}_{22}\text{N}_3\text{O}_3^+$  304.1656; found 304.1654  $[\text{M} + \text{H}]^+$ .



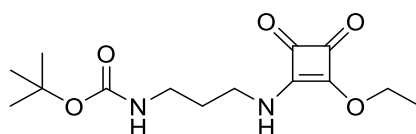
3-(4-((2-chloro-3,4-dioxocyclobut-1-en-1-yl)amino)-1-oxoisindolin-2-yl)piperidine-2,6-dione (**29**). 111 mg (0.43 mmol) of lenalidomide and 78 mg (0.51 mmol) of squaric acid dichloride are dissolved in anhydrous THF (2 mL) under Ar atmosphere at 0 °C. The reaction mixture is therefore left to evolve to room temperature for 2h and the resulting solid is filtered out, washed with hexane and dried under vacuum. Pale yellow solid, 139 mg (yield 87%).  $^1\text{H}$  NMR (300 MHz, DMSO- $d_6$ )  $\delta$  2.02 (m, 1.1H), 2.40 (m, 1H), 2.63 (m, 1.0H), 2.95 (m, 1.1H), 4.56 (m, 1.9H), 5.17 (dd,  $J = 6.0\text{ Hz}$ ), 7.66 (br s, 2.6H), 11.03 (s, 0.9H), 11.36 (br s, 0.5H), 11.70 (br s, 0.4H). ESI-HRMS (+)  $m/z$  (%):

calcd  $C_{17}H_{12}N_3O_5ClNa^+$   $[M + Na]^+$  396.0358; found 396.0358, 428.0622  $[M+Na+MeOH]^+$ .

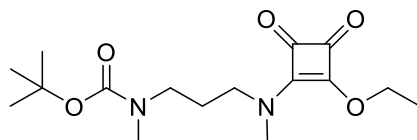


tert-butyl (3-((3-chloro-4-((2-(2,6-dioxopiperidin-3-yl)-1-oxoisindolin-4-yl)amino)-2-oxobut-3-enamido)propyl)carbamate (**30**). 135 mg (0.36 mmol) of **29** and 76 mg (0.43 mmol) of N-Boc-propane-1,3-diamine are dissolved in  $CH_3CN$  (5mL) and stirred at room temperature for 16h. After the reaction time, the solvent is removed under vacuum and the resulting crude is purified by column chromatography ( $SiO_2$ ,  $CH_2Cl_2:MeOH$ , 95:5). Brown-yellowish solid, 46 mg (yield 23%).  $^1H$  NMR (600 MHz,  $DMSO-d_6$ ):  $\delta$  1.35 (s, 9.6H), 1.56 (m,  $J = 6.9$  Hz, 2.1H), 2.02 (m, 1.1H), 2.37 (dq,  $J = 13.1, 4.4$  Hz, 1.0H), 2.62 (d,  $J = 16.5$  Hz, 1.1H), 2.92 (q,  $J = 6.4$  Hz, 3.1H), 3.13 (q,  $J = 6.6$  Hz, 2.0), 4.60 (dd,  $J = 17.4$  Hz, 2.0H), 5.17 (dd,  $J = 13.3, 5.2, 1.0$ H), 6.78 (t,  $J = 6.2$  Hz, 0.9H), 7.52 (m, 1.0H), 7.59 (m, 2.0H), 8.75 (t,  $J = 6.5$  Hz, 1.0H), 9.19 (d,  $J = 13.3, 1.0$ H), 9.79 (d,  $J = 14.4, 1.0$ H), 11.04 (s, 1.0H).  $^{13}C$  NMR (150 MHz,  $DMSO-d_6$ ):  $\delta$  23.0, 28.7, 29.6, 31.6, 38.0, 46.5, 52.0, 78.0, 106.5, 120.3, 123.5, 130.2, 133.2, 134.0, 136.6, 156.1, 163.5, 167.9, 171.4, 173.3, 179.0. ESI-HRMS (+)  $m/z$  (%): calcd  $C_{25}H_{30}N_5O_7ClNa^+$   $[M + Na]^+$  570.1726; found 570.1730.

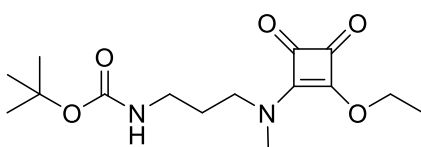
*General procedure for synthesis of squaramate esters 31a-c.* The corresponding N-Boc-diamine (1 equiv) was added dropwise to a solution of diethyl squarate (1.1 equiv) in  $CH_3CN$  (0.02M). The solution was stirred overnight at room temperature. After reaction time, the solvent was removed and the crude was further purified either by precipitation or by silica-gel chromatography.



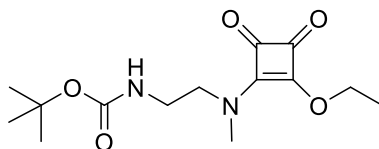
tert-butyl (3-((2-ethoxy-3,4-dioxocyclobut-1-en-1-yl)amino)propyl)carbamate (**31a**). Compound renamed after squaramate ester **13a**, chapter 2.



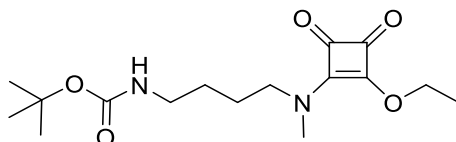
*tert-butyl (3-((2-ethoxy-3,4-dioxocyclobut-1-en-1-yl) (methyl) amino) propyl) (methyl) carbamate (31b)*. Silica-gel column chromatography (CH<sub>2</sub>Cl<sub>2</sub>:MeOH gradient, 1:0 to 20:1). Pale oil, 379 mg (yield 90%). <sup>1</sup>H NMR (300 MHz, CDCl<sub>3</sub>): δ 1.43 (s, 9.1H), 1.48 (t, *J* = 4.5, 3.2H), 1.81 (m, 2H), 2.87 (s, 3.1H), 3.17 (t, *J* = 6.5, 1.9H), 3.15 (s, 2H), 3.36 (s, 1.1H), 3.45 (t, *J* = 7.1, 0.9H), 3.73 (t, *J* = 6.5, 1.1H), 4.77 (q, *J* = 6.5, 2H), 5.06 (br s, 0.5H). ESI-HRMS (+) *m/z* (%): Calcd for C<sub>16</sub>H<sub>26</sub>N<sub>2</sub>O<sub>5</sub>Na<sup>+</sup> [M + Na]<sup>+</sup> 349.1734, found: 349.1734.



*tert-butyl (3-((2-ethoxy-3,4-dioxocyclobut-1-en-1-yl) (methyl) amino) propyl) carbamate (31c)*. Silica-gel column chromatography (CH<sub>2</sub>Cl<sub>2</sub>:MeOH gradient, 1:0 to 20:1). Pale oil, 351 mg (yield 98%). <sup>1</sup>H NMR (300 MHz, CDCl<sub>3</sub>): δ 1.44 (s, 9H), 1.47 (t, *J* = 4.8, 3H), 1.80 (m, 2H), 3.15 (t, *J* = 6.5, 2 H), 3.15 (s, 2H), 3.34 (s, 1H), 3.45 (t, *J* = 7.1, 0.8H), 3.73 (t, *J* = 6.5, 1.2H), 4.77 (q, *J* = 6.5, 2H), 5.06 (br s, 0.5H). ESI-HRMS (+) *m/z* (%): Calcd for C<sub>15</sub>H<sub>24</sub>N<sub>2</sub>O<sub>5</sub>Na<sup>+</sup> [M + Na]<sup>+</sup> 335.1577, found: 335.1560.



*tert-butyl (2-((2-ethoxy-3,4-dioxocyclobut-1-en-1-yl) (methyl) amino) ethyl) carbamate (31d)*. Precipitation with Et<sub>2</sub>O, white solid. 295 mg (yield 55%). <sup>1</sup>H NMR (300 MHz, CDCl<sub>3</sub>): δ 1.44 (s, 9H), 1.47 (t, *J* = 4.8, 3H), 3.22 (s, 2H), 3.39 (s, 1H), 3.40 (q, *J* = 5.8, 2 H), 3.47 (t, *J* = 5.8, 0.7H), 3.71 (t, *J* = 5.6, 1.4H), 4.64 (br s, 0.5H) 4.74 (q, *J* = 7.1, 2H). ESI-HRMS (+) *m/z* (%): Calcd for C<sub>14</sub>H<sub>22</sub>N<sub>2</sub>O<sub>5</sub>Na<sup>+</sup> [M + Na]<sup>+</sup> 321.1421, found: 321.1421.

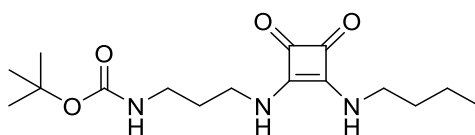


*tert-butyl (4-((2-ethoxy-3,4-dioxocyclobut-1-en-1-yl) (methyl) amino) butyl) carbamate (31e)*. Silica-gel column chromatography (CH<sub>2</sub>Cl<sub>2</sub>:MeOH gradient, 1:0 to 20:1). Pale oil, 166 mg, yield 34 %. <sup>1</sup>H NMR (300 MHz, CDCl<sub>3</sub>): δ 4.77 (qd, *J* = 7.0, 2.0, 2H), 4.63 (br s, 0.5H), 4.55 (br s, 0.5H), 3.69 (t, *J* = 7.1, 1.2H), 3.41 (t, *J* = 7.1, 1H), 3.32 (s,

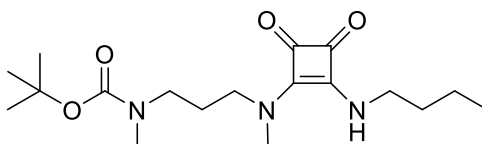
1.5H), 3.16 (s, 1.5H), 3.16 (t,  $J = 6.5$ , 2 H), 1.6 (m, 2H), 1.50 (m, 2H), 1.47 (m, 2H), 1.46 (t, 3H), 1.44 (s, 9H). ESI-HRMS (+)  $m/z$  (%): Calcd for  $C_{16}H_{26}N_2O_5Na^+$  [ $M + Na$ ] $^+$  349.1734, found: 349.1734.

*General procedure for synthesis of amino butylamine-self-immolative systems 33a-e.*

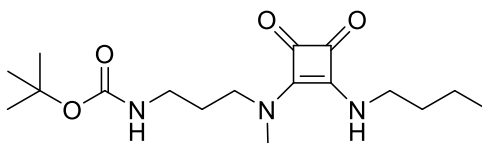
The corresponding squaramate ester **31a-e** (1 equiv) and *n*-butylamine (1.1 equiv) were dissolved in EtOH (0.05M). The reaction mixture was stirred overnight at room temperature. After reaction time, the solvent was removed and further purified either by precipitation or by silica-gel chromatography. The resulting *N*-Boc protected compound is treated with HCl or trifluoroacetic acid to afford the final product as an ammonium salt.



*tert-butyl (3-((2-(butylamino)-3,4-dioxocyclobut-1-en-1-yl) amino) propyl) carbamate (32a).* Precipitation with Et<sub>2</sub>O. White amorphous solid, 136 mg (yield 62%). <sup>1</sup>H NMR (600 MHz, CDCl<sub>3</sub>):  $\delta$  0.86 (t,  $J = 7.3$  Hz, 4.3H), 1.28 (m,  $J = 7.4$  Hz, 2.1H), 1.35 (s, 9.4H), 1.47 (m,  $J = 7.4$  Hz, 3.3H), 1.60 (m,  $J = 6.7$  Hz, 2.1H), 2.94 (q,  $J = 7.0$  Hz, 2H), 3.46 (br s, 5H), 6.81 (br s, 0.8H), 7.32 (br s, 2H). ESI-HRMS (+)  $m/z$  (%): Calcd for  $C_{16}H_{27}N_3O_4Na^+$  [ $M + Na$ ] $^+$  348.1894, found: 348.1891.

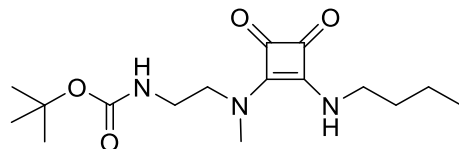


*tert-butyl (3-((2-(butylamino) -3,4-dioxocyclobut-1-en-1-yl) (methyl) amino) propyl) (methyl)carbamate (32b).* Silica-gel column chromatography (CH<sub>2</sub>Cl<sub>2</sub>:MeOH gradient, 40:1 to 20:1). Pale oil, 76 mg (yield 72%). <sup>1</sup>H NMR (300 MHz, CDCl<sub>3</sub>):  $\delta$  0.94 (t,  $J = 7.2$  Hz, 3.1H), 1.38 (m,  $J = 7.3$  Hz, 2.1H), 1.43 (s, 9.1H), 1.62 (m, 2H), 1.81 (m, 2H), 2.87 (s, 3.1H), 3.17 (t,  $J = 6.5$ , 1.9H), 3.15 (s, 2H), 3.36 (s, 1.1H), 3.45 (t,  $J = 7.1$ , 0.9H), 3.73 (t,  $J = 6.5$ , 1.1H), 4.77 (q,  $J = 6.5$ , 2H), 5.06 (br s, 0.5H). ESI-HRMS (+)  $m/z$  (%): Calcd for  $C_{18}H_{31}N_3O_4Na^+$  [ $M + Na$ ] $^+$  376.2207, found: 376.2207.

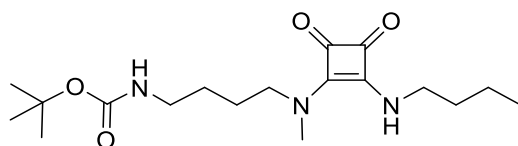


*tert-butyl (3-((2-(butylamino)-3,4-dioxocyclobut-1-en-1-yl) (methyl) amino) propyl) carbamate (32c).* Silica-gel column chromatography (CH<sub>2</sub>Cl<sub>2</sub>:MeOH gradient, 40:1 to 20:1). Pale oil, 378 mg (yield 97%). <sup>1</sup>H NMR (600 MHz, CDCl<sub>3</sub>):  $\delta$  0.95 (t,  $J = 7.3$  Hz,

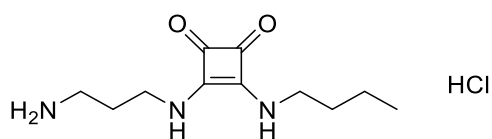
3H), 1.38 (m,  $J = 7.6$  Hz, 2.3H), 1.44 (s, 9.6H), 1.62 (m, 4.3H), 1.84 (m,  $J = 6.6$  Hz, 2H), 3.16 (q,  $J = 6.2$  Hz, 2.2H), 3.24 (s, 2.8H), 3.57 (t,  $J = 7.8$  Hz, 2H), 3.74 (q,  $J = 6.8$  Hz, 2H), 5.10 (s, 0.8H), 5.66 (s, 0.7 H). ESI-HRMS (+)  $m/z$  (%): Calcd for  $C_{17}H_{29}N_3O_4Na^+$   $[M + Na]^+$  362.2050, found: 362.2051.



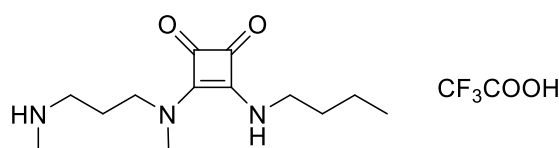
*tert-butyl (2-((2-(butylamino)-3,4-dioxocyclobut-1-en-1-yl) (methyl) amino) ethyl) carbamate (32d)*. Precipitation with pentane, white solid. 277 mg yield (90%).  $^1H$  NMR (300 MHz,  $CDCl_3$ ):  $\delta$  0.93 (t,  $J = 7.3$ , 2H), 1.39 (m,  $J = 7.1$ , 2H), 1.44 (s, 9H), 1.63 (m,  $J = 7.3$ , 2H), 3.26 (m, 2H), 3.38 (s, 5H), 3.76 (q,  $J = 6.6$ , 2H), 5.04 (t,  $J = 5.8$ , 1H), 7.61 (br s, 0.6H). ESI-HRMS (+)  $m/z$  (%): Calcd for  $C_{16}H_{27}N_3O_4Na^+$   $[M + Na]^+$  348.1894, found: 348.1892.



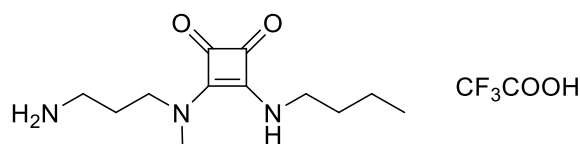
*tert-butyl (4-((2-(butylamino)-3,4-dioxocyclobut-1-en-1-yl) (methyl) amino) butyl) carbamate (32e)*. Silica-gel column chromatography ( $CH_2Cl_2$ :MeOH gradient, 40:1 to 20:1). Pale oil, 109 mg (yield 65%).  $^1H$  NMR (300 MHz,  $CDCl_3$ ):  $\delta$  0.94 (t,  $J = 7.3$ , 3H), 1.40 (m, 2H), 1.44 (s, 9H), 1.54 (m, 2H), 1.68 (m, 2H), 3.48 (q,  $J = 7.1$ , 2H), 3.29 (s, 3H), 3.48 (t,  $J = 7.08$ , 1H), 3.76 (q,  $J = 6.6$ , 2H), 4.66 (br s, 0.9H). ESI-HRMS (+)  $m/z$  (%): Calcd for  $C_{18}H_{31}N_3O_4Na^+$   $[M + Na]^+$  376.2207, found: 376.2206.



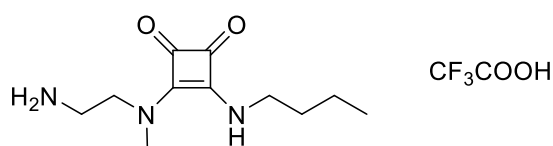
*3-((2-(butylamino)-3,4-dioxocyclobut-1-en-1-yl) amino) propan-1-aminium (33a)*. Grey amorphous solid. 27 mg (yield 88%).  $^1H$  NMR (300 MHz,  $D_2O$ ):  $\delta$  0.91 (t,  $J = 7.4$  Hz, 3.1H), 1.37 (m,  $J = 7.5$ , 2.1H), 1.60 (m,  $J = 7.1$ , 2.0), 2.02 (m,  $J = 7.1$ , 2.0), 3.09 (t,  $J = 7.6$  Hz, 2.1), 3.61 (br s, 1.9H), 3.71 (br s, 1.9H).  $^{13}C$  NMR (150 MHz,  $D_2O$ ):  $\delta$  13.0, 19.0, 28.4, 32.4, 36.7, 41.1, 44.2, 168.2, 168.5, 181.2, 182.0. ESI-HRMS (+)  $m/z$  (%): Calcd for  $C_{11}H_{20}N_3O_2^+$   $[M + H]^+$  226.1539, found: 226.1542.



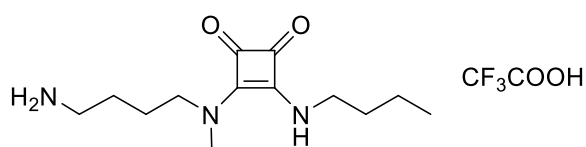
3-((2-(butylamino)-3,4-dioxocyclobut-1-en-1-yl) (methyl) amino) -N-methylpropan-1-aminium-trifluoroacetate (**33b**). Pale oil, 45 mg (yield 91 %).  $^1\text{H}$  NMR (600 MHz,  $\text{D}_2\text{O}$ ):  $\delta$  0.82 (t,  $J = 7.4$  Hz, 2.9H), 1.26 (m,  $J = 7.4$  Hz, 2H), 1.51 (m,  $J = 7.2$  Hz, 2.3H), 1.98 (m,  $J = 7.3$ , 3.7H), 2.63 (s, 2.7H), 2.99 (t,  $J = 7.8$  Hz, 2.7H), 3.15 (s, 3.1H), 3.54 (t,  $J = 6.9$  Hz, 1.8H), 3.64 (t,  $J = 6.6$  Hz, 2H).  $^{13}\text{C}$  NMR (150 MHz,  $\text{D}_2\text{O}$ ):  $\delta$  13.6, 19.1, 23.4, 23.9, 32.2, 33.1, 43.0, 45.3, 54.4, 167.0, 167.4, 181.9, 182.2. ESI-HRMS (+) m/z (%): Calcd for  $\text{C}_{13}\text{H}_{24}\text{N}_3\text{O}_2^+$  [M + H] $^+$  254.1863, found: 254.1862.



3-((2-(butylamino)-3,4-dioxocyclobut-1-en-1-yl) (methyl) amino) propan-1-aminium-trifluoroacetate (**33c**). Digestion with pentane. Pale oil, 412 mg (yield 98%).  $^1\text{H}$  NMR (300 MHz,  $\text{DMSO-}d_6$ ):  $\delta$  0.82 (t,  $J = 7.2$  Hz, 2.9H), 1.32 (m,  $J = 7.4$  Hz, 2H), 1.54 (m,  $J = 7.2$  Hz, 2H), 1.83 (m,  $J = 7.2$ , 1.9H), 2.80 (m,  $J = 7.5$  Hz, 1.9H), 3.15 (s, 3.1H), 3.57 (m, 3.6 H), 7.72 (s, 2.8H).  $^{13}\text{C}$  NMR (75 MHz,  $\text{DMSO-}d_6$ ):  $\delta$  13.6, 19.1, 25.7, 33.1, 36.3, 43.2, 48.1, 167.5, 181.8, 182.4. ESI-HRMS (+) m/z (%): Calcd for  $\text{C}_{12}\text{H}_{22}\text{N}_3\text{O}_2^+$  [M + H] $^+$ : 240.1707. Found: 240.1696.

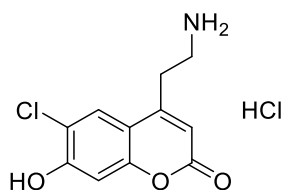


2-((2-(butylamino)-3,4-dioxocyclobut-1-en-1-yl) (methyl) amino) ethan-1-aminium-trifluoroacetate (**33d**). Precipitation from pentane. White amorphous solid, 270 mg (yield 95%), white solid.  $^1\text{H}$  NMR (300 MHz,  $\text{CDCl}_3$ ):  $\delta$  0.89 (t,  $J = 7.9$  Hz, 3H), 1.32 (m,  $J = 7.4$  Hz, 2H), 1.50 (m,  $J = 7.2$  Hz, 2H), 2.60 (t,  $J = 6.5$  Hz, 2.7H), 3.12 (m,  $J = 6.0$  Hz, 2H), 3.52 (s, 1.6H), 3.76 (q,  $J = 6.1$  Hz, 1.9H), 7.62 (s, 1.4H), 7.85 (s, 0.3H), 8.53 (s, 1.7H).  $^{13}\text{C}$  NMR (150 MHz,  $\text{DMSO-}d_6$ ):  $\delta$  13.5, 19.0, 32.6, 32.7, 43.0, 48.9, 158.2, 158.4, 182.3. ESI-HRMS (+) m/z (%): Calcd for  $\text{C}_{11}\text{H}_{20}\text{N}_3\text{O}_2^+$  [M + H] $^+$  226.1550, found: 226.1538.

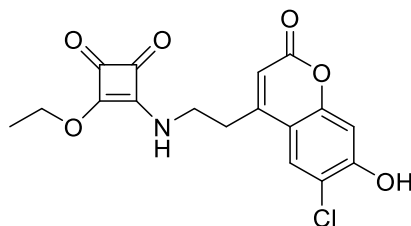


4-((2-(butylamino)-3,4-dioxocyclobut-1-en-1-yl) (methyl) amino) butan-1-aminium-trifluoroacetate (**33e**). Digestion with pentane. Pale oil, 102 mg (yield 91%).  $^1\text{H}$  NMR (300 MHz,  $\text{CDCl}_3$ ):  $\delta$  0.89 (t,  $J = 7.4$  Hz, 3H), 1.31 (m,  $J = 7.4$  Hz, 2H), 1.52 (m, 4H), 1.59 (m,  $J = 7.5$  Hz, 2H), 2.81 (m,  $J = 6.5$  Hz, 2H), 3.14 (s, 2.9H), 3.55 (q,  $J = 6.9$  Hz,

3.7H), 7.68 (s, 3.7H).  $^{13}\text{C}$  NMR (150 MHz, DMSO- $d_6$ ):  $\delta$  13.7, 19.1, 23.7, 24.1, 33.1, 36.1, 38.5, 43.1, 50.0, 158.1, 158.3, 167.6, 181.8, 182.2. ESI-HRMS (+)  $m/z$  (%): Calcd for  $\text{C}_{13}\text{H}_{24}\text{N}_3\text{O}_2^+$   $[\text{M} + \text{H}]^+$ : 254.1863, found: 240.1857.

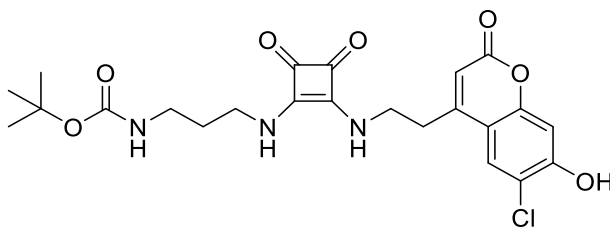


*2-(6-chloro-7-hydroxy-2-oxo-2H-chromen-4-yl)ethan-1-aminium chloride (FFN102)*.  
The data obtained are in agreement with those reported on the literature.<sup>223</sup>

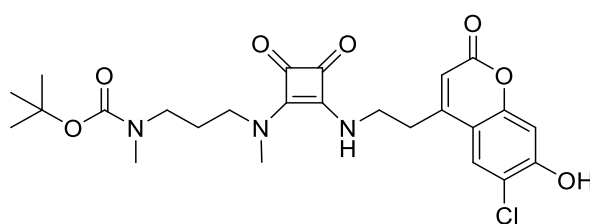


*3-((2-(6-chloro-7-hydroxy-2-oxo-2H-chromen-4-yl)ethyl)amino)-4-ethoxycyclobut-3-ene-1,2-dione (34)*. 180 mg (0.65 mmol) of **FFN102** and 122 mg (0.72 mmol) of diethyl squarate are suspended in a mixture of EtOH: Borax buffer pH 9 (1:1, 10 mL) and stirred overnight at room temperature for 16 h. After the reaction time, the resulting yellow solid is filtered out and washed with  $\text{H}_2\text{O}$  ( $3 \times 10$  mL) and EtOH ( $3 \times 5$  mL) and dried under vacuum and  $\text{P}_2\text{O}_5$ . Pale yellow amorphous solid, 318 mg (yield 90%).  $^1\text{H}$  NMR (300 MHz DMSO- $d_6$ ):  $\delta$  1.26 (t,  $J = 7.1$  Hz, 2.1H), 1.35 (t,  $J = 7.2$  Hz, 1.4H), 3.00 (t,  $J = 6.4$  Hz, 2.1H), 3.58 (q,  $J = 6.6$  Hz, 1.2H), 3.76 (q,  $J = 7.1$  Hz, 0.9H), 4.54 (q,  $J = 7.1$  Hz, 1H), 4.61 (q,  $J = 7.1$  Hz, 1H), 6.18 (s, 0.9H), 6.90 (s, 1H), 7.85 (s, 0.6H), 7.88 (s, 0.3H), 8.63 (t,  $J = 6.2$  Hz, 0.4H), 8.83 (t,  $J = 5.6$  Hz, 0.5H), 11.39 (s, 0.6H). ESI-HRMS (+)  $m/z$  (%): Calcd for  $\text{C}_{17}\text{H}_{14}\text{NO}_6\text{ClNa}^+$   $[\text{M} + \text{Na}]^+$  386.0402, found: 386.0402.

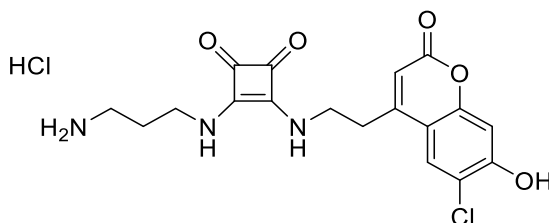
*General procedure for the synthesis of coumarin-loaded self-immolative systems 36a and 36b*. Squaramate ester **34** (1 equiv), the corresponding amine (1.1 equiv) and  $\text{K}_2\text{CO}_3$  (2 equiv) are suspended in EtOH (0.01M) and the suspension is stirred at 60 °C for 16 h. The resulting solution is cooled down to 0 °C in a water-ice bath and the resulting solid is centrifuged, washed with  $\text{H}_2\text{O}$  ( $3 \times 2$  mL) and dried under vacuum with  $\text{P}_2\text{O}_5$ . Then, the Boc-protected system was treated with a HCl 1N:EtOH (1:1, 0.05M) at 50 °C for 16 h. After the reaction time, the solvent was removed by rotary evaporation and the resulting solid was washed with  $\text{H}_2\text{O}$  ( $3 \times 2$  mL) and dried under vacuum and  $\text{P}_2\text{O}_5$  to afford the final products as ammonium salts.



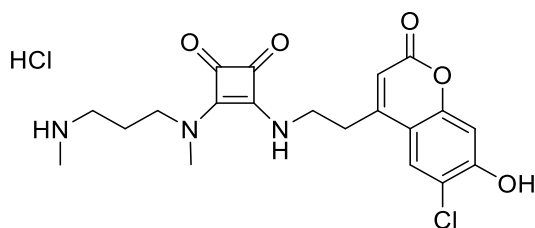
*tert-butyl (3-((2-((2-(6-chloro-7-hydroxy-2-oxo-2H-chromen-4-yl) ethyl) amino) -3,4-dioxocyclobut-1-en-1-yl) amino) propyl) carbamate (35a)*. Pale yellow amorphous solid, 116 mg (yield 34%).  $^1\text{H}$  NMR (300 MHz, DMSO- $d_6$ ):  $\delta$  1.42 (s, 9.5H), 1.71 (s, 2H), 3.08 (dt, 4.1H), 3.56 (s, 1.8H), 3.91 (2H), 6.02 (s, 1H), 6.53 (0.5H), 7.69 (s, 0.9H). ESI-HRMS (+)  $m/z$  (%): Calcd for  $\text{C}_{23}\text{H}_{26}\text{N}_3\text{O}_7\text{ClNa}^+$   $[\text{M} + \text{Na}]^+$  514.1351, found: 514.1358.



*tert-butyl (3-((2-((2-(6-chloro-7-hydroxy-2-oxo-2H-chromen-4-yl) ethyl) amino) -3,4-dioxocyclobut-1-en-1-yl) (methyl) amino) propyl) (methyl) carbamate (35b)*. Yellow amorphous solid, 30 mg (yield 84%).  $^1\text{H}$  NMR (300 MHz, DMSO- $d_6$ ):  $\delta$  1.41 (s, 9.1H), 1.79 (s, 2H), 2.8 (s, 2.5H), 3.09 (s, 4.7H), 3.28 (s, 2.7H), 3.65 (s, 1.2H), 3.99 (2H), 6.06 (s, 1H), 6.54 (s, 0.5H), 7.73 (s, 0.8H). ESI-HRMS (-)  $m/z$  (%): Calcd for  $\text{C}_{25}\text{H}_{29}\text{N}_3\text{O}_7\text{Cl}^-$   $[\text{M}]^-$  518.1700, found: 518.1696.

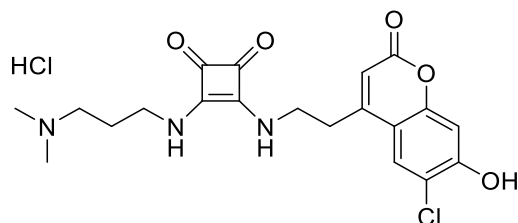


*3-((2-((3-((2-(6-chloro-7-hydroxy-2-oxo-2H-chromen-4-yl) ethyl) amino) propyl) amino)-3,4-dioxocyclobut-1-en-1-yl) amino)propan-1-aminium chloride (36a)*. Pale yellow amorphous solid, 29 mg, (yield 93%).  $^1\text{H}$  NMR (300 MHz,  $\text{D}_2\text{O}$ , 10% DMSO- $d_6$ ):  $\delta$  1.96 (m,  $J = 7.0$  Hz, 2H), 3.04 (t,  $J = 7.6$  Hz, 2.1H), 3.12 (t,  $J = 5.9$  Hz, 2.2H), 3.60 (t,  $J = 6.7$  Hz, 2H), 3.92 (t,  $J = 6.7$  Hz, 2.1H), 6.33 (s, 1H), 6.97 (0.8H), 7.87 (s, 1H).  $^{13}\text{C}$  NMR (600 MHz, DMSO- $d_6$ ):  $\delta$  28.9, 33.2, 36.3, 40.4, 42.2, 103.6, 111.8, 111.9, 117.1, 126.0, 152.8, 153.3, 156.4, 159.8, 168.0, 182.2, 182.4. ESI-HRMS (+)  $m/z$  (%): Calcd for  $\text{C}_{18}\text{H}_{19}\text{N}_3\text{O}_5\text{Cl}^+$   $[\text{M} + \text{H}]^+$  392.1008, found: 392.1008, 414.0828  $[\text{M} + \text{Na}]^+$ .

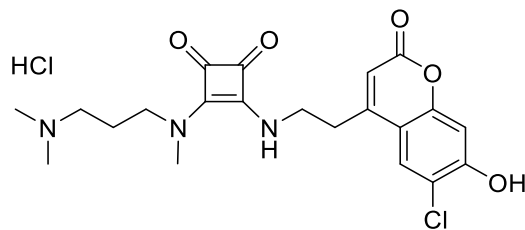


3-((2-((2-(6-chloro-7-hydroxy-2-oxo-2H-chromen-4-yl)ethyl)amino)-3,4-dioxocyclobut-1-en-1-yl)(methyl)amino)-N-methylpropan-1-aminium (**36b**). Yellow solid, 20 mg (yield 99%).  $^1\text{H}$  NMR (300 MHz,  $\text{D}_2\text{O}$ , 10%  $\text{DMSO-d}_6$ ):  $\delta$  2.02 (m, 2.6H), 2.74 (s, 3.7H), 2.76 (3H), 3.03 (t, 2.7H), 3.67 (q, 2.7H), 3.95 (t, 2.2H), 6.36 (s, 1H), 6.99 (s, 1H), 7.93 (s, 1H).  $^{13}\text{C}$  NMR (600 MHz,  $\text{DMSO-d}_6$ ):  $\delta$  23.9, 38.5, 32.2, 33.3, 42.6, 45.2, 103.6, 111.9, 112.2, 117.1, 126.1, 153.3, 156.3, 159.8, 167.4, 180.4, 181.5. ESI-HRMS (+)  $m/z$  (%): Calcd for  $\text{C}_{20}\text{H}_{23}\text{N}_3\text{O}_5\text{Cl}^+ [\text{M} + \text{H}]^+$  420.1321, found: 420.1320.

*General procedure for the synthesis of coumarin-loaded systems 36c and 36d.* Squaramate ester **34** (1 equiv), the corresponding amine (1.1 equiv) and  $\text{K}_2\text{CO}_3$  (2 equiv) are suspended in EtOH (0.01M) and the suspension is stirred at 60 °C for 16 h. The resulting solution is cooled down to 0 °C in a water-ice bath and the resulting solid is centrifuged and redissolved in hot water. The solution is acidified with HCl 1N until no more precipitate is observed. The solid is filtered out and dried under vacuum and  $\text{P}_2\text{O}_5$ .



3-((2-((2-(6-chloro-7-hydroxy-2-oxo-2H-chromen-4-yl)ethyl)amino)-3,4-dioxocyclobut-1-en-1-yl)amino)-N,N-dimethylpropan-1-aminium chloride (**36c**). Pale yellow solid, 40 mg (yield 42%).  $^1\text{H}$  NMR ( $\text{D}_2\text{O}$ , 10%  $\text{DMSO-d}_6$ ):  $\delta$  1.92 (m, 2H), 2.90 (s, 6.3H), 3.09 (m, 4.3H), 3.57 (m, 2.2H), 3.94 (m, 2.2H), 6.07 (s, 1H), 6.54 (s, 0.5H), 7.72 (s, 1H).  $^{13}\text{C}$  NMR (600 MHz,  $\text{DMSO-d}_6$ ):  $\delta$  26.6, 33.1, 40.8, 42.3, 43.0, 54.6, 103.6, 111.4, 111.5, 117.5, 125.9, 153.0, 153.5, 157.2, 159.9, 168.0, 182.3, 182.5. ESI-HRMS (+)  $m/z$  (%): Calcd for  $\text{C}_{20}\text{H}_{23}\text{N}_3\text{O}_5\text{Cl}^+ [\text{M} + \text{H}]^+$  420.1321, found: 420.1321.



3-((2-((2-(6-chloro-7-hydroxy-2-oxo-2H-chromen-4-yl)ethyl)amino)-3,4-dioxocyclobut-1-en-1-yl)(methyl)amino)-N,N-dimethylpropan-1-aminium chloride (**36d**). Yellow solid, 15 mg (yield 36%).  $^1\text{H}$  NMR ( $\text{D}_2\text{O}$ , 10%  $\text{DMSO-d}_6$ ):  $\delta$  1.94 (m, 2.3H), 2.75 (s, 9.5H), 2.97 (t, 1.5H), 3.04 (m), 3.13 (m) (10H), 3.83 (t, 2.2H), 6.20 (s, 1.1H), 6.95 (s, 1.4H), 7.96 (s, 1H), 8.00 (br s, 0.8H), 8.86 (br s, 0.2H).  $^{13}\text{C}$  NMR (600 MHz,  $\text{DMSO-d}_6$ ):  $\delta$  22.2, 25.8, 29.2, 30.1, 33.3, 42.0, 48.0, 53.7, 103.5, 111.8, 111.2, 117.1, 126.0, 153.2, 153.4, 156.3, 159.8, 169.3, 181.3, 182.4. ESI-HRMS (+)  $m/z$  (%): Calcd for  $\text{C}_{21}\text{H}_{25}\text{N}_3\text{O}_5\text{Cl}^+ [\text{M} + \text{H}]^+$  434.1477, found: 434.1479.

#### 5.5.4. NMR Spectra of Selected Compounds

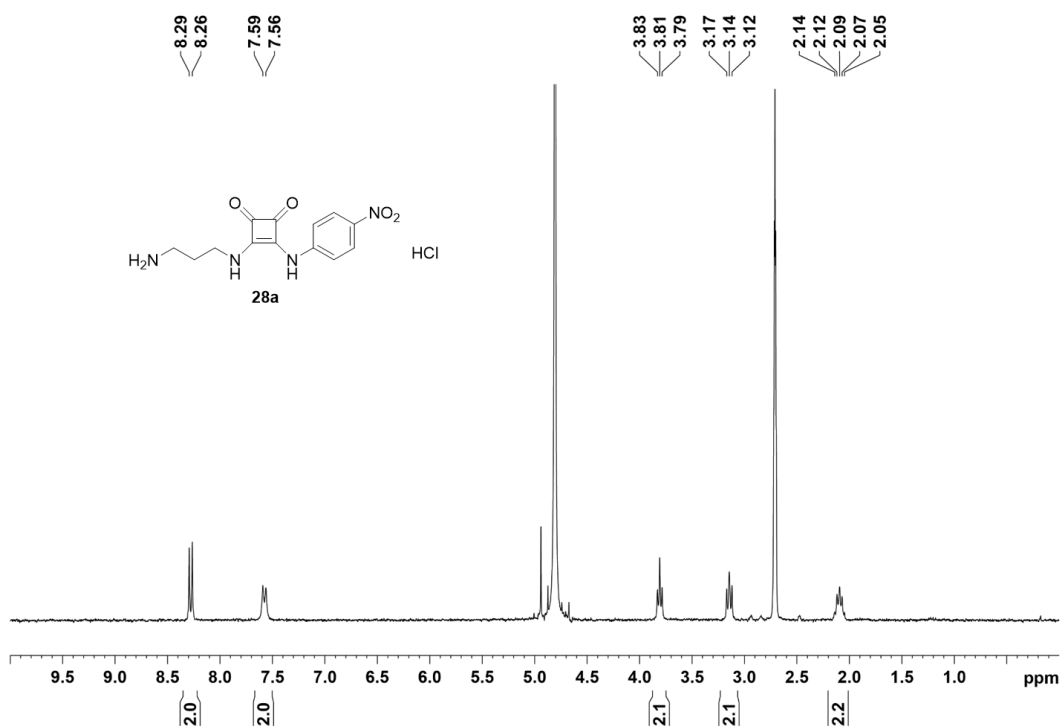


Figure 5.36.  $^1\text{H}$  NMR spectrum of **28a** in  $\text{D}_2\text{O}$ , 10%  $\text{DMSO-d}_6$ , 300 MHz, 298 K.

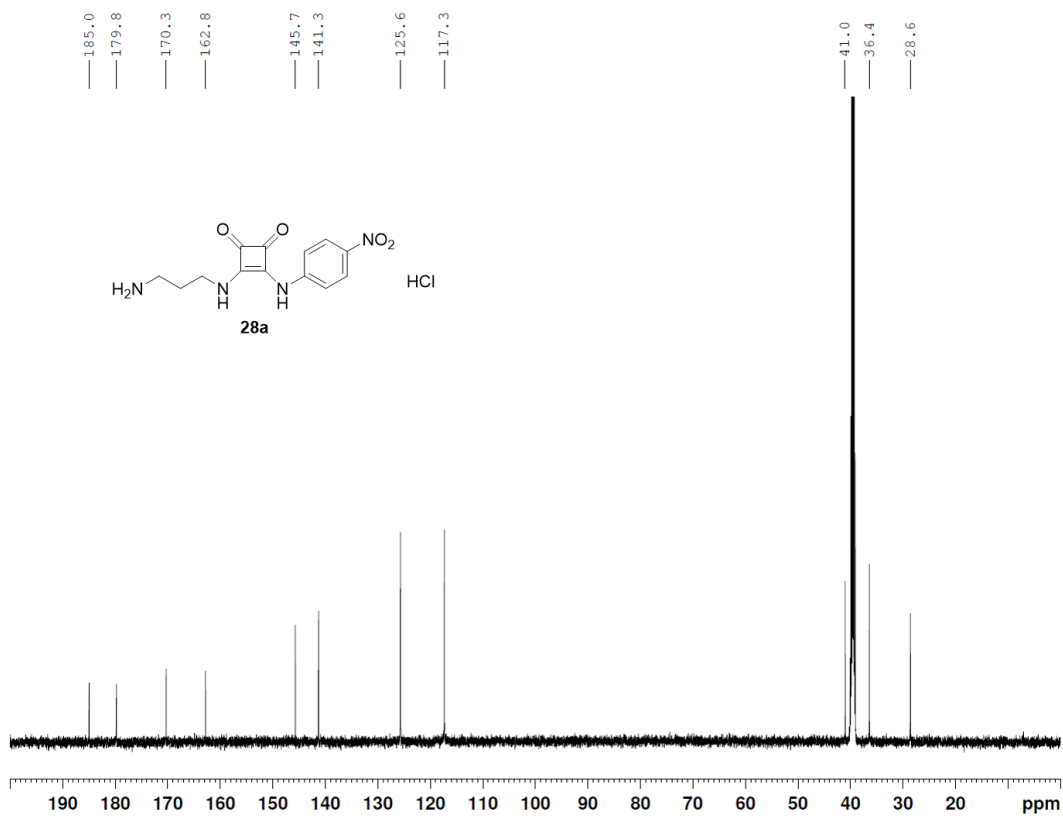


Figure 5.37. <sup>13</sup>C NMR spectrum of **28a** DMSO-*d*<sub>6</sub>, 150 MHz, 298 K.

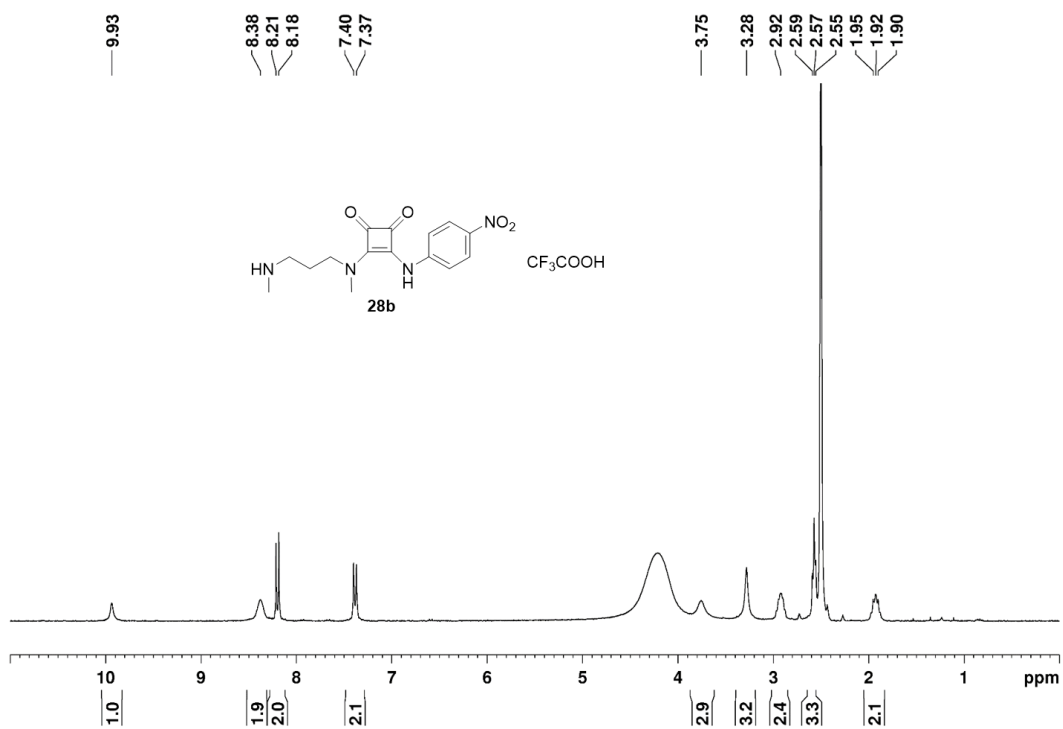


Figure 5.38. <sup>1</sup>H NMR spectrum of **28b** DMSO-*d*<sub>6</sub>, 300 MHz, 298 K.

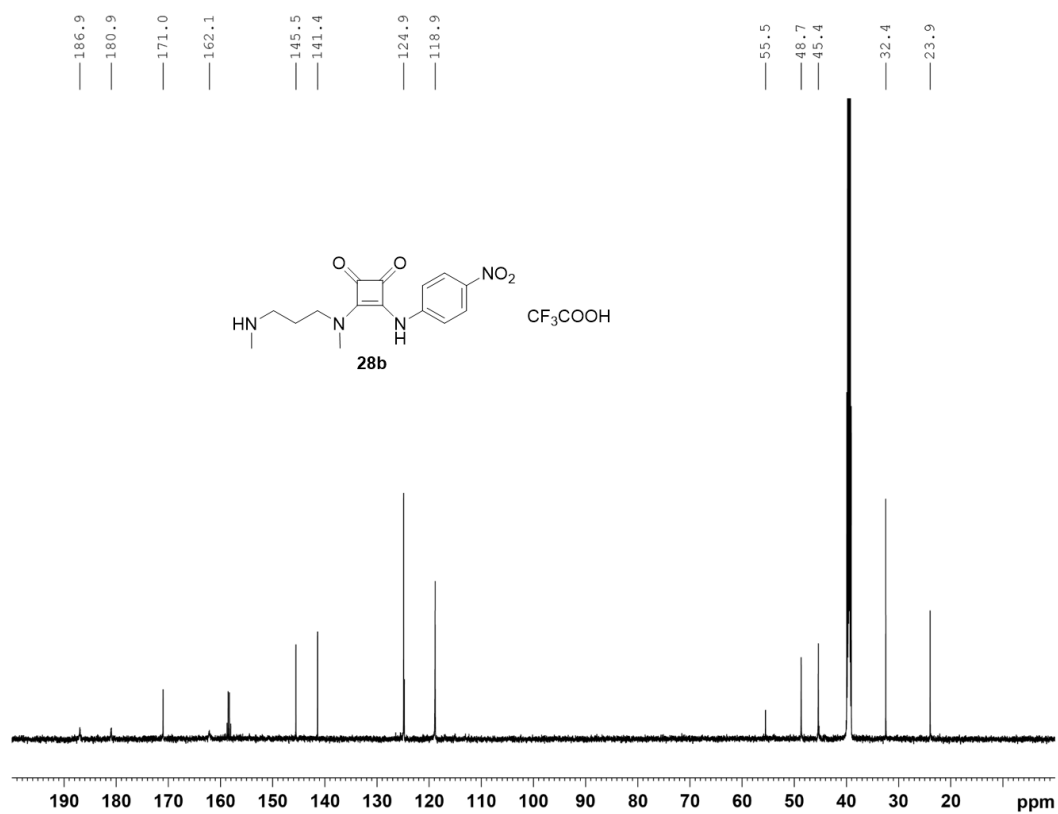


Figure 5.39.  $^{13}\text{C}$  NMR spectrum of **28b** DMSO- $d_6$ , 150 MHz, 298 K.

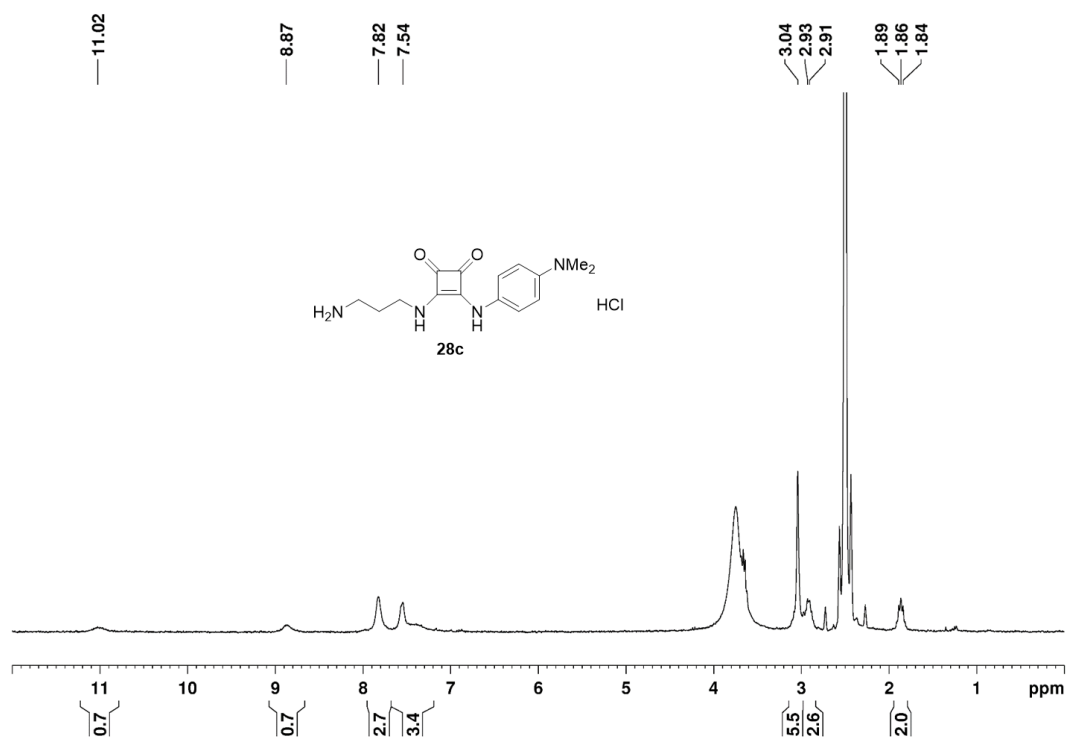


Figure 5.40.  $^1\text{H}$  NMR spectrum of **28c** DMSO- $d_6$ , 300 MHz, 298 K.

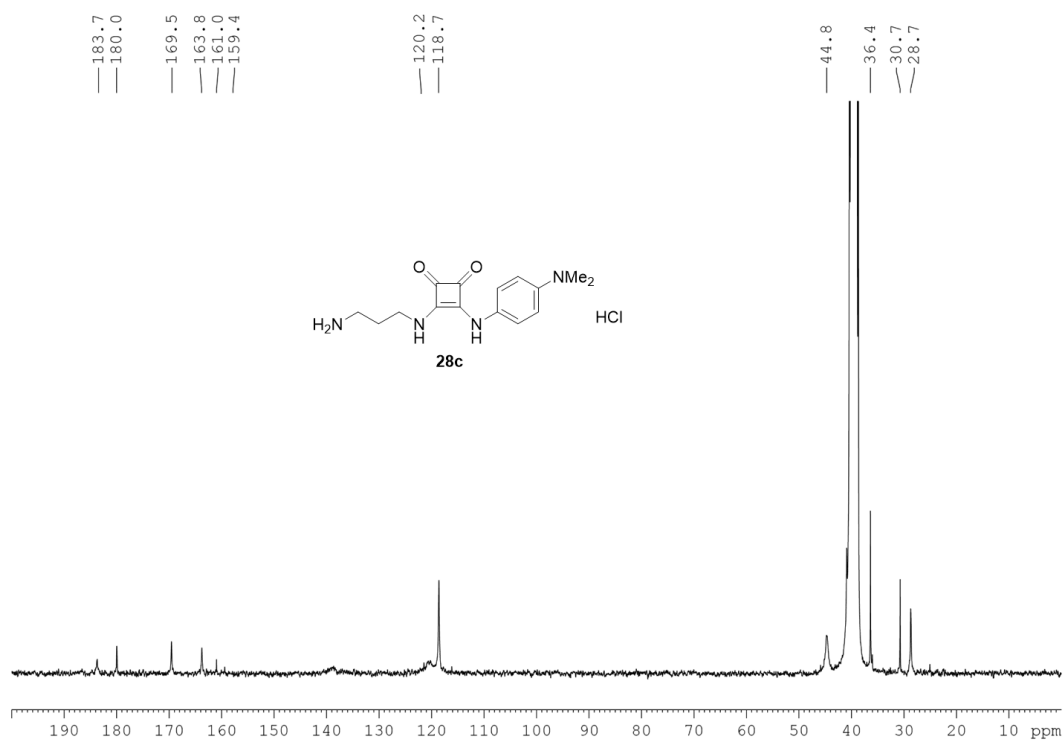


Figure 5.41.  $^{13}\text{C}$  NMR spectrum of **28c** DMSO- $d_6$ , 75 MHz, 298 K.

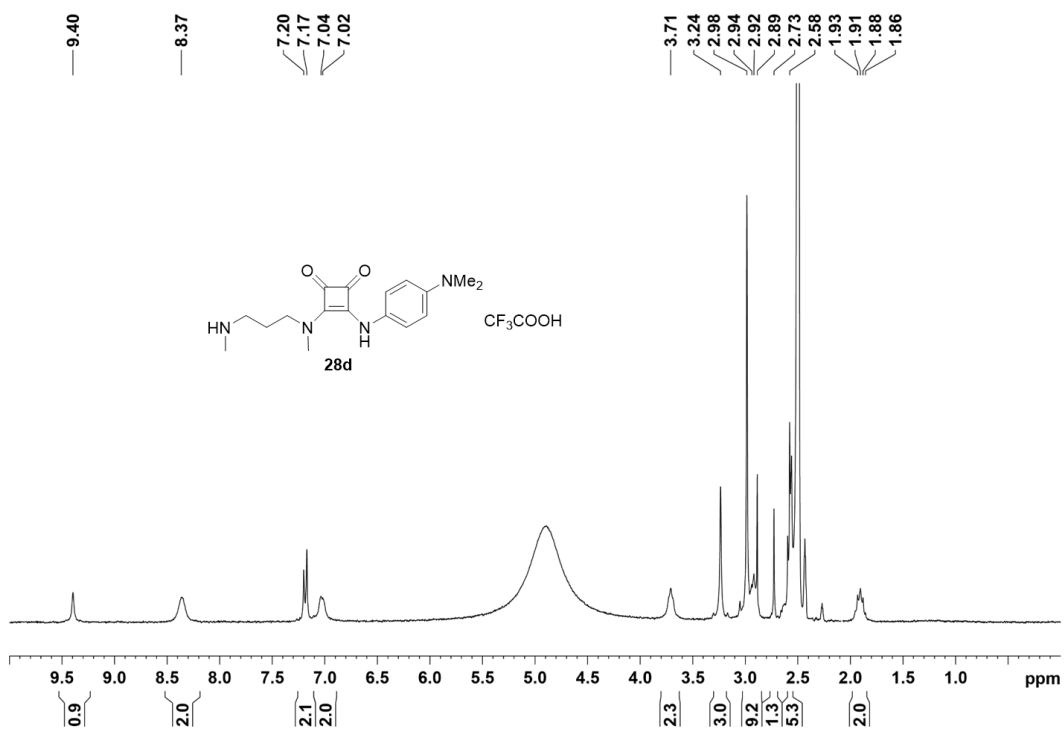


Figure 5.42.  $^1\text{H}$  NMR spectrum of **28d** DMSO- $d_6$ , 300 MHz, 298 K.

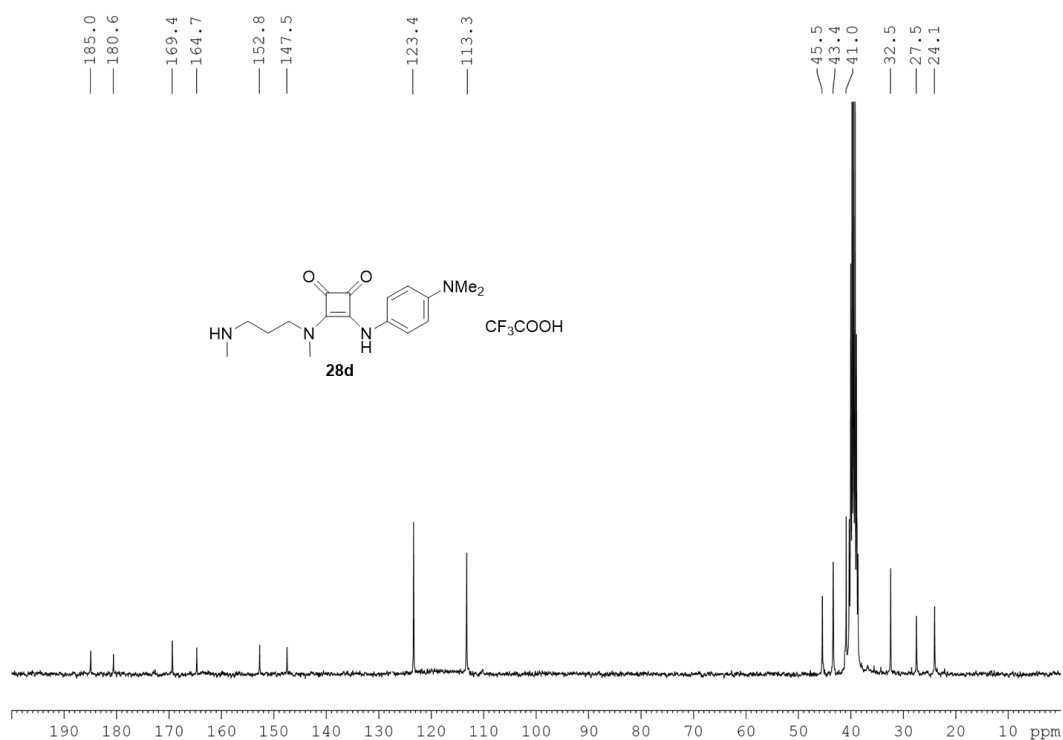


Figure 5.43. <sup>13</sup>C NMR spectrum of **28d** DMSO, 75 MHz, 298 K.

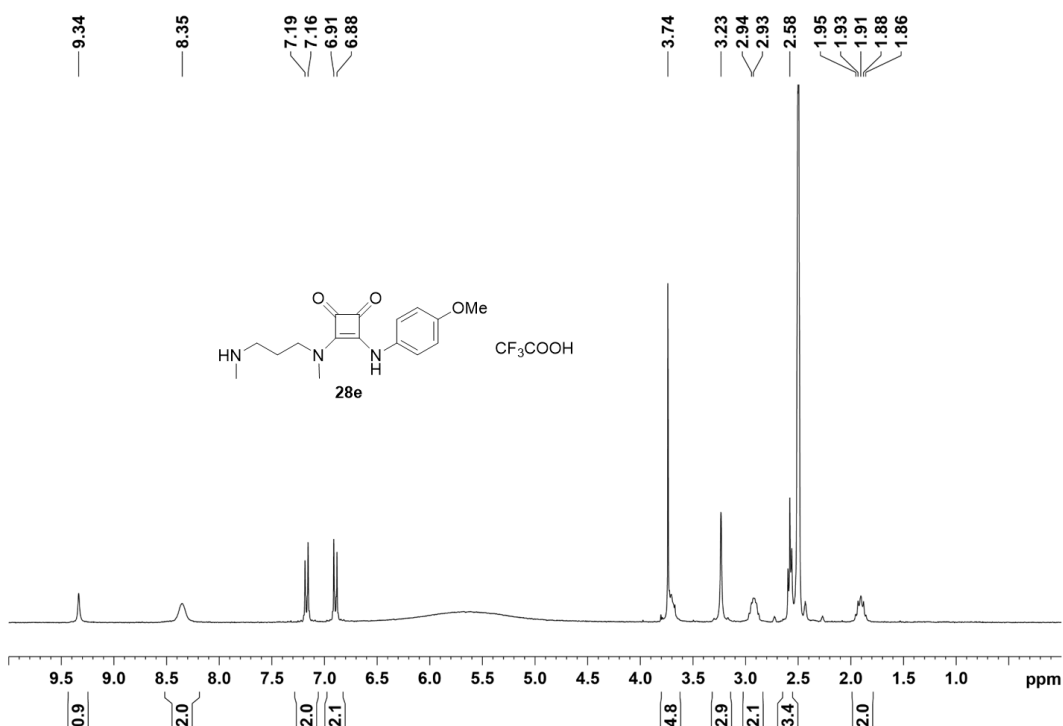


Figure 5.44. <sup>1</sup>H NMR spectrum of **28e** DMSO-*d*<sub>6</sub>, 300 MHz, 298 K.

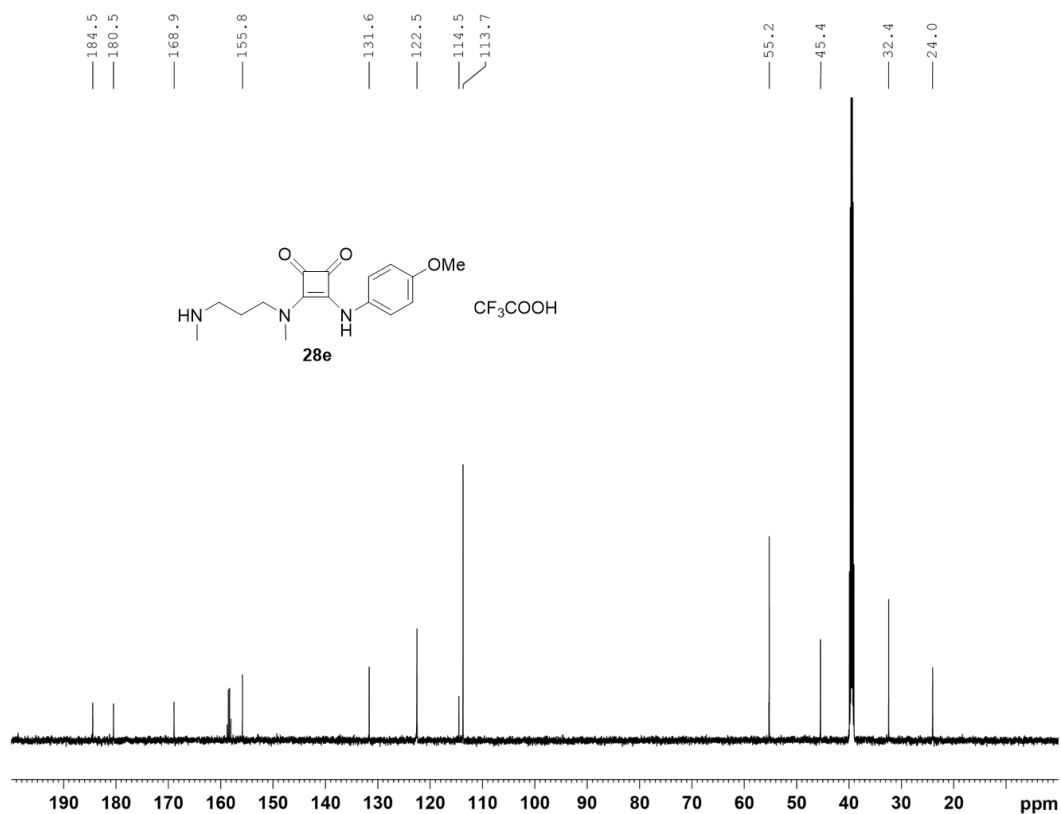


Figure 5.45.  $^{13}\text{C}$  NMR spectrum of **28e** DMSO, 75 MHz, 298 K.

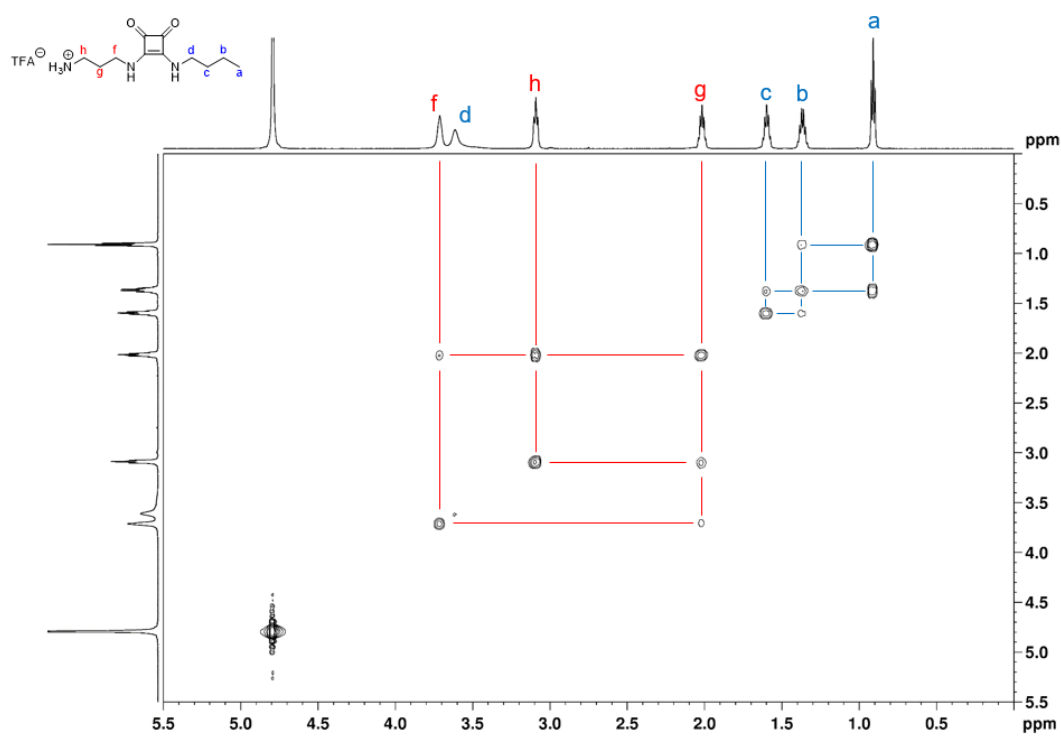


Figure 5.46.  $^1\text{H}$ - $^1\text{H}$ -COSY spectrum of **33a** in  $\text{D}_2\text{O}$ , 600 MHz, 298 K.

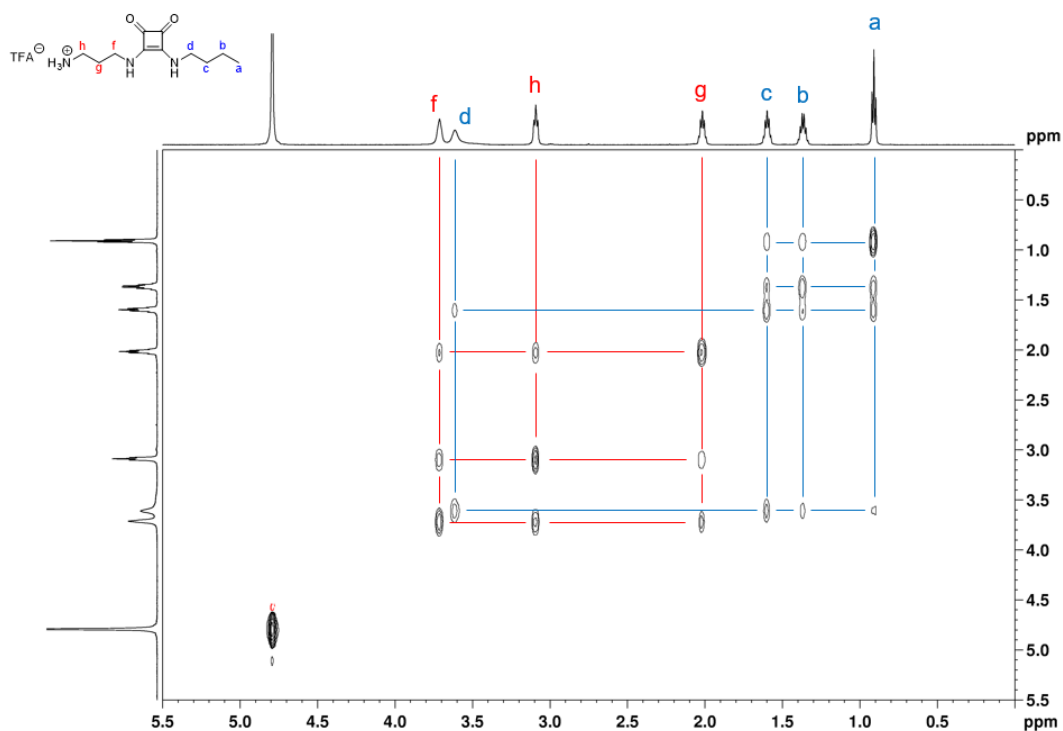


Figure 5.47.  $^1\text{H}$ - $^1\text{H}$ -TOCSY spectrum of **33a** in  $\text{D}_2\text{O}$ , 600 MHz, 298 K.

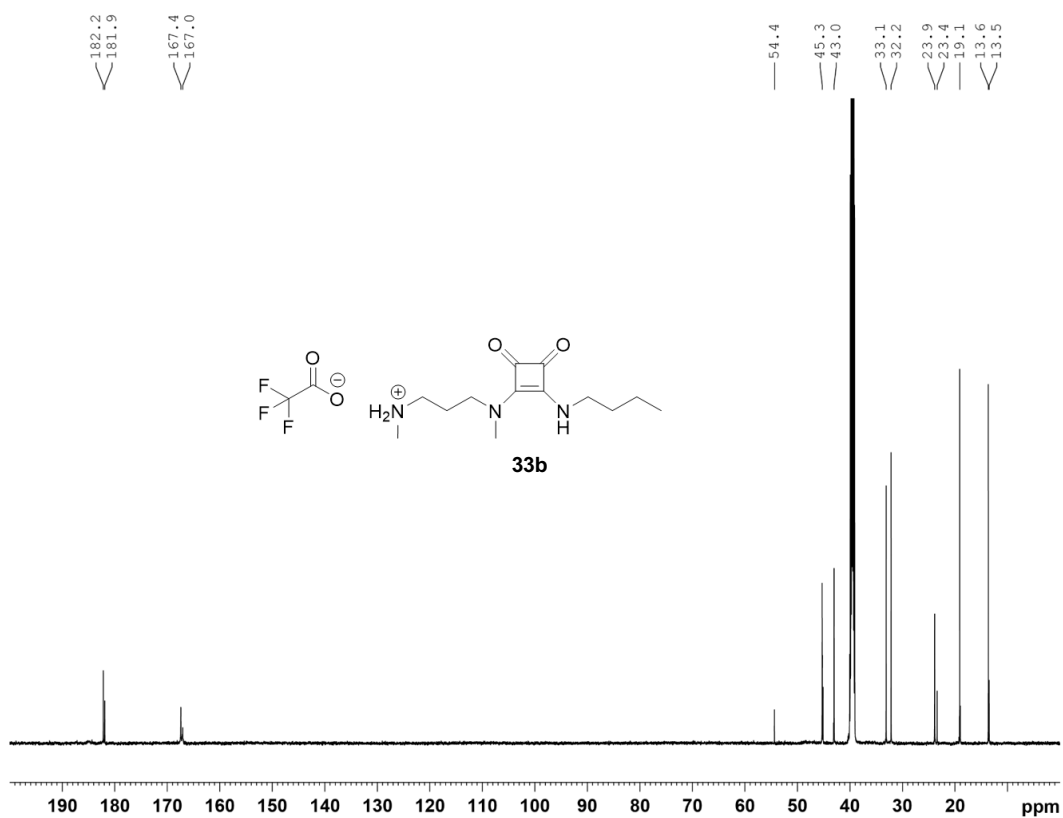
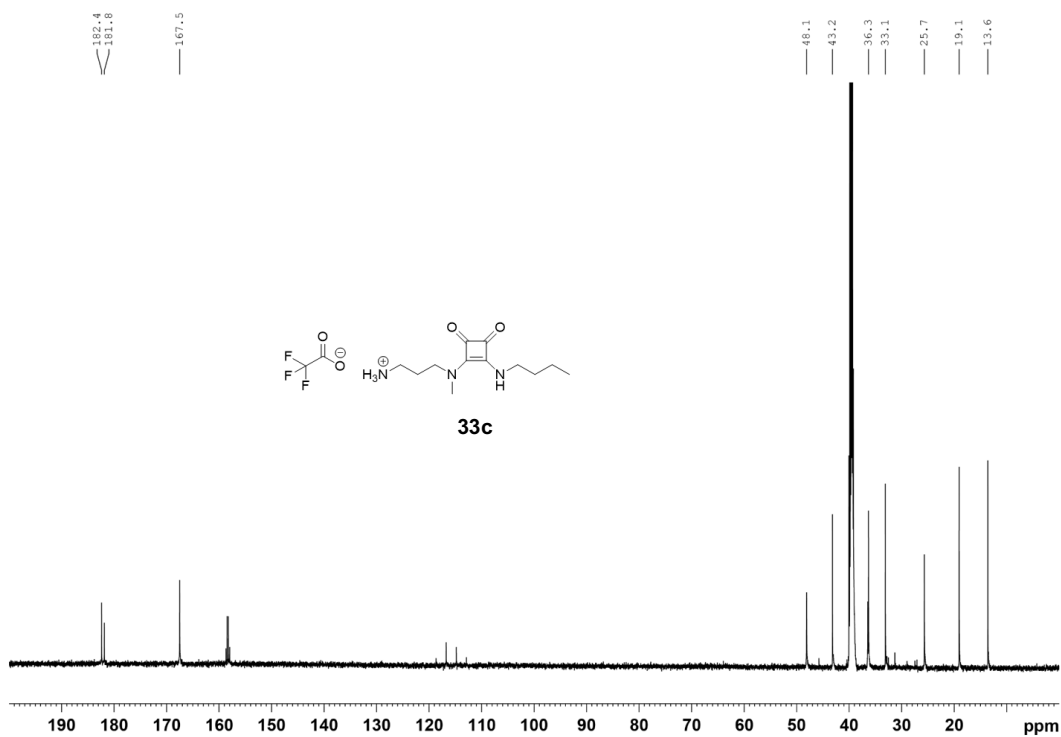
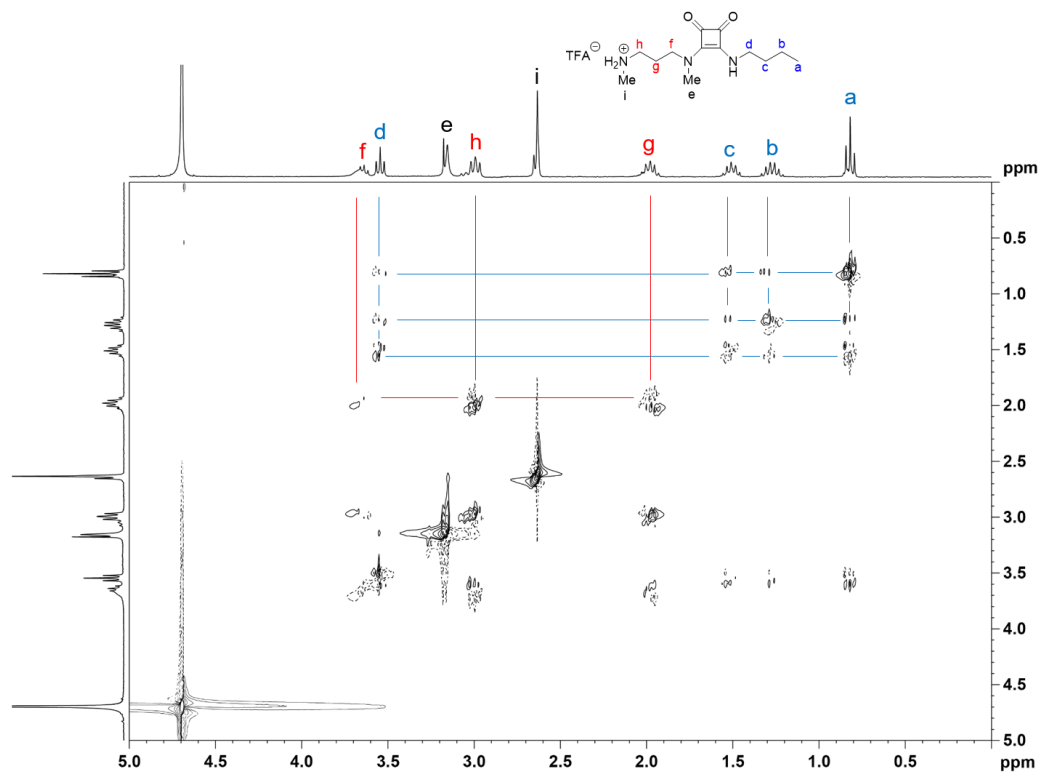


Figure 5.48.  $^{13}\text{C}$  NMR spectrum of **33b** in  $\text{DMSO-}d_6$ , 600 MHz, 298 K.



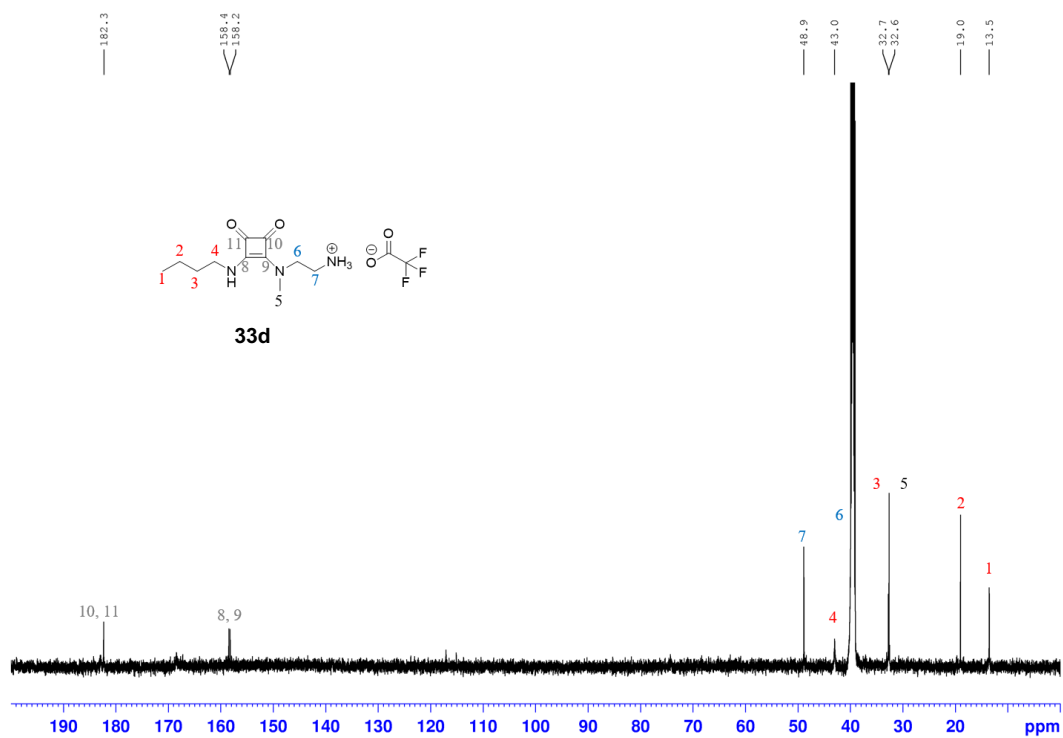


Figure 5.51.  $^{13}\text{C}$  NMR spectrum of **33d** in  $\text{DMSO-}d_6$ , 600 MHz, 298 K.

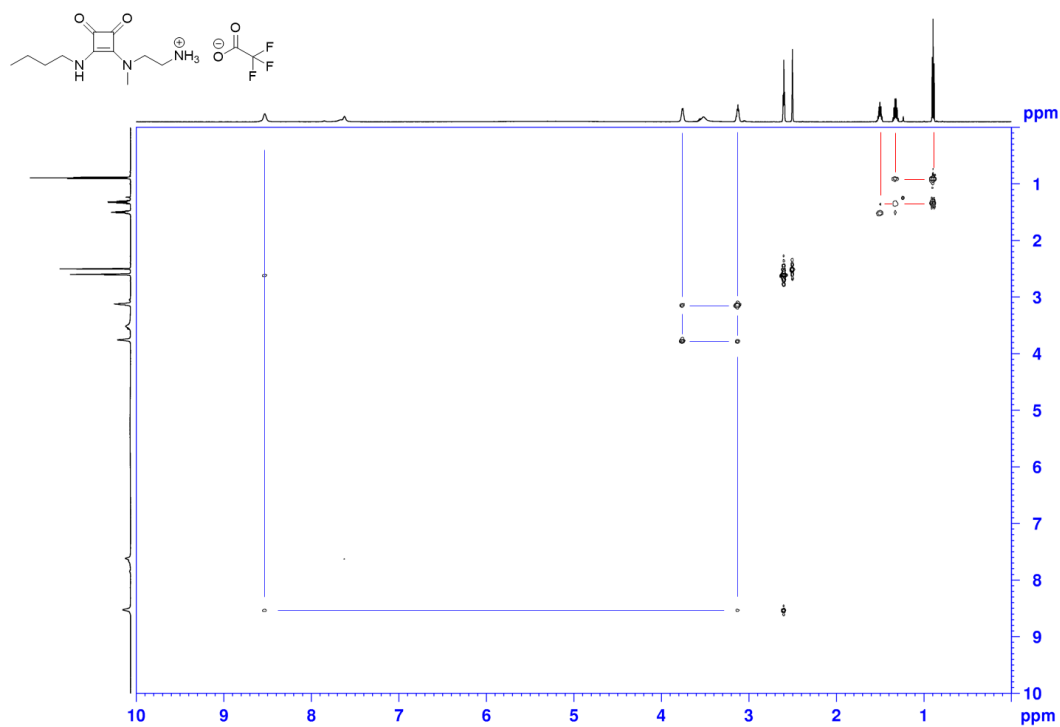


Figure 5.52.  $^1\text{H-}^1\text{H}$  COSY experiment of **33d** in  $\text{DMSO-}d_6$ , 600 MHz, 298 K.

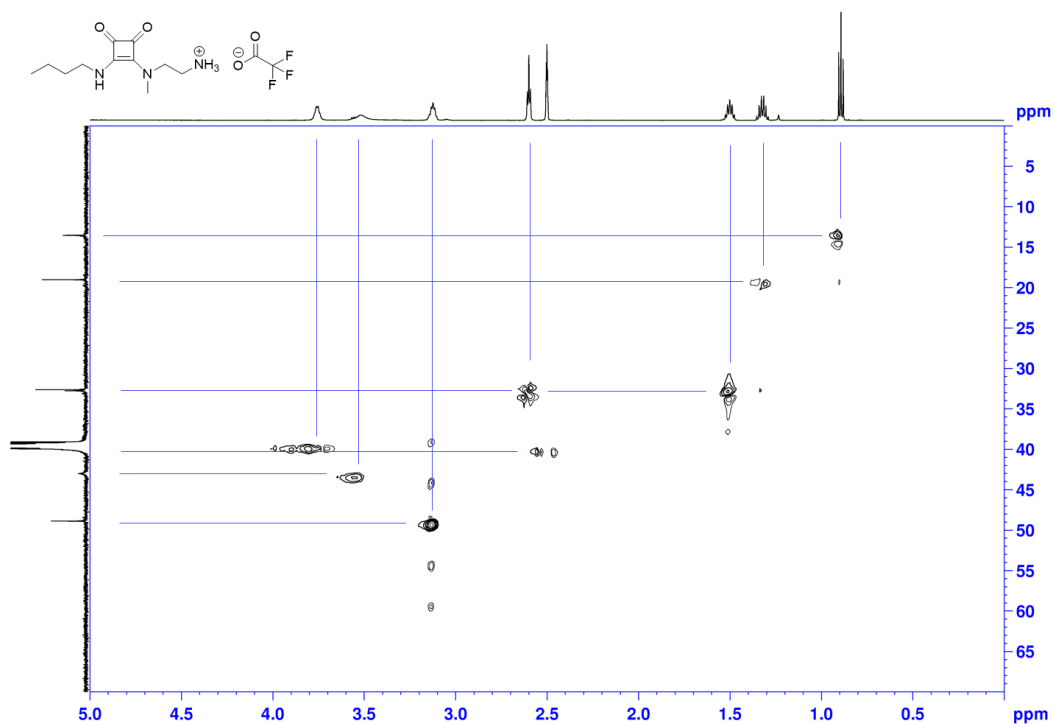


Figure 5.53.  $^1\text{H}$ - $^{13}\text{C}$  HSQC experiment of **33d** in  $\text{DMSO-}d_6$ , 600 MHz, 298 K.

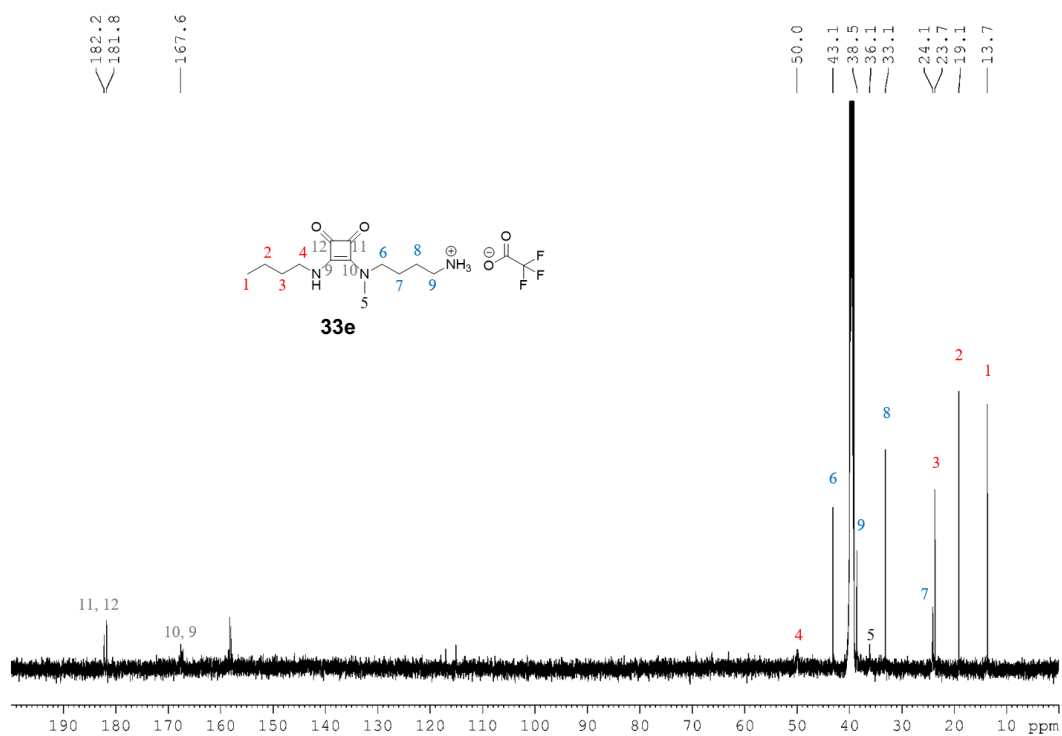
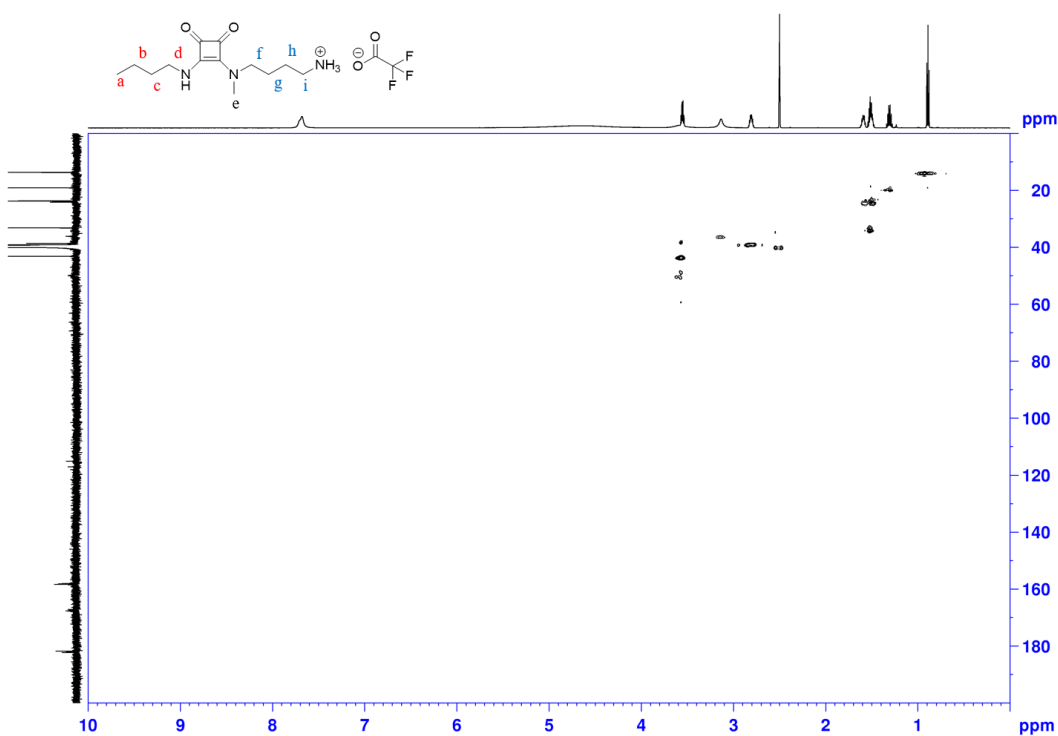
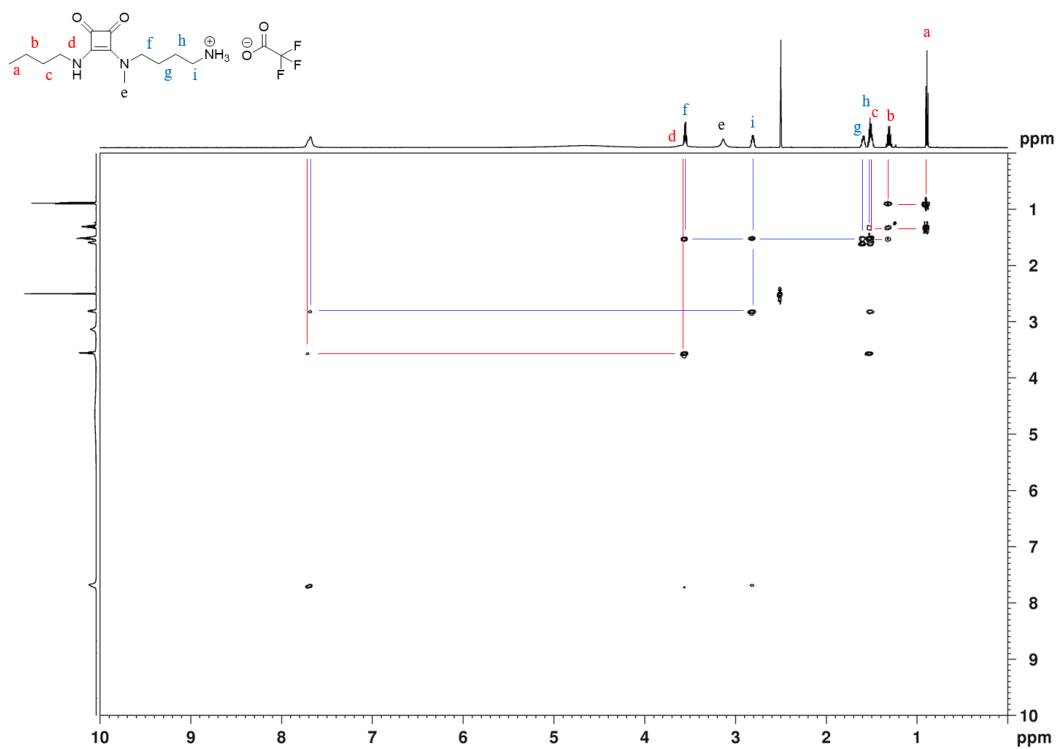


Figure 5.54.  $^{13}\text{C}$  NMR spectrum of **33e** in  $\text{DMSO-}d_6$ , 600 MHz, 298 K.



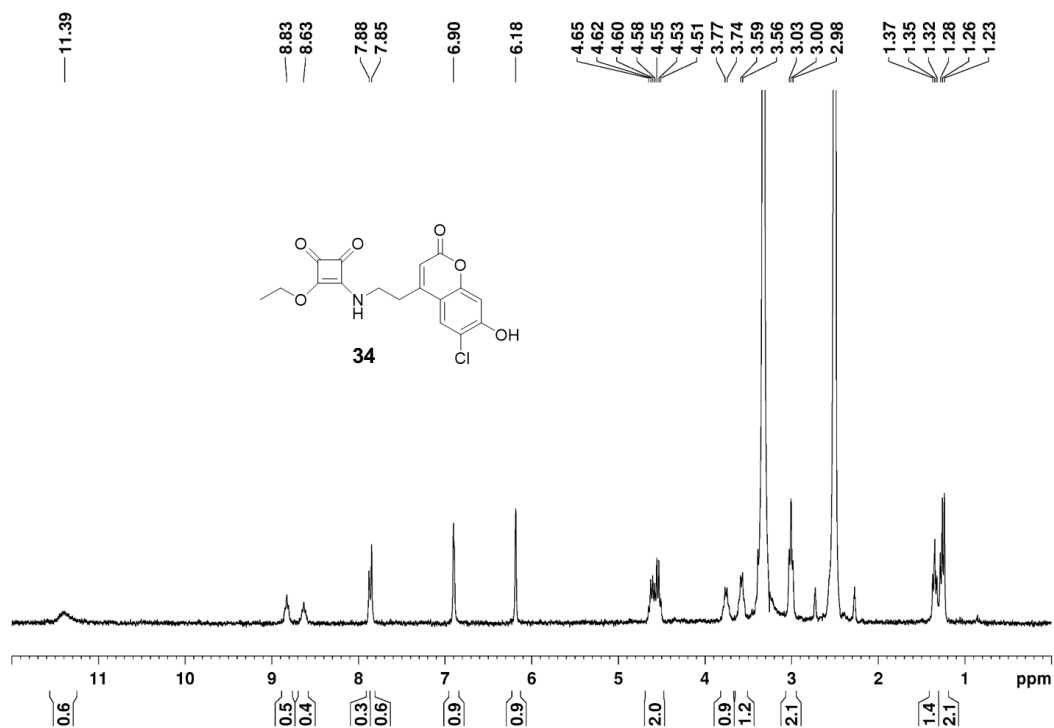


Figure 5.57.  $^1\text{H}$  NMR experiment of **34** in  $\text{DMSO-}d_6$ , 300 MHz, 298 K.

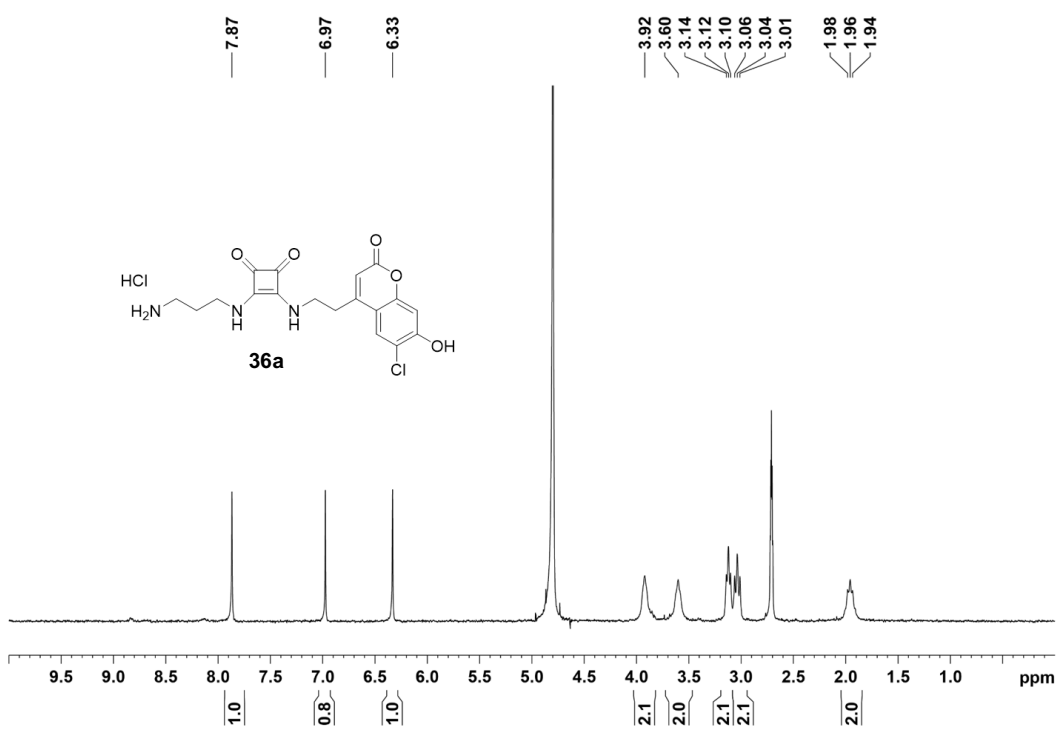


Figure 5.58.  $^1\text{H}$  NMR experiment of **36a** in  $\text{D}_2\text{O}$ , 5%  $\text{DMSO-}d_6$ , 300 MHz, 298 K.

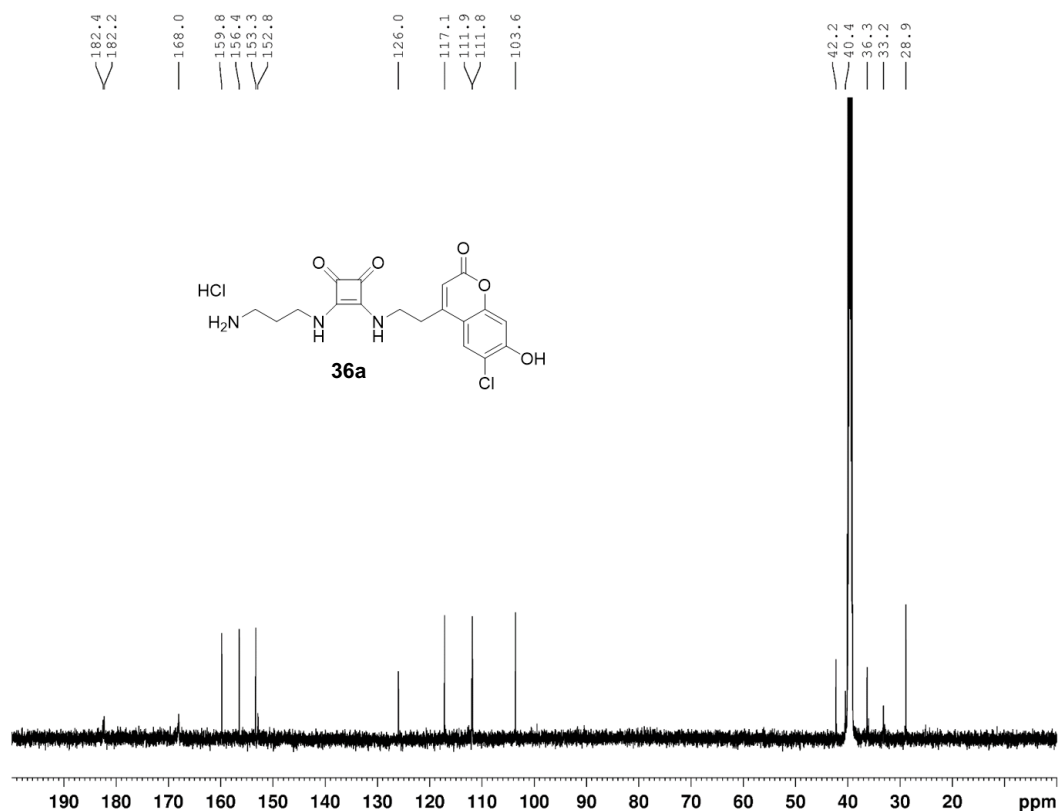


Figure 5.59.  $^{13}\text{C}$  NMR experiment of **36a** in  $\text{DMSO-}d_6$ , 600 MHz, 298 K.

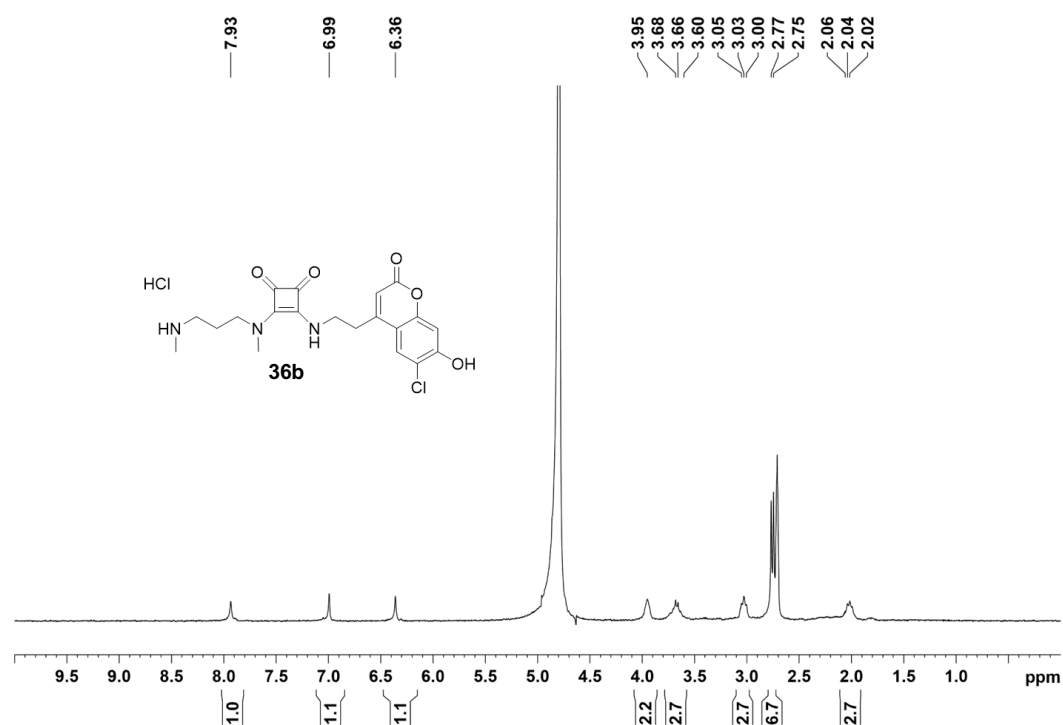


Figure 5.60.  $^1\text{H}$  NMR experiment of **36b** in  $\text{D}_2\text{O}$ , 5%  $\text{DMSO-}d_6$ , 300 MHz, 298 K.

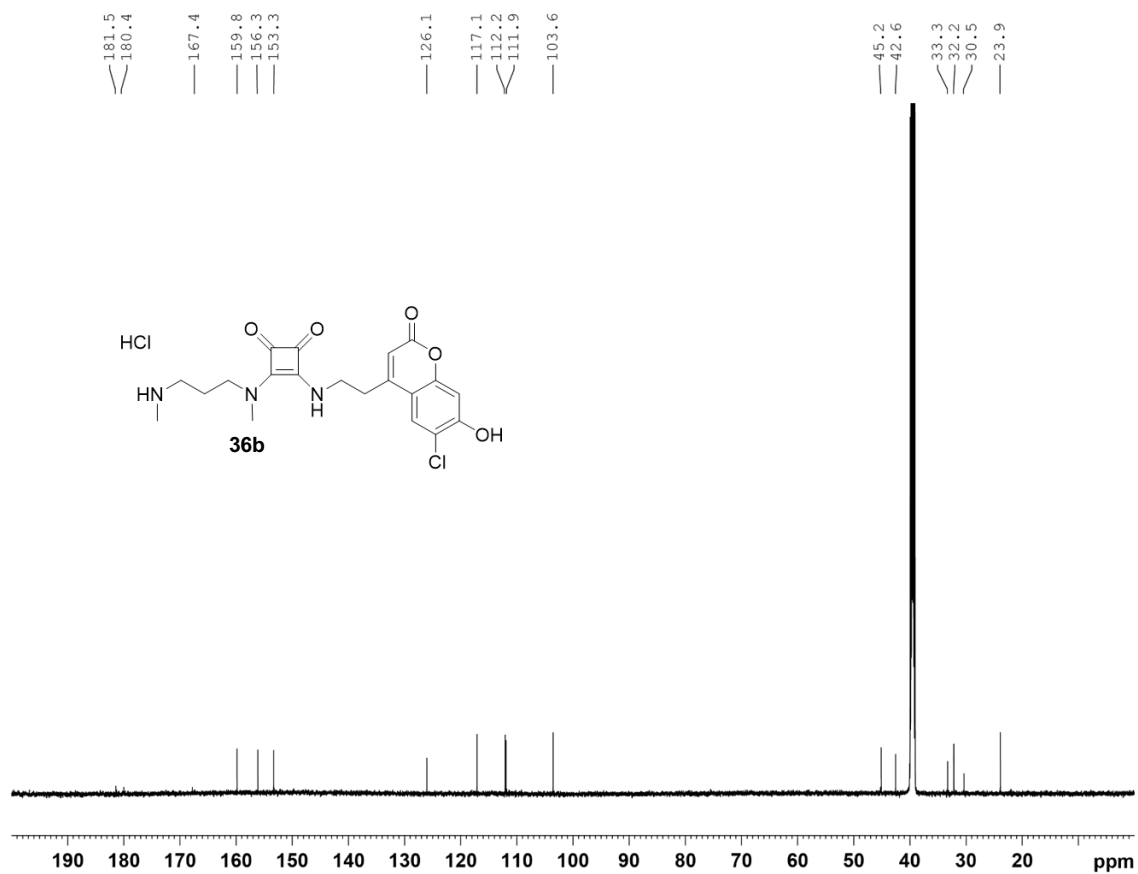


Figure 5.61.  $^{13}\text{C}$  NMR experiment of **36b** in  $\text{DMSO-}d_6$ , 600 MHz, 298 K.

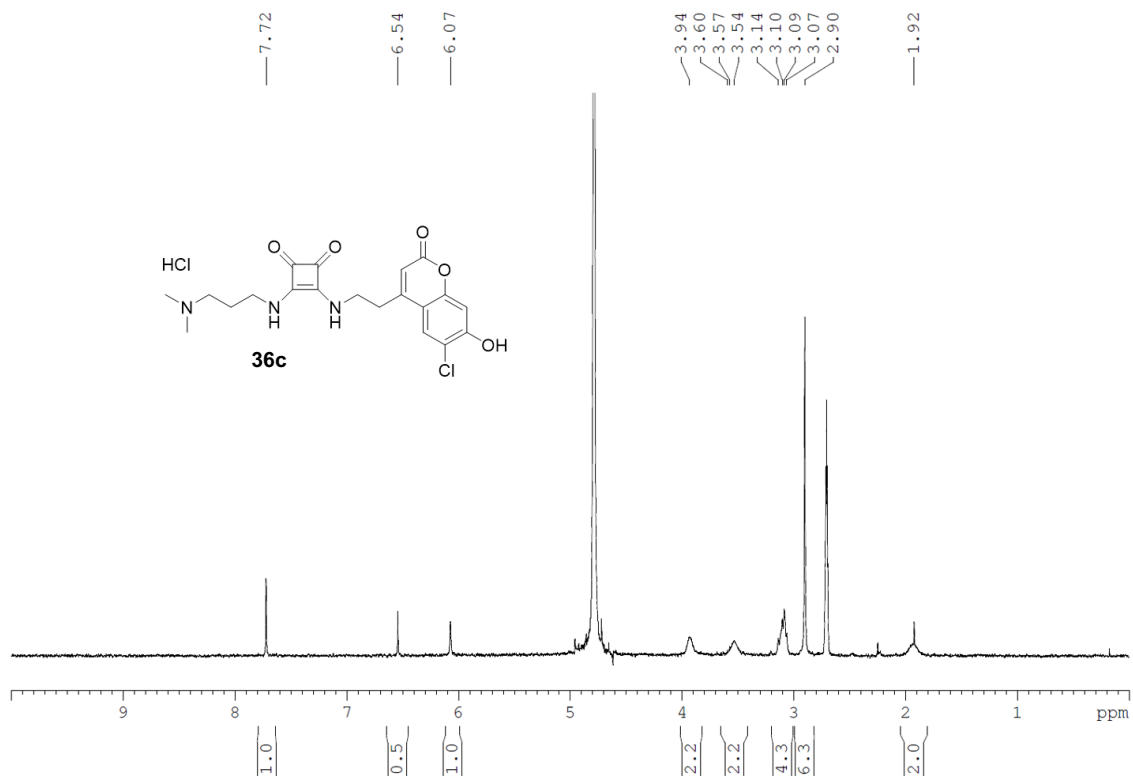


Figure 5.62.  $^1\text{H}$  NMR experiment of **36c** in  $\text{D}_2\text{O}$ , 5%  $\text{DMSO-}d_6$ , 300 MHz, 298 K.

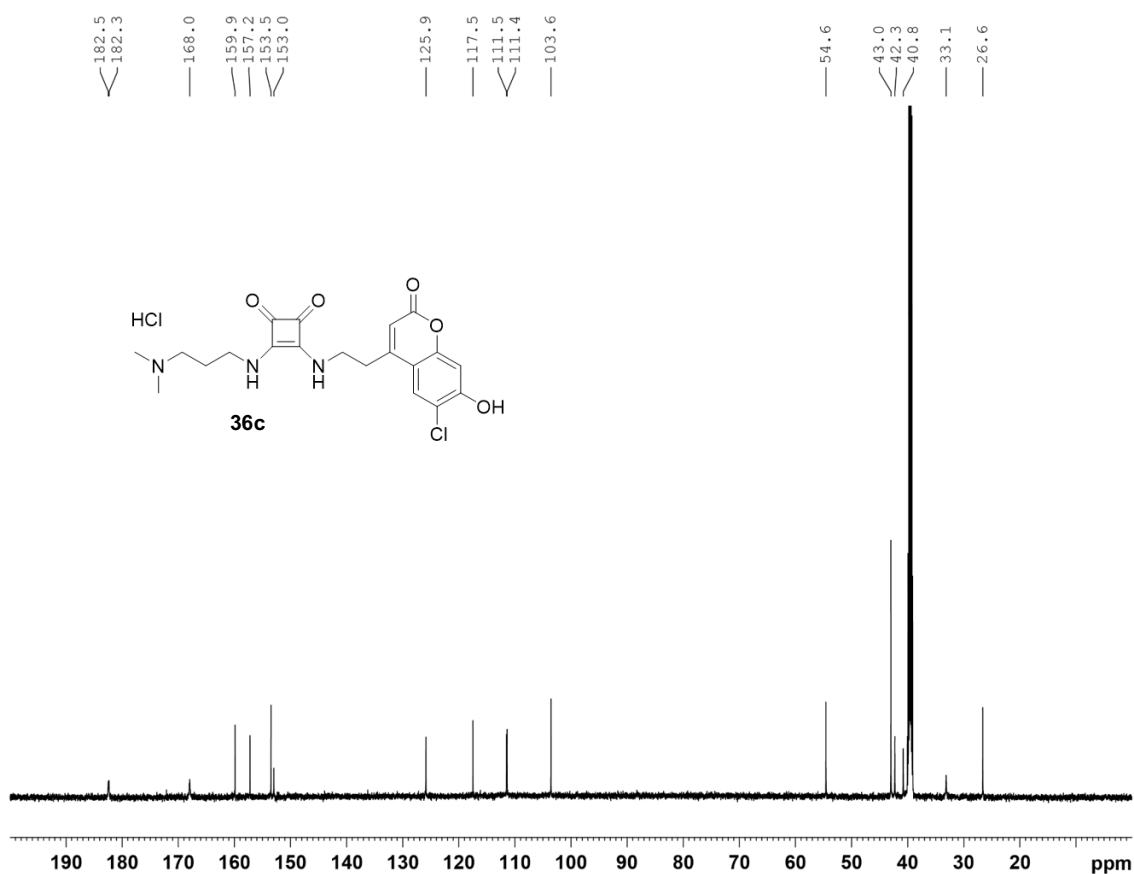


Figure 5.63.  $^1\text{H}$  NMR experiment of **36c** DMSO- $d_6$ , 600 MHz, 298 K.

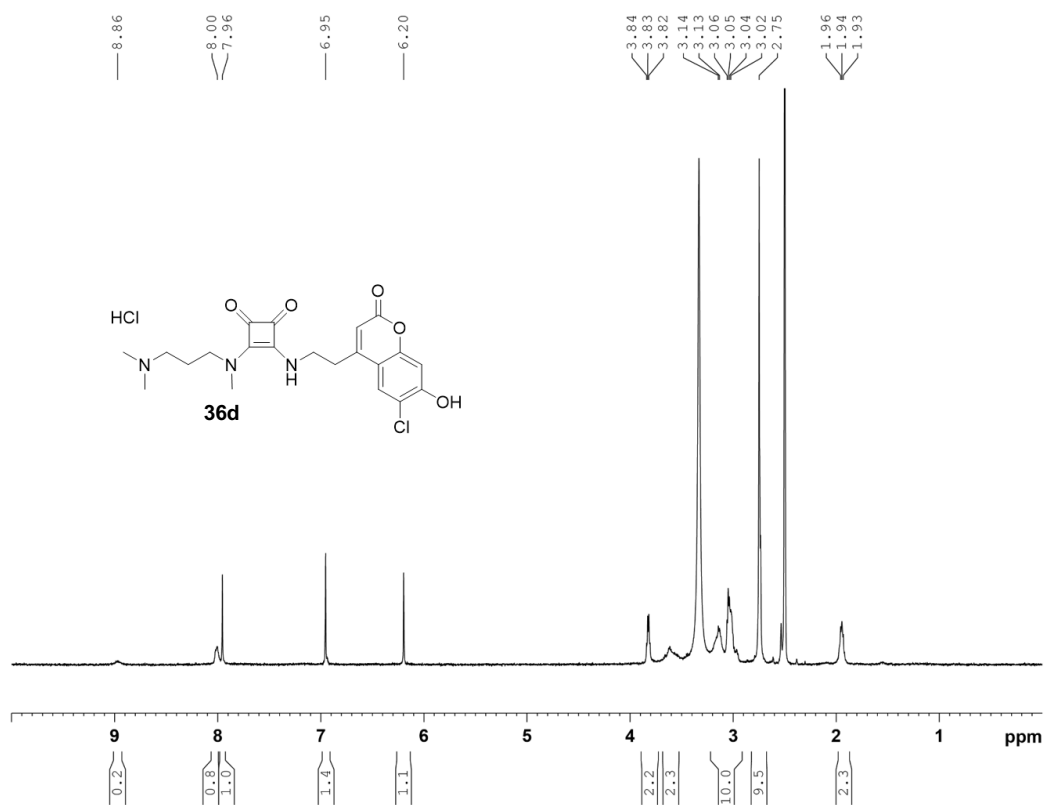


Figure 5.64.  $^1\text{H}$  NMR experiment of **36d** in DMSO- $d_6$ , 300 MHz, 298 K.

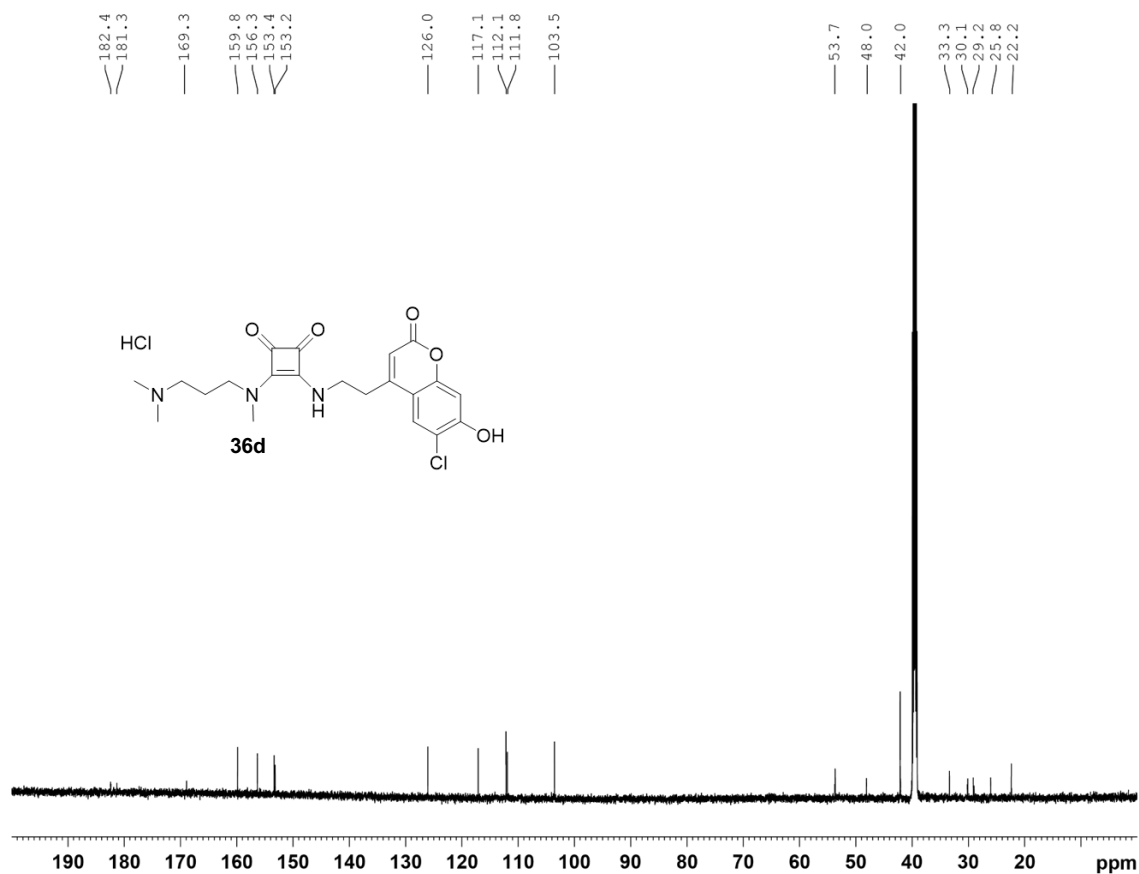
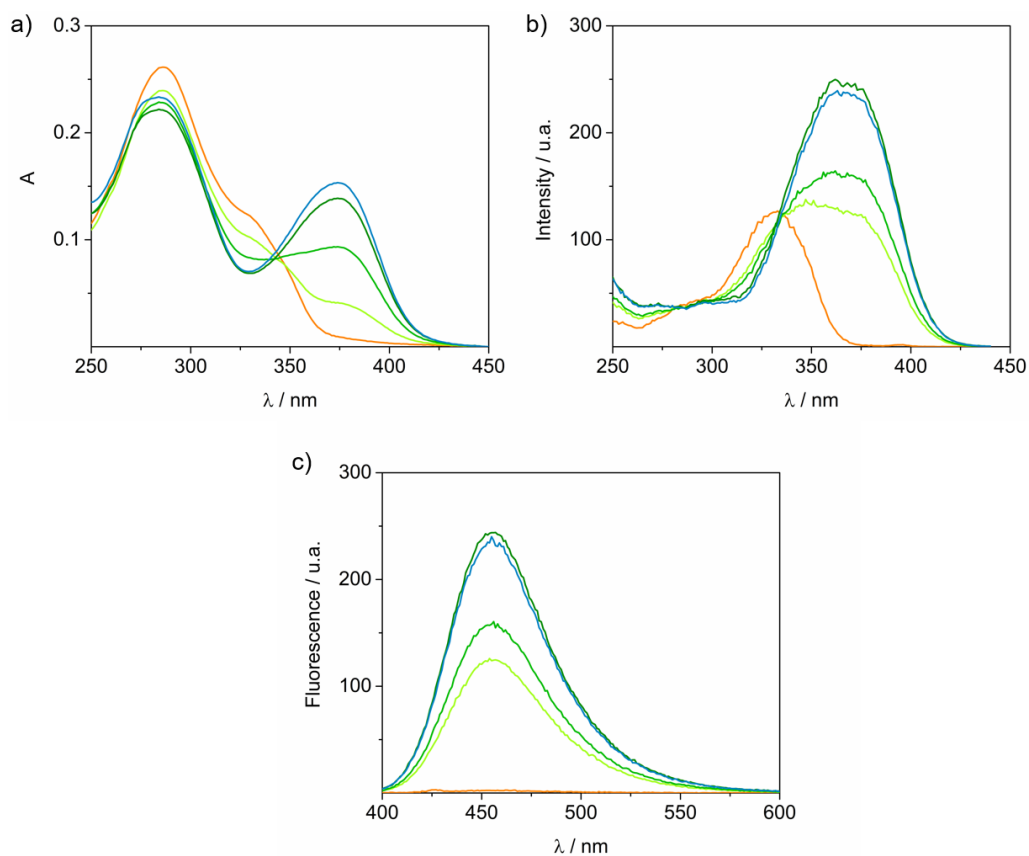


Figure 5.65.  $^{13}\text{C}$  NMR experiment of **36d** in  $\text{DMSO-}d_6$ , 600 MHz, 298 K.

### 5.5.5. Spectroscopic Data of Compounds **36a-d**

Spectroscopic characterization of 10  $\mu\text{M}$  solution of **36a-d** in 10 mM aqueous buffered solutions at pH 3 (orange), 5 (light green), 6 (green), 7 (dark green) and 8 (blue). All the emission spectra of **36a-d** were obtained at optimal excitation wavelengths at different pH values according to their excitation spectra obtained. Do to the fluorescence quenching by the squaramide moiety, a 10 nm acquisition bandwidth was used.



**Figure 5.66.** Absorption a), excitation b) and emission c) spectra of 10  $\mu\text{M}$  36a.

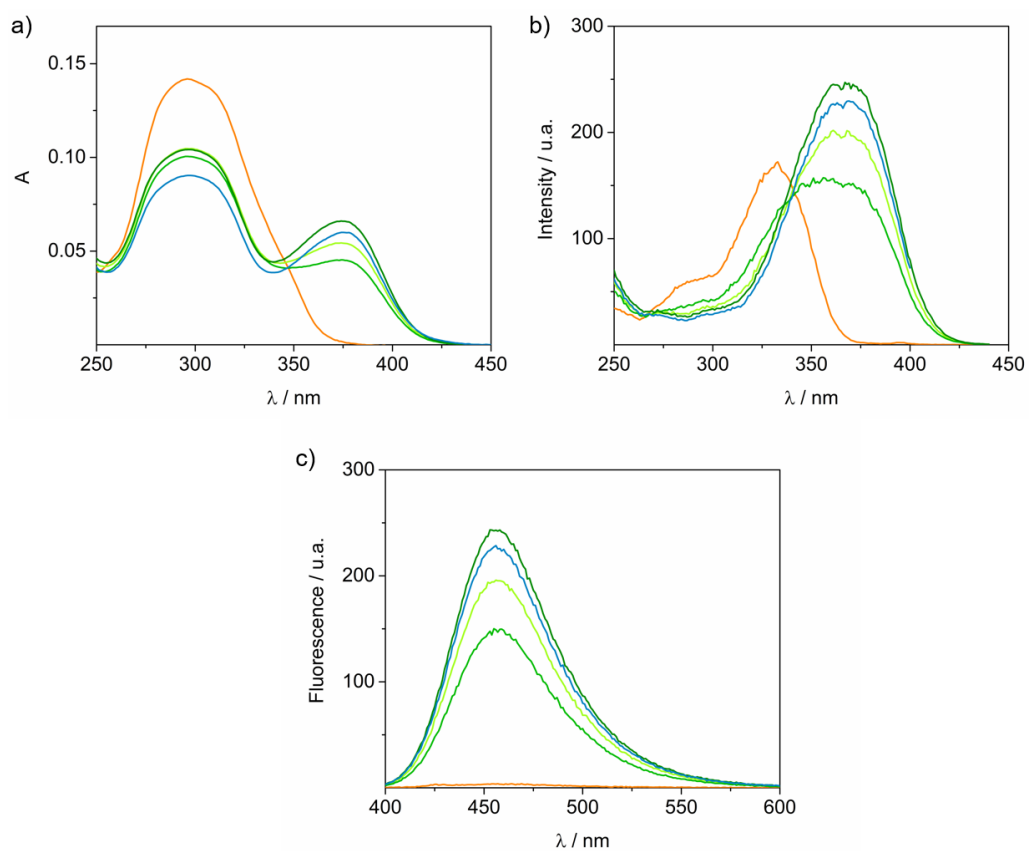


**Figure 5.67.** Absorption a), excitation b) and emission c) spectra of 10  $\mu\text{M}$  36b.

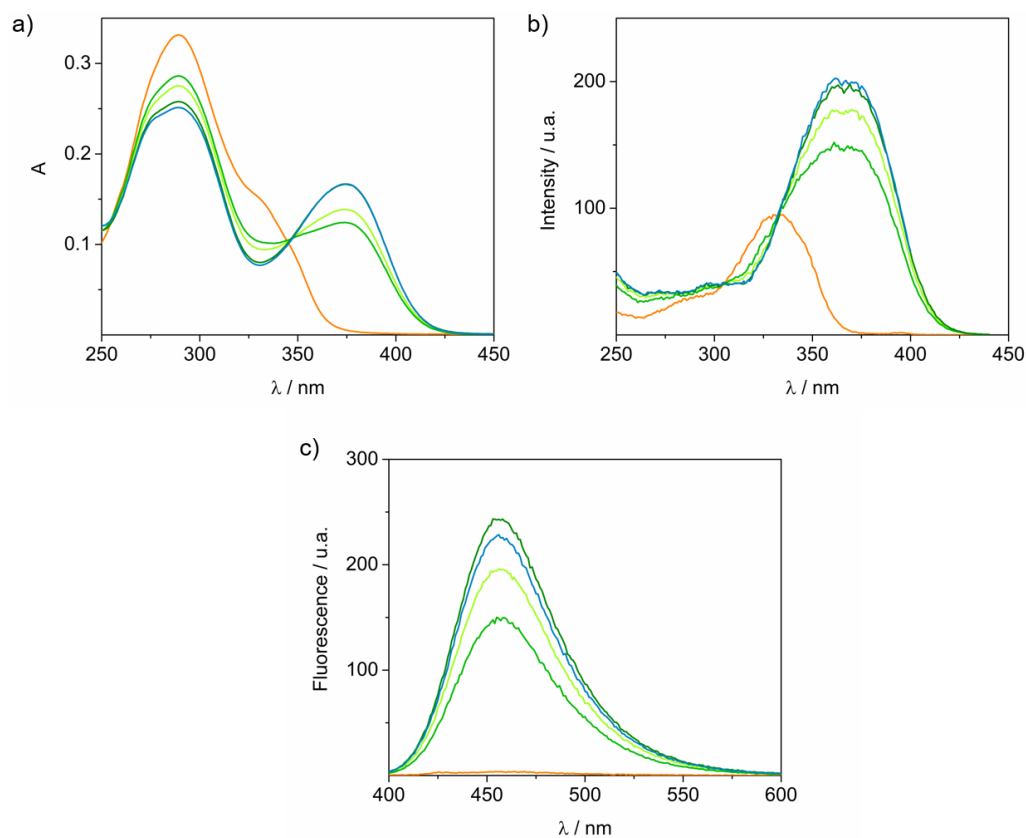


**Figure 5.68.** Absorption a), excitation b) and emission c) spectra of 10  $\mu\text{M}$  36c.

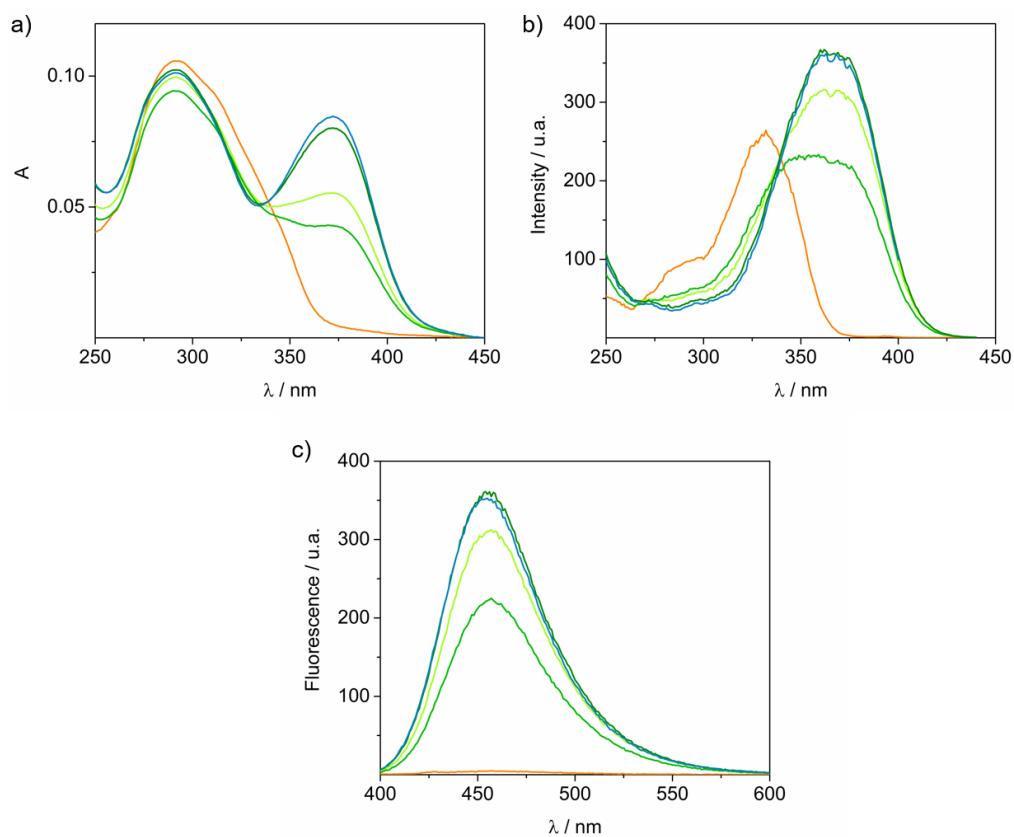


**Figure 5.69.** Absorption a), excitation b) and emission c) spectra of 10  $\mu\text{M}$  36d.

**6**

---

**Squaramide-Based Self-Immolative  
Spacers in Action**



## 6.1. PRODRUG DESIGN

In the previous chapters the ability of the self-immolative squaramide system to successfully release a model payload has been explored. When comparing the reaction rate profiles obtained for the release of aliphatic alcohols (ROH), anilines (ArNH<sub>2</sub>), and aliphatic amines (RNH<sub>2</sub>), the differences found in their kinetics were closely related with the nucleofugacity of the leaving group. Thus, the rate of release of an aliphatic amine was 10<sup>4</sup> times lower compared with those found for the release of an aniline or an alcohol (both around the same order of magnitude, Figure 6.1). Despite showing a similar kinetic constant, the main difference between the release of an alcohol and the aniline was the useful pH interval for each type of compound. Remarkably, whereas cyclization for aniline derivatives is mainly handicapped by the protonation status of the nucleophilic terminal amine, the cyclization of squaramic esters takes place even in moderate acidic pHs, allowing the release of the cargo.

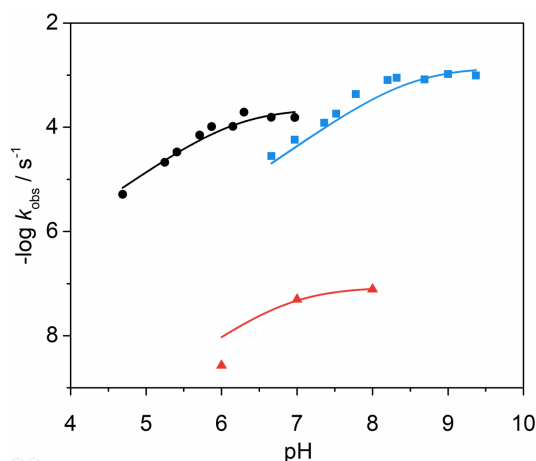


**Figure 6.1.** Summary of representative examples of pH-rate profiles obtained from the kinetic studies described in chapters 3 and 5 for the cyclization reaction of self-immolative models showing the influence of the chemical functionality of the leaving group: aliphatic alcohol (black), aniline (blue) and aliphatic amine (red).

Considering the hard synthetic access to squaramate esters and taking into account that the final aim is to develop a prodrug system that would work at physiological conditions (pH~7.4), we decided to work with aromatic amino derivatives to design the prodrug. Thus, we selected an aniline-containing bioactive compound to first, enhance its chemical stability through squaramide-conjugation and second, study its release to the medium under the action of a specific external stimulus.

As a proof of concept, we selected as a payload, a nitrogen mustard derivative as the parent chemotherapeutic agent to build up the model prodrug, where our squaramide self-immolative linker was in the bone structure.

### 6.1.1. Drug/Cargo Selection

Despite the enormous cost in human lives, during both World Wars and the interwar period there were great advances in science and technology. Much of the research focused on warfare found civilian uses after the war and helped to shape today's world. One of the most remarkable outcomes was the development of chemotherapeutics derived from the mustard gas or sulphur mustard, widely used as a chemical weapon. In 1919 a first report revealed some insights on its mechanism of action, finding leukopenia in the poisoned patients.<sup>237</sup> In the following decades, new derivatives followed, finding their pharmaceutical activity as DNA alkylating agents. Nowadays nitrogen mustards (NMs) constitute one of the most powerful families of antitumor agents used in the treatment of cancer such as non-Hodgkin's lymphoma, chronic leukemia, and lung, ovarian, and breast cancer.<sup>238</sup> Figure 6.2 shows the evolution of the chemical structures of NMs, highlighting the most representative derivatives.<sup>239</sup>

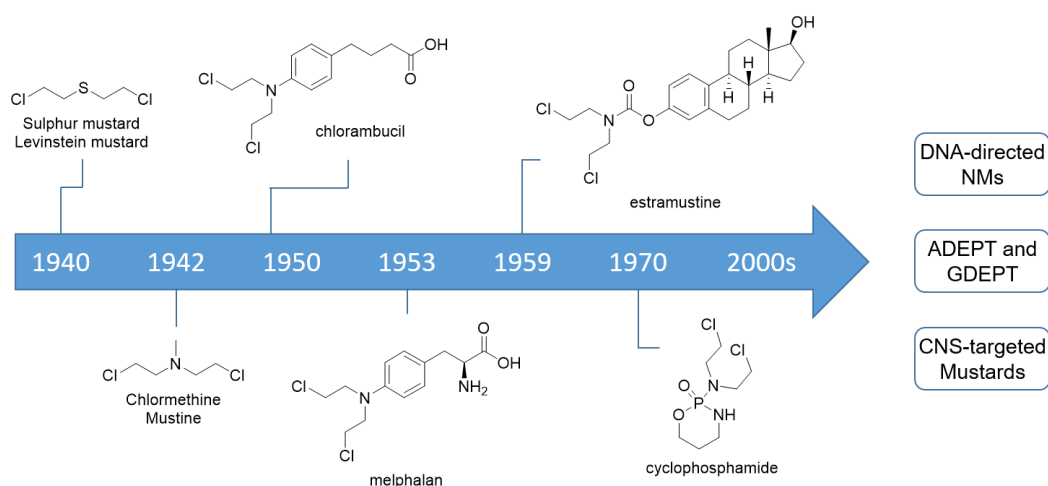


**Figure 6.2.** Historical evolution of mustard agents for therapeutic applications.

Although NMs have been extensively used in medicine, the main drawback of NMs-based chemotherapies is their lack of specificity and high cytotoxicity. Hence, in the last decades, researchers have worked thoughtfully in the development of targeted delivery systems such as prodrugs or directed enzyme therapies (such as ADEPT and GDEPT

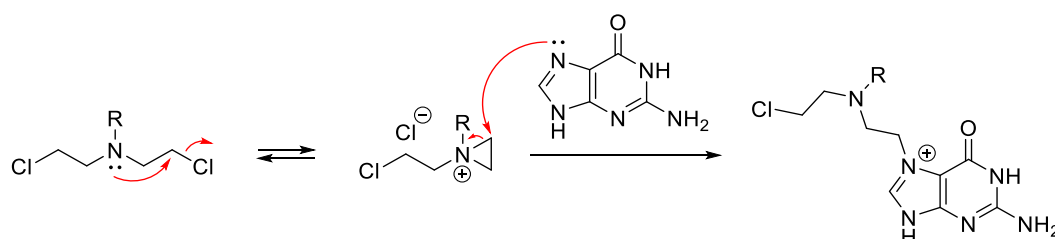
<sup>237</sup> E. B. Krumbhaar, *J. Am. Med. Assoc.* **1919**, 72, 39–41.

<sup>238</sup> a) B. Fisher, B. Sherman, H. Rockette, C. Redmond, R. Margolese, E. R. Fisher, *Cancer* **1979**, 44, 847–857. b) L. Jacobson, T. J. Wachowski, *Bull. North Shore Branch Chicago Med. Soc.* **1947**, 3. c) A. S. Weisberger, B. Levine, J. P. Storaasli, *JAMA, J. Am. Med. Assoc.* **1955**, 159, 1704–1707.

<sup>239</sup> a) R. C. Fuson, D. M. Burness, R. E. Foster, R. D. Lipscomb, *J. Org. Chem.* **1946**, 11, 499–503. b) A. Gilman, F. S. Philips, *Science* **1946**, 103, 409–436. c) A. Gilman, *Am. J. Surgery* **1963**, 105, 574–578. d) R. K. Singh, S. Kumar, D. N. Prasad, T. R. Bhardwaj, *Eur. J. Med. Chem.* **2018**, 151, 401–433.

using antibodies or gene vectors respectively) which would direct the active drug preferably to the targeted tumour.<sup>239d</sup>

**Mechanism of action.** NMs react with the  $N^7$  position of DNA guanine residues through a reactive aziridinium intermediate (Scheme 5.1).<sup>240</sup>



**Scheme 6.1.** General mechanism of guanine alkylation by nitrogen mustards. Formation of a reactive aziridinium intermediate.

Due to the high reactivity of the nitrogen of NMs to form the aziridinium intermediate, researchers have focused their efforts in reducing the nucleophilicity of the nitrogen lone pair and thus reducing its ability to form the aziridinium intermediate. A common strategy is its conjugation to an acceptor  $\pi$  system, which lowers the reactivity of the mustard. Currently, several NMs derivatives are being used in the clinic:<sup>241</sup>

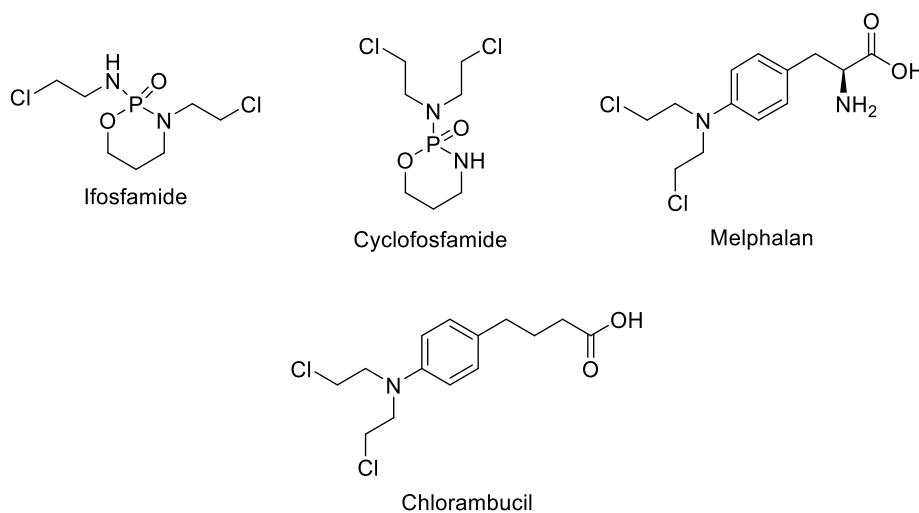


**Chart 6.1.** Structure of  $\pi$ -conjugated NMs derivatives approved for medical use.

Based on the ability of our squaramide-based self-immolative system (SSIS) to efficiently release aniline derivatives, we chose the aniline nitrogen mustard  $N^1, N^1$ -bis(2-chloroethyl)benzene-1,4-diamine (ANM), an aniline conjugated NM derivative as a drug candidate from which design and construct our model prodrug.

<sup>240</sup> A. Polavarapu, J. A. Stillabower, S. G. W. Stubblefield, W. M. Taylor, M. H. Baik, *J. Org. Chem.* **2012**, *77*, 5914–5921.

<sup>241</sup> O. M. Colvin, *Alkylating Agents. Encyclopedia of Cancer* **2002**, 35–42. DOI:10.1016/b0-12-227555-1/00001-0

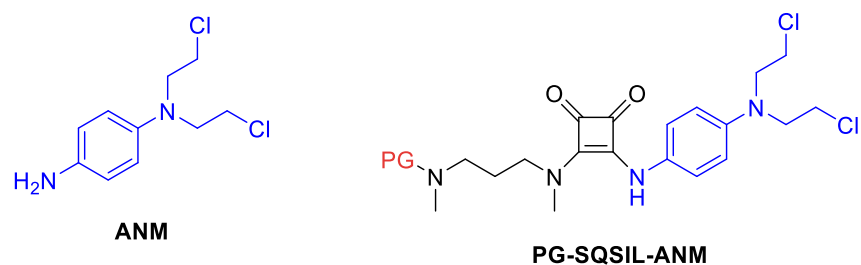


**Chart 6.2.** Chemical structure of parent Aniline Nitrogen Mustard (ANM) and proposed conjugation to the self-immolative spacer (PG-SQSIL-ANM).

In analogy to the previously studied self-immolative systems bearing anilines, we decided to conjugate the cargo (drug) directly to the squaryl moiety. In the design of our SSIS, we chose the *N,N'*-dimethylated linker since in our experience, *N*-methylated squaramides showed faster cyclization rates and better aqueous solubility than the corresponding non-methylated compounds.

To complete our design, it was also necessary to find a suitable trigger group (PG) for the terminal amine. As it was exposed in chapter 1, protective groups provide the chemical stability to the prodrug system but, under a particular external stimuli, the PG cleavage triggers the cascade reaction which results in the system disassembly and consequent cargo release.

### 6.1.2. Trigger Selection

As it was briefly commented in chapter 1, Directed Enzyme Prodrug Therapy (DEPT) uses exogenous enzymes (commonly non-human) to activate the prodrugs at a particular site of the body. If that enzyme is codified within the target cell by the previous administration of a gene by gene therapy, it is known as Gene-Directed Enzyme Prodrug Therapy (GDEPT). This strategy is of great interest to face cancer disease since it normally demands high specificity to avoid undesired toxicity in healthy cells. For cancer treatment, GDEPT it is also known as *Suicide Gene Therapy* because activation of the prodrugs causes cell apoptosis. In 2000, prodrug-suicide therapies constituted around the 15 % of clinical trials of chemotherapies<sup>242</sup> and this approach keeps increasing over the last years.

GDEPT comprises a three-component system: 1) an inactivated drug (prodrug), 2) a gene coding for an enzyme that activates the prodrug and 3) a carrier. Firstly, the coding gene for the specific enzyme is delivered to a tumour cell. There, the transcription of that gene into an mRNA and subsequent translation leads to the production of the enzyme inside the tumour cell. Finally, the prodrug is administered and converted into the active parent drug only inside the tumoral cell, which contains the activating

<sup>242</sup> W. F. Anderson, *Nat. Med.* **2000**, *6*, 862–863.

enzyme. One of the major requirements of GDEPT is the use of enzymes which are expressed exclusively or with a high ratio in tumour cells over healthy cells. Hence, the prodrug is mainly converted in the tumoral environment reducing the collateral damage to the rest of the tissues.<sup>243</sup>

Over the last two decades many enzyme/prodrug systems have been investigated but the most extensively studied are herpes simplex virus thymidine kinase (HSV-TK) with ganciclovir (GCV),<sup>244</sup> cytosine deaminase (CyD) of *E. coli* with 5-fluorocytosine (5-FC),<sup>245</sup> cytochrome P450 with cyclophosphamide/ifosfamide (CPA/IFA),<sup>246</sup> and nitroreductase with **CB1954**.<sup>247</sup>

This latter example is quite interesting because since the first discovery of inhibitory activity of 5-Azirinidinyl-2,4-dinitrobenzamide (**CB1954**) against the Walker 256 carcinoma<sup>248</sup> in 1969,<sup>249</sup> this prodrug has been introduced in the development of GDEPT and VDEPT to enhance selectivity against certain types of tumours.<sup>247a,250</sup>

---

<sup>243</sup> J. Zhang, V. Kale, M. Chen, *AAPS J.* **2015**, *17*, 102–110.

<sup>244</sup> a) C. Beck, S. Cayeux, S. D. Lupton, B. Dörken, T. Blankenstein, *Hum. Gene Ther.* **1995**, *6*, 1525–1530. b) S. O. Freytag, B. Movsas, I. Aref, H. Stricker, J. Peabody, J. Pegg, Y. Zhang, K. N. Barton, S. L. Brown, M. Lu, A. Savera, J. H. Kim, *Mol. Ther.* **2007**, *15*, 1016–1023.

<sup>245</sup> a) F. Koyama, H. Sawada, T. Hirao, H. Fujii, H. Hamada, H. Nakano, *Cancer Gene Ther.* **2000**, *7*, 1015–1022. b) S. O. Freytag, J. H. Kim, H. Stricker, J. Pegg, S. L. Brown, M. Lu, *Cancer Res.* **2006**, *13*, 7497–7506.

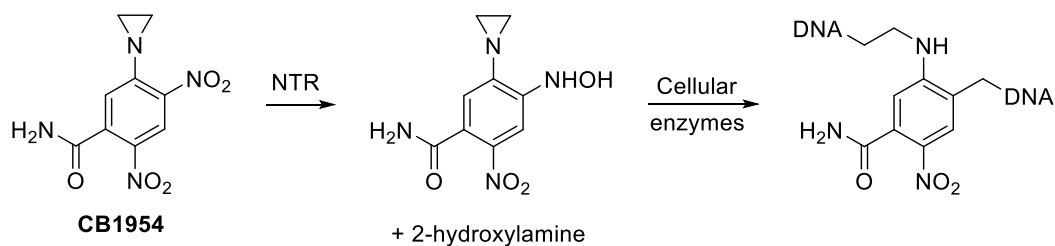
<sup>246</sup> a) C.-S. Chen, J. T. Lin, K. A. Goss, Y. He, J. R. Halpert, D. J. Waxman, *Mol. Pharmacol.* **2004**, *65*, 1278–1285. b) G. Vredenburg, S. den Braver-Sewradj, B. M. A. van Vugt-Lussenburg, N. P. E. Vermeulen, J. N. M. Commandeur, J. C. Vos, *Toxicol. Lett.* **2015**, *232*, 182–192.

<sup>247</sup> a) R. J. Knox, F. Friedlos, R. F. Sherwood, R. G. Melton, G. M. Anlezark, *Biochem. Pharmacol.* **1992**, *44*, 2297–2301. b) Y. Ju, X. Mu, J. Chi, G. Teng, Y. Yang, H. Hua, *Mol. Med. Rep.* **2016**, *14*, 5164–5170.

<sup>248</sup> R. J. Knox, D. A. Lydall, F. Friedlos, C. Basham, C. J. Rawlings, J. J. Roberts, *Mutat. Res. Repair* **1991**, *255*, 227–240.

<sup>249</sup> L. M. Cobb, T. A. Connors, L. A. Elson, A. H. Khan, B. C. V. Mitchley, W. C. J. Ross, M. E. Whisson, *Biochem. Pharmacol.* **1969**, *18*, 1519–1527.

<sup>250</sup> G. Chung-Faye, D. Palmer, D. Anderson, J. Clark, M. Downes, J. Baddeley, S. Hussain, P. I. Murray, P. Searle, L. Seymour, P. A. Harris, D. Ferry, D. J. Kerr, *Clin. Cancer Res.* **2001**, *7*, 2662–2668.



**Scheme 6.2.** Activation of **CB1954** by *E. coli* nitroreductase (NTR). Only 2- or 4- nitro group are reduced but equally.

5-Azirinidiny-2,4-dinitrobenzamide (**CB1954**) is enzymatically activated by an exogenous nitroreductase which reduces either 2- or 4- nitro group to hydroxylamine.<sup>251</sup> The reduction reaction is not selective so both metabolites are equally formed (Scheme 6.2).

In addition to dinitrobenzamide **CB1954**, nitroreductases have been extensively used in GDEPT for the reduction of dinitrobenzamide mustards, *p*-nitrobenzylcarbamates and nitroindolines, therefore they are active against a relatively broad scope of substrates.<sup>252</sup> For our research purpose, *p*-nitrobenzylcarbamates (*p*NBzC) are of particular interest for the development of self-immolative spacers since carbamates are widely used in the protection of amino groups in organic synthesis.<sup>253</sup>

Given the good prospects of the tandem NTR/prodrug in suicide gene therapy we decided to use the *p*NBzC residue as the protecting group for our squaramide-based self-immolative prodrug and study the disassembly process under enzymatic activation:

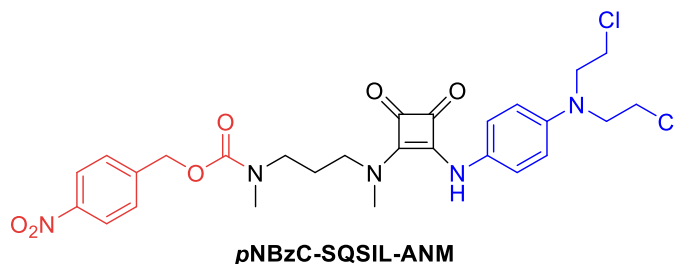


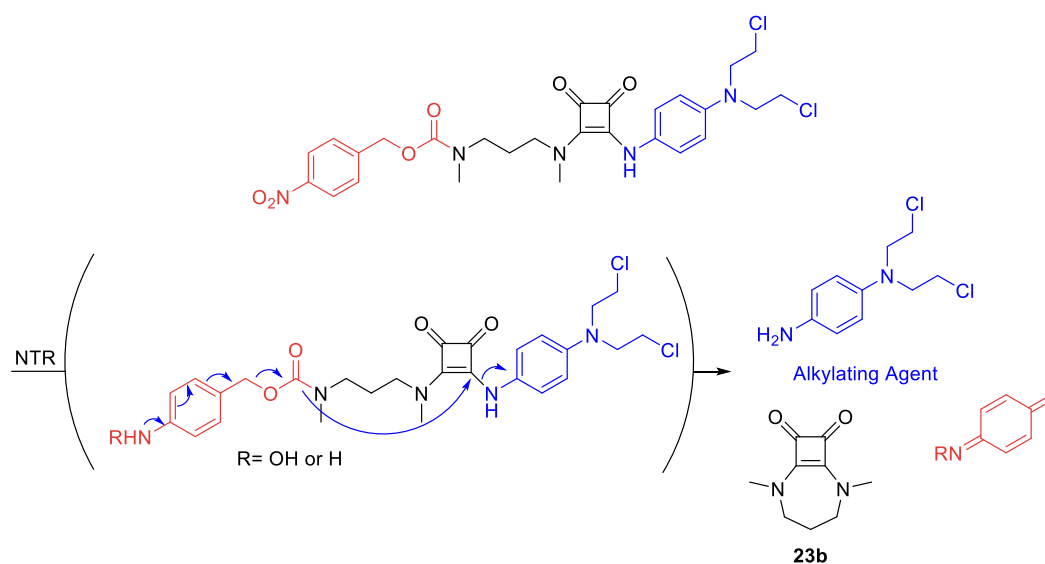
**Chart 6.3.** Structure of squaramide-based self-immolative prodrug. Building blocks: Trigger (*p*NBzC) in red, self-immolative linker in black (SQSIL) and ANM payload in blue.

Based on the suicide gene therapy used for the alkylating agent **CB1954**, our system would be converted into the toxic active form after reduction of the *p*-nitrobenzyl into the corresponding hydroxylamine or amine following the pathway shown in Scheme 6.3:

<sup>251</sup> G. N. Parkinson, J. V. Skelly, S. Neidle, *J. Med. Chem.* **2000**, *43*, 3624–3631.

<sup>252</sup> W. A. Denny, *J. Biomed. Biotechnol.* **2003**, *2003*, 48–70.

<sup>253</sup> P. G. M. Wuts, T. W. Greene. (2007) *Greene's Protective Groups in Organic Synthesis*, 4<sup>th</sup> ed., John Wiley & Sons, Inc, DOI: 10.1002/0470053488



**Scheme 6.3.** Structure of the designed NTR/squaramide-based self-immolative prodrug disassembly.

In addition to the release of the alkylating agent, an azaquinone methide derivative (red) and compound **23b** (black) would be released.

## 6.2. OBJECTIVES

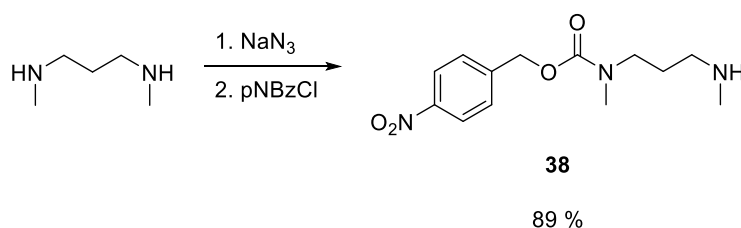
The main aim of this chapter is to design and test as a proof of concept a self-immolative system applied to the drug delivery in cancer therapy. The design will be based on the knowledge acquired from the kinetic studies and the disassembly performance of the self-immolative models studied in Chapter 5. To reach this goal, we have defined the particular following aims:

- To design and synthesize a self-immolative model prodrug.
- To perform *in vitro* studies on the kinetics of prodrug disassembly process.
- To study the mechanism of action of both the prodrug and parent drug *in vitro*.
- To study the biological activity of the prodrug in comparison with the parent drug in cultured cell lines.
- To expand the payload scope of the designed self-immolative prodrug by tuning the spacer moiety.

## 6.3. RESULTS AND DISCUSSION

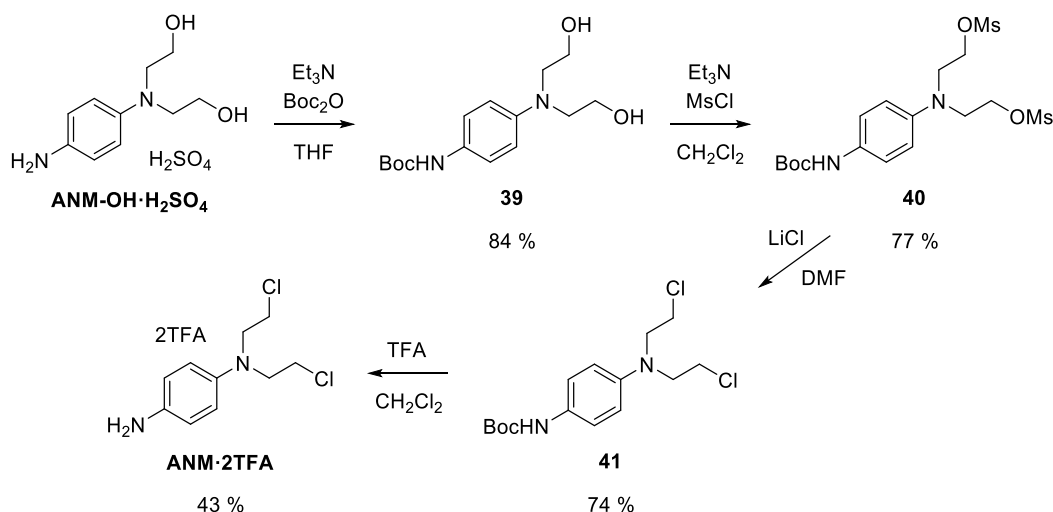
### 6.3.1. Synthesis of the Self-Immolative Nitrogen Mustard Prodrug

The synthesis of the self-immolative system was carried in a cunning-like fashion to avoid premature disassembly. Initially, it was necessary to monoprotect the diamine linker before its conjugation with the squaryl residue. By adapting a reported procedure,<sup>254</sup> *N,N'*-dimethyl-1,3-propanediamine was efficiently monoprotected with *p*-nitrobenzyl chloroformate (*p*NBzCl) affording compound **38** in a high yield (89%).



**Scheme 6.4.** Synthesis of the monoprotected *p*NBz carbamate diamine **38**.

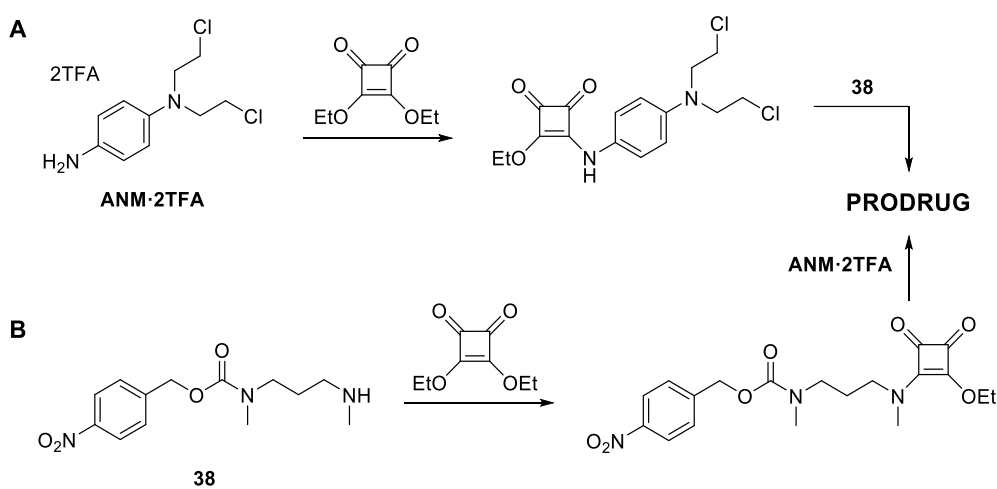
In parallel, synthesis of the aniline nitrogen mustard (ANM) parent drug was carried out using *N,N*-bis(2-hydroxyethyl)-1,4-phenylenediamine sulphate as starting material (ANM-OH). In a first step, the primary amine was Boc-protected using Boc<sub>2</sub>O in the presence of an excess of Et<sub>3</sub>N using THF as solvent (**39**). Then, the alcohols were converted into the corresponding mesyl derivatives by reaction with mesyl chloride in anhydrous CH<sub>2</sub>Cl<sub>2</sub> (**40**). Subsequent treatment with LiCl in anhydrous DMF afforded the Bis-chloro-derivative **41** which was then deprotected with TFA to afford the aniline nitrogen mustard ANM as a TFA ammonium salt.



**Scheme 6.5.** Four-step synthesis of parent chemotherapeutic ANM.

<sup>254</sup> Y. C. Huang, C. Cao, X. L. Tan, X. Li, L. Liu, *Org. Chem. Front.* **2014**, *1*, 1050–1054.

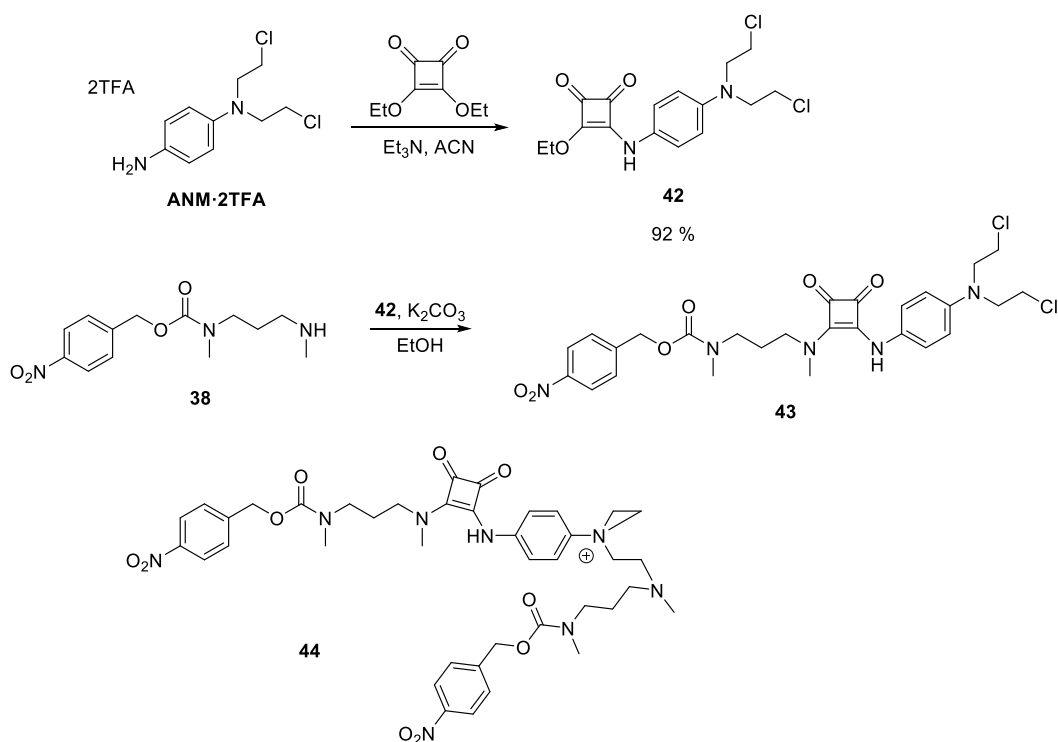
As discussed in Chapter 5, one of the synthetic handicaps when coupling anilines with diethyl squarate or squaramic esters is the low reactivity of the aniline due to the partial conjugation of the nitrogen lone pair to the aromatic residue. On the other hand, electrophilicity of squaramic esters is lower than the corresponding squaric ester so it also hinders the normal reaction pathway. For these reasons, we proposed two alternative pathways. Pathway **A** tackle the synthesis of the self-immolative prodrug starting by the condensation of the mustard to the diethyl squarate. Once the squaramic ester is obtained, the last step requires to connect the protected diamine **38** with the parent drug **ANM** through a squaryl linker.



**Scheme 6.6.** Proposed synthetic pathways to access the squaramide-based self-immolative linker prodrug.

Conversely, pathway **B** proceeds by the first coupling of compound **38** with ethyl squarate followed by reaction with the mustard drug **ANM** (Scheme 6.6). Due to the low reactivity of the aniline, a priori pathway **A** would lead to a better yield because the aniline reacts easier with ethyl squarate than with squaramic ester derivatives. However, the main drawback is the presence of reactive chlorine groups which could also be attacked by the incoming amino nucleophile in the second step.

Despite the uncertainty of the chemoselectivity, path **A** was tested as described in Scheme 6.7. Squaramic ester **42** was firstly synthesized by reaction of **ANM·2TFA** with ethyl squarate in the presence of  $\text{Et}_3\text{N}$ . Then, it was coupled with amino **38** in  $\text{EtOH}$  in the presence of  $\text{K}_2\text{CO}_3$ .



**Scheme 6.7.** Synthesis of prodrug **43** by pathway A. Byproduct **44** is mainly obtained over the desired product **43**.

The crude reaction was analysed by HRMS and two main compounds were identified: 1) the aziridinium undesired byproduct (801.3562,  $[\text{M}]^+$ ) and 2) the desired prodrug (592.1723,  $[\text{M}+\text{H}]^+$ ) in much lower proportion (Figure 6.3). Additionally, several other byproducts could not be identified.

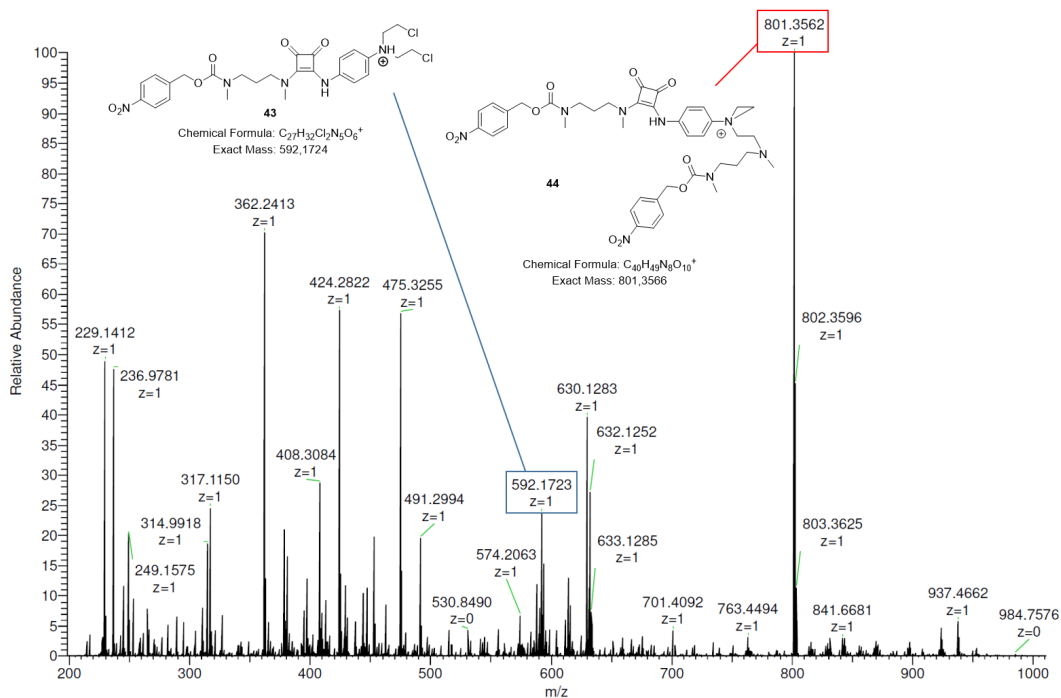
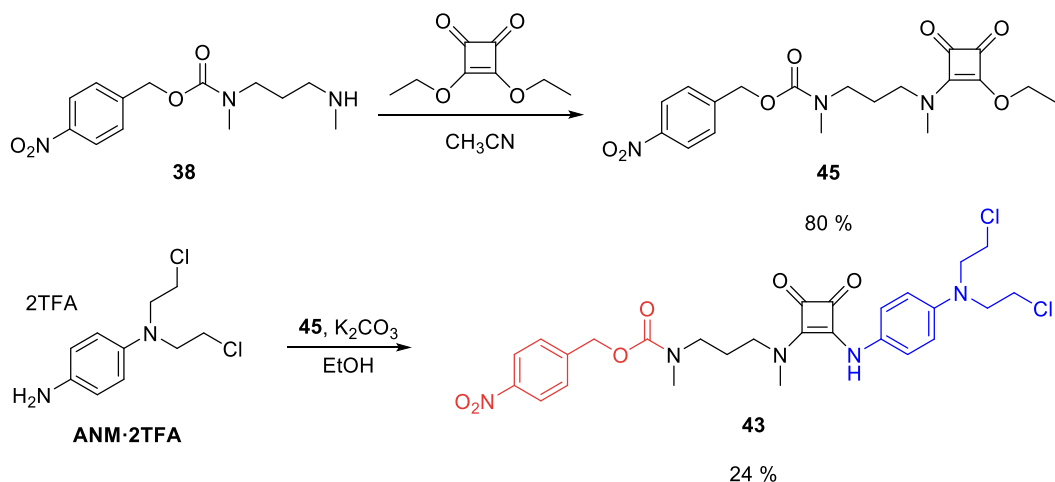


**Figure 6.3.** HRMS analysis of crude reaction from pathway A. Highlighted in red: main byproduct **44**. Highlighted in blue: self-immolative prodrug **43**.

Clearly, the presence of the bis-chloro electrophilic moiety handicapped the synthetic access to the prodrug **43** severely. To overcome such difficulty the alternative synthetic route B was tried, even though the expected yield would be lower. Hence, protected amino **38** was reacted with ethyl squarate to obtain the corresponding squaramic ester **45**. The subsequent reaction with ANM-2TFA in EtOH under  $K_2CO_3$  led to prodrug **43** in 24 % yield:



**Scheme 6.8.** Synthesis of self-immolative prodrug **43** by synthetic pathway B.

The full characterization of the self-immolative prodrug **43** was carried by 1D and 2D NMR experiments (see Figure 6.4, 6.5 and experimental section), and supported by ESI-HRMS.

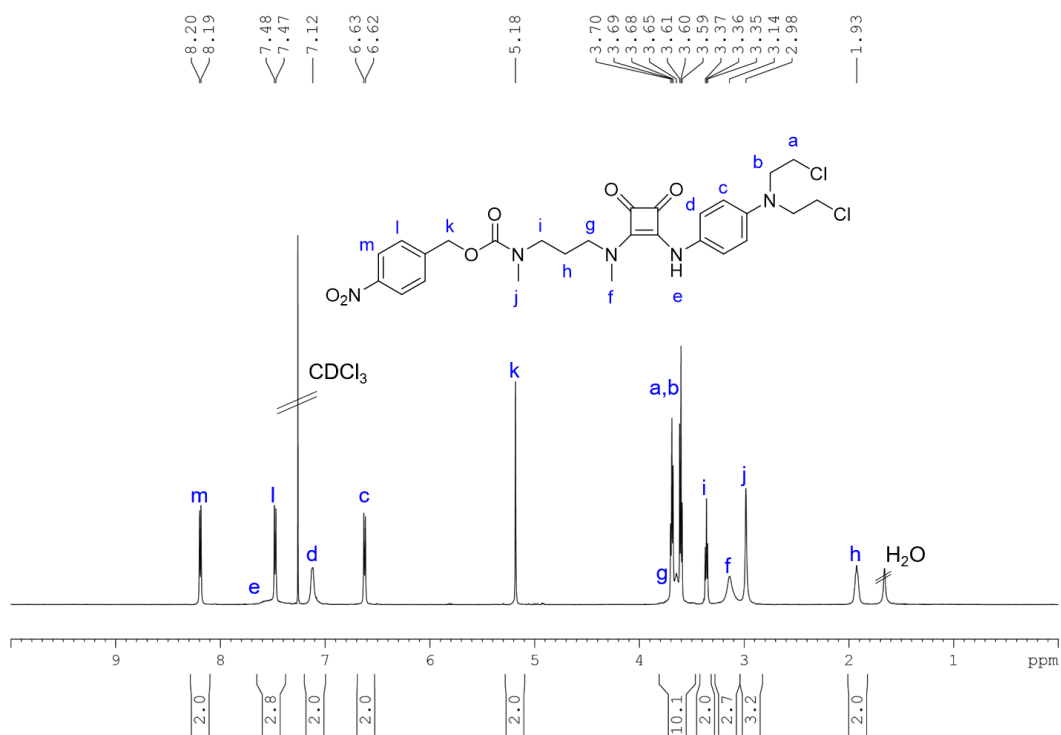


**Figure 6.4.**  $^1\text{H}$  NMR spectrum of compound 43 (CDCl<sub>3</sub>, 600 MHz, 298K) and the corresponding signal assignment.

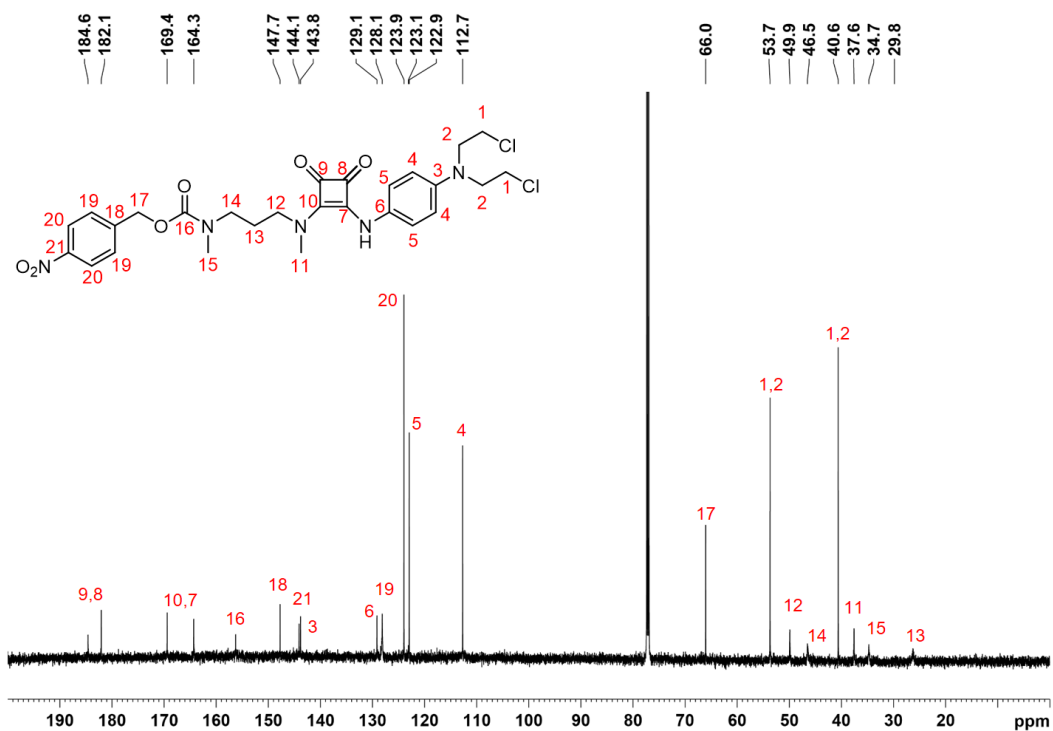


**Figure 6.5.**  $^{13}\text{C}$  NMR spectrum of compound 43 (CDCl<sub>3</sub>, 150 MHz, 298K) and the corresponding signal assignment.

### 6.3.2. DNA Cross-Linking

Nitrogen mustards (NMs) belong to the family of alkylating agents. As explained before, the mechanism of action consists of the irreversible alkylation of the DNA. Such damage is critical since it blocks the ability of the DNA to replicate and develop its further biological activity. Generally, the irreversible DNA damage leads to cell apoptosis. Hence, alkylating agents are being widely used for cancer treatment because tumour cells tend to replicate faster than normal cells and therefore, they are more sensitive to DNA damage.

*Mustard alkylation of Drew-Dickerson Dodecamer:* To examine the reactivity of prodrug **43** towards DNA, we performed *in vitro* experiments with a representative DNA. We selected the Drew-Dickerson Dodecamer (DDD), a prototypical B-DNA with a self-complementary CGCGAATTCGCG sequence.<sup>255</sup> Figure 6.6 shows the configurations of single- and double-strand DNA, (a) ssDDD and (b) dsDDD respectively. Figure 6.6c displays the dsDNA coloured by residues where cytosine = yellow, guanine = green, adenine = red and thymine = blue, for clarification.<sup>256</sup>

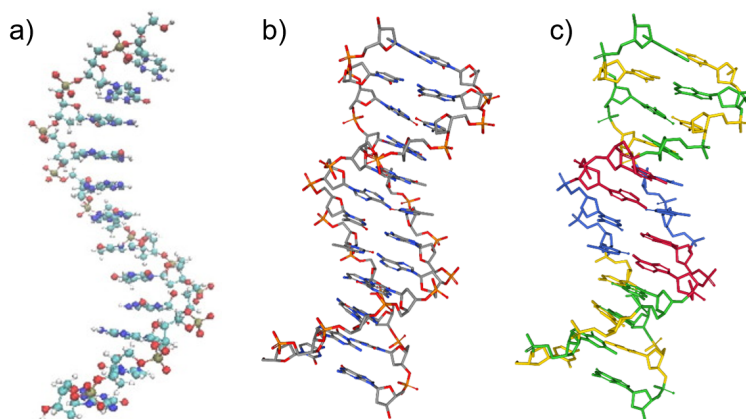


**Figure 6.6.** Representative configurations of a) native configuration of the ssDDD and b), c) dsDDD-piperazine complex (in both cases the piperazine ligand is omitted for clarity). Reproduced from reference 255d and 256.

To determine the reactivity of prodrug **43** and parent mustard **ANM** towards DDD the reaction products were analysed by High Resolution Mass Spectrometry (HRMS) using Electrospray Ionization (ESI) in negative mode. The initial analysis of a 10  $\mu$ M solution

<sup>255</sup> a) H. R. Drew, R. M. Wing, T. Takano, C. Broka, S. Tanaka, K. Itakura, R. E. Dickerson, *PNAS* **1981**, *78*, 2179–2183. b) T. Dršata, A. Pérez, M. Orozco, A. V Morozov, J. Šponer, F. Lankaš, *J. Chem. Theory Comput.* **2013**, *9*, 707–721. c) P. D. Dans, L. Danilāne, I. Ivani, T. Dršata, F. Lankaš, A. Hospital, J. Walther, R. I. Pujagut, F. Battistini, J. L. Gelpí, R. Lavery, M. Orozco, *Nucleic Acids Res.* **2016**, *44*, 4052–4066. d) S. Ghosh, H. Dixit, R. Chakrabarti, *Chem. Phys.* **2015**, *459*, 137–147.

<sup>256</sup> PDB ID: 1D44. J. R. Quintana, R. E. Dickerson, A. A. Lipanov, *Biochemistry* **1991**, *30*, 10294–10306.

of untreated commercial DDD revealed a multicharged species distribution detecting only the parent compound as a single strand DNA in three main charged states, highlighted in orange: 1214.2109 ( $z = 3$ ), 910.4071 ( $z = 4$ ) and 728.1243 ( $z = 5$ ). Figure 6.7 shows the mass spectrogram.

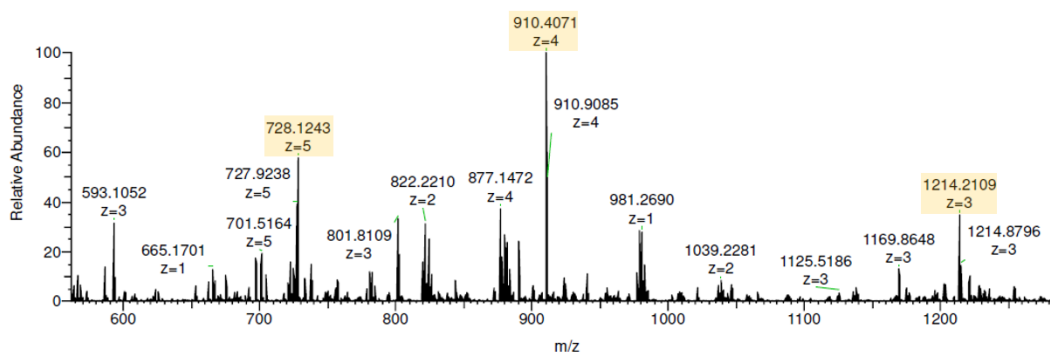
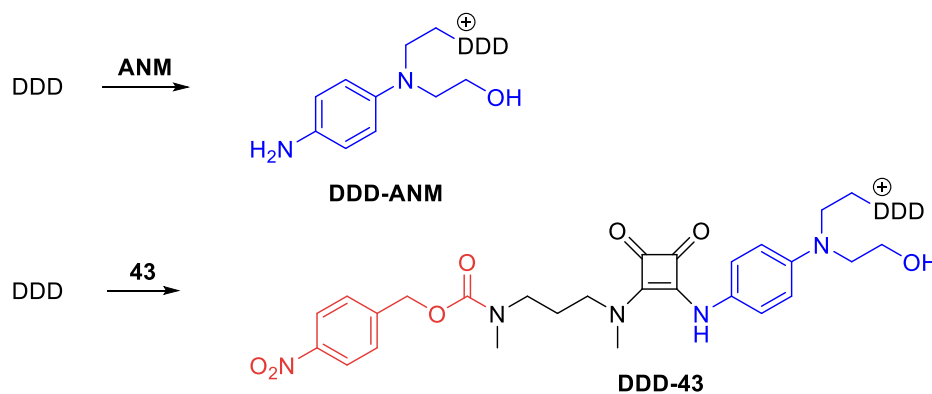


**Figure 6.7.** HRMS spectrogram, showing the multicharged species distribution of ssDDD.

Once the parent DNA was identified, DDD ( $10 \mu\text{M}$ ) was incubated with the corresponding alkylating agent (ANM or **43** at  $40 \mu\text{M}$ ) at  $37^\circ\text{C}$  for 48 h in 1 mM Tris buffer (pH 7.4). The analysis of the crude reactions by HRMS revealed the appearance of the respective mono-alkylated species, while the remaining chloride residue appeared hydrolysed:



**Scheme 6.9.** DNA alkylated adducts detected by HRMS after treatment of  $10 \mu\text{M}$  DDD with  $40 \mu\text{M}$  parent ANM and self-immolative **43** respectively.

The mono alkylated DNA adducts were also distributed among different multicharged species (highlighted in blue) finding a monoisotopic mass of 3822.7633 ( $z = 1$ ) for DDD-ANM adduct and 4180.8627 ( $z = 1$ ) for DDD-**43** (Figure 6.8 and 6.9 respectively). Along with the alkylated DNA adducts, DDD was also detected (highlighted in orange).

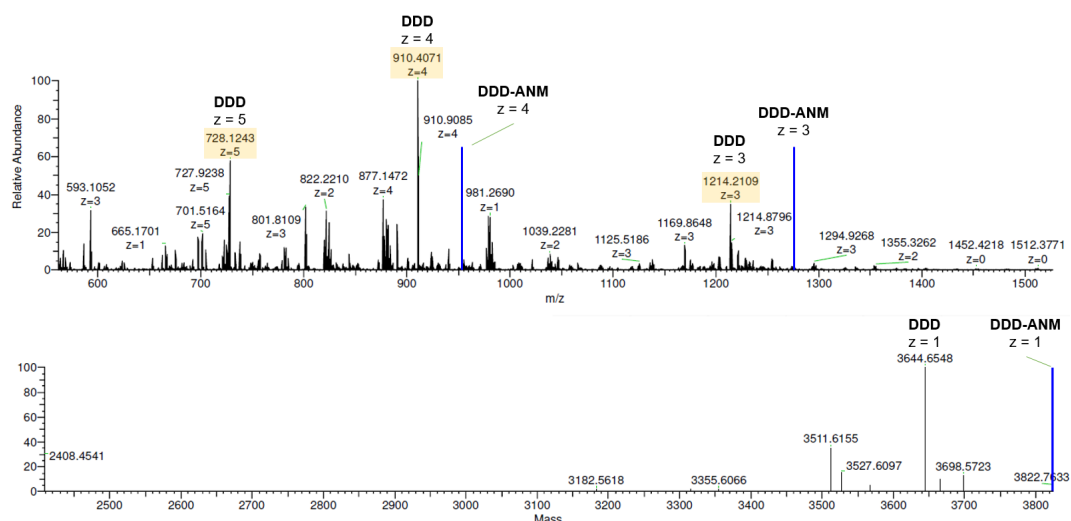


**Figure 6.8.** Spectrogram of 10  $\mu\text{M}$  DDD incubated with 40  $\mu\text{M}$  ANM for 48 h at 37  $^{\circ}\text{C}$ .

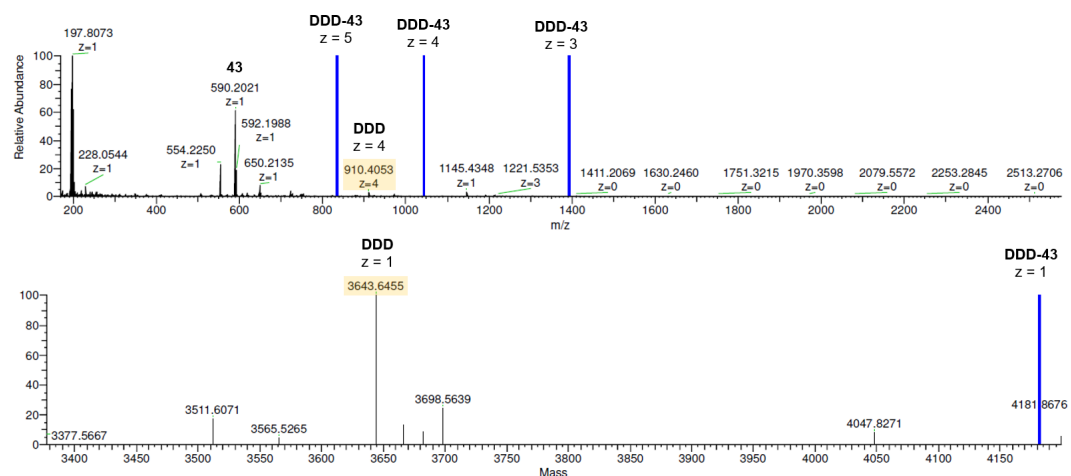
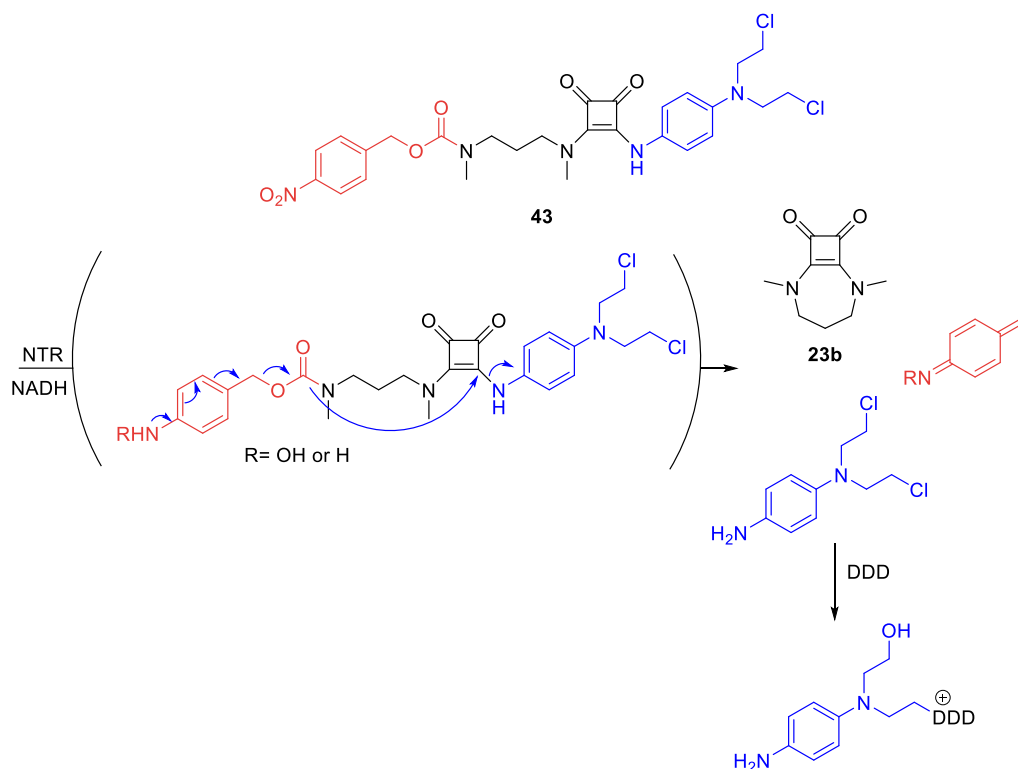


**Figure 6.9.** Spectrogram of 10  $\mu\text{M}$  DDD incubated with 40  $\mu\text{M}$  **43** for 48 h at 37  $^{\circ}\text{C}$ .

Since mass spectrometry is not a quantitative technique the percentage of DNA alkylation could not be quantified but the experiment demonstrates that both compounds react with DNA forming irreversible covalent bonds.

After testing the intrinsic reactivity of ANM and prodrug **43** towards DDD, the enzymatic activation of our prodrug was tested. Thus, a 10  $\mu\text{M}$  solution of DDD was treated with **43** (40  $\mu\text{M}$ ) and, for the activation of the self-immolative process, nitroreductase (NTR) and NADH were added (5  $\mu\text{g}/\text{mL}$  and 35  $\mu\text{M}$  respectively). Analogously, the crude reaction mixture was incubated for 48 h at 37  $^{\circ}\text{C}$  and then it was injected for mass analysis. The reaction would proceed as follows:



**Scheme 6.10.** Mechanism of activation of prodrug **43** by the tandem NTR/NADH and subsequent DDD adduct formation.

A close analysis on the crude reaction mixture showed the mass peak corresponding to the adduct DDD-ANM which indicates the complete release of the mustard by self-immolation of **43** (Figure 6.10). Additionally, in ESI(+) mode we could detect the monoisotopic mass corresponding to cyclosquaramide **23b**, the expected cyclic squaramide product (Figure 6.10, inset).

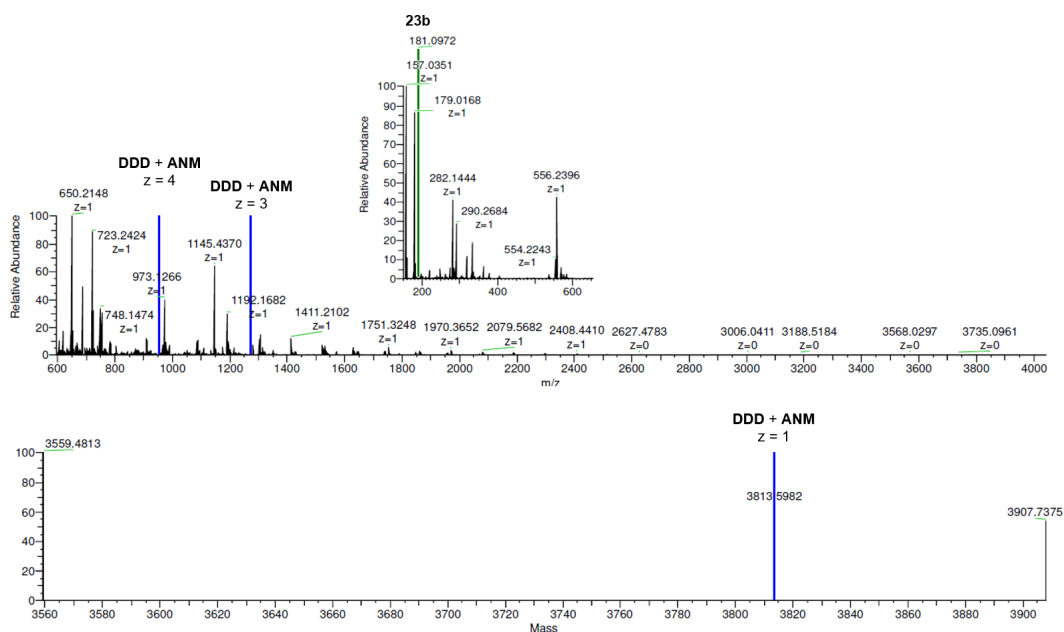


**Figure 6.10.** Spectrogram of 10  $\mu\text{M}$  DDD incubated with 40  $\mu\text{M}$  **43** under activation by 5  $\mu\text{g/mL}$  of NTR and 35  $\mu\text{M}$  NADH for 96 h at 37  $^{\circ}\text{C}$ .

### 6.3.3. Cell Viability Analysis

The biological activity of parent mustard **ANM** and prodrug **43** were tested against two cultured human glioblastoma tumoral cell lines, U87 and T98G, in a cell viability assay. These two cell lines were selected due to their positive response to mustard alkylating agents. To determine the effectivity of the self-immolative prodrug **43**, we performed a cell viability assay, measuring the number of living cells in a population after the treatment with the prodrug **43** and by comparison with the same amount of untreated cells. In our case, the viability of the cultured cells was tested using CellTiter-Glo Luminescent Cell Viability Assay (Promega, Madison, WI). This is a homogeneous method to determine the number of viable cells in a cell culture based on the quantization of the ATP present as the indicator of metabolically active cells. The assay was performed by incubating the cells for a 48 h and 96 h with the agents under assay at 10  $\mu\text{M}$ . After the treatment, the luminescence of viable cells was measured and quantified.<sup>257</sup> For comparison purposes, we tested the both the prodrug **43** and the parent drug **ANM**.

The results are shown in Table 6.1 and Figure 6.11.

<sup>257</sup> T. L. Riss, R. A. Moravec, A. L. Niles, S. Duellman, H. A. Benink, T. J. Worzella, L. Minor. Cell Viability Assays. 2013 May 1 [Updated 2016 Jul 1]. In: Sittampalam GS, Coussens NP, Brimacombe K, *et al.*, editors. Assay Guidance Manual [Internet]. Bethesda (MD): Eli Lilly & Company and the National Center for Advancing Translational Sciences; **2004**. From: <https://www.ncbi.nlm.nih.gov/books/NBK144065/>

**Table 6.1.** Viability % values obtained after the treatment of glioblastoma cell lines with ANM and **43** (10  $\mu$ M) at 48 h and 96 h respectively.

Agent/ cell line	Viability (%) 48 h		Viability (%) 96 h	
	U87	T98G	U87	T98G
<b>ANM</b>	80	105	26	40
<b>43</b>	146	98	151	67

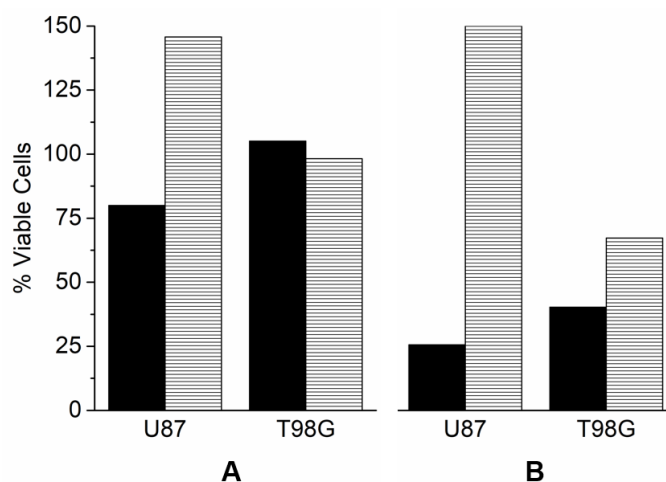


**Figure 6.11.** Effect on the cell viability of cells U87 and T98G after incubation with ANM (10  $\mu$ M, solid black) and **43** (10  $\mu$ M, lined) for A) 48 h and B) 96 h, respectively.

Analysis of the effect on U87 cells shows that the activity of the parent mustard **ANM** increases with time, from 80 % down to 26 % viability. Conversely, the prodrug **43** does not cause any observable effect on the cell activity even after 96 h of treatment.

On the other hand, the effect on T98G cells is similar for both compounds, at 48 h either of the compounds have any effect on the cell viability but after 96 h, this percentage falls to 40 % and 67 % for **ANM** and **43**, respectively. These behaviour suggests that T98G cells are more sensitive to the tested agents than U87 cells.

To deep in the knowledge of the biological effect that the self-immolative prodrug could have and test its capability to cause DNA damage, we performed a clonogenic assay with glioblastoma tumorous cells (LN229). A clonogenic assay is a cell biology technique used for testing the effectiveness of specific agents on damaging the DNA of certain cells evaluating their capability of proliferation. It consists of incubating living cells with the agent under assay for 1 hour. After cell exposure, the incubation media is renewed with fresh culture media and the cells are allowed to grow for a long period. In our case, cells were incubated for 9 days. Finally, the colonies produced are fixed, stained and counted. Depending on the effectiveness of the agent, the number of surviving colonies will vary.

Along with prodrug **43**, temozolomide (**TMZ**), a common DNA damaging agent<sup>258</sup> was tested as the control. For comparison purposes, the parent nitrogen mustard drug **ANM** and the corresponding hydrolysis product ANM-OH were also included in the assay.

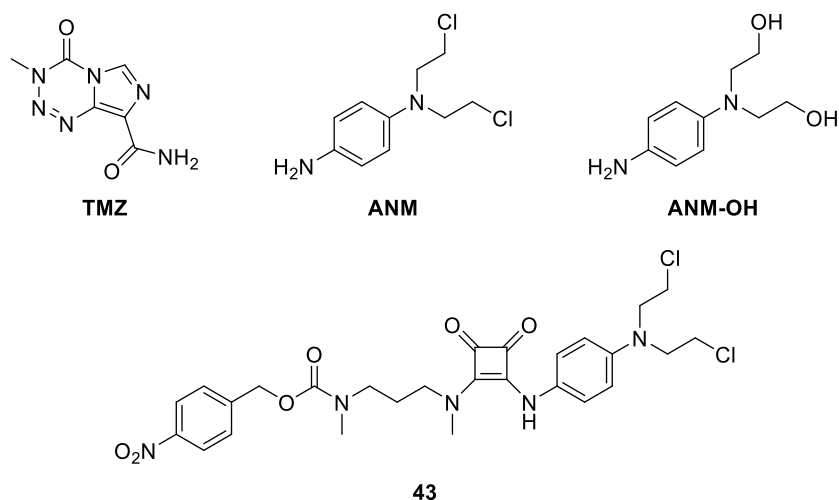


**Chart 6.4.** Chemical structures of the alkylating agents used in the clonogenic assay.

LN229 cells were exposed to a 10  $\mu$ M solution of the drug agent for 1h. Then, the solution was renewed and the cells were allowed to grow for nine days. Finally, the cells were fixed, stained with crystal violet and counted. For additional details, see the experimental section.

**Table 6.2.** LN229 clones formed and survival factor (SF) after the treatment with antitumor agents.

Cell line / Agent	LN229 <sup>a</sup>		
	200 cells	500 cells	SF %
<b>CONT</b>	144	197	100
<b>TMZ</b>	83	116	58
<b>ANM</b>	155	209	106
<b>ANM-OH</b>	194	218	122
<b>43</b>	30	55	24

Plate efficiency: <sup>a</sup>56 %

<sup>258</sup> J. Zhang, M. F.G. Stevens, T. D. Bradshaw, *Curr. Mol. Pharmacol.* **2012**, 5, 102–114.

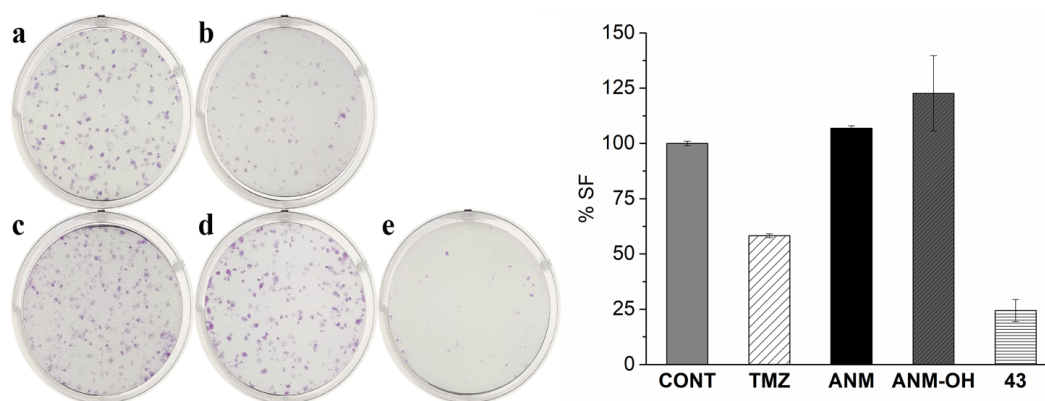


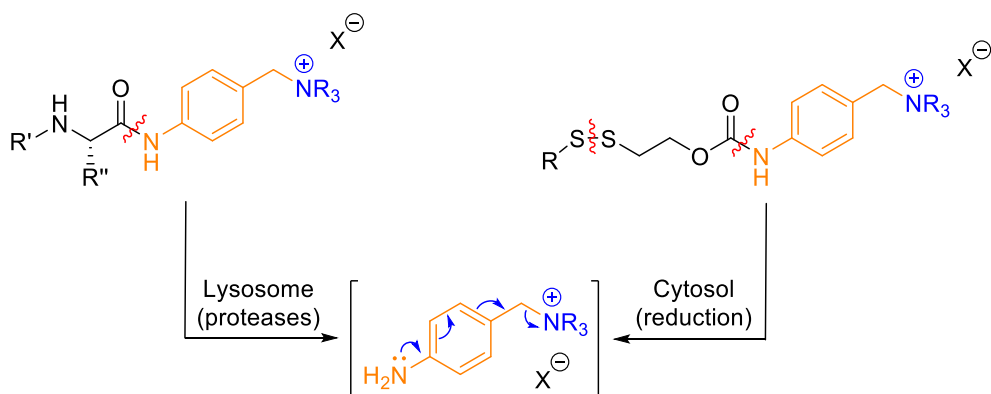
**Figure 6.12.** Left. Representative example of a clonogenic assay performed in six-well plates, with clones produced by seeding 200 LN229 glioblastoma cells. (a) Untreated control (CONT) (b) After temozolomide (TMZ) treatment (c,d) After parent mustard treatment (ANM and ANM-OH) (e) After treatment with **43**. Right. Average surviving fraction (SF) after 9 days of incubation (500 and 200 cells seeded respectively).

As shown in Table 6.2 and Figure 6.12, the number of viable cells significantly decreased to 24 % under treatment with prodrug **43**, in comparison with the parent drug (c, ANM) and the corresponding hydrolysed mustard (d, ANM-OH). In these latter cases the exposure to the drug did not show any effect on the cell proliferation. Remarkably, the effectiveness of **43** was noticeably better than the observed with temozolomide, which showed a surviving factor of 58 %. Similar survival results were found for the clonogenic assay with U87 cells (see Experimental Section).

#### 6.3.4. Further Perspectives

The studies performed with compound **43** demonstrate the ability of squaramides to act as self-immolative linkers for drug delivery. As exposed in the previous chapters, aniline derivatives are suitable cargos to be released, obtaining good disassembly velocities compared to aliphatic amines. Although this fact may limit the usefulness of our self-immolative linker, we took advantage of this limitation and expanded the scope of the conjugable functionalities. Recently, Pillow and colleagues developed a bioreversible linkage system based on quaternary ammonium groups to connect a broad array of tertiary- and heteroaryl- amines to a carrier protein.<sup>259</sup>

<sup>259</sup> L. R. Staben, S. G. Koenig, S. M. Lehar, R. Vandlen, D. Zhang, J. Chuh, S. F. Yu, C. Ng, J. Guo, Y. Liu, A. Fourie-O'Donohue, M. Go, X. Linghu, N. L. Segraves, T. Wang, J. Chen, B. Wei, G. D. L. Phillips, K. Xu, K. R. Kozak, S. Mariathasan, J. A. Flygare, T. H. Pillow *Nat. Chem.* **2016**, *8*, 1112–1119.

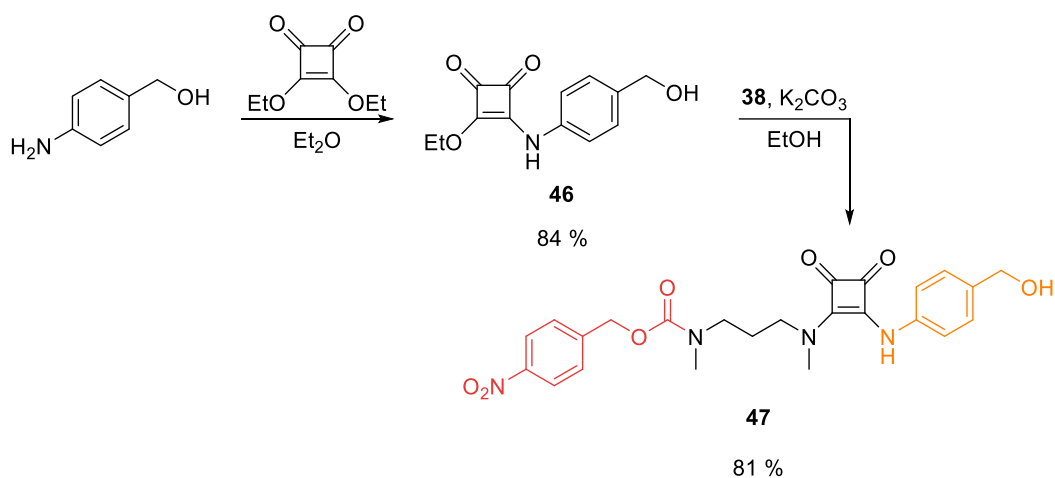


**Scheme 6.11.** Pillow's self-immolative bioconjugable linkage (orange) for the traceless release of tertiary amines (blue).

This strategy resulted in a general method for the conjugation of anticancer drugs as Auristatin, Carfilzomib, Tubulysin, Vinblastine, Indibulin, Duocarmycin and Gefitinib and antibacterial agents as Retapamulin, dmDNA31 and DNA31, Rifabutin and Clindamycin. All of them containing tertiary- or heteroaryl- amines.

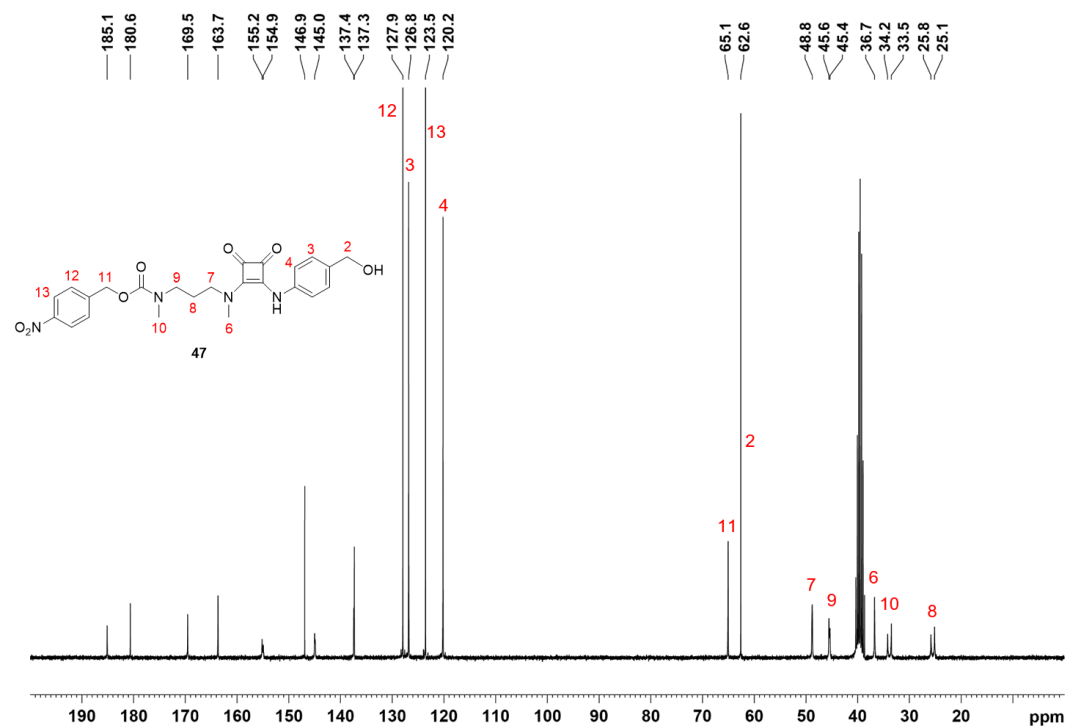
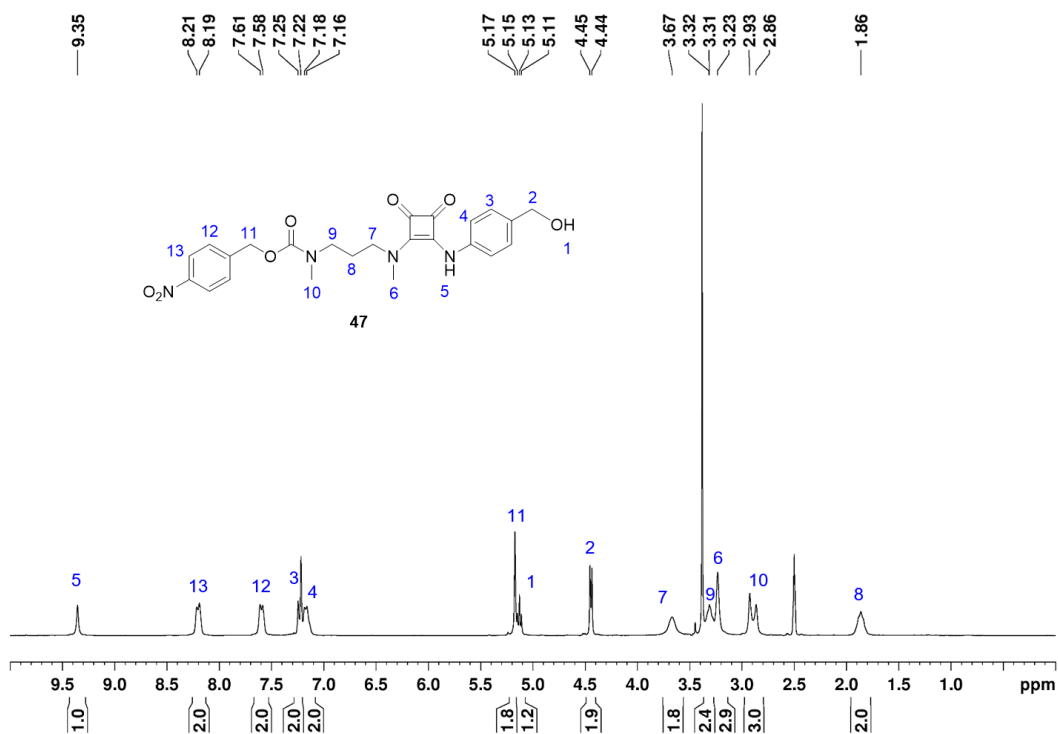
Based on these precedents, we conjugated the self-immolative tunable *p*-amino benzyl alcohol to our squaramide-based self-immolative linker to expand the cargo scope through the posterior conjugation of a suitable drug to the methylene position of the new linker.

*Synthesis of the squaramide-based self-immolative building block 47 for the conjugation of amines.* Given the lower reactivity of anilines in comparison with aliphatic amines, the synthesis of the unsymmetric squaramide **47** was achieved by first, the equimolar reaction of *p*-amino benzyl alcohol and diethyl squarate which afforded squaramate ester **46** and second, the subsequent reaction with carbamate-protected amino **38** led to the desired self-immolative system **47** in good yield (81%).

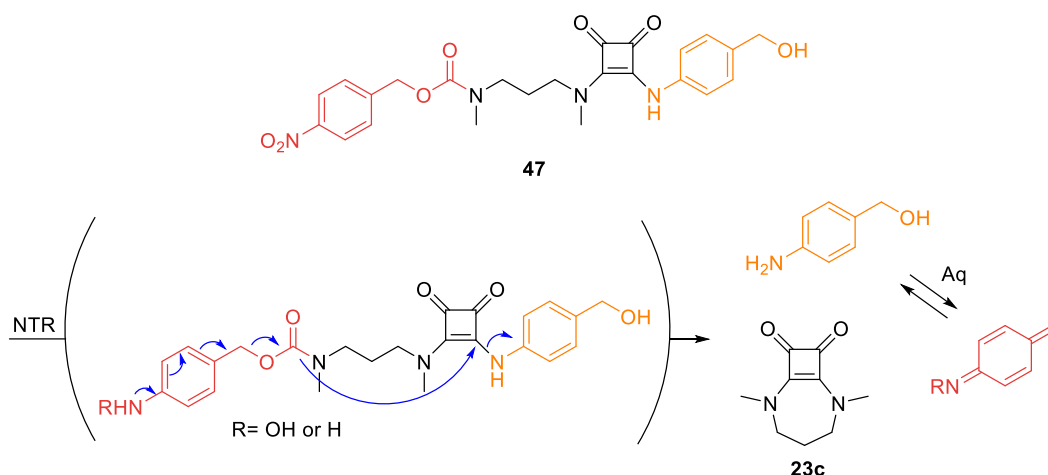


**Scheme 6.12.** Synthesis of the self-immolative parent squaramide **47**. Protective moiety is highlighted in red and the self-immolative aniline, in orange.

Full characterisation of **47** was achieved by ESI-HRMS and 1D and 2D NMR spectroscopy.



In analogy with system **43**, the trigger (red, *p*NBzC) would be cleaved under bioreductive conditions (NTR with NADH) which would result in the subsequent chain reaction:



**Scheme 6.13.** NTR/NADH triggered disassembly of self-immolative system **47**.

It is worth to notice that the released *p*-aminobenzyl alcohol and the carbamate cleavage product are interconvertible in aqueous media. Analogously to the reactivity of quinone methide derivatives, the hydration process occurs by the nucleophilic addition of water to the conjugated methide.<sup>260</sup>

*Study of the disassembly process of self-immolative system 47.* Like the previously prepared self-immolative prodrug **43** (bearing a nitrogen mustard as the cargo), system **47** can also be disassembled under reductive conditions. Thus, the self-immolative system **47** (50  $\mu$ M) was incubated in a Tris buffered solution (10 mM, 5 % DMSO, pH 7.4) in the presence of NTR and NADH (1  $\mu$ g/mL and 500  $\mu$ M) at 37  $^{\circ}$ C.

The reaction crude was monitored by HPLC (0.8 mL/min, H<sub>2</sub>O 0.1 % formic acid/CH<sub>3</sub>CN) by taking samples at variable time intervals. Figure 6.15 shows representative chromatograms of samples taken at 5 min, 16 h and 72 h, respectively. Disappearance of **47** led to the formation of cyclic squaramide **23**.

<sup>260</sup> Y. Chiang, A. J. Kresge, Y. Zhu, *J. Am. Chem. Soc.* **2000**, *122*, 9854–9855.

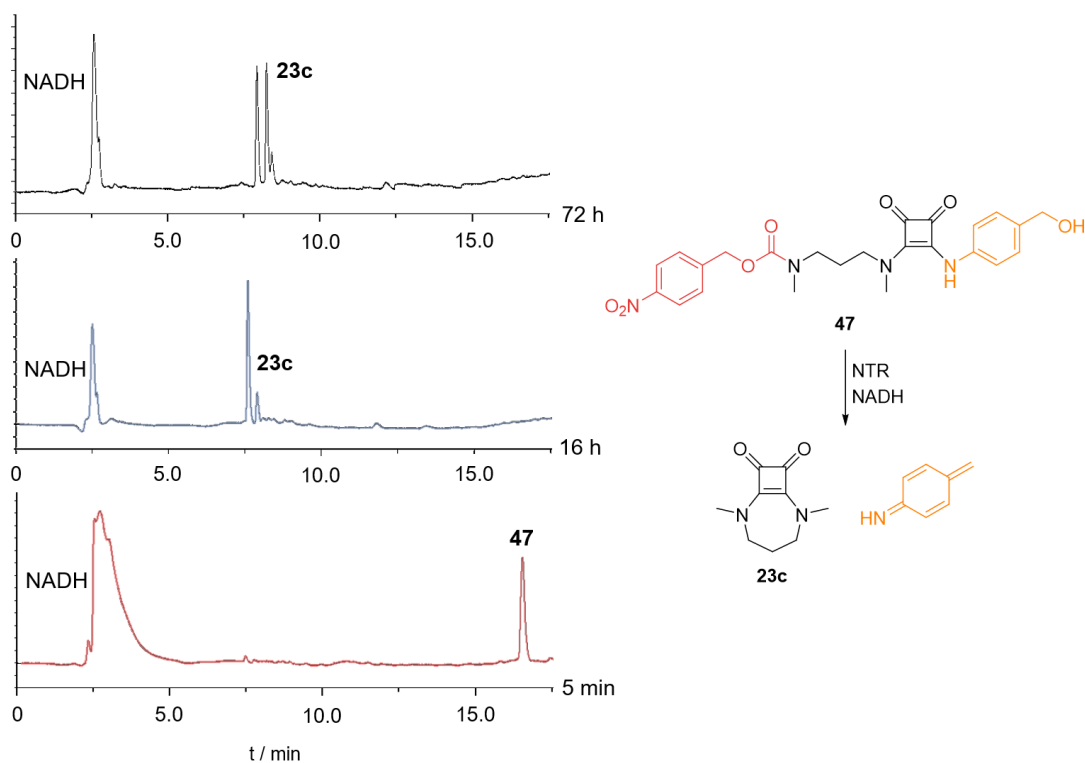


**Figure 6.15.** HPLC study of the disassembly of system **47** by UV-vis detection of sample traces ( $\lambda = 290 \text{ nm}$ ). *p*-amino benzyl alcohol is not detected at this wavelength because of its instability in water.

In addition to the UV detection, we analysed the reaction crude by coupling the HPLC column to a Q Exactive High Resolution Mass Spectrometer (Figure 6.16). In addition to the formation of cyclic squaramide **23c** we could detect the carbamate deprotected self-immolative system **47'** (304.1656,  $M+H^+$ ) which after intramolecular cyclization affords cyclic squaramide **23c** (181.0977,  $M+H^+$ ).

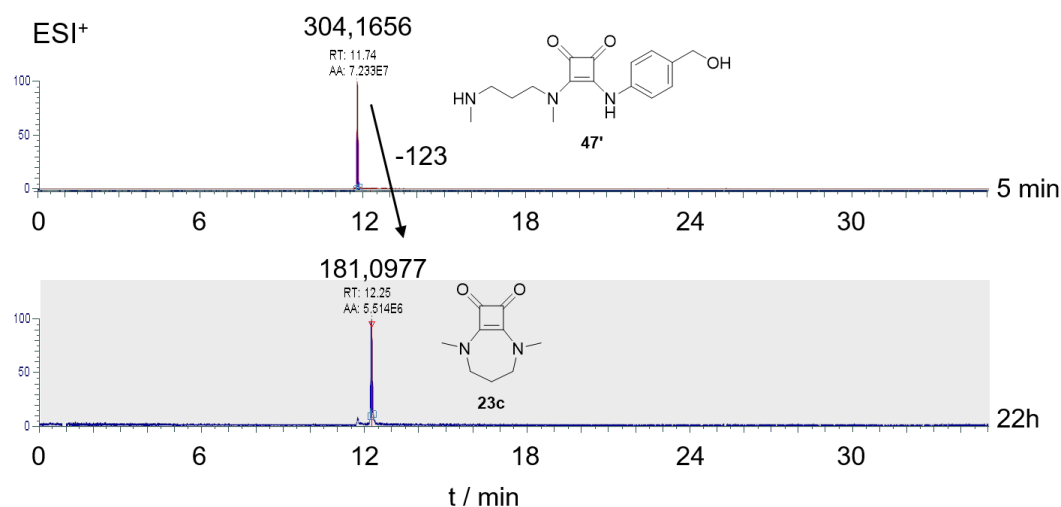
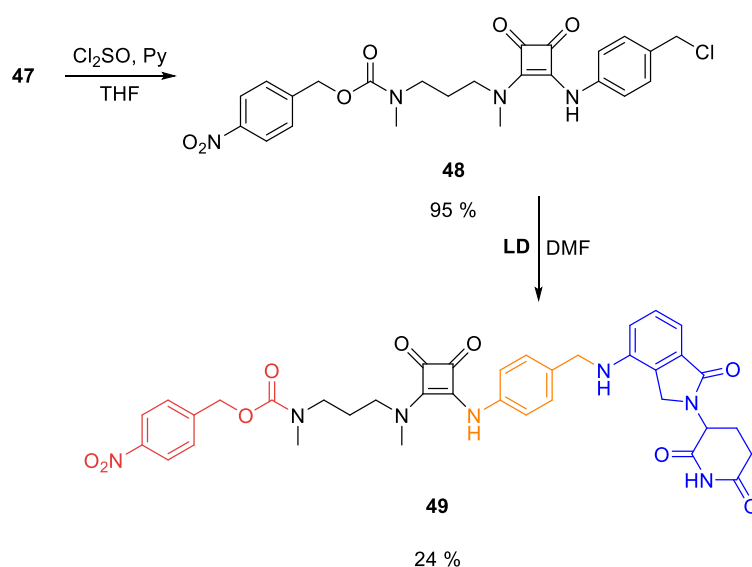


**Figure 6.16.** HPLC-HRMS analysis in ESI<sup>+</sup> mode of NTR/NADH-triggered self-immolative disassembly of system **47**.

*System 49. A model for amine conjugation:* Given the good behaviour of the parent SIS **47**, we decided to go one step further and use that tunable system to conjugate chemical functionalities that failed to be attached to the parent squaramide for a proper release. Thus, as a proof of concept, we chose the previously used lenalidomide (**LD**) as an example of a bioactive compound showing a handicapped reactivity.

Successfully, we could afford system **49** by firstly transforming the parent compound **47** into **48** and then coupling it with lenalidomide. Thus, the reaction of **47** with thionyl chloride in THF in the presence of pyridine led to the benzyl chloride **48**. The subsequent reaction with **LD** in DMF afforded **49**, which was purified by preparative HPLC (see details in the experimental section).



**Scheme 6.14.** Synthesis of the Lenalidomide prodrug conjugate **49**.

Full characterisation of **49** was achieved by HRMS and 1D and 2D NMR spectroscopy.

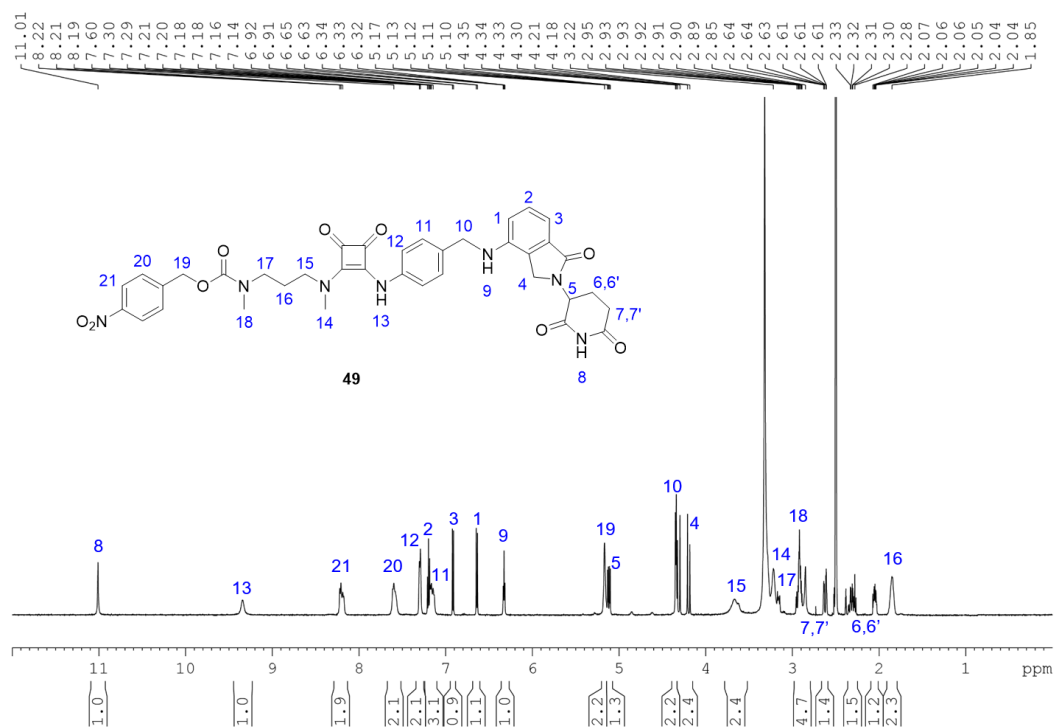


**Figure 6.17.**  $^1\text{H}$  NMR spectrum of compound **49** (DMSO- $d_6$ , 600 MHz, 298K) and the corresponding signal assignment.

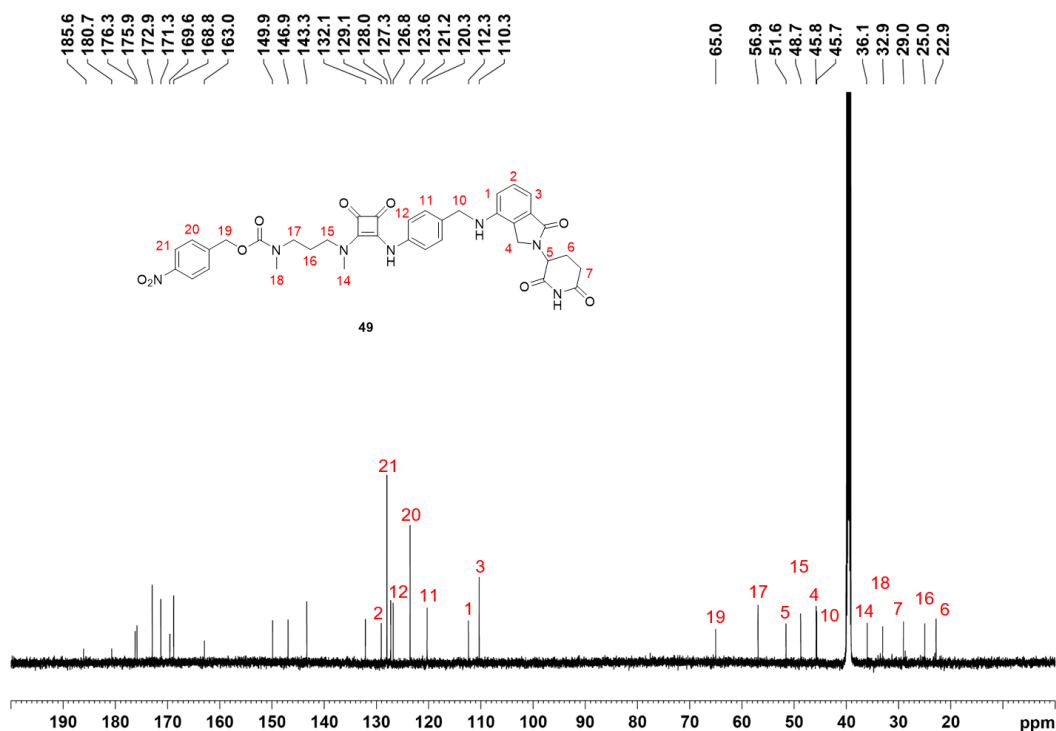


**Figure 6.18.**  $^{13}\text{C}$  NMR spectrum of compound **49** (DMSO- $d_6$ , 150 MHz, 298K) and the corresponding signal assignment.

In analogy with the parent SIS **47**, we evaluated the effectiveness of disassembly by incubation of self-immolative compound **49** (50  $\mu\text{M}$ ) in a Tris buffered solution (10 mM, 5 % DMSO, pH 7.4) with nitroreductase (1  $\mu\text{g}/\text{mL}$ ) in presence of NADH (500

$\mu\text{M}$ ) at  $37^\circ\text{C}$  for 22h. The products formation was followed by HPLC-HRMS analysis (Figure 6.16). First of all, we detected as a main product the peak corresponding to the carbamate-protected system **49'**, with a mass of 545.2507 ( $\text{M} + \text{H}^+$ ). After incubation for 22 h at  $37^\circ\text{C}$  we detected the corresponding disassembly products: cyclosquaramide **23c** and lenalidomide ( $\text{M} + \text{H}^+$ , 181.0977 and 260.1030 respectively), demonstrating the efficacy of the self-immolation process.

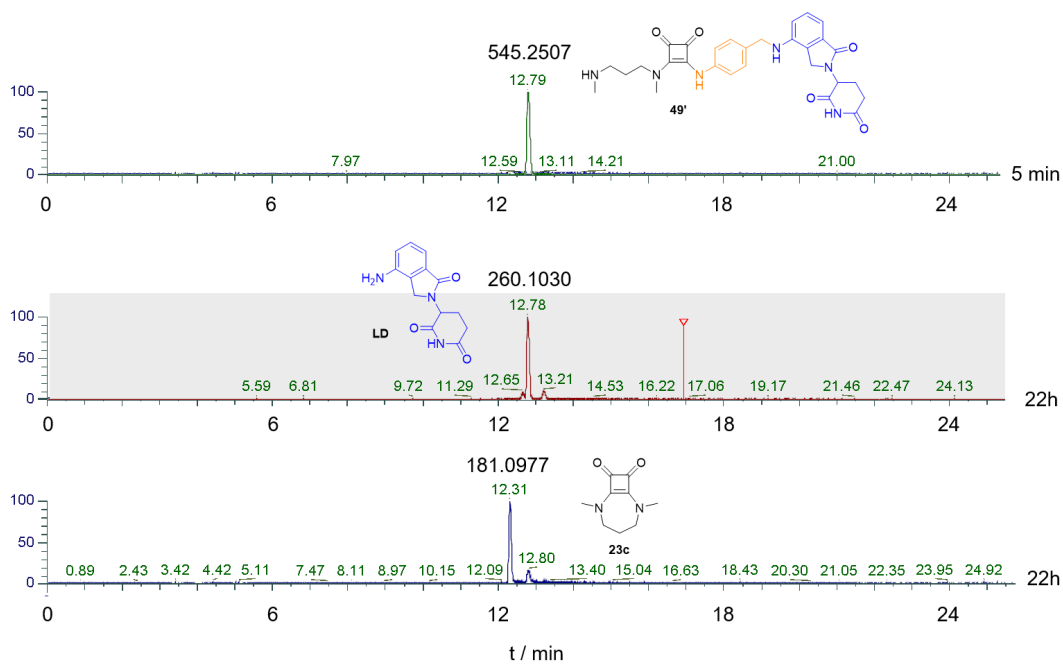


**Figure 6.19.** HPLC-HRMS analysis in  $\text{ESI}^+$  mode of NTR/NADH-triggered self-immolative disassembly of system **49**.

## 6.4. CONCLUSIONS

Based on the previously optimized self-immolative spacer, we designed and synthesised a squaramide-based self-immolative prodrug capable of releasing an alkylating agent upon activation with NTR/NADH.

*In vitro* experiments with Drew-Dickerson Dodecamer (ssDNA) allowed us to corroborate the ability of the released drug to covalently bond to the DNA.

The activity of the prodrug and the parent compounds was tested in human glioblastoma cultured cells through a long-exposure experiment (Cell Viability Assay) and by short-exposure experiment (Clonogenic Assay). Cell Viability Assay performed on U87 glioblastoma cells showed an inhibition on the cell growth by treatment with the prodrug **43**, while the treatment with parent mustard **ANM** caused a decrease in the viability to 26 %. The same experiments performed on T98G cells showed a significant effect on the cell proliferation lowering the viability to 40 % when treated with **ANM** and 67 % with prodrug **43**.

The clonogenic assay performed with LN229 cells showed no effect on the cell growth after treatment with the parent mustard **ANM** for 9 days. However, the survival factor fell down to 24 % after exposing the cells to prodrug **43**. This result is quite outstanding since temozolomide, a common antitumor agent used in the treatment of brain cancers, showed a survival factor of 58 %.

The design and development of compounds **47** and **49**, proved the expansion of the drug/cargo scope, by introducing a *p*-aminobenzyl group, a second self-immolative moiety. The tunability of the self-immolative system was demonstrated, henceforth proving their ability to conjugate and release poor reactive anilines, such as lenalidomide.

## 6.5. EXPERIMENTAL SECTION

The various chemicals were of commercial origin (Aldrich or Scharlau) and were used as received.  $^1\text{H}$ ,  $^{13}\text{C}$  and 2D NMR spectra (at 300 and 600 MHz) and  $^{13}\text{C}$  (at 75 and 150 MHz) spectra were recorded on 300 and 600 MHz spectrometers in  $\text{CDCl}_3$  or  $\text{DMSO-}d_6$  solutions at the specified temperature. The residual proton signal was used as a reference. Chemical shifts ( $\delta$ ) are given in ppm and coupling constants ( $J$ ) in Hz. ESI-HRMS mass spectra were recorded on a magnetic sector on an Orbitrap mass spectrometer.

*HRMS detection of Interstrand Cross-Linking:* Drew-Dickerson Dodecamer (DDD) was purchased from Invitrogen (Thermo Fisher Scientific). DDD (10  $\mu\text{M}$ ) was incubated with the corresponding drug (40  $\mu\text{M}$ ) at 37  $^\circ\text{C}$  for 48 h in 1 mM Tris buffer (pH 7.4). For the activation of the self-immolative system, nitroreductase (NTR) and NADH were added (5  $\mu\text{g}/\text{mL}$  and 35  $\mu\text{M}$  respectively). The solutions were injected to the mass spectrometer and ionization was performed in ESI(-) mode.

*Clonogenic Assay:* The clonogenic survival assay was performed by modification of van Bree *et al.* procedure.<sup>261</sup> 500000 cells were plated in six-well plates to a final volume of 2 mL/well. Then, the media was removed and cells were treated with the corresponding alkylating agent for 1h. The cells are trypsinised, counted and plated at two concentrations (200 and 500 cells/well respectively). The cell culture was allowed to grow for 9 days. At the termination of the assay, cells were rinsed with PBS. Colonies thus formed were stained for 45 minutes with 0.5 % (w/v) crystal violet prepared in 70 % (v/v) ethanol solution, rinsed with water, and finally air-dried.

*Cell Viability Analysis:* Cell lines were plated in a 96-well plate, 2500 cells/well in a final volume of 200  $\mu\text{L}$ . Cells were treated with the appropriate amount ( $\mu\text{L}$ ) of a 10 mM solution of the alkylating agent in DMSO to reach a final 10  $\mu\text{M}$  concentration in culture medium, and evaluated at 48 and 96 h. After the treatment, cells were incubated with 25  $\mu\text{L}$  of culture medium and 25  $\mu\text{L}$  CellTiter-Glo reagent. Luminescence was measured using a Synergy Mx microplate reader (Biotek, Winooski, VT). All experiments were performed in triplicate. The luminescence obtained for the untreated control is considered as the 100 % viability and the treated cells are referred to this.

*Methods for the analysis on HPLC and HPLC-HRMS, 47 and 49:* The stock solutions of SIS were prepared in DMSO (1 mM) and were stored at 4  $^\circ\text{C}$ . Nitroreductase (NTR) was purchased from Sigma-Aldrich in powder. The stock solution of NTR was prepared in 10 mM PBS (pH 7.4, 1 mg/mL) and preserved in small batches at -20  $^\circ\text{C}$ .  $\beta$ -

---

<sup>261</sup> N. A. P. Franken, H. M. Rodermond, J. Stap, J. Haveman, C. van Bree, *Nat. Protoc.* **2006**, *1*, 2315–2319.

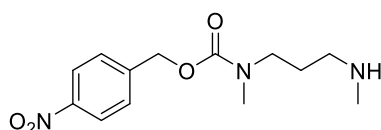
Nicotinamide adenine dinucleotide, reduced disodium salt hydrate (NADH) was purchased from Sigma-Aldrich in powder. The stock NADH solution was prepared in water (5 mM) and stored at 4 °C.

The SIS (50  $\mu$ L, 50  $\mu$ M) and NADH (100  $\mu$ L, 500  $\mu$ M), were added to 835  $\mu$ L of Tris buffer (10 mM, pH 7.4). To the above mixture 15  $\mu$ L of NTR were added and the resulting mixture was incubated at 37 °C in a microtube shaker incubator. At the given reaction times, samples were analysed by HPLC-UV or/and HPLC-HRMS.

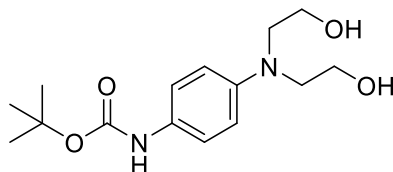
HPLC-UV was performed in a Gilson HPLC system. Samples were analysed at 0.8 mL/min using H<sub>2</sub>O (0.1 % formic acid) and CH<sub>3</sub>CN as eluent by C18 reverse phase chromatography. The 30-min gradient of elution was H<sub>2</sub>O:CH<sub>3</sub>CN, 5:95 for the first 5 min and then 60:40 in the next 20 min. Detection was performed using a Diode Array at 290 nm.

HPLC-HRMS were determined in a Thermo Scientific Q Exactive orbitrap mass spectrometer. Samples were directly injected at 0.5 mL/min using a 26-min isocratic gradient of H<sub>2</sub>O (0.1 % formic acid):CH<sub>3</sub>CN, 5:95. Detection was performed in ESI<sup>+</sup> mode.

### 6.5.1. Synthesis

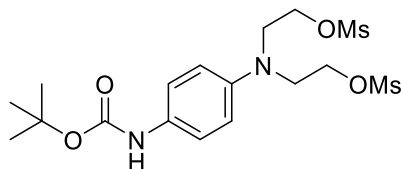


*4-nitrobenzyl methyl(3-(methylamino)propyl)carbamate (38)*. The product was prepared according to a reported procedure.<sup>254</sup> Pale oil, 1230 mg (yield 89 %). <sup>1</sup>H NMR (300 MHz, CDCl<sub>3</sub>)  $\delta$ : 1.74 (m, 2.4H), 2.41 (s, 3.1H), 2.57 (t,  $J = 7.0$ Hz, 2H), 2.96 (s, 2.9H), 3.38 (t,  $J = 7.1$ Hz, 2.2H), 5.22 (s, 2H), 7.52 (d,  $J = 8.9$ Hz, 1.7H), 8.22 (d,  $J = 8.9$ Hz, 1.6H).

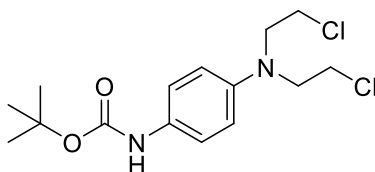


*tert-butyl (4-(bis(2-hydroxyethyl)amino)phenyl)carbamate (39)*. 682 mg (2.32 mmol) of ANM-OH sulphate and 1 mL (6.95 mmol) of Et<sub>3</sub>N were dissolved in CH<sub>2</sub>Cl<sub>2</sub> (20 mL). The reaction was stirred for 1h to achieve the complete deprotonation of amine starting material. Then, 632 mg (2.90 mmol) of Boc<sub>2</sub>O dissolved in CH<sub>2</sub>Cl<sub>2</sub> were added and the reaction was stirred at room temperature for 8h. After the reaction time, the solvent was removed under rotary evaporation and the crude residue was purified by silica-gel

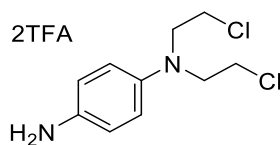
column chromatography (CH<sub>2</sub>Cl<sub>2</sub>/MeOH 30:1 v/v) to afford **39** as an amorphous white solid. 578 mg (yield 84 %). <sup>1</sup>H NMR (300 MHz, CDCl<sub>3</sub>) δ: 1.44 (s, 9.1H), 3.49 (q, *J* = 5.9Hz, 4.4H), 4.71 (t, *J* = 5.6 Hz, 2.1H), 6.57 (d, *J* = 9.4Hz, 2.1H), 7.18 (d, *J* = 9.6Hz, 2H), 8.85 (br s, 0.9H).



(( 4 - (tert-butoxycarbonyl) amino) phenyl) azanediyl bis (ethane-2,1-diyl) dimethane-sulfonate (**40**). 578 mg (1.95 mmol) of **39** and 0.82 mL (5.85 mmol) of distilled Et<sub>3</sub>N were dissolved in anhydrous CH<sub>2</sub>Cl<sub>2</sub> (15 mL) and cooled to 0°C in an ice bath under argon atmosphere. Then, 0.41 mL (5.27 mmol) of MsCl were added dropwise and the reaction was stirred for 0.5h at 0°C. Afterwards, the reaction was quenched with 50 mL of NaHCO<sub>3</sub> 5 % and the product was extracted with CH<sub>2</sub>Cl<sub>2</sub> (3 × 10 mL). The organic phase was dried with brine (2 × 10 mL) and Na<sub>2</sub>SO<sub>4</sub> and concentrated under rotary evaporation to afford **40** as pale yellow oil. 682 mg (yield 77 %). <sup>1</sup>H NMR (300 MHz, CDCl<sub>3</sub>) δ: 1.45 (s, 8.2H), 3.14 (s, 5.9H), 3.66 (t, *J* = 5.8Hz, 4H), 4.27 (t, *J* = 5.6 Hz, 3.8H), 6.71 (d, *J* = 9.6Hz, 2.2H), 7.27 (d, *J* = 8.2Hz, 2H), 8.98 (br s, 1.2H).

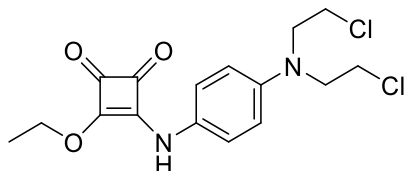


tert-butyl (4-(bis(2-chloroethyl)amino)phenyl)carbamate (**41**). 682 mg (1.51 mmol) of dimesylate **40** and 192 mg (4.52 mmol) of LiCl were dissolved in 2 mL of anhydrous DMF and heated to 117°C under argon atmosphere. After 0.5h the reaction was cooled down to 0°C in an ice-bath and 10 mL of HCl 3N were added. The product was extracted with CH<sub>2</sub>Cl<sub>2</sub> (3 × 10 mL) and the organic phase was dried with brine (2 × 10 mL) and Na<sub>2</sub>SO<sub>4</sub>. The solvent was removed under rotary evaporation and the crude was digested with hexane to afford **41** as an amorphous white solid. 371 mg (yield 74 %). <sup>1</sup>H NMR (300 MHz, CDCl<sub>3</sub>) δ: 1.45 (s, 8.7H), 3.67 (m, 8H), 6.66 (d, *J* = 9.1Hz, 2H), 7.26 (d, *J* = 8.3Hz, 1.8H), 8.97 (br s, 0.9H).

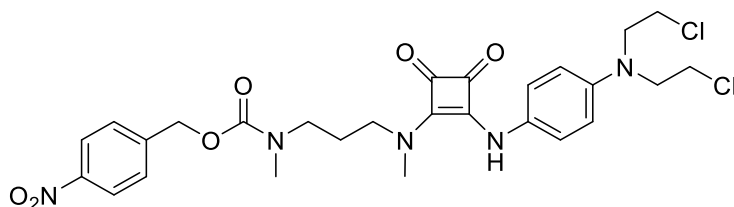


*N*<sup>1</sup>,*N*<sup>1</sup>-bis(2-chloroethyl)benzene-1,4-diaminium trifluoroacetate (**ANM·2TFA**). 371 mg (1.11 mmol) of boc-protected compound **41** were dissolved in CH<sub>2</sub>Cl<sub>2</sub> (5 mL) and 0.86

mL (11 mmol) of TFA were added and the reaction was stirred at 30 °C for 48h. After the reaction time the solvent was removed by rotary evaporation and the resulting oil crude was digested with hexane to afford **ANM·2TFA** as a brown amorphous solid. 219 mg (43 % yield). <sup>1</sup>H NMR (300 MHz, CDCl<sub>3</sub>) δ: 3.72 (s, 7.4H), 6.83 (d, *J* = 8.9Hz, 2.1H), 7.15 (d, *J* = 8.9Hz, 2H), 9.50 (br s, 3.1H).

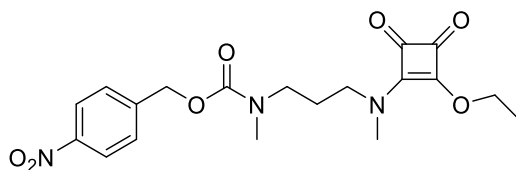


*3-((4-(bis(2-chloroethyl)amino)phenyl)amino)-4-ethoxycyclobut-3-ene-1,2-dione* (**42**). 211 mg (0.46 mmol) of **ANM·2TFA** and 0.13 mL (0.92 mmol) of Et<sub>3</sub>N were dissolved in Et<sub>2</sub>O (10 mL). Then, 93 mg (0.55 mmol) of ethyl squarate dissolved in 5 mL of Et<sub>2</sub>O were added dropwise and the reaction was stirred at room temperature for 16h. After the reaction time, the resulting yellow suspension was filtered and washed with Et<sub>2</sub>O (3 × 2 mL) and dried under vacuum. Yellow amorphous solid, 150 mg (yield 92 %). <sup>1</sup>H NMR (300 MHz, CDCl<sub>3</sub>) δ: 1.40 (t, *J* = 7.0Hz, 1.6H), 3.71 (s, 8.3H), 4.73 (q, *J* = 7.1Hz, 1.1H), 6.76 (d, *J* = 9.8Hz, 2H), 7.21 (br s, 1H), 7.35 (d, *J* = 8.9Hz, 1H), 9.60 (br s, 0.5H), 10.56 (br s, 0.5H). ESI-HRMS (+) *m/z* (%): calcd for C<sub>16</sub>H<sub>18</sub>N<sub>2</sub>O<sub>3</sub>Cl<sub>2</sub>Na<sup>+</sup> [*M* + Na]<sup>+</sup> 379.0587; found 379.0587, 737.1250 [*2M* + Na]<sup>+</sup>.

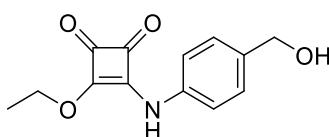


*4-nitrobenzyl 3-((2-((4-(bis(2-chloroethyl)amino)phenyl)amino)-3,4-dioxocyclobut-1-en-1-yl)(methyl)amino)propyl(methyl)carbamate* (**43**). 34 mg (0.08 mmol) of ester **45** were dissolved in EtOH (5 mL) and 25 mg (0.18 mmol) of K<sub>2</sub>CO<sub>3</sub> were added and the suspension was stirred at room temperature. Then 46 mg of **ANM·2TFA** (0.10 mmol) dissolved in EtOH (5 mL) were added dropwise and the reaction was stirred at room temperature for 16h. After the reaction time, the solvent was removed by rotary evaporation and the resulting crude was purified by silica-gel column chromatography (CH<sub>2</sub>Cl<sub>2</sub>/MeOH 20:1 v/v) to afford **43** as an amorphous brown solid, 12 mg (yield 24 %). <sup>1</sup>H NMR (600 MHz, CDCl<sub>3</sub>) δ 1.93 (s, 2H), 2.98 (s, 3.2H), 3.14 (s, 2.7H), 3.36 (t, *J* = 6.9Hz, 2H), 3.60 (t, *J* = 6.9Hz, 4.6H), 3.64 (s, 1.4H), 3.69 (t, *J* = 7.0Hz, 4.2H), 5.18 (s, 2H), 6.62 (d, *J* = 8.8Hz, 2H), 7.12 (s, 2H), 7.48 (d, *J* = 8.2Hz, 2.4H), 7.56 (br s, 0.4H) 8.19 (d, *J* = 8.2Hz, 2H). <sup>13</sup>C NMR (150 MHz, CDCl<sub>3</sub>) δ 29.8, 34.7, 37.6, 40.6, 46.5, 49.9, 53.7, 66.0, 112.7, 122.9, 123.1, 123.9, 128.1, 129.1, 143.8, 144.1, 147.7,

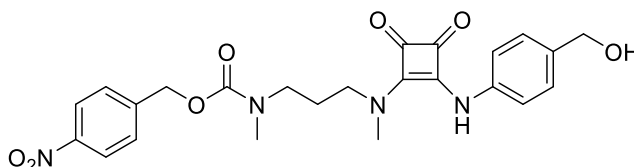
164.3, 169.4, 182.1, 184.6. ESI-HRMS (+)  $m/z$  (%): calcd for  $C_{27}H_{31}N_5O_6Cl_2Na^+$  [ $M + Na$ ] $^+$  614.1544; found 614.1546.



4-nitrobenzyl 3-((2-ethoxy-3,4-dioxocyclobut-1-en-1-yl)(methyl)amino)propyl(methyl) carbamate (**45**). 677 mg (2.41 mmol) of protected amine **38**, 491 mg (2.89 mmol) of ethyl squarate and 0.4 mL (2.89 mmol) of  $Et_3N$  were dissolved in  $Et_2O$  (15 mL) and the reaction was stirred for 16h at room temperature. After the reaction time, the solvent was removed by rotary evaporation and the resulting crude residue was purified by silica-gel column chromatography ( $CH_2Cl_2/MeOH$  40:1 v/v) to afford **45** as pale oil. 782 mg (yield 80 %).  $^1H$  NMR (300 MHz,  $CDCl_3$ )  $\delta$ : 1.45 (m,  $J = 6.7Hz$ , 3.7H), 1.90 (m,  $J = 7.3Hz$ , 2H), 2.98 (s, 2.7H), 3.10 (m, 1.1H), 3.16 (s, 1.1H), 3.35 (s, 2.9H), 3.43 (t,  $J = 8.0Hz$ , 1H), 3.72 (t,  $J = 7.0Hz$ , 1.3H), 4.76 (q,  $J = 7.0Hz$ , 2.1H), 5.2 (s, 2H), 7.52 (d,  $J = 8.9Hz$ , 1.5H), 8.23 (dd,  $J = 8.8, 2.2Hz$ , 1.5H). ESI-HRMS (+)  $m/z$  (%): calcd for  $C_{19}H_{24}N_3O_7^+$  [ $M + H$ ] $^+$  406.1609; found 406.1607.

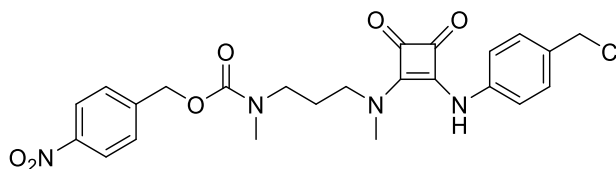


3-ethoxy-4-((4-(hydroxymethyl)phenyl)amino)cyclobut-3-ene-1,2-dione (**46**). A solution of 209 mg (1.70 mmol) of *p*-aminobenzyl alcohol dissolved in  $Et_2O$  (15 mL) was added to a 5 mL solution of ethyl squarate (318 mg, 1.87 mmol) and the reaction was stirred at room temperature for 16 h. After the reaction time, the resulting precipitate was filtered out and washed with  $Et_2O$  ( $3 \times 3$  mL) and dried under vacuum to afford **46** as a white amorphous solid. 354 mg (yield 84 %).  $^1H$  NMR (300 MHz,  $DMSO-d_6$ )  $\delta$ : 1.41 (t,  $J = 7.3Hz$ , 3.1H), 4.45 (d,  $J = 4.4Hz$ , 2.1H), 4.76 (q,  $J = 7.1Hz$ , 2.1H), 5.15 (br t,  $J = 6.2Hz$ , 1H), 7.29 (m, 4H), 10.74 (br s, 1H). ESI-HRMS (+)  $m/z$  (%): calcd for  $C_{13}H_{14}NO_4^+$  [ $M + H$ ] $^+$  248.0917; found 248.0918.

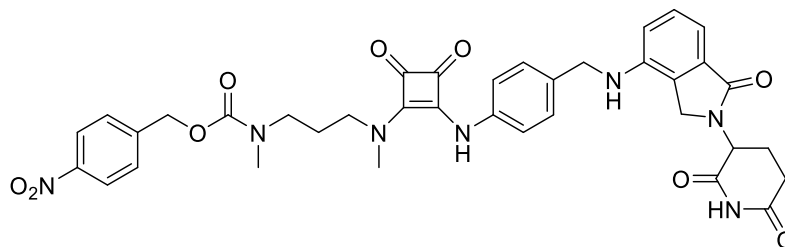


4-nitrobenzyl 3-(2-(4-(hydroxymethyl)phenyl)amino)-3,4-dioxocyclobut-1-en-1-yl(methyl)amino)propyl(methyl) carbamate (**47**). 208 mg (0.74 mmol) of carbamate-protected amine **38**, 219 mg (0.89 mmol) of squaramate ester **46** and 123 mg (0.89

mmol) of  $K_2CO_3$  were dissolved in 10 mL of EtOH and the reaction was stirred at room temperature for 16 h. After the reaction time, the solvent was removed by rotary evaporation and the crude residue was suspended in water. The resulting solid was filtered out, washed with water ( $3 \times 5$  mL) and dried under vacuum and  $P_2O_5$  to afford **47** as an orange amorphous solid. 289 mg (yield 81 %).  $^1H$  NMR (300 MHz, DMSO- $d_6$ )  $\delta$ : 1.86 (m, 2H), 2.86 and 2.93 (s, 3H), 3.23 (s, 2.9H), 3.31 (s, 2.4H), 3.67 (s, 1.8H), 4.44 (d,  $J = 5.4$  Hz, 1.9H), 5.13 (t,  $J = 5.7$  Hz, 1.2H), 5.17 (s, 1.8H), 7.17 (d,  $J = 6.6$  Hz, 2H), 7.23 (d,  $J = 8.4$  Hz, 2H), 7.59 (d,  $J = 8.8$  Hz, 1.9H), 8.20 (d,  $J = 8.6$  Hz, 1.9H), 9.35 (s, 1H).  $^{13}C$  NMR (300 MHz, DMSO- $d_6$ )  $\delta$ : 25.1, 25.8, 33.5, 34.2, 36.7, 45.4, 45.6, 48.8, 62.6, 65.1, 120.2, 123.5, 126.8, 127.9, 137.3, 137.4, 145.0, 146.9, 154.9, 155.2, 163.7, 169.5, 180.6, 185.1. ESI-HRMS (+)  $m/z$  (%): calcd for  $C_{24}H_{27}N_4O_7^+$  [ $M + H$ ] $^+$  483.1874; found 483.1874, 505.1697 [ $M + Na$ ] $^+$ .



*4-nitrobenzyl 3-(2-((4-(chloromethyl) phenyl) amino) -3,4-dioxocyclobut-1-en-1-yl) (methylamino)propyl(methyl)carbamate (48)*. 297 mg (0.62 mmol) of **47** were dissolved in anhydrous THF (5 mL) and cooled to 0-4 °C under argon atmosphere. Then, 59  $\mu$ L (0.74 mmol) of  $SOCl_2$  and 59  $\mu$ L (0.74 mmol) of pyridine were added while stirring. An orange precipitate appeared, and the reaction was let to evolve to room temperature. After 16 h of reaction, the solvent was removed by rotary evaporation and the crude residue was purified by silica-gel column chromatography ( $CH_2Cl_2/MeOH$  20:1 v/v) to afford **48** as an orange amorphous solid. 292 mg (yield 95 %).  $^1H$  NMR (300 MHz,  $CDCl_3$ )  $\delta$ : 1.94 (m, 2.1H), 2.14 and 2.17 (s, 3.8H), 3.00 (s, 3.1H), 3.20 (s, 2.9H), 3.38 (s, 5.6H), 4.41 (s, 2.2H), 5.18 (s, 2.2H), 7.48 (d,  $J = 8.8$  Hz, 2H), 8.21 (d,  $J = 8.6$  Hz, 1.6H).



*4-nitrobenzyl 3-(2-(4-(2-(2,6-dioxopiperidin-3-yl) -1-oxoisindolin-4-yl) amino) methyl) phenyl) amino) -3,4-dioxocyclobut-1-en-1-yl) (methyl) amino) propyl) (methyl) carbamate (49)*. 102 mg (0.20 mmol) of chloride **48** and 48 mg (0.19 mmol) of lenalidomide were dissolved in 2 mL of anhydrous DMF under argon atmosphere. The reaction was heated to 50 °C and stirred for 16h. After the reaction time, the crude

residue was injected on an HPLC system for purification eluting with 5-60 % 0.1 % formic acid in water:acetonitrile to afford **49** as a pale yellow solid. 32 mg (24 % yield).  $^1\text{H}$  NMR (600 MHz,  $\text{DMSO-}d_6$ )  $\delta$ : 1.85 (s, 2.3H), 2.05 (m, 1.2H), 2.32 (m, 1.5H), 2.52 (m), 2.64 (m, 1.4H), 2.85 (s, 1.6H), 2.92 (m, 3.2H), 3.16 (m, 0.8H), 3.22 (s, 3H), 3.66 (s, 2.4H), 4.25 (m, 2.4H), 4.34 (d,  $J = 5.9\text{Hz}$ , 2.3H), 5.12 (m, 1.3H), 5.17 (s, 2.2H), 6.33 (t,  $J = 5.9\text{Hz}$ , 1H), 6.64 (d,  $J = 8.1\text{Hz}$ , 1.1H), 6.92 (d,  $J = 7.3\text{Hz}$ , 0.9H), 7.15 (m, 1.7H), 7.20 (t,  $J = 7.8\text{Hz}$ , 1.4H), 7.30 (d,  $J = 7.3\text{Hz}$ , 2.1H), 7.60 (m, 2.1H), 8.20 (m, 1.8H), 9.34 (s, 1H), 11.01 (s, 1H).  $^1\text{H}$  NMR (150 MHz,  $\text{DMSO-}d_6$ )  $\delta$ : 22.9, 25.0, 29.0, 32.9, 36.1, 45.7, 45.8, 51.6, 56.9, 65.0, 110.3, 112.3, 120.3, 121.2, 123.6, 126.8, 127.3, 128.0, 129.1, 132.1, 143.3, 146.9, 149.9, 163.0, 168.8, 169.6, 171.3, 172.9, 175.9, 176.3, 180.7, 185.6. ESI-HRMS (+)  $m/z$  (%): calcd for  $\text{C}_{37}\text{H}_{37}\text{N}_7\text{O}_9\text{Na}^+$   $[\text{M} + \text{Na}]^+$  746.2545; found 746.2544, 724.2726  $[\text{M} + \text{H}]^+$ , 762.2284  $[\text{M} + \text{K}]^+$ .

### 6.5.2. NMR Spectra of Selected Compounds

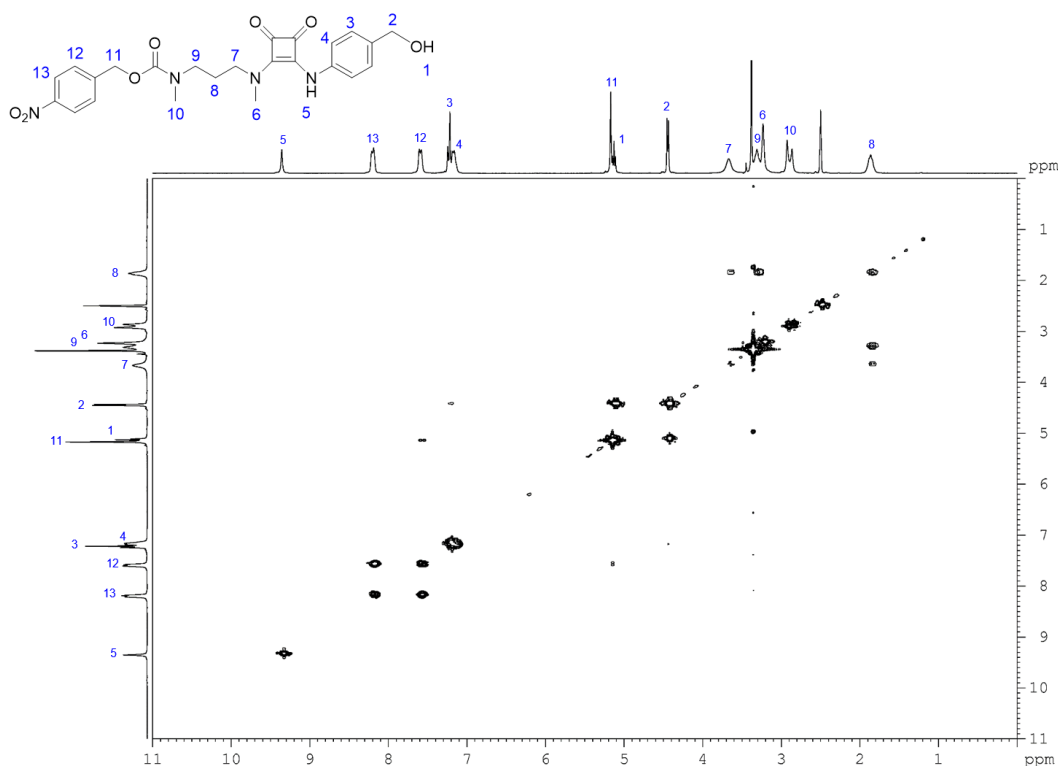


Figure 6.20.  $^1\text{H}$ - $^1\text{H}$  COSY experiment of compound **47** ( $\text{DMSO-}d_6$ , 298K).

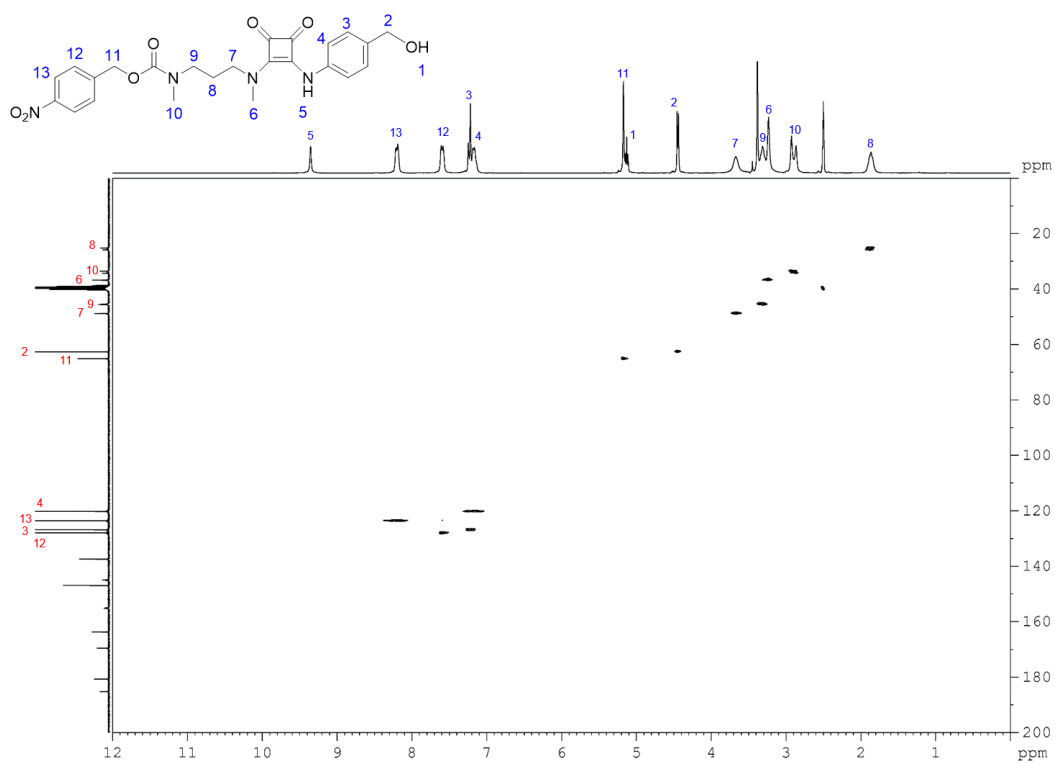


Figure 6.21.  $^1\text{H}$ - $^{13}\text{C}$  HSQC experiment of compound 47 (DMSO- $d_6$ , 298K).

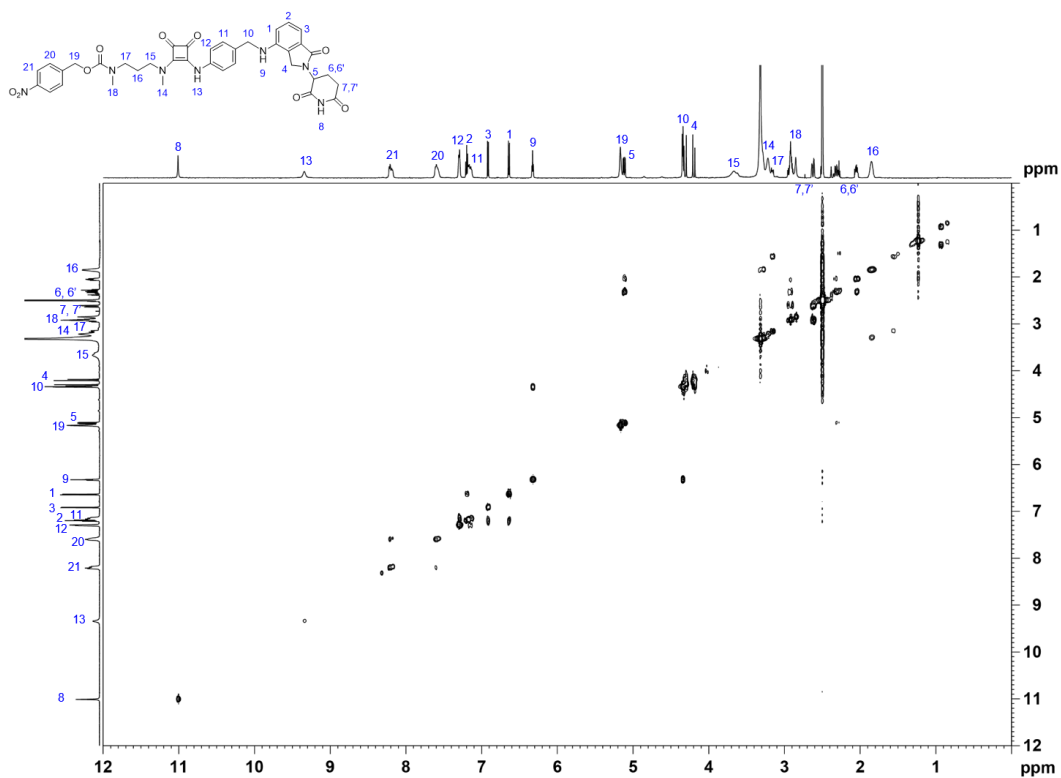


Figure 6.22.  $^1\text{H}$ - $^1\text{H}$  COSY experiment of compound 49 (DMSO- $d_6$ , 298K).

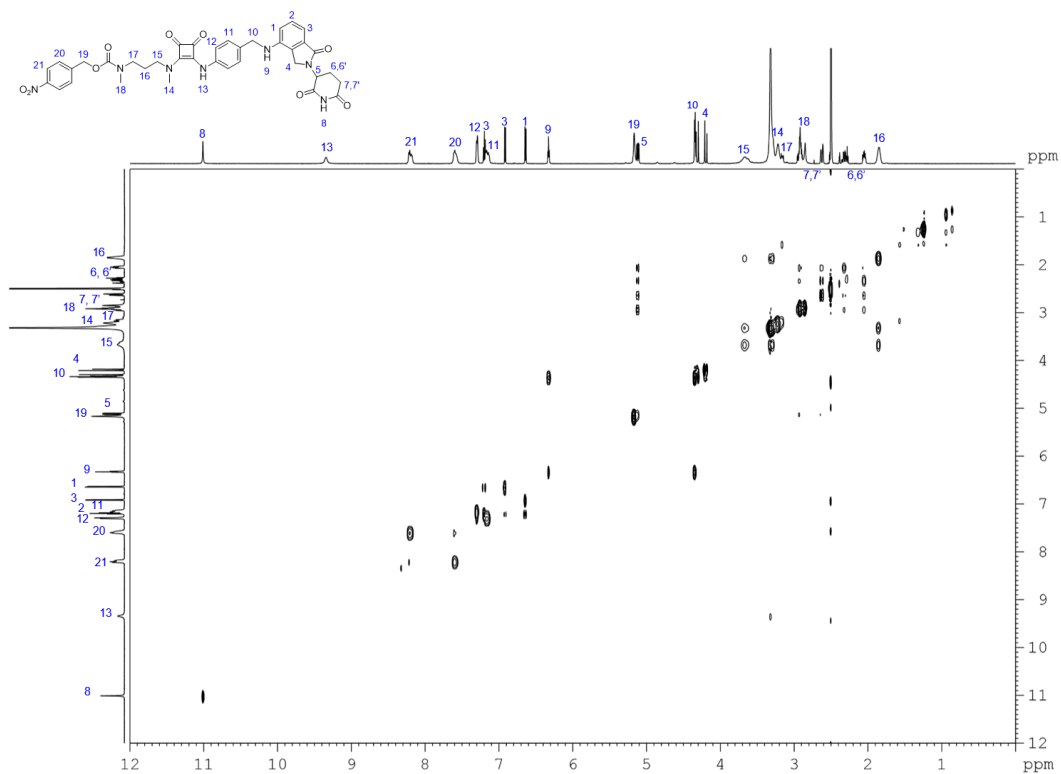


Figure 6.23.  $^1\text{H}$ - $^1\text{H}$  TOCSY experiment of compound **49** ( $\text{DMSO-}d_6$ , 298K).

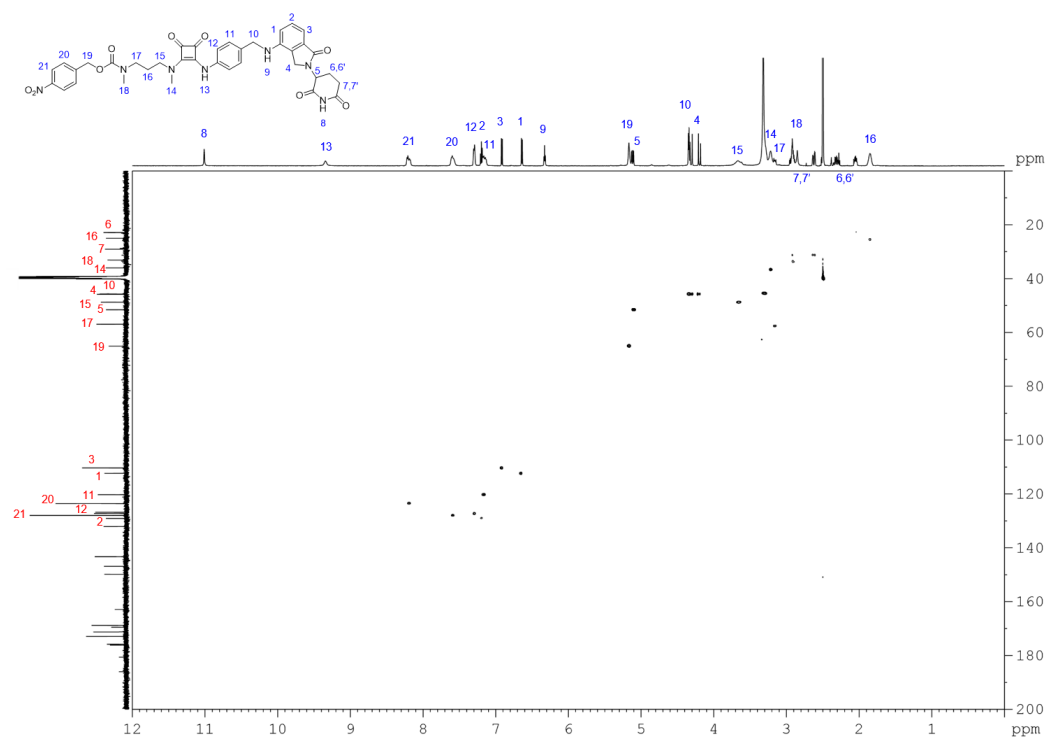


Figure 6.24.  $^1\text{H}$ - $^{13}\text{C}$  HSQC experiment of compound **49** ( $\text{DMSO-}d_6$ , 298K).

### 6.5.3. Clonogenic Assay

**Table 6.3.** U87 clones formed and survival factor (SF) after the treatment with antitumor agents.

Cell line / Agent	U87 <sup>a</sup>		
	200 cells	500 cells	SF %
<b>CONT</b>	127	165	100
<b>TMZ</b>	38	53	31
<b>ANM</b>	106	172	94
<b>ANM-OH</b>	109	152	89
<b>43</b>	43	51	32

Plate efficiency: <sup>a</sup>48 %.

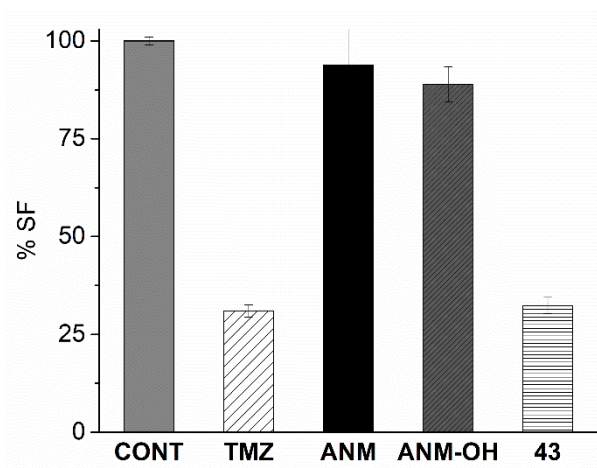


**Figure 6.25.** Average surviving fraction (SF) after 9 days of incubation (500 and 200 U87 glioblastoma cells seeded respectively). From left to right: Untreated control (CONT), treatment with temozolomide (TMZ), parent mustard treatment (ANM and ANM-OH), treatment with prodrug 43.



## **Conclusions**



## Conclusions

The present thesis describes the design and synthesis of a series of self-immolative models based on squaramides to evaluate their ability to release a payload under external stimuli.

We have designed and synthesised a small collection of squaryl derivatives bearing different functionalities as the leaving group. Both amino and thiol group have proved to be suitable nucleophiles to undergo the self-immolative cyclisation reaction. The kinetic studies performed at physiological conditions and pH variable defined the key features for an optimal squaramide-based self-immolative linker: 1) propanediamino as the trigger chain 2) aniline as the leaving group and 3) *N*-methylation of the squaryl ring.

Based on these features, we have designed and synthesised the prodrug **43**, bearing an alkylating agent as the drug/cargo (**ANM**). The amino trigger group was protected as a *p*-nitrobenzyl carbamate which was enzymatically activated with nitroreductase using NADH as the reductive agent. The optimized self-immolative spacer can be tuned to conjugate chemical functionalities that fail to be attached to the parent squaramide for a proper release. This modified SIS has shown a good performance releasing lenalidomide.

The biological activity of both prodrug **43** and the parent drug **ANM** was tested against glioblastoma cancer cells. The survival factor of LN229 cells after the treatment with **43** was 24 % while the parent **ANM** did not cause any effect on the cell proliferation. Such a result is quite outstanding since temozolomide showed a 58 % survival factor.

In parallel with the main line of the thesis, we studied the formation of crystalline hydrates of cyclosquaramides **23a-c**. The difference in the degree of *N*-methylation changed the occurrence of water clusters leading to water tapes in **23a**, 2D hexagonal water layers in **23b**, and 1D water chains in **23c**.